USARTL-TR-78-55A

LEVEL III

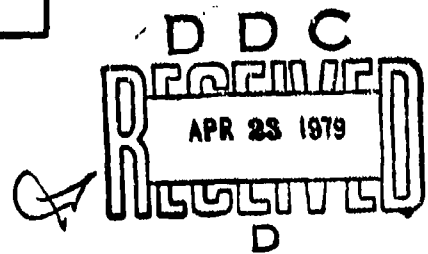COMBUSTOR DESIGN CRITERIA VALIDATION
Volume I - Element Tests and Model Validation

T. W. Bruce, H. C. Mongia, R. S. Reynolds
AiRESEARCH MANUFACTURING CO. OF ARIZONA
111 SOUTH 34th STREET
PHOENIX, ARIZ. 85034

March 1979

Final Report for Period 2 July 1975 - 31 October 1978
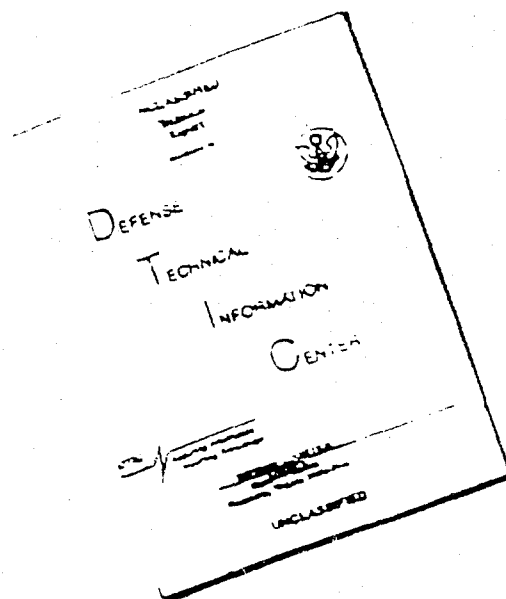
Approved for public release;
distribution unlimited.

DDC
RECEIVED
APR 23 1979
D

79 04 19 001

DISCLAIMER NOTICE

THIS DOCUMENT IS BEST QUALITY AVAILABLE. THE COPY FURNISHED TO DTIC CONTAINED A SIGNIFICANT NUMBER OF PAGES WHICH DO NOT REPRODUCE LEGIBLY.

APPLIED TECHNOLOGY LABORATORY POSITION STATEMENT

This report d scribes an effort undertaken to improve small gas turbine combustor design techniques. This analytical procedure is viewed as a significant step toward reducing the design and development time and the cost associated with future Army gas turbine combustors while simultaneously achieving a more durable and fuel-efficient design. The reader is referred to the report documentation page for a description of each of the three volumes of this report. It is considered worthy of widespread application with the turbine industry. Any critique or other response regarding its use should be addressed to this agency.

Mr. Kent Smith of the Propulsion Technical Area, Aeronautical Technology Division, served as Project Engineer for this effort.

REPORT DOCUMENTATION PAGE	READ INSTRUCTIONS BEFORE COMPLETING FORM

1. REPORT NUMBER	2. GOVT ACCESSION NO.	3. RECIPIENT'S CATALOG NUMBER
USARTL TR-78-55A		

4. TITLE (and Subtitle)	5. TYPE OF REPORT & PERIOD COVERED
COMBUSTOR DESIGN CRITERIA VALIDATION. VOLUME I. Element Tests and Model Validation	Final Report. 2 July 1975 — 31 Oct 1978
	6. PERFORMING ORG. REPORT NUMBER
	75-211682(38)-1

7. AUTHOR(s)	8. CONTRACT OR GRANT NUMBER(s)
T. W. Bruce H. C. Mongia R. S. Reynolds	DAAJ02-75-C-0044

9. PERFORMING ORGANIZATION NAME AND ADDRESS	10. PROGRAM ELEMENT, PROJECT, TASK AREA & WORK UNIT NUMBERS
AiResearch Manufacturing Co. of Arizona 111 South 34th Street Phoenix, Arizona 85034	62209A 1F262209AH76 00 79 EK

11. CONTROLLING OFFICE NAME AND ADDRESS	12. REPORT DATE
Applied Technology Laboratory, U.S. Army Research and Technology Laboratories (AVRADCOM) Fort Eustis, Virginia 23604	March 1979
	13. NUMBER OF PAGES
	388

14. MONITORING AGENCY NAME & ADDRESS(if different from Controlling Office)	15. SECURITY CLASS. (of this report)
391 p.	Unclassified
	15a. DECLASSIFICATION/DOWNGRADING SCHEDULE

16. DISTRIBUTION STATEMENT (of this Report)

Approved for public release; distribution unlimited.

17. DISTRIBUTION STATEMENT (of the abstract entered in Block 20, if different from Report)

18. SUPPLEMENTARY NOTES

Volume I of a three-volume report

19. KEY WORDS (Continue on reverse side if necessary and identify by block number)

Small Gas Turbines
Analytical Models

20. ABSTRACT (Continue on reverse side if necessary and identify by block number)

This report describes the 37-month program for the development of analytical models applicable to small gas turbine combustors. Six analytical models were developed and validated with element tests. The inputs and correlations obtained from the element tests along with basic developments to the models and the numerics provided analytical models which, when used in judicious conjunction with traditional empirical design and development of two different advanced reverse flow annular combustor concepts. One concept met all program performance goals without any major design modifications and

DD FORM 1473 EDITION OF 1 NOV 65 IS OBSOLETE

the second concept required only one modification to meet the objectives. Therefore, the analytical models, when used in the proper context in conjunction with empirical methodology will reduce the design and development time and cost associated with gas turbine combustion systems. In addition, the models add to the fundamental understanding of the physical processes occurring within the combustor which affect its performance.

Extensive performance mapping of the two developed combustor concepts was conducted. This data was used to validate and update the computer models. The degree of correlation between model predictions and test measurements is generally good for this stage of development.

This is Volume I of the three-volume final report covering the combustor element tests and model validation that took place in Task 1 of the program. Volume II reports the results of program Tasks II and III on the design, fabrication, and rig test of the two different combustors (described above) designed to specific goals utilizing the analytical procedures. Volume III is the User's Manual for the models and includes a description of the models and a listing of the computer codes with instructions on usage.

ABSTRACT

The Combustor Design Criteria Validation Program was conducted by the AiResearch Manufacturing Company of Arizona under Contract DAAJ02-75-C-0044 with the Applied Technology Laboratory, U.S. Army Research and Technology Laboratories (AVRADCOM). The primary objective of the three-phase program was to develop and validate computer analytical models for application to small gas turbine engine propulsion combustion systems.

This report is presented in three volumes. Volume I describes the formulation and validation through element testing of six computer models conducted under Task I. Volume II describes the application of the computer models to the design and development of two combustor concepts conducted under Tasks II and III. Volume III consists of a description of the analytical models and a listing of the computer codes with instructions on usage.

The Program Manager was Mr. T. W. Bruce and the Principal Investigator was Dr. H. C. Mongia. Principal contributing engineers were Mr. R. S. Reynolds, who directed the development of the analytical models and Mr. E. B. Coleman who directed the design and testing efforts. The program was monitored by Mr. K. Smith from the Applied Technology Laboratory, U.S. Army Research and Technology Laboratories, Fort Eustis, Virginia.

TABLE OF CONTENTS

LIST OF ILLUSTRATIONS

LIST OF ILLUSTRATIONS (CONTD)

15

LIST OF TABLES

19

LIST OF TABLES (CONTD)

I. INTRODUCTION

A. General Information

Past approaches to the design of turbo-propulsion combustion
systems have relied largely on empirical correlations derived
from previous development experience and based on theoretical
considerations of the fundamental combustion processes involved.
These correlation parameters have proved quite useful for prelim-
inary design predictions and interpretation of experimental re-
sults in the iterative series of development tests that normally
follow. With the increasing demands for improvements in combus-
tion system performance and particularly since the focus of
attention is on combustion pollutant emission reduction, there
has been a recognized need to obtain a more thorough understand-
ing of the basic combustion processes. Towards this objective
various mathematical models have been developed. The models
have ranged from the perfectly-stirred and plug-flow reactors
where chemical kinetics are considered to be the primary control-
ling factor to the more rigorous combustor-flow models that also
account for the effects of heat, mass, and momentum transfer.

Under a previous program sponsored by the U.S. Army
(Advanced, Small, High-Temperature-Rise Combustor Program), an
analytical design technique was developed that used various
individual models to analyze component processes of the combus-
tion system such as fuel injection, primary zone performance,
dilution-zone mixing, and film cooling. The primary-zone model
was a two-dimensional, finite-difference recirculating-flow pro-
gram that computed flow-field velocities, temperatures, and
species concentrations. This program demonstrated the feasi-
bility of mathematical modeling as a promising aid in combustor
design as a potential means for helping to reduce the time and
cost of development.

21

The present program represents an extension and refinement of the previous effort with specific application to the design requirements of advanced, small, high-temperature-rise combustors for aircraft engines in the 0.91- to 2.27-kilogram-per-second flow range. This program was performed for the Applied Technology Laboratory, U.S. Army Research and Technology Laboratories (AVRADCOM), Fort Eustis, Virginia, by the AiResearch Manufacturing Company of Arizona during the period July 1975 to October 1978. The program is documented in this three-volume report.

B. Objectives.

The primary objective of this program was to further develop and validate existing analytical combustor design procedures that can be used to significantly shorten the design and development cycle of small advanced gas turbine engine combustors.

The basic approach of this program consisted of a concentrated analytical treatment of key combustion phenomena affecting combustor performance complemented by rig tests. The rig test culminated in a complete series of performance mapping to validate the empirical/analytical combustor design procedure in an environment matching an actual operating engine.

The program was initially comprised of four technical tasks:

Task I   - Analytical-Model Refinement

Task II - Full-Scale Combustor Design, Fabrication, and Preliminary Tests

Task III - Combustor-Performance Mapping

Task IV - Limited Modification and Retest

The Task I technical effort is described herein. A complete description of the Task II and Task III activities is presented in Volume II. The computer codes for the combustor design that evolved from that effort are fully documented in Volume III. The combustor performance goals were achieved in Tasks II and III; thus Task IV was cancelled.

The computer models are based upon the numerical solution of the governing aero/thermo equations applicable to turbo-propulsion combustor environment, and are, therefore, applicable for analyzing internal flowfield of can, can-annular, and annular combustor geometries. Both the in-line and reverse-flow combustor configurations can be analyzed.

The cost-effectiveness of the empirical/analytical design procedure was to be demonstrated by undertaking the design and development testing of two full-scale annular combustors based on the following engine/combustor configurations, parameters, and goals:

1. Engine/Component Configuration.

   - Annular-combustor configurations

   - Centrifugal compressor (last stage)

   - First-stage axial turbine

   - Nonregenerative cycle

2. Parameters and Goals.

   - Engine airflow, W_{a3} = 1.30 kg/s

   - Combustor inlet pressure (P_3) = 1013 kPa

   - Compressor efficiency = 78.4 percent (total-to-static)

   - Combustor inlet temperature = 622K

23

- Combustion efficiency = 99.5 percent (100 percent power)

  = 98.0 percent (5 percent power)

- Combustor pressure loss $\dfrac{P_{T3} - P_{T4}}{P_{T3}}$ = 3 percent

- Combustor discharge temperature (T_{4avg}) = 1533 K

- Maximum circumferential pattern factor (PF) ≤ 0.23

  where $\quad PF = \dfrac{T_{4\ max} - T_{4\ avg}}{T_{4avg} - T_3}$

- Average radial temperature profile compatible with typical turbine blade requirements

- Maximum radial pattern factor (RPF) ≤ 0.075

  where $\quad PF = \dfrac{T_{4\ avg\ rad\ max} - T_{4\ avg}}{T_{4\ avg} - T_3}$

  $T_{4\ avg\ rad\ max}$ = peak value of the circumferentially averaged radial temperature profile

- Good light-off/relight capability to 6091 meters altitude and ambient-temperature conditions per MIL-E-5007D, Paragraph 3.2.5.1 (dated 15 October, 1973)

- No visible carbon formation with hot fuel or at high-altitude conditions

- Multifuel capability, including JP-4 and JP-5

24

- Fuel manifold operational capability to run for
  20 hours with contaminated JP-4 fuel in accordance
  with MIL-E-8593A, Table X

- The combined CO and HC exhaust emissions will be
  sufficiently low to meet the previously noted com-
  bustion efficiency goals at 100- and 5-percent
  rated power. The NO_x LTO emissions level will
  be at or below the 1979 EPA NO_x standards. The
  maximum smoke number will be below the threshold
  of the exhaust plume visibility

- Acceptable component temperature levels and gradients
  to ensure long combustion system life and reliability.

- Reasonable cost and weight

C. Summary.

The following six computer codes were developed and refined
during Task I of the program:

- Annulus-flow model

- 3-D combustor-performance model

- Liner-cooling model

- Transition-liner mixing model

- Gaseous-emissions model

- Fuel-insertion model

A one-dimensional annulus-flow model is used to calculate the pressure losses and airflow distribution around the combustor liner. Information provided by this model on the jet velocities and efflux angles for the various orifices around the combustor liner is used for specifying the boundary conditions required by combustor internal flow programs.

The internal flow-field characteristics, including combustion efficiency, exhaust-temperature quality, and lean blowout can be predicted by a 3-D recirculating (elliptic) reacting program. The program is based upon a computer code procured from Professor D. B. Spalding, and uses a variant of the numerical scheme described in Reference 1. The program is used to analytically assess the effect of detail design changes on combustor performance.

An accurate prediction of the practical cooling-band performance and attendant liner-temperature levels and gradient is essential for estimating liner life. A 2-D parabolic program based upon the efficient numerics of Patankar and Spalding[2] is used for analyzing the flow region adjacent to the liner. Appropriate initial, edge, and boundary conditions are supplied by the combustor performance model and the annulus flow model. The 2-D parabolic program is also used to predict the mixing rate in the transition liner of the reverse-flow annular combustors.

A 2-D parabolic program incorporating a 16-step kinetic scheme was developed to predict gaseous emissions. The fuel-insertion model provides a rough estimate of fuel-nozzle system performance in a specified combustor flow field.

---

[1]Patankar, S.V., "Numerical Prediction of Three-Dimensional Flows," Studies in Convection: Theory, Measurement and Applications, Volume 1 (B.E. Launder), Academic Press (1975)

The following element tests were conducted to furnish data for validating the analytical models:

- Sauter mean diameter (SMD) measurements of practical air-assist airblast nozzles and air-assist pressure atomizers.

- Film effectiveness of a conventional film-cooling scheme, and three advanced cooling concepts under simulated combustor environments.

- Mixing of cold transverse jets with a confined hot stream.

- Can combustor mapping

  - Nonreacting 3-D velocity and pressure measurement

  - Internal profiles of emissions with Jet-A and natural gas.

  - Radiation measurements.

- Transition liner mixing.

A reasonably good agreement was achieved between measurements and models incorporating a two-equation turbulence model, a two-step kinetic scheme, and a realistic spray combustion model.

A description of combustor-design procedures is presented in Section II. A brief description of the six combustor

[2]Patankar, S.V., and D.B. Spalding, "Heat and Mass Transfer in Boundary Layers," Intertext Books (1970).

analytical models is given in Section III (see Volume III for a detail description of the models and associated computer codes). Section IV presents experimental data obtained from different element tests. Model validation is presented in Section V. Conclusions of the present study and some thought for future combustor-modeling activities are summarized in Section VI.

II. COMBUSTOR DESIGN PROCEDURES

Design considerations for a turbo-propulsion combustor must address the following performance and operational factors:

- Combustion efficiency

- Lean flame stability and altitude relight

- Ground idle/starting

- Carbon and smoke formation

- Gaseous emissions

- Exhaust temperature quality (radial and circumferential profiles)

- Liner-wall temperature and permissible wall-temperature gradients

Many of these requirements have to be compromised in order to achieve acceptable combustor performance over the entire engine flight envelope.

Due to the complexities associated with the combustion processes and flow field in gas turbine combustors, the evolution of combustor-design technology has proceeded along two distinct paths. Practical engineers faced with hardware problems have developed a number of design correlations and empirical design procedures, such as presented in Section II.A. On the other hand, researchers involved in studying fundamental aspects of reactive flows have developed a number of analytical models that address specific phenomena.

29

The communication gap between practical combustion engineers and fundamental researchers is quite wide. This program concentrated on bridging that gap, and making available to the gas turbine engine industry a cost-effective combustor design procedure that makes use of "experience" correlations as well as combustor analytical models based on well-tried, successful, mathematical models of turbulence, chemical kinetics, spray combustion, and radiation. A complete set of advanced analytical design tools has been put together to address and analyze important aspects of gas turbine combustion phenomena, as explained in Section III.

A typical conventional empirical design approach is outlined in Section II.A. The coupling of an empirical approach with combustor analytical models is explained in Section II.B. The use of new design techniques has been rewarding at AiResearch in the design and development testing of a number of advanced combustion concepts. It is hoped that with continued improvement in understanding of reactive flows, and with a judicious blend of hardware and modeling experience, the empirical/analytical combustor-design procedure will become universally applicable.

A.   Empirical Design and Development Procedures.

The conventional approach to the design and development of combustion systems for gas turbine engines involves extensive use of empirical correlations derived from experimental analysis, followed by a series of component-development tests. Through the years, a number of empirical and semi-empirical correlations have been developed by engine manufacturers to provide guidelines for the initial design of a combustion system, and to predict attainable performance on the basis of experience trends.

30

The empirical-design approach differs from company to company, and between individuals of the same company. Nevertheless, the design approach must give consideration to numerous design criteria including combustion efficiency, lean flame stability, altitude relight, ground idle/starting, carbon and smoke formation, gaseous emissions, exhaust-temperature quality, combustor pressure drop, and liner durability.

High combustion efficiency, over the entire engine operating range, is a prime objective in turbo-propulsion combustion system design, as it directly affects specific fuel consumption. Inefficiencies in the combustion process can be explained by using detailed flow models, such as the 3-D Combustor-Performance Model described in Section III.B. However, simple semi-empirical correlations, such as Lefebvre's air-loading parameter or its minor modification, shown in Figure 1, are quite useful for estimating initial combustor-size requirements for a given application.

Other parameters that are used for scaling combustors are heat-release rate and reference velocity shown in Figure 2 (from Reference 3). The cross-sectional dimension can be established consistent with experience correlations between reference Mach number and allowable pressure loss, such as typically shown in Figure 3(a).

The required dilution-zone volume, length, and channel height can be estimated by using simple curves, shown in Figure 3(b). In this curve, the general trend for combustor pattern factor is shown to be an inverse function of the pressure-loss factor ($\Delta P/q_{ref}$) and the dilution zone length-to-height ratio.

[3]Carlson, N.G., "Development of High-Temperature Subsystem Technology to a Technology Readiness State: Phase I Topical Report, Preliminary Combustor Design," Technical Report FE-2292-11, November 1977, Work Performed Under Contract No. EX-76-C-01-2292.
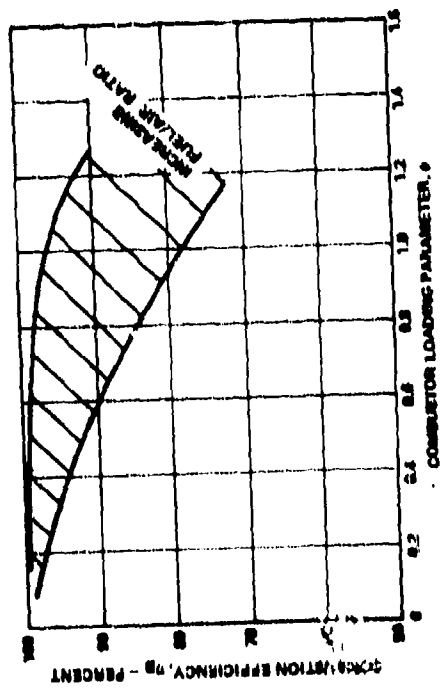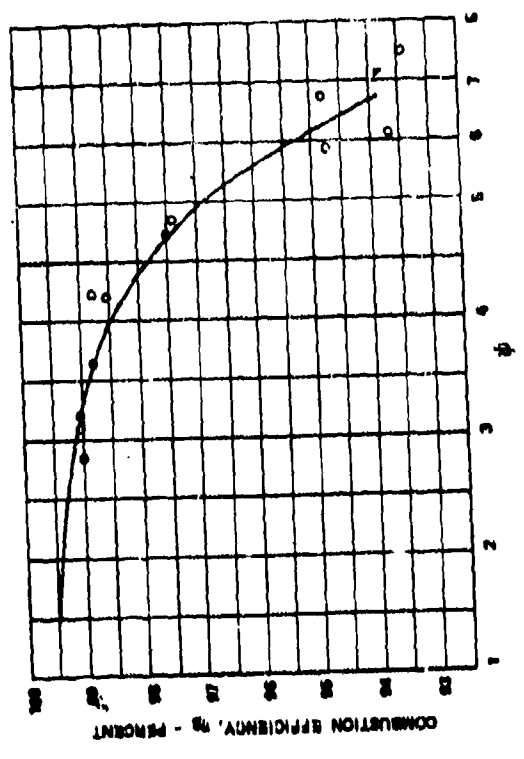
(b) AiResearch Combustor

(a) Typical Efficiency

Figure 1. Combustion Efficiency As A Function of Air Loading Parameter.
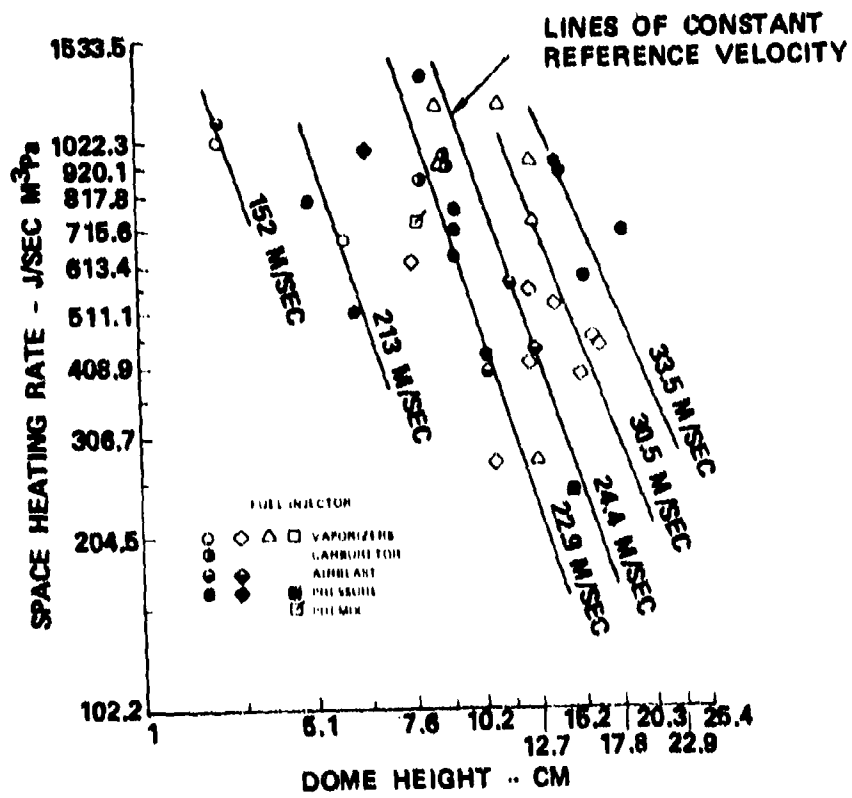
Figure 2. Relationship of Space Heating Rate to Annular Combustor Size.
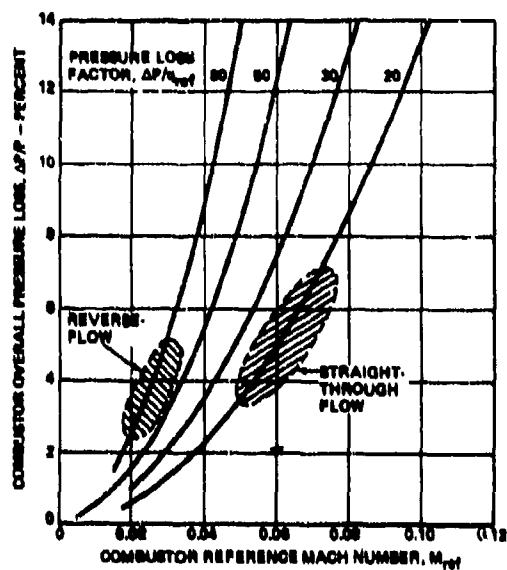
(a)
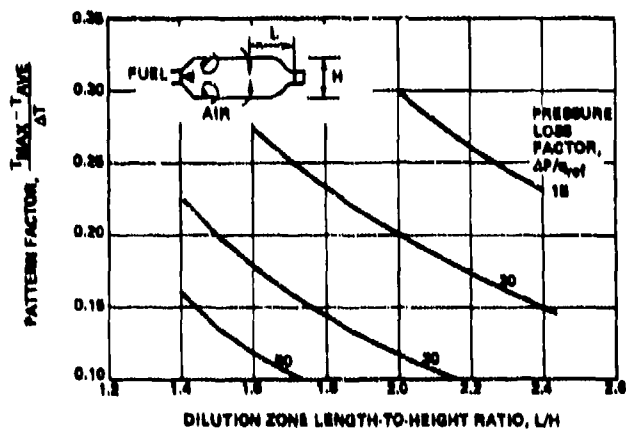
(b)

Figure 3.   Overall Pressure Loss and
            Discharge Pattern Factor.

The liner cooling-air requirements have been estimated by using a variety of correlations, as presented in Figures 4(a)[3] and 4(b)[4], or the following simple expression from Reference[5]:

Percent Film Cooling = 0.1 T_i - 30 ($\pm$10 percent)

The selection of a fuel-injection system is less rigorous compared to combustor geometrical configuration and the liner-cooling-air requirements. Experience indicates that in addition to air or fuel-loading parameters, the fuel-injection process has a significant effect on combustion efficiency (particularly at low-power points). The fuel-injection system also affects exhaust-temperature quality, smoke and carbon formation, lean blowout, and fuel impingement on the liner wall with attendant liner hot spots. Turbo-propulsion combustors have employed a variety of fuel-injection systems in regard to nozzle configurations (pressure atomizers, including simplex/duplex or airblast), mode of insertion into the liner (axial versus radial/tangential), axial location from the dome and orientation relative to the recirculation zone, and fuel-nozzle characteristics such as droplet size and cone angle. So numerous are the possible combinations that the successful development of a realistic semi-empirical correlation involving aero/fuel-nozzle interaction is a remote possibility.

Once the initial combustor configuration is established, the subsequent design and development approach is varied. Some engineers prefer performing calculations by using a number of simple computer programs. The following paragraphs give a

[4]Wood, M. P., and K. M. Johansen, "Advanced, Small, High-Temperature-Rise Combustor Program; Volume II Design and Test of Full-Scale Combustion System," AiResearch Manufacturing Co., USAAMRDLTR-74-38, Eustis Directorate, U.S. Army Air Mobility R&D Laboratory, Fort Eustis, Va., AD776978, February 1974.

[5]Odgers, J., "Combustion Modeling Within Gas Turbine Engines," AIAA Paper No. 77-52.
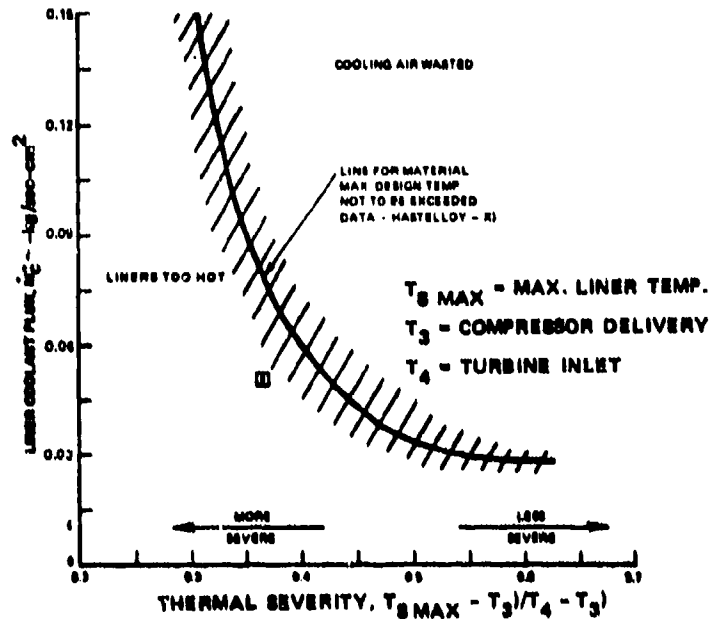
(A)
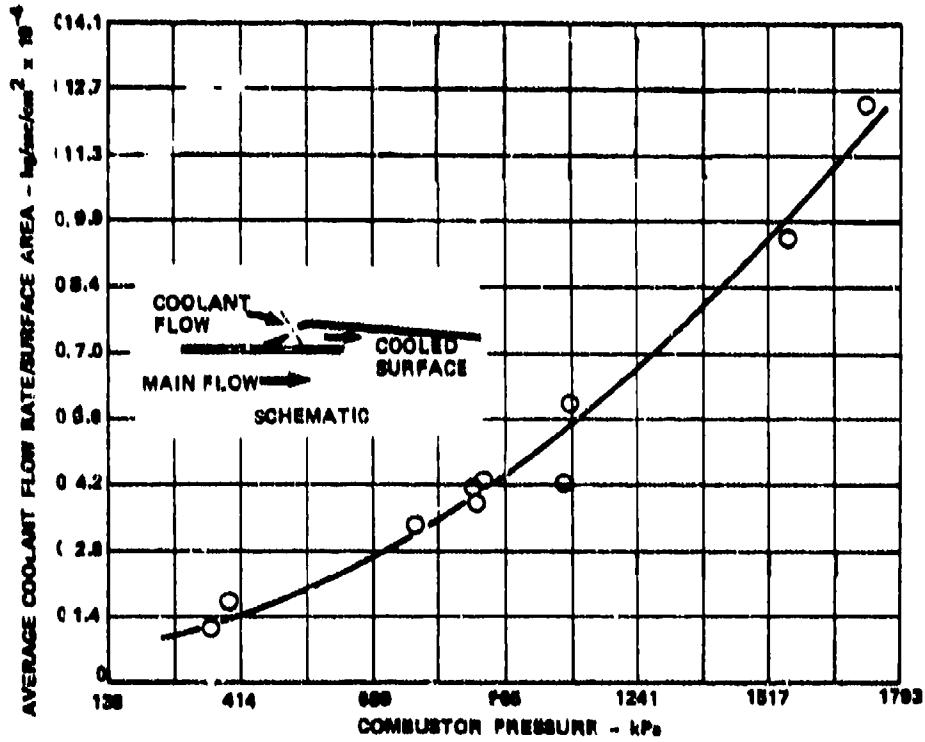
(B)

Figure 4. Typical Experience Curves for Liner Cooling
Flow Requirement.

36

brief description of the use of simple calculation methods based upon the computer codes documented in Reference 6.

A one-dimensional annulus flow model is used to calculate the pressure losses and airflow distribution around the combustor liner. The analysis includes the effects of area change, heat transfer, friction, drag due to nozzle shrouds and service struts, and mass addition. The model calculates the flow-discharge coefficients and efflux angles for the orifices along the annulus.

An impinging-jet recirculation model predicts the effects of multiple three-dimensional radial jets and the recirculation caused with the impinging jets. The control volume axis for model development is the centerline of the jet-impingement region. The flow momentum is related to the pressure differential that results from jet blockage with use of the momentum balance. Knowing the number and geometry of the primary orifices, and assuming that the primary-zone exit flow experiences a sudden expansion loss when flowing past the impinging jets, the model calculates the fraction of the primary orifice flow rate that recirculates upstream.

A dilution jet trajectory model is used to predict dilution jet trajectory, mass entrainment, velocity, temperature decay, jet spread, and profile changes after jet mixing.

Fuel-spray trajectory models are used for predicting spray characteristics of various fuel injectors. These models are of considerable benefit in the selection of fuel injectors and their optimum location in a specified combustor internal flow field.

[6]Hunter, S.C., K. M. Johansen, H. C. Mongia, and M. P. Wood, "Advanced, Small, High-Temperature-Rise Combustor Program, Volume I, Analytical Model Derivation and Combustor-Element Rig Tests (Phases I and II)," AiResearch Manufacturing Co., USAAMRDL TR74-3A, Eustis Directorate, U.W. Army Air Mobility R&D Laboratory, Fort Eustis, Va., AD 778766, February 1974.

A one-dimensional wall-cooling model, similar to Reference 7, is used for calculating the liner-wall temperature levels. The analysis includes flame radiation to the wall, convection on both sides of the wall, radiation from the cold side of the wall to the plenum, and film-cooling effectiveness. The heat-conduction loss through a single or multiple material thickness is also included.

With the help of the above models, it is possible to identify potential problem areas with the preliminary combustor configurations. The designs are modified as required. Detail drawings are prepared, parts fabricated, and component-development testing initiated. During these tests it is important to relate experimental results back to the empirical parameters that were used for preliminary design. A systematic means of collecting the relevant data for correlation purposes and future reference is highly desirable.

An empirical approach, as delineated above, has worked reasonably well with combustor configurations that have evolved from well-proven concepts. The design/development time duration and cost can vary enormously, depending upon the target goals. With increasingly stringent levels of design requirements, the inadequacy of simple one-dimensional calculation procedures is quite obvious. Consequently, the interpretation of the experimental data becomes more qualitative in nature, with a resultant increase in development time and cost.

B. Empirical/Analytical Design Procedure.

A more cost-effective design procedure can be developed if the experimental results are properly evaluated. Not only does it help in planning a correct approach for the component

---

Ballal, D. R., and A. H. Lefebvre, "A Proposed Method for Calculating Film Cooled Wall Temperatures in Gas Turbine Combustion Chambers," ASME Paper 72-WA/HT-24.

38

rig tests, but well-scrutinized experimental data is also useful
for further improving empirical correlations and for future
reference. The empirical/analytical design procedure is a first
milepost along the path of establishing the combustor design and
development as a scientific approach, rather than the "cut and
try" approach that has been used for so long. The approach does
not minimize the importance of the empirical data base. On the
contrary, it (with the help of advanced combustor analytical
models) improves our fundamental understanding of the various
physico-chemical process occurring in gas turbine combustors.
The choice as to which analytical models should be used is very
critical, as it will directly affect the level of success
achieved.

Due to the complexities associated with the combustion
process and flow field in gas turbine combustors, the development
of combustor analytical models has proceeded along two distinct
paths:

- Simplified or detailed reaction mechanisms with
  simplified flow models, and

- Detailed flow models with simplified or detailed
  reaction mechanisms.

A majority of combustor analytical models have utilized
idealized flow models comprised of well-stirred or partially-
stirred reactors and plug flow models. Both simple and complex
kinetic schemes have been used for predicting fuel/air reaction
rates. These models have been quite useful for data interpre-
tation, but their application as combustor analytical design
tools is quite limited. The model limitations[8] are associa-
ted with the inability to accurately predict the effect of com-
bustor geometrical details on residence time and fuel/air ratio
distribution.

[8]Mosier, S. A., and R. Roberts, "Low-Power Turbopropulsion
Combustor Exhaust Emissions, Volume 3, Analysis,"
Technical Report AFAPL-TR-73-36, 1974.

The development of detailed flow models has been slow due to a number of reasons including numerics, incomplete understanding in regard to turbulence, chemical kinetics, spray combustion, and radiation. As progress is made in these areas, the flow models that numerically integrate the 2-D or 3-D field equations will become more popular. This approach provides the ultimate prospects of analyzing the effect of detail design changes on combustor performance, and eventual quantitative interpretation of experimental data with resultant improvement in empirical correlations.

The performance of a combustor is determined by its internal flow-field characteristics, which are influenced strongly by a number of variables. These include:

- Primary-zone volume and equivalence ratio

- Level and scale of mixedness

- Fuel-nozzle spray characteristics and orientation with respect to the recirculation zone

- Combustor-inlet pressure and temperature, and temperature rise

- Combustor residence time

For correlating and interpreting combustor data, analytical models are expected to give quantitative predictions (from an engineering point-of-view) of the following parameters:

- Combustion efficiency, especially at low power conditions

- Exhaust-temperature quality

40

- Liner-wall temperature levels and gradients, including hot spots

- Gaseous emissions

- Fuel-nozzle performance

- Liner pressure drop and airflow distribution

A number of questions must be resolved in order to achieve a most economical engineering tool for combustor design. These concern:

- Mathematical models of turbulence, chemical kinetics, spray combustion, and radiation

- Numerical scheme

- Boundary conditions

These have been discussed in detail in Volume III. Simple and well-tried mathematical models of turbulence and its effect on combustion, spray combustion, chemical kinetics, and radiation were employed. The models used are a two-equation turbulence model, a two-step kinetic scheme, and a six-flux radiation model, as described in Section II of Volume III. The numerical schemes in the elliptic and parabolic programs are variants of the numerics described in References 1 and 2. Further details on the numerics and boundary conditions are given in Sections III and IV of Volume III.

Due to computer-memory limitations and extended computation times with a fully elliptic numerical scheme, all of the combustor-performance parameters cannot be economically predicted by a single computer code. Consequently, a multi-level analysis

approach has been developed, as presented in the empirical/
analytical combustor-design procedure logic chart of Figure 5.
A brief description of the following six analytical models is
given in Section III.

- Annulus-flow model

- 3-D combustor-flow model

- Transition-mixing model

- Wall-cooling model

- Emission model

- Fuel-insertion model

The manner in which the empirical-design approach is inte-
grated with analytical models is described in the following
paragraphs.

After a new engine envelope, associated component con-
straints, and the engine fuel schedule have been defined, a
preliminary combustor sizing is executed by utilizing various
"experience" correlations. Simplified one-dimensional models,
such as described in Section II.A, are then used to define a
preliminary combustor design. With the help of these simple
and economical calculations, it is relatively easy to study a
number of different design concepts to arrive at the most
promising configuration.

Further improvement in the basic design is undertaken by
using the advanced analytical models shown in Figure 5. The
necessity of using this approach becomes more apparent if the
new engine envelope forces the consideration of combustor con-
cepts that lie outside the designer's experience and/or
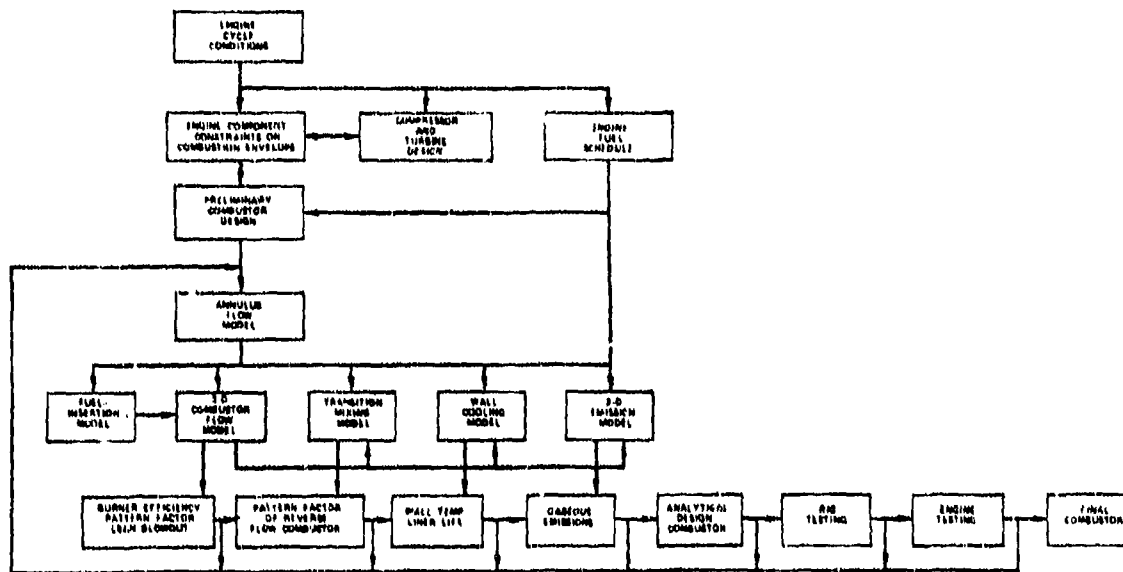
Figure 5. Empirical/Analytical Combustor Design
Procedure Logic Chart.

empirical correlations. The models can be used to parametrically study the effects of detail design changes on combustor performance. A number of combustor modifications may have to be run before arriving at an acceptable engineering compromise. The computer-iteration process might involve many man-weeks of effort, with attendant computer cost.

A relative comparison has to be made between computer cost and hardware test expenditure. It is not expected that analytical experience alone can shorten the combustor-development time. It is a judicious blend of analytical model predictions and development experience that would significantly reduce the time and cost. As technical advances are made in computer technology, numerical fluid mechanics, and physical understanding of various combustion phenomena, the extent to which personal judgement is required will be minimized. In addition, with the application of the new design technique to a variety of combustor configurations and back-correlating with relevant data, it is hoped that the technique will become more useful and cost-effective as a design tool.

III. ANALYTICAL MODELS DESCRIPTION

A brief description of the six analytical models is presented below. For a more detailed description, see Volume III.

A. Annulus Flow Model.

The annulus flow model is used to calculate pressure losses and airflow distribution within the annulus external to the combustor liner.

Annulus losses and flow distribution are computed from the generalized influence-coefficient method given by Shapiro.[9] This method leads to the following equation for loss in total pressure for a small finite-length of duct:

$$\frac{dP_t}{P_t} = -\frac{KM^2}{2}\left[\frac{dT_t}{T_t} + \frac{4fdx}{D} + C_D\frac{dA_B}{A} + 2(1-y)\frac{dw}{W}\right]$$

where:
- P_t = total pressure
- M = average Mach number in element
- T_t = total temperature
- f = wall friction factor
- dx = element length
- D = duct hydraulic diameter
- C_D = drag coefficient of inserted bodies
- A_B = frontal area of inserted body
- A = duct area
- y = velocity of injected mass/duct velocity
- dW = injected mass flow
- W = duct mass flow

---

[9] Shapiro, A. H., "The Dynamics and Thermodynamics of Compressible Fluid Flow," The Ronald Press Company (1953).

The Mach number is obtained from a similar influence coefficient equation given by Shapiro.[9] The above analysis includes the effect of area change, heat transfer, friction, drag, and mass addition.

Swirl effects are accounted for by solving the previous equations in the direction of actual flow, together with an equation for angular momentum with friction losses. The computer program for this model generates a pictorial representation of the combustor, and tabulates the flow parameters at specified stations. A typical computer-output plot is shown in Figure 6. The program can calculate pressure drop from an assigned fixed-orifice geometry, or can size orifices for a desired pressure drop and an assigned flow distribution.

The annulus-flow model calculates boundary conditions, such as flow distribution around the combustor liner, jet velocity and angle, etc., which are required by the combustor internal-flow models.

B.   3-D Combustor-Performance Model.

The combustor internal flow-field characteristics are strongly influenced by airflow distribution around the liner, jet velocities and efflux angles, nozzle-spray properties, fuel/air ratio, and dwell times of different zones. The governing aero/thermo equations are coupled and nonlinear, and defy analytical solutions of all but a few academic problems.

A 3-D combustor-performance model has been developed based upon a code supplied by Professor D.B. Spalding. The model numerically integrates the governing equations for the following variables:

46

Figure 6. Typical Computer Plot for Annulus Flow Program Output.

47

- Axial, radial, and tangential velocity components

- Turbulence kinetic energy (k) and dissipation rate (ϵ)

- Unburned hydrocarbons ($C_x H_y$), CO, and composite fuel-mass fraction

- Stagnation enthalpy

- Radiation vectors along X, Y, and Z directions

- Spray droplet size and distribution

The two-equation turbulence model, requiring solution of k and ϵ, is moderately complex, and is considered to be superior to other models having a similar or lesser degree of complexity. This model has been extensively used by many researchers, and has proved to be adequate in a wide range of flow conditions, including the complex combustor flow-field mapped in this program and described in Sections IV and V. More advanced turbulence models, such as those based upon the Reynolds stress-modeling approach, are not yet sufficiently developed to warrant their use in complex combustor flow-field problems.

The combustion rate is computed via a two-step kinetic scheme wherein:

$$C_x H_y + \left(\frac{x}{2} + \frac{y}{4}\right)(O_2 + n N_2) \xrightarrow{R_f} x\, CO + \frac{y}{2} H_2O + \left(\frac{x}{2} + \frac{y}{4}\right)n\, N_2$$

$$x\, CO + \frac{x}{2}(O_2 + n N_2) \xrightarrow{R_{CO}} x\, CO_2 + \frac{x}{2} n\, N_2$$
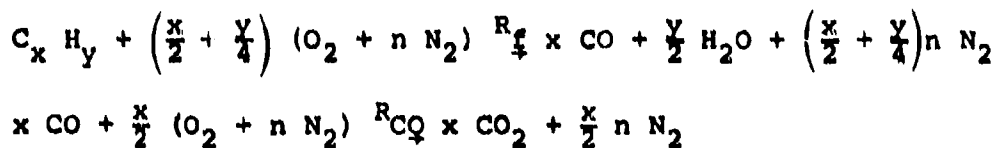
The effective reaction rate (R_f) for fuel oxidation is computed from the minimum of the reaction rate controlled by chemical kinetics, fuel-mixing rate, or oxygen-mixing rate. Similarly, R_{CO} denotes the minimum of the reaction rates of CO

48

combustion as controlled by chemical kinetics, mixing rate of CO and/or oxygen. Such a scheme has given good correlation with measured internal-species profiles from a number of combustion systems.

The 3-D combustor-performance model was validated with experimental data on:

- Mixing of cold transverse jets with a confined hot stream

- Can combustor mapping

  - Nonreacting 3-D velocity and pressure measurement

  - Internal profiles of emissions with natural gas and Jet-A

  - Radiation measurements.

C. Wall-Cooling Model.

An accurate assessment of the liner wall-temperature levels and gradients is very important as it directly affects the liner life. If a wall-cooling model underpredicts liner temperature by 56 K, the liner life will be reduced by approximately 40 percent, as reported by Sturgess.[10] Conventional, one-dimensional, wall-cooling models are inadequate for predicting liner-wall temperatures of current-technology combustors[10]. A full 3-D elliptic solution for predicting liner-wall temperature is desirable, but is not economical due to the extended computer time required to get a sufficient number of nodes near the wall for achieving a grid-independent solution.

---

[10] Sturgess, G. J., "Gas Turbine Combustor Liner Durability-The Hot-Streak Problem," Project Squid (ONR) Workshop on Gas Turbine Combustor Design Problems, 1978.

Since the velocity vectors near the wall are predominantly in the same direction as the main flow, a parabolic solution procedure can be efficiently used to compute liner-wall temperatures. A 2-D parabolic program was developed for this purpose. The program solves for axial velocity, swirl velocity, turbulence, kinetic energy and dissipation, a two-step kinetic scheme, spray combustion, a two-flux radiation model, and stagnation enthalpy. The model uses a two-equation turbulence model of Launder and Jones.[11] The numerical scheme is based upon Reference 2.

The appropriate initial/boundary and edge conditions are supplied by the 3-D combustor-performance model and the annulus-loss model, as described in Volume III. This program is quite flexible in that single or multiple cooling bands, both in the primary and secondary zones, can be analyzed. It is possible to handle both annular and can geometries.

D. Transition-Mixing Model.

A reverse-flow annular combustor, for a turbine engine that employs a centrifugal compressor as its last stage of compression and axial turbine for its high-pressure spool, has a reverse-flow transition liner. The flow in practical transition liners usually does not have a negative streamwise velocity component. Significant jet mixing has taken place in the straight section upstream of the transition liner. However, the mixing in the region of the transition liner, where flow changes from axial to radial and fully completes a 180-degree bend, must be computed to predict the pattern factor of a reverse-flow combustor that feeds and axial turbine.

---

[11] Jones, W. P., and B. E. Launder, "The Calculation of Low-Reynolds Number Phenomena with a Two-Equation Model of Turbulence," ASME Paper 72-HT-20.

The geometry of practical transition liners is too complex
to make efficient use of the 3-D combustor-performance code.
If the flow variations within the transition liner along the
circumferential direction are small and can be neglected, a 2-D
parabolic program can be used to predict mixing rates along
different Z-r planes, where Z is the streamwise coordinate.
A 2-D parabolic program was therefore developed using numerics
and mathematical models similar to those of the wall-cooling
model described in Section III.C. It should be noted that for
nonrecirculating flows in axisymmetric geometries with stream-
line curvature, the elliptic effects of pressure along the Z
direction must be taken into account. However, this was not
incorporated in the model as it was beyond the scope of this
program; the cross-stream variation in pressure, due to stream-
line curvatures, was taken into account.

E.   2-D Emissions Model.

With the emergence of public concern for air pollution, an
increased emphasis has been made by industry, including
AiResearch, to improve the fundamental understanding of various
processes leading to the formation of harmful pollutants.
Numerous detailed kinetic schemes have appeared in the literature
for predicting HC, CO, and NO_x. In addition, different tech-
niques have been put forward to compute gaseous emissions from
gas turbine engines, such as References 8 and 12. Most of these
calculation procedures use either a simplified flow-field
model[8] or estimate "exchange coefficients" from some detailed
flow-field computations based upon simple kinetic schemes.[12]
However, some work has been reported in parabolic flow computa-
tion with detailed kinetics, such as Reference 13.

[12] Sanborn, J. W., R. S. Reynolds, and H. C. Mongia, "A Quasi-
Three-Dimensional Calculation Procedure for Predicting the
Performance and Gaseous Emissions of Gas Turbine Combustors,"
AIAA Paper No. 76-682.

[13] Edelman, R., J. Boccio, and G. Weilerstein, "The Role of
Mixing and Kinetics in Combustion Generated NOx," Paper
presented at Aiche Symposium on Control of NOx Emissions
in Direct Combustion Power Sources, 1973.

A 2-D parabolic program with a 16-step kinetic scheme was developed based upon modified Patanker-Spalding numerics.[2] The modification was made in regard to computing chemical-species source terms for a coupled-set of equations. This resulted in a significant reduction in computation time. Other important features of this model are:

- Effect of turbulence in combustion, as explained in Volume III.

- Spray combustion of complex fuel, such as JP-4 and JP-5.

- A two-flux radiation model.

F. Fuel-Insertion Model.

Small, high-pressure-ratio and high-temperature-rise reverse-flow combustors pose a major problem with respect to the selection of an optimum fuel-injection system. A major part of the problem is created by excessive or uncontrolled impingement of fuel on the combustor wall. To minimize fuel impingement, it is of paramount importance to attain an optimum matching between fuel-nozzle characteristics and combustor internal-flow field. It may be recalled that the 3-D combustor-performance model considers spray evaporation/combustion of complex fuels, such as JP-4 and JP-5. Consequently, the program can be used for defining an optimum fuel-injection system, as reported in Section III of Volume II.

A fuel-insertion model was developed to save computer time and facilitate a quick selection of an injection system. This program computes Sauter mean diameter (SMD) of the pressure atomizer (simplex or duplex), air-assist pressure atomizer, and airblast and air-assist airblast nozzles. The droplet heat-up, evaporation, and combustion are calculated based on

the Priem and Heidman model[14] modified to take into account variable properties of the jet fuels. The droplet drag coefficient is calculated from:

$$C_d = C_{d_s}/(1+B)$$

where C_{d_s} is the drag coefficient of a nonreacting sphere, and B is the evaporation/burning rate constant.

The spray is initially divided into five droplet-size groups. The trajectory of each of the droplet sizes is computed for uniform flow on any specified flow field. Knowing a combustor internal-flow field (as computed by the 3-D combustor-performance model), the effect of spray-cone angle, SMD, fuel-nozzle pressure drop, fuel physical properties on the spray trajectory, and amount of fuel impingement on the liner wall can be easily computed with the fuel-insertion model.

[14] Priem, R. J., and M. F. Heidmann, "Vaporization of Propellants in Rocket Engines," ARS Journal, Nov. 1959, pp. 836-842.

IV. ELEMENT TESTS

A parallel experimental investigation was conducted during Task I to verify analytical models described in Section III, and to identify potential problems associated with small, high-pressure-ratio, high-temperature-rise combustors. Major design problems encountered in the development of advanced small combustors are generally concerned with the following components and performance parameters:

- Liner cooling

- Discharge-temperature quality

- Gaseous emissions, particularly idle combustion efficiency

- Fuel injection

Element tests were therefore conducted during Task I to afford a significantly improved understanding of the design constraints imposed by each of these.

The performance of conventional and advanced cooling concepts was measured under a simulated combustor environment, as summarized in Section IV.A. Experimental data on the mixing of cold transverse jets with the hot-gas stream of a can combustor was taken (as described in Section IV.B) to better understand the mixing characteristics of the impinging jets in order to minimize the dilution-air requirement. The internal flow-field characteristics of a typical Garrett/AiResearch can combustor were measured with and without combustion, as summarized in Sections IV.C and IV.D. The data was taken with both gaseous and liquid fuels.

A limited amount of test data was collected on the radiation heat loading and is summaried in Section IVE. The ignition characteristics of a piloted airblast Nozzle and an air-assist airblast nozzle were measured and are summarized in Section IV.F.

Fuel-nozzle characteristics, including mean droplet size and spray cone, strongly influence the combustor performance, such as idle emissions, light-off and blowout characteristics, dome and liner wall carbon-formation tendencies, and temperature levels and gradients. A droplet-measurement apparatus was therefore developed under this program and described in Section IV.G. The Sauter mean diameters of an air-assist pressure atomizer and air-assist airblast nozzles were measured and correlated. The mixing rate in a typical reverse-flow combustor transition liner is summarized in Section IV.H.

A. Liner Cooling.

Liner cooling for a combustor matched to the last stage of a centrifugal compressor and an axial or radial turbine imposes severe limitations on the design of low-airflow, high-pressure, high-temperature-rise gas generators. The cooling-air requirement for a combustor using conventional cooling-film geometries can exceed 75 percent of the engine total airflow rate in order to achieve long combustor-life objectives.

Although conventional film-cooling concepts are suitable for low-pressure ratio combustors, and are inexpensive to fabricate, their disadvantages and limitations provide impetus for evaluation of more advanced cooling concepts. Disadvantages of conventional film-cooling concepts include

- Saw-tooth wall temperatures resulting from pure film cooling without attention to the cold side of the liner

55

- Performance that is strongly region-dependent

- Fair-to-poor coolant-flow control

- Degradation of pattern factor

- Overcooling at low power, thus quenching the
  combustion reactions and contributing to HC and
  CO emissions.

Quantitative knowledge about many frequently used film-
cooling configurations under combustor-operating conditions is
limited because of the difficulty encountered in obtaining
detailed and reliable data with known coolant-flow distribution.

Most of the practical cooling-slot geometries, Figure 7,
generate a 3-D flow-field downstream of the lip. The most
significant geometric parameters governing the film-cooling
performance are metering-hole-area/slot open area and the
relative cover-plate length L/S^6. It was experimentally
observed (for the low temperature difference and low turbulence
level) that design correlations derived for the impingement
film configuration also apply to pinched impingement film and
wiggle-strip geometries. The hole step design did not perform
as well as the other configurations.

The above tests were conducted at approximately ambient
pressure and temperature. The effect of the ratio of the main
(hot) stream to the cooling stream gas temperatures (or the
density ratio) significantly affects the cooling-slot perform-
ance. This was reported by Burns and Stollery[15], and shown
typically in Figure 8. Therefore, the performance of a

[15]Burns, W. K. and J. L. Stollery, "The Influence of Foreign
Gas Injection and Slot Geometry on Film Cooling Effective-
ness," Int. J. Heat and Mass Transfer, Vol. 12, pp. 935-951,
1969.
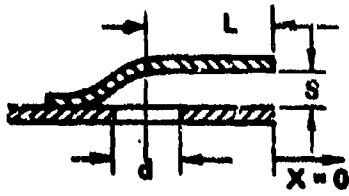
IMPINGEMENT FILM
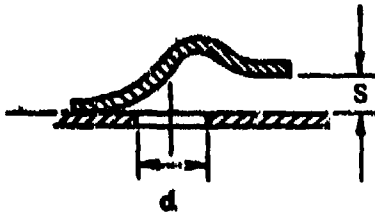
PINCHED-IMPINGEMENT FILM
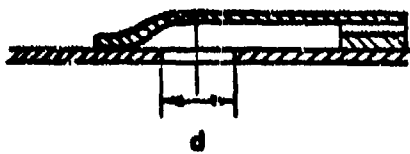
IMPINGEMENT FILM WITH WIGGLE STRIP

HOLE-STEP

Figure 7. Combustor Film Cooling Configurations.
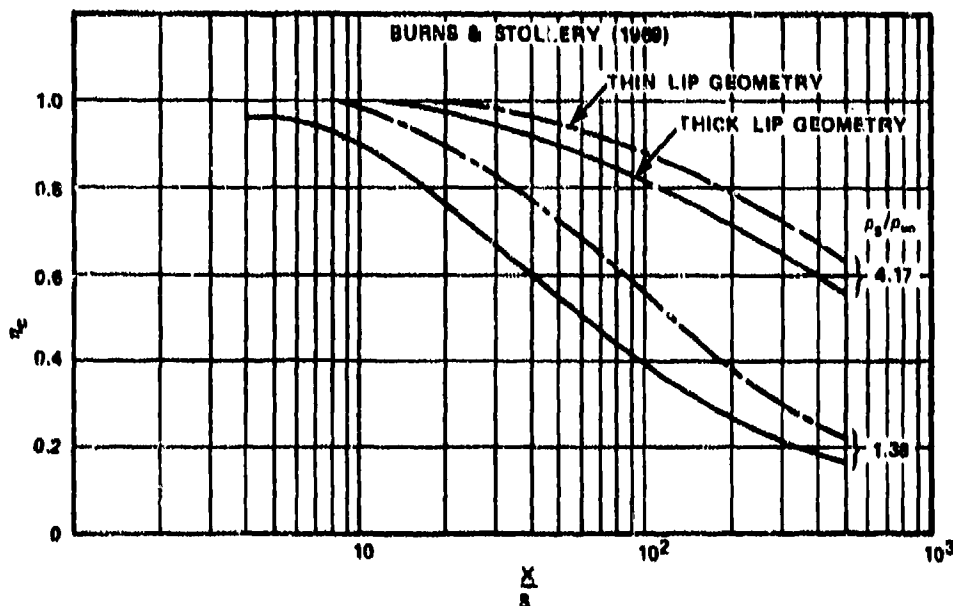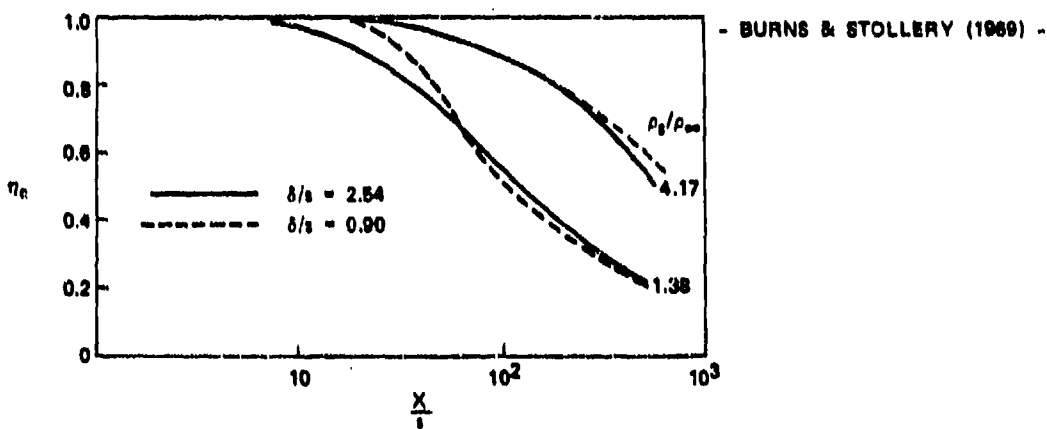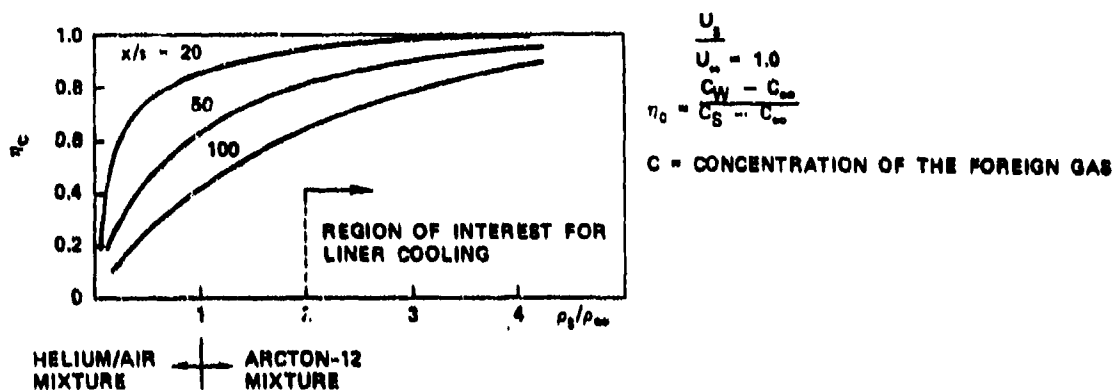
Figure 8. Effect of Density Ratio, ρ_s/ρ_∞, Lip Geometry and Main Stream Boundary Layer Thickness on Impermeable Wall Effectiveness, η_c, as Reported by Burns and Stollery[15].

58

practical cooling-band configuration was experimentally measured
under simulated combustor temperature environment as listed in
Table 1. The temperature ratio (density ratio) and jet-to-hot-
stream velocity ratio were varied over the range of interest in
a typical combustor environment.

The test rig and associated instrumentation is described
in Section IV.A.1. The description and data for the four cooling
concepts listed in Table 1 are given in Section IV.A.2 through
IV.A.5. Finally, a comparison between three cooling concepts
(namely, conventional film, conventional film/extended surface,
and impingement/film) as inferred from wall-temperature levels
and gradients determined by thermal-sensitive paint (Thermindex
OG-6), is given in Section IV.A.6.

1. Liner-Cooling Test Rig and Instrumentation

A general layout of the test rig is shown in Figure 9. A
slave can combustor was used to supply a hot airstream for the
liner-cooling or jet-mixing test sections. Different test
sections can be flanged to the combustor, as shown in the
layout. The test-section plenum was made compatible with
different test-section liners.

The cooling and annulus airflow rates were measured at the
inlets, shown in Figure 9. The air for the test sections
enters the annulus through 60 orifices of 7.2 mm diameter,
arranged in six staggered rows, giving approximately a 5-percent
pressure drop at the design condition. A settling length of
approximately 20 cm (9 times the annulus hydraulic diameter) was
provided for the flow to settle before entering orifices of the
conventional film/convection cooling band. Airflow rates at the
outlet were measured. The difference between the measured flow
rates at the inlet and outlet constituted the cooling airflow
rate. Annulus air static pressure and temperature were measured
at a plane 3.9 cm upstream from the cooling-slot discharge lip.

TABLE 1. LINER COOLING TEST GEOMETRIES AND FLOW CONDITIONS.

Cooling Configurations

- Conventional Film/Convection Cooling
- Conventional Film/Extended Surface Convection Cooling
- Impingement/Film/Convection Cooling
- Coarse-Pore Transpiration/Convection Cooling

Range of Flow Parameters

Combustor Inlet Pressure	=	2 - 10 atm
Annulus Air Temperature	=	300 - 600K
Hot Stream Velocity	=	35 - 45 m/s
Hot Stream Temperature	=	1100 - 1300K
Coolant Jet Velocity	=	30 - 100 m/s
T_{hot}/T_{ann}	=	2.2 - 4.3
U_{jet}/U_{hot}	=	0.8 - 2.5
Annulus Velocity	=	20 - 45 m/s

60
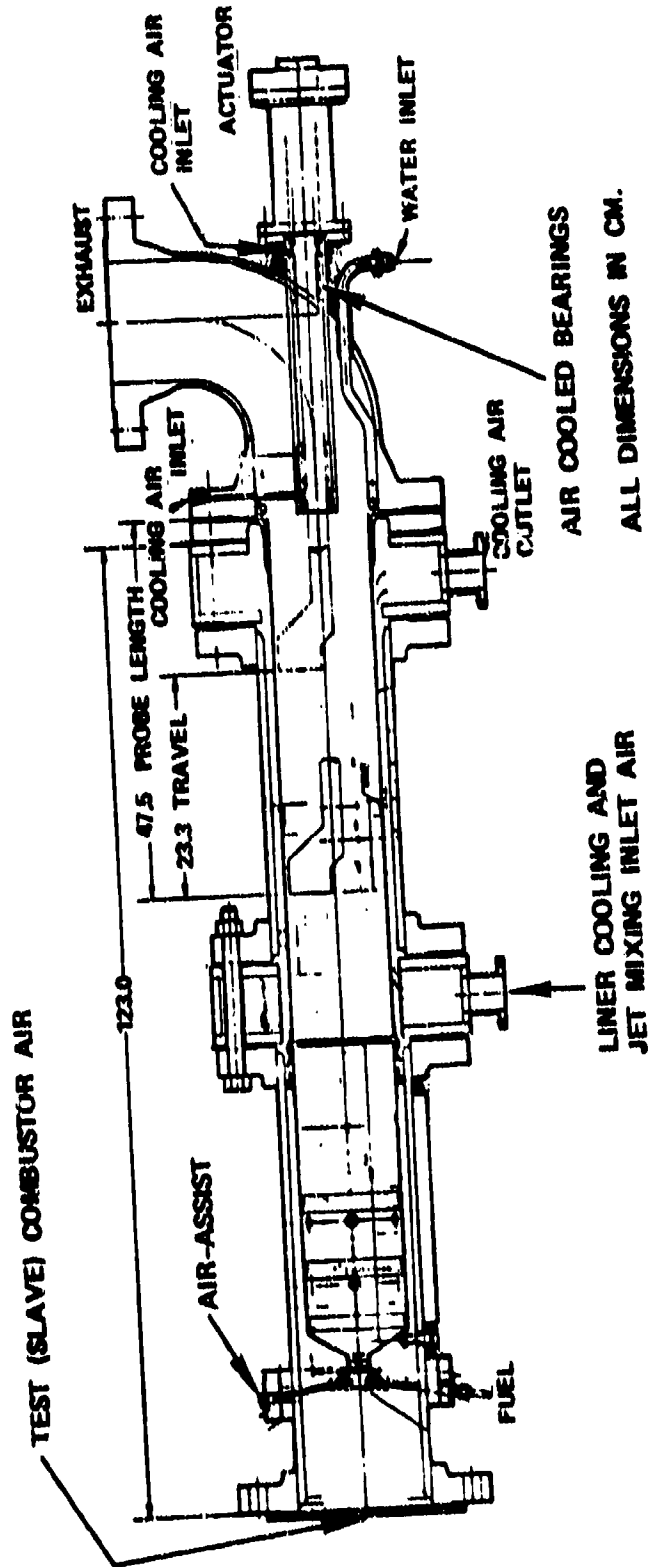
Figure 9. A Schematic Layout and Liner Cooling/Impinging Jets/Can Combustion Rig.

61

Annulus air temperatures were measured by two rows of thermo-
couples, inline and in-between the orifices, starting 1.91 mm
(one slot height) downstream from the lip. Each row consisted
of 11 chrome/alumel (CA) thermocouples of 1.02 mm diameter.
The axial locations of the annulus air thermocouples, as
measured from the cooling-slot lip, are listed in Table 2.
The annulus air temperature was maintained close to ambient
so as to minimize the heat loss to the surroundings.

The initial internal velocity and temperature profiles were
measured at 3.81 mm downstream from the lip. Velocity was
calculated by taking P_t traverses and using a wall static tap.
A Kiel probe was used for measuring the P_t profile. Internal
temperature profiles were measured by a CA thermocouple rake,
which had two degrees of freedom (along the axial and circum-
ferential directions). The rake was mounted on a 2.54 cm diam-
eter water/air cooled shaft operated by an actuator shown in
Figure 10. This actuator, operated by a 24-volt dc motor, can
traverse an axial distance of 30.5 cm, with an angular sweep of
180 degrees.

The slave combustor-discharge temperature profile was quite
acceptable, with a pattern factor of 0.08, at a combustor
temperature rise of 1068K. Figures 11 and 12 show the rig setup
in the combustion test cell. The same rig was modified to
conduct other element tests as described in Sections IV.B through
IV.G.

2.   Performance of Conventional Film/Convection Cooling Scheme

The performance of a typical cooling film band, shown
in Figure 13, was measured at the different flow conditions
given in Table 2. The cooling band has 60 equally-spaced
orifices of 2.31 mm diameter, giving a total geometric area of
252 mm^2. The slot height is 1.91 mm, and the corresponding
slot open area-to-orifices area ratio is 2.90. The orifice

62

TABLE 2.   AXIAL LOCATION OF ANNULUS AIR AND
WALL THERMOCOUPLES.

Station No.	Axial Distance, mm
1	1.91
2	5.72
3	11.43
4	17.15
5	22.86
6	28.58
7	38.10
8	47.63
9	57.15
10	66.68
11	76.20

ATTACHMENT TO RIG

ELECTRICAL SUPPLY

COUNTER
ROTATIONAL
MOTION

LIMIT SWITCH
ROTATIONAL MOTION

LIMIT SWITCH
AXIAL MOTION

COUNTER
AXIAL MOTION

ATTACHMENT TO
INSTRUMENTATION SHAFT
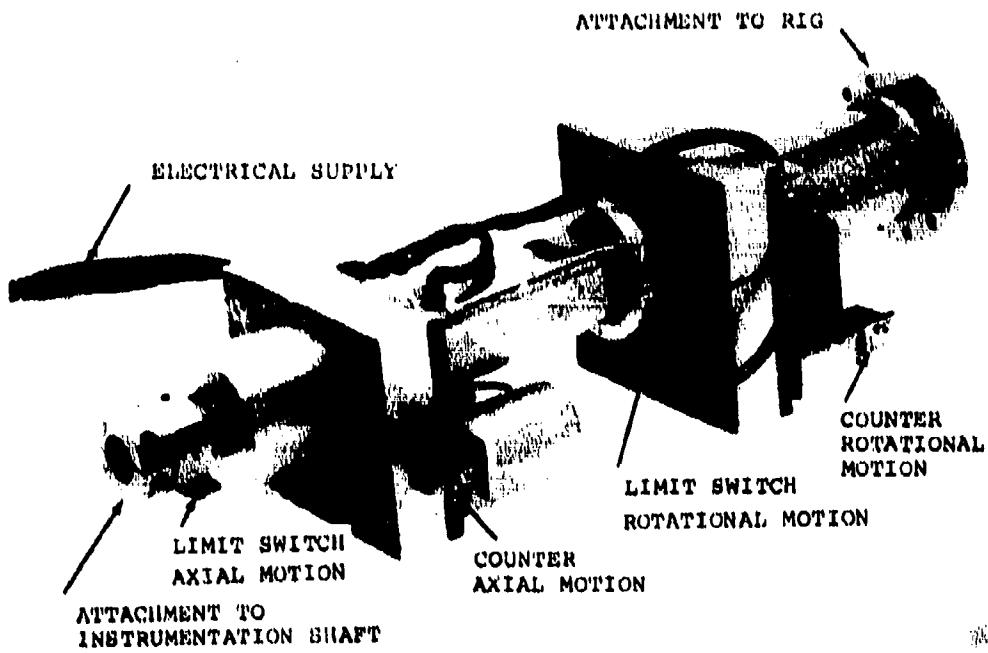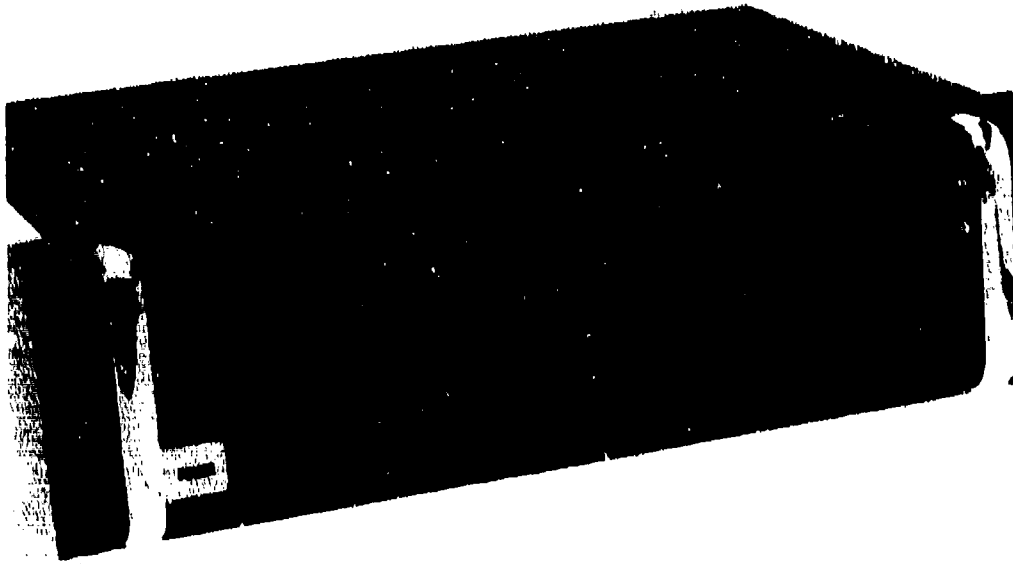
Figure 10. Probe Actuator.

64
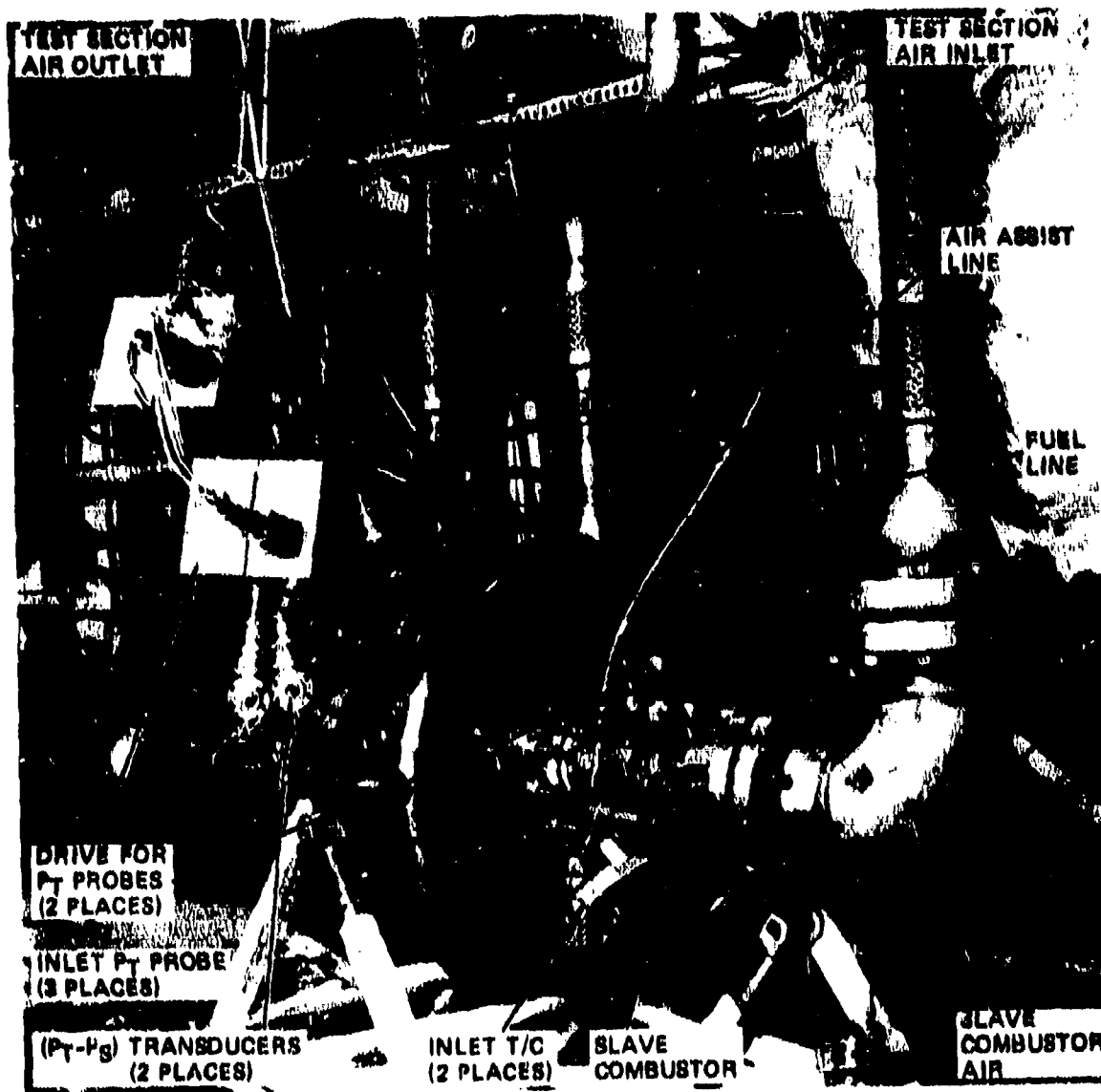
Figure 11. Liner Cooling/Impinging Jets/Can Combustor Rig.

ANNULUS AIR T/C's
(22 PLACES)

ACTUATOR

WATER SUPPLY
ELBOW COOLING

SLAVE COMBUSTOR
AIR FLOW

INLET ANNULUS
AIR STATIC PRESSURE
(4 PLACES)

Figure 12.   Liner Cooling/Impinging Jet Test Section.

66

SLOT HEIGHT = 1.91 mm
SLOT TO METERING AREA RATIO = 2.9
LIP THICKNESS = 1.02 mm
CAN DIAMETER = 12.66 cm

60 - 2.31 mm HOLES IN ONE ROW
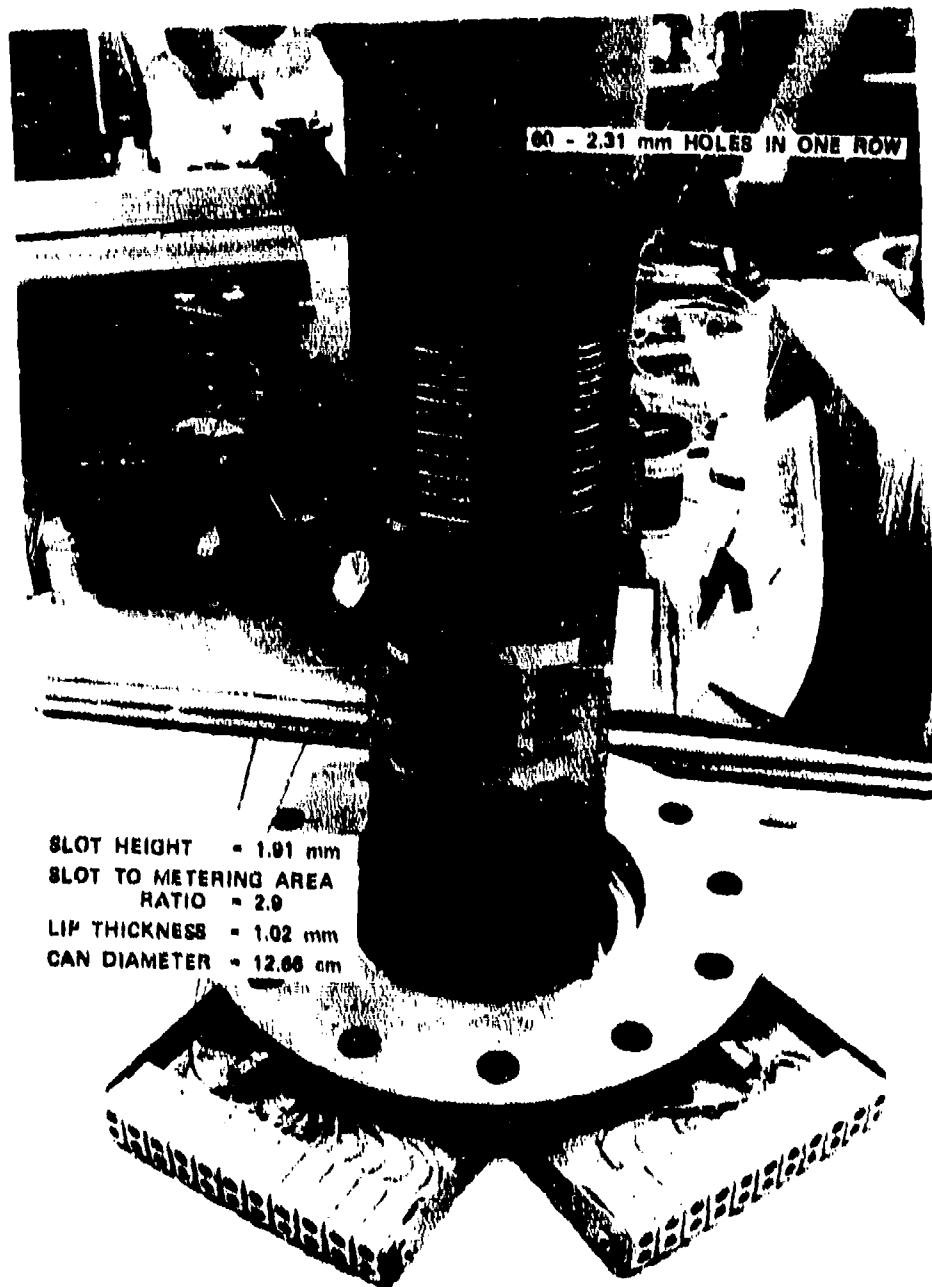
Figure 13.   Conventional Film/Convection Cooling Scheme.

spacing, based upon the can diameter of 12.66 cm, is 2.87 hole
diameters. The cooling-band lip is located 6.86 mm downstream
from the center of the metering orifices, giving an axial length
of 3 diameters for the impinging jets to spread before exiting
the impingement plate. The lip thickness is 0.53 times the slot
height. Twenty two CA thermocouples were tack welded to the
liner wall and covered by a nichrome strip to minimize convection
heat loss from the junction. The thermocouples were placed
inline and in-between the metering orifices, shown in Figure 13,
covering a total distance of 762 mm downstream from the lip, or
approximately 40 slot heights. Thus wall-temperature measure-
ments were made for the region of interest in a typical com-
bustor liner.

Table 3 tabulates the test conditions for which the
liner wall-temperature measurements were made. The hot-stream
flow conditions including density and velocity were maintained
relatively constant, as shown in the table. The test-section
pressure was varied independently, thus setting pressure drop
across the cooling orifices from 0.81 to 5.88 percent of the
test-section pressure (identified here as annulus pressure).
The corresponding jet velocity ratios varied from 0.86 to 2.37.
The annulus air velocity was kept around 20 m/s. The parameters
of general interest are listed such as the ratios of density,
velocity, mass velocity, and momentum. It can be seen that the
measurements were made over a wide range of parameters for the
density ratio normally encountered in the primary zone of gas
turbine combustors.

Figures 14 and 15 give the measured wall temperatures along
planes inline and in-between the metering holes for all five sets
of data. The figures also show the fluctuations in wall-
temperature values, as obtained over more than 10 scans of
internal-profile measurements. Table 4 presents the measured
data in terms of "film effectiveness" defined as:

$$n_F = \frac{T_{hot} - T_{wall}}{T_{hot} - T_{ann}}$$

TABLE 3. TEST CONDITIONS FOR CONVENTIONAL FILM COOLING.

	Set-1	Set-2	Set-3	Set-4	Set-5
Hot Stream					
Airflow, kg/s	1.412	1.417	1.417	1.411	1.414
Temperature, K	1270	1270	1270	1270	1270
Pressure, kPa	974	976	976	977	976
Velocity, m/s	43.4	43.5	43.5	43.3	43.4
Cold Stream					
Orifice pressure drop, % P_{ann}	0.81	1.63	2.63	4.25	5.88
Cooling Airflow, kg/s	0.0853	0.1225	0.1562	0.1998	0.2368
Temperature, K	295	293	293	295	295
Annulus Velocity, m/s	22.9	22.0	21.4	20.7	20.1
Parameters					
ρ_{SLOT}/ρ_{HOT}	4.30	4.33	4.34	4.31	4.31
V_{jet}/U_{HOT}	0.86	1.22	1.55	2.01	2.37
$(\rho V)_{jet}/(\rho U)_{HOT}$	3.69	5.28	6.73	8.65	10.23
$(\rho V^2)_{jet}/(\rho U^2)_{HOT}$	3.16	6.43	10.45	17.37	24.28
U_{slot}/U_{hot}	0.296	0.420	0.536	0.693	0.819
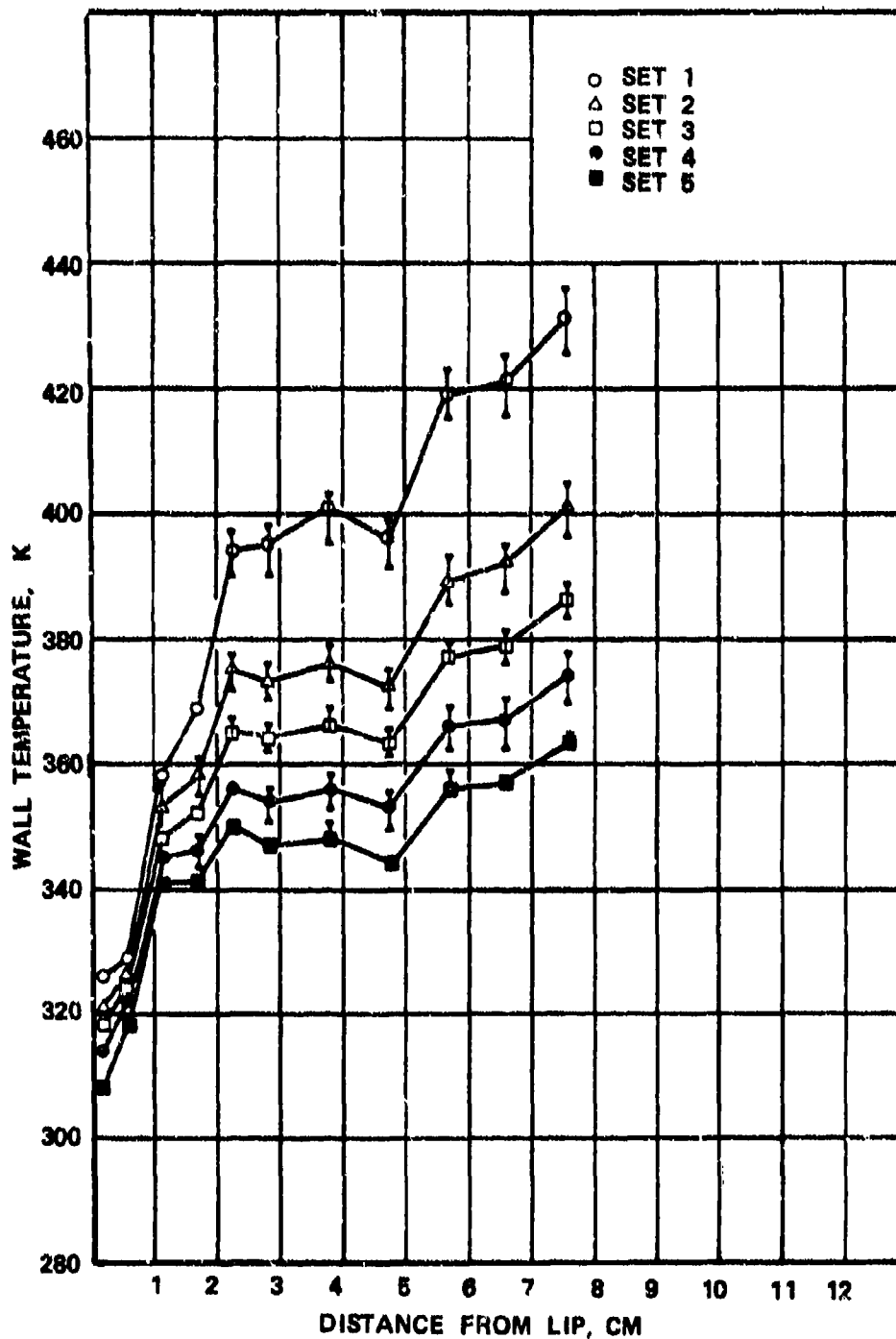
Figure 14. Measured Wall Temperatures of Conventional
Film In Line With Orifice.

70
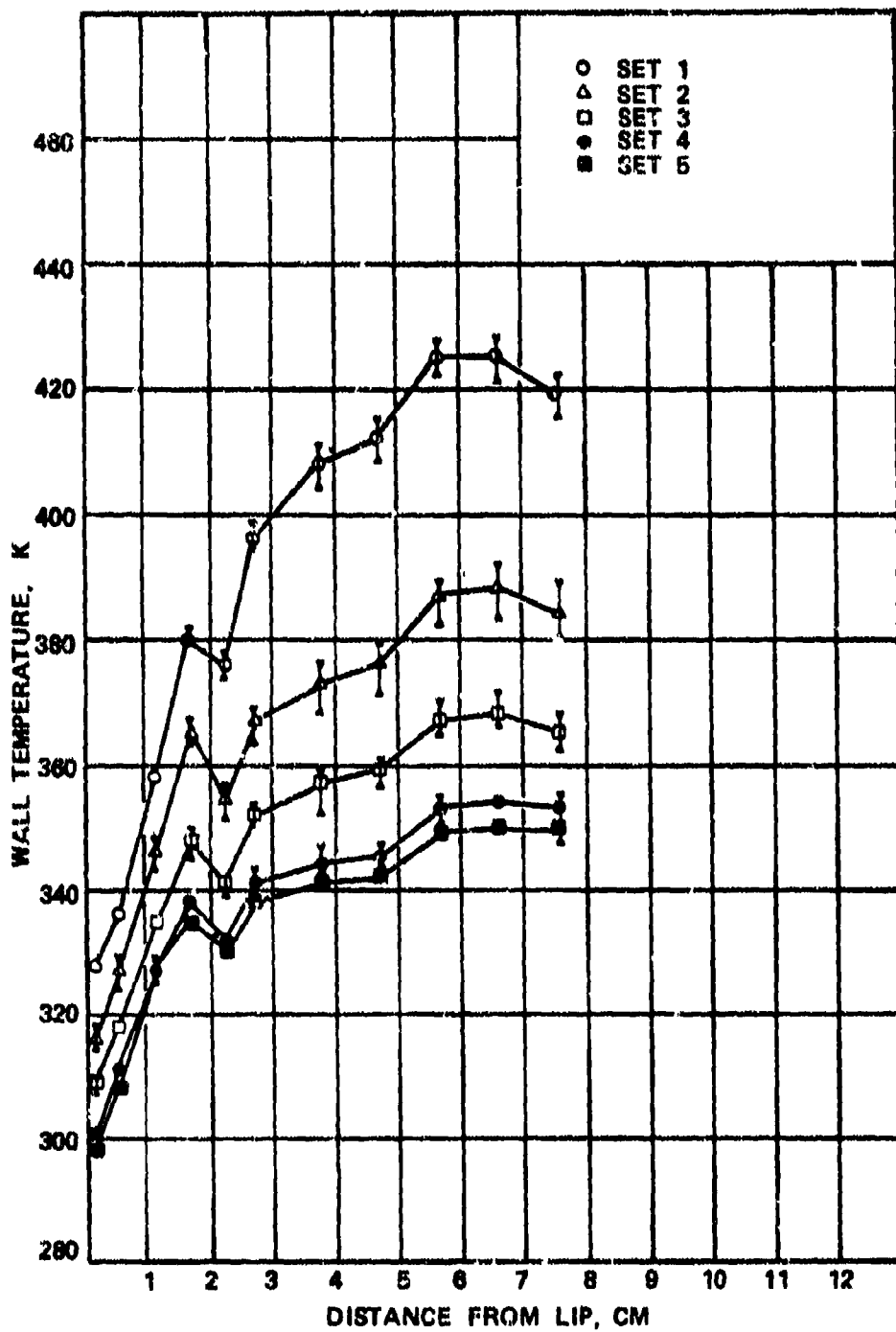
Figure 15. Measured Wall Temperatures of Conventional Film In Between Cooling Orifices.

71

TABLE 4. MEASURED "FILM EFFECTIVENESS" OF CONVENTIONAL FILM COOLING SCHEME.

Inline with Cooling Orifice

T/C #	Axial Dist. X/S	Film Effectiveness, η_f				
		Set 1	Set 2	Set 3	Set 4	Set 5
1	1.0	0.968	0.971	0.974	0.981	0.987
2	3.0	0.965	0.966	0.968	0.972	0.976
3	6.0	0.935	0.939	0.944	0.949	0.953
4	9.0	0.924	0.933	0.940	0.948	0.953
5	12.0	0.898	0.916	0.926	0.937	0.944
6	15.0	0.897	0.918	0.927	0.939	0.947
7	20.0	0.891	0.915	0.925	0.937	0.946
8	25.0	0.896	0.919	0.928	0.941	0.950
9	30.0	0.873	0.902	0.914	0.927	0.937
10	35.0	0.871	0.899	0.912	0.926	0.936
11	40.0	0.861	0.889	0.905	0.919	0.930

In-Between Cooling Orifices

T/C #	Axial Dist. X/S	Film Effectiveness, η_f				
		Set 1	Set 2	Set 3	Set 4	Set 5
12	1.0	0.966	0.976	0.984	0.994	0.997
13	3.0	0.958	0.965	0.974	0.984	0.987
14	6.0	0.935	0.946	0.957	0.967	0.967
15	9.0	0.913	0.931	0.944	0.956	0.958
16	12.0	0.917	0.938	0.951	0.962	0.964
17	15.0	0.896	0.924	0.940	0.953	0.956
18	20.0	0.884	0.918	0.934	0.950	0.953
19	25.0	0.880	0.915	0.933	0.949	0.952
20	30.0	0.867	0.904	0.924	0.941	0.945
21	35.0	0.867	0.903	0.923	0.939	0.944
22	40.0	0.873	0.907	0.926	0.941	0.944

It was observed that the η_F variation between the two
θ-planes is quite small, and that the cooling jets had picked
up heat from the splash plate to give effectiveness less than
1.0 at the first axial station (located one slot downstream
from the lip). In order to facilitate a comparison with
other researchers, it was therefore assumed that the cooling-film
temperature at the lip exhaust is equal to the wall temperature
at $\frac{X}{S} = 1.0$.

The modified film-effectiveness data for the plane in line
with the orifice is presented in Figure 16. The annulus air-
temperature rise over the test-section length of 76 mm was
approximately 5K for Set-1, and approximately 0 for Set-5,
indicating that the system was close to the adiabatic assumption.
Nevertheless, the main objective of the liner-cooling tests was
to show relative comparison between the various cooling schemes,
followed by a can-combustor demonstration of the most promising
schemes, as summarized in Section IV.A.F. Consequently, small
errors in measured film effectiveness due to nonadiabacity of
the system was not considered so critical.

The measured data (Figure 16) illustrates the effect of
slot-to-main velocity ratio on the performance of the conven-
tional film-cooling scheme. The film effectiveness for the
smallest velocity ratio of 0.296 decreases to 0.89 at 40
slot distance downstream from the lip. As the velocity ratio
increases, the film effectiveness improves, giving 0.94 at a
velocity ratio of 0.819. Burns and Stollery reported only a
limited amount of impervious film-effectiveness data for the
region close to the lip (Figure 16) for a velocity ratio of
unity. Their data is comparable to the measurements of this
program.

Design correlations for clean, 2-D cooling slots in low-
turbulence levels and low-temperature-difference applications
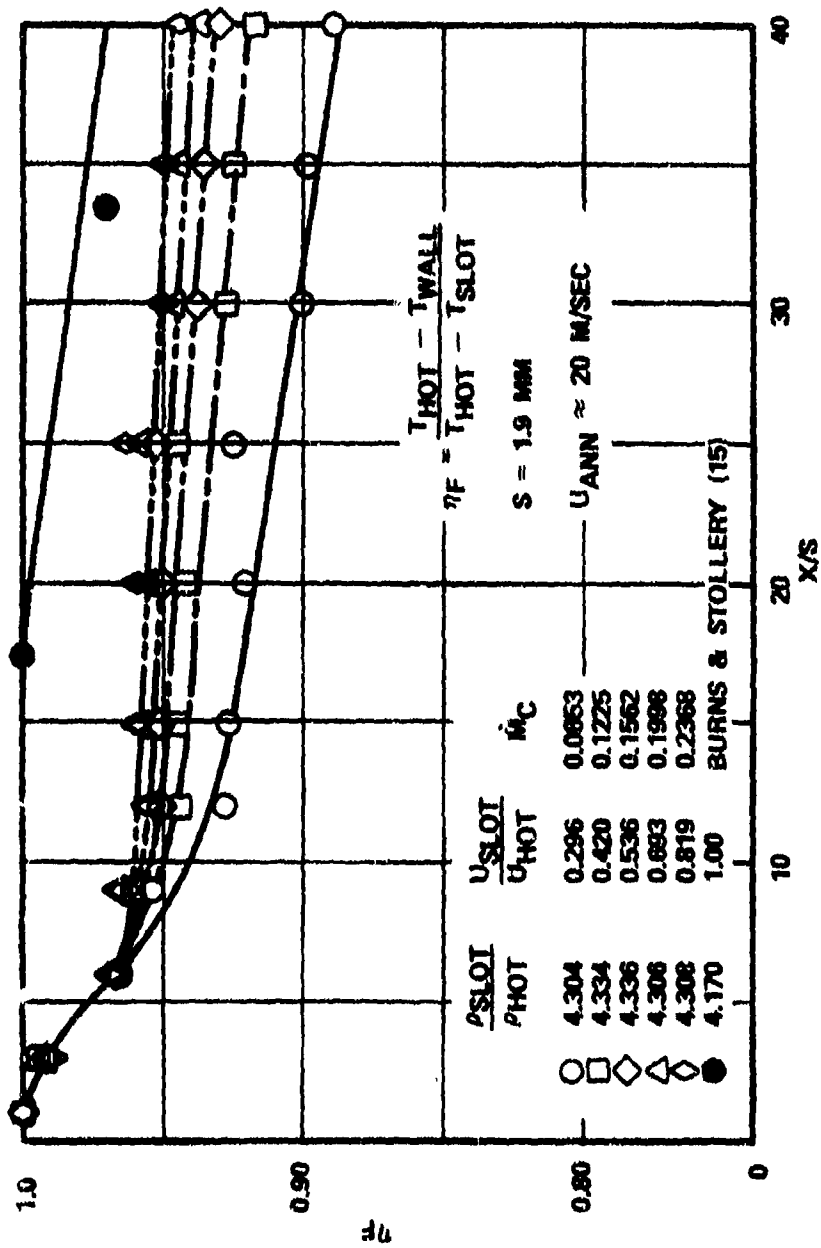
Figure 16. Film Effectiveness of Conventional Film Cooling Scheme and Comparison with Burns and Stollery Data.

74

are well established, shown in Figure 17 (taken from Goldstein[16]). The correlating parameter $X/S \, M \, Re_s^{1/4}$ has not been verified for the region less than 2 due to the lack of data. The present data is plotted in Figure 18, indicating the applicability of the correlation with practical cooling geometries, with typical parameters of interest to a combustion engineer.

3. <u>Performance of Impingement Film/Convection-Cooling Scheme</u>

An impingement film-cooling scheme is a simple extension of a conventional film-cooling scheme in that a longer impingement plate is used. The splash-plate cooling is accomplished by the impinging rows of jets. Therefore, the temperature of the cooling film exiting the lip is generally higher than that of a conventional cooling film, with attendent loss in the film effectiveness of the former scheme. The objectives of the test series were to document the degradation in the film effectiveness downstream from the lip, compared to conventional film, and to make limited wall-temperature measurements of the splash plate.

A simple impingement-film configuration was selected, as shown in Figure 19. The splash plate was similar to that of the conventional film except for length. The lip is located 22.1 mm from the center of the first row of orifices, compared to 6.46 mm for the film-cooling geometry. It has three staggered orifice rows, as shown, consisting of a total of 180 holes of 1.24 mm, with circumferential spacing of 5.35 mm hole diameters, and axial spacing of 6.71 mm diameters. The total geometric area of 219 mm^2 is slightly less than that of the film-cooling band 252 mm^2. The slot-to-orifice area ratio is 3.33 mm.

---

[16]Goldstein, R.J., "Film Cooling," Advances in Heat Transfer V. 7 (1971).
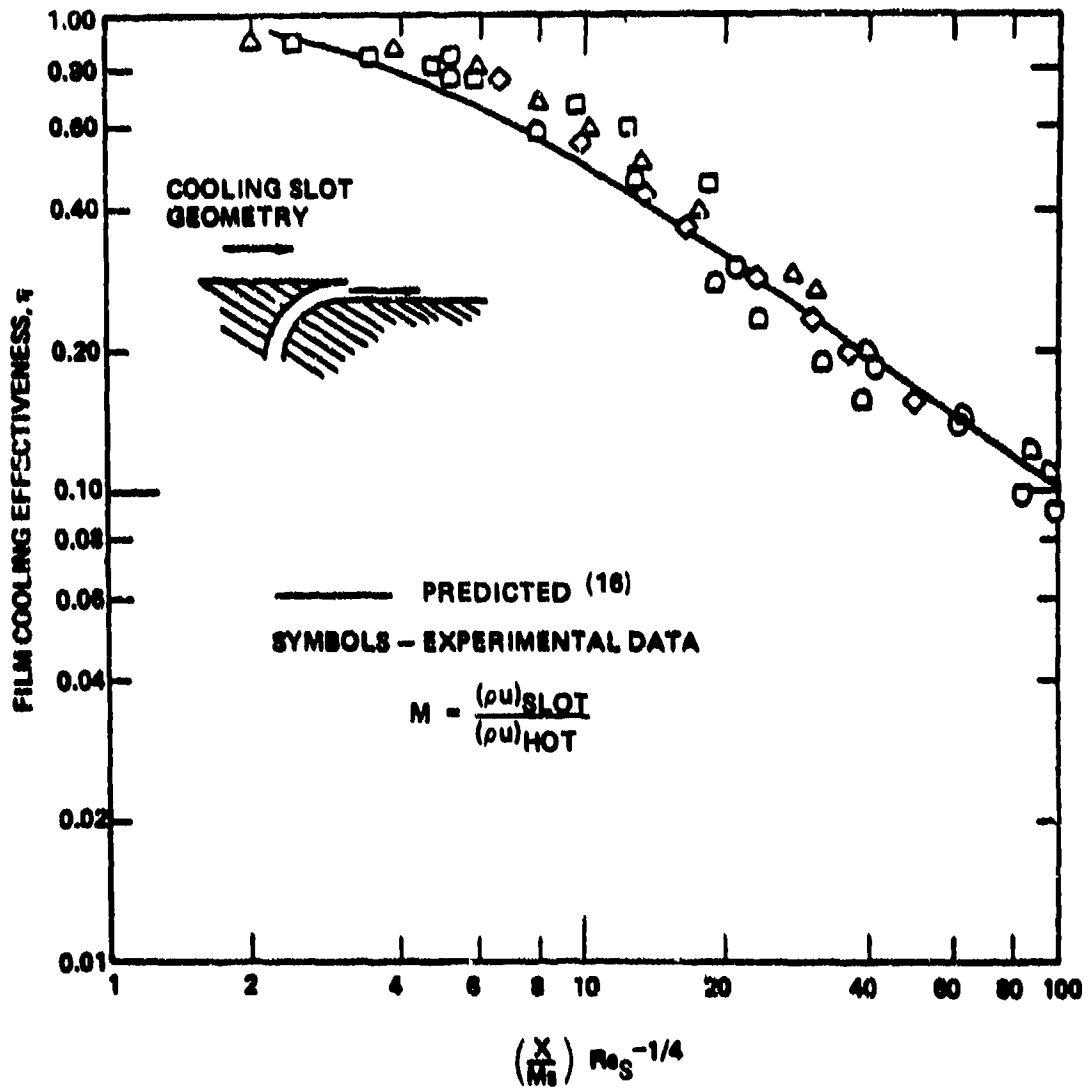
Figure 17. Film Cooling Effectiveness Measured
in Low ΔT and Turbulence Level
Environment.
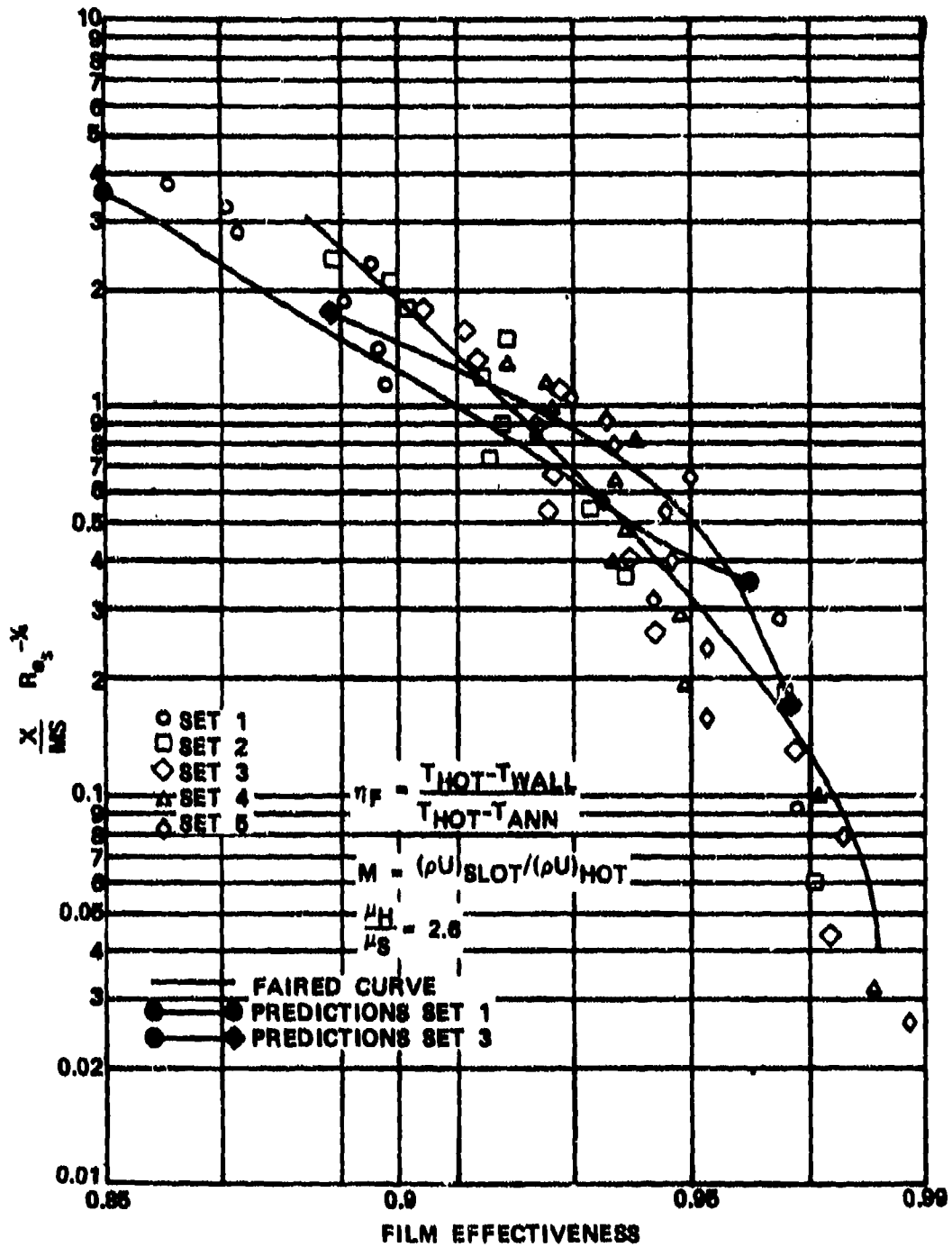
Figure 18. Film Effectiveness of Conventional Film Cooling Scheme.

77

Figure 19.   Impingement Film/Convection Cooling Scheme.

78

The wall temperatures downstream of the lip were measured
by 22 CA thermocouples, similar to those used in the conven-
tional film. Five thermocouples of 0.5 mm diameter were
welded on the inside of the splash plate, as shown in Figure 19
(numbered 23 through 27), to measure wall temperatures directly
under the radial jets, and at two axial stations in between the
three rows. Data on wall temperatures was taken for the test
conditions listed in Table 5. Twelve sets of data were taken
with the slot-to-main stream velocity ratios varying from 0.27
to 0.90, and the density ratio varying from 1.8 to 4.3.

Figure 20 shows a typical wall temperature of the splash
plate as a function of axial distance from the center of the
first row of orifices, with orifice pressure drop and density
ratio as parameters. The wall-temperature levels follow a saw-
tooth profile, and there is a decrease in wall temperatures
with an increase in pressure drop. The effectiveness defined
in a manner similar to film effectiveness is comparable to the
performance of a typical cooling slot at approximately 40 slot-
heights downstream from the lip, as shown in Table 3. The
corresponding performance of the cooling film exiting from the
slot is shown in Figure 21.

As shown by Figure 21 the film effectiveness of the
impingement/film configuration in the region downstream from
the lip is lower than that of the conventional film (Table 3).
This can be explained partly by observing that the film tempera-
ture at the lip is slightly higher with the impingement config-
uration. The modified film-effectiveness variation with X/S
is shown in Figure 22 by assuming that the film temperature at
the lip is equal to wall temperature at $\frac{X}{S}$ = 1.0.

The performance of both films is comparable, as inferred
from Figures 16 and 22, although the impingement/film is slightly

TABLE 5. TEST CONDITIONS FOR IMPINGEMENT/FILM COOLING SCHEME.

Parameters	Set-1	Set-2	Set-3	Set-4	Set-5	Set-6	Set-7	Set-8	Set-9	Set-10	Set-11	Set-12
Hot Stream												
Airflow, kg/s	1.4.6	1.411	1.410	1.413	1.415	1.414	0.273	0.273	0.272	0.273	0.274	0.274
Temperature, K	1276	1270	1270	1270	1270	1270	1097	1105	1112	1107	1102	1106
Pressure, kPa	975	977	976	975	976	975	196	197	197	196	196	196
Velocity, m/s	43.5	43.3	43.2	43.5	43.4	43.4	36.1	36.2	36.3	36.5	36.4	36.5
Cold Stream												
Pressure Drop, %	0.89	1.87	2.76	4.88	6.59	9.17	0.34	0.85	1.52	0.51	1.02	1.53
Cooling Airflow, kg/s	0.0825	0.1159	0.1458	0.1845	0.2316	0.2777	0.00714	0.01126	0.01509	0.01057	0.01483	0.01805
Temperature, K	292	293	295	294	292	296						
Annulus Velocity, m/s	22.6	22.0	21.7	20.8	20.8	19.0						
Parameters												
ρ_{SLOT}/ρ_{HOT}	4.35	4.34	4.30	4.32	4.35	4.38	1.82	1.82	1.83	2.69	2.63	2.61
V_{jet}/U_{HOT}	0.90	1.31	1.61	2.12	2.51	3.00	0.96	1.52	2.43	0.96	1.37	1.69
$(\rho V)_{jet}/(\rho U)_{HOT}$	3.89	5.68	6.91	9.17	10.91	13.12	1.75	2.76	3.71	2.59	3.62	4.40
$(\rho V^2)_{jet}/(\rho U^2)_{HOT}$	3.49	7.44	11.10	19.45	27.40	29.35	1.68	4.18	7.53	2.49	4.97	7.43
U_{SLOT}/U_{HOT}	0.27	0.39	0.48	0.64	0.75	0.94	0.29	0.46	0.61	0.29	0.41	0.51
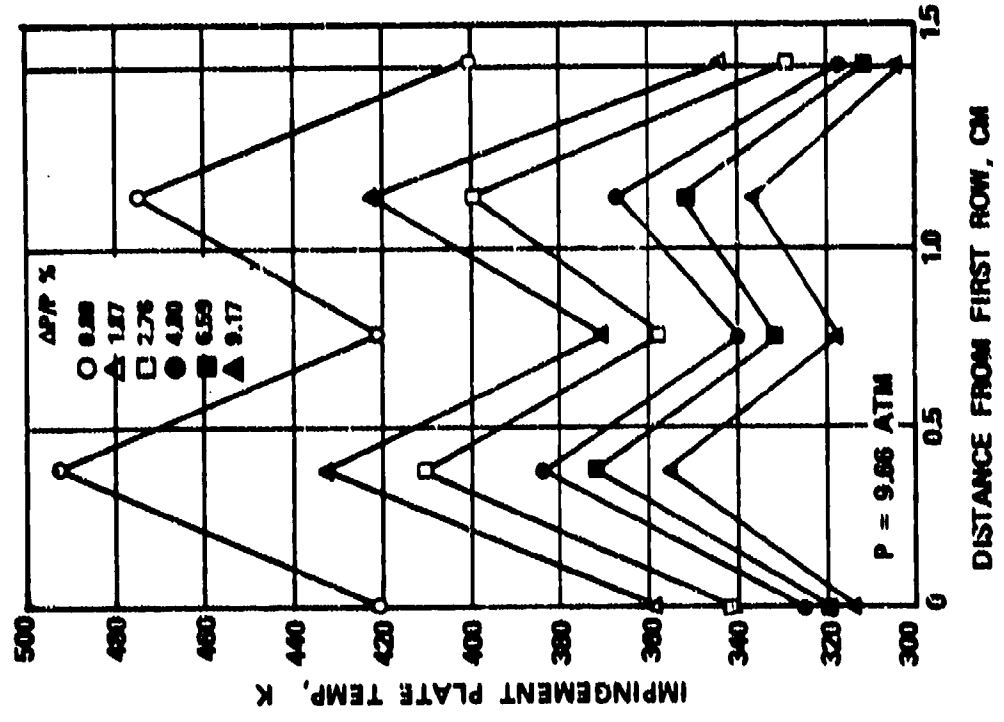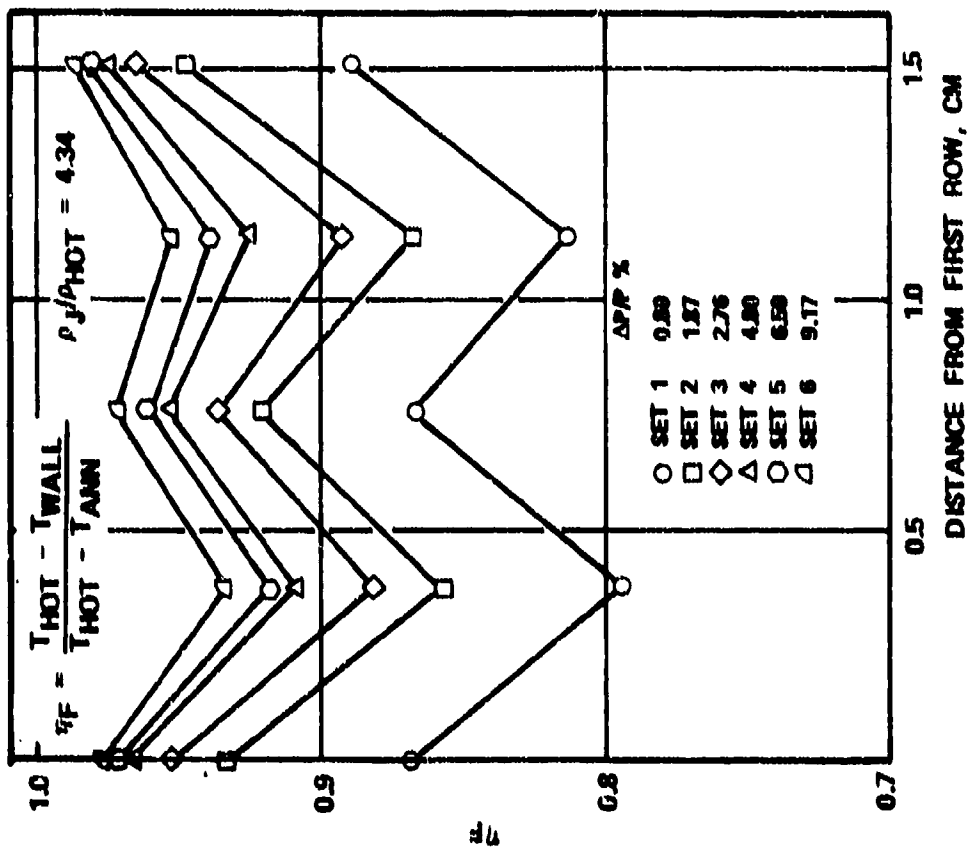
Figure 20. Performance of Splash Plate of the Impingement/Film Configuration.
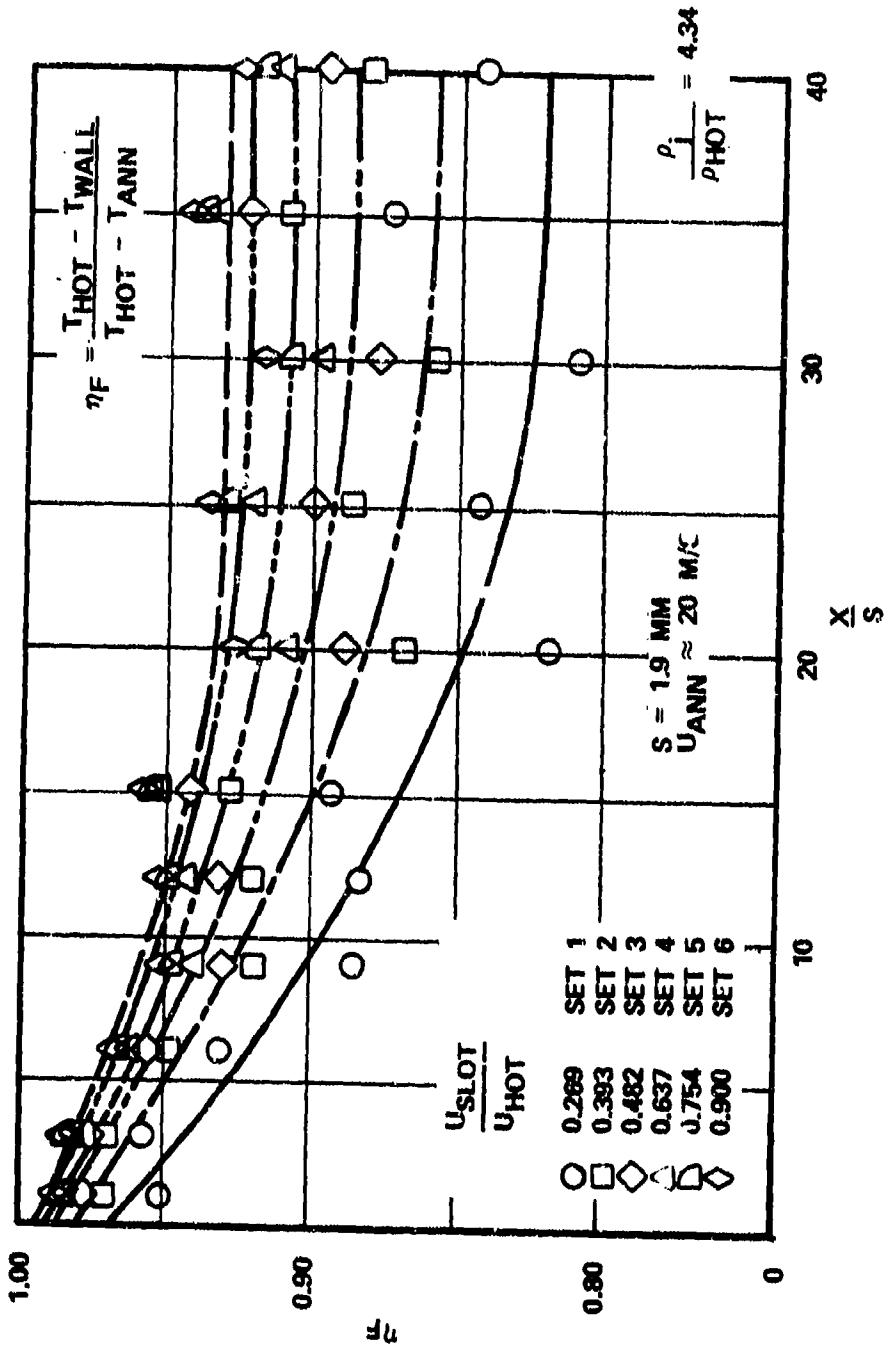
Figure 21. Performance of the Film of Impingement/Film Configuration.

82
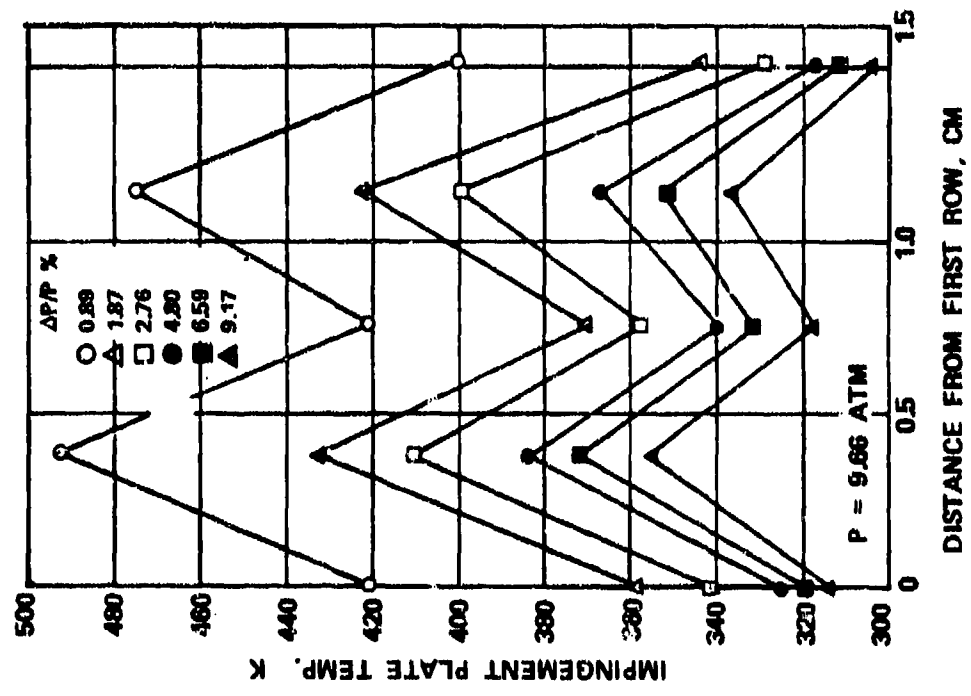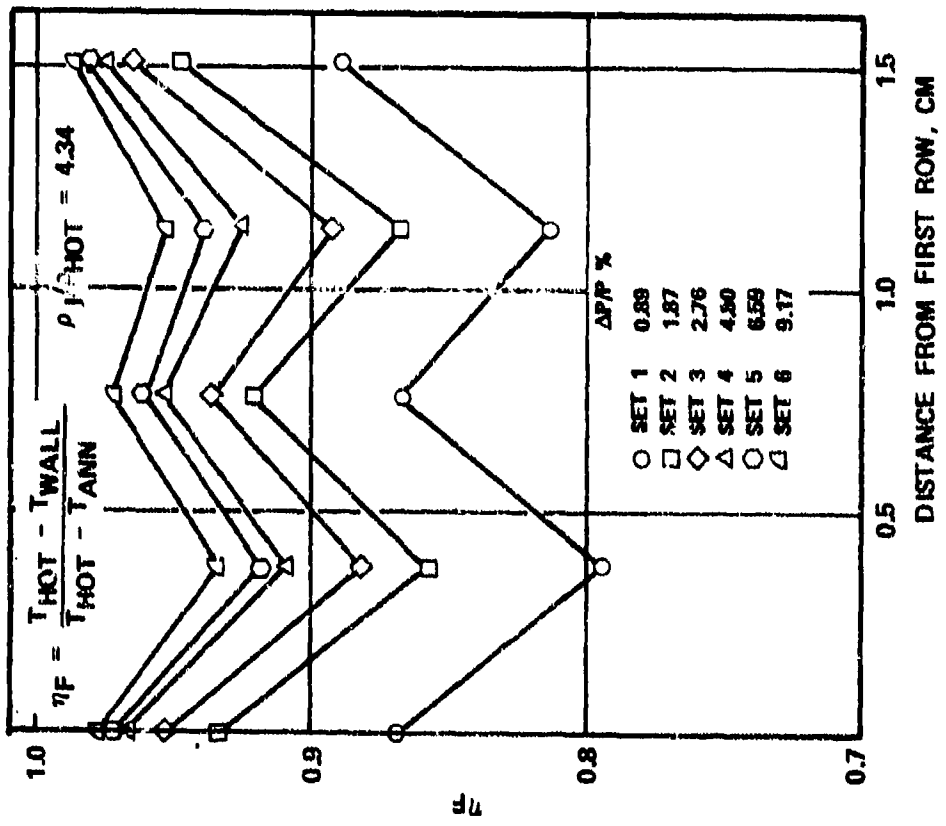
Figure 20.   Performance of Splash Plate of the Impingement/Film Configuration.
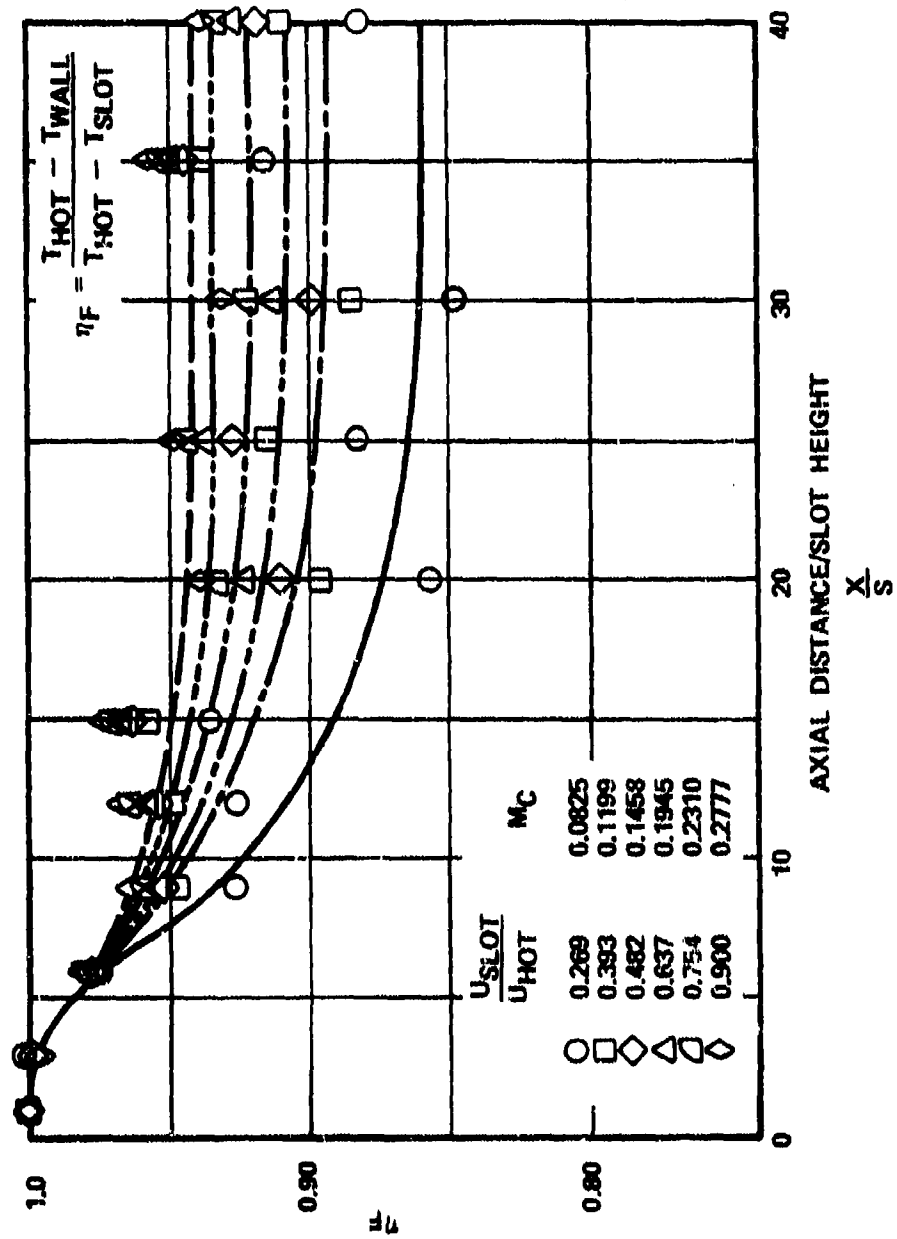
Figure 22. Performance of Impingement/Film Cooling Scheme.

83

inferior. However, a total distance of 9.83 cm is being protected by the impingement/film, as compared to 8.31 cm with the conventional film configuration--which in turn reduces the cooling air requirement per unit surface area by approximately 15 percent. Another advantage of the impingement/film configuration is that the entrainment of the cooler film air by the main combustion air is delayed as compared to the conventional film, thus minimizing wall quenching with attendent improvement in idle efficiency.

The performance of the scheme for density ratios equal to 1.82 and 2.65 at low liner-pressure drop, typical of AiResearch reverse-flow annular combustors, is shown in Figure 23. The film effectiveness is significantly lowered, as expected. Finally, Figure 24 gives a design-correlation plot for the film effectiveness of the impingement/film configuration as a function of the film-correlating parameter, $X/MS \left(\frac{\mu_S}{\mu_{HOT}} Re_S\right)^{0.25}$. This figure can be compared with Figure 18 for the conventional film-cooling band performance. For obtaining comparable performance with both cooling concepts, approximately 3 percent more cooling air would be required with the impingement/film configuration. Since the surface area covered by the impingement/film band was 15-percent larger than the conventional film, the net reduction in the cooling-air requirement would be approximately 12 percent.

4. **Performance of Conventional Film/Extended Surface Convection Cooling Scheme**

The conventional film test section was modified to install an extended-surface geometry, as shown in Figure 25. The extended-surface configuration consisted of square fins of 1.57 mm height and width machined with center-to-center spacing of 5.08 mm, or 3.24 times the fin height. The fin is located 4.11 cm downstream from cooling holes, or 17.9 slot-heights
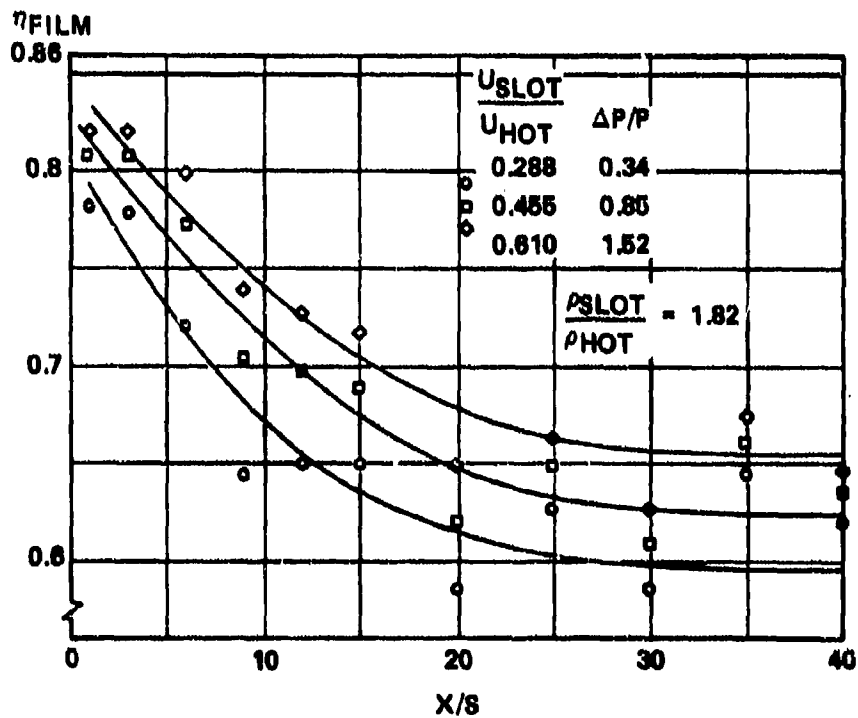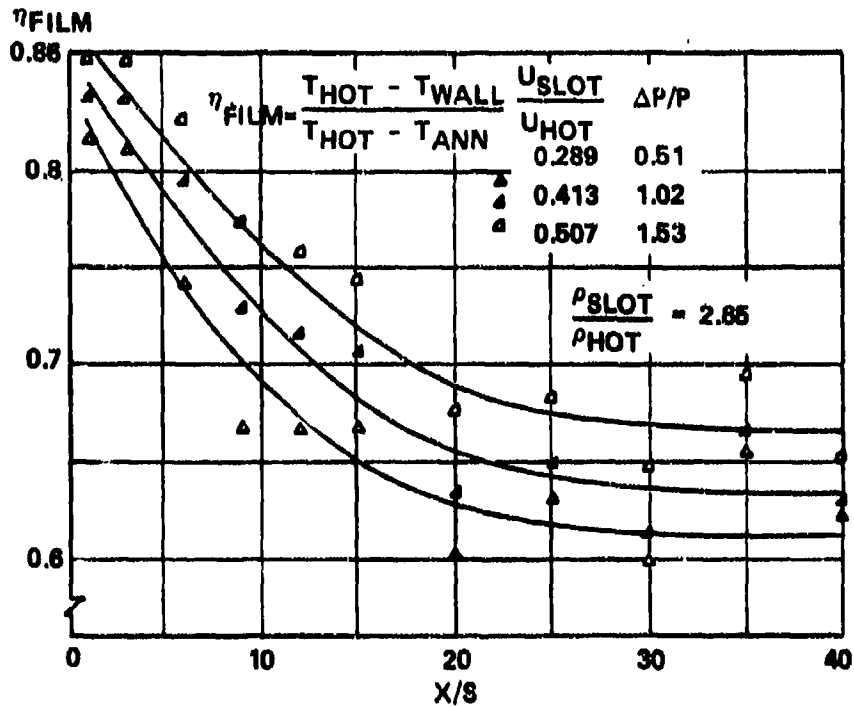
Figure 23. Film Effectiveness of Impingement/Film Cooling Scheme with Density Ratio as Parameter.
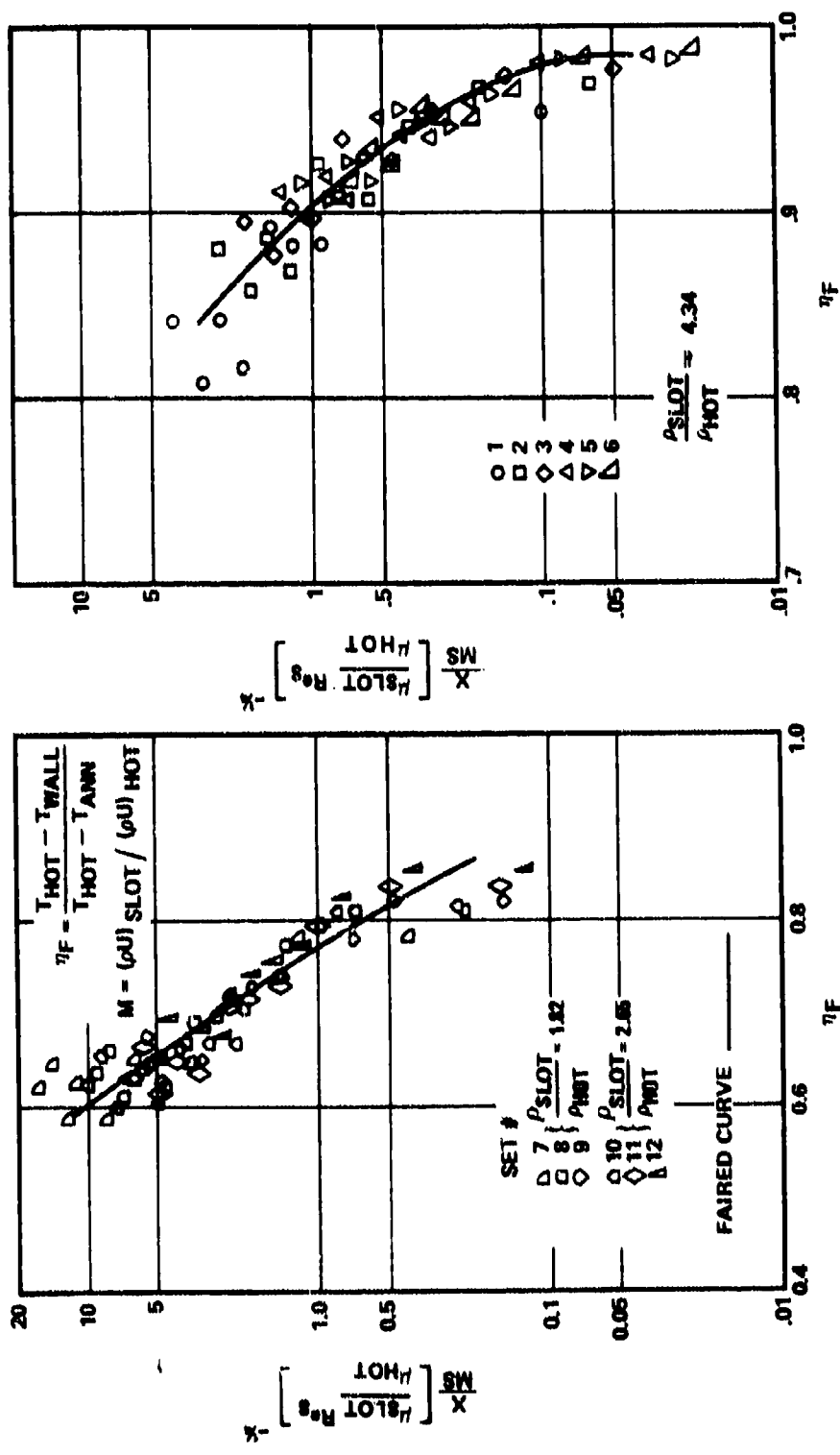
Figure 24. Performance of Impingement/Film Geometry.

86
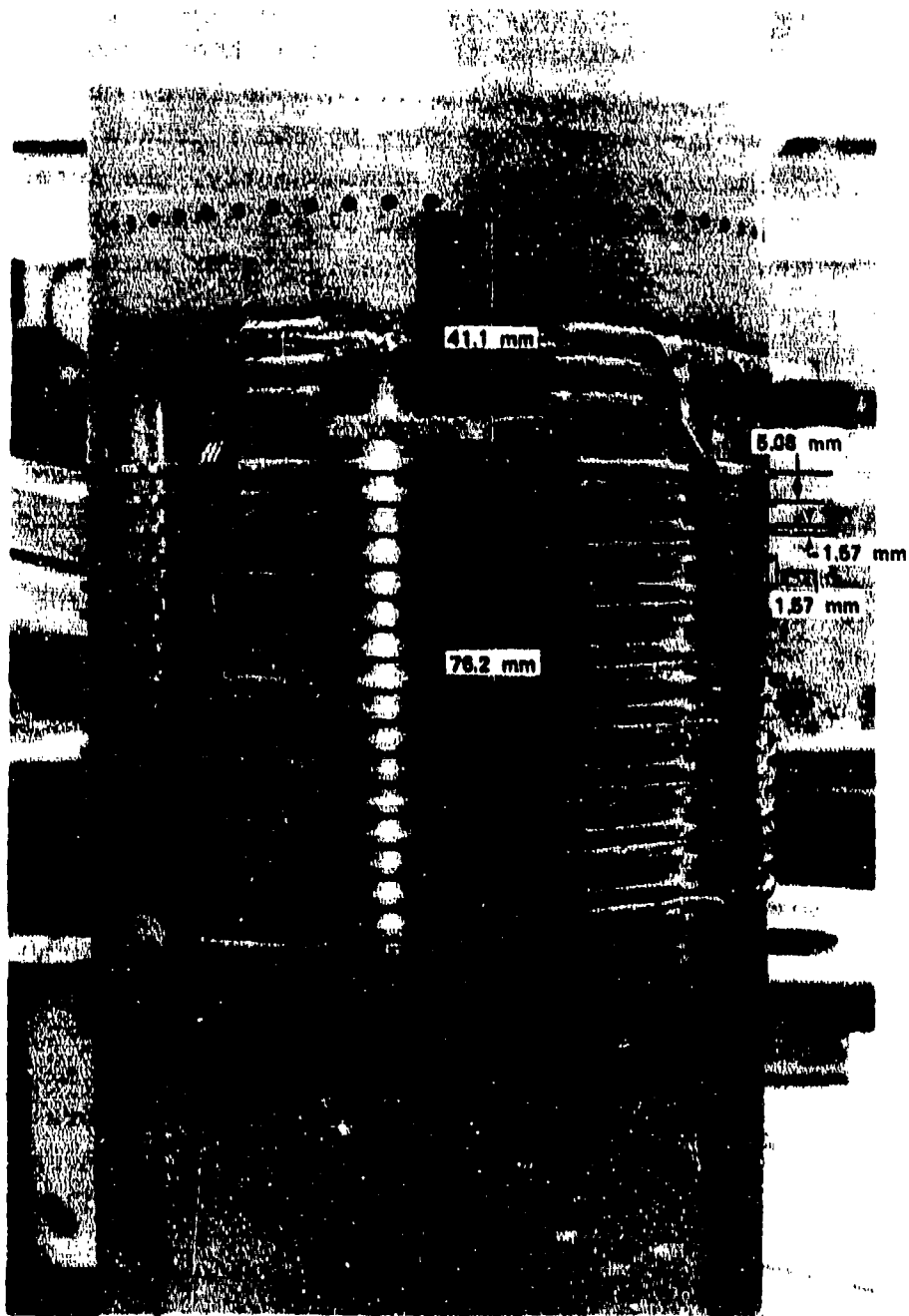
Figure 25.   Film/Extended Surface Convection Cooling Scheme.

downstream from the lip of the splash plate. Consequently, this part of the test section was protected by the cooling film. The presence of the fins increased the cold-side heat transfer. This was due to an increase in the turbulence level caused by tripping the boundary layer, and also by the increase in surface area by approximately 63 percent. Consequently, the deterioration in the film effectiveness beyond 17.9 slot-heights is compensated by the enhanced cold-side heat-transfer process.

The test section wall-temperature measurements were made for different orifice pressure drops and density ratios, as listed in Table 6. Figure 26 shows the measured film effectiveness with density and velocity ratios as parameters. The extended-surface geometry performance at 50 slots downstream from the lip was comparable to that of the conventional film at $\frac{X}{S} = 40$, as shown in Table 3. This means that the cooling air requirement with the advanced scheme is reduced by approximately 20 percent.

5.   Performance of Coarse-Pore Transpiration Cooling Scheme.

A coarse-pore transpiration cooling scheme, as shown in Figure 27, was experimentally studied at the test conditions listed in Table 7. The geometry consisted of eight staggered rows of 0.83-mm diameter orifices. Each row consists of 60 equally-spaced holes around the can of 26.66 cm diameter giving center-to-center spacing of 8 mm hole diameters. The axial spacing of the rows is 6.65 mm or 8.01 mm hole diameters, as shown in Figure 27. The total geometric area of the holes is 257 mm^2, as compared to 252 mm^2 of the conventional film-cooling scheme.

Thirty-two fine CA thermocouples of 0.51-mm diameter were tackwelded as shown in Figure 27. The thermocouples numbered 1 through 10 were placed in line with one of the orifices of the first row, whereas numbers 23 through 32 lay along a line

TABLE 6. TEST CONDITIONS FOR CONVENTIONAL FILM/
EXTENDED SURFACE COOLING SCHEME.

Parameters	Set-1	Set-2	Set-3	Set-4	Set-5	Set-6	Set-7	Set-8	Set-9
Hot Stream									
Airflow, kg/s	1.41	1.42	1.42	1.42	1.41	1.42	0.275	0.274	0.271
Temperature, K	1270	1270	1270	1270	1270	1270	1116	1115	1112
Pressure, kPa	977	977	977	977	976	976	195	196	196
Velocity, m/s	43.3	43.4	43.4	43.4	43.4	43.5	37.2	36.7	36.6
Cold Stream									
Pressure Drop, %	0.94	1.80	2.74	4.69	6.58	9.04	0.52	0.85	1.52
Cooling Airflow, kg/s	0.0933	0.1297	0.1611	0.2123	0.2523	0.299	0.0095	0.0123	0.0166
Temperature, K	290	289	288	290	293	294	608	608	606
Annulus Velocity, m/s	22.3	21.5	20.9	20.2	19.7	18.9	48.4	47.5	4.65
Parameters									
ρ_{SLOT}/ρ_{HOT}	4.38	4.39	4.41	4.38	4.34	4.32	1.84	1.84	1.84
V_{jet}/U_{HOT}	0.92	1.27	1.58	2.09	2.51	2.98	1.15	1.49	2.01
$(\rho V)_{jet}/(\rho U)_{HOT}$	4.03	5.59	6.95	9.15	10.89	12.89	2.11	2.75	3.70
$(\rho V^2)_{jet}/(\rho U^2)_{HOT}$	3.71	7.11	10.95	19.11	27.35	32.45	2.42	4.10	7.43
U_{SLOT}/U_{HOT}	0.32	0.44	0.54	0.72	0.87	1.03	0.40	0.51	0.69
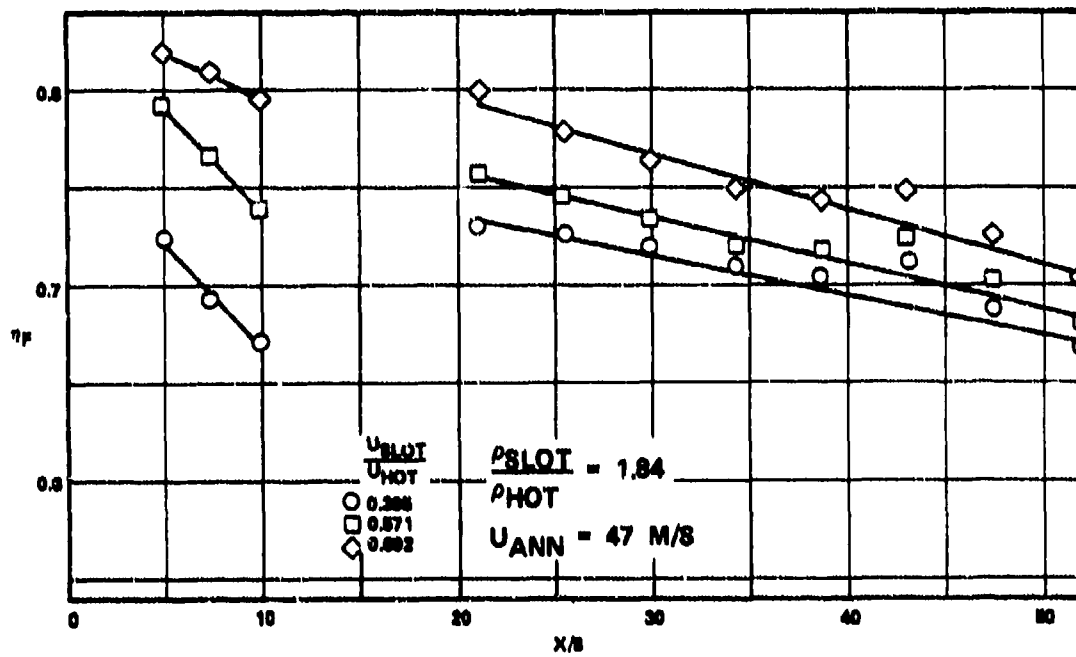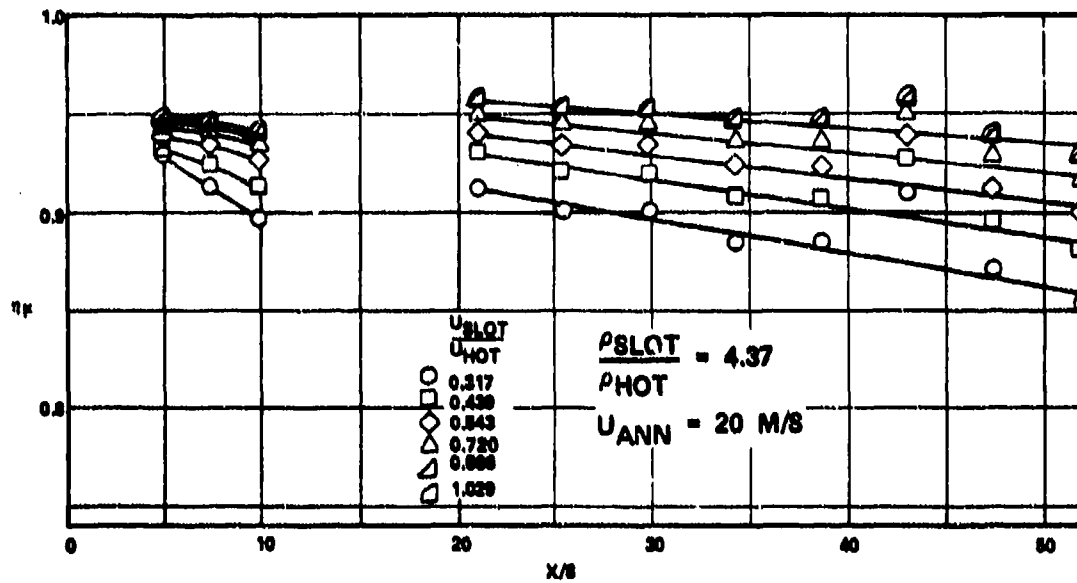
Figure 26. Performance of Film/Extended
Surface Convection Cooling Scheme.

90

Figure 27.   Coarse-Pore Transpiration Cooling Scheme.

TABLE 7. TEST CONDITIONS FOR COARSE-PORE TRANSPIRATION COOLING SCHEME.

Parameters	Set-1	Set-2	Set-3	Set-4	Set-5	Set-6
Hot Stream						
Airflow, kg/s	1.414	1.414	1.415	1.413	1.417	1.416
Temperature, K	1270	1270	1270	1270	1270	1270
Pressure, kPa	977	977	977	977	976	976
Velocity, m/s	43.4	43.3	43.4	43.3	43.5	43.4
Cold Stream						
Pressure Drop, %	0.91	1.93	2.74	4.66	6.35	9.07
Cooling Airflow, kg/s	0.0938	0.1375	0.1639	0.2171	0.2565	0.3124
Temperature, K	293	293	295	292	289	287
Annulus Velocity, m/s	22.5	21.7	21.4	20.2	19.4	18.2
Parameters						
ρ_{SLOT}/ρ_{HOT}	4.34	4.33	4.30	4.35	4.39	4.42
V_{jet}/U_{HOT}	0.91	1.33	1.60	2.10	2.44	2.96
$(\rho V)_{jet}/(\rho U)_{HOT}$	3.93	5.77	6.87	9.11	10.74	13.09
$(\rho V^2)_{jet}/(\rho U^2)_{HOT}$	3.57	7.67	10.97	19.10	26.25	38.71
$M=\dot{m}_c''/(\rho U)_{Hot}$	0.0436	0.0639	0.0762	0.101	0.119	1.145

$\dot{m}_c''$ = Cooling flow rate based upon the test section length of 4.66 cm.

in between the orifices. Figure 28 shows typical wall temperatures measured along lines A and B marked on Figure 27. There are only minor differences in the overall performance along both lines. Figure 29 shows the computed film effectiveness versus X/d along line A, with orifice-pressure drop as a parameter. η_F increased with $\frac{X}{d}$ due to addition of cooling air from different rows. The increase in η_F continues approximately 10 orifice diameters beyond the last row of holes, as shown in Figure 29. However, beyond that, there is exhibited a decrease in η_F. There is an increase in η_F with increasing ΔP and attendent blowing parameter ($\frac{\dot{m}_c "_F}{\rho_{Hot} U_{Hot}}$) up to 2.74 percent, beyond which the jets overpenetrate with resulting loss in η_F.

Recently LeBrocq,[17] et al., reported their experimental data on a coarse-pore transpiration-cooling geometry comprised of 1.59 mm diameter orifices drilled in a flat plate at a 8 hole diameter spacing. Figure 30 shows typical results or the impervious wall effectiveness as a function of the blowing parameter (M) with density ratio as a parameter. With freon (ρ_s/ρ_∞ = 4.23), the maximum effectiveness was obtained at M=0.0625, as compared to M=0.0762 in the present study. The variation of η_C with X is also given in Figure 30, showing an increase in η_C with X, similar to that measured in the present study.

The limited amount of measured data on the coarse-pore transpiration configuration indicated that the scheme is quite suitable with a low-pressure drop combustion system up to a momentum ratio of around 11. However, the performance is quite inferior compared to other schemes investigated. Its use

[17]LeBrocq, P.V., B.E. Launder, and C.H. Priddin, "Discrete Hole Injection as a Means of Transpiration Cooling; An Experimental Study," Proceeding Instn. Mech. Engrs., 1973.
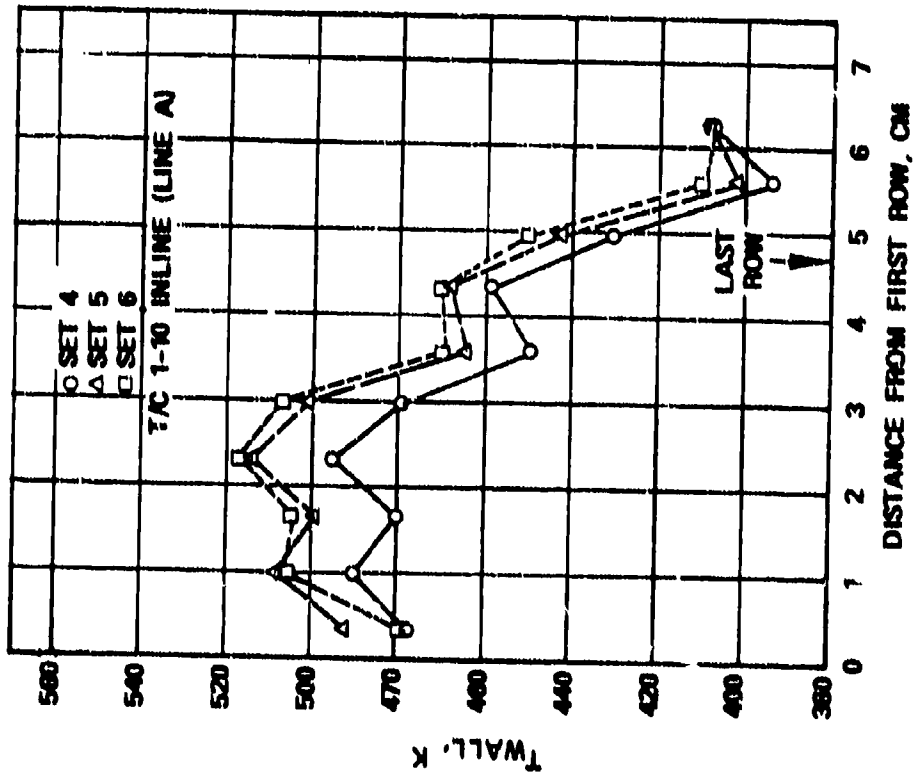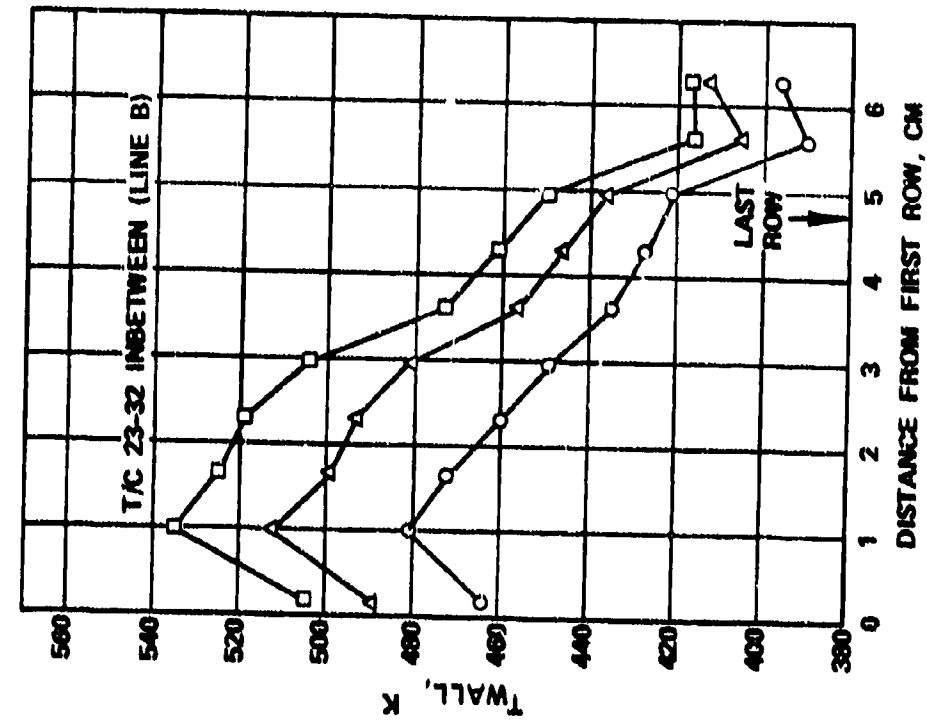
Figure 28. Wall Temperatures of Coarse-Pore Transpiration Cooling Scheme.
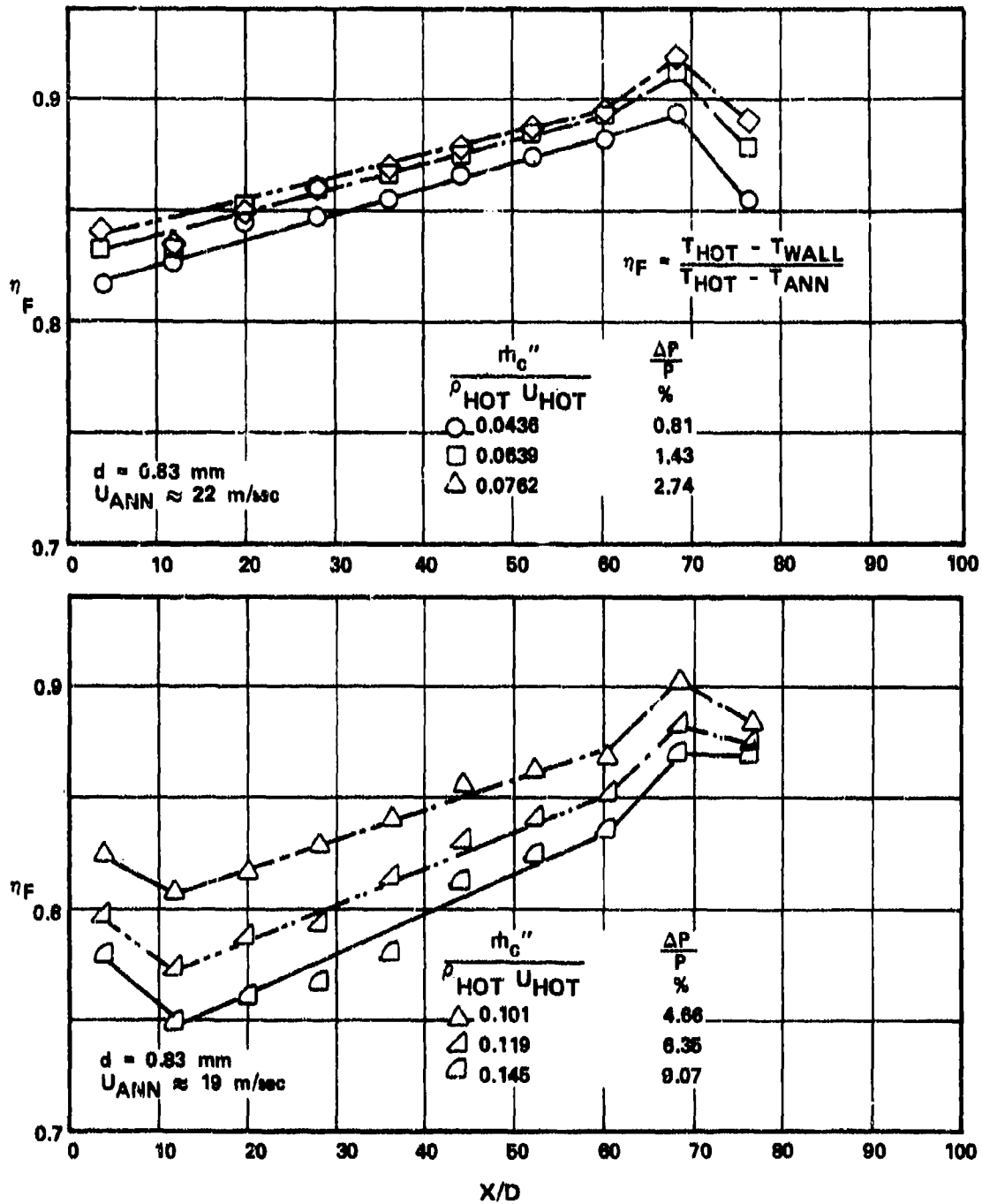
Figure 29. Performance of Coarse-Pore Transpiration
Cooling Scheme.

$$\eta_c = \frac{C_{WALL} - C_\infty}{C_{SLOT} - C_\infty}$$
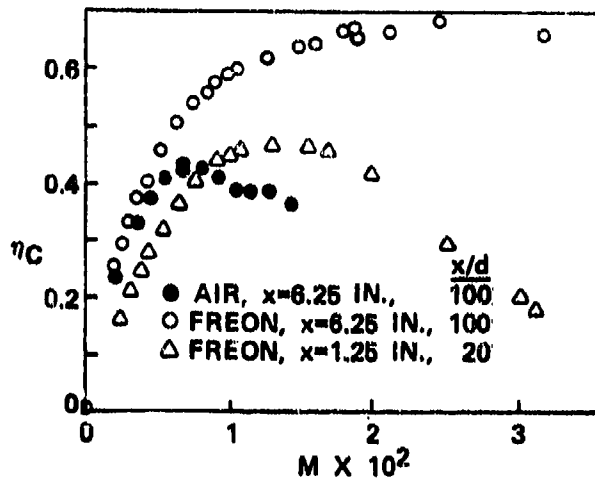
DEPENDENCE OF FILM EFFECTIVENESS
ON BLOWING RATE, $M = \dot{m}_c'' / \rho_\infty U_\infty$
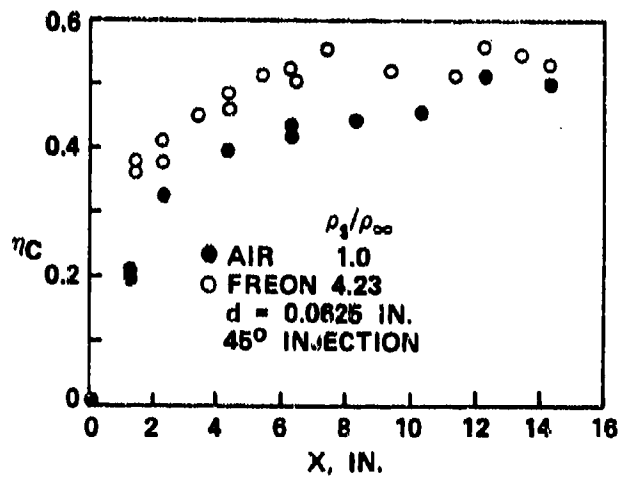
FILM EFFECTIVENESS VERSUS AXIAL
DISTANCE, M = 0.0065

Figure 30. Film Effectiveness of Coarse-
Pore Transpiration Measured by BROCQ.

therefore, should be limited to local cooling of potential hot
spots, such as behind the igniter and the fuel-nozzle grommets,
or where geometrical constraints make other more efficient
cooling concepts less desirable.

6. Relative Comparison of Cooling Schemes

The performance of the four cooling schemes was investigated
under a nonreacting flow environment with the temperature ratio
varying over the range of interest in gas turbine combustors.
The results have been presented in the previous four sections.
Figure 31 shows a relative comparison of the four cooling schemes
at low-to-moderate pressure drops for a 4.34 temperature ratio,
which is typically encountered in the combustor primary zone.
Based upon the measurements, the best cooling scheme appeared
to be film/extended-surface geometry. The second best was
the impingement film configuration. Three combustor cans were
fabricated to compare the performance of the following schemes,
deduced from the temperature-sensitive paint:

- Conventional film

- Impingement/Film

- Conventional film/extended surface

Figure 32 gives wall-temperature characteristics and a
description of the important geometric details of a can combustor
that employed a conventional cooling band. The recirculation
zone is established by primary jets and dome louver air that
enters the combustor with 90-degree swirl angle. The cooling-
slot height is approximately 2 mm. The lip of the slot extends
6.4 mm beyond the center of the cooling air holes. Cooling air
for the primary and intermediate panels meters through 30 ori-
fices of 4.4- and 4.8-mm diameter, respectively, with the corres-
ponding circumferential spacing of 3 and 2.8 mm hole diameters.

97
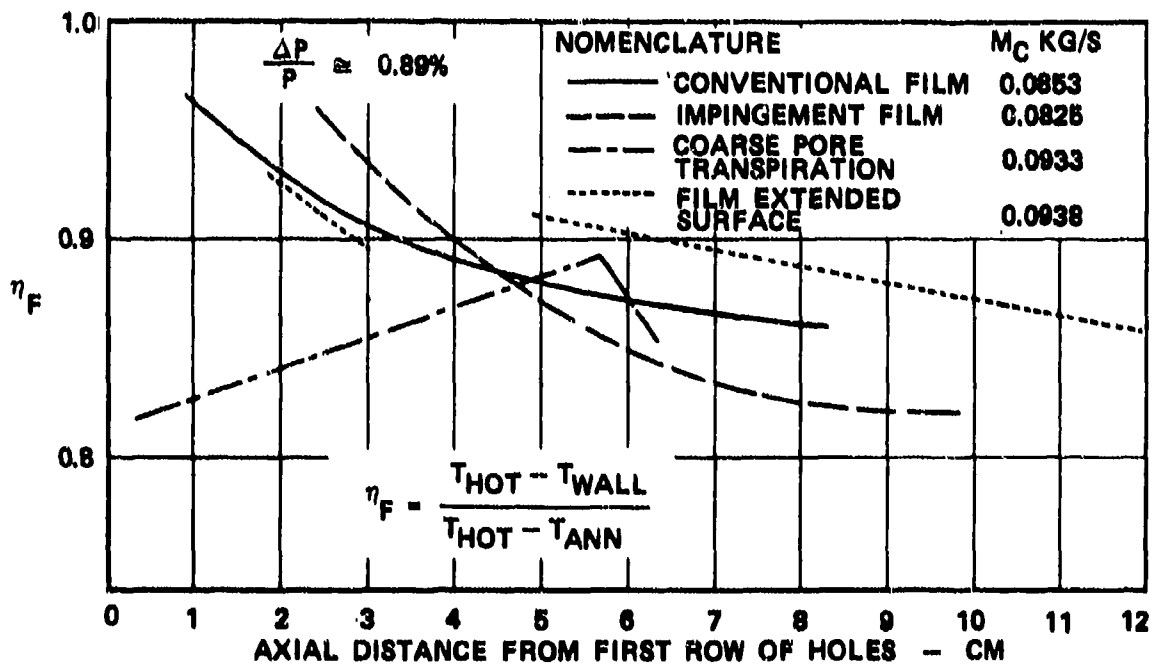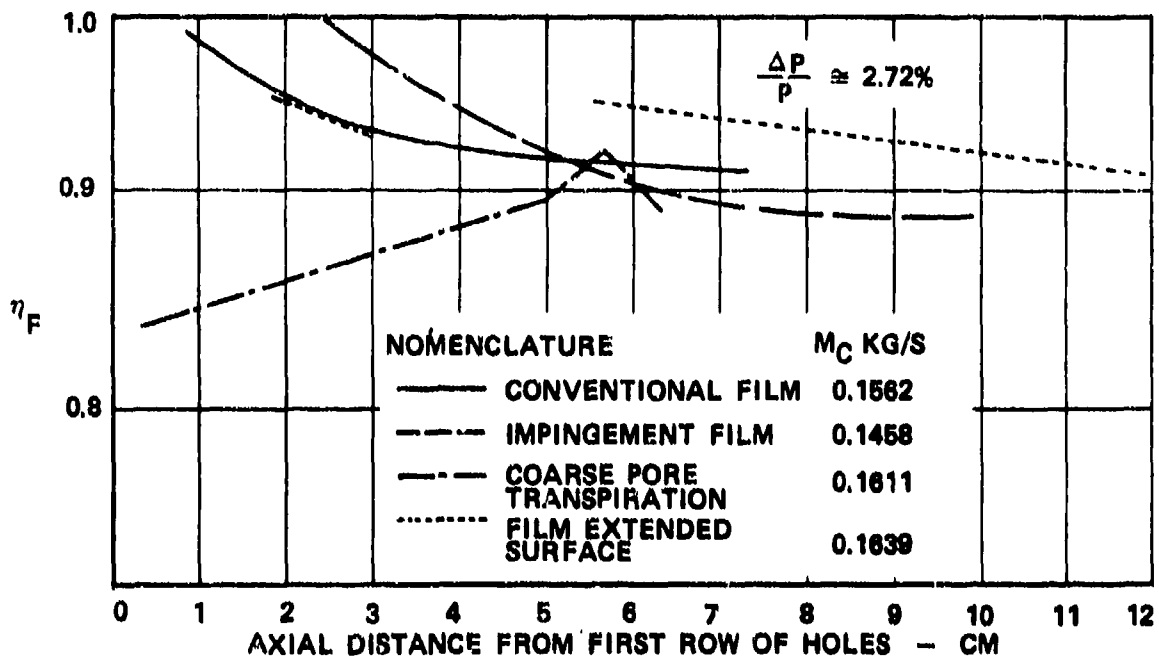
Figure 31. Comparison of the Four Cooling Schemes in Nonreacting Flow Fields.

	AIRFLOW (% TOTAL)
— 30 HOLES OF 3.6 mm DIAMETER	7.7
— 30 – 4.4 mm HOLES	11.7
— 6 – 1.12 cm HOLES	15.0
30 – 4.8 mm HOLES	13.8
6 – 1.42 cm HOLES	24.2

P_3 = 1000 kPa
W_{a_3} = 1.4 kg/s
T_3 = 622 K
T_4 = 1422 K

CAN DIAMETER = 12.66 cm
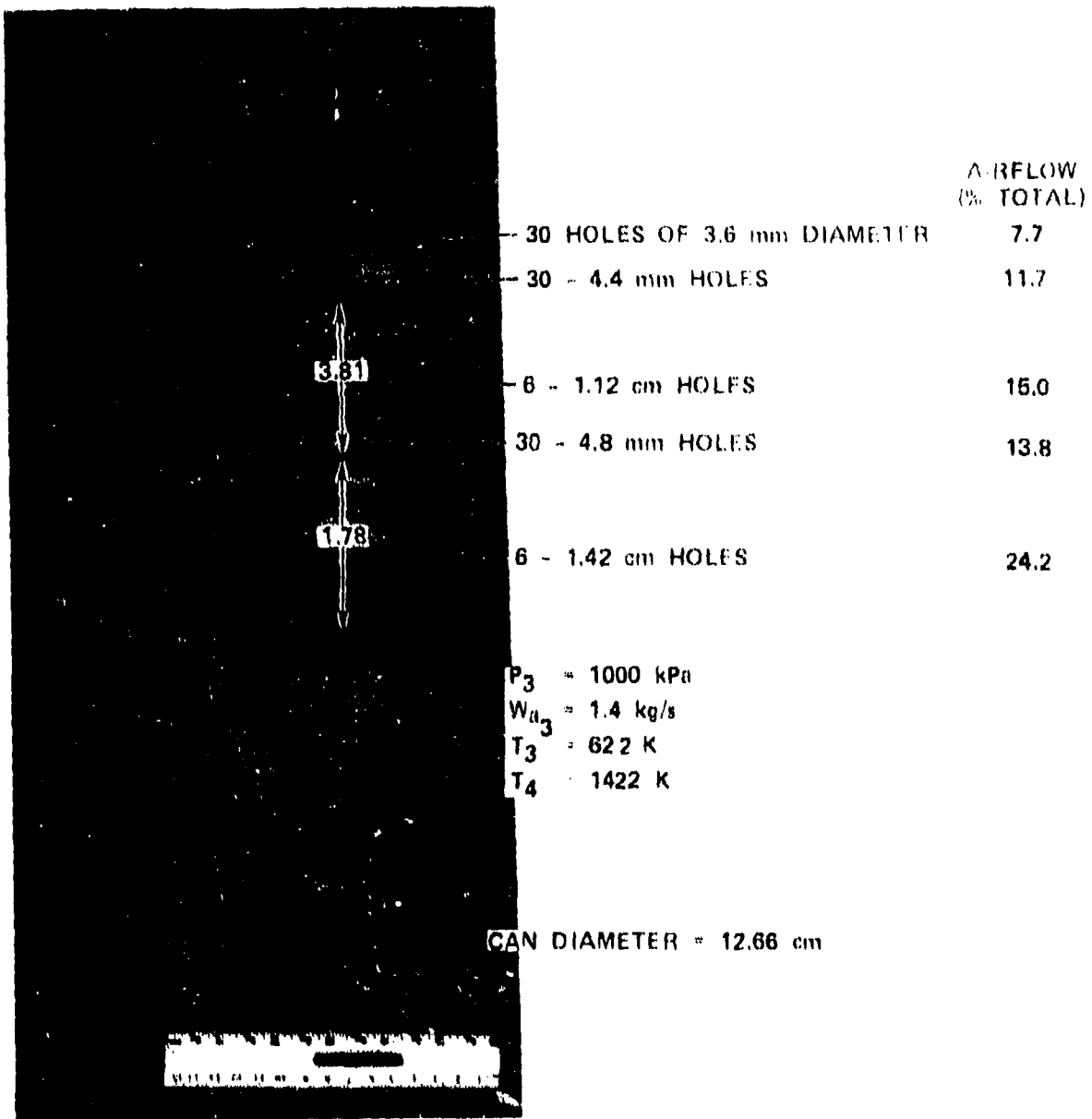
Figure 32. Wall Temperature Characteristics as
Determined by Thermindex OG-6 of
Conventional Cooling Scheme.

This insured a relatively uniform film exiting the lip. The center-to-center distances for the first and second cooling-film bands are 7.14 and 8.22 cm, respectively, which corresponds to 35 and 41 mm slot heights. The computed cooling-airflow rate for both the primary and secondary panels was 0.58 g/s cm^2, which corresponds to a typical cooling flow-rate requirement for a can combustor with inlet pressure equal to 10 atmospheres.

A typical temperature-sensitive paint run of the can combustor with conventional cooling scheme is shown in Figure 32 for a combustor inlet pressure and temperature of 10 atmospheres and 622 K, respectively. The maximum wall-temperature levels of 1172 K obtained at a combustor-exit temperature of 1422 K was considered to be high for a long-life combustor.

The combustor was modified to incorporate an extended surface geometry, as shown in Figure 33. Four fins of 1.57 mm height and 1.57 mm width were machined starting 38.1 mm downstream from the first cooling orifices. The center-to-center spacing of the fins was 5.1 mm. Similarly, 10 fins were machined for the secondary panel as shown. Because of the fins, the surface area increased locally by approximately 63 percent with an attendent increase in local heat-transfer coefficient. Consequently, the resultant hot spot was reduced by approximately 470 K compared to the conventional film-cooling configuration.

Figure 34 shows a typical thermal paint run on a can combustor that used an impingement/film cooling configuration. A total of 240 holes of 1.57 mm diameter were drilled, as shown, forming a four-row staggered arrangement. The splash plate with 2 mm height was welded with the lip extending 6.4 mm beyond the last row. The same orifice size and arrangement was used for the secondary panel also. This resulted in approximately a 15-percent reduction in the cooling-flow rate for the secondary panel, compared to the baseline combustor

FIN DIMENSIONS = 1.57 x 1.57 mm
PITCH = 5.1 mm

Figure 33. Wall Temperature Characteristics of
Film/Extended Surface Cooling Scheme.
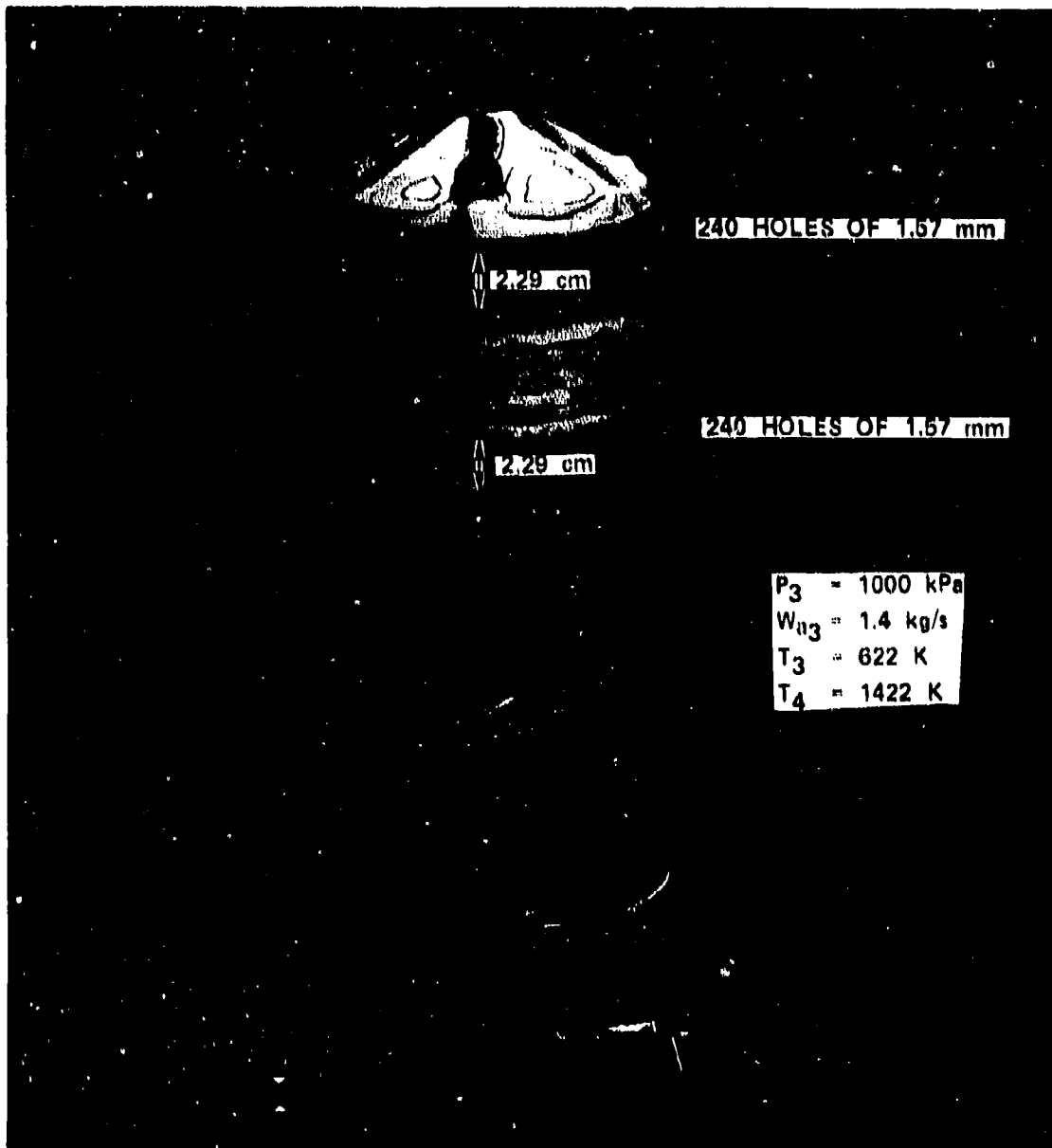
Figure 34.   Wall Temperature Characteristics of
Impingement/Film Cooling Scheme.

(Figure 31). Hot spots of the impingement/film configuration
reduced to 1089 K as compared to 1172 K obtained with the
conventional film can.

B. Jet Mixing

In advanced, high-temperature-rise, small combustors, a
small fraction of the combustor air is available for dilution
and trimming of the exhaust-temperature profile. Measurements
weie therefore made to study mixing characteristics of impinging
dilution jets in a can test section of 12.6 cm diameter. A
slave combustor (shown in Figure 9), supplied the air for
the test section at a relatively constant temperature of 1200 K.
The dilution jet air temperature was maintained at approximately
300 K. A number of orifice arrangements were studied, as listed
in Table 8. Internal-temperature profiles were measured by a
10-thermocouple rake which had 2 degrees-of-freedom along longi-
tudinal and circumferential directions.

The orifice configurations were selected to allow a rela-
tively wide range of circumferential spacing between the orifices.
The geometrical spacing to the orifice diameter ratio was varied
from 8.3 to 20.3. In order to facilitate a comparison with the
data of Holdeman and Walker[18] on the mixing of multiple jets into
a heated cross flow in rectangular test sections, the effective
spacing of the jet was defined based upon the same equivalent
cross-stream flow area per jet in a rectangular test section
of height R, where R is the can radius; i.e.,

$$S_{EFF} \; R = \frac{\pi R^2}{n}$$

Realizing that the circumferential spacing between n
orifices on a can is given by $S_{GEOM} = 2\pi R/n$, S_{EFF} is simply
half of the S_{GEOM}.

[18]Holdeman, J.D., and R.E. Walker, "An Empirical Model for the
Mixing of a Row of Dilution Jets with a Confined Crossflow,"
AIAA Paper 76-48.

103

TABLE 8. MIXING CHARACTERISTICS OF IMPINGING JETS.

IMPINGING JET CONFIGURATIONS	R/D	$(S/D)_{GEOM}$	$(S/D)_{EFF}$
- 2 Opposed Plunged Orifices of 9.8 mm	6.5	20.3	10.15
- 4 Opposed Plunged Orifices of 9.8 mm	6.5	10.15	5.07
- 6 Opposed Orifices of 8.0 mm	7.9	8.3	4.14

       Single Row

       Two rows Inline Separated by $\Delta X = 42.4$ mm $= 5.3D$

       Two rows Staggered Separated by $\Delta X = 42.4$ mm $= 5.3D$

RANGE OF FLOW PARAMETERS

- Pressure = 10 ATM
- Orifice Pressure Drop = 1 - 10 Percent

$$T_{HOT} \approx 1200K$$

$$T_{ANN} \approx 300K$$

$$U_{HOT} \approx 40 \ M/S$$

$$V_{JET} = 40 - 150 \ M/S$$

$$\text{JET MOMENTUM RATIO} \ \frac{\left(\rho_j \ V_j\right)^2}{\left(\rho_{HOT} \ U_{HOT}\right)^2} = 4 - 60$$

The six-orifice configuration gave effective spacing of
4.14D. This configuration was more thoroughly studied by
measuring the mixing characteristics of single row and two rows
axially separated by 4.22 cm. Both inline and staggered con-
figurations were investigated and a typical commparison is
shown in Figures 35 and 36. The hot stream and initial jet
velocites and density, as listed for both configurations, were
slightly different, with the resulting jet momentun ratios being
13.5 and 11.1, respectively, for the staggered and inline jets
of the first rows. No appreciable difference between the jets
is evident in the region upstream of the second row. The
measured data shows the splitting of the core of the jets into
two separate vortices (regions of minimum temperature) at 3.53
to 4.95 Dj downstream from the first row in case of the staggered
configuration. On the other hand, it happens between 2.48 and
3.80 Dj for the inline rows. The spreading of the inline jet
appears to be slightly more than that of the staggered jet. The
mixing characteristics are quite different for both geometries
in the region downstream from the second row, as shown in Figure
36, which is located at $\frac{X}{D} = 5.9$. The jet penetration slightly
downstream from the second row is relatively more with the
inline configuration due in part to the low pressure region
created by the first jet. The inline jet further strengthens
the first jet; whereas in the staggered configuration the mixing
region is established in the region previously occupied by the
first jet. The spreading of the jets with attendent uniformity
in the circumferential direction is more pronounced with the
staggered jets; however an increased penetration is obtained
with the inline configuration of dilution rows.

The measurements for different jet configurations are sum-
marized in Sections IV.B.1 through IV.B.4.
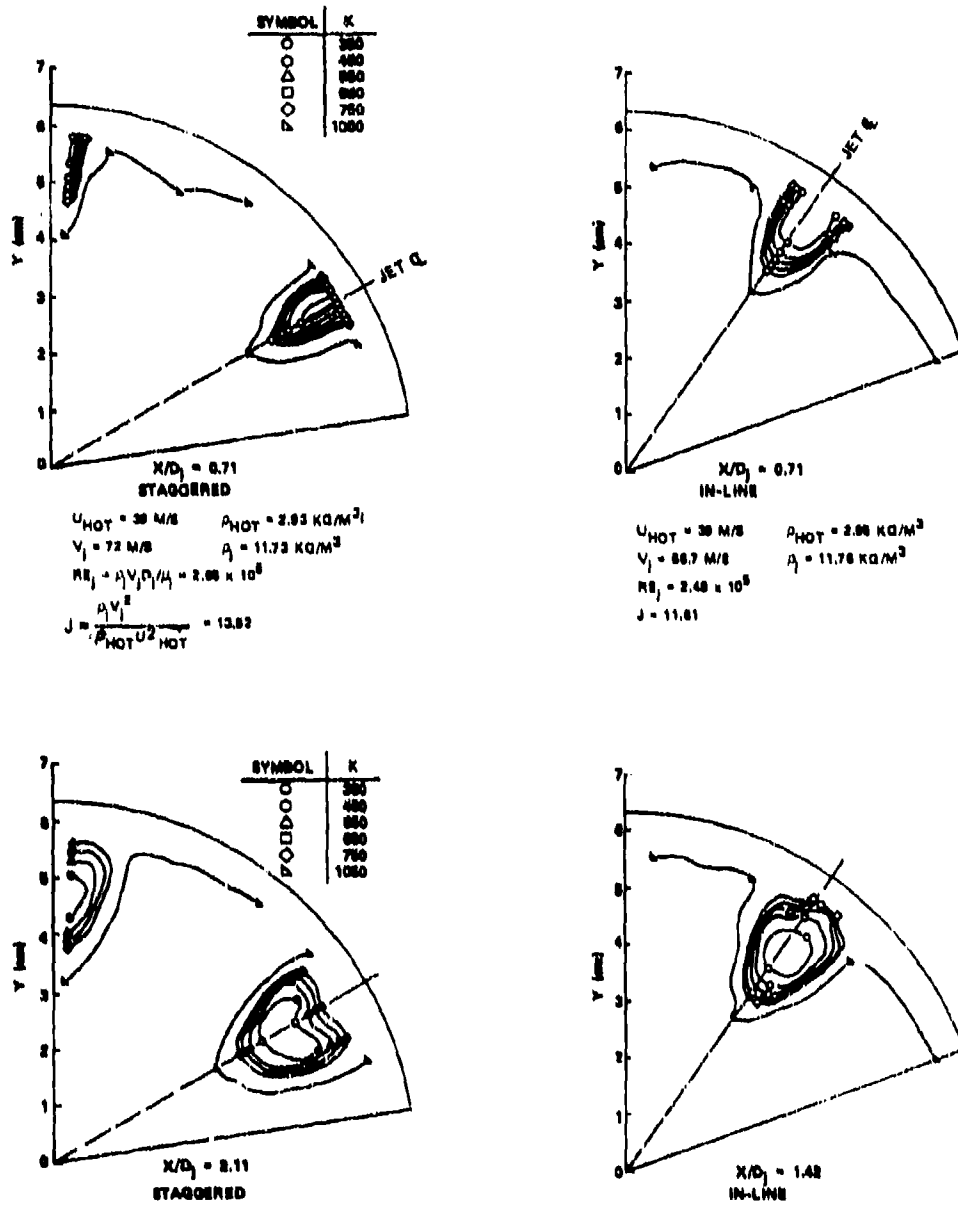
SYMBOL	K
O	350
O	450
△	550
O	650
O	750
◁	1050

$X/D_j = 0.71$
STAGGERED

$U_{HOT} = 39$ M/S $\rho_{HOT} = 2.93$ KG/M^3
$V_j = 72$ M/S $\rho_j = 11.73$ KG/M^3
$RE_j = \rho_j V_j D_j / \mu_j = 2.06 \times 10^5$

$J = \dfrac{\rho_j V_j^2}{\rho_{HOT} U^2_{HOT}} = 13.52$

$X/D_j = 0.71$
IN-LINE

$U_{HOT} = 39$ M/S $\rho_{HOT} = 2.96$ KG/M^3
$V_j = 66.7$ M/S $\rho_j = 11.76$ KG/M^3
$RE_j = 2.48 \times 10^5$
$J = 11.61$

$X/D_j = 2.11$
STAGGERED

$X/D_j = 1.42$
IN-LINE

Figure 35.   A Typical Comparison Between Mixing Characteristics
of In-Line and Staggered Rows of Dilution Jets
Upstream of the Second Row (Sheet 1 of 3).

106
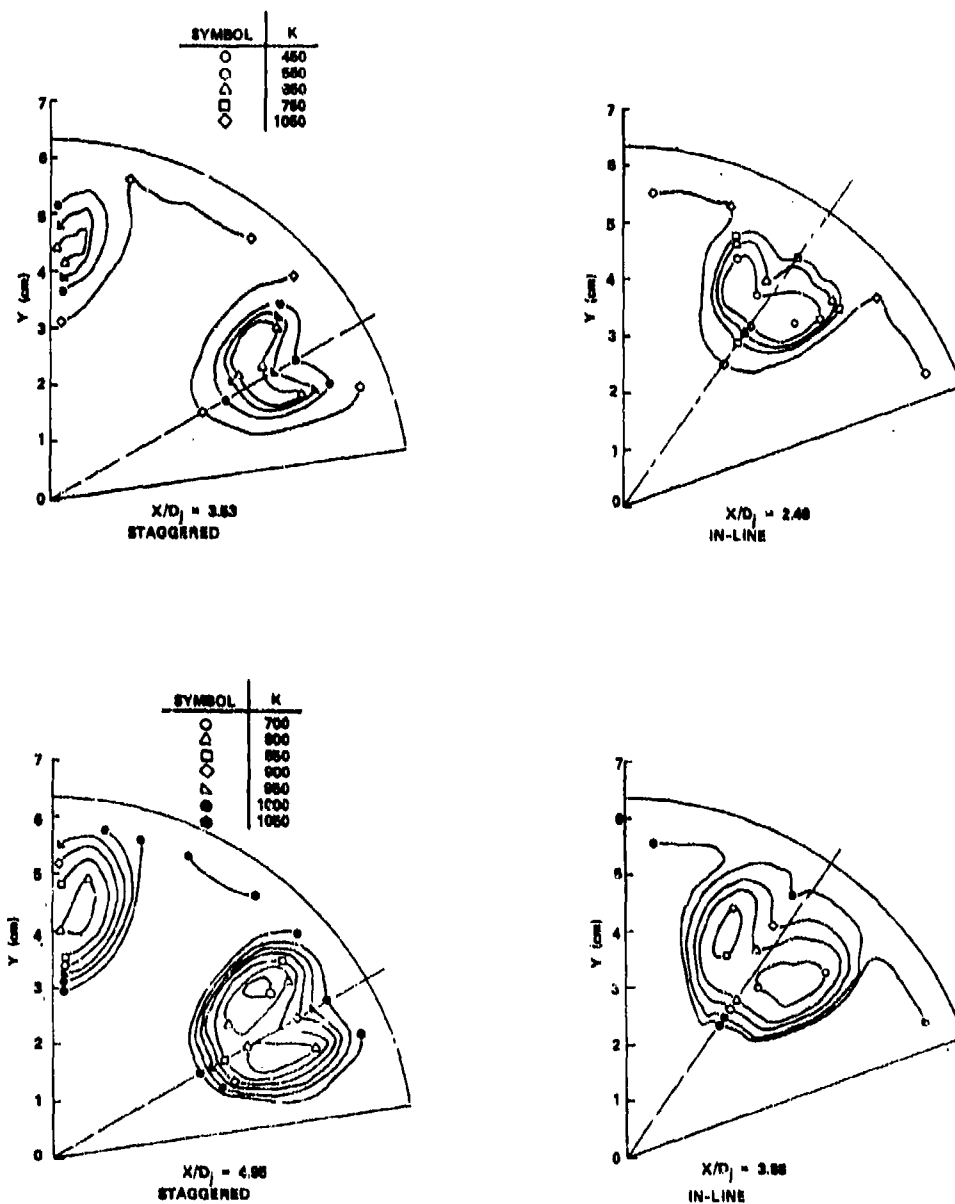
Figure 35. A Typical Comparison Between Mixing Characteristics of In-Line and Staggered Rows of Dilution Jets Upstream of the Second Row (Sheet 2 of 3).
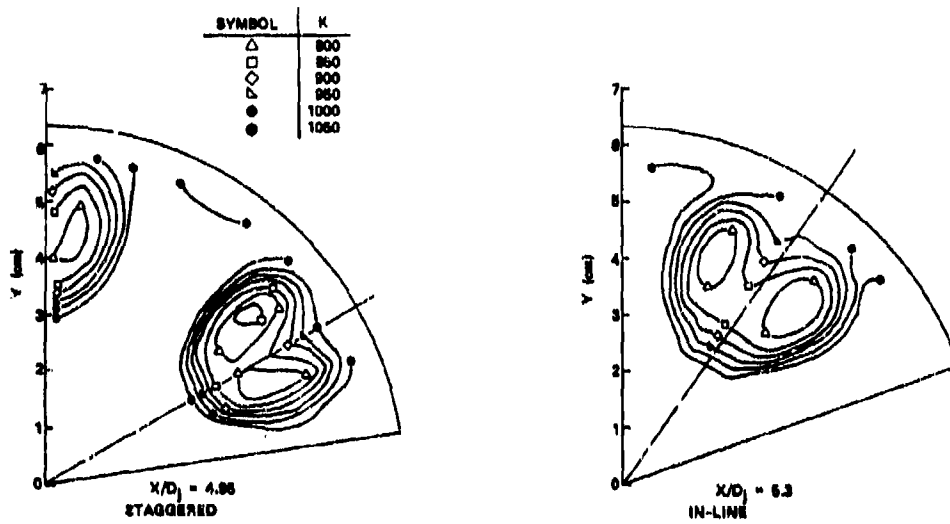
Figure 35. A Typical Comparison Between Mixing Characteristics
of In-Line and Staggered Rows of Dilution Jets
Upstream of the Second Row (Sheet 3 of 3).
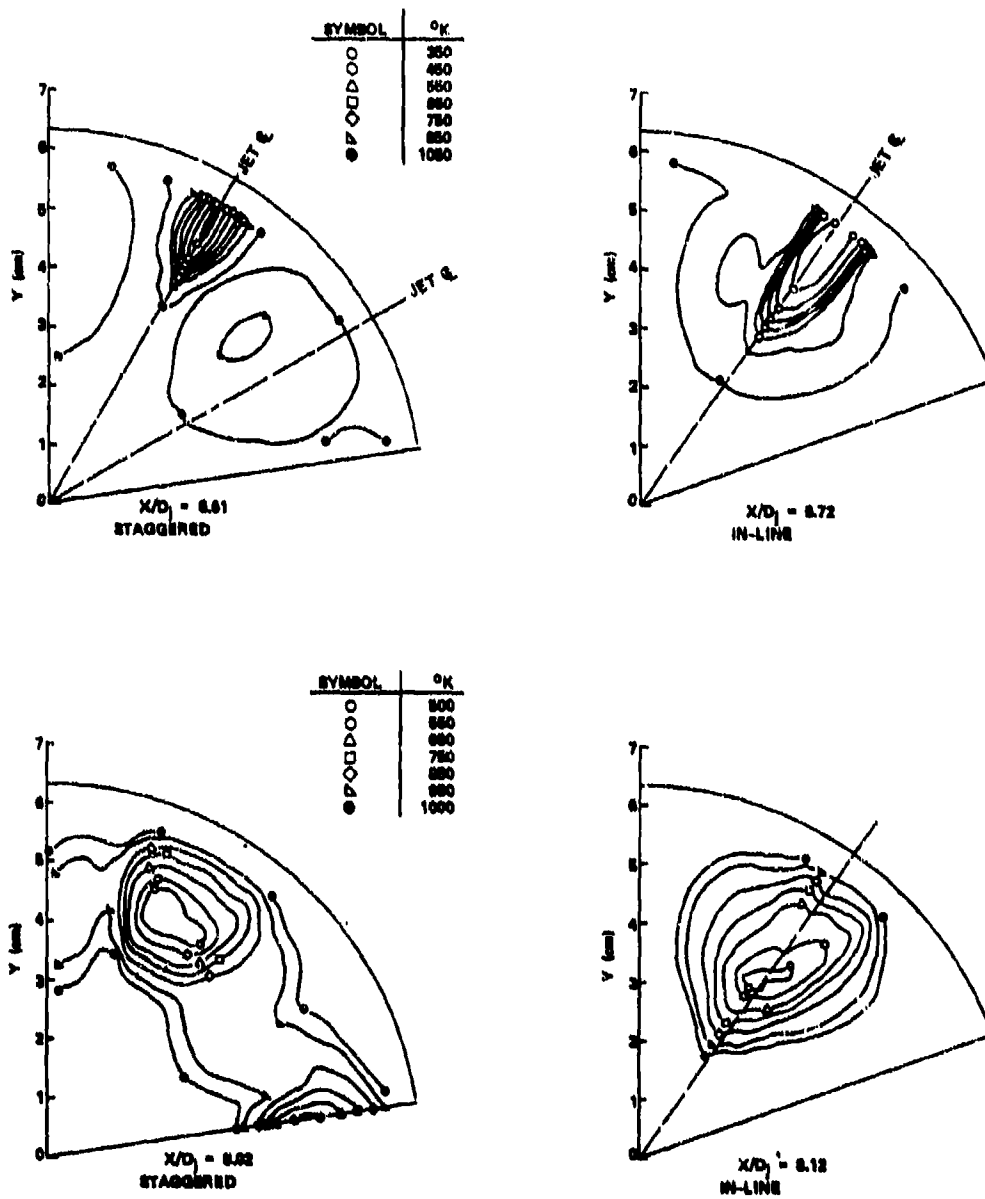
Figure 36. A Typical Comparison Between Mixing Characteristics of In-Line and Staggered Rows of Dilution Jets the Region Downstream of the Second Row (Sheet 1 of 2).
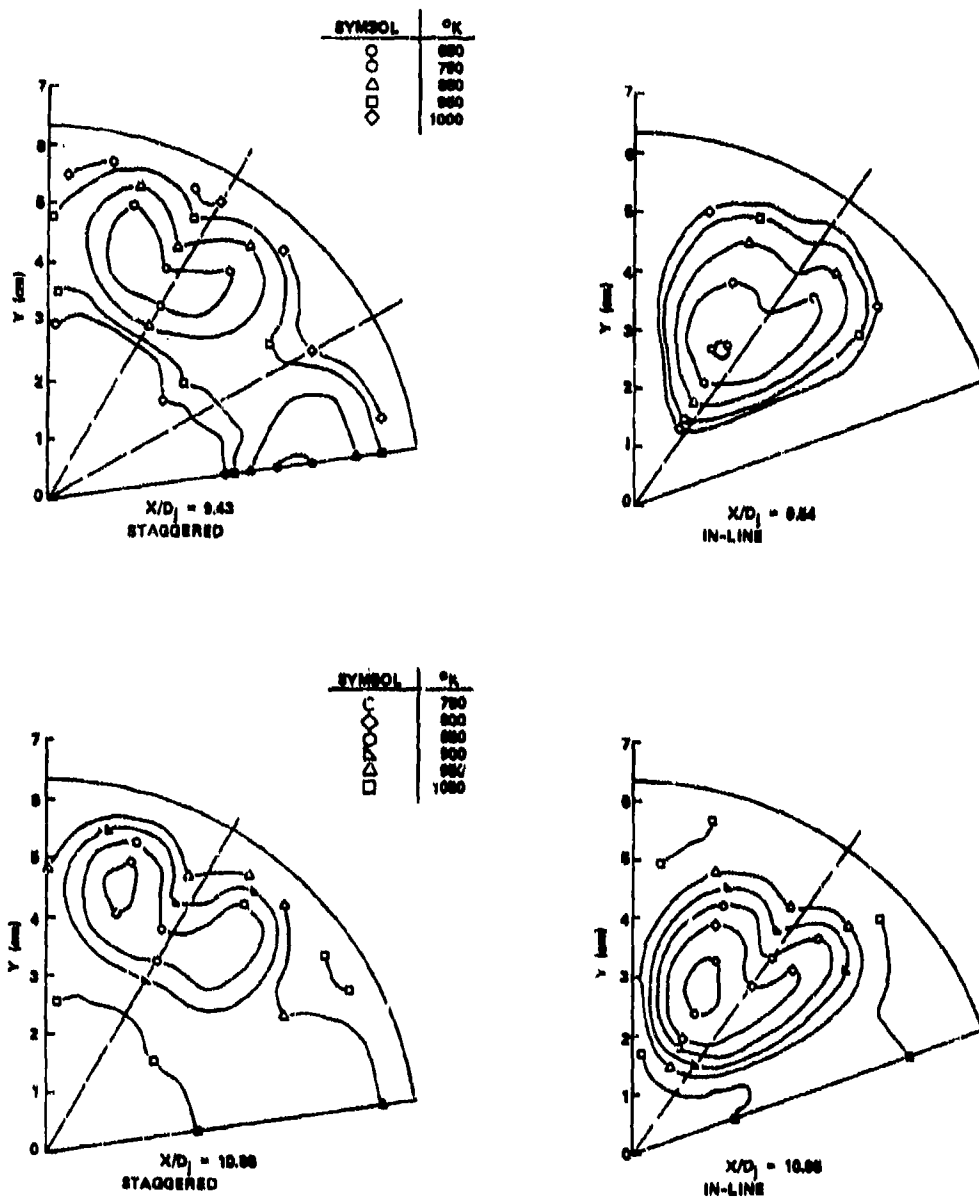
109

X/D$_j$ = 9.43
STAGGERED

X/D$_j$ = 9.54
IN-LINE

X/D$_j$ = 10.96
STAGGERED

X/D$_j$ = 10.96
IN-LINE

Figure 36. A Typical Comparison Between Mixing Characteristics of In-Line and Staggered Rows of Dilution Jets in the Region Downstream of the Second Row (Sheet 2 of 2).

1. Mixing Characteristics of Two Opposing Jets

Mixing characteristics of the jets emanating from two diametrically opposed plunged orifices were studied for a range of pressure drops from 1.16- to 12.04-percent, as listed in Table 9. The corresponding mass-velocity ratio varied from 4.53 to 15.28, with attendent range of jet-momentum ratio from 4.74 to 60.46.

The jet penetration, centerline temperature, and the jet half-widths, reduced from the data in line with the center of the orifice, are shown in Figure 37. Here jet penetration is defined as radial distance of the jet centerline from the test-section wall. The maximum possible jet penetration of the opposing jets can be equal to the can radius (R) of 6.33 cm. The jet half-width is defined by the following equation:

$$\pi/4 \; D_w{}^2 = A_{j1/2}$$

where $A_{J1/2}$ is the jet half-area measured at an axial distance X downstream from the dilution orifice. The minimum jet temperature T_{jc} is presented by the normalized temperature θ_{CO} defined as

$$\theta_{CO} = \frac{T_{HOT} - T_{jc}}{T_{HOT} - T_j}$$

where: T_j = Initial jet temperature at X = 0.

A number of empirical correlations have been proposed by different researchers for predicting the mixing characteristics of unbounded jets. However only a limited number of investigations have been conducted on jets in a confined stream[18]. An effort was therefore made to correlate the present data with both original and slightly modified relations developed by Holdeman and Walker. The modified Holdeman corelations over-

111

TABLE 9. TEST CONDITIONS OF TWO-OPPOSING JETS.

Parameters	Set-1	Set-2	Set-3	Set-4	Set-5
Hot Stream					
Airflow, kg/s	1.40	1.37	1.41	1.40	1.41
Temperature, K	1247	1268	1221	1184	1113
Pressure, kPa	978	1016	975	977	974
Velocity, m/s	42.19	40.50	41.68	40.03	38.12
Dilution Jet					
Pressure drop, %	1.16	2.24	5.16	8.07	12.04
Temperature, K	289	290	289	288	288
ρ_j, kg/m^3	11.74	12.15	11.70	11.77	11.73
V_j, m/s	44.23	61.92	95.20	120.7	150.8
Parameters					
$(\rho V)_j / (\rho U)_{HOT}$	4.53	6.69	9.65	12.4	15.28
$(\rho V^2)_j / (\rho U^2)_{HOT}$	4.74	10.22	22.04	37.38	60.46
$Ra_j \times 10^{-5}$	2.01	2.91	4.31	5.49	6.84
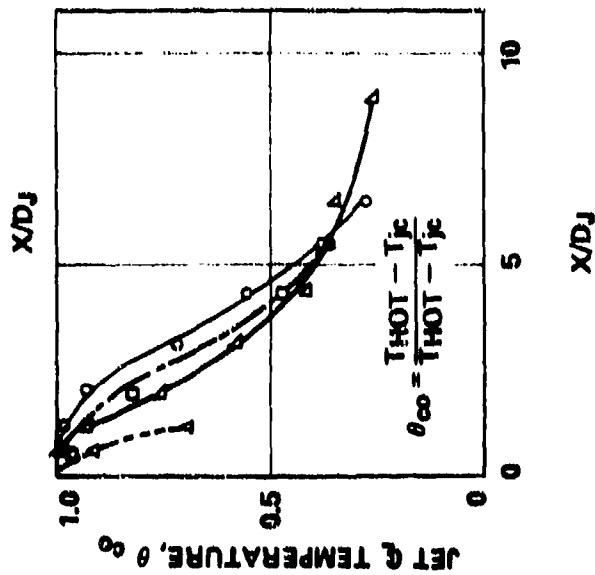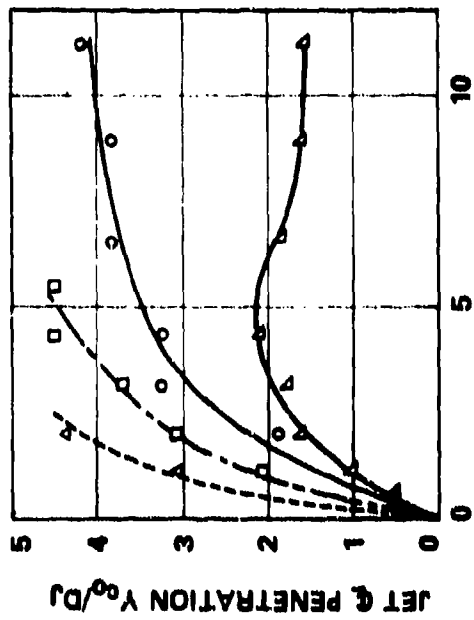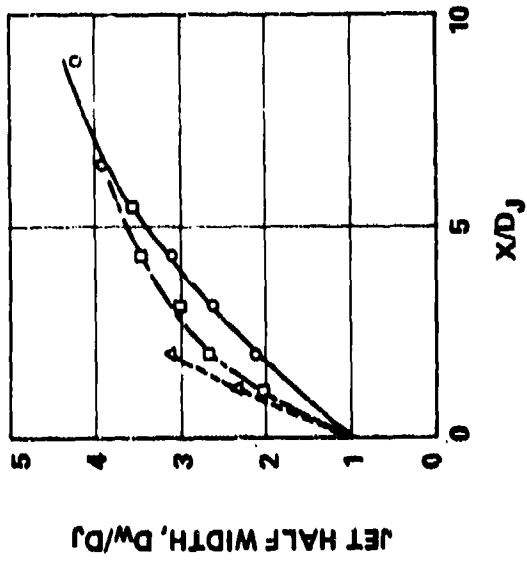
Figure 37, Mixing Characteristics of Two-Impinging Jets With Momentum Ratio (J) As a Parameter.

113

predicted the jet penetration. The agreement with the jet
centerline temperature and half width was generally poor.
Development of a new set of empirical relations was considered
beyond the scope of the present program, and therefore was not
pursued. However, an extensive comparison between the 3-D model
predictions and measurements was made for all of the jet mixing
cases, as summarized in Section VB. The agreement was reasonably
good.

2. Mixing Characteristics of Four Opposing Jets

Internal temperature measurements were made for a four-
opposing plunged orifice configuration with different jet-to-
cross-stream momentum ratios as listed in Table 10. The orifice
diameter of 9.8 mm was equal to that of the two-opposing jet
configuration reported in the previous section.

The reduced data on the centerline jet trajectory, jet
half-width, and the centerline temperature versus axial distance
from the orifice center is shown in Figure 38. This data can be
directly compared with that of the two-opposing jets to discern
the differences between the mixing characteristics of two- and
four-opposing jets. An in-depth comparison is given in Section
IV.B.6, where mixing characteristics of different orifice config-
urations are summarized.

The jet penetrated approximately up to 2 D_j at the lowest
momentum ratio of 2.88, which increased to 4.5 when J = 11.9.
As J was increased to 20.89 the asymptotic jet penetration did
not increase, although the slope of the jet trajectory was con-
siderably increased. Further increase in J to 41.84 and 65.14
brought significant change in the shapes of the isothermal lines
in the region beyond a 2 D_j downstream from the jet origin, as
shown in Figure 39.

114

TABLE 10. TEST CONDITIONS OF FOUR OPPOSING JETS.

Parameters	Set-1	Set-2	Set-3	Set-4	Set-5
Hot Stream					
Airflow, Kg/s	1.39	1.42	1.41	1.40	1.42
Temperature, K	1135	1138	1097	1085	1017
Pressure, kPa	977	973	975	975	973
Velocity, m/s	39.95	39.37	37.54	36.82	35.08
Dilution Jet					
Pressure drop, %	0.67	2.73	4.45	8.32	12.03
Temperature, K	292	289	289	288	287
ρ_j, kg/m^3	11.61	11.67	11.71	11.75	11.76
V_j, m/s	33.68	68.45	88.08	122.7	150.4
Parameters					
$(\rho V)_j / (\rho U)_{HOT}$	3,421	6.846	8.90	12.55	15.19
$(\rho V^2)_j / (\rho U^2)_{HOT}$	2.88	11.9	20.89	41.83	65.14
$Re_j \times 10^{-5}$	1.51	3.09	3.99	5.57	6.84
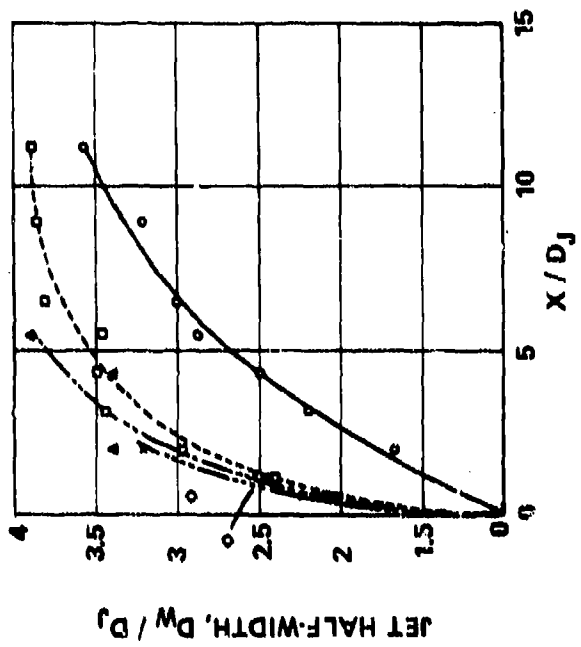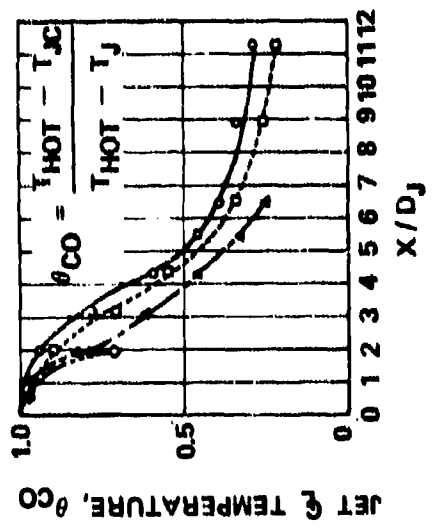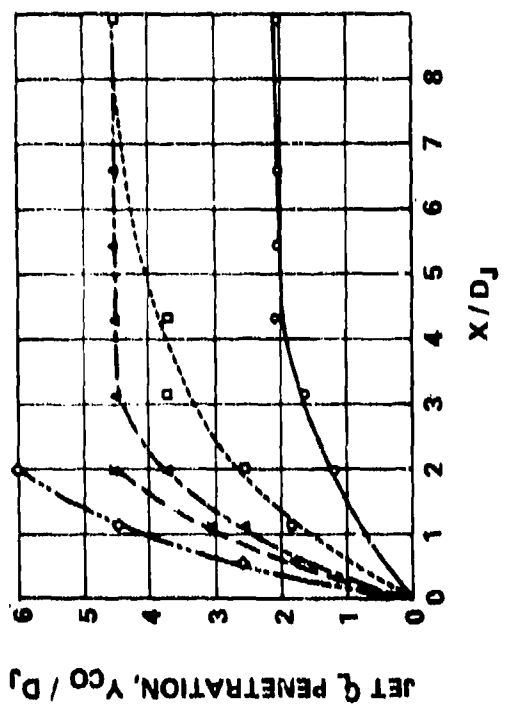
Figure 38. Measured Mixing Characteristics of Four Opposing Jets.
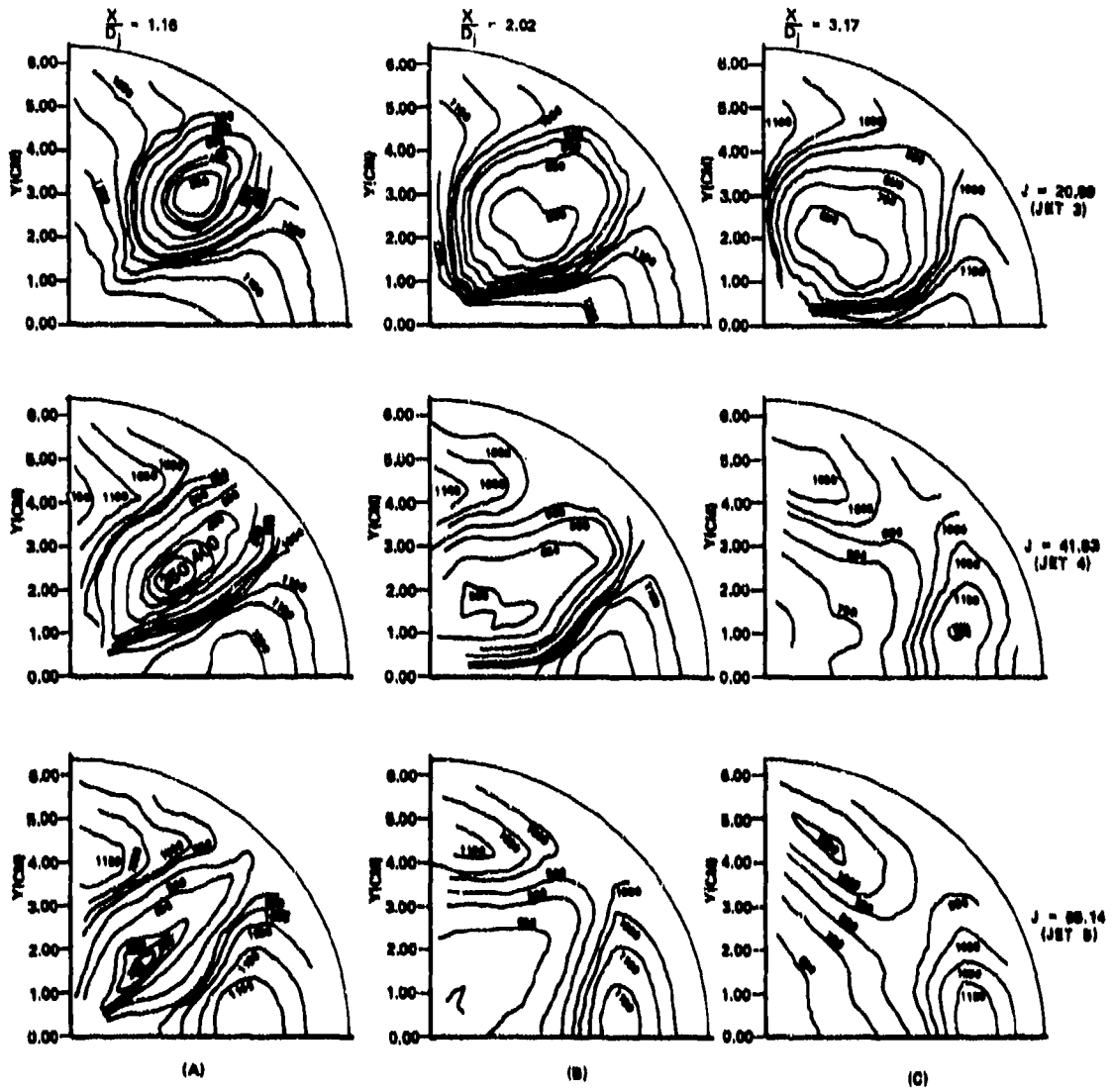
Figure 39. Measured Mixing Characteristics of Four Opposing Jets.

Figure 39(a) presents the measured isothermal plots at $\frac{X}{D_j}$
= 1.16 as affected by the jet momentum ratio, J = 20.89 (Jet 3),
J = 41.03 (Jet 4) and J = 65.14 (Jet 5). The jet shapes are
relatively similar with discernable jet cores. However, at
$\frac{X}{D_j}$ = 2.02, the profiles are quite different. Jet 3 maintains
a relatively intact shape. Jet 4 is about to break, whereas
the decay of Jet 5 has already begun. Jet 3 development
continues at $\frac{X}{D_j}$ = 3.17; it has not penetrated up to the center-
line of the combustor. In the case of other jets, the minimum
temperature is near the centerline, although the jets have
already broken. Consequently, with high jet-momentum ratios, the
conventional jet correlations for trajectory and mixing rate are
useful only for a relatively small axial distance downstream from
the jet origin. There does not exist any simple correlation for
predicting the mixing rates in the region downstream from the
jet breakup. However, the 3-D combustor performance model can
be used for correlating the jet-mixing data in all of the regions
of interest including jet development, jet decay, and mixing
region. This comparison is presented in Section V.B.

3. Mixing Characteristics of Six-Opposing Jets

Internal temperature profiles were measured for a 6-flush-
orifice configuration at different test conditions, as listed in
Table 11. The reduced data on jet trajectory, jet half-width,
and jet centerline temperature is presented in Figure 40. Like
in the four-opposing jet case, there was no increase in jet
penetration with jet-momentum ratios higher than 41. Similarly,
there is a negligible increase in the jet half-width beyond
J = 41.

TABLE 11. TEST CONDITIONS OF SIX-OPPOSING JETS.

Parameters	Set-1	Set-2	Set-3	Set-4	Set-5
Hot Stream					
Airflow, Kg/s	1.39	1.41	1.40	1.41	1.41
Temperature, K	1239	1204	1140	1072	1083
Pressure, kPa	980	977	980	976	972
Velocity, m/s	41.36	41.06	38.59	36.51	37.25
Dilution Jet					
Pressure drop, %	0.77	2.63	3.78	8.13	11.96
Temperature, K	294	292	290	289	289
ρ_j, kg/m^3	11.60	11.60	11.72	11.72	11.67
V_j, m/s	36.24	67.03	81.04	121.5	150.4
Parameters					
$(\rho V)_j / (\rho U)_{HOT}$	3.69	6.73	8.26	12.34	15.13
$(\rho V^2)_j / (\rho U^2)_{HOT}$	3.23	10.99	17.34	41.06	61.08
$Re_j \times 10^{-5}$	1.33	2.46	3.00	4.50	5.54

JET HALF-WIDTH, D_W / D_J

$$\theta_{CO} = \frac{T_{HOT} - T_{JC}}{T_{HOT} - T_J}$$

JET Q TEMPERATURE, θ_{CO}

JET Q PENETRATION, Y_{CO} / D_J

X / D_J

J	
○	3.24
○	10.99
□	17.34
△	41.06
◇	61.08

$D_J = 7.19$ mm
CAN RADIUS = 8.8 D_J
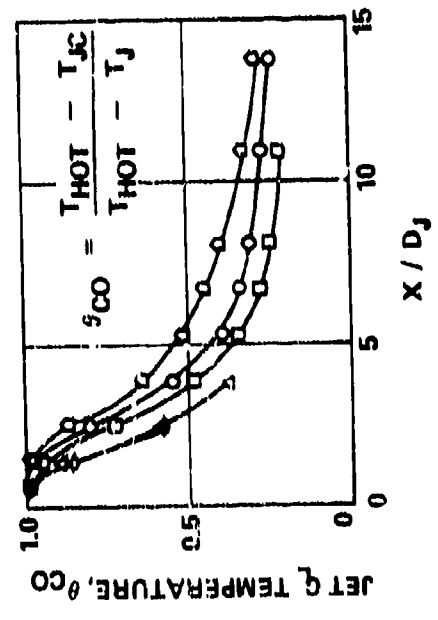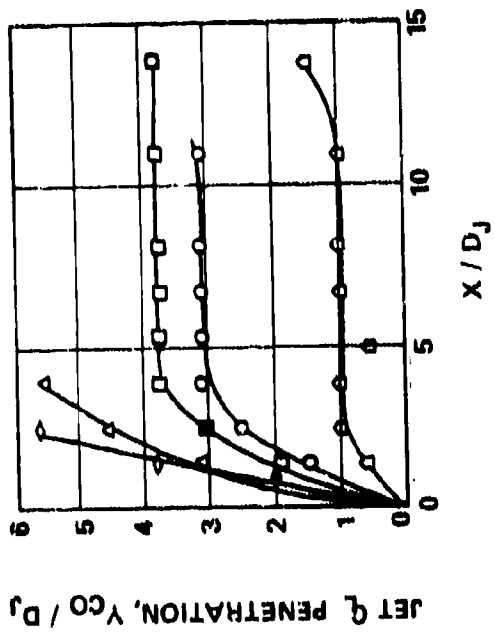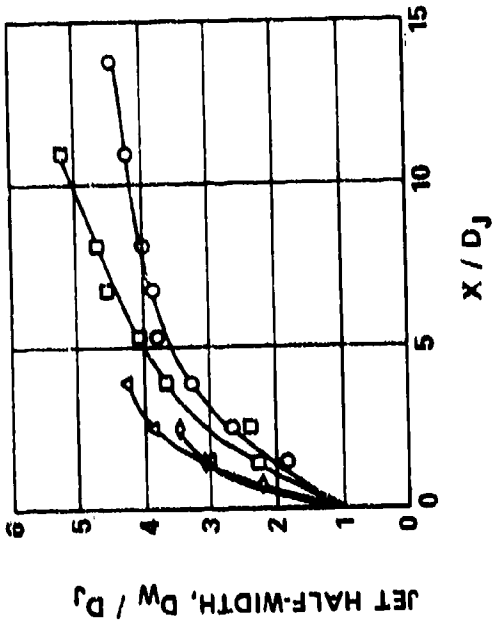
Figure 40. Mixing Characteristics of Six-Impinging Jets with Momentum Ratio (J) As a Parameter.

120

4. Mixing Characteristics of Inline and Staggered Rows of Six Opposing Jets

The mixing characteristics of the two rows of six-opposing jets emanating from flush orifices were studied for both inline and staggered configurations. The test conditions for inline and staggered arrangement are presented in Tables 12 and 13, respectively. A typical comparison for the jet development, decay, and mixing characteristics of both configurations was previously presented in Figures 35 and 36.

The reduced data on the jet penetration, jet half-width, and jet centerline temperature for both the first and the second jets for the inline configuration is presented in Figure 41. The corresponding data for the staggered-row geometry, where the second-row jets lie in between the first-row jets, is shown in Figure 42.

In the case of the inline configuration (Figure 41), the jet penetration and half width of the second-row jets were more than that of the first-row jets, due in part to a low-pressure region created by the latter. It should be noted that the second row was located 5.9 D_j downstream from the first row. The jet-centerline temperature was higher for the second row than for the first-row jets. The results for the staggered geometry were quite different as shown in Figure 42. For the lowest jet-momentum ratio case ($J=4.5$), the penetration and mixing rate (D_w/D_j) of the second jet were slightly higher than for the first jet. At higher jet-momentum ratios, the trend was opposite to that of the inline. The higher velocity region created by the first jet, in the region in between the jets, resulted in reducing the penetration of the second jet. Some reduction in the second jet penetration was expected since a slightly higher through-flow was passing across the jet. This implies that if the cross-stream flow rates were equal for both the first and

TABLE 12. TEST CONDITIONS OF TWO ROWS OF INLINE
          SIX-OPPOSING JETS.

Parameters	Set-1	Set-2	Set-3
Hot Stream			
Airflow, kg/s	1.41	1.40	1.41
Temperature, K	1177	1150	1126
Pressure, kPa	974	977	976
Velocity, m/s	40.34	39.12	38.49
Dilution Jet			
Pressure drop, %	0.88	2.61	4.38
Temperature, K	288	288	288
ρ_j, kg/m^3	11.73	11.76	11.76
V_j, m/s	38.31	66.70	87.24
Parameters			
$(\rho V)_j / (\rho U)_{HOT}$	3.88	6.81	8.86
$(\rho V^2)_j / (\rho U^2)_{HOT}$	3.69	11.61	20.09
$Re_j \times 10^{-5}$	1.42	2.48	3.24

TABLE 13. TEST CONDITIONS OF TWO ROWS OF STAGGERED SIX-OPPOSING JETS.

Parameters	Set-1	Set-2	Set-3	Set-4
Hot Stream				
Airflow, kg/s	1.41	1.39	1.40	1.41
Temperature, K	1166	1156	1126	1091
Pressure, kPa	975	977	979	976
Velocity, m/s	40.02	38.95	38.25	37.30
Dilution Jet				
Pressure drop, %	1.06	2.98	4.16	8.51
Temperature, K	289	289	288	289
ρ_j, kg/m^3	11.70	11.73	11.78	11.72
V_j, m/s	42.3	71.58	84.99	124.5
Parameters				
$(\rho V)_j / (\rho U)_{HOT}$	4.26	7.35	8.69	12.61
$(\rho V^2)_j / (\rho U^2)_{HOT}$	4.51	13.52	19.3	42.08
$Re_j \times 10^{-5}$	1.56	2.65	3.16	4.61
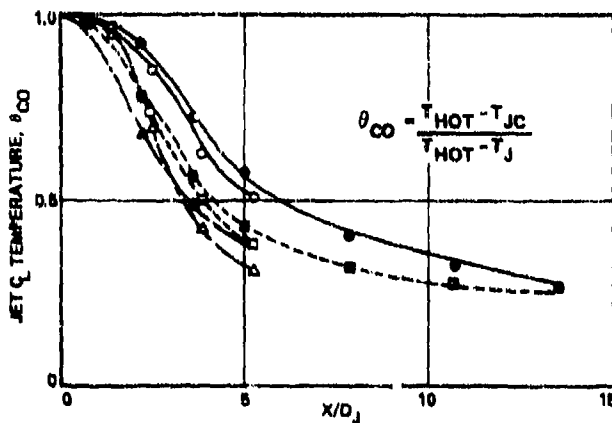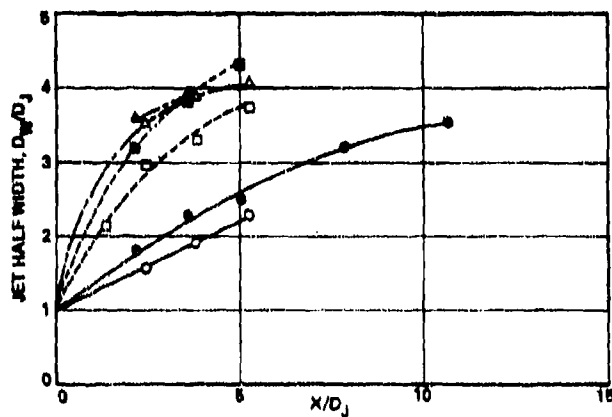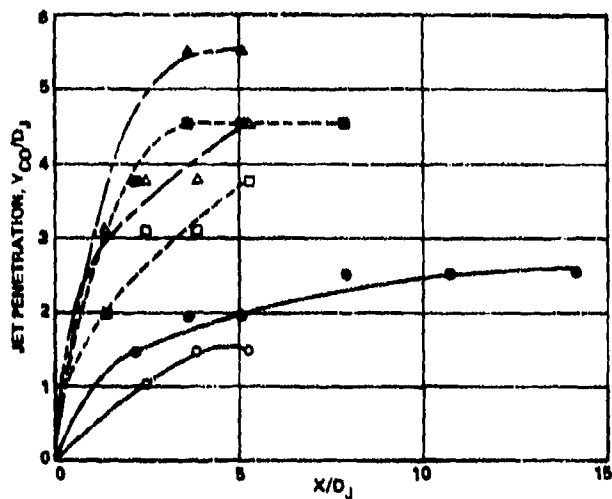
J	FIRST JET	SECOND JET
3.69	○	●
11.61	□	■
20.09	△	▲

AXIAL DISTANCE BETWEEN JETS = 5.9 D_J
D_J = 7.19 MM   CAN RADIUS = 8.8 D_J
X = AXIAL DISTANCE FROM ORIGIN OF FIRST JET

$$\theta_{CO} = \frac{T_{HOT} - T_{JC}}{T_{HOT} - T_J}$$

Figure 41.   Measured Mixing Characteristics of the In-line Six-Opposing Jets.

124
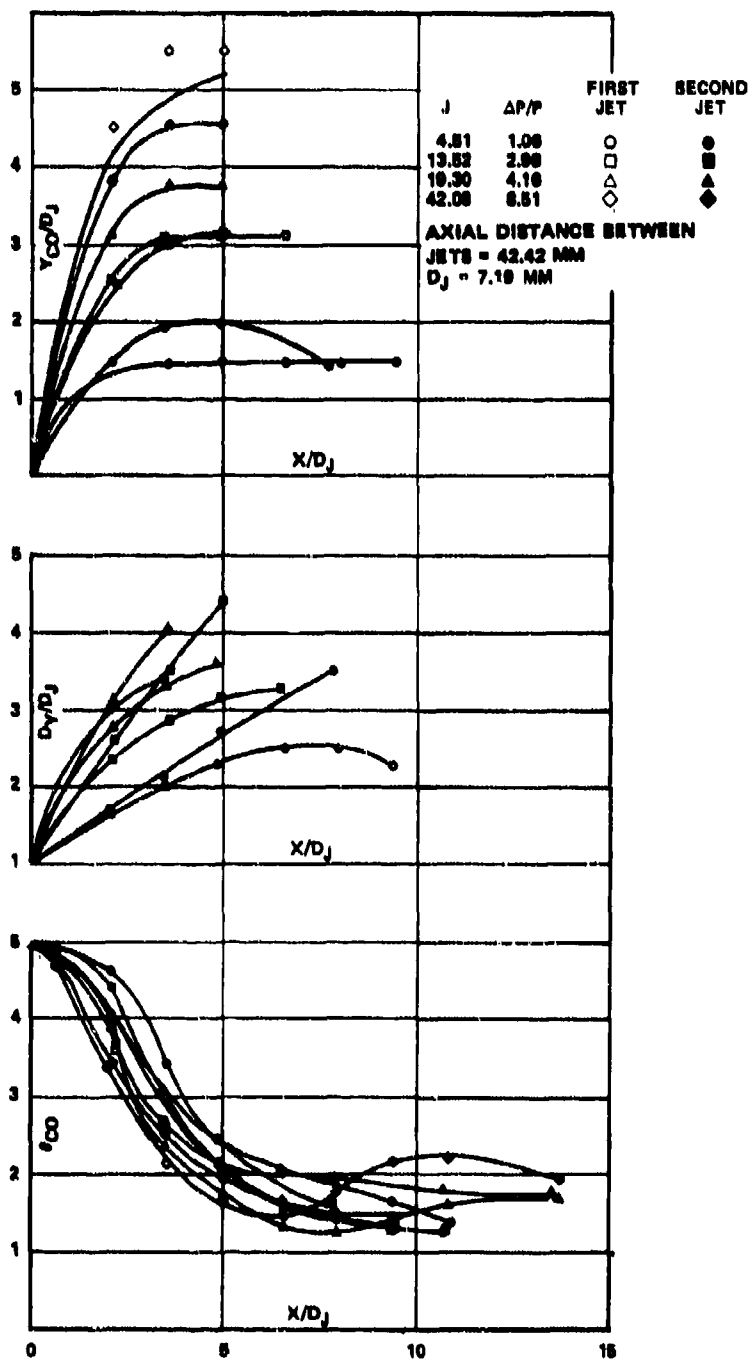
Figure 42. Measured Mixing Characteristics of the Staggered Six-Opposing Jets.

second row of jets, the penetration of the second jet would be slightly higher than presented in Figures 41 and 42.

C. Can Combustor Cold-Flow Mapping

A can combustor, presented in Figure 43, was used for cold-velocity mapping. The combustor has three cooling skirts with slot height equal to approximately 2 mm. The discharge face of the fuel nozzle was nearly flush with the conical dome leading edge, i.e., 2.01 cm from the top face giving a combustor length of 39.5 cm. Axial locations of each of the air-injection points (measured from the face of the fuel nozzle) along with orifice size and geometric area are given in Table 14.

Cold velocity traverses were taken at 21 stations; the axial and circumferential locations are indicated in Figure 43. Four traverses were made in the primary zone, seven in the intermediate zone and ten in the dilution zone. The symmetry of the internal flow field around a primary jet and a dilution jet was checked at two axial stations, namely at X = 5.99 and 12.85 cm.

Most of the velocity-measurement ports were fitted with alignment grommets to minimize air leakage. A calibrated five-hole pyramid (described below) passed through a tube seated on the grommet seat in order to minimize air leakage across the velocity port. The velocity ports not in use were covered by plugs.

CAN RADIUS = 6.35 CM
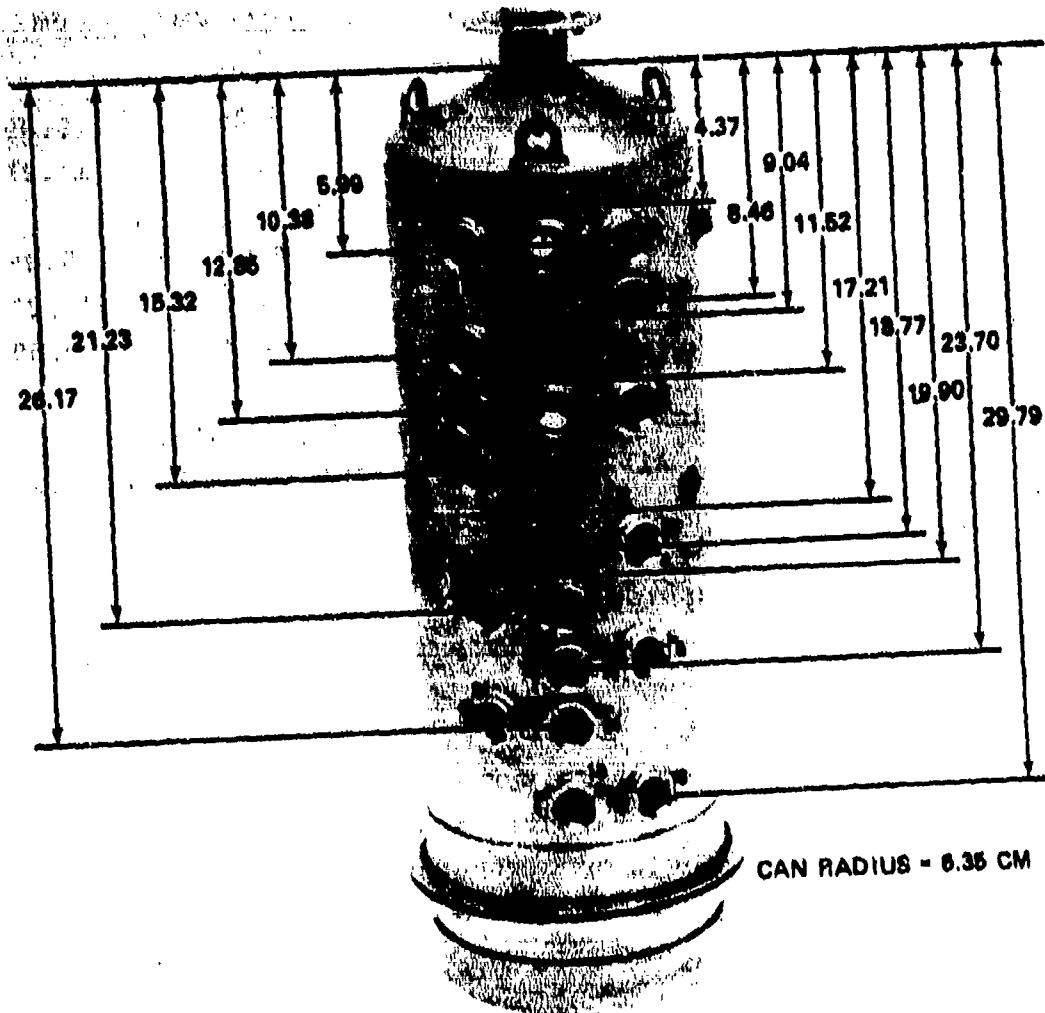
Figure 43. Can Combustor for Cold Velocity Mapping.

TABLE 14. COLD FLOW CAN COMBUSTOR GEOMETRICAL
DETAILS.

Orifice Type	Number of Orifices	Orifice Size, cm	Geometric Area, cm^2	Axial Distance, cm
Dome louvers	30	0.36	3.02	--
Primary	6	1.12	5.89	9.09
Dilution	6	1.42	9.53	17.21
Cooling slot lip				
No. 1	30	0.44	4.60	5.05
No. 2	30	0.48	5.43	12.20
No. 3	30	0.48	5.43	20.59

The combustor was installed in a test rig presented
previously in Figure 9. Air entered the test assembly plenum
through a baffle which had 40 orifices providing a 10-percent
pressure drop at a design corrected flow rate of 0.2 kg/s.
This baffle along with approximately 20 cm of settling length
was provided to achieve a relatively uniform annulus airflow
distribution.

A schematic of the five-hole pyramid probe for measuring
three velocity components, and static and total pressures is
shown in Figure 44. Calibration of the pyramid probe was obtained
on a flow rig, also presented in Figure 44. The probe yaw-angle
setting was obtained by installing the probe and the actuator on
a lathe bed, as shown. The probe was clamped in position where
both of the yaw pressures were equal. The zero-yaw setting
could be repeated within ±0.5 degree. The pitch-angle calibra-
tion was obtained by immersing the probe in the nozzle jet at a
known pitch angle. The data was recorded for every 5-degree
interval over the range of -45 to +30 degrees pitch angle at
different flow Mach numbers ranging from 0.04 to 0.3.
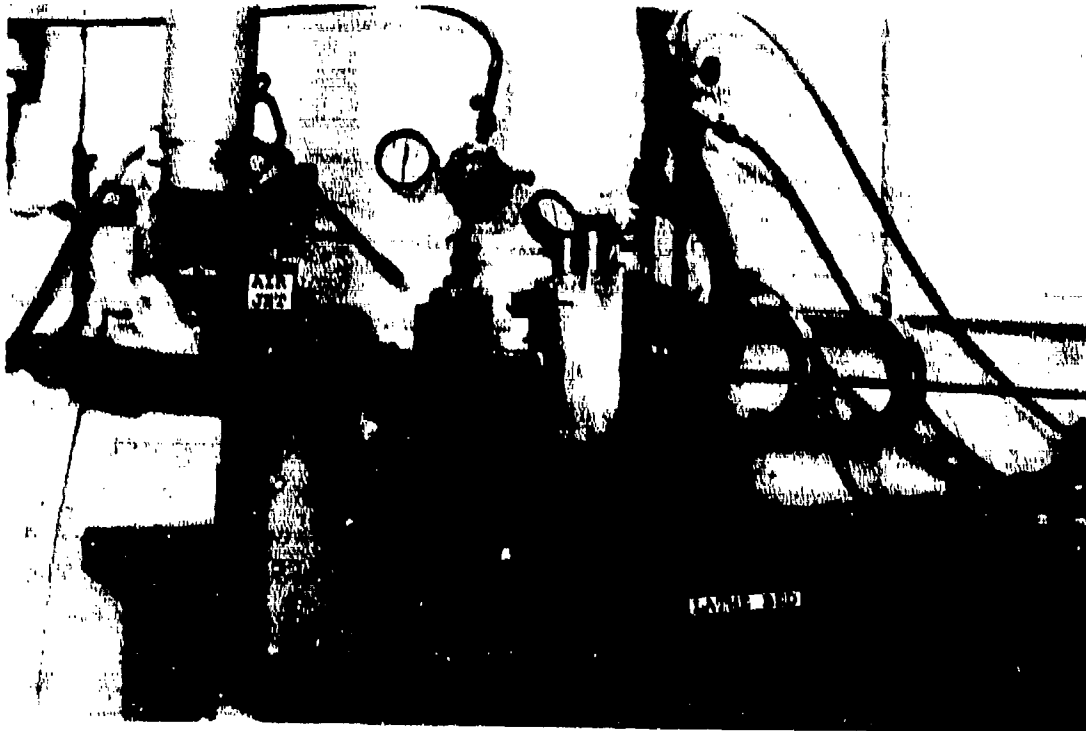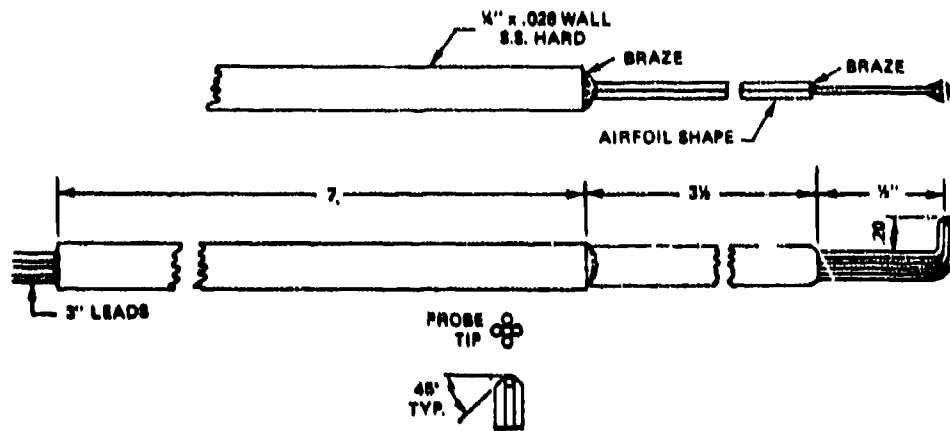
Figure 44.   A Five-Hole Pyramid Probe and Calibration
Set-up.

An electronic micromanometer (Datametrics Barocel Electronic
Manometer No. 1173), which could accurately read the pressure
differential over the range 0.001 to 100 inch of water, was used
for recording the pressures.

The measured data was reduced and correlated with the
following three parameters:

- Total pressure parameter, $PP_1 = \dfrac{P_t - P_1}{q}$

- Static pressure parameter, $PP_2 = \dfrac{P_s - P_{yaw}}{q}$

- Pitch parameter, $PP_3 = \dfrac{P_U - P_L}{q}$

where:

P_t	=	true total pressure
P_s	=	true static pressure
P_1	=	probe total pressure
P_{yaw}	=	probe yaw (static) pressure
$P_U - P_L$	=	pressure difference between upper and lower pitch ports of the probe
q	=	true kinetic head.

All of the three parameters were found to be independent of
the Mach number over the range M=0.04 to 0.3. The data was best
fitted by polynominals of different orders. Little reduction in
the mean square errors of the parameters PP_1 and PP_2 was
observed beyond a sixth-order polynominal. On the other hand, a
fifth-order polynominal gave the best fit for the PP_3 data. The
results along with the best-fit expressions for one of the two
probes calibrated is presented in Figure 45.

Three isothermal (cold) flow-mapping tests were conducted
with the can combustor installed in the rig. A close-up view of
the test setup and test conditions are presented in Figure 46.
Two probe stops, indicated as lower and upper stops in
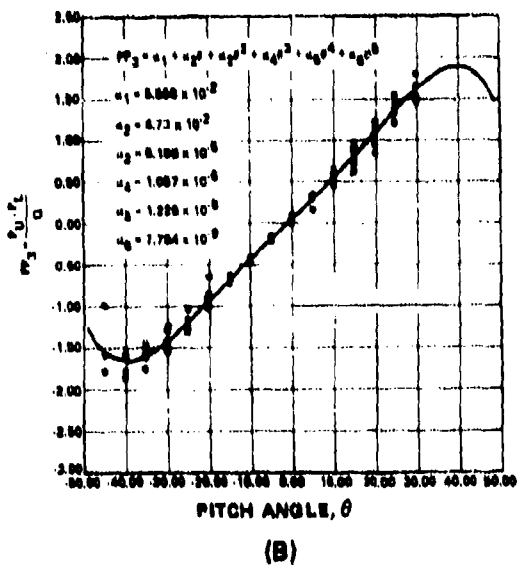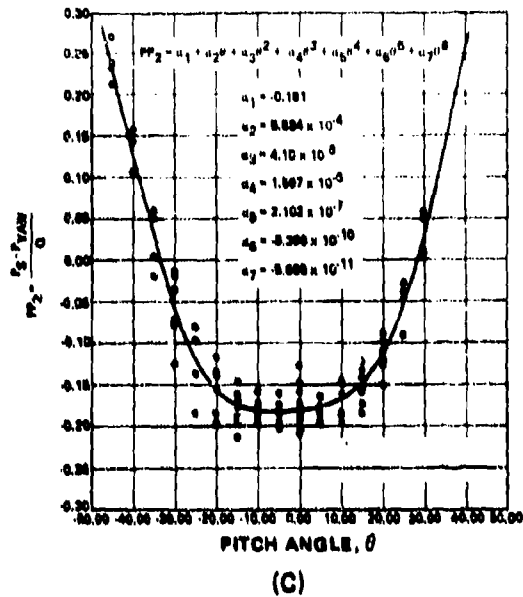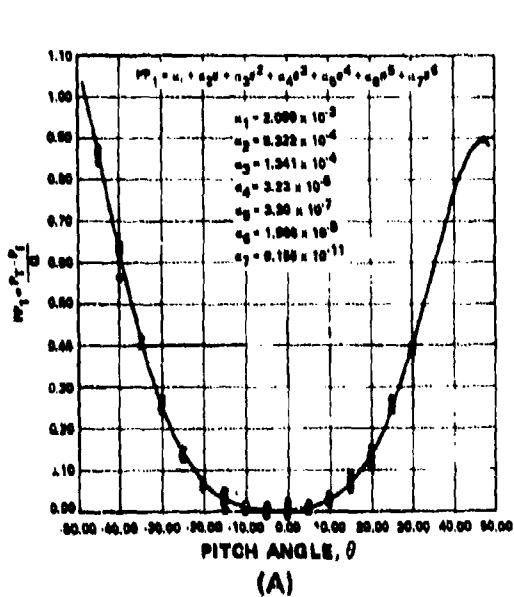
130

$$PP_1 = a_1 + a_2\theta + a_3\theta^2 + a_4\theta^3 + a_5\theta^4 + a_6\theta^5 + a_7\theta^6$$

$a_1 = 2.000 \times 10^{-3}$
$a_2 = 5.322 \times 10^{-4}$
$a_3 = 1.341 \times 10^{-4}$
$a_4 = 3.23 \times 10^{-6}$
$a_5 = 3.30 \times 10^{-7}$
$a_6 = 1.900 \times 10^{-9}$
$a_7 = 9.194 \times 10^{-11}$

PITCH ANGLE, θ

(A)

$$PP_2 = a_1 + a_2\theta + a_3\theta^2 + a_4\theta^3 + a_5\theta^4 + a_6\theta^5 + a_7\theta^6$$

$a_1 = -0.181$
$a_2 = 5.584 \times 10^{-4}$
$a_3 = 4.10 \times 10^{-6}$
$a_4 = 1.997 \times 10^{-5}$
$a_5 = 2.103 \times 10^{-7}$
$a_6 = -5.390 \times 10^{-10}$
$a_7 = -9.890 \times 10^{-11}$

PITCH ANGLE, θ

(C)

$$PP_3 = a_1 + a_2\theta + a_3\theta^2 + a_4\theta^3 + a_5\theta^4 + a_6\theta^5$$

$a_1 = 5.500 \times 10^{-2}$
$a_2 = 4.73 \times 10^{-2}$
$a_3 = 8.100 \times 10^{-5}$
$a_4 = 1.907 \times 10^{-6}$
$a_5 = 1.229 \times 10^{-8}$
$a_6 = 7.764 \times 10^{-9}$

PITCH ANGLE, θ

(B)

P_T = TRUE TOTAL PRESSURE
P_S = TRUE STATIC PRESSURE
P_1 = PROBE TOTAL PRESSURE
P_{YAW} = PROBE YAW (STATIC) PRESSURE
$P_U - P_L$ = PRESSURE DIFFERENCE BETWEEN UPPER AND LOWER PITCH PORTS OF THE PROBE
Q = TRUE KINETIC HEAD

Figure 45.   A Five-Hole Pyramid Probe and Calibration Setup.

131

○ **TEST CONDITIONS**

COND #	P3 (ATM)	T3 (K)	Wa3 (Kg/s)	ΔP/P (%)
1	10.00	288	1.818	3.25
2	10.03	288	2.263	5.01
3	9.98	288	2.736	7.39

Figure 46. Cold Flow Can Combustor Mapping.

Figure 46, were provided so that the probe would traverse a prescribed length of 11.7 cm, whereas the combustor internal diameter was 12.5 cm. When the probe was at its lower stop, its distance from the lower wall was 3.8 mm; similarly when at the upper stop, the distance from the upper wall was 3.8 mm. These stops were provided to avoid any structural damage to the probe. The combustor-inlet pressure and temperature were measured by three total-pressure probes and two CA thermocouples. The probe traverse of 11.7 cm was made with an existing traversing mechanism that provided an automatic yaw null. The transducer pressure traces and yaw angle were recorded on Hewlett-Packard chart recorders. Typical traces are shown in Figure 47. The top half of the figure shows the variation of yaw angle (looking down on the probe) and the difference in pressures measured at the upper and lower pitch holes. Note that the pressure fluctuations of up to 100 cm of water were measured indicating a high level of flow-velocity fluctuations. The probe total pressure (P_1) was measured with respect to the combustor inlet pressure (P_3) in order to eliminate any possible inlet line pressure fluctuations. The yaw pressure was measured with respect to the probe total pressure. Fluctuations of up to 60 cm of water in the total pressure and the probe kinetic heat ($P_1 - P_{yaw}$) were observed. These fluctuations were greater than the combustor exit mean kinetic head of 5.1 cm-H_2O corresponding to an airflow rate of 1.367 kg/s. Consequently, it was quite difficult to make a good estimate of time-mean values of the probe output.

A computer program was used to expedite the raw data reduction. Since a large quantity of data was obtained, typical axial-velocity profiles are presented here as an illustration: The rest of the data, along with the 3-D model predictions, is shown in Section V.C. Figures 48 through 51 present axial-velocity profiles for a total of 16 ports at test condition No. 1.

133
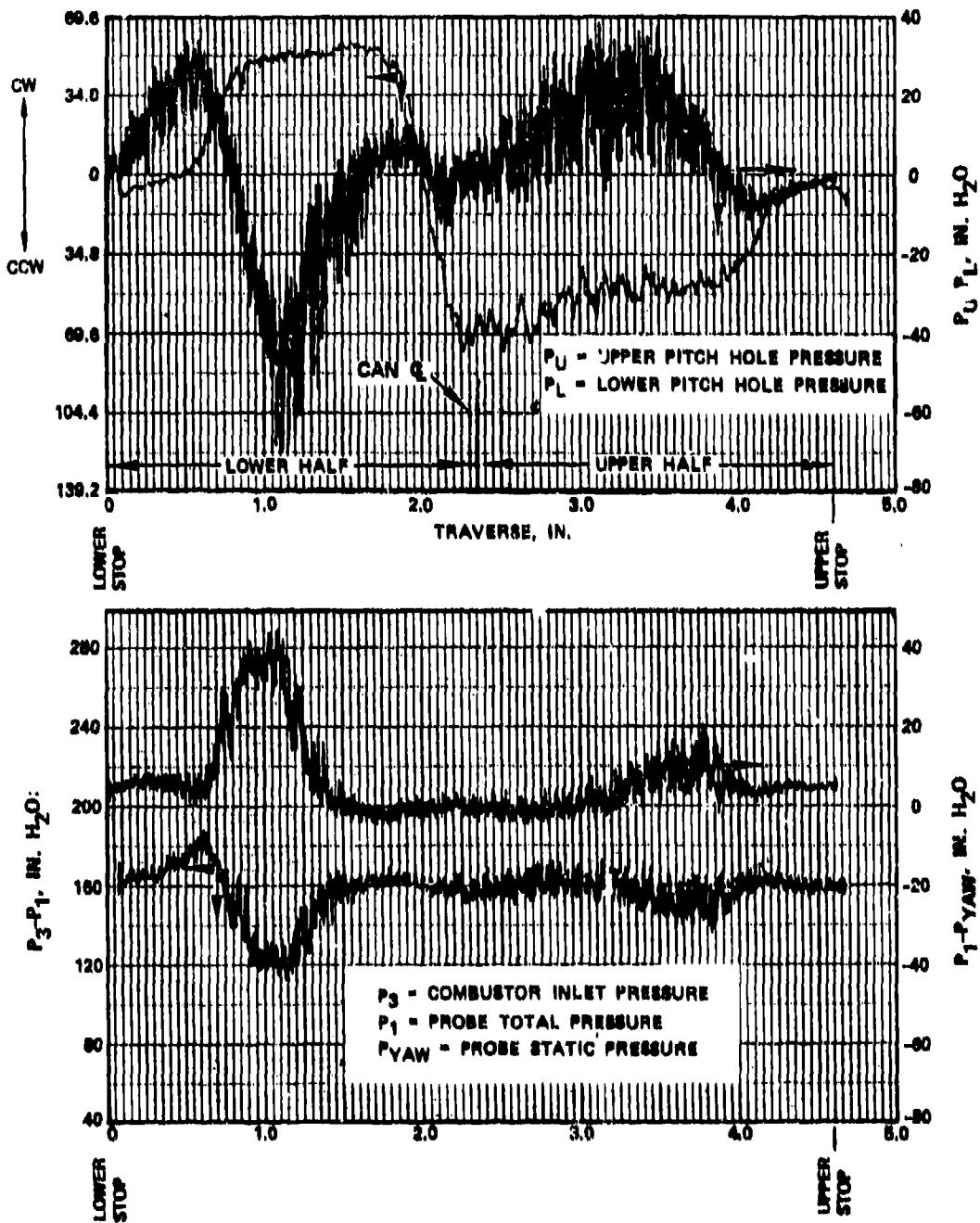
Figure 47. Typical Pressure and Yaw Angle Traces.

134
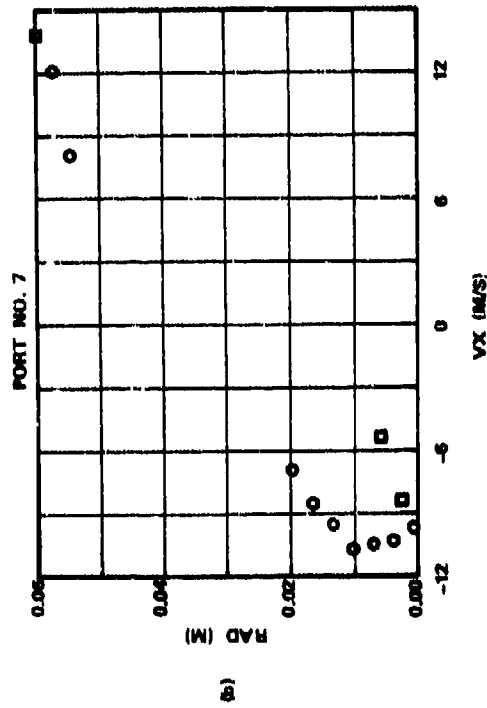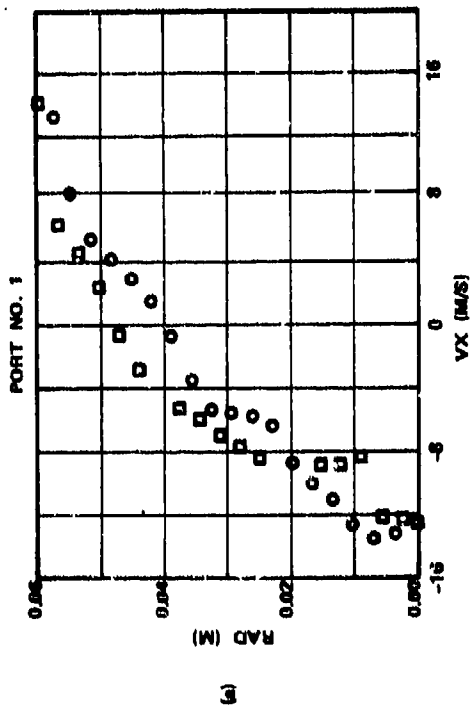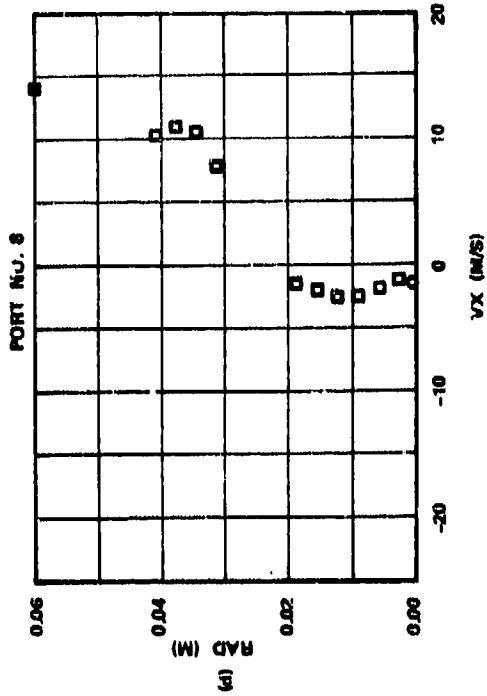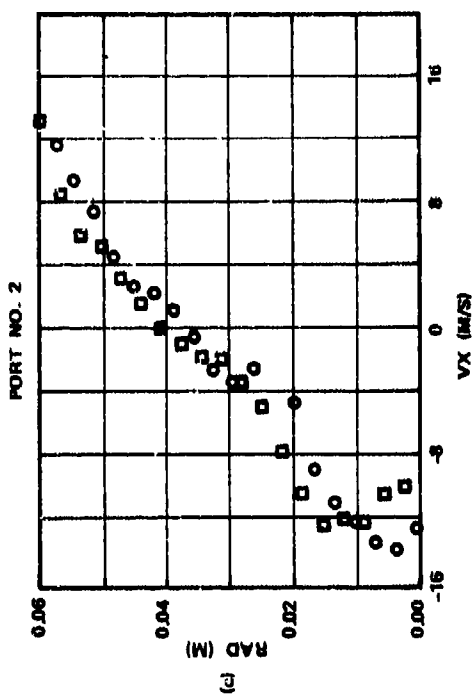
Figure 48. Axial Velocity Profiles for Condition No. 1.
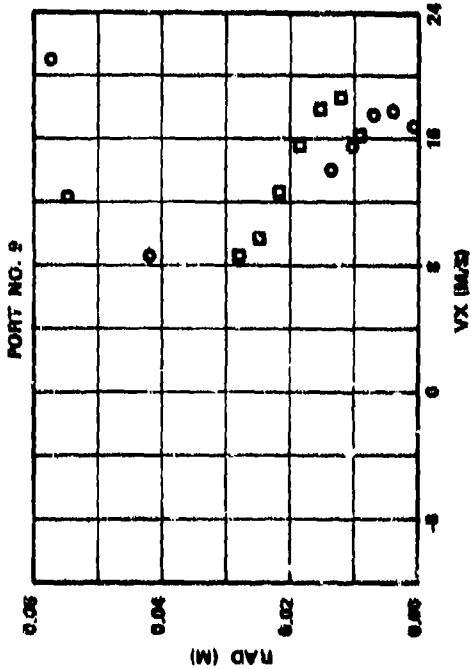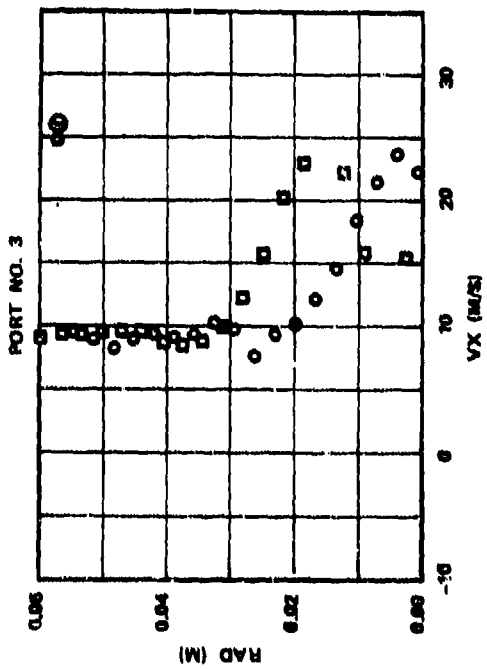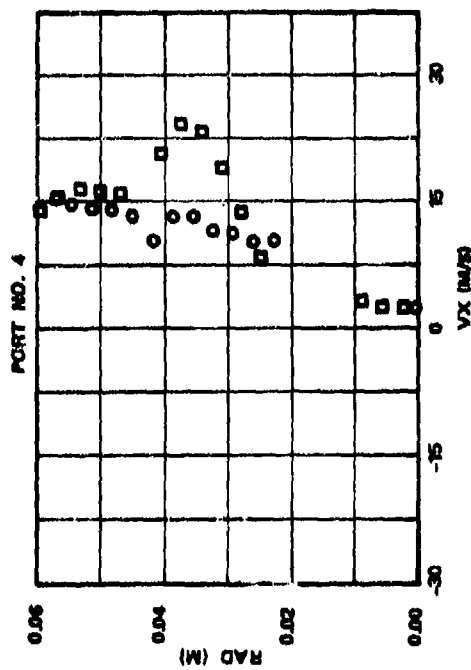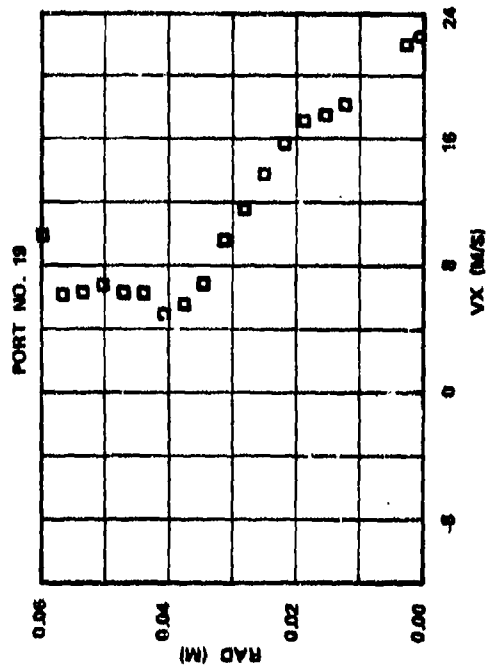
Figure 49. Axial Velocity Profiles
for Condition No. 1.

136
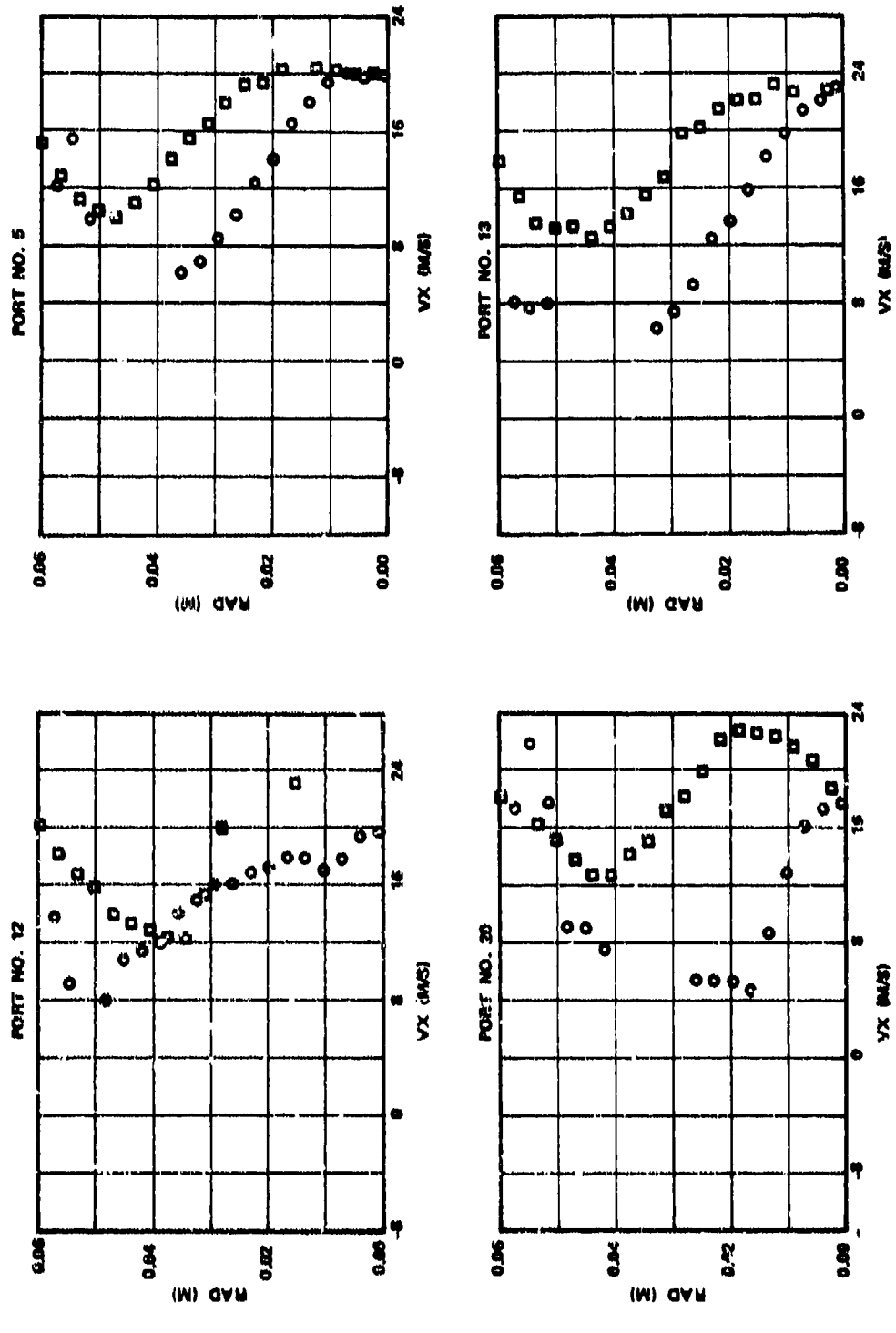
Figure 50.   Axial Velocity Profiles for Condition No. 1.

137
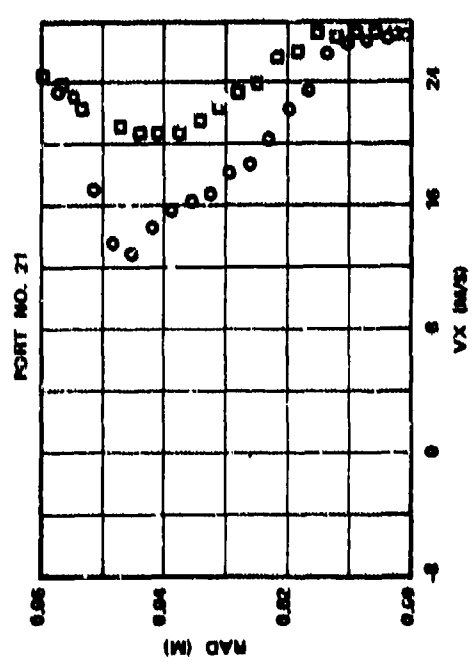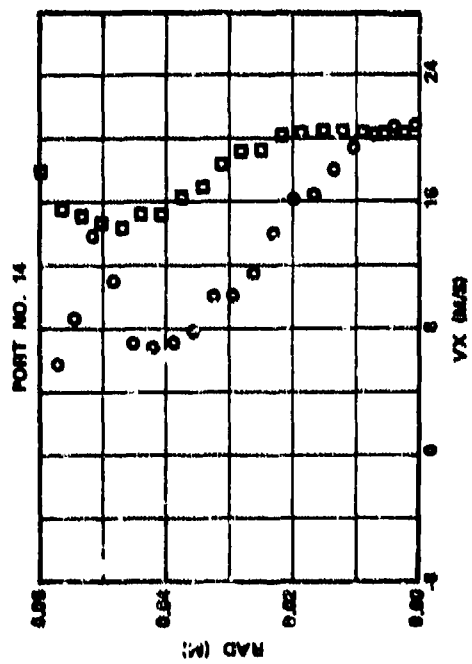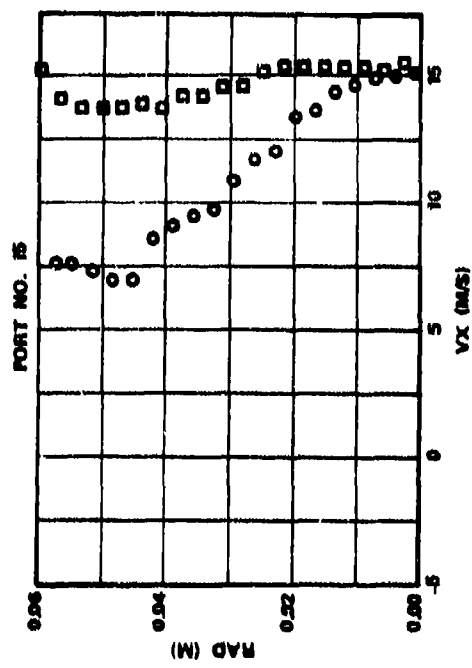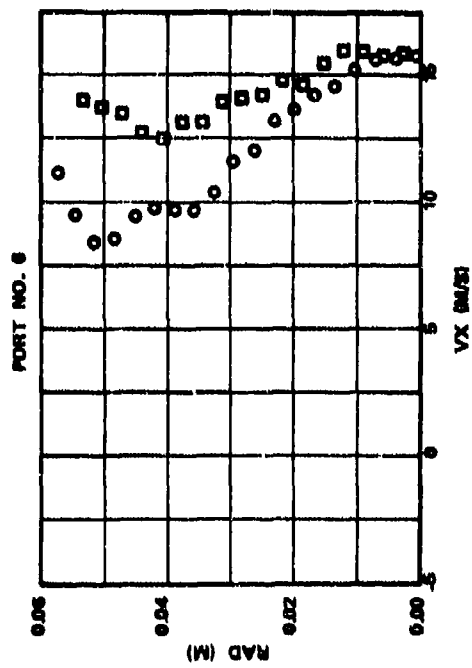
Figure 51. Axial Velocity Profiles for Condition No. 1.

138

Figure 48 shows radial profiles of axial velocity at axial Stations 1, 2, and 7 in the primary zone, and Station 8 which is immediately downstream from the primary jet. At port No. 1 (approximately 1 cm downstream from the lip of cooling slot No. 1 and 3 cm upstream from the primary orifice, and lying in between the primary jets) the measured recirculation height was approximately 4.5 cm or 0.72 of the can radius. There is some difference between the radial profiles on both sides of the can centerline. However, the small difference could be caused by: (a) airflow distribution around the liner, (b) the blockage caused by the 21 tubes/plugs through the outer annulus, and (c) inaccuracy in calculating time-mean values. The results for port No. 7, which was located in line with a primary orifice, were similar to those of port No. 1. At this location, the probe could not be nulled at many of the radial stations. However, it is interesting to note that the axial velocity near the wall and the can centerline at port No. 7 were approximately equal to those of port No. 1, thus lending confidence to the measurements. The measured recirculation-zone height at port No. 2, which was located between primary orifices and 5 mm upstream of the primary orifice row, was approximately 4 cm. A slight reduction in the axial velocity near the wall may be noticed as expected. The recirculation zone was terminated by the primary jets, as shown by measurements at port No. 8 located 1.3 cm downstream from the primary orifice.

The experimental data for port No. 3 (Figure 49) appear to be suspect in that the velocity peak near the wall, created by the cooling film, is not evident except by an isolated point (numbered 1). This observation is further supported by the data for port No. 9, where a velocity peak near the wall was observed as expected. A reduction in the cooling-film velocity with axial distance downstream from the lip is quite obvious, as shown for port No. 19. The data for port No. 4 appears suspect when compared with that of port No. 19.

Although there was more scatter in data for ports No. 12 and No. 20, as shown in Figure 50, a peak in the axial-velocity profile (caused by the presence of the cooling film) is obvious. Further reductions in the peak value with axial distance can be noted for ports No. 5 and No. 13. Other data for the dilution zone is presented in Figure 51.

From a general review of the data, it was concluded that the data was valid; although some discrepancies were noted between the data from the lower and upper halves of the combustor. These discrepancies are consistent, and can be explained. It is apparent that for highly turbulent recirculating flows, a measurement system should be utilized that minimizes flow-field distortion.

D.   Can Combustor Reacting Flow Mapping

A can combustor, presented in Figure 52, was used for mapping radial profiles of CO, CO_2, NO_x, and HC at different axial stations. The mapping was conducted with both gaseous (natural gas) and liquid fuels (Jet-A). The can combustor was similar to that used for cold-flow mapping, except for a fourth cooling slot shown in Figure 52.

A water/steam cooled stainless steel emission probe (Figure 53), with 10 individual radial points was designed and fabricated under this program. Heated water at approximately 423 K and under pressure entered the emission probe. The water-flow rate was adjusted to maintain the probe-head surface temper- ature at approximately 423 K. A hot water/ condensing unit was used for supplying the required hot water flow rate, and for condensing the water/steam mixture exiting the emission probe. A detailed thermal and stress analysis was conducted for the emission probe to insure proper quenching of the sample and dura- bility of the probe. The probe was successfully used for

CAN RADIUS = 6.35 cm

ALL DIMENSIONS IN CENTIMETERS
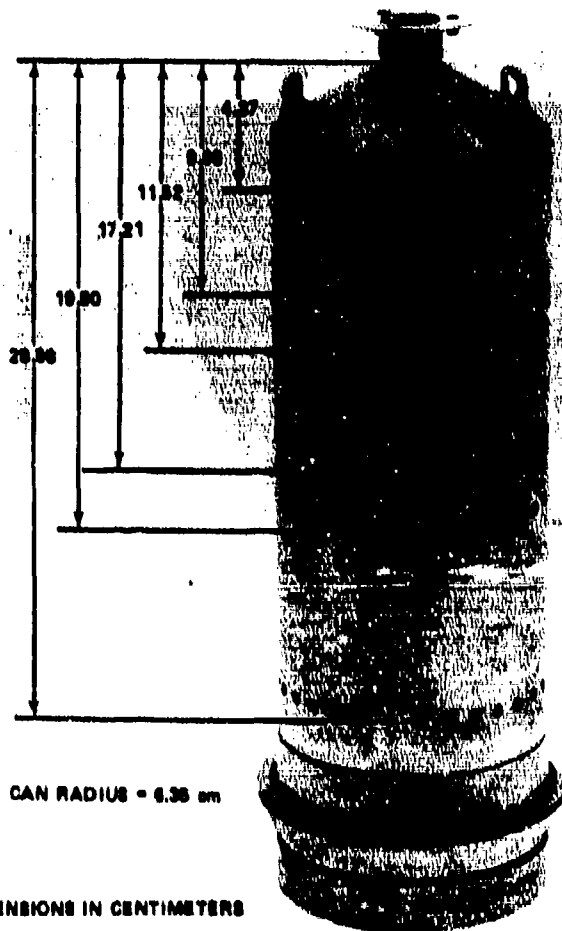
REACTING FLOW CAN COMBUSTOR GEOMETRICAL DETAILS

ORIFICE TYPE	NO. OF ORIFICES	SIZE (cm)	GEOMETRIC AREA, cm^2	AXIAL DISTANCE (cm)
DOME LOUVERS	30	0.36	3.02	--
PRIMARY	6	1.12	5.89	9.09
DILUTION	6	1.42	9.53	17.21
COOLING SLOT LIP				
#1	30	0.44	4.6	5.05
#2	30	0.48	5.43	12.20
#3	30	0.48	5.43	20.59
#4	30	0.48	5.43	29.67

Figure 52. Can Combustor for Reacting Flow Mapping.
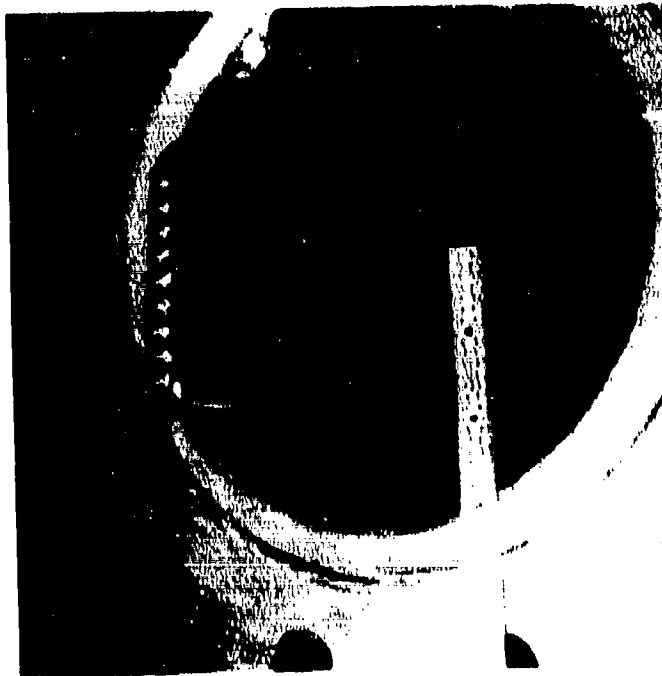
EMISSIONS PROBE

HOT WATER/CONDENSING UNIT

Figure 53. Emission Probe and Hot Water/Steam Condensing Unit.

142

measuring emissions for all of the 13 test conditions listed
in Tables 15 and 16 without incurring any structural deterioration.

A natural gas nozzle with nozzle-exit diameter of 7.67 mm,
and an air-assist airblast nozzle, as presented in Figure 54,
were used for the can combustor mapping. The reduced data of
radial profiles at different axial stations is given in Appendix
A. A circumferential position of 0 degrees lies along a plane
midway between the primary jets, whereas an x-r plane in line
with the center of the primary jet is denoted by 30 degrees.
The axial distance is measured from the face of the nozzle that
was installed flush with the combustor dome. The unburned
hydrocarbons (expressed as $C_{1.127} H_{4.254}$ for natural gas, and
$C_{10} H_{19.28}$ for Jet-A), CO, and NO_x are expressed as parts-per-
million (PPM) wet; whereas CO_2 is presented as percent moles of
the products.

TABLE 15. COMBUSTOR FLOW CONDITIONS AND PARAMETERS FOR EMISSIONS MAPPING WITH NATURAL GAS.

Parameters	Set-1	Set-2	Set-3	Set-4	Set-5	Set-6	Set-7
Combustor airflow, kg/s	0.372	0.374	0.227	0.749	1.115	1.109	1.959
Combustor inlet pressure, atm	2.01	2.00	2.00	4.02	6.02	6.04	6.03
Fuel/air ratio	0.00607	0.00974	0.00635	0.01004	0.00606	0.01009	0.00635
T_3, K	370	369	369	366	371	372	369
T_4, K	643	796	654	805	644	813	654
ΔP, % Pt_3	3.23	3.28	1.21	3.24	3.24	3.20	9.94
W_c, kg/s	0.462	0.466	0.283	0.463	0.463	0.460	0.811
$\dfrac{Wa_3}{P_3^{1.75}\, e^{\frac{T_3}{300}}}$, kg/s	0.0319	0.0325	0.0197	0.0194	0.0140	0.0138	0.0247

Composition of natural gas

Component	CH_4	C_2H_6	C_3H_8	C_4H_{10}	CO_2	He	N_2
Mole fraction	0.8702	0.0852	0.0180	0.0009	0.0009	0.0002	0.0246

Equivalent fuel = $C_{1.127} H_{4.254}$

TABLE 16. COMBUSTOR FLOW CONDITIONS AND PARAMETERS FOR EMISSIONS MAPPING WITH JET-A FUEL.

Parameters	Set-8	Set-9	Set-10	Set-11	Set-12	Set-13
Combustor airflow, kg/s	0.369	0.672	0.667	0.931	0.929	1.435
Combustor inlet pressure, atm	2.02	4.02	4.02	6.03	6.02	9.99
Fuel/air ratio	0.01035	0.01109	0.0169	0.00999	0.01492	0.01478
T_3, K	371	450	453	533	534	623
T_4, K	790	888	1097	922	1098	1170
ΔP, % P_{t_3}	3.09	3.16	3.12	3.18	3.18	3.23
W_c, kg/s	0.21	0.21	0.21	0.21	0.21	0.21
$\dfrac{W_{a_3}}{P_3^{1.75} \ e^{\frac{T_3}{300}}}$, kg/s	0.0313	0.0131	0.0129	0.0068	0.0068	0.0032
Sauter mean dia, microns	46	28	33	20	22	17
Nozzle spray cone, degrees	90	90	90	90	90	90

Composition of Jet-A fuel

Aromatics, % by vol = 17.0
Naphthalenes, % by wt = 0.9
Hydrogen content, % by wt = 13.54
Hydrogen/carbon weight ratio = 0.157
Lower heating value = 4.308 x 10^7 Joules/kg
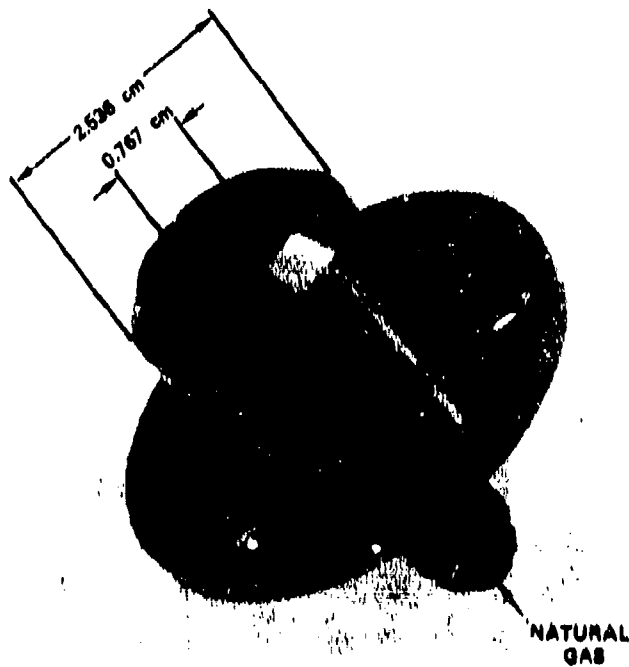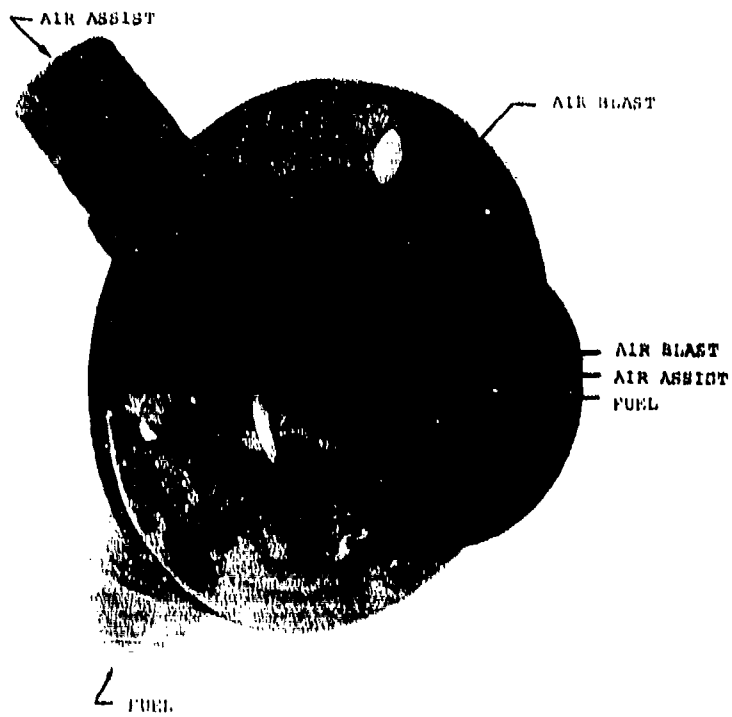
Figure 54. Natural Gas Nozzle and Airblast Nozzle Used for the Can Combustor Mapping.

146

Radial profiles were measured at up to eight axial stations, namely x = 6.0, 8.5, 10.4, 12.9, 15.4, 18.8, 21.3, and 26.2 cm. Up to five circumferential stations were mapped to measure variations of the profiles along different x-y planes. It is well known that there is a measurement error involved with perturbing types of probes such as used in the present study. Every effort was made to minimize the probe cross-dimension; however, the measurement errors were expected to be quite high in the primary zone and near the liner wall. In addition, the errors in measured HC were the highest. Consequently, only limited measurements were taken upstream of the primary orifices.

Figure 55 shows typical HC radial profiles for the six axial stations along two circumferential planes, inline and in-between the primary jet. The presented results are for Set-1 listed in Table 15. The radial profiles at θ = 0 and θ = 30 degrees at approximately 3 cm upstream from the primary orifices were relatively similar, and the peak is close to the can combustor centerline. However, at 1.3 cm downstream from the primary orifice, the profiles were considerably different. There was approximately two orders of magnitude reduction in HC near the can combustor center, compared to the upstream station at x = 6 cm. The peak in the HC profile was close to the liner wall for θ = 0, but was near the can combustor centerline for θ = 30 degrees. However, 1.5 cm further downstream at x = 12.9 cm, the radial profiles of HC along θ = 0 and 30 degrees were approximately similar. At 1.6 cm downstream from the dilution orifice, x = 18.8 cm, a minimum HC value of 40 ppm occurred at 3.0 cm radius for the plane inline with the dilution jet. At x = 26.2 cm, the profiles are relatively one-dimensional.

Figures 56 through 59 present average axial profiles of HC, CO, and NO_x for Set-1 through Set-13 to illustrate the effect of different parameters, including fuel/air ratio, combustor inlet-flow conditions, and the type of fuel on combustor performance.

147
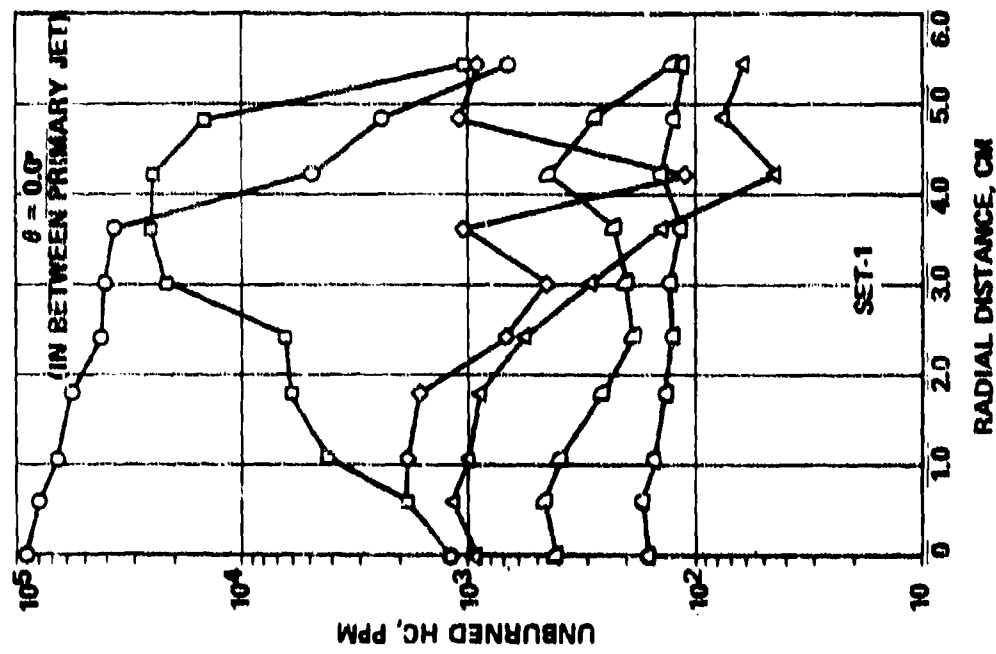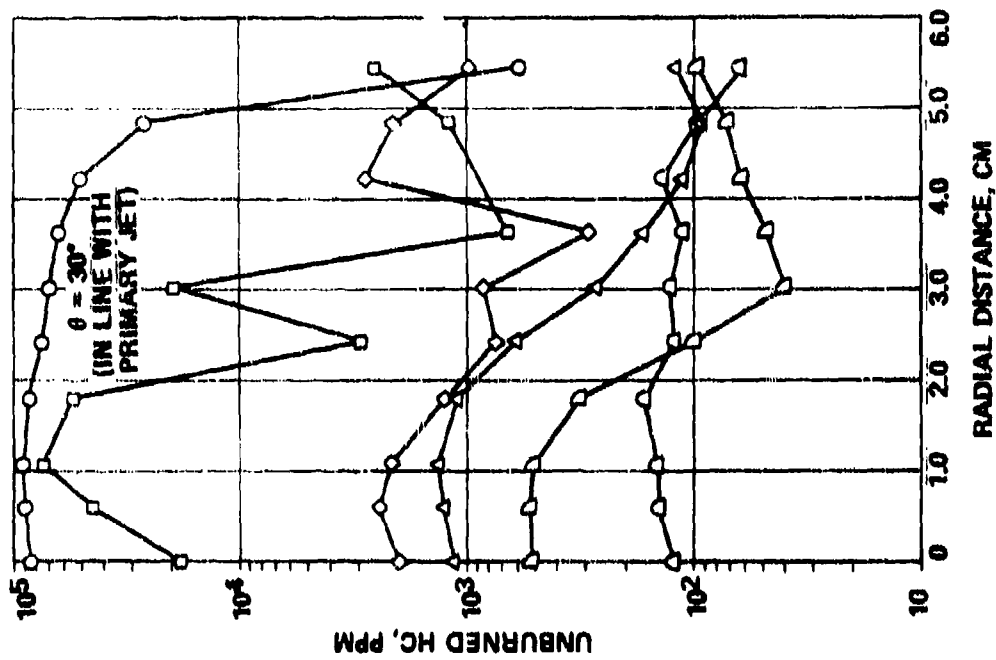
Figure 55. Measured Unburned Hydrocarbon Profiles In Line and In Between Primary Jet for Set-1.

148
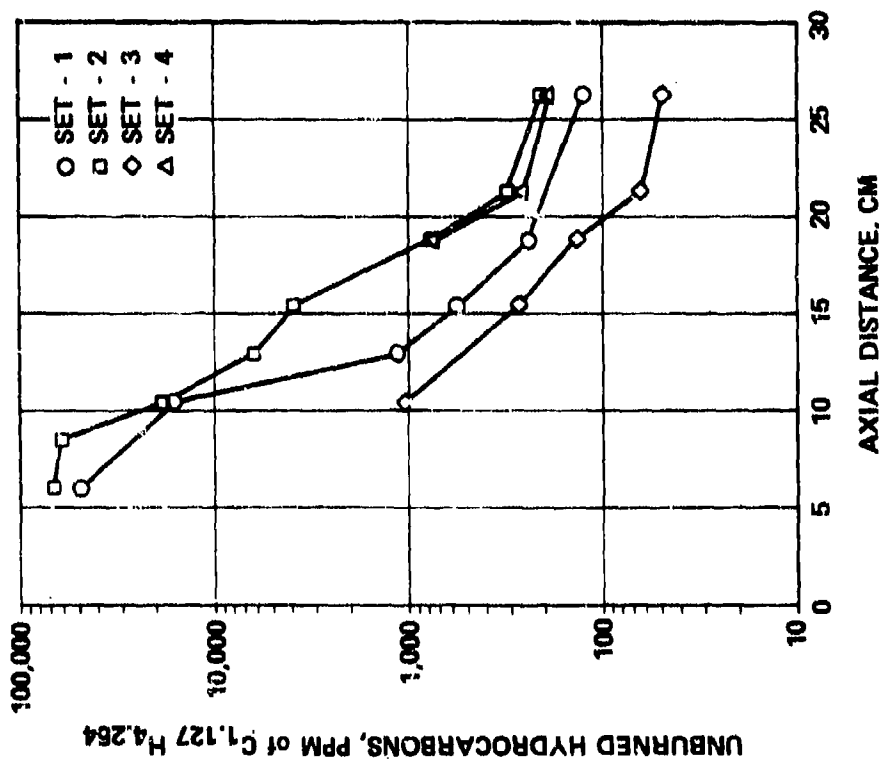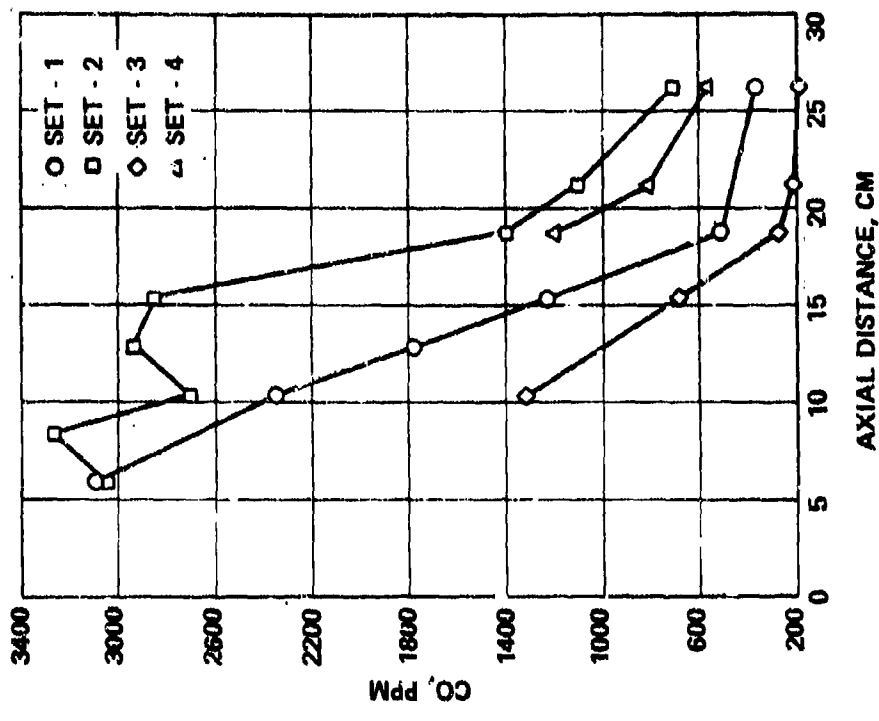
Figure 56. Average Profiles of HC and CO for Set-1 Through Set-4.

149
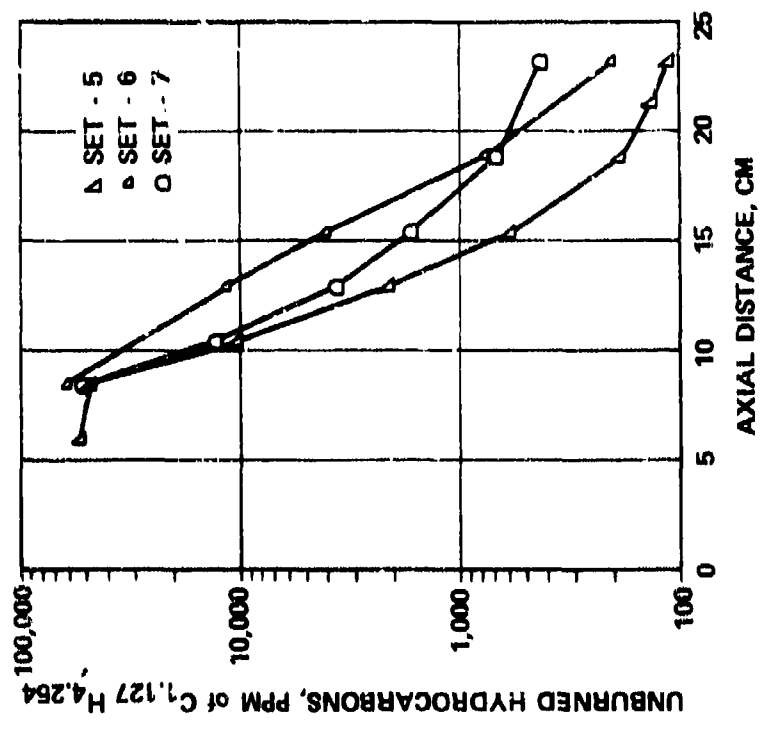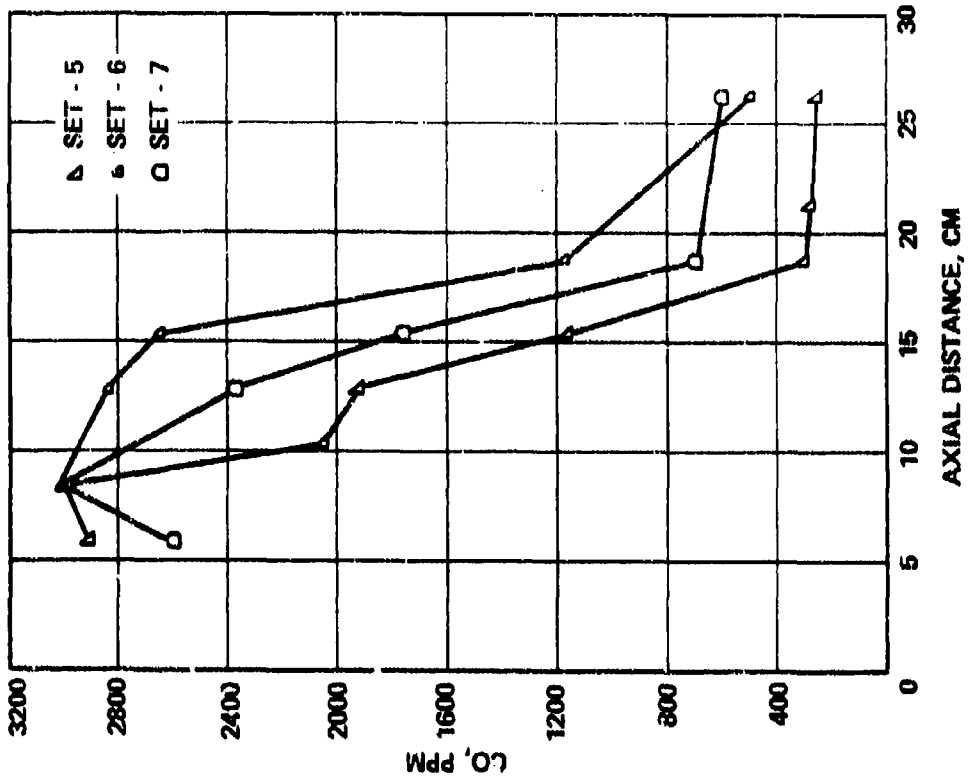
Figure 57. Average Profiles of HC and CO for Set-5 through Set-7.
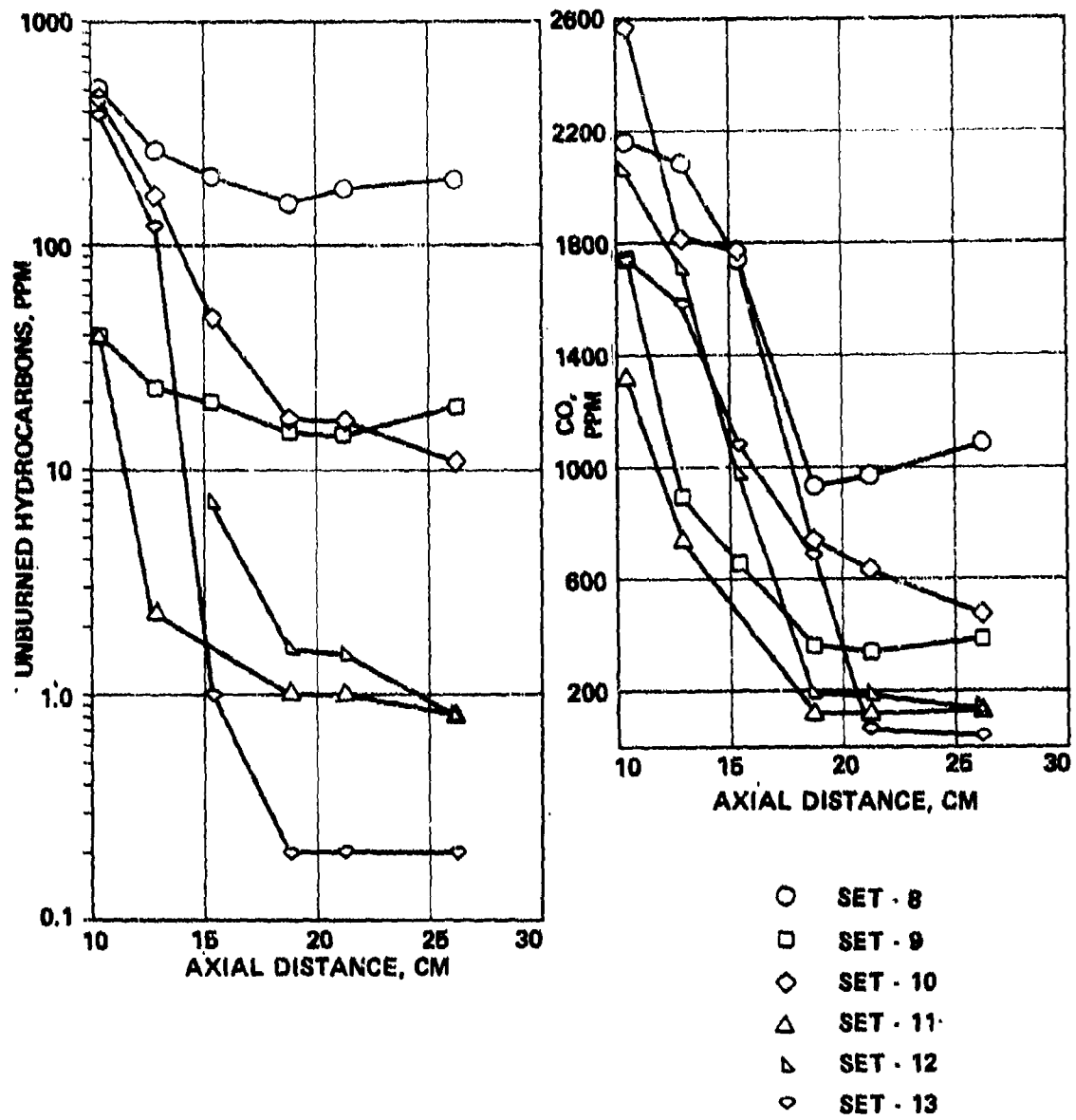
Figure 58. Average Profiles of HC and CO for Set-8 Through Set-13.
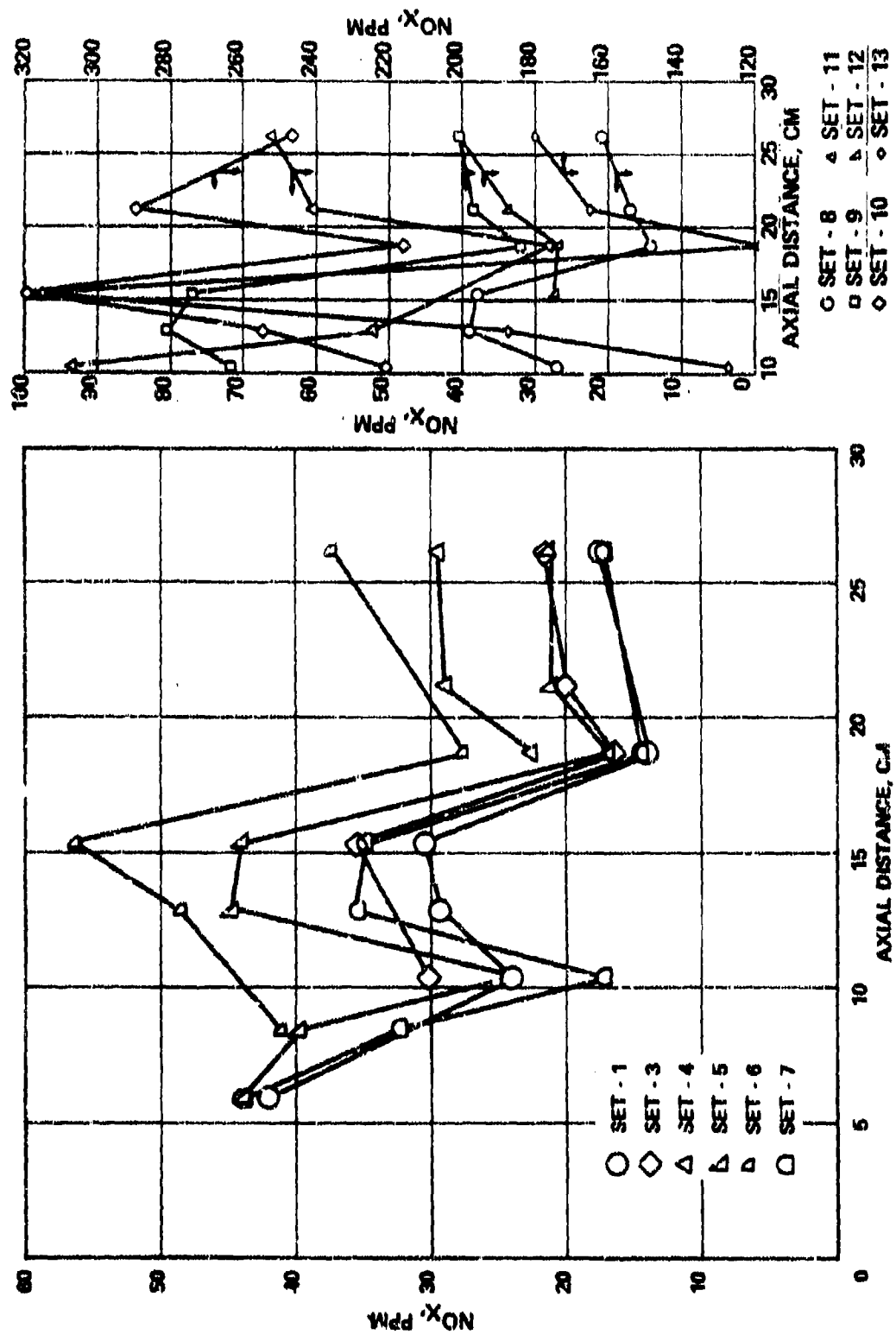
Figure 59. Average Profiles for NO_x for Set-1 Through Set-13.

First, the results with gaseous fuel will be discussed. With
increasing fuel/air ratio (such as Set-1 versus Set-2, and Set-5
versus Set-6) there was an increase in HC and CO, as shown in
Figures 56 and 57. An increase in pressure resulted in a
decrease in HC and CO. An increase in combustor residence time
(as in Set-1 versus Set-3, and Set-7 versus Set-5) resulted in
a decrease in HC and CO.

The fuel-nozzle characteristics strongly affect combustor
performance, shown by test results of Set-2 and Set-8. The
natural gas nozzle had approximately a zero spray angle, com-
pared to a 90-degree spray angle of the airblast nozzle. Set-2
had 15,000 ppm of HC at $x = 10.4$ cm, compared to 500 ppm in
Set-8. However, at $x = 26.2$ cm, the results were comparable.
On the other hand, at $x = 10.4$ cm the CO levels were comparable
with both natural gas and liquid fuel, whereas at $x = 26.2$ cm
the natural gas had a lower CO level. Increasing fuel/air ratio
had a minor effect on exhaust HC and CO emissions. An increase
in pressure caused a decrease in exhaust HC and CO emissions. A
comparison between NO_x emitted with gaseous and liquid fuels is
presented in Figure 59. Both Set-2 and Set-8 gave similar exit
NO_x emissions.

A comparison between analytical predictions and measure-
ments is presented in Section V.D.

E. Radiation Flux Measurements.

The thermal radiation from the can combustor (Figure 52) at
two axial locations, namely through primary and dilution
orifices, was measured with a Leeds and Northrup Ray-O-Tube.
The two sapphire windows were cooled by a double filtered plant
air line. The radiometer was focused at 38.1 cm from the
centerline of the can.

153

Since the radiometer was viewing through the primary and dilution orifices, the background (wall) radiation was negligible. The instrument had a background emf of 0.005 mV, and was approximately independent of the combustor inlet pressure and temperature. On the other hand, the emf reading through the primary orifice with P_{t3} = 1013 KPa, T_3 = 933 K, and f/a = 0.0215 was 3.05 mV. A typical fluctuation in the emf reading of the instrument was 0.05 mV. Therefore, the background radiation contribution could be neglected. Table 17 summarizes the radiation flux measured through the primary orifice with natural gas as the fuel. The measured radiation flux increased with pressure and fuel/air ratio as expected.

Table 18 presents the measured radiation flux through the primary orifice with Jet-A fuel. Again, expected results were obtained. The radiation flux with Jet-A was considerably higher than with natural gas, as may be seen by comparing Tables 17 and 18. The measured data cannot be compared with semi-empirical relationships, such as Reeve's Expression, which are strictly applicable to calculating radiation flux from a relatively uniform hot stream. The measured emissions profiles at stations 1.3 cm downstream from the primary orifice and 1.58 cm downstream from the dilution hole showed significant variations in the radial direction, as shown typically in Figures 60 and 61 for the test Set-13 of Table 16, respectively. As shown in Figure 60, approximately two orders of magnitude variation in radial profiles of CO, CO_2, and consequently water vapor, exist slightly downstream of the primary orifice. Consequently, the measured data will be compared with the prediction of the 3-D elliptic program that includes a six-flux radiation model.

154

TABLE 17. RADIATION FLUX THROUGH THE PRIMARY ORIFICE WITH NATURAL GAS.

Test No.	P_{t3} (kPa)	T_3 (K)	Wa_3 (g/s)	Fuel/Air Ratio	Radiation Flux $(J/s-m^2)$
1-2	508.7	497.5	757.5	0.0042	5.83×10^4
2-2	507.6	498.0	760.2	0.0082	8.83×10^4
3-2	508.7	500.8	755.8	0.0152	7.88×10^4
1-3	1013.3	626.4	1376.5	0.0043	11.35×10^4
3-3	1012.2	618.3	1368.2	0.0110	16.07×10^4

TABLE 18. RADIATION FLUX THROUGH THE PRIMARY ORIFICE WITH JET-A FUEL.

Test No.	P_{t3} (kPa)	T_3 (K)	Wa_3 (g/s)	Fuel/Air Ratio	Radiation Flux $(J/s-m^2)$
1-9	407.3	448.9	508.6	0.0148	3.15×10^5
1-10	406.3	450.8	506.4	0.0220	3.74×10^5
1-11	509.7	531.7	702.1	0.0133	4.41×10^5
1-12	610.0	532.2	703.5	0.0195	5.36×10^5
1-13	1013.3	622.8	1073.9	0.0215	7.25×10^5
1-14	1013.3	622.2	1069.8	0.0132	6.62×10^5
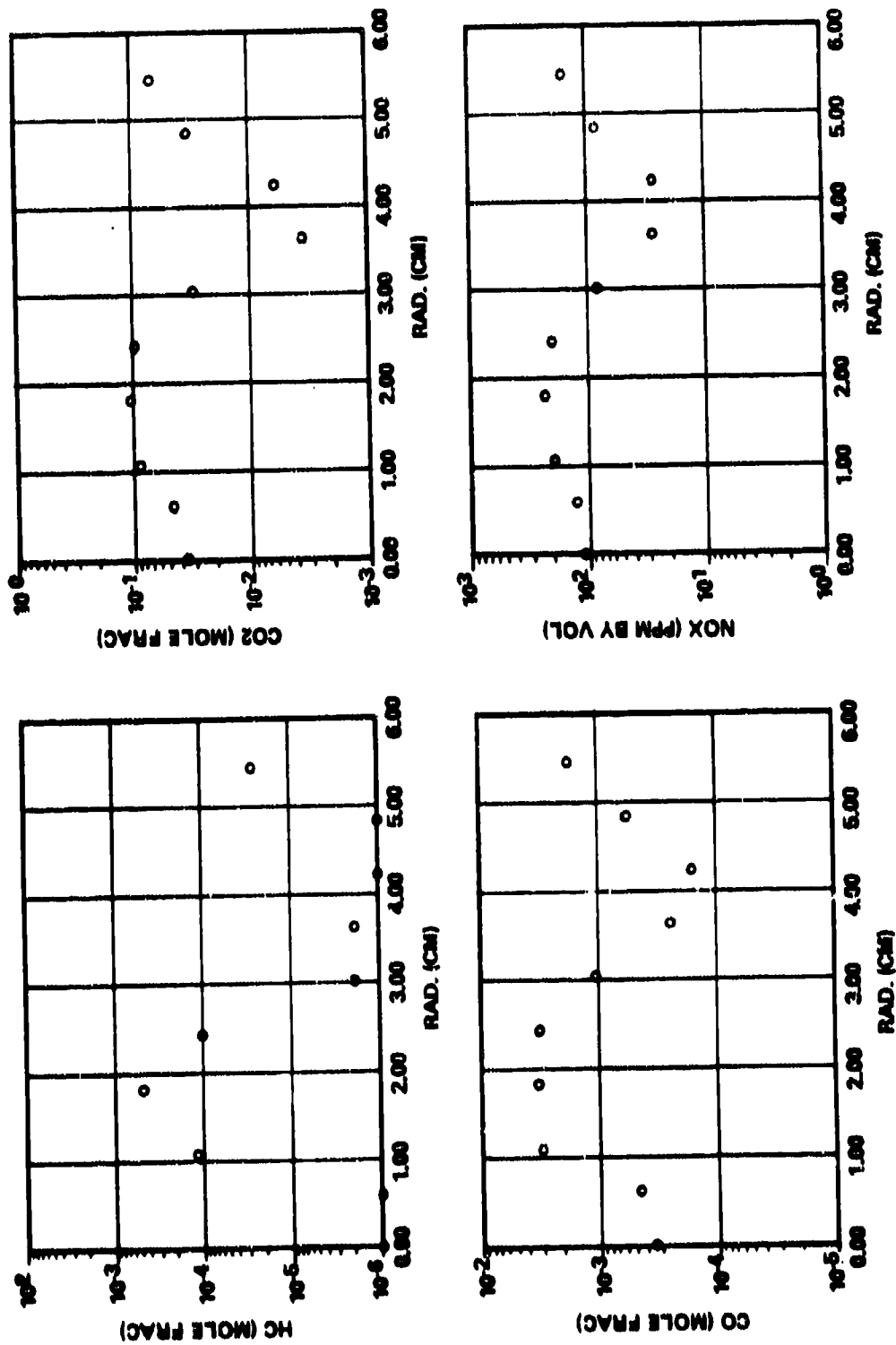
Figure 60. Measured HC, CO_2, CO, and NO_x Profiles at 13mm Downstream From, and In Line With, the Primary Hole for Set-13 of Table 16.
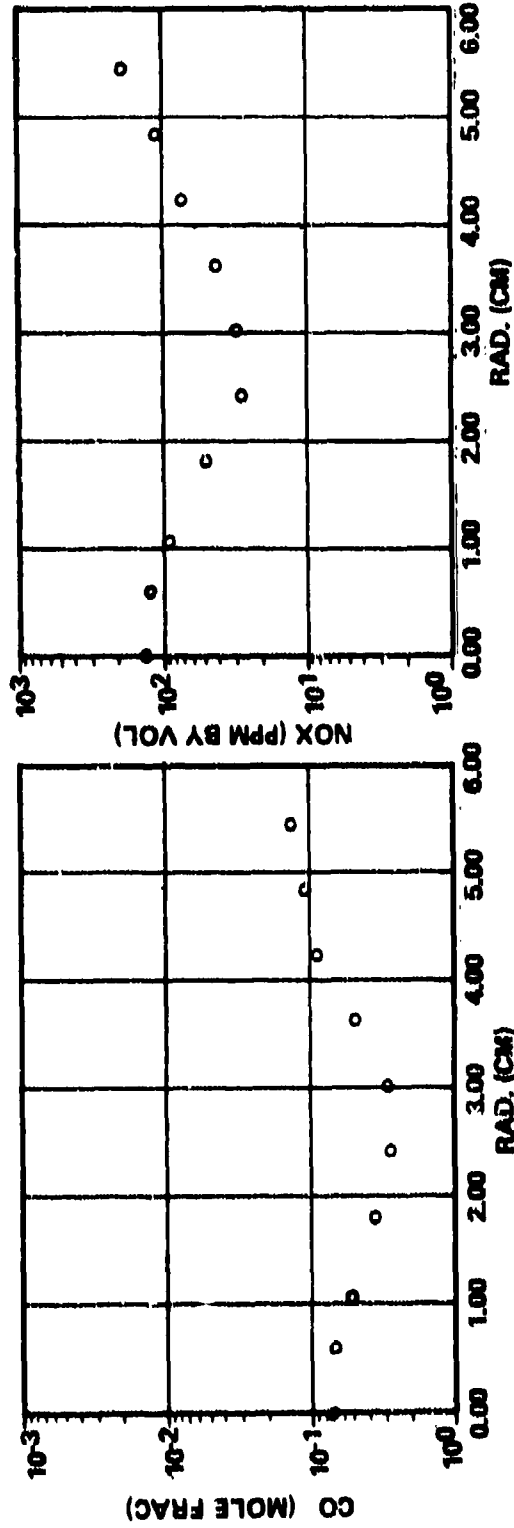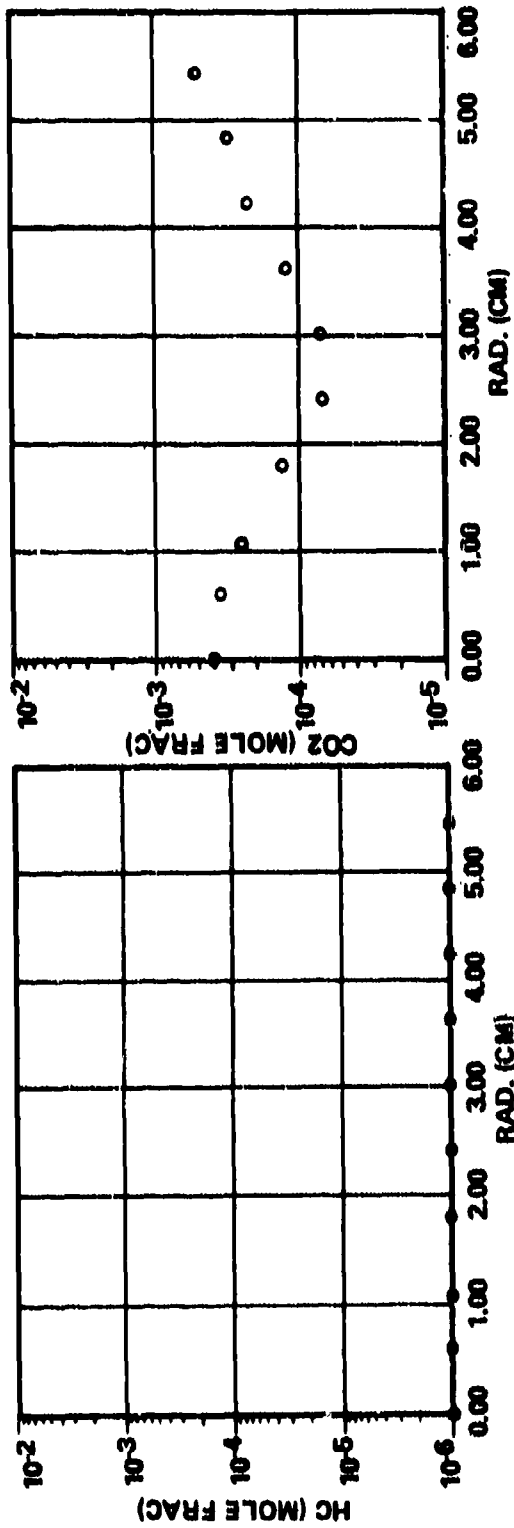
Figure 61. Measured HC, CO_2, CO, and NO_x Profiles at 15.6mm Downstream From, and In Line With, the Dilution Hole for Set-13 of Table 16.

157

TABLE 19.   RADIATION FLUX THROUGH THE DILUTION
HOLE WITH JET-A FUEL.

Test No.	P_{t3} (kPa)	T_3 (K)	Wa_3 (g/s)	Fuel/Air Ratio	Radiation Flux ($J/s-m^2$)
2-9	406.3	452.2	507.7	0.0148	0.69×10^5
2-10	405.2	452.8	509.3	0.0219	1.99×10^5
2-11	609.0	535.6	711.6	0.0133	0.74×10^5
2-12	608.0	536.1	711.2	0.0193	2.49×10^5
2-13	1013.3	621.4	074.5	0.0216	4.41×10^5
2-14	1012.2	621.1	1072.3	0.013	0.91×10^5

A significant decrease in the radiation flux through the
dilution hole was obtained, as shown in Table 19, compared to
that through the primary orifice. The reduction in the flux was
due to a lower local fuel/air ratio and gas temperature. The
measured radiation fluxes will be correlated with the 3-D
elliptic model predictions.

F.   Ignition Tests with Airblast Nozzles.

Ignition tests of the can combustor (Figure 52) with an air-
blast, air-assist/airblast, and piloted-airblast nozzle operating
on JP-4 fuel were completed. The ignition tests were conducted
with a reference velocity equal to 1.5 m/s which simulated a 10-
percent engine cranking speed) and 3.05 m/s at flow conditions
corresponding to standard-day sea level, 3048 and 6096 meter
altitudes. The combustor inlet temperature was maintained close
to 300 K. The measured ignition fuel/air ratio data are listed
in Table 20.

The pure airblast (AB) nozzle required an ignition fuel/
air ratio greater than 0.025 (Test No. 1-2) even at the sea-level
point. However, the light-off fuel/air ratio of the piloted AB
nozzle was much lower at 0.0132 (Test No. 4-2). The ignition
fuel/air ratio of air-assisted (AAB) nozzle was similar at a
boost pressure ratio of 1.6, as shown by Test No. 3-2. On the
other hand, the AAB nozzle exhibited lower ignition fuel/air
ratios at higher simulated ignition altitudes compared to the
piloted AB nozzle.

TABLE 20.   LIGHT-OFF FUEL/AIR RATIO OF A CAN
COMBUSTOR WITH JP-4 FUEL.

Test No.	P_{t3} (kPa)	Air-Assist Press./P_{t3}	Wa3 (g/s)	T_3 (K)	Reference Velocity (m/s)	Light-Off Fuel/Air Ratio
Pure Airblast						
1-2	122.0	-0-	0.076	298.9	4.2	>0.0252
Air-Assist Airblast						
2-2	122.0	1.20	0.076	298.3	4.2	0.0163
3-2	122.0	1.61	0.076	298.9	4.2	0.0137
2-3	84.8	1.20	0.027	299.4	2.1	0.0204
2-4	85.2	1.19	0.052	298.9	4.2	0.0121
3-3	84.8	1.60	0.027	299.4	2.1	0.0204
3-4	84.8	1.60	0.053	296.7	4.2	0.0127
2-4	85.2	2.30	0.052	298.9	4.2	0.0121
Piloted Airblast						
4-2	122.3	0	0.077	297.2	4.2	0.0132
4-3	84.7	0	0.026	299.4	2.1	0.0307
4-4	84.7	0	0.053	300.0	4.3	0.0154
4-6	47.4	0	0.017	300.6	2.4	0.0450

G. Nozzle Spray Sauter Mean Diameter Measurements.

The combustor efficiency, gaseous and particulate emissions, discharge-temperature quality, lean-flammability limits, and light-off characteristics of small, high-pressure-ratio, and high-temperature-rise combustors depend upon internal flow-field characteristics and major features of the fuel nozzle (such as Sauter mean diameter (SMD) and spray-cone angle). Although spray cones may be easily photographed, very elaborate test facilities have been required to measure SMD until recently.[19] A less costly optical device was built in parallel with this program to determine the mean droplet diameter of an atomizer spray from an analysis of the diffractively scattered light intensity. The apparatus was used to measure the SMD of an air-assist pressure atomizer and an air-assist airblast nozzle.

1. Description of Apparatus

The main advantage of the light-scattering technique is that it does not affect the nozzle-spray pattern or secondary atomization, as do other methods. The technique, as developed by Dobbins, Crocco, and Glassman[19], is based on the forward scattering of a parallel beam of monochromatic light that is passed through the spray. The angle through which the light is scattered by the droplets can be theoretically related to the mean droplet size.

The optical system is shown schematically in Figure 62. Laser light, collimated into a beam approximately 1 cm in diameter, is passed through the atomizer spray, and is focused upon an aperture in front of a photomultiplier tube. The intensity of the scattered light can then be determined by traversing the photomultiplier tube aperture across the light beam.

---

[19]Dobbins, R.A., Crocco, L., and Glassman, I., "Measurement of Mean Particle Sizes of Sprays From Diffractively Scattered Light," AIAA J. 1, 1882-1886 (1963)

[20]Rizkalla, A.A., and A.H. Lefebvre, "The Influence of Air and Liquid Properties on Airblast Atomization,"" ASME Journal of Fluids Engineering, Sept. 1975.
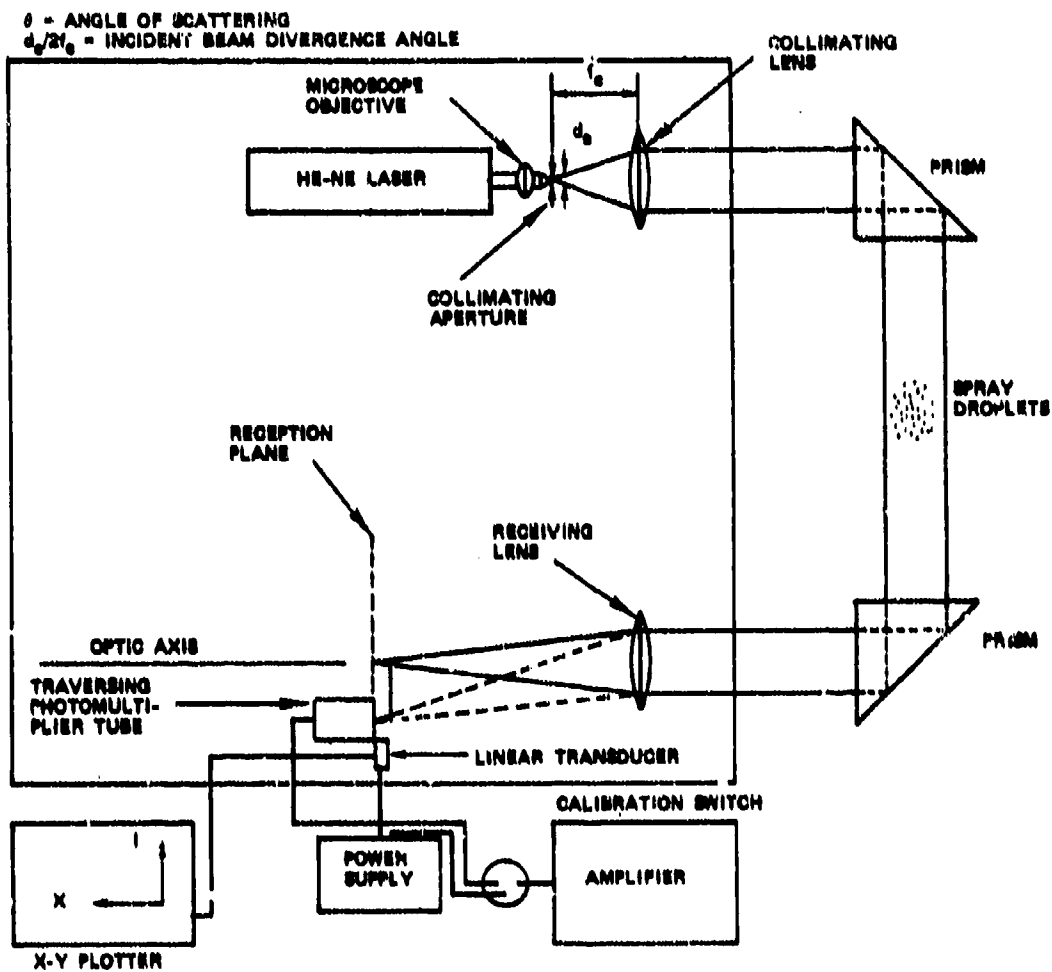
Figure 62. Schematic of Optical Apparatus used in Light-Scattering Technique.

A 5.0-milliwatt helium-neon laser produces the source of light with a wavelength of 632.8 nm, and a microscope objective lens focuses the laser beam onto a 25-micron collimating aperature. This aperature provides a point source of light at the focal point of the 11.5 cm focal length acromatic collimator lens, thus forming a parallel beam of light.

The ratio of the collimating aperature diameter to twice the collimating lens focal length is the divergence angle of the incident beam, which must be small compared to the angle of scattering. Since the angle of scattering decreases as particle size increases, the divergence angle determines the upper limit of mean droplet size that can be measured. The divergence angle of the system is equal to 0.012 degree, which is smaller than the 0.021 degree of the apparatus of Professor A. H. Lefebvre using a mercury arc lamp light source.[20]

The laser beam is reflected by a 45-, 90-, and 45-degree prism through the spray onto an identical prism, which reflects the light to the receiver lens. Again, the length of the system is shortened by the use of the prisms. The receiver lens focuses the light onto a 25-micron aperture in an otherwise light-tight photomultiplier box. The RCA photomultiplier tube has a maximum sensitivity at 420 nm, utilizes a 0-1600 VDC power supply, and is connected to a logarithmic amplifier.

The photomultiplier box can be traversed at right angles to the optical axis up to 2.54 cm. A micrometer adjustment gives the position of the photomultiplier box (relative to the optical axis) to an accuracy of 0.025 mm. The position of the photomultiplier box is indicated on the x-axis of the x-y plotter by a liner position transducer, and the light intensity at a given scattering angle is recorded on the y-axis on four-cycle semilogarithmic paper. The entire optical system is mounted on an air-suspended table, and is shown in Figure 53. An enclosure that shields the system from stray light was removed for the photograph.
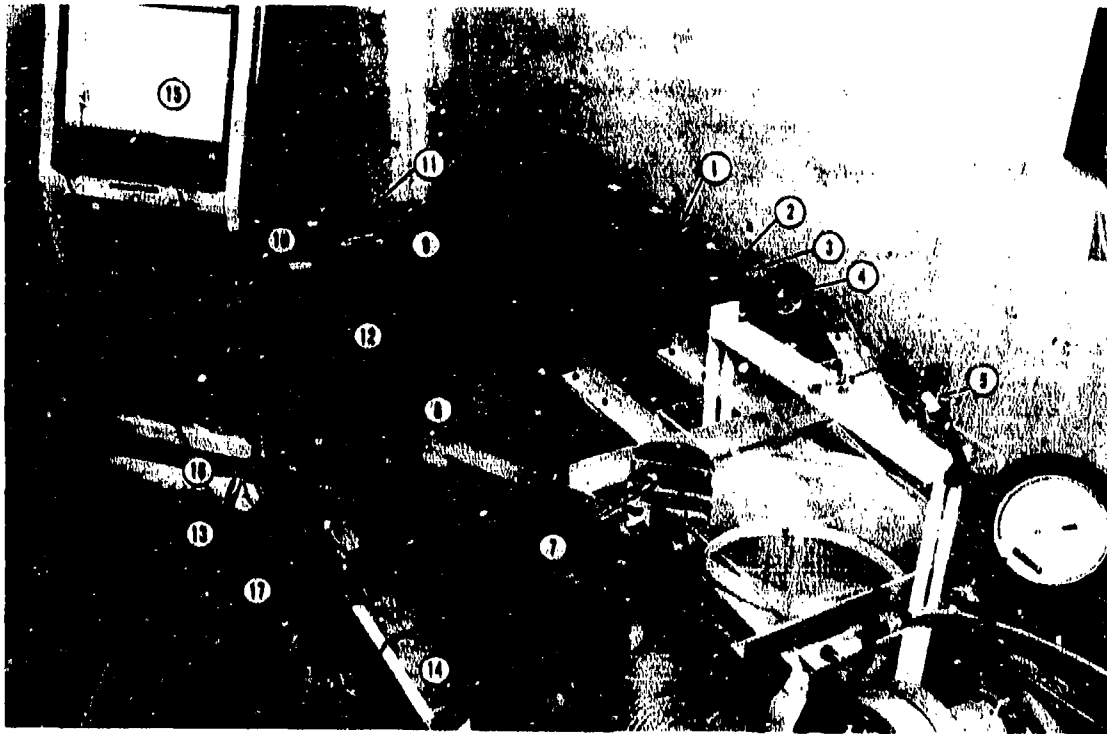
1. HELIUM NEON LASER
2. MICROSCOPE OBJECTIVE
3. 25 MICRON COLLIMATING APERATURE
4. CONVEX-CONVEX ACHROMATIC COLLIMATING LENS
5. 45°, 90°, 45° PRISM
6. FUEL NOZZLE (DOWNWARD SPRAY)
7. 45°, 90°, 45° PRISM
8. CONVEX-CONVEX ACHROMATIC RECEIVING LENS
9. 25 MICRON PHOTOMULTIPLIER APERATURE
10. LINEAR POSITION TRANSDUCER
11. TRANSVERSING PHOTOMULTIPLIER TUBE
12. AIR SUSPENDED TABLE
13. DC POWER SUPPLY 0-1600V
14. AUTOMATIC LOGARITHMIC CONVERTER
15. X-Y PLOTTER
16. LASER POWER SUPPLY
17. POWER SUPPLY FOR LINEAR TRANSDUCER

Figure 63.   Light Scattering Optical Apparatus.

2. Theory

The theory for the scattering of light by a polydispersion of dielectric spherical particles of size number α (equal to $\pi D/\lambda$, where D is the particle diameter, and λ is the wavelength of incident light) makes the following assumptions:

- The incident radiation is planar and monochromatic

- The forward angle of scattering, θ, is small

- The particle size number α and the phase shift 2α (M-1) are large (M is the refractive index)

- The particles are nonabsorbing

- The distance between the particle and observer is large compared to D^2/λ

- All the particles are illuminated equally; i.e., the attenuation of the incident beam is slight because the optical depth is small (Dobbins, et al. found the effects of finite optical depths to be negligible).

The intensity of the scattered light due to the polydispersion, normalized by dividing by the intensity of the light scattered in the forward direction $\theta = 0$, is equal to the following expression from Reference 20.

$$I(\theta) = \frac{\int_0^{D_m} \frac{2J_1(\alpha\theta)}{\alpha\theta} N_r(D)D^4 dD}{\int_0^{D_m} N_r(D)D^4 dD}$$

164

where D_m is the maximum particle diameter, J_1 is a Bessel function, and N_r (D) is the particle diameter distribution function. The upper limit distribution function proposed by Mugele and Evans[21] has been shown to be quite adequate in describing experimentally-measured droplet-size distributions, and was used to define N_r (D) by Dobbins et al.[20] The two variables of importance in describing a particular distribution are the skewness (most probable to maximum diameter ratio $\bar{D}/D_m$), and the spread of the distribution function (a monodispersion having the smallest spread). Roberts and Webb[22] found that when the scattered light intensity, $I(\theta)$, is plotted against the reduced angle, $\pi D_{32}\theta/\lambda$, (D_{32} is the volume-to-surface mean diameter or SMD), the scattered light intensity is almost independent of the particle-size distribution function. For wide distributions, and narrow ones approaching monodispersions, and for $0.13 < \bar{D}/D_m < 0.8$, the theoretical illumination profiles were nearly coincident; the mean illumination profile from Reference 22 is shown in Figure 64. The minimum standard deviation from the mean (about 1 percent) occurs when $I(\theta) = 0.08$. For convenience, the point to fit an experimentally-determined illumination profile to Figure 64 is chosen as $I(\theta) = 0.1$ and $\pi D_{32}\theta/\lambda = 2.647$. Therefore, by measuring the angle θ to the position where the light intensity is equal to 10 percent of the intensity of the forward scattered light ($\theta = 0$), the SMD can be calculated knowing the wavelength of the incident light.

A typical light-intensity profile plot obtained using the AiResearch equipment is shown in Figure 65 for an airblast atomizer spraying water. The unscattered light masks the forward scattered light near $X = 0$ requiring an extrapolation of the scattered-light intensity. The extrapolation should

[21] Mugele, R.A. and Evans, H.D., "Droplet Size Distribution in Sprays," Ind. Eng. Chem. 43, 1317-1324 (1951)

[22] Roberts, J.H. and Webb, M.J., "Measurements of Droplet Size for Wide Range Particle Distributions," AIAA J. 2, 583-585 (1964).
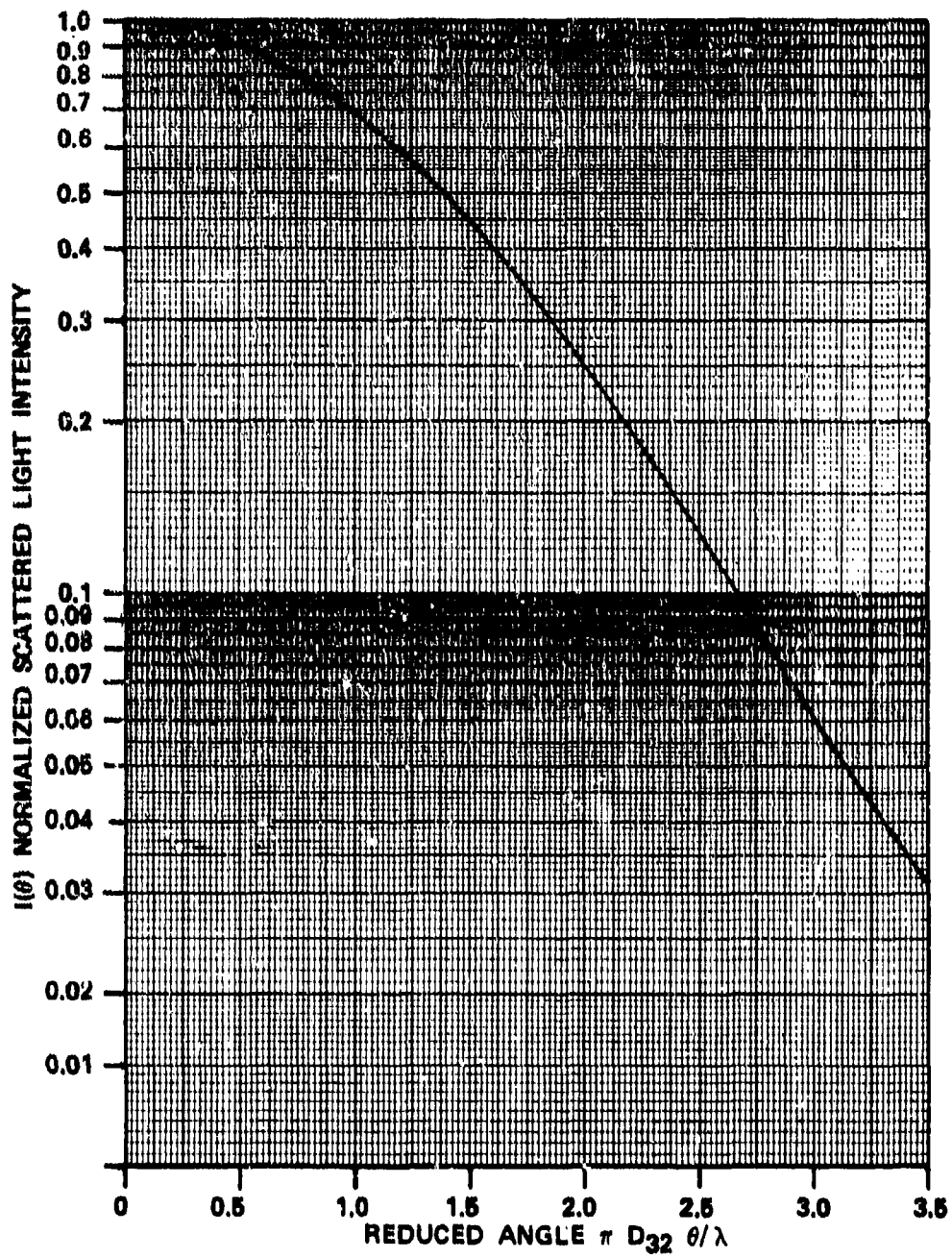
Figure 64.   Mean Theoretical Illumination Profile.
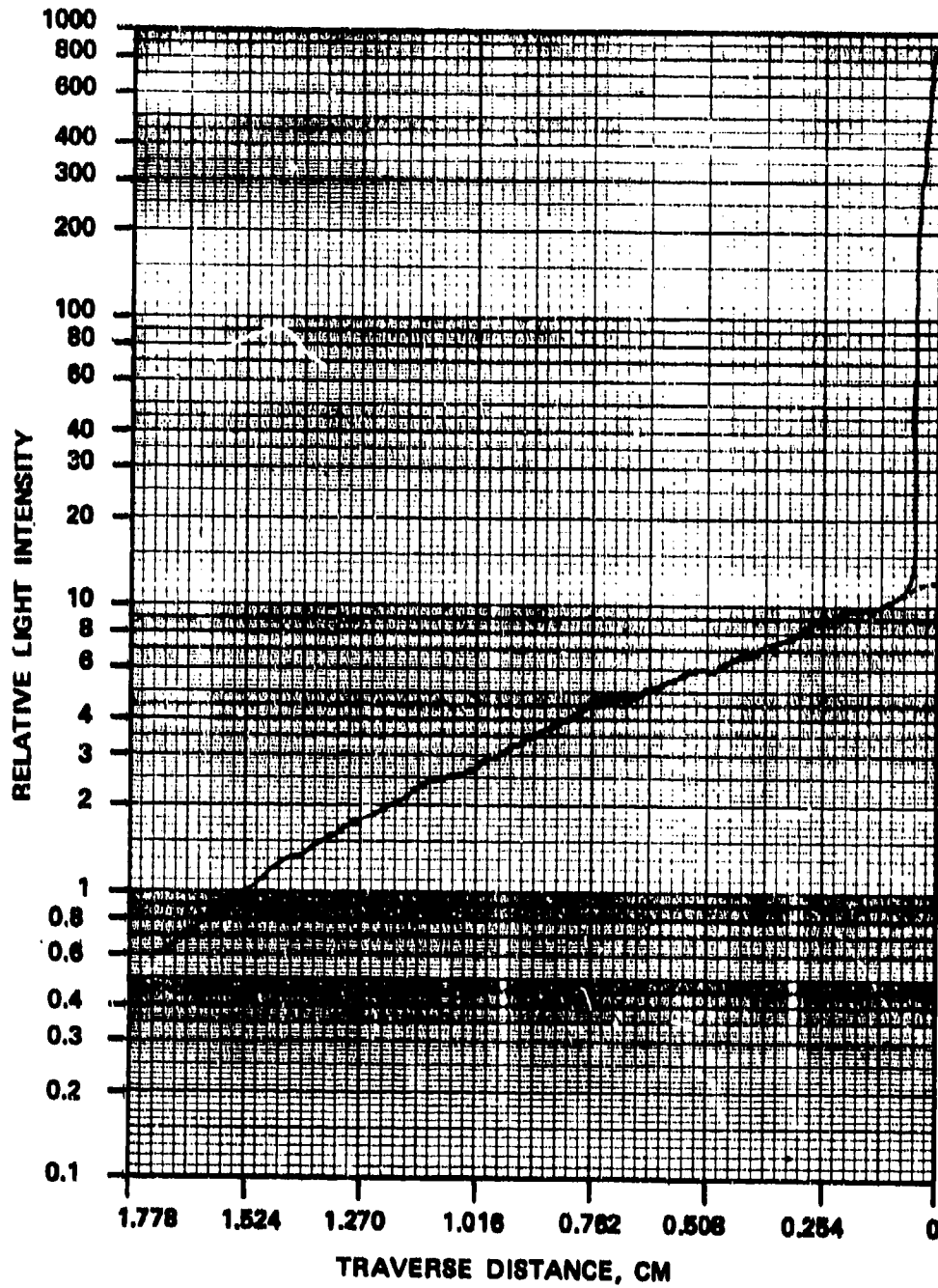
Figure 65.   Typical Experimental Light Intensity Profile.

follow the shape of the mean theoretical illumination profile,
and a typical extrapolation is shown as a dotted line in
Figure 65. The point on the scattered-light intensity is
10 percent of the forward scattered light intensity, and is also
shown in Figure 65. The traverse distance to the subject point
can be seen to be equal to 1.5 cm. Therefore, the SMD can be
calculated in meters from the following equation:

$$SMD = 2.647 \ \lambda/\pi \ \tan^{-1}(x/f_c)$$

where: $\lambda = 632.8 \times 10^{-9} m$

$f_c = 762$ mm

x = traverse distance

Droplet-size measurements taken at Cranfield Institute
of Technology on an airblast nozzle are compared in Table 21 to
the measurements using the AiResearch apparatus. The agreement
varies from very good to poor; however, the AiResearch data is
self consistent and some of the error may be attributed to the
difficulty in reproducing the experimental conditions exactly.
The Cranfield data was taken using kerosine and the AiResearch
apparatus is limited to water only; therefore, the AiResearch
data was corrected to kerosine using the following equation for
low viscosity liquids from Rizkalla and Lefebvre:[20]

$$\frac{SMD_{kerosine}}{SMD_{H_2O}} = \sqrt{\frac{\sigma_k \ \rho_k}{\sigma_{H_2O} \rho_{H_2O}}} = 0.544 \ \text{at} \ 289K$$

$$SMD_{JETA}/SMD_{H_2O} = 0.512 \ \text{at} \ 289K$$

Another comparison between Cranfield and AiResearch data is
provided in Table 22 for a pressure atomizer with and without
external air assist; the external air assist being provided
through the secondary fuel passage. Again, the agreement varies
from poor to good, but the AiResearch data is self-consistent.

TABLE 21. COMPARISON OF DROPLET SIZE MEASUREMENTS TAKEN AT C.I.T. AND AIRESEARCH ON AIRBLAST NOZZLE.

Airblast Pressure Drop (Percent)	Air Assist Pressure (kPa)	Fuel Flow Rate (kg/h)	SMD Cranfield/AiResearch (Microns)	
4.0	0	2.7	56	58
4.0	69		29	25
4.0	207		17.5	16
5.5	0		45	51
5.5	69		28	22
5.5	207		16.5	14.5
7.0	0		30	29.5
7.0	69		22.5	21.5
7.0	207	2.7	15.5	13
4.0	0	3.6	59	61.5
4.0	69		33	23
4.0	207		18.5	16
5.5	0		47	52
5.5	69		29	21.5
5.5	207		17	14
7.0	0		32	35
7.0	69		27*	20
7.0	207	3.6	16	12

*24.5µ using nitrogen freezing technique

TABLE 22. COMPARISON OF DROPLET SIZE MEASUREMENT TAKEN AT C.I.T. AND AIRESEARCH ON PRESSURE ATOMIZER.

Fuel Flow Rate (kg/h)	Air-Assist Pressure (kPa)	SMD Cranfield/AiResearch (microns)	
3.2	0	53	76
3.2	69	40	43
3.2	207	27	32
4.5	0	53	43
4.5	69	41	36
4.5	207	29	29

3. SMD Correlation

The SMD data from two air-assist airblast nozzles was correlated by using a modified Riskalla and Lefebvre expression,[20] wherein airblast air velocity V_a was replaced by V_{eff} as defined below:

$$\dot{m}_{a_{Total}} V_{eff} = \dot{m}_a V_a + \eta_{conv} \dot{m}_{aa} V_{aa}$$

where:

$$m_{a_{Total}} = m_a + m_{aa}$$

$\dot{m}_a$ = Airblast airflow rate

$\dot{m}_{aa}$ = Air-assist airflow rate

V_a = Airblast air velocity

V_{aa} = Air-assist air velocity

The conversion efficiency η_{conv} is a function of air-assist passage pressure drop and nozzle geometry.

A typical correlation with a pure/air-assist airblast nozzle atomization characteristics is presented in Figure 66. By using the above-mentioned expression for V_{eff} and η_{conv} equal to unity, a single equation successfully correlated SMD data of the airblast nozzle with and without external air-assist.

A production air-assist pressure atomizer nozzle was used for studying the effect of external air-assist pressure drop on SMD. The measured data, presented in Table 23, could not be correlated with a modified Parker-Hannifin expression,[8] shown by Curve 1 in Figure 67. However, the data was successfully correlated by the following expression:

TABLE 23. PRESSURE ATOMIZER SMD DATA.

Test No.	Air-Assist Pressure (kPa)	Fuel Flow (kg/h)	SMD (Micron)
1	0	3.2	53
2	69		40
3	207		27
4	345	3.2	Unstable
5	0	4.5	53
6	69		41
7	207	4.5	29
8	0	6.8	50
9	69		43
10	207	6.8	30
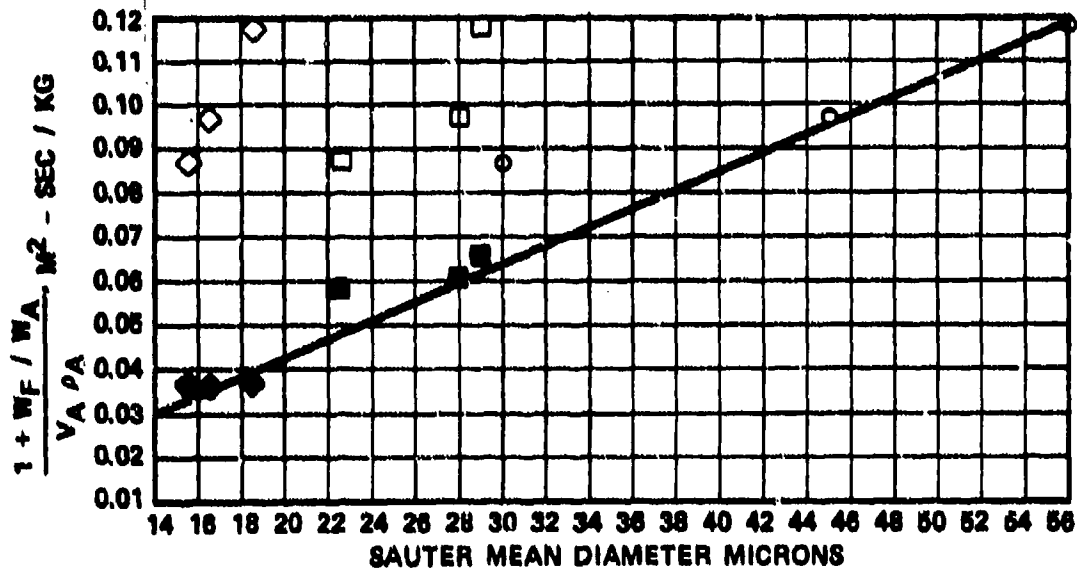
W_F = 2.72 KG/HR ○ WITHOUT AIR ASSIST ΔP/P = 0.04, 0.055, 0.07

68.9 kPa AIR ASSIST
□ V_A AND W_A GIVEN BY COMBUSTOR ΔP
■ V_A = V_{EFF}, W_A = TOTAL AIRFLOW

206.8 kPa AIR ASSIST
◇ V_A AND W_A GIVEN BY COMBUSTOR ΔP
◆ V_A = V_{EFF}, W_A = TOTAL AIRFLOW

Figure 66.   Typical Pure/Air-Assist Airblast Nozzle
             Atomization Characteristics.

172
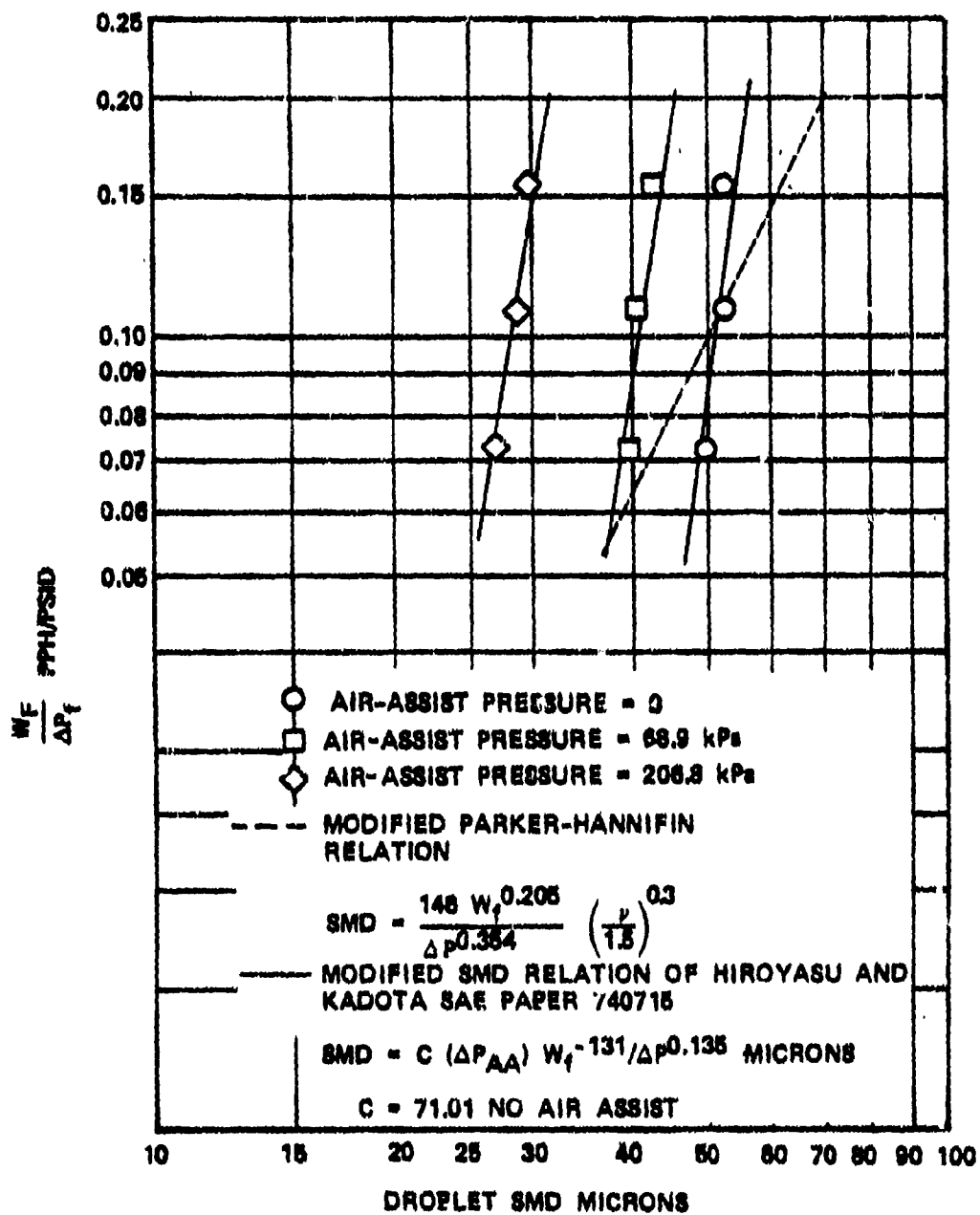
Figure 67. External Air Assisted Pressure Atomizer SMD Characteristics.

173

$$SMD = C \ (\Delta P_{AA}) \ W_F^{0.131}/\Delta P_f^{0.135}$$

where C is a function of nozzle air-assist pressure drop. The exponents of fuel-flow rate (W_F, PPH) and fuel pressure drop (ΔP_f, psid) were taken from Hiroyasu and Kadota.[23] The constant C was fitted as a function of air-assist pressure drop. The predicted values are in good agreement with measurments as shown in Figure 67. The variation of the constant C with air-assist ΔP_{AA} is shown in Figure 68.

H. Transition Liner Mixing Tests.

A transition section mixing rig was used to measure mixing of hot and cold streams in a transition section wherein the combustor exit flow is turned through 180° to the turbine inlet. The rig (shown schematically in Figure 69) involved minor modifications to an existing combustor and rig. A photograph of the modified combustor is shown in Figure 70. Figure 71 shows photographs of the rig installed in the test facility.

All original combustor air orifices were blocked. One air stream was provided from a manifold and entered through what previously were five start-nozzle ports and 10 run-nozzle ports, shown in Figure 70. Fifteen orifices were provided on the ID of the combustor liner to admit the second air stream via the combustor annulus. Circumferential locations of these orifices coincided with those of the start- and run-nozzle ports.

A splitter plate was provided (Figure 70) to separate the cold and hot streams at the inlet to the transition section. The splitter plate length of 8.13 cm was estimated to be adequate in order to provide enough mixing of the individual streams before joining at the transition section inlet.

---

[23] Hiroyasu, H., and T. Kadota, "Fuel Droplet Size Distribution in Diesel Combustion Chamber," SAE Paper 740715, 1974.
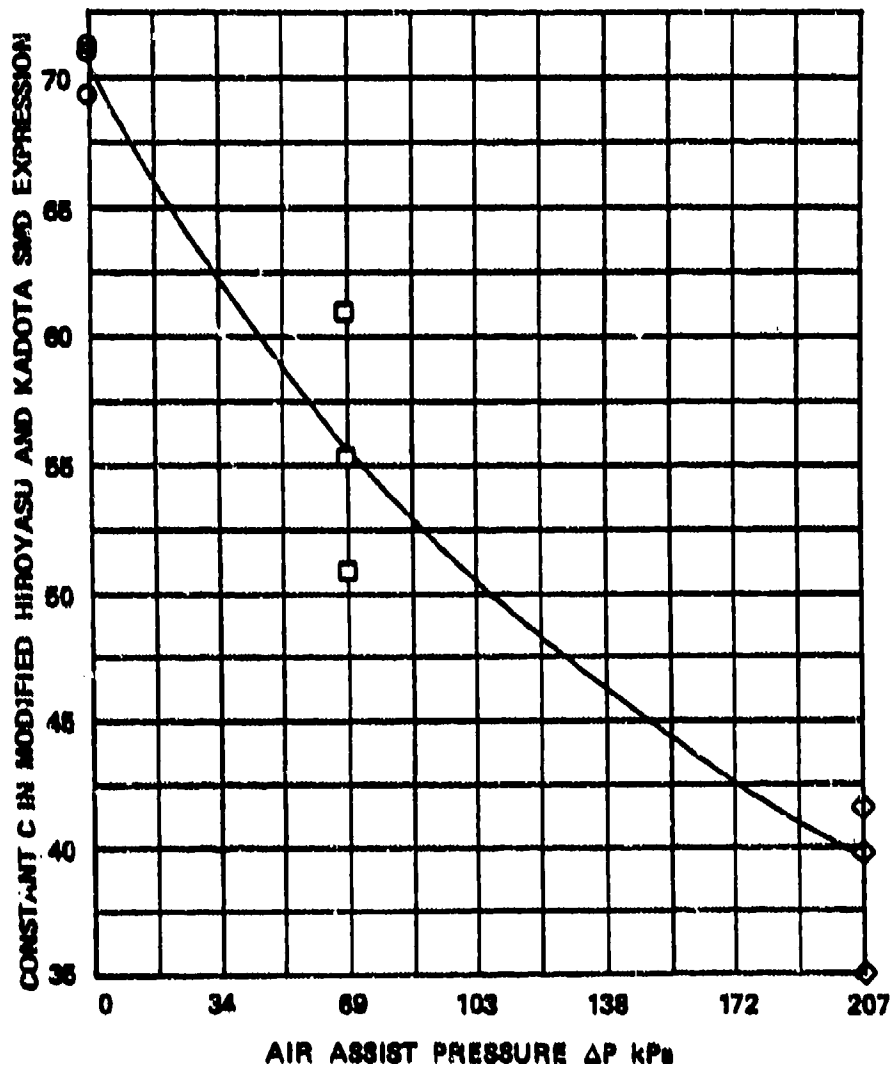
Figure 68.   Effect of Air Assist Pressure on SMD
            Expression Constant C.

175

COLD OR HOT FLOW
THROUGH 5 RADIAL
AND 10 AXIAL JETS

HOT OR COLD FLOW
THROUGH 15 RADIAL
JETS

17.65 CM

5.59 CM

13.16 CM RADIUS

9.02 CM

7.52 CM
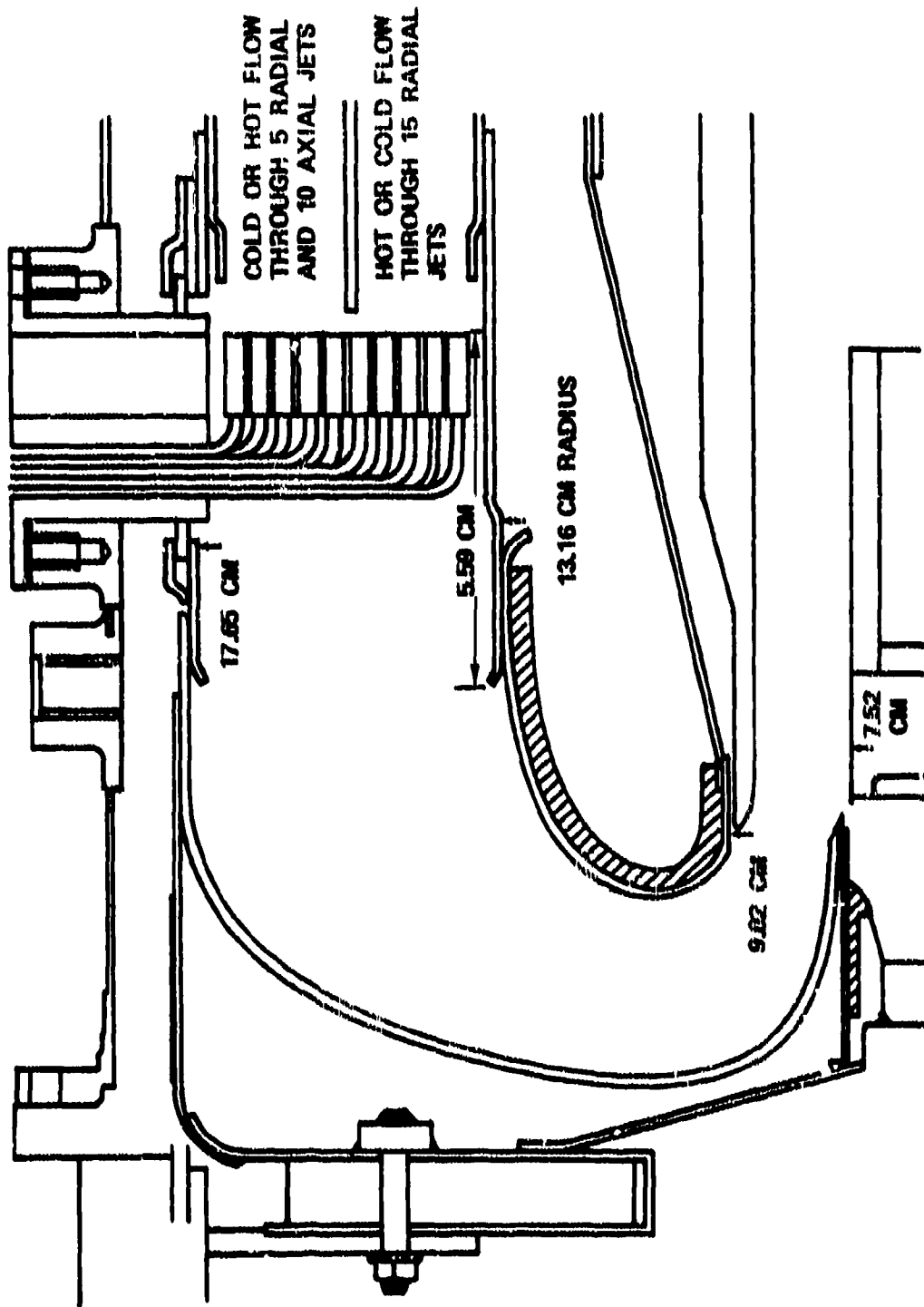
Figure 69. A Schematic of the Transition Mixing Rig.

OUTER PANEL
ORIFICES

INNER PANEL
ORIFICES

INSTRUMENTATION
GROMMET

SPLITTER PLATE
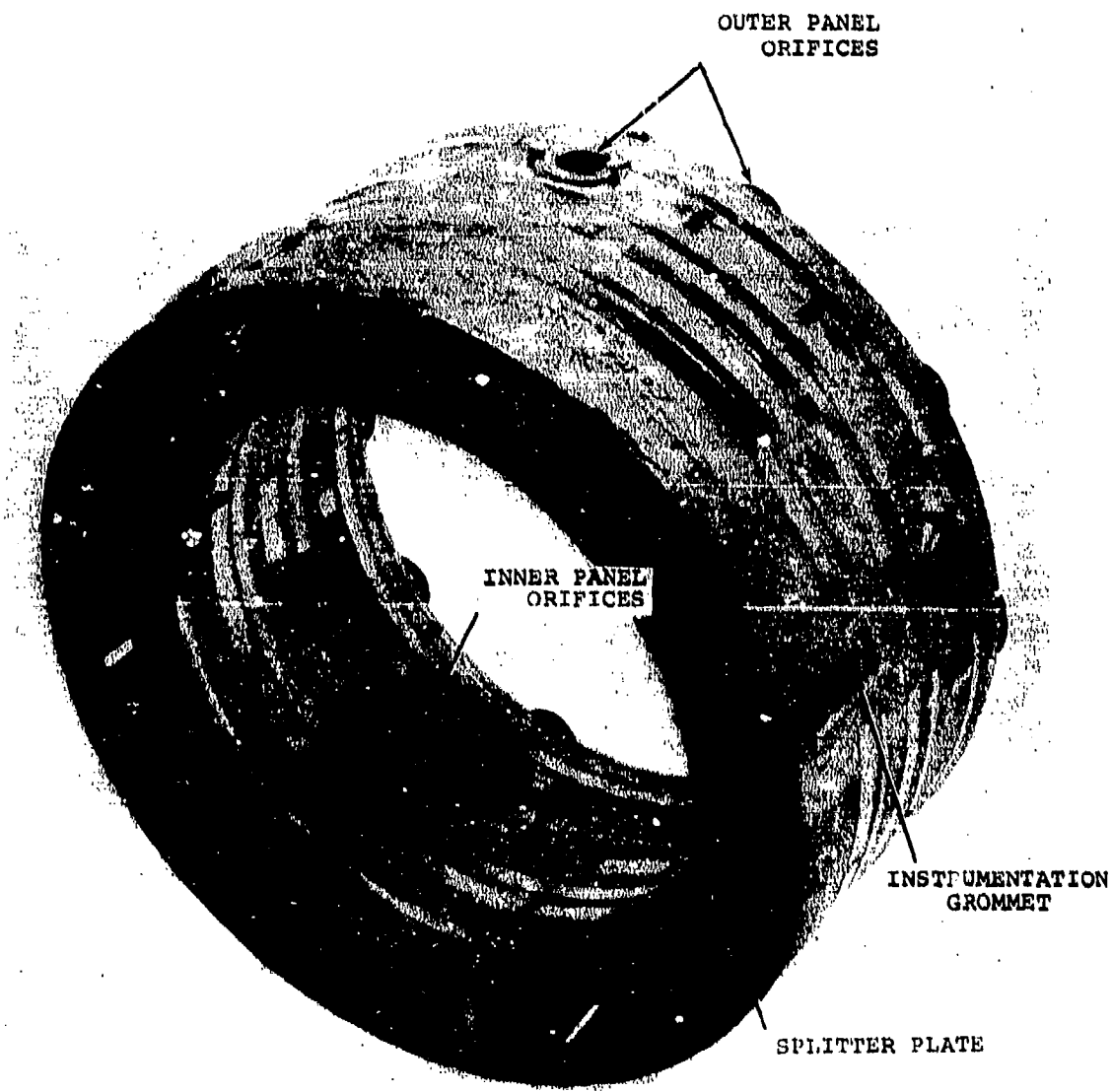
Figure 70.   Modified Combustor Used for Transition Mixing Tests.

177
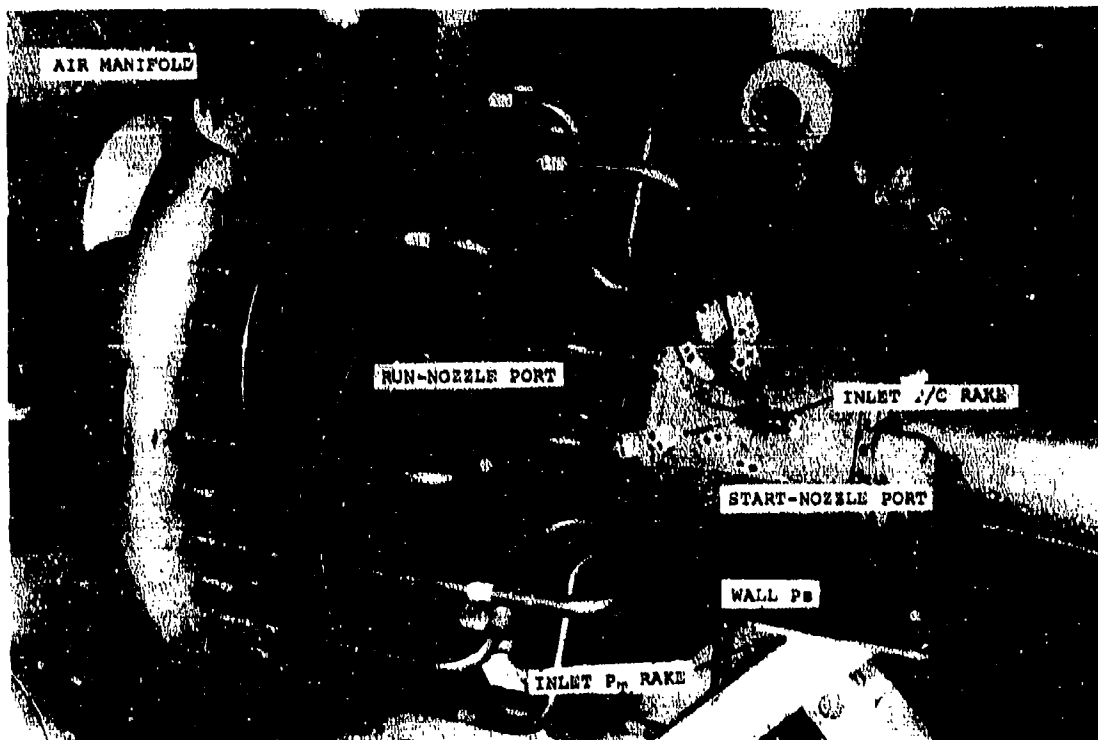
Figure 71. Transition Mixing Rig.

Three total temperature (T_t) and one total pressure (P_t)
rakes were located 5.59 cm upstream of the transition section
inlet. One of these stationary 10-element thermocouple rakes was
positioned in line with one of the start-nozzle ports, its cir-
cumferential position being 36 degrees counterclockwise from
the rig top dead center. The second thermocouple rake was placed
in line with a run-nozzle port at 126 degrees counterclockwise
and the third thermocouple rake was placed at 228 degrees
counterclockwise between a start- and run-nozzle port. A sta-
tionary 10-element P_t (Kiel) rake was placed at 216 degrees
counterclockwise, between nozzle ports. Four wall static pres-
sure elements were used to measure the static pressure distribu-
tion immediately downstream from the splitter plate. The tran-
sition liner inlet channel height was 4.5 cm.

The transition liner exit had inside- and outside-radii of
7.52 and 9.02 cm, respectively, giving the exhaust channel
height of 1.5 cm. The transition liner equivalent mixing length
(defined as liner volume/ inlet flow area) was 15 cm or 2.9
times the inlet channel height.

The temperature profile at the transition liner exit was
measured by a rotating 7-element thermocouple rake which made a
complete 360-degree sweep at 15-degree intervals.

The thermocouples numbered 3, 5, and 7 were located at
the same radial distance, but at different circumferential loca-
tions. Therefore, the measurements by these thermocouples were
used for checking the repeatability of the exhaust profile
measurement.

A set of five data points was first obtained with the cold
stream flowing through the upper channel of the combustor.
Another set of five data points was obtained with the cold
stream flowing through the lower half of the combustor. Inlet

flow rates, pressure, maximum and minimum temperatures, and
exit average temperature and pattern factor of these 10 runs
are listed in Table 24.

The cold stream temperature varied from 229 to 450 K,
whereas the hot-stream temperature varied from 511 to 678 K.
Inlet flow rates were changed from 0.57 to 1.7 kg/s; and inlet
pressure was maintained at approximately 1013 kPa.

Although there were significant variations between the
inlet temperature profiles at the three circumferential stations
measured, the difference between the average and minimum values
of the cold stream was quite small. The same observation can be
made for the hot stream.

The inlet circumferential pattern factor (PF) as defined
below is the maximum local value, and did not consistently occur
at the same circumferential locations.

$$PF = \frac{T_{max} - T_{avg}}{T_{avg}}$$

By comparing Scans 1 and 2-1, one can deduce the influence
of the location of the cold stream with respect to the hot
stream with other parameters remaining the same. At first it
was postulated that the residence times of the hot and cold
streams and the residence-time ratios would influence the mixing
rate. By defining the transition liner mixing parameters as
$[(PF)_{initial} - (PF)_{final}]/(PF)_{initial}$, the effect of the
residence times and attendant ratios on mixing were quanti-
fied as tabulated in the last four columns of Table 24; where
the residence time, τ, is defined as

$$\tau = \frac{\text{Upper (lower) Half Transition Liner Volume}}{\text{Initial Volume Flow Rate Through Upper (Lower) Half of Combustor}}$$

TABLE 24

TRANSITION MIXING RIG INITIAL (DOWNSTREAM OF SPLITTER PLATE) AND FINAL (EXHAUST) PROFILE DATA.

By comparing these mixing parameters to the residence-time variations it is quite evident that the postulate of mixing dependence upon residence time is not valid over the ranges tested. It does appear, however, that the location of the hot and cold inlet stream, i.e., whether the cold flow is from the outer and inner combustor annulus, significantly influence the mixing rate, as nearly twice the mixing rates were achieved with cold flow from the inner annulus.

The exit-temperature profile for Scan-1, shown in Figure 72, is three dimensional. A flat average-temperature profile for this run, as well as other test cases, was obtained as shown in Figure 73. The difference between maximum and minimum temperature profiles is quite large. The exit-temperature profiles for the other nine runs exhibited similar three-dimensional characteristics. At first glance, it could be concluded that due to the 3-D flow effects, none of these tests can be used for validation of the transition mixing model. Although better controlled transition mixing tests (which would provide 2-D inlet as well as exit profiles along with more information on the inlet profiles variation along the circumferential direction) would be desirable, this data can be used for a "first level" validation of the transition mixing model by using data from selected sectors of the transition liner as explained in the following paragraphs.

Figure 74 shows the inlet-temperature profile in line with the start nozzle located at 36 degrees for Scan 1; also shown are exit-temperature profiles at 30 and 45 degrees. The exit average temperature of 490 K at 45 degrees is quite close to the inlet T_{avg} of 509 K, whereas at 30 degrees T_{avg} = 580 K. It was also noticed that exit T_{avg} at 60 degrees was 437 K. It therefore appears that there was probably some swirl in the inlet stream which caused this circumferential temperature shift. The inlet PF of 0.579 was reduced to 0.155 and 0.075 at 30 and 45 degrees, respectively. Similar data for the sector in line
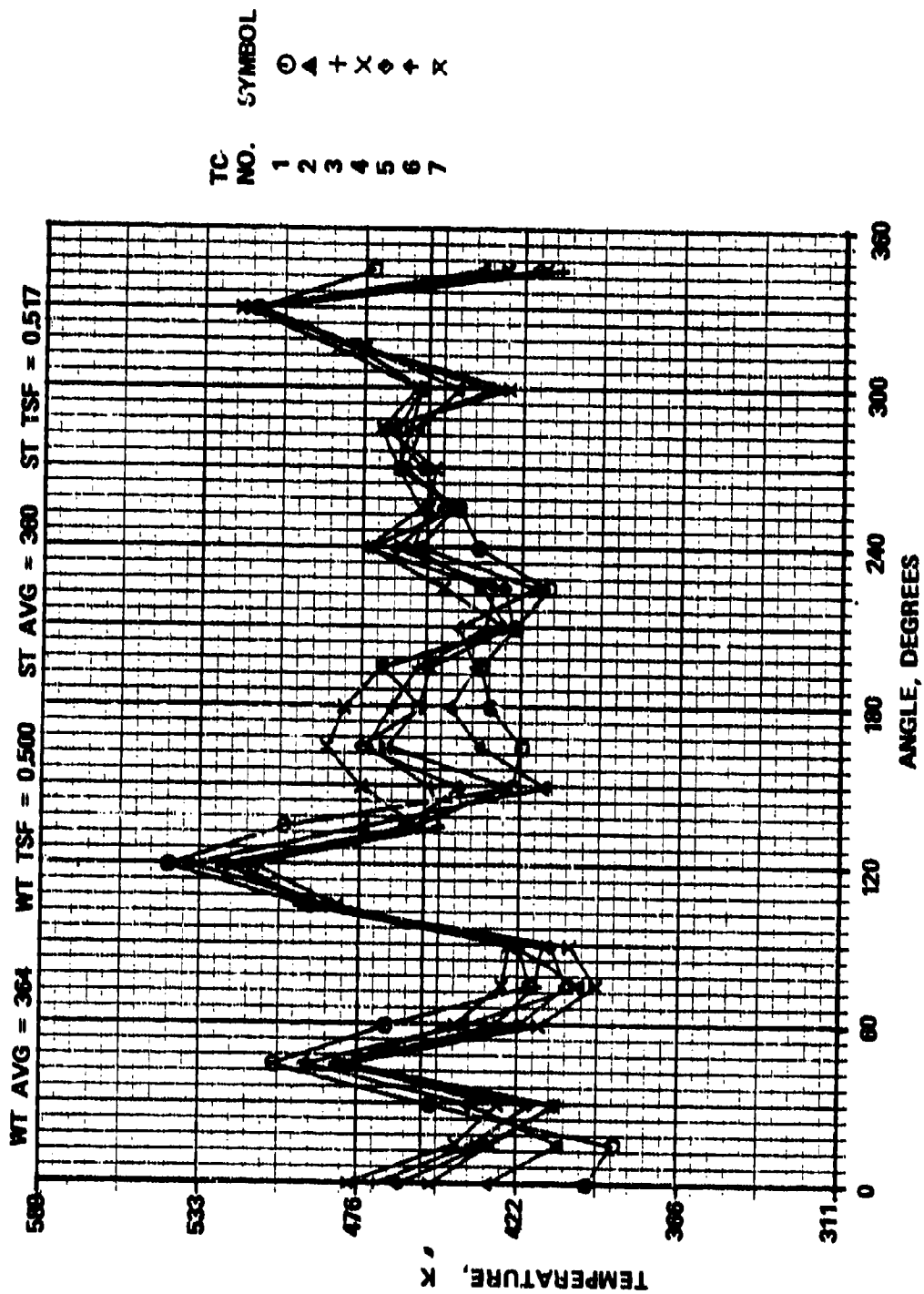
Figure 72. Transition Mixing Tests, Scan -1.

183
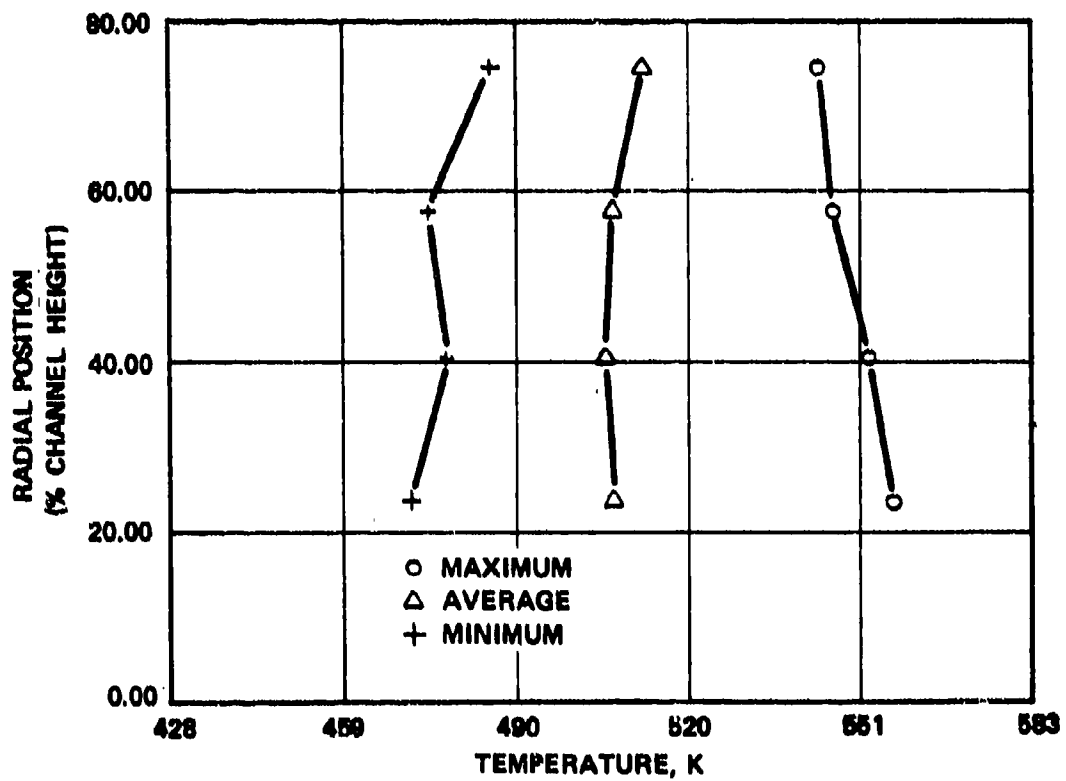
Figure 73.   Transition Mixing Tests, Scan-1.

with the main nozzle port is shown in Figure 74. The inlet T_{avg}
was equal to 490 K at 126 degrees; the exit T_{avg} being 527 and
469 K at 120 and 135 degrees, respectively. Again, a circum-
ferential shift in temperature can be seen. The inlet PF was
equal to 0.72, the exit PFs at 120 and 135 degrees were 0.063 and
0.169, respectively.

From the figures and results from other test conditions,
it was concluded that the flow can be considered approximately
two dimensional in a given sector, and can therefore be analyzed
by the 2-D transition mixing model.

Figure 75 summarizes all experimental results in terms of
the mixing parameter, the residence time of the hot stream, and
ratio of the residence times. Solid symbols denote results for
the cases where the cold stream flows through the inner annulus
of the combustor, whereas open symbols are for the cold stream
through the outer portion. The global mixing rate, as deter-
mined for the T_4-traverse and shown as rectangles, clearly
demonstrates that improved mixing is obtained when the hot
stream is through the upper half of the combustor. It may be
noted that the global mixing-rate characteristics, and not the
local (sector-wise) mixing, are generally of greater interest to
the combustor designer. This limited set of data shows only a
weak dependence of the transition liner length (residence time)
and the ratio of residence times on the mixing rate. The signi-
ficant observation is that the global mixing-rate characteristics
are influenced more by the radial profile of temperature exiting
from the primary, and not by the residence time. The equivalent
mixing length, and the radii of curvature of the liner are
important because it is the latter which favors the transfer of
hot gases toward the center of curvature of the liner surface
and enhances the mixing between the hot gases from the O.D. with
cold gases from the inner annulus of the combustor.
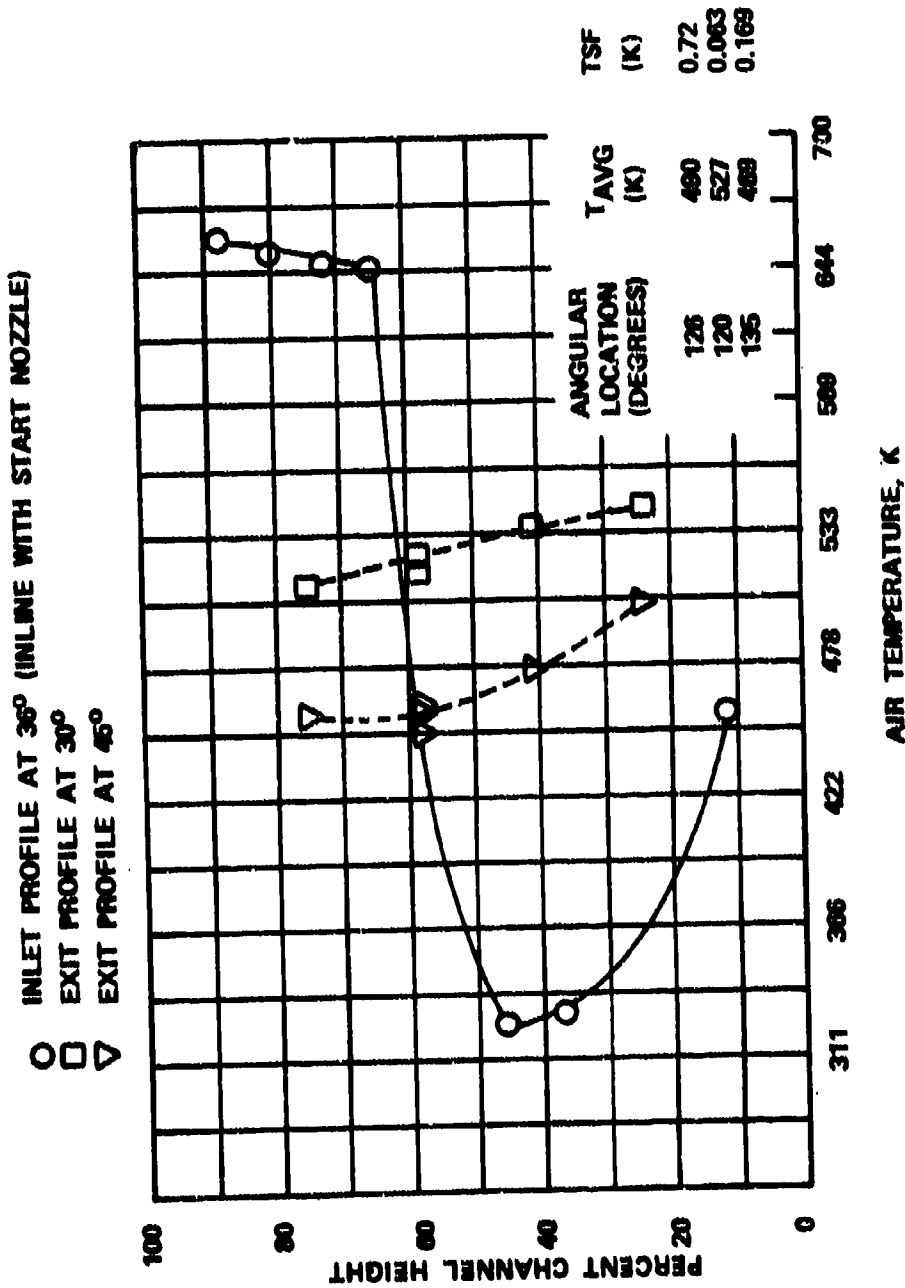
Figure 74. Transition Mixing Test, Scan 1.

186
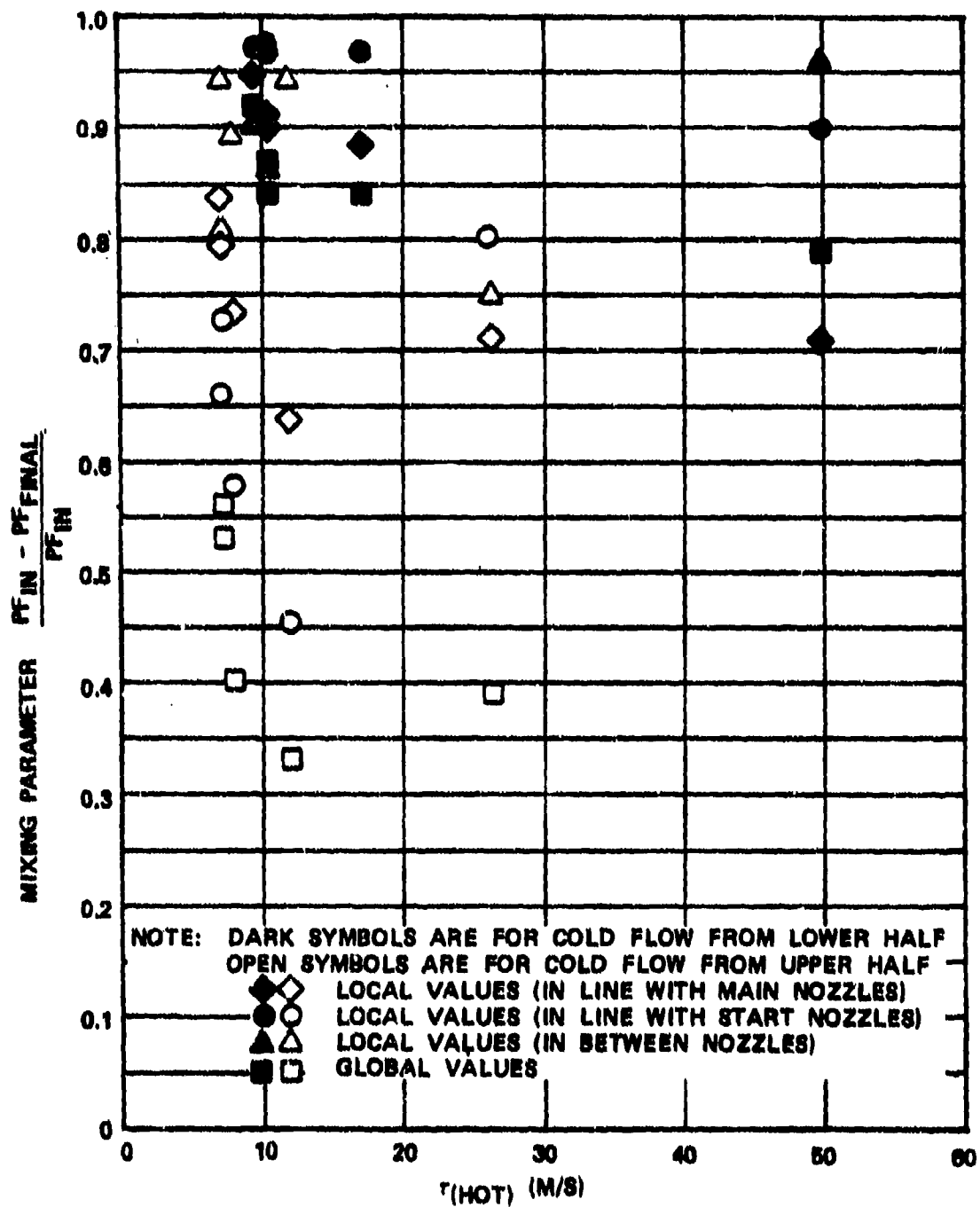
Figure 75. Mixing Parameter Versus $\tau_{(Hot)}$.

187

V.   MODEL VALIDATION

There were three main objectives of the model-valid   on
phase.   First, different mathematical models had to be validated
before they could be used with some confidence to design and
test two full-scale combustor systems   (the main objective of
Tasks II and III of the program).   Second, validation was done
for the test combustors, which closely simulated the test con-
ditions usually encountered in turbopropulsion combustion sys-
tems.   The third, and perhaps the most important objective,
was to make predictions for the element tests with minimum
information regarding initial and boundary conditions.

Consider a typical combustion system, as shown schematically
in Figure 76.   In order to predict combustor performance param-
eters, it is necessary to predict the combustor internal flow-
field, which in turn requires information concerning the follow-
ing:

- Airflow distribution around the liner

- Velocity components of radial jets

- Swirler vane discharge velocity components

- Velocity profiles at the lip exit of cooling bands

- Spray characteristics including droplet distribution,
  initial droplet velocity distribution, and spray cone
  angle

- Turbulence properties, such as turbulence kinetic
  energy and length scale, of air entry points
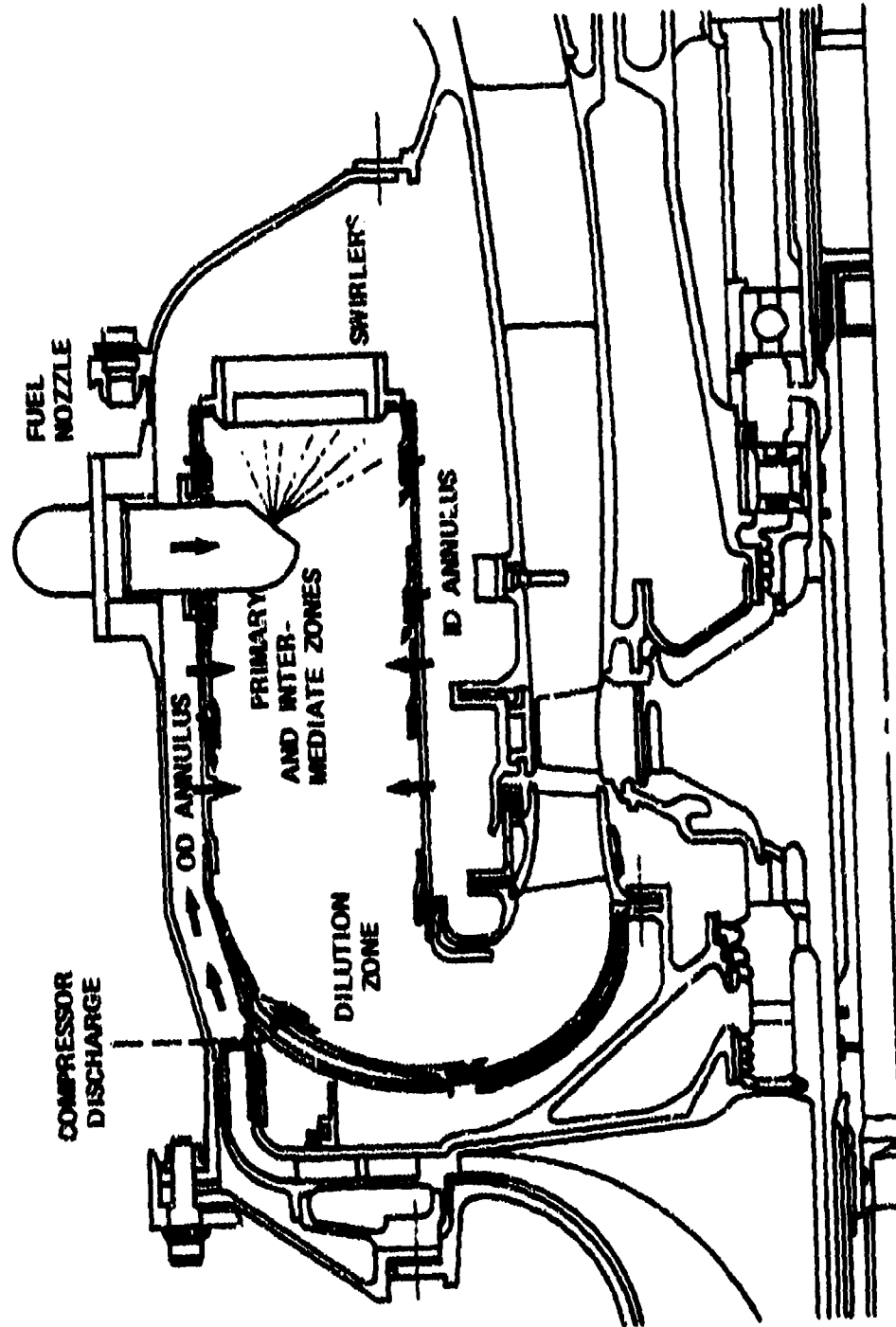
Figure 76. A Typical Reverse-Flow Annulus Combustion System.

- Heat-transfer coefficient on the cold side of
  liner walls.

- Flow distortion at the compressor discharge; and
  local distortions created by different obstacles
  such as nozzle shrouds and utility struts, etc.

The airflow distribution around the combustor liner can be
calculated in principle by using an annulus flow model, which
could be as simple as a 1-D or as complicated as a 3-D flow
model. If a 3-D annulus flow model is used, it will require a
more accurate description of the compressor-discharge conditions
than is currently known. Moreover, the airflow distribution
will be strongly influenced not only by compressor-discharge
profiles, but also by geometrical details of the liner (including
details of plenum and different local obstructions in the flow).
Since the information on the latter is not available, and since
manufacturing tolerances cause variations in the flow distribu-
tion anyway, the 3-D annulus flow model is not needed during the
initial combustor-design phase. Instead, a simple 1-D annulus
flow model is adequate for the time being.

With the 1-D annulus flow model, it is possible to compute
airflow distribution around the liner, velocity components of
radial jets, and average heat-transfer coefficients for the cold
side at different liner axial stations. The Sauter mean diameter
and the fuel nozzle spray-cone angle can be easily measured on a
nozzle spray rig, but not as easily in actual combustor-flow
conditions.

The remainder of the boundary conditions cannot be measured
easily, and must be specified. Even if extensive measurements
are taken to document these boundary conditions for a combustor
installed in an engine, there is no guarantee that another engine
will give the same boundary conditions. In addition, if a new

190

combustion system is to be developed, such measurements cannot be made as no engine exists. So it appears that the design of a new combustion system, or the analysis of an existing production combustor, will have to be undertaken with insufficiently specified boundary conditions.

Consequently, most of the Task I element tests were conducted with some of the boundary conditions known; whereas others, which cannot be easily measured on production combustors, had to be assumed. The objective was to study the sensitivity of the predictions to the boundary conditions.

The following topics are currently under intensive investigation by a number of researchers:

- Turbulence

- Effect of turbulence on combustion

- Transfer of passive scalars such as temperature

- Spray dynamics, evaporation, and combustion

- Radiation

- Smoke

In the present study, emphasis was put on the first four topics. The objective was to compare measurements with predictions of the model that are based on currently well-developed and well-tried mathematical models and their minor modifications, as described in Volume III. The validation of liner cooling, jet mixing, can combustor cold flow and reacting flow, radiation, and transition-liner mixing is presented in this chapter.

A. Liner Cooling

A number of studies have been reported to evaluate the performance of different liner-cooling schemes. The study reported in the following paragraphs is limited in scope in that the emphasis is placed on computing hot-side heat-transfer rate only. By using suitable expressions for the cold-side heat-transfer coefficients, the approach presented here can be used for predicting wall-temperature levels and gradients of combustor liners that employ advanced cooling schemes. Therefore, results are presented only for the conventional flow-cooling geometry experimentally studied in this program, and as reported in Section IV.A.2. The corresponding flow conditions were previously reported in Table 3.

A 2-D elliptic program was used to compute initial profiles of velocity, temperature, turbulence kinetic energy and dissipation rate in the region immediately downstream from the cooling-slot lip. The initial free-stream velocity and temperature profiles were taken to be uniform. The turbulence kinetic energy and length scale were taken to be $0.003\ U_{\infty}^2$ and $0.02\ \Delta y$, where U_{∞} is the free-stream velocity, and Δy is the normal distance from the wall. For the cooling slot, turbulence kinetic energy and length scale were assumed to be equal to $0.02\ U_s^2$ and $0.02\ h_s$, respectively; where U_s and h_s are the slot velocity and slot height, respectively. The initial slot-stream temperature was assumed to be equal to the measured annulus air temperature. Annulus air velocity and slot velocity were taken from the measurements.

For the downstream region, which did not have a reverse-flow region created by the splash plate, the wall-cooling model was used for predicting liner wall temperature as a function of X and liner-pressure drop. The liner test section was divided into 200 cross-stream nodes, with 60 of these distributed within the slot height of 1.91 mm. The marching step size was taken to

be 0.1 h_s. Figures 77 through 81 show a comparison between
predicted and measured wall temperatures for Set-1 through
Set-5 listed in Table 2. The effect of the initial slot-
velocity profile on predictions is shown in the figures. The
slot axial-velocity profile was computed by:

$$U_s = \bar{U}_s \ \frac{1-C^a}{b}$$

where:

$$C = 2 \ \text{Abs} \ (\frac{\Delta y}{h_s} - 0.5)$$

$$b = 0.83$$

$$a = \frac{1}{1-b} - 1$$

where $\bar{U}_s$ is the average slot velocity, and Δy is the distance
from the liner wall or splash plate.

As shown in Figures 77, 78, and 79 for the case of pressure
drops encountered in reverse-flow combustors, the agreement
between predictions and data is quite good. However, the cor-
relation is not so good with higher pressure-drop cases, as shown
in Figures 80 and 81, due to the following reasons. Because of
the high pressure drop with attendant high jet velocity, the
initial slot-velocity profile is significantly different from
the assumed symmetric profile. In addition, the turbulence
level is greatly increased. Nevertheless, predictions are
reasonable enough to ensure the usefulness of the wall-cooling
model for predicting liner-wall temperatures for reacting flows.

B.   Jet Mixing.

The 3-D elliptic program was used to correlate jet-mixing
data presented previously in Section IV.B. The computation was
started with initial conditions specified for an x-y plane
6.35 cm upstream from the jet centerline. Temperature profiles
were measured at the initial plane. The axial velocity was
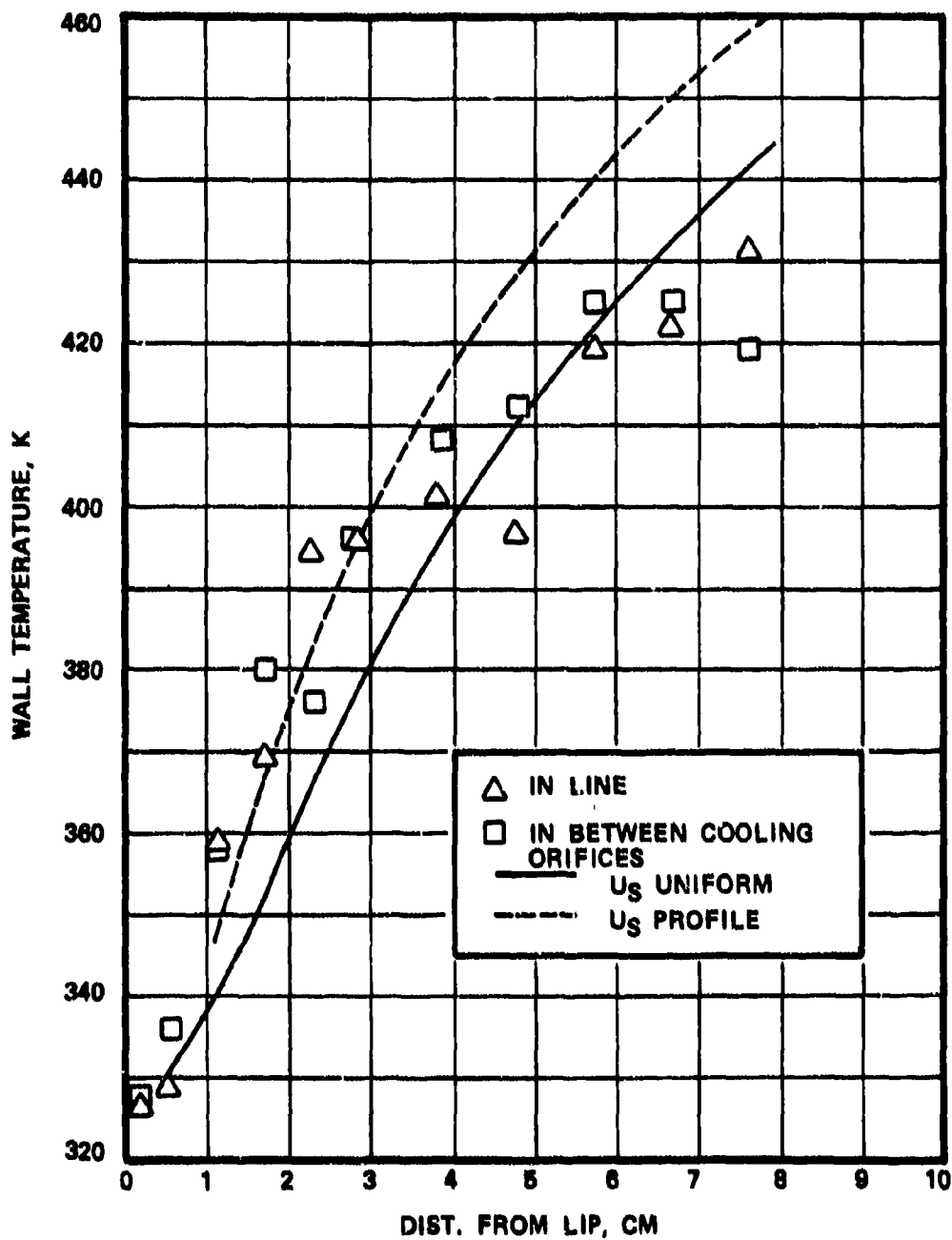
Figure 77. A Comparison Between Predicted and Measured
Liner Wall Temperatures for Set-1 of Table 2.

$U_{slot}/U_\infty = 0.3$
Liner $\Delta P = 0.8\%$
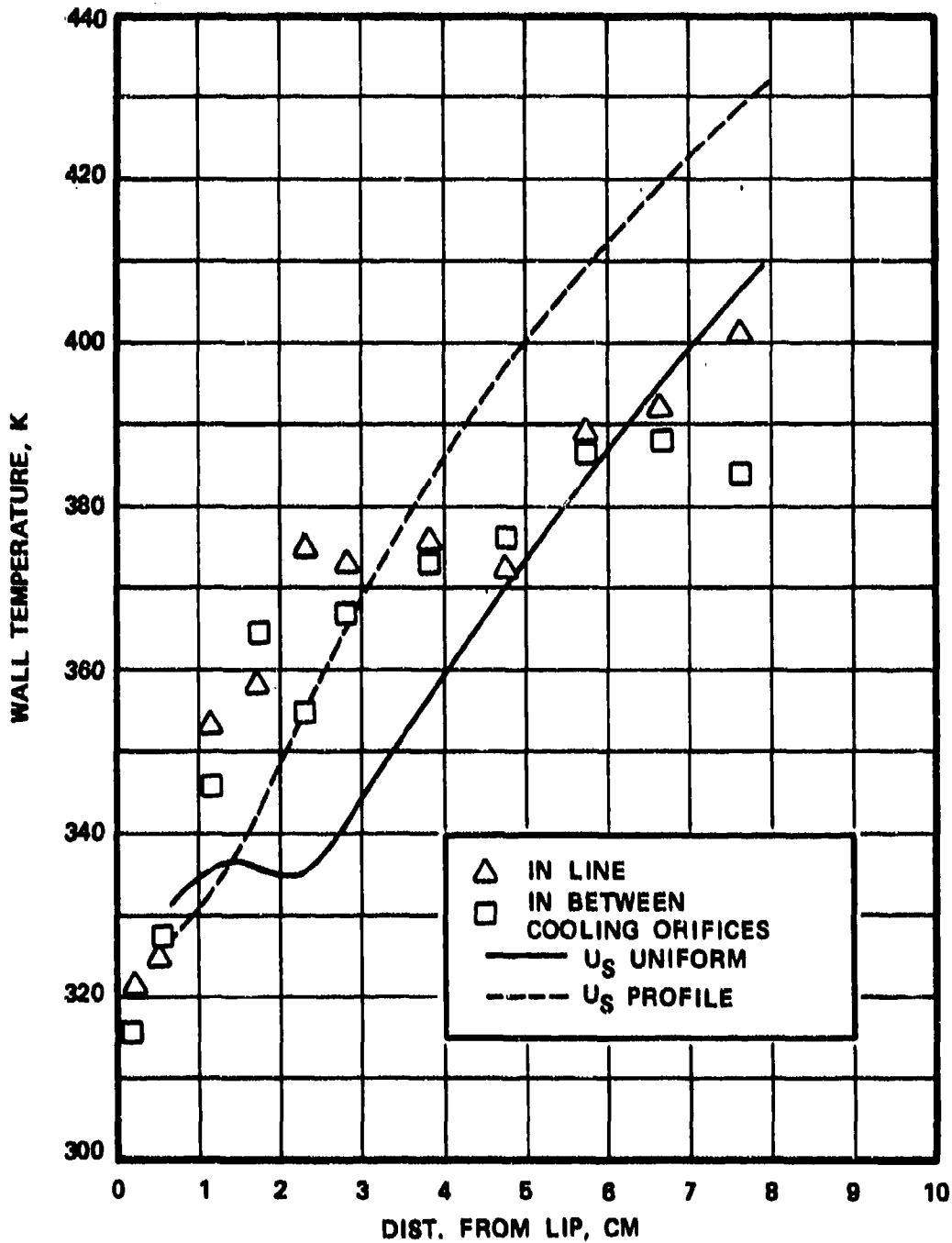
Figure 78. A Comparison Between Predicted and Measured
Liner Wall Temperatures for Set-2 of
Table 2.

$U_{slot}/U_\infty = 0.4$
Liner $\Delta P = 1.6\%$
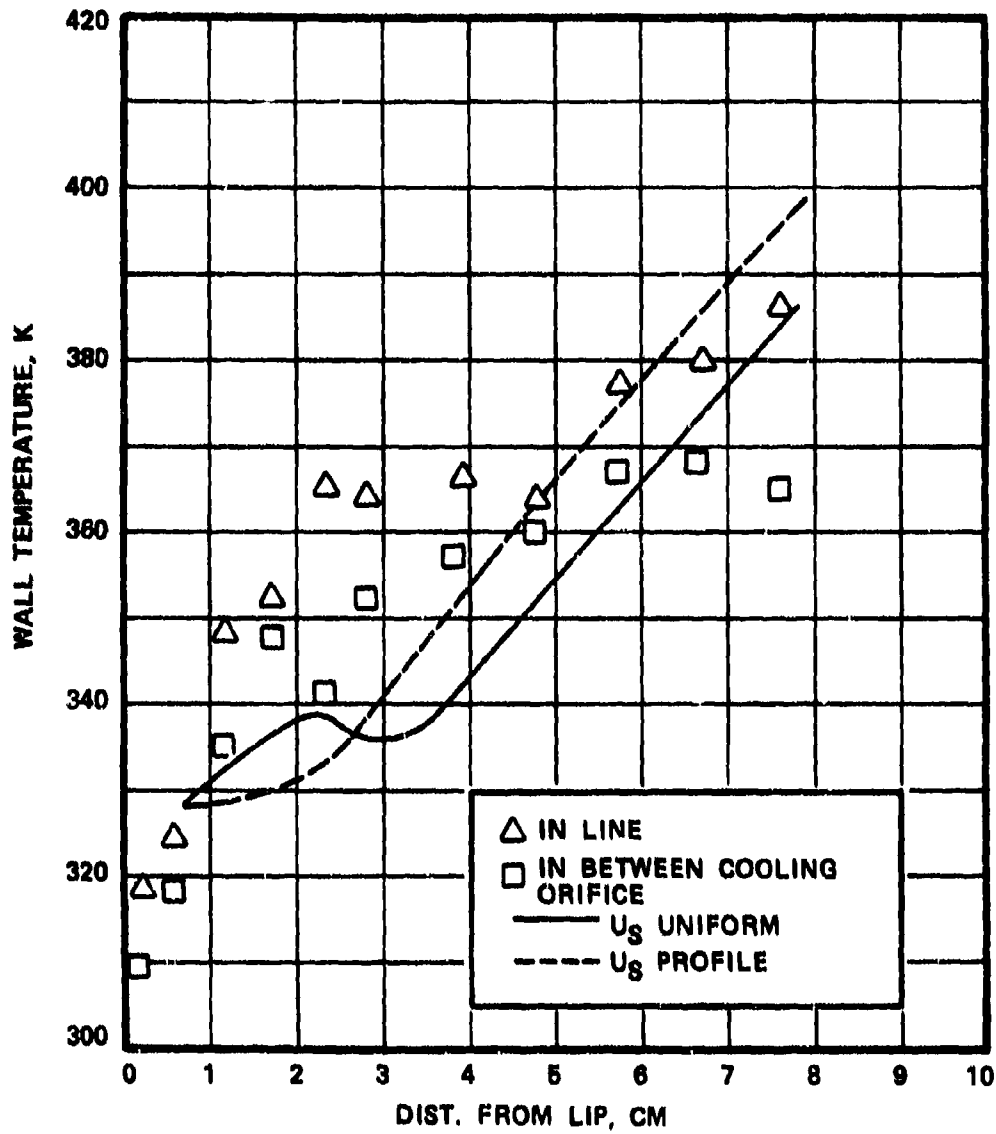
Figure 79. A Comparison Between Predicted and Measured
Liner Wall Temperatures for Set-3 of
Table 2.

$U_{slot}/U_\infty = 0.5$
Liner $\Delta P = 2.6\%$
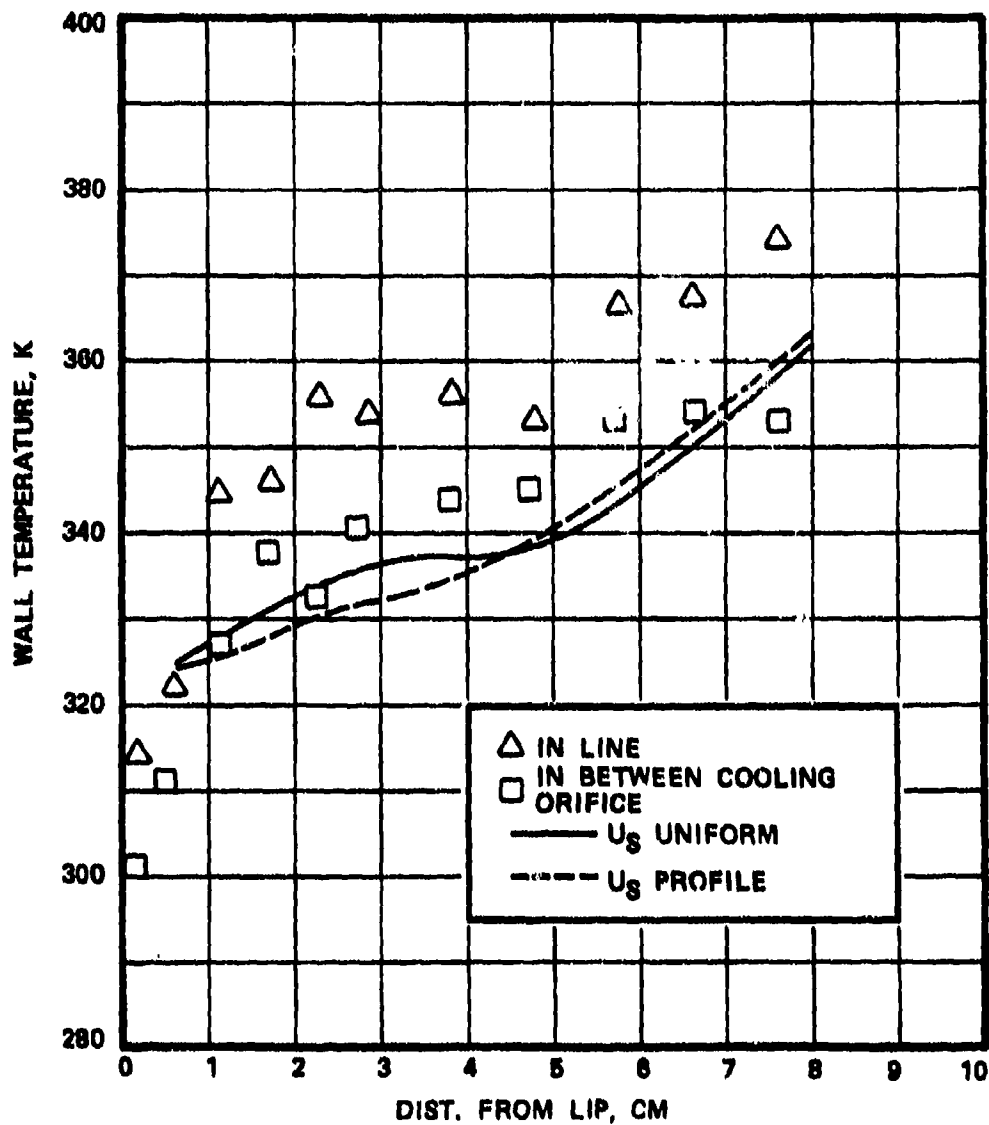
Figure 80. A Comparison Between Predicted and Measured
            Liner Wall Temperatures for Set-4 of
            Table 2.

            $U_{slot}/U_\infty = 0.7$
            Liner $\Delta P = 4.3\%$

197
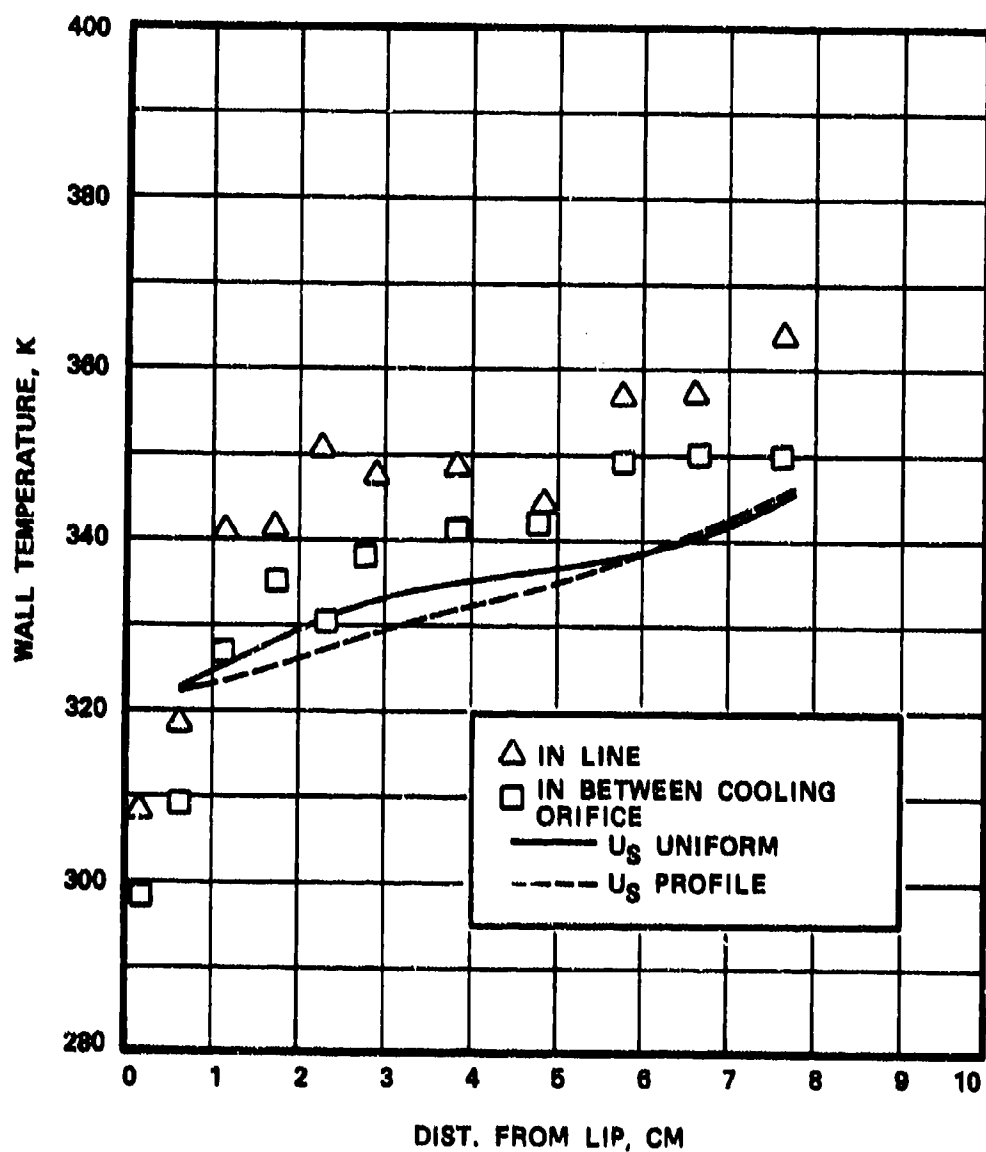
Figure 81. A Comparison Between Predicted and
Measured Liner Wall Temperatures
for Set-5 of Table 2.

$U_{slot}/U_\infty = 0.8$
Liner $\Delta P = 5.9\%$

assumed to be uniform and was calculated from the measured mass
flow rate and arithmetically averaged temperature and known main-
stream pressure. The mainstream and jet turbulence kinetic
energy was assumed to be:

$$k = 0.003 \; U^2$$

The length scale distribution for the mainstream was assumed to
be given by:

$\ell = 0.238 \; y$, where y is the radial distance from the wall.
On the other hand, for an orifice of diameter D, $\ell = 0.238D$.

Based on the total and static pressure drops across the
test section liner wall, the jet angle was assumed at 80 degrees.
The jet velocity was calculated from the liner pressure drop.

The test section of interest was divided into a number of
unevenly-spaced finite-difference nodes, such as presented in
Figure 82 for the 4-opposing jet case. A 90-degree sector of
the test section was divided into 30 x 15 x 18 nodes along the
axial, radial, and circumferential directions, respectively.
The dilution jet was represented by 4 nodes, as shown in Figure
82. The major criterion of convergence was cumulative mass resid-
ual defined as:

$$S = \Sigma_{ijk} \; |S_{ijk}|$$

where S_{ijk} is the mass continuity error for the node (i,j,k).
The convergence was assumed to be achieved when $S \leq 0.001$. The
maximum S_{ijk} was of the order of 0.00001, and the corresponding
variation in the axial velocity component between the last two
iterations was around 0.2 percent. Typically, 100 iterations
were needed to achieve convergence with a new case.
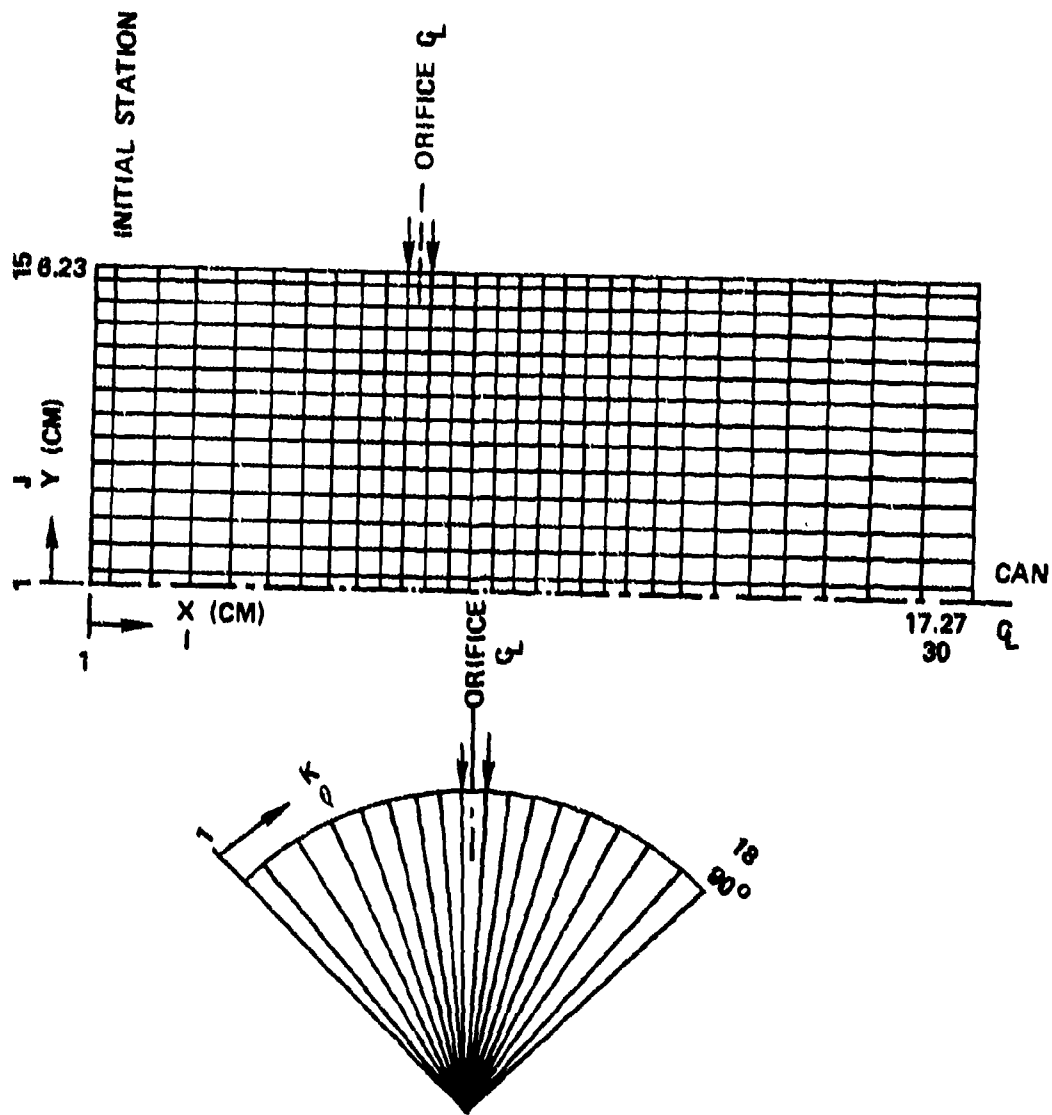
Figure 82. Finite Difference Grid Spacing for Four Opposing Jets.

Figure 83 presents the effect of cumulative mass residual, S, on predicted isothermal lines along an x-y plane in line with the dilution jet. Predicted profiles in the region upstream and slightly downstream from the jet origin are relatively unchanged from S = 0.01 to 0.002. However, further downstream the profiles are quite different.

The effect of initial jet angle on the predicted profiles is shown in Figure 84 for the x-y plane in line with the jet. The predicted jet trajectory agrees reasonably well with the data when the jet angle equals 80 degrees. As expected, the results were significantly affected by initial jet angle.

Model predictions were made by assuming an effective Prandtl number equal to 0.9, and an effective Schmidt number for turbulence kinetic energy equal to 0.9. As presented in Figure 85, the effect of change in effective Prandtl number from 0.7 to 0.9 on predicted isothermal lines is negligible.

Figures 86 through 91 present typical comparisons between predicted and measured jet trajectories and isothermal profiles. The effect of jet-momentum ratio on the predicted profiles, along an x-y plane in line with the orifice center, is shown in Figure 86 for the four-opposing jet configuration. Reference should be made to Table 10 in Section IV.B for the test flow conditions and other parameters, including mass-velocity ratio, density ratio, and pressure drop. Predicted jet trajectory, defined by the locus of minimum temperature, agrees reasonably well with the data. A comparison between predicted and measured profiles is presented in Figures 87 and 88 at different axial stations for typically selected isothermal lines. Figure 87(a) and 87(b) present measured isothermal lines of 800 and 1100 K, respectively, at x = 6.86 cm, whereas the jet origin is at x = 6.35 cm. Predicted results, shown by dotted lines, are for x = 6.57 and 7.00 cm. As is evident, the model overpredicts the jet

SYM-VAL ⊙ 300, ▲ 350, + 450, ✕ 500, ◇ 800, ✦ 950, ✕ 1000, Z 1050, Y 1100, ✕ 115
SYM-VAL ✕ 1200, ✕ 1250, (K)
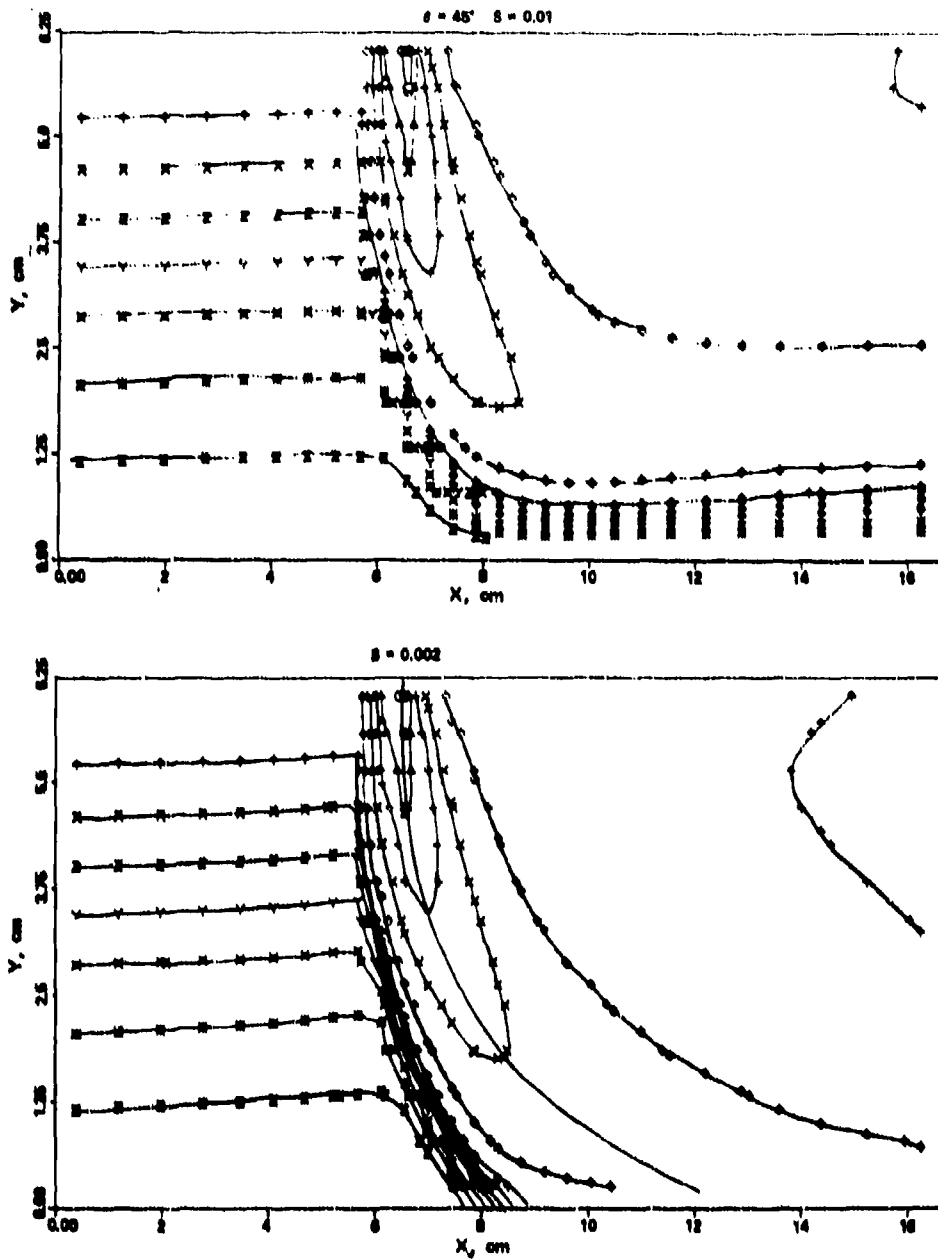
Figure 83. Effect of Cumulative Mass Residual (S) on
Predicted Isothermal Profiles of Set-3 of
Table 10.

JET ANGLE = 60°

● MEASURED JET CENTER LINE
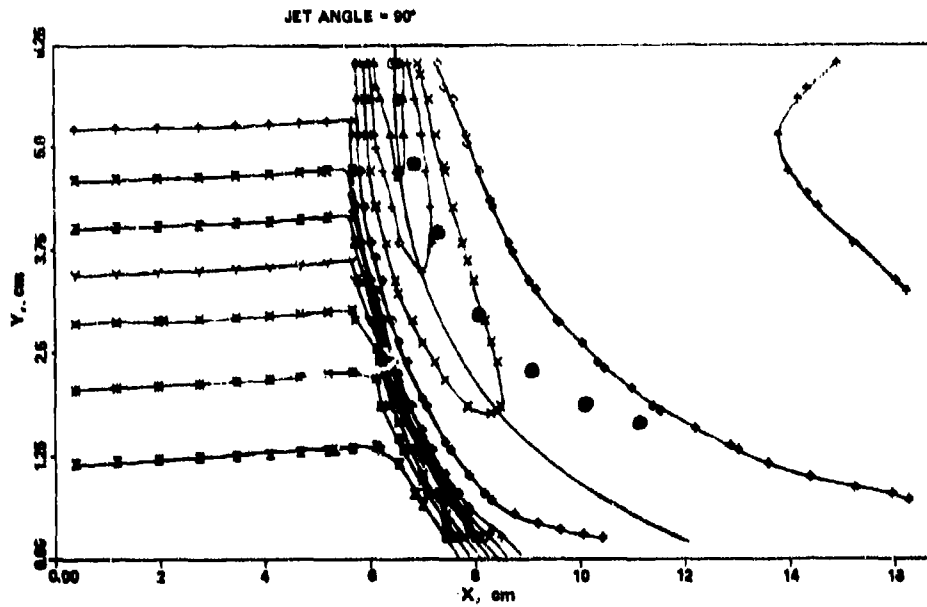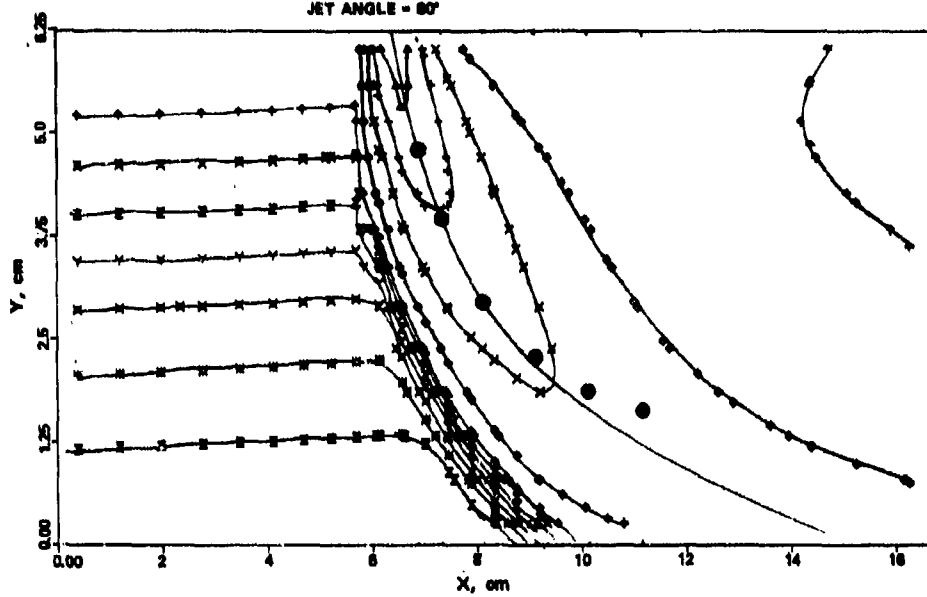
JET ANGLE = 90°

Figure 84. Effect of Jet Angle on Predicted Isothermal Lines of Set-3 of Table 10.

203

θ = 45°
PREFF = 0.9

● MEASURED JET
CENTER LINE

PREFF = 0.7
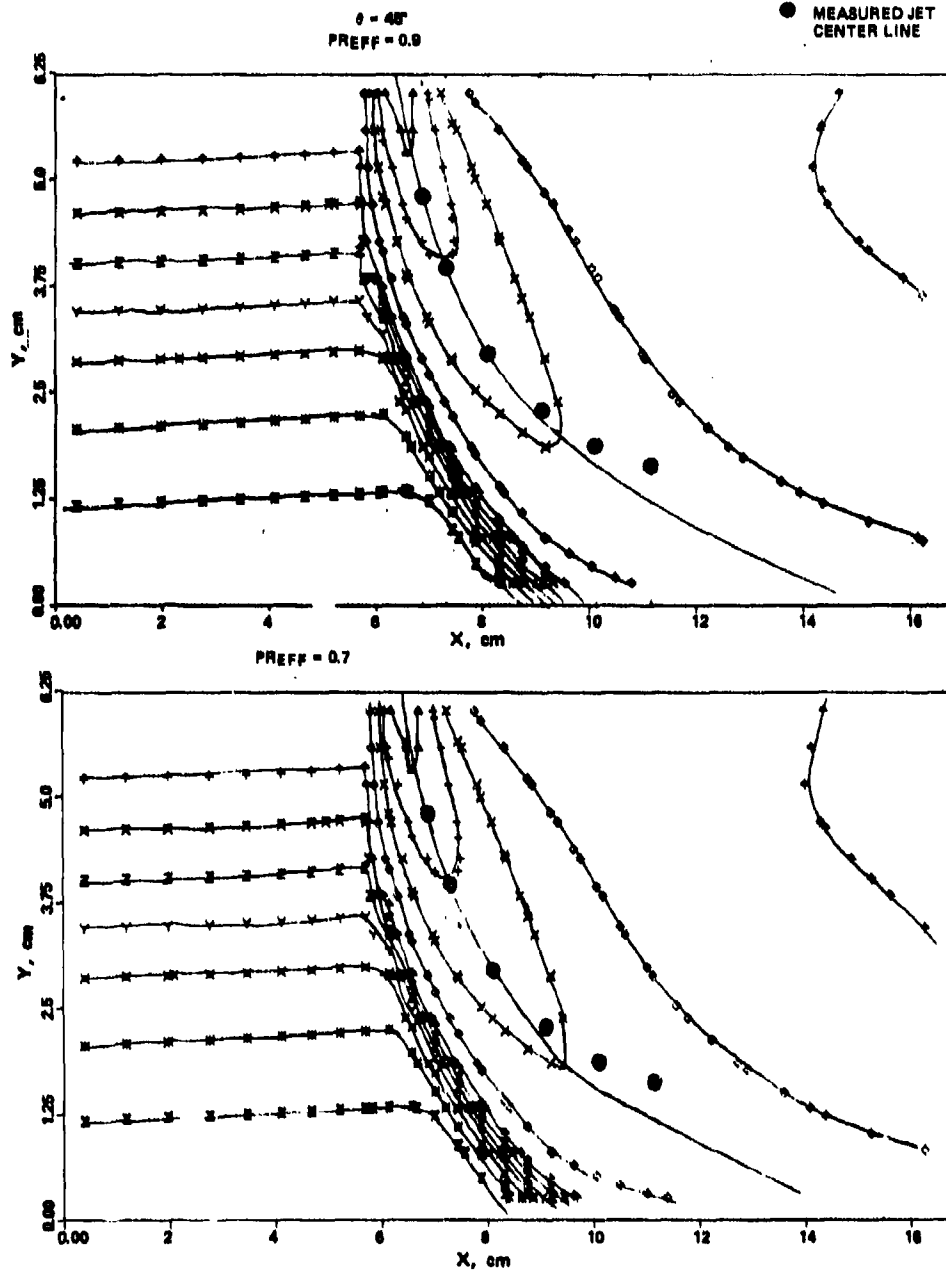
Figure 85.   Effect of Prandtl Number on Predicted
            Isothermal Plots of Set-3 of Table 10.

204
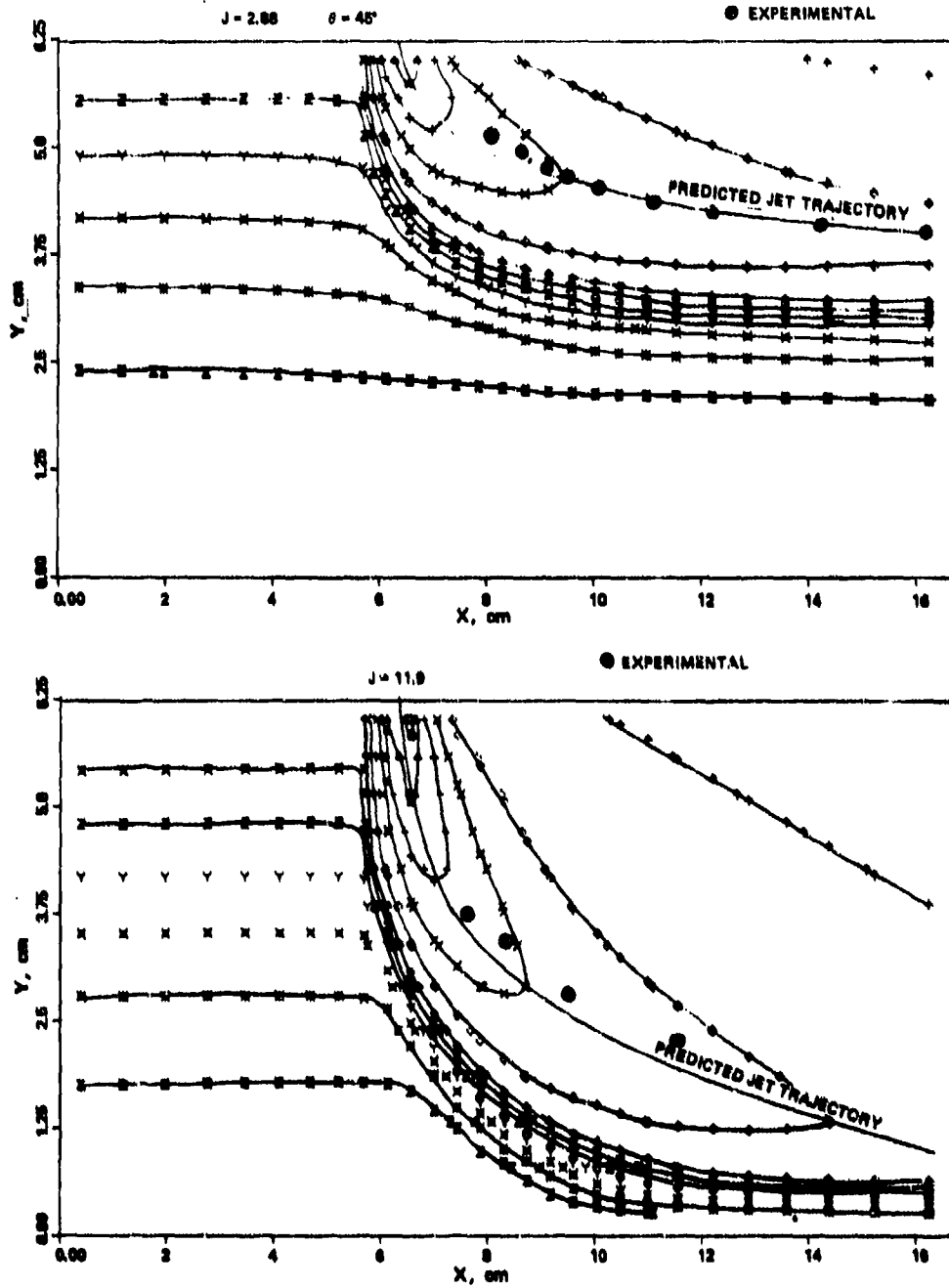
Figure 86.   Comparison Between Predicted and Measured
Jet Trajectories of Four-Opposing Jets
With Jet Momentum Ratio As a Parameter;
Refer to Table 10 for Other Details.

205

expansion rate. The same observation is valid for another down-stream plane at x = 7.37 cm, as shown in Figure 87(c) and (d). However, further downstream at x = 8.13 cm, the jet core (T = 800 K) is underpredicted whereas the peripheral isothermal line is overpredicted, until x = 9.14 cm, shown in Figure 87(h). Beyond x = 9.14 cm, shown in Figure 88, the model underpredicts the area under T = 1100 K isothermal lines. Nevertheless, the model gives reasonably good agreement with the data considering ten radial thermocouples were used to define the profiles. Figures 89 and 90 present comparison for moderate and high jet-momentum ratios of 20.9 and 65.1, respectively. For the moderate J, the model underpredicts jet expansion along the circumferential direction, except in the region close to the jet origin. However, for J = 65.1, the model slightly overpredicts the jet shapes, as shown in Figure 90.

Figure 91 shows a comparison between predicted and measured jet trajectories of the six-opposing jets at different jet-momentum ratios. The model overpredicts jet penetration at low values of jet-momentum ratio, but gives good agreement for moderate-to-high jet-momentum ratios. The corresponding jet shapes are shown in Figures 92 through 96.

Finally, Figure 97 shows results for a two-row staggered six-opposing jet configuration at a low jet-momentum ratio of 4.5. The model overpredicts penetration for the first jet, but gives good agreement with the second-jet data.

It therefore can be concluded that 3-D model predictions are in reasonably good agreement with measurements. Further improvement is needed in regard to the jet expansion rate. Nevertheless, the 3-D model can be used for studying mixing of transerve cold jets with confined hot stream. Figures 98 and 99 present predicted isothermal plots for a two-row inline six-opposing dilution jet with a liner pressure drop of 2 percent. The first-row jet originates at x = 6.35 cm, whereas the
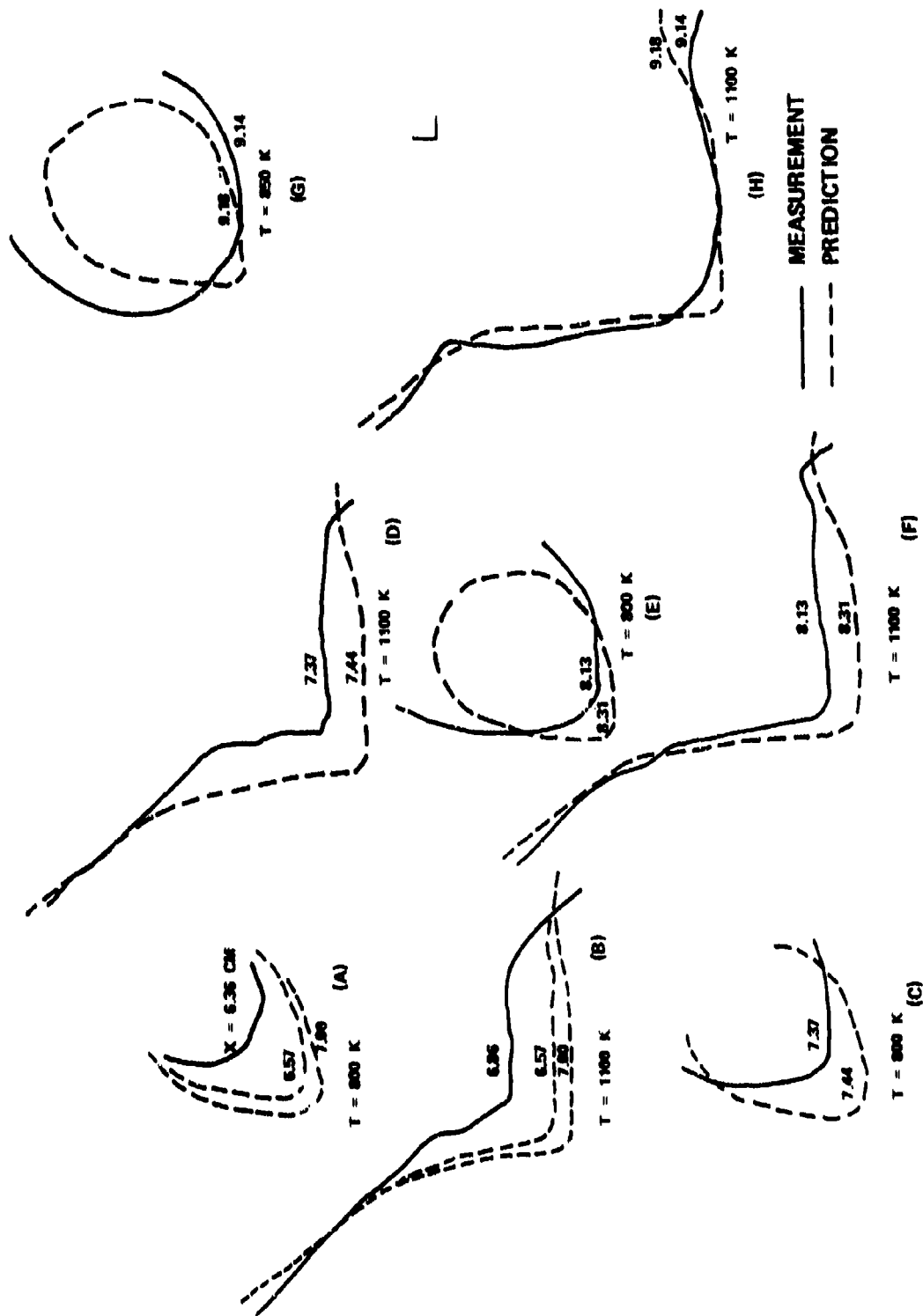
Figure 87. Comparison Between Measured and Predicted Isothermal Lines of a Four-Opposing Jet Case, J = 2.9, Set-1 of Table 10.

207
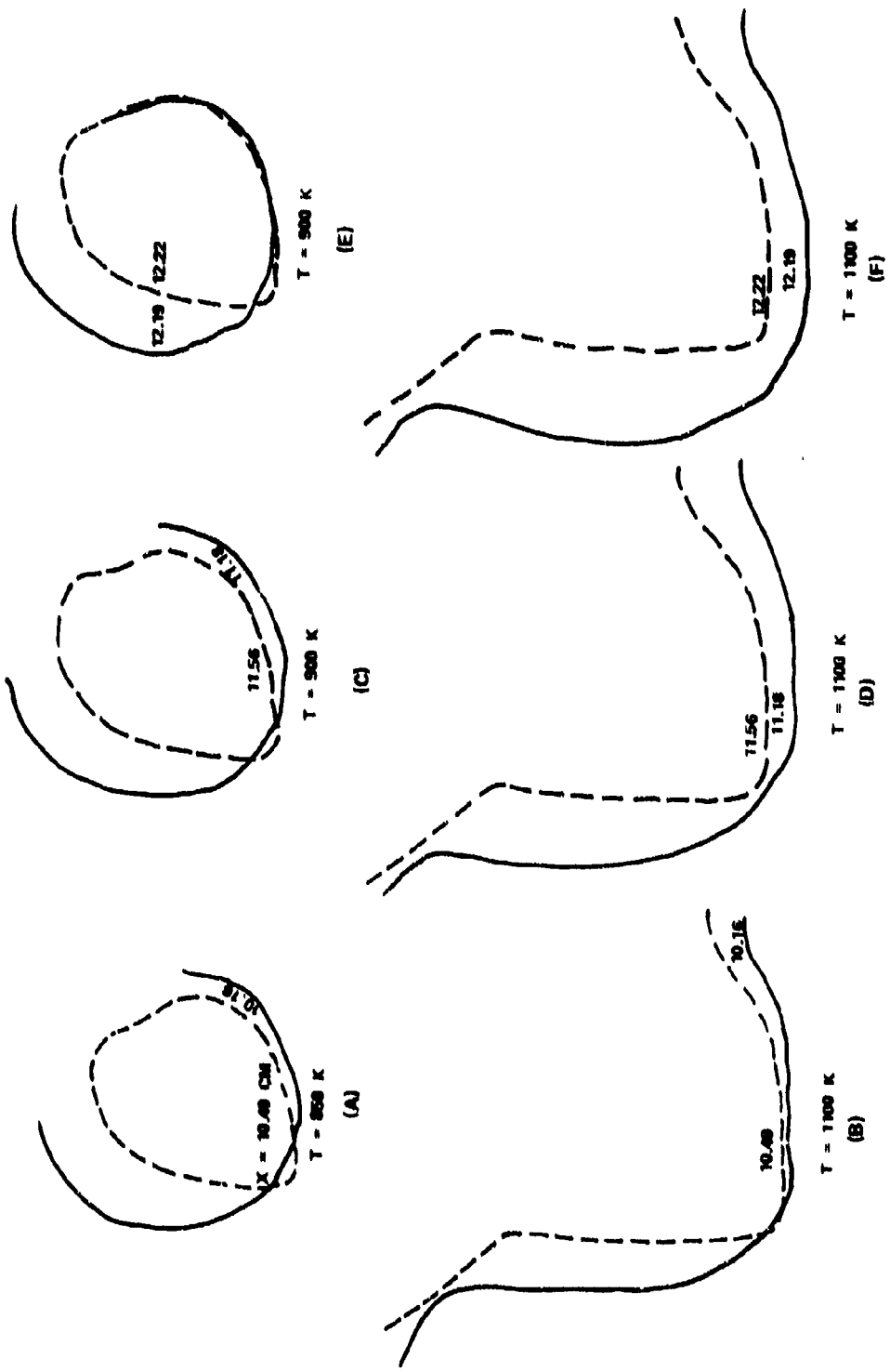
Figure 88. Comparison Between Predicted and Measured Isothermal Lines of a Four-Opposing Jet Case J = 2.9, Set-1 of Table 10.

DATA
PREDICTION

208
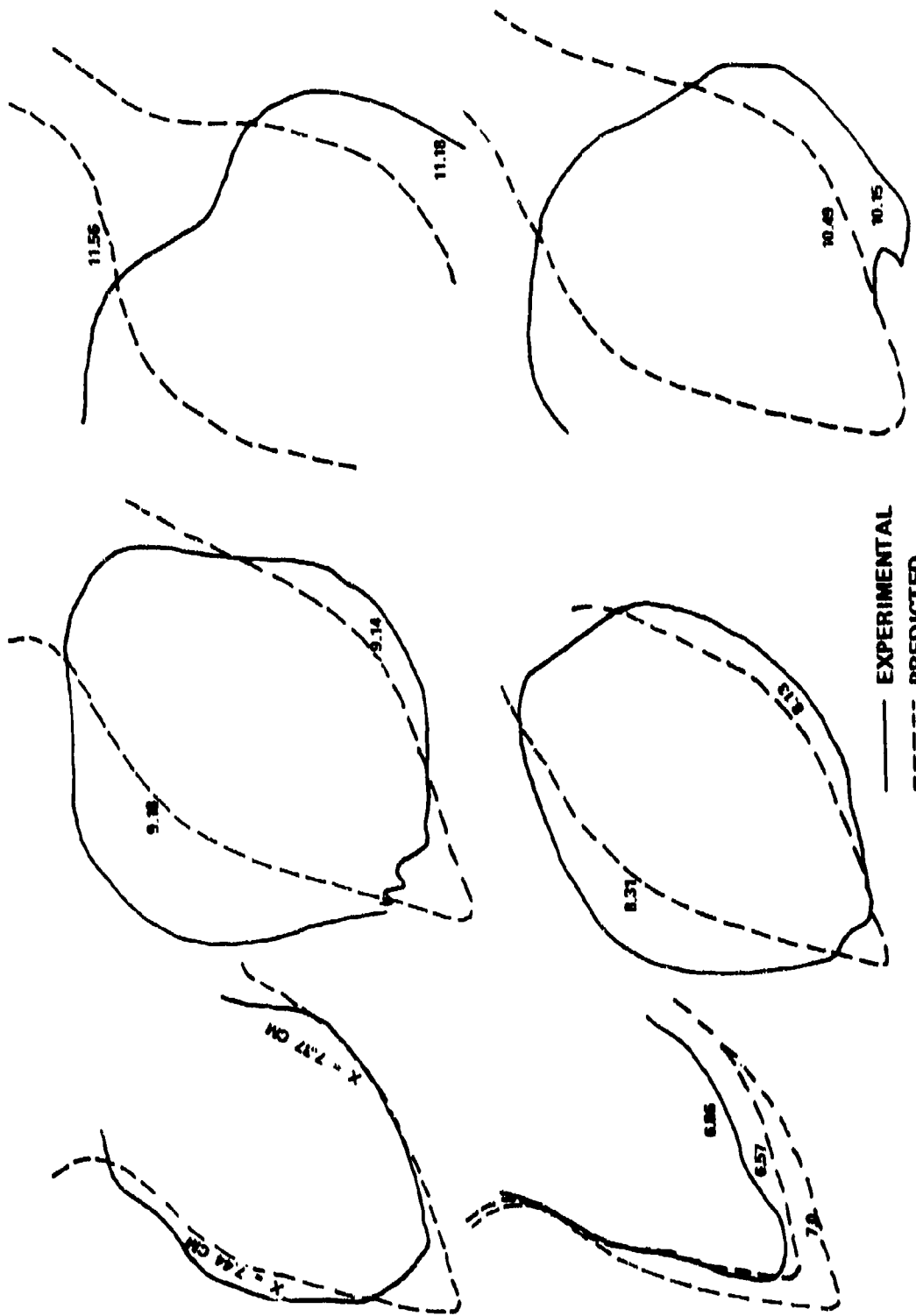
Figure 89. Comparison Between Predicted and Measured Isothermal Line (T = 900 K) of a Four-Opposing Jet Case, J = 20.9, Set-3 of Table ".

EXPERIMENTAL
PREDICTED
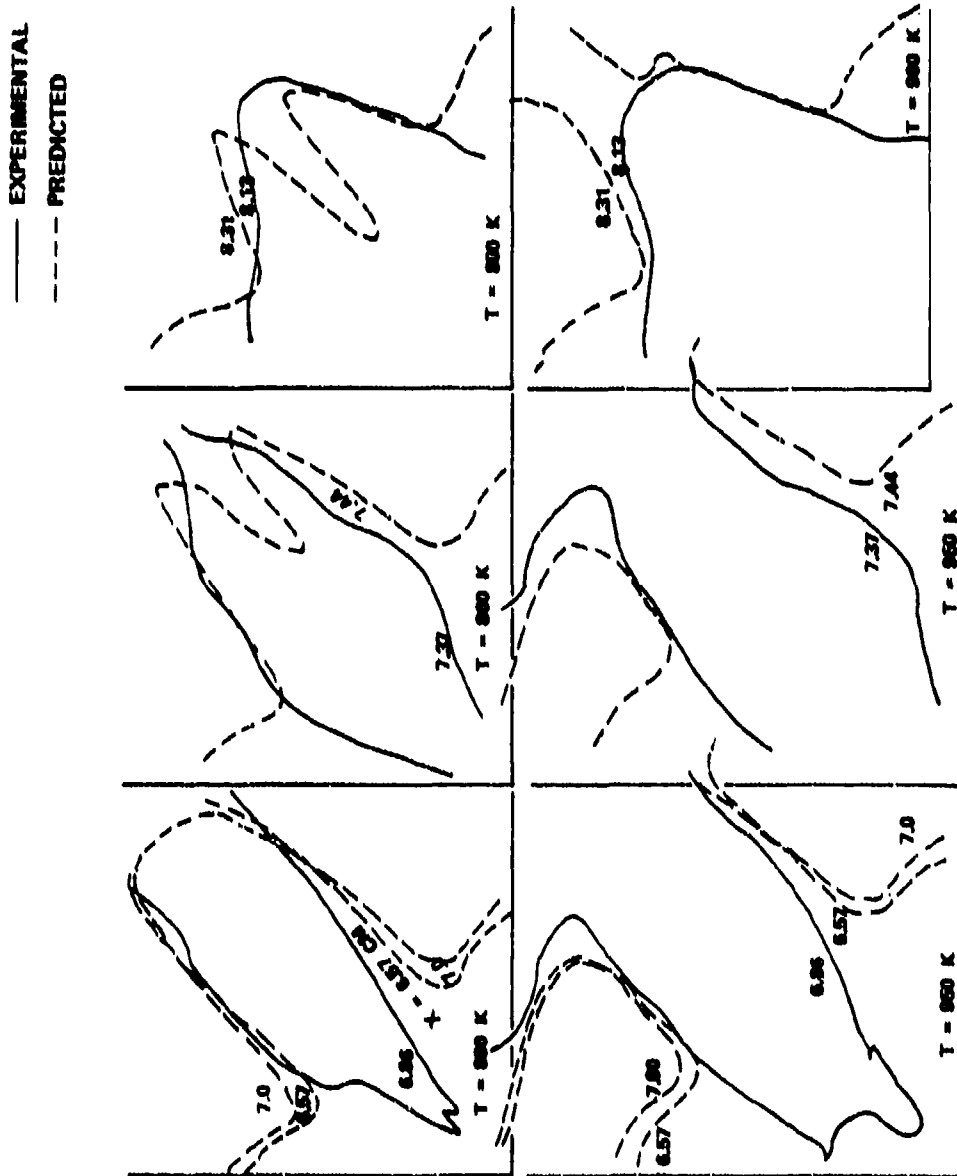
Figure 90. Comparison Between Predicted and Measured Isothermal Lines of a Four-
Opposing Jet Case, J = 65.1, Set-5 of Table .i.

210

J = 3.2   δ = 30°

J = 11.0

**Figure 91.   Comparison Between Predicted and Measured Jet
Trajectories of Six-Opposing Jets With Jet
Momentum Ratio As a Parameter.
(Sheet 1 of 3)**

211

J = 17.3

J = 41.1
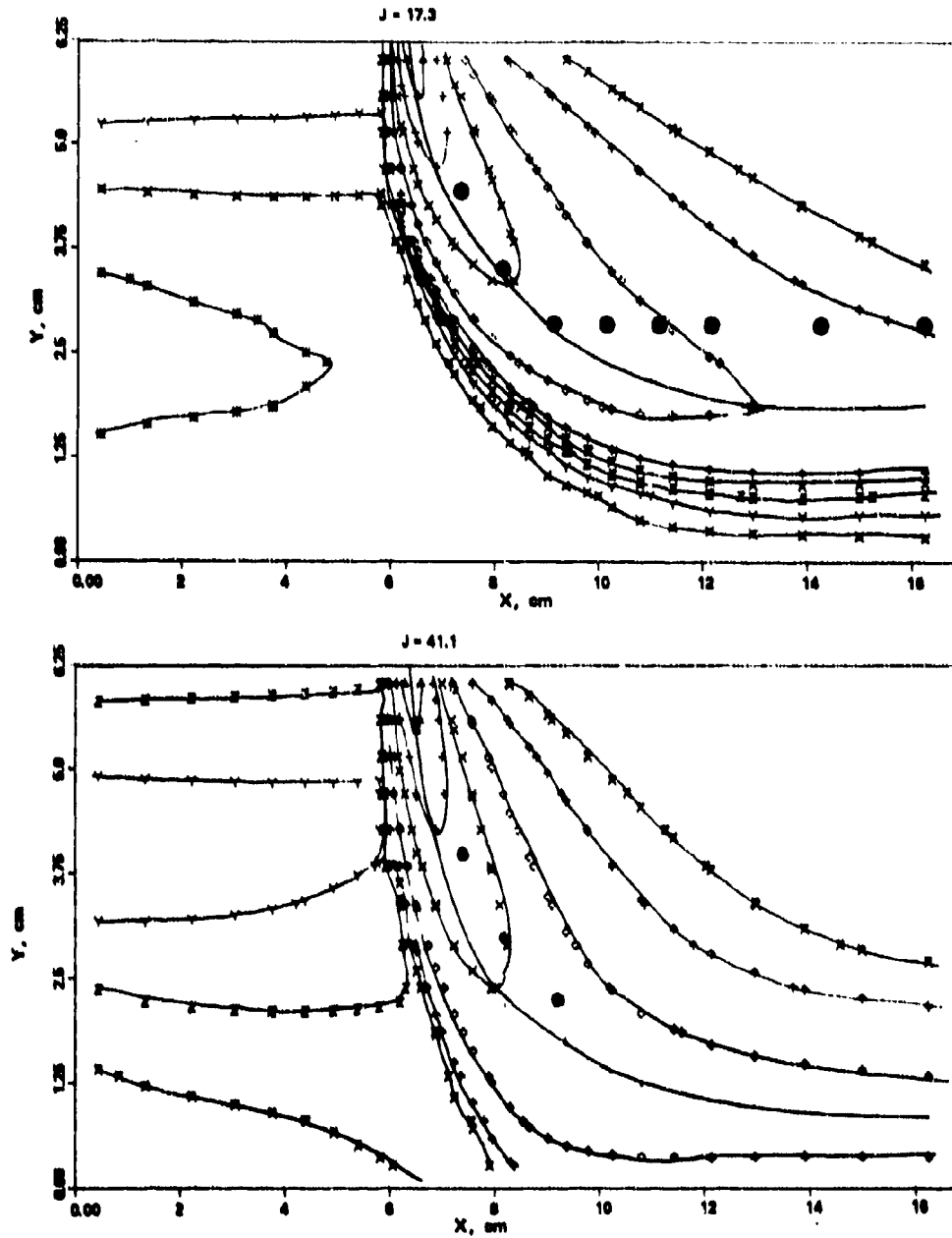
Figure 91.   Comparison Between Predicted and Measured Jet
             Trajectories of Six-Opposing Jets With Jet
             Momentum Ratio As a Parameter.
             (Sheet 2 of 3)

Figure 91. Comparison Between Predicted and Measured Jet
Trajectories of Six-Opposing Jets With Jet
Momentum Ratio As a Parameter.
(Sheet 3 of 3)

Figure 92. Comparison Between Predicted and Measured Isothermal Lines of a Six-Opposing Jet, J = 3.2, Set-1 of Table 11.

214
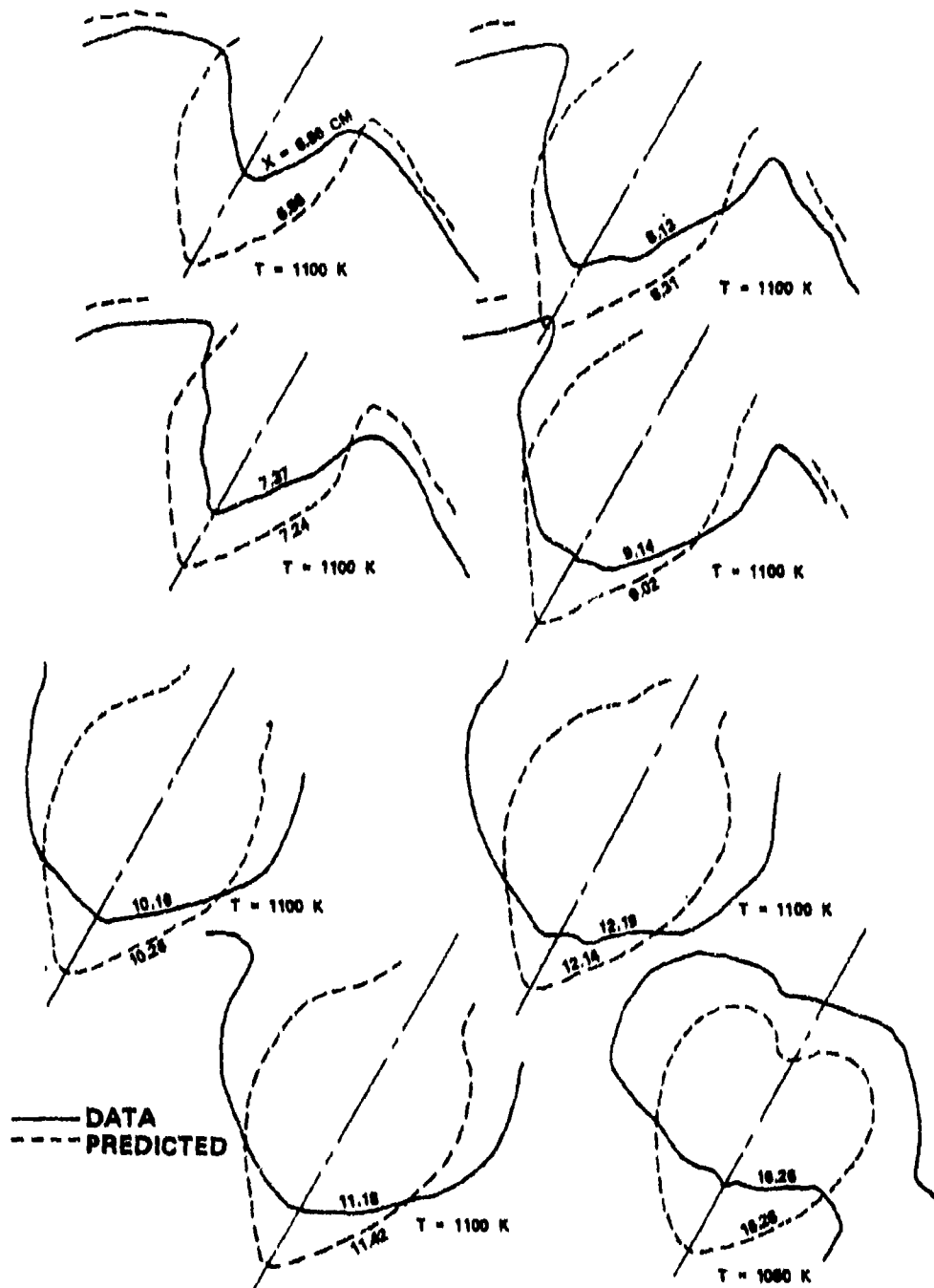
Figure 93. Comparison Between Predicted and Measured Isothermal Lines of a Six-Opposing Jet, J = 11.0, Set-2 of Table 11.
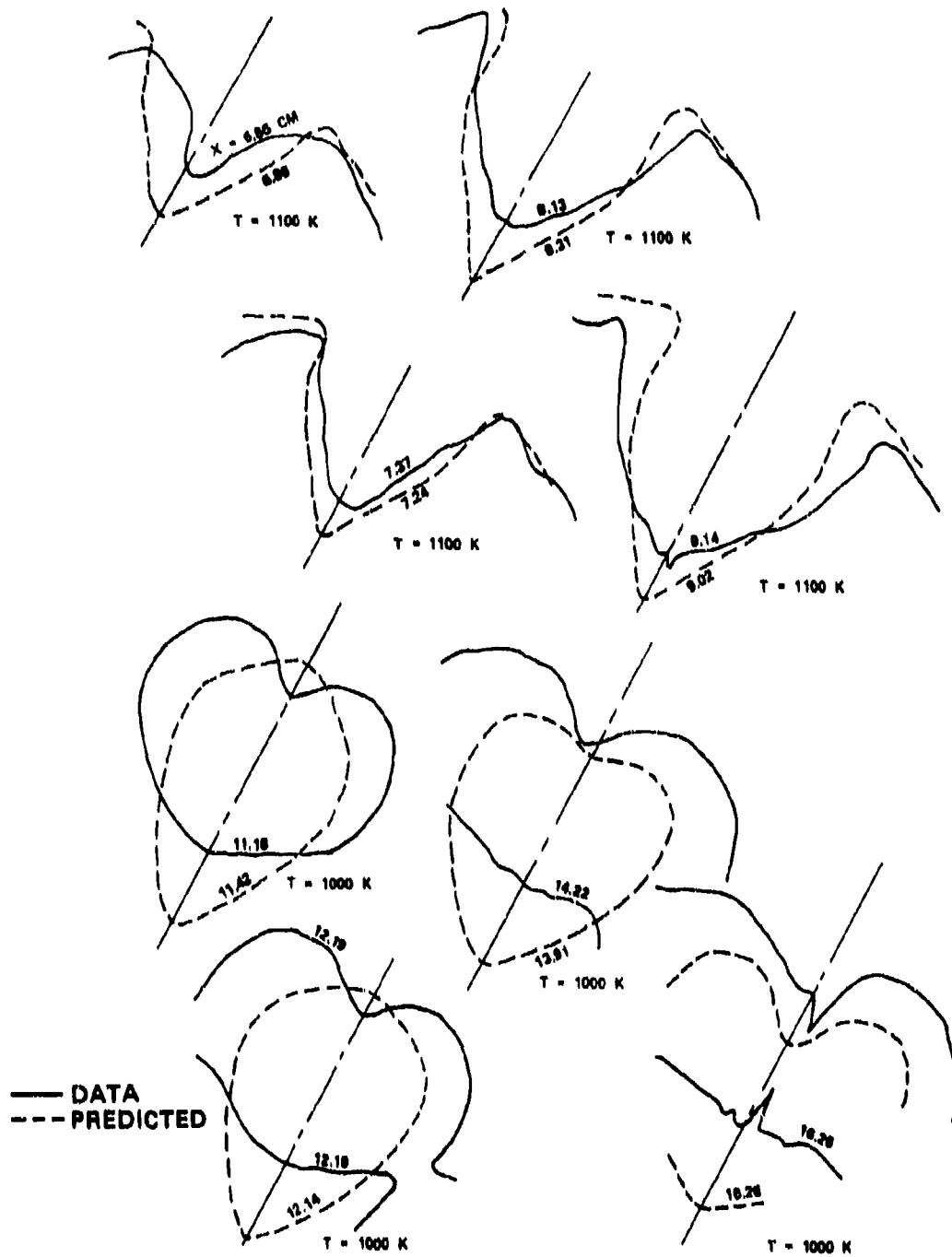
Figure 94. Comparison Between Predicted and Measured
Isothermal Lines of a Six-Opposing Jet,
J = 17.3, Set-3 of Table 11.
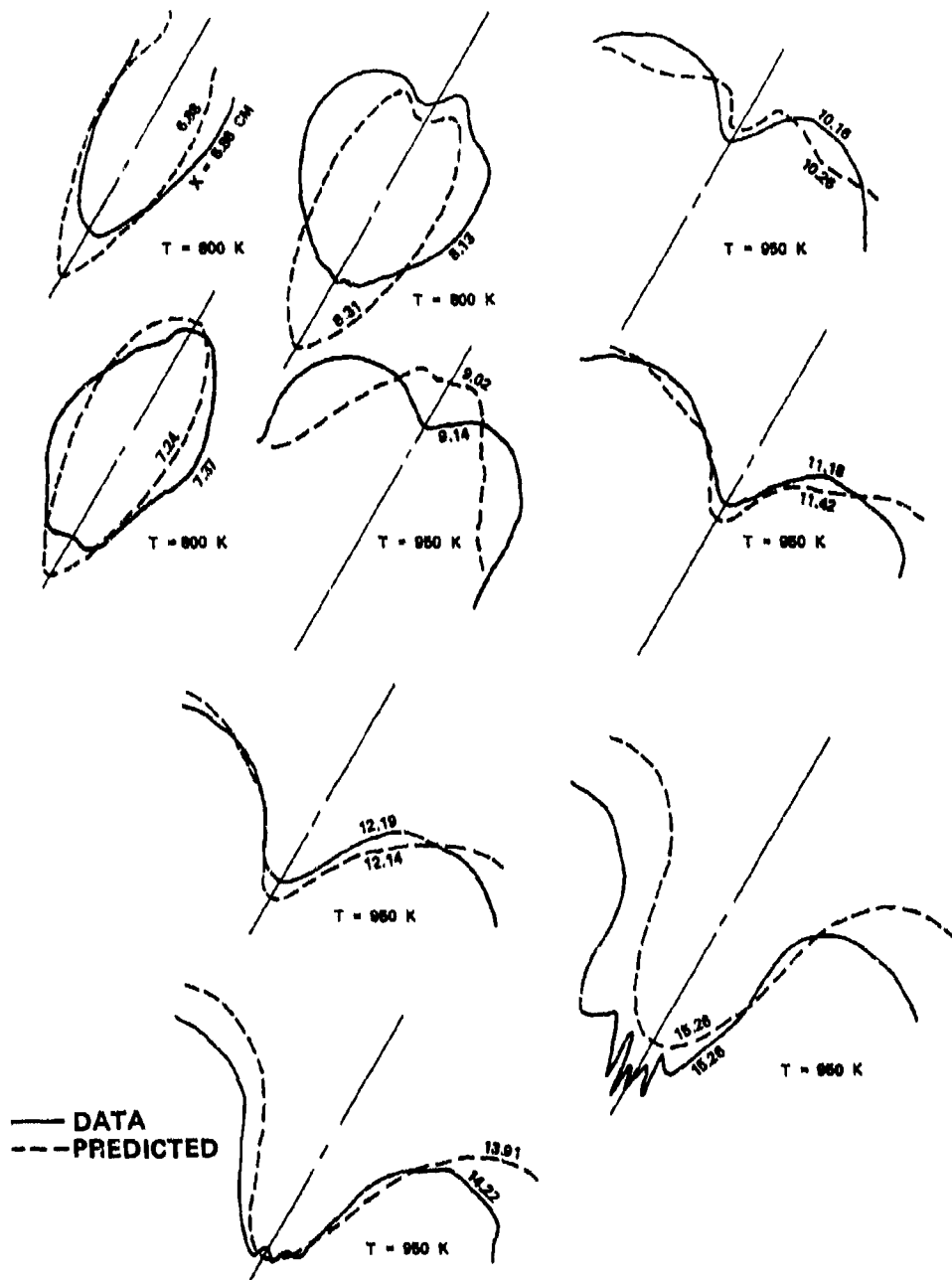
Figure 95. Comparison Between Predicted and Measured
Isothermal Lines of a Six-Opposing Jet,
J = 41.1, Set-4 of Table 11.
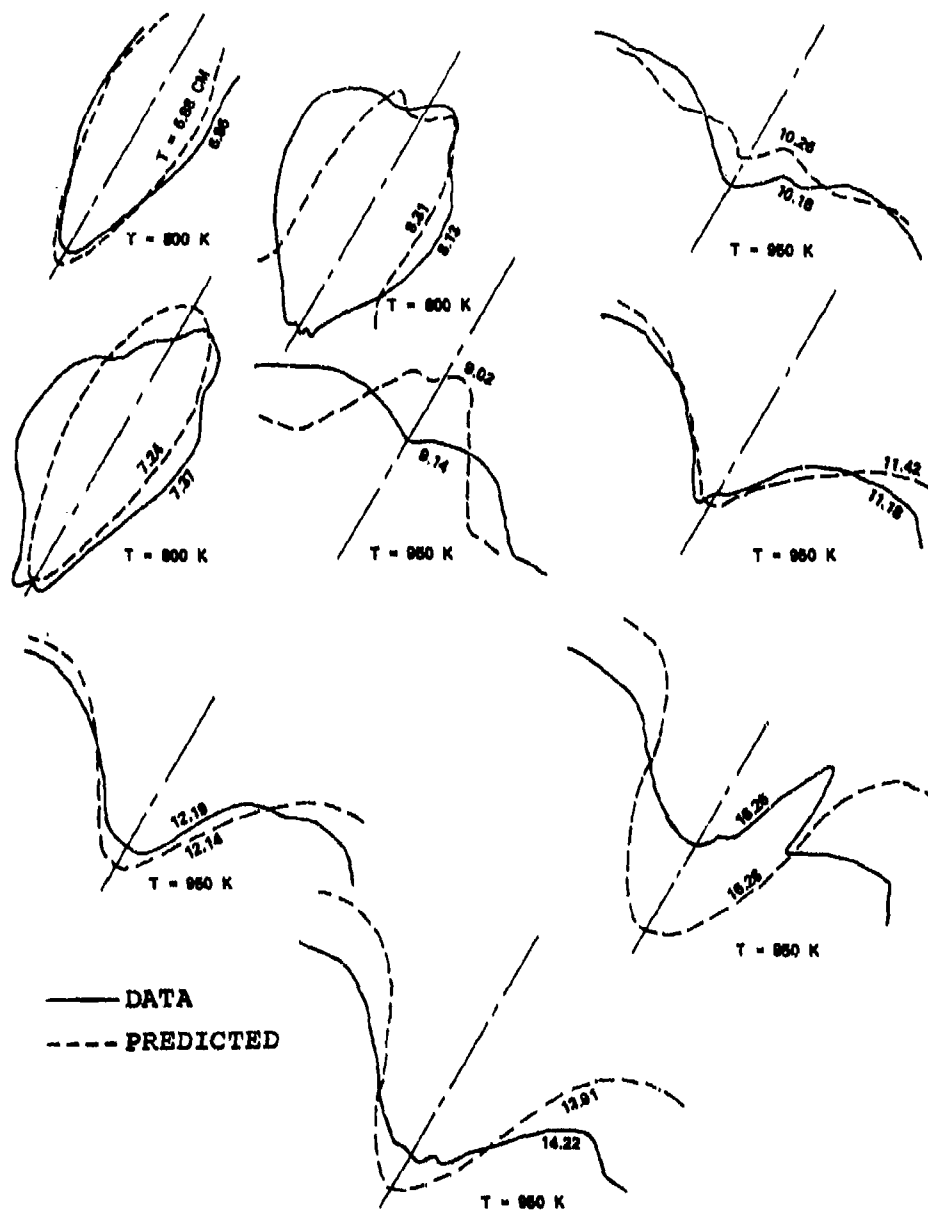
Figure 96. Comparison Between Predicted and Measured
Isothermal Lines of a Six-Opposing Jet,
J = 61.1, Set-5 of Table 11.

218
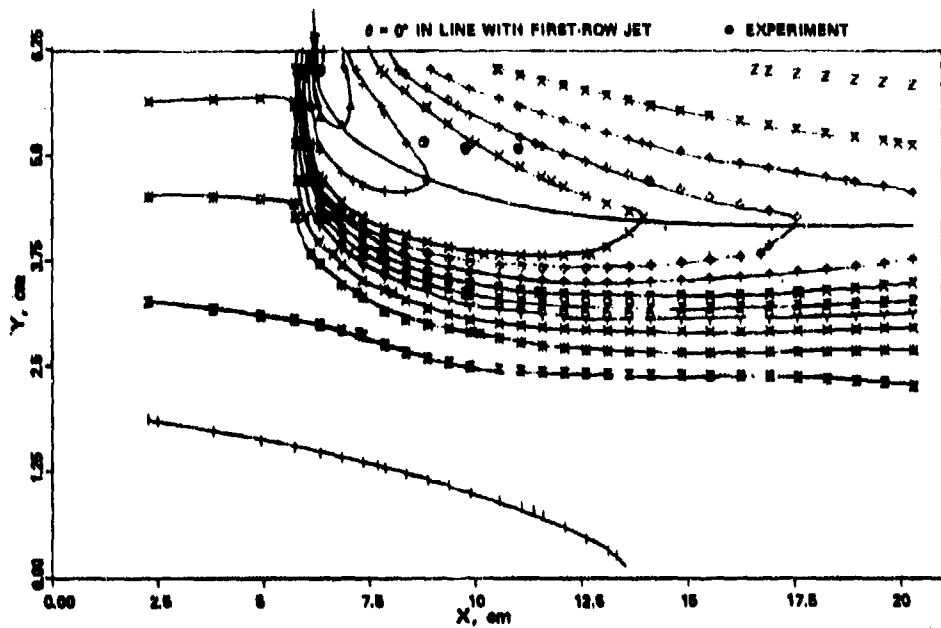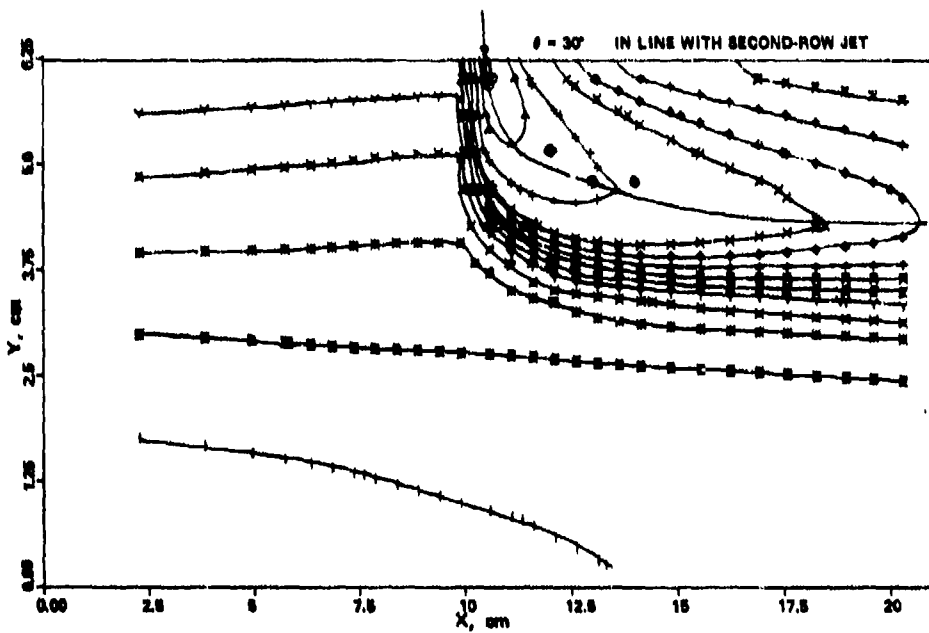
Figure 97. Comparison Between Predicted and Measured Jet Trajectories of Two Staggered Rows of Six-Opposing Jets; Jet Momentum Ratio = 4.5.
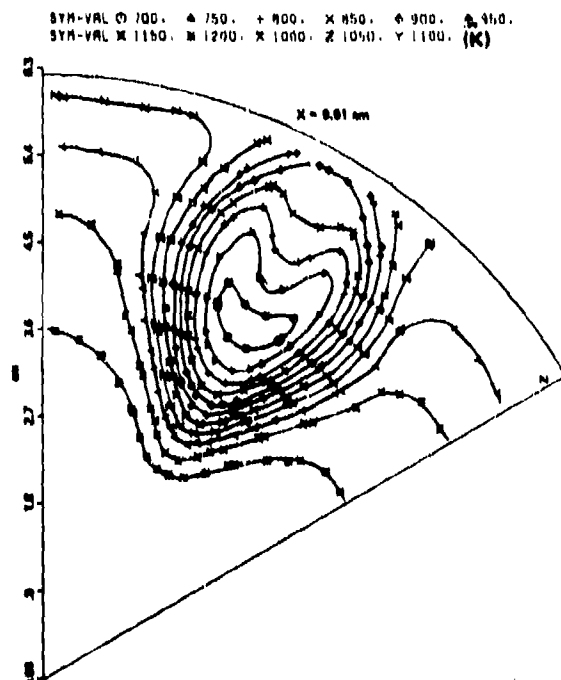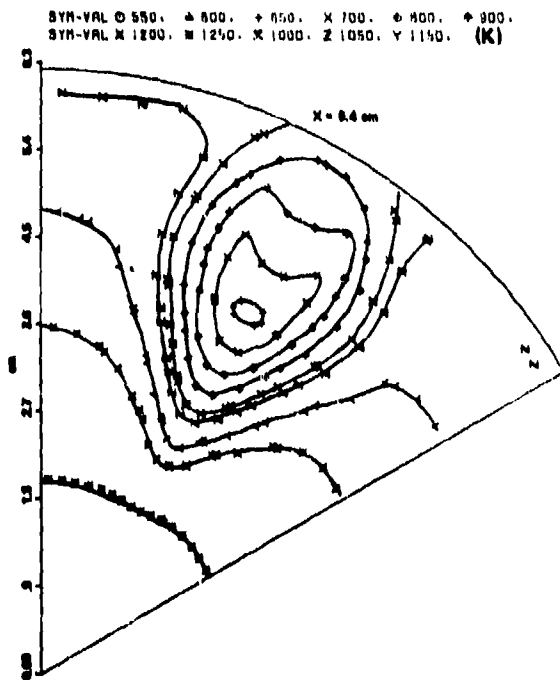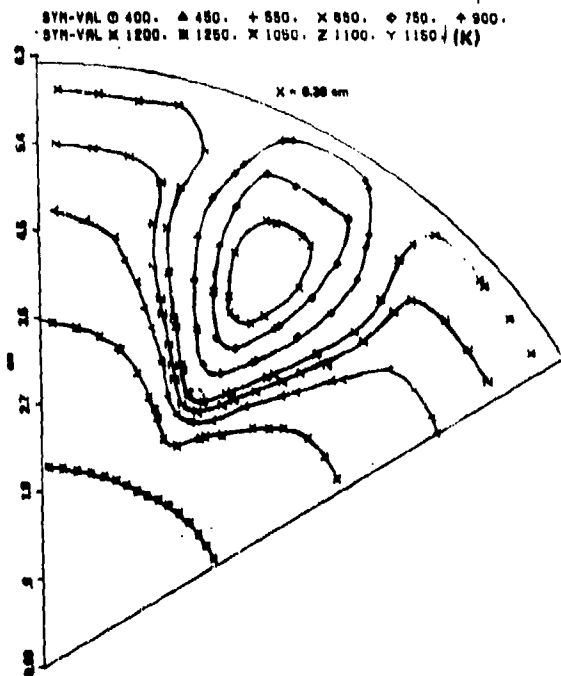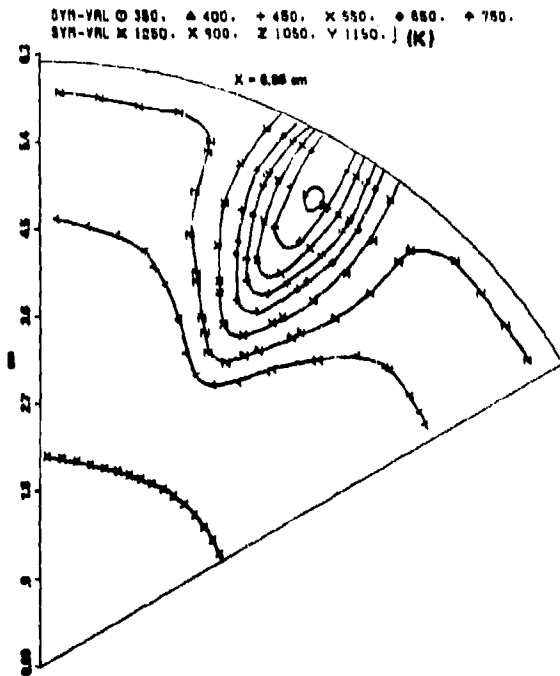
Figure 98.   Predicted Mixing Characteristics of a First-Row
Jet of Two In-Line Rows of Six-Opposing Jets
Configuration; Location of First Row x = 6.35 cm.
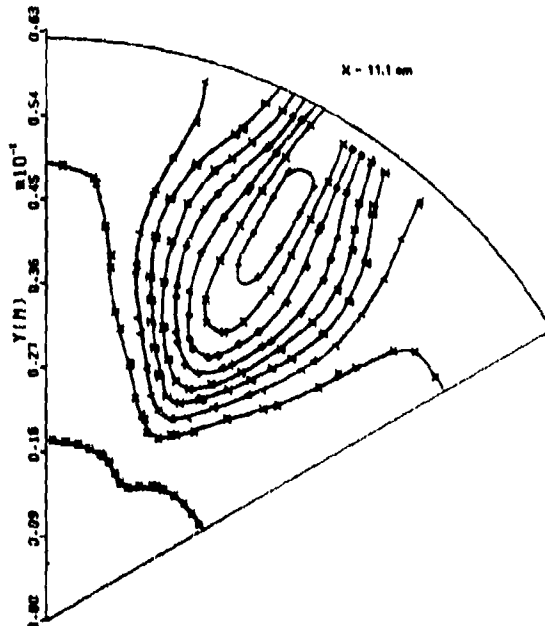
220

X = 11.1 cm

X = 12.12 cm

X = 16.59 cm

X = 30.32 cm
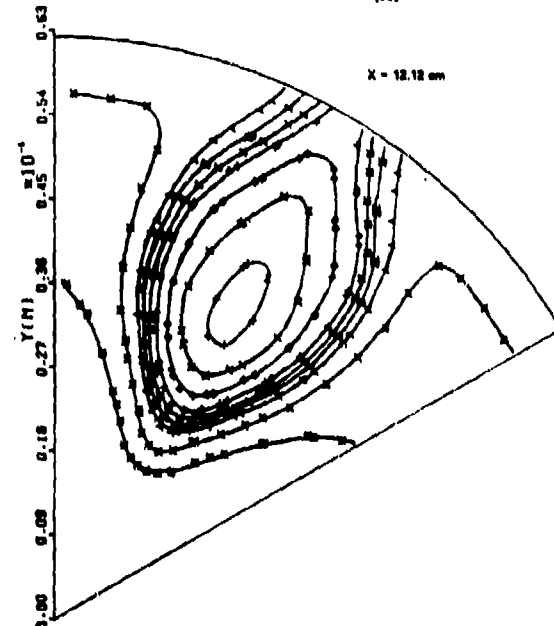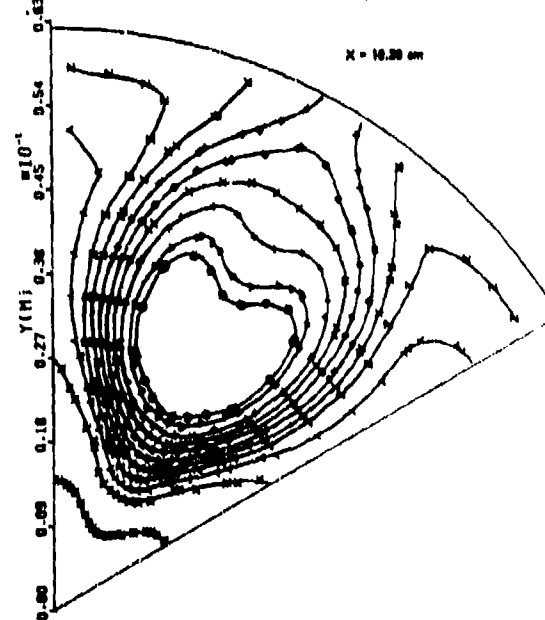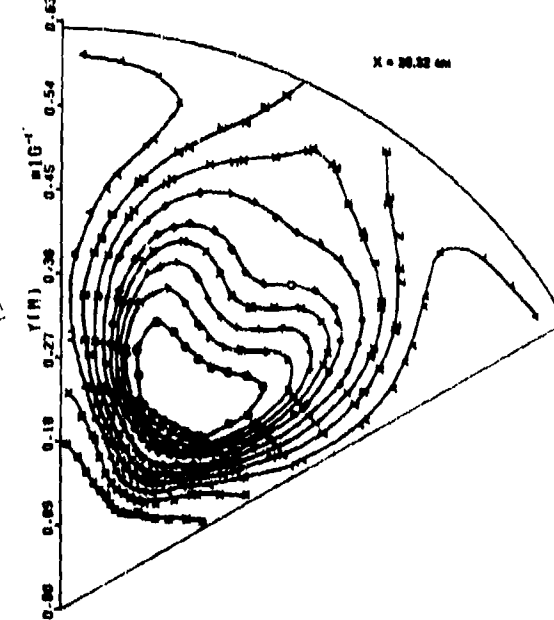
Figure 99.   Predicted Mixing Characteristics of a Second-Row
Jet of Two In-Line Rows of Six-Opposing Jets
Configuration; Location of Second Row x = 10.59 cm.

221

second-row orifice is located at x = 10.59 cm. The development
of the first-row jet continues and is fully developed at
x = 9.91, which is located 0.68 cm upstream from the second row.
The jet has penetrated a radial distance of 2.1 cm. The corres-
ponding hot stream maximum temperature is less than the initial
maximum temperature of 1250 K. Figure 99 shows the development
of the second-row jet. The jet shape is maintained up to x =
20.32 cm; i.e., 9.73 cm downstream from the second row. The
corresponding jet penetration is 3.6 cm. Consequently, the hot
core of 1200 K near the can centerline has not been dissipated
by employing 2 rows of 12 jets.

C. Can Combustor Cold-Flow Mapping

The 3-D elliptic flow program was used to predict internal
profiles of the can combustor, shown previously in Figure 43;
the corresponding test conditions were presented in Figure 46.
A 60-degree sector of the combustor was divided into 32 x 16 x 14
finite-difference nodes along axial, radial, and circumferential
directions, respectively. Figure 100 shows the grid spacing.
The primary jet was simulated by six finite-difference nodes,
whereas the dilution jet was simulated by four nodes. Airflow
distribution around the liner was calculated by the annulus flow
model. Jet velocities were calculated from measured liner-
pressure drop and the Mach tables. The radial jet angle was
estimated to be 90-degrees. The turbulence kinetic energy and
length scale of the radial jet were assumed to be 0.003 V_j^2 and
0.02 D_j, respectively; where V_j and D_j are the radial jet vel-
ocity and diameter. Similarly, turbulence kinetic energy and
length scale associated with cooling-slot air were 0.003 U_s^2
and 0.02 S, respectively. Here, U_s denotes slot-air velocity
and S is the slot height, respectively. The dome inclined wall
was simulated by broken lines indicated in Figure 100, where a
continual increase in the flow area was substituted by three jumps

222
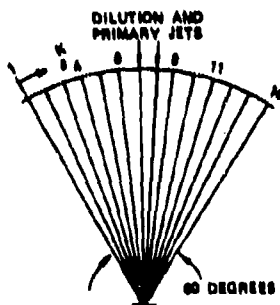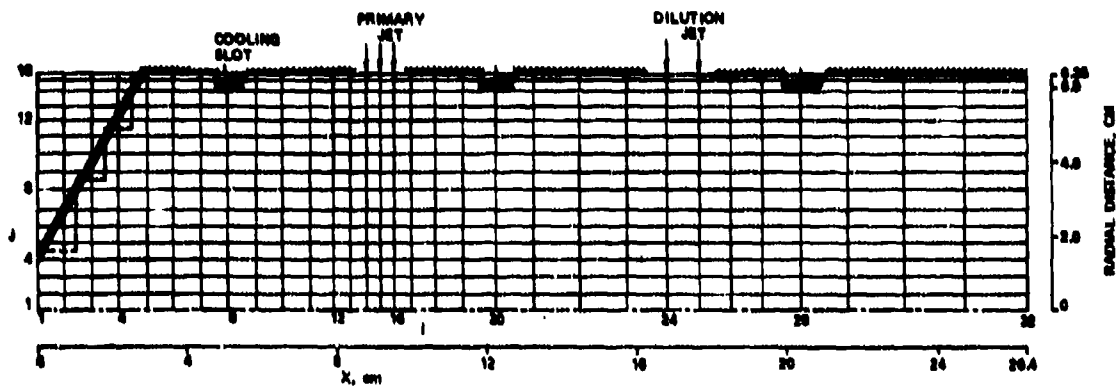
Figure 100. Grid Spacing Used For Can Combustor Model Validation.

223

in the cross-section flow area. Further improvement in the
inclined-wall simulation could be achieved by increasing the
number of X-nodes near the inlet with a loss in the resolution
somewhere else in the flow field.

The calculations were initiated for all of the three test
cases with assumed uniform profiles so that the convergence rate
could be checked as a function of combustor pressure drop and
airflow rate. Convergence was checked by comparing maximum
nodal mass residual; cumulative mass residual; total mass flux
error at the combustor exit plane; the variations in pressures
for the nodes (2, 15, 2) and (31, 15, 2); and variations in
axial, radial, and tangential velocity components for the node
having the maximum mass residual. The convergence rate was
quite fast for achieving a cumulative mass residual of 0.05 W_{a_3};
it was moderate for achieving an error of 0.01 W_{a_3}, and quite slow
for getting down to 0.005 W_{a_3}. The corresponding maximum nodal
mass residual was typically 3.0 x 10^{-5} W_{a_3}, and the exit plane
mass residual was 1.0 x $10^{-4}W_{a_3}$. The pressure variations
between successive iterations were of the order of 0.5 percent.
The maximum nodal mass residual was generally at a node with
either small velocity components or with large gradients.
Typical variations in axial, radial, and tangential velocity
components for the node with maximum mass residual were of the
order of 0.04 m/s.

Figures 101 through 106 present a comparison between pre-
dicted and measured axial-velocity profiles for the three test
sets at different x-y planes lying in line and in between the
primary jet (shown previously in Figure 43). The accuracy of
the measured data was less than satisfactory, as explained in
Section IV.C; due in part to high turbulence levels, and
errors introduced by the perturbing velocity probe. Since the
pyramid probe used in this study was originally designed for
measuring high subsonic flows, such as encountered in compressor
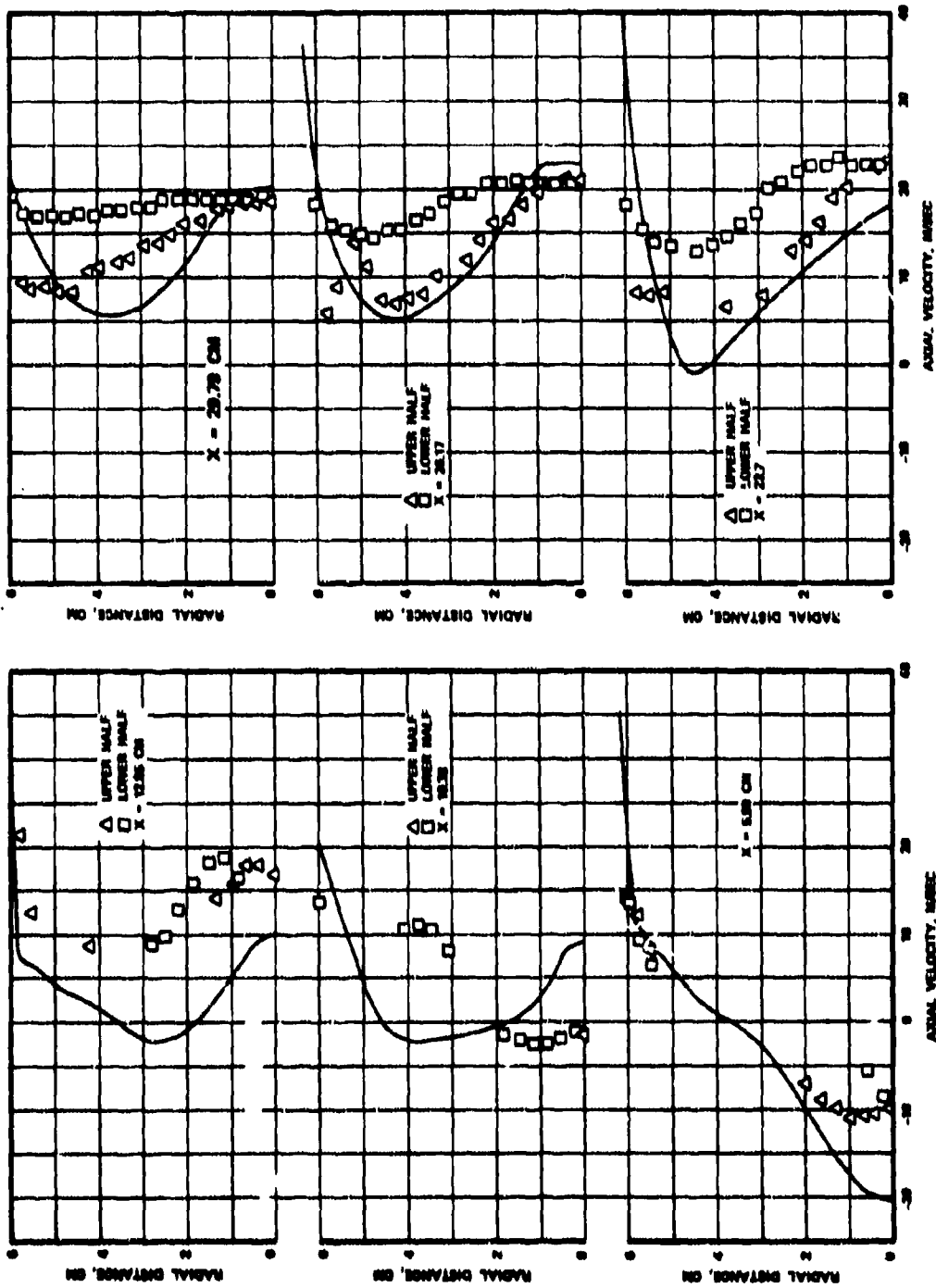
Figure 101. Comparison Between Predicted and Measured Axial Velocity Profiles in Different X-Y Planes In Line With Primary Jet; Combustor Airflow Rate = 1.82 kg/s.
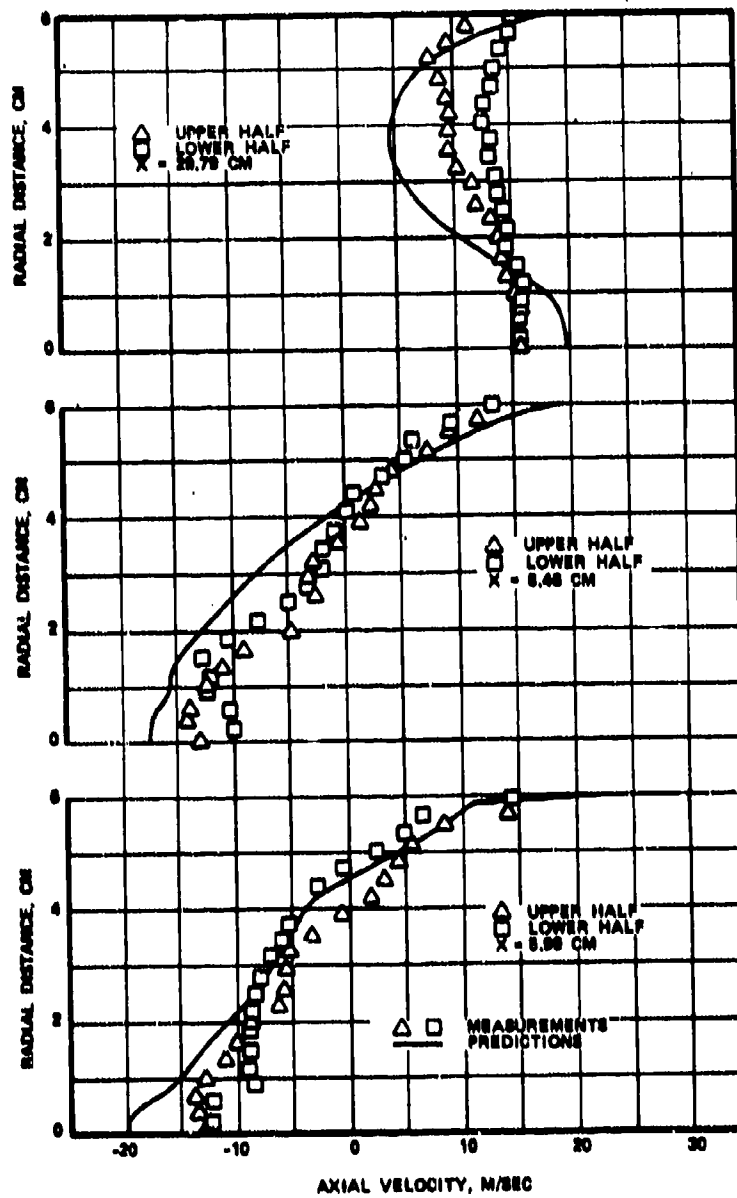
Figure 102. Comparison Between Predicted and Measured Axial
Velocity Profiles in Different X-Y Planes In
Between Primary Jet; Combustor Airflow Rate =
1.82 kg/s.
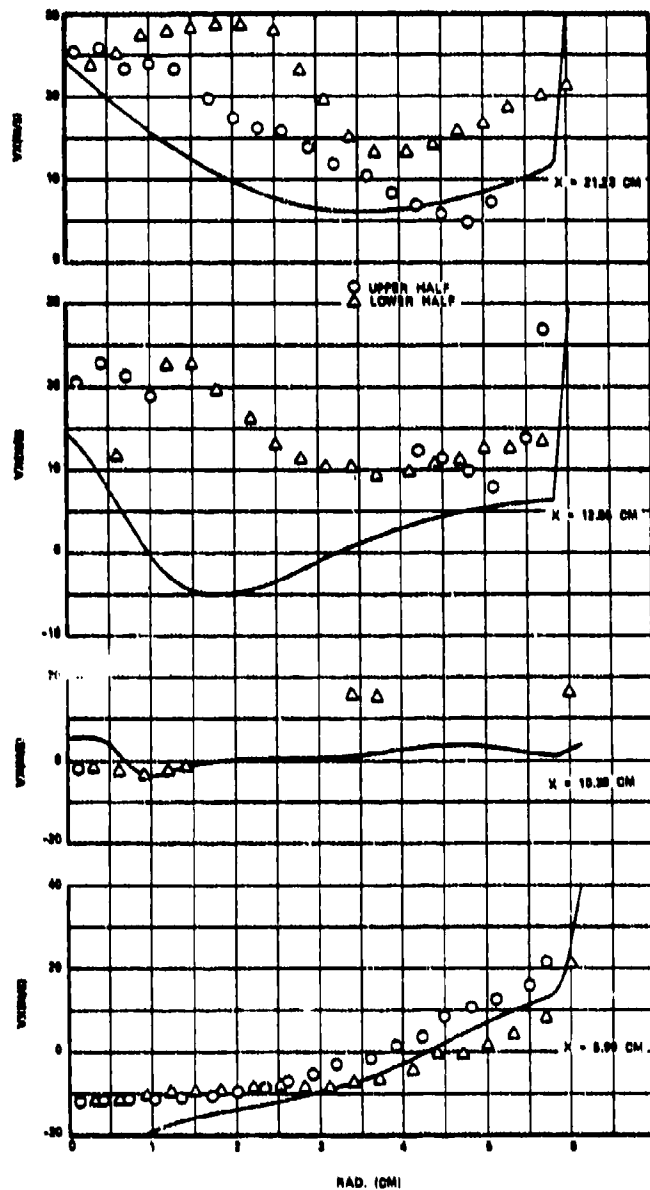
Figure 103. Comparison Between Predicted and Measured
Axial Velocity Profiles in Different X-Y
Planes In Line With Primary Jet; Combustor
Airflow Rate = 2.26 kg/s.
(Sheet 1 of 2)

Figure 103. Comparison Between Predicted and Measured Axial Velocity Profiles in Different X-Y Planes In Line With Primary Jet; Combustor Airflow Rate = 2.26 kg/s. (Sheet 2 of 2)

228
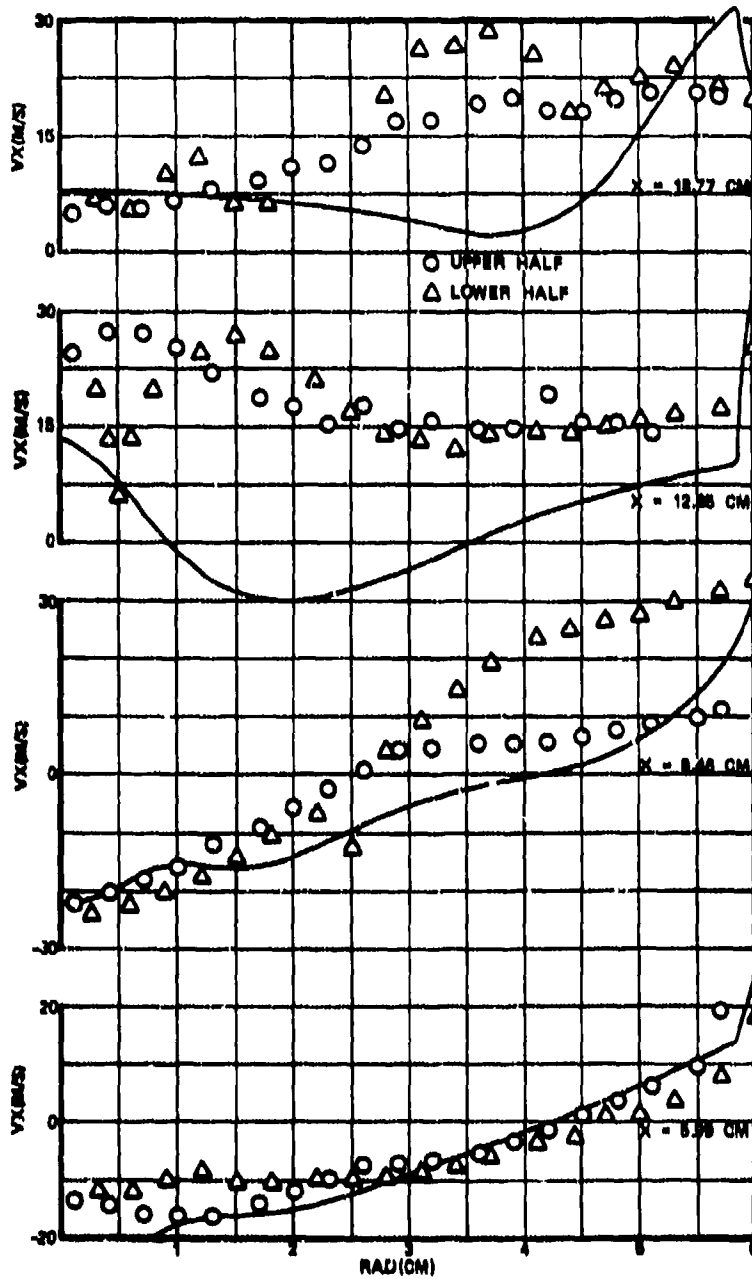
Figure 104. Comparison Between Predicted and Measured
Axial Velocity Profiles in Different X-Y
Planes In Between Primary Jet; Combustor Air-
flow Rate = 2.26 kg/s.
(Sheet 1 of 2)

Figure 104. Comparison Between Predicted and Measured
Axial Velocity Profiles in Different X-Y
Planes In Between Primary Jet; Combustor Air-
flow Rate = 2.26 kg/s.
(Sheet 2 of 2)

Figure 105. Comparison Between Predicted and Measured Axial
Velocity Profiles in Different X-Y Planes In Line
With Primary Jet; Combustor Airflow Rate = 2.74
kg/s.(Sheet 1 of 2)

231

Figure 105. Comparison Between Predicted and Measured Axial
Velocity Profiles in Different X-Y Planes In Line
With Primary Jet; Combustor Airflow Rate = 2.74
kg/s. (Sheet 2 of 2)

232
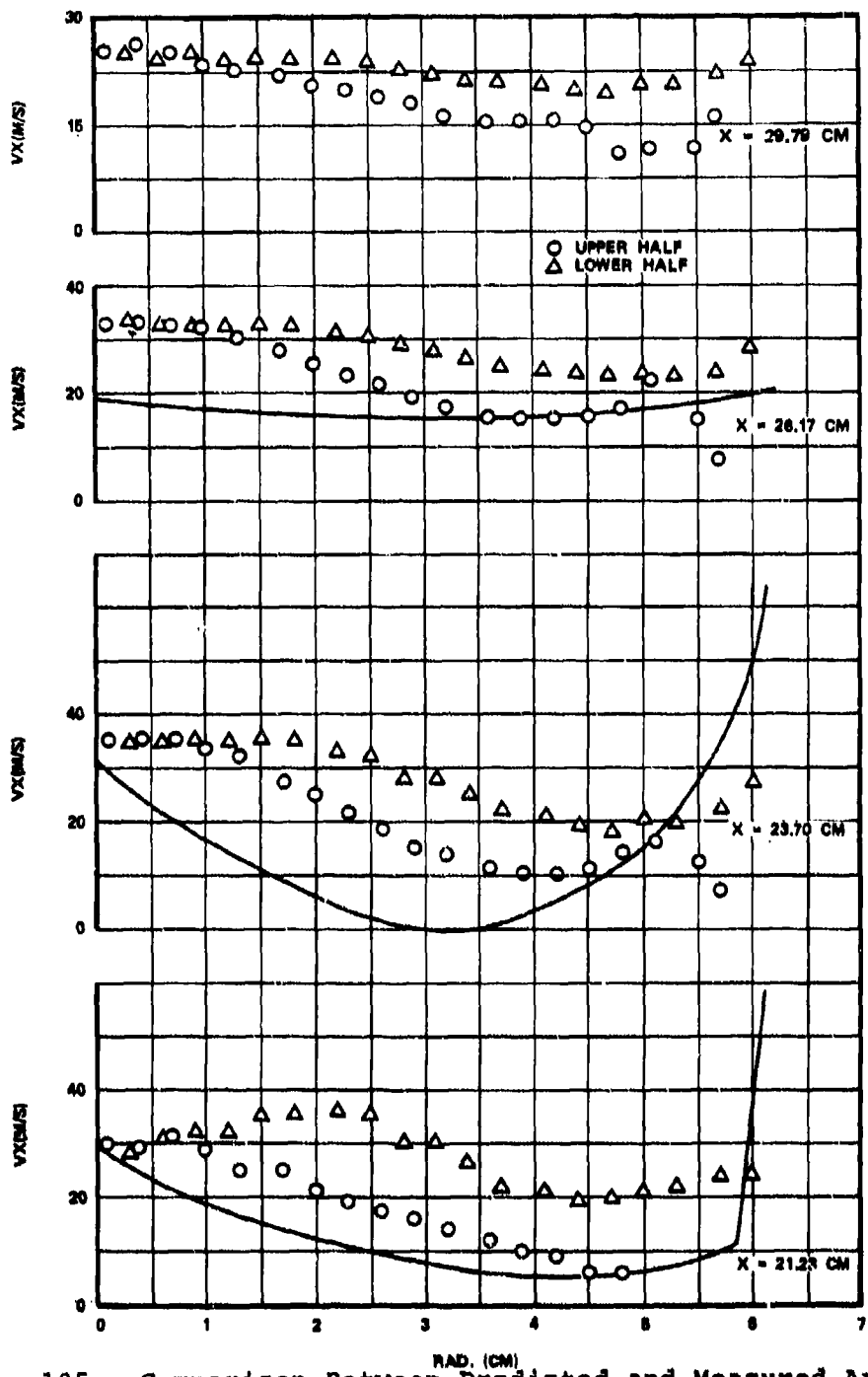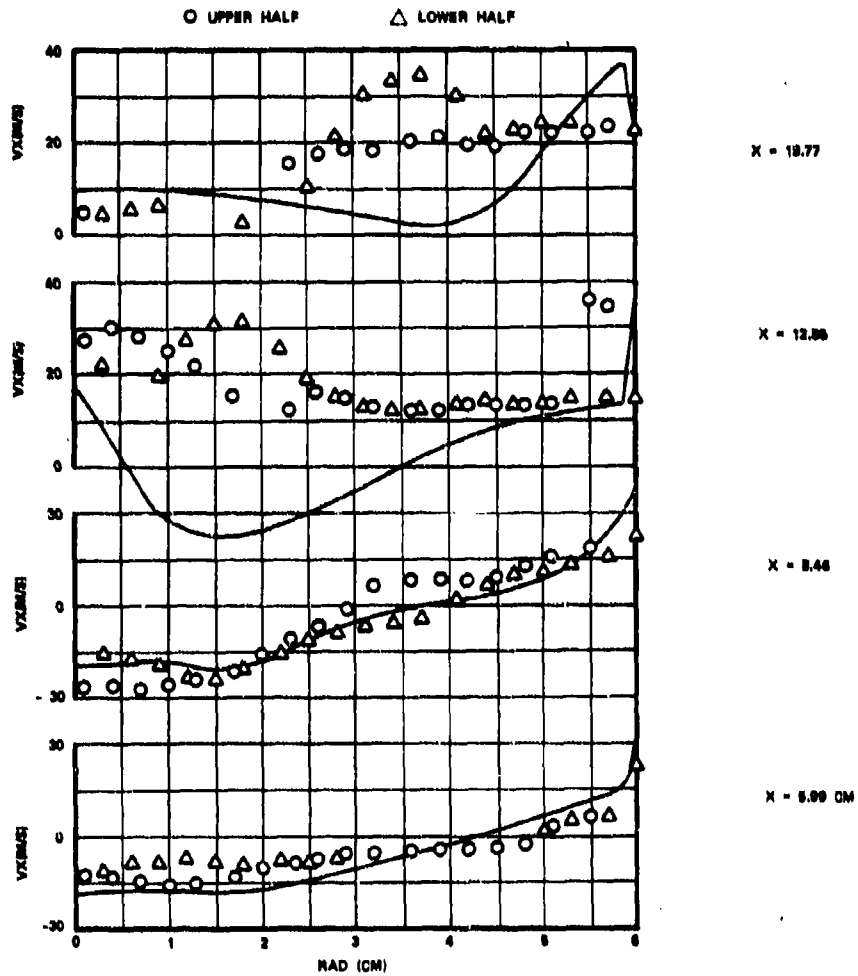
Figure 106. Comparison Between Predicted and Measured Axial Velocity Profiles in Different X-Y Planes In Between Primary Jet, Combustor Airflow Rate = 2.74 kg/s.(Sheet 1 of 2)

Figure 106. Comparison Between Predicted and Measured Axial
Velocity Profiles in Different X-Y Planes In
Between Primary Jet, Combustor Airflow Rate =
2.74 kg/s.(Sheet 2 of 2)

vane passages, its accuracy at low velocities was questionable. Figure 101 and 102 present the comparison for the lowest-airflow-rate case; i.e., 1.82 kg/s with the corresponding combustor reference velocity of 11.7 m/s. The predicted results were in reasonably good agreement with measurements in the high-velocity region, such as near the liner wall, close to the combustor dome at x = 5.99 cm for both x-y planes in line and in between the primary jets. In general, it can be said that the predictions are in qualitatively good agreement with measured axial-velocity profiles. A similar level of qualitative correlation was obtained for both radial and tangential velocity components. In order to further improve the flow model, it will be desirable to undertake internal velocity measurements of the can combustor by using a laser-Doppler velocimeter.

The 3-D elliptic program can provide detailed understanding of the combustor internal flow field, including turbulence properties. Figure 107 presents the predicted reverse-flow region for both isothermal and reacting flow fields. The cold-flow recirculation zone extends up to the dilution orifices, and encompasses two small positive-velocity regions located slightly downstream from the dome and near the can center (around x = 9 and 12 cm). With reacting flow, however, such as shown for Set-13 of Table 16, the recirculation extension beyond the primary orifice is quite small. The recirculation-zone volume was relatively unaffected by the reference velocity. On the other hand, the turbulence kinetic-energy profiles changed with the reference velocity. Figures 108 and 109 show predicted profiles of turbulence kinetic energy (k) at liner-pressure drops of 5 and 7.4 percent, respectively. The results are shown for the three x-y planes along θ = 0, 14, and 27.7 degrees; whereas the primary and dilution jets are located at θ = 30 degrees. The profiles of the θ = 0- and 14-degree planes are approximately similar, but the profiles for the plane close to the transverse jets are quite different. The transverse jets create a high turbulence region behind the jet, as well as along the radial

235
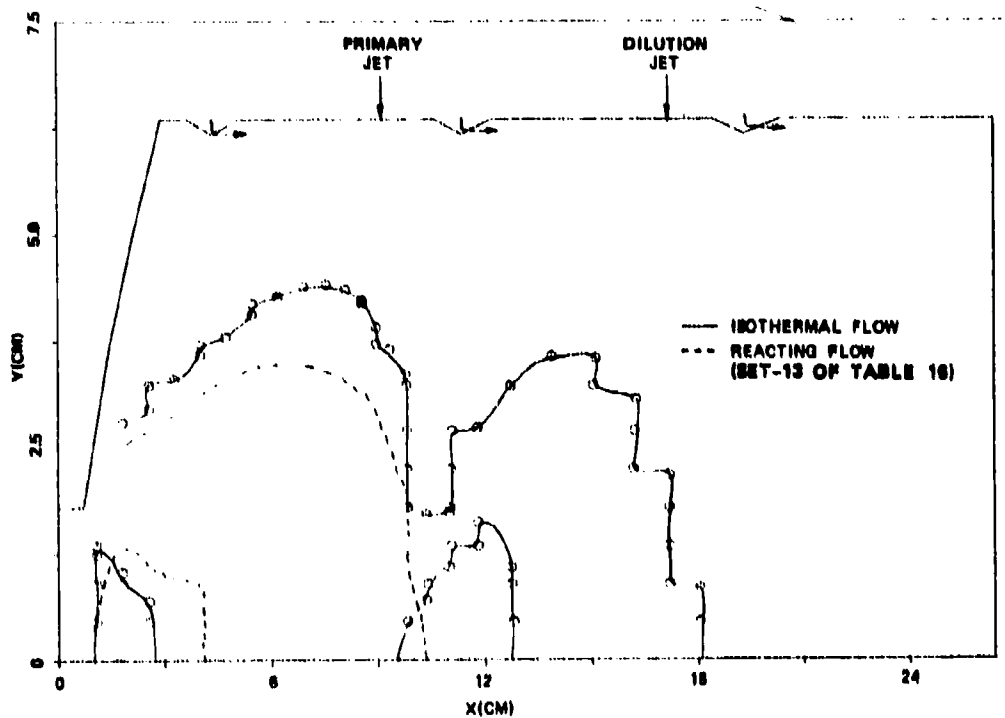
Figure 107. Predicted Reverse-Flow Region $(V_x < 0)$ With and Without Combustion for the Plane In Line With Primary Jet.

direction. Whereas the primary jet creates a maximum k value along the radial direction in the plane in line with the jet, the dilution jet creates more turbulence near $\theta = 14$ degrees. The level of k increases with an increase in liner-pressure drop, as inferred from Figures 108 and 109.

D. Can Combustor Reacting Flow Mapping.

The 3-D combustor-performance model was used to predict internal profiles of the can combustor, shown previously in Figure 52, to correlate emission data with natural gas and Jet-A fuel. The relevant combustor-flow conditions and parameters for emissions mapping were tabulated in Tables 15 and 16. A 60-degree sector of the combustor was divided into 32 x 16 x 14 finite-difference nodes along axial, radial, and circumferential directions, respectively. A number of computer runs were made to achieve an acceptable two-step reaction scheme that gives reasonably good comparison with measured data. The reaction rate for fuel is taken to be the minimum of the following three rate expressions:

$$R_{fu,ch} = K_1 \, \rho^n \, (m_{fu})^{n_1} \, (m_{H_2O})^{n_2} (m_{ox})^{n_3} e^{-E/RT} \tag{1}$$

$$R_{fu,Turb} = C_{R_1} \, \rho \, m_{fu} \, \frac{\epsilon}{k} \tag{2}$$

$$R_{fox,Turb} = C_{R_1} \, \rho \, \frac{m_{ox}}{i} \, \frac{\epsilon}{k} \tag{3}$$

Equation (1) represents the fuel oxidation rate as determined by chemical kinetics. The overall reaction order (n) is equal to $n_1 + n_2 + n_3$. The first computer run for natural gas was made with k_1, n, n_1, n_2 and E, as given by Williams, Hottel, and Morgan[24], expressed in S.I. units:

---

[24]Williams, G.C., H.C. Hottel, and A.C. Morgan, "The Combustion to Methane in a Jet-Mixed Reactor," Twelfth Symposium (International) on Combustion, The Combustion Institutes (1969).
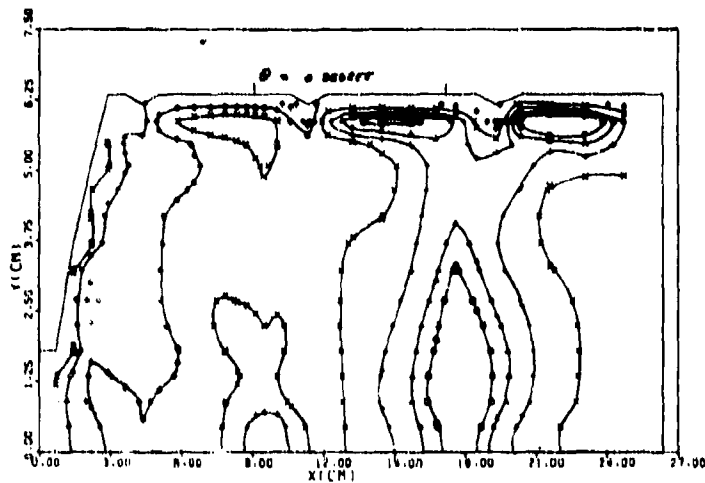
LEGEND

○ 0.875 k_{MAX}

△ 0.750 k_{MAX}

+ 0.625 k_{MAX}

× 0.500 k_{MAX}

◇ 0.375 k_{MAX}
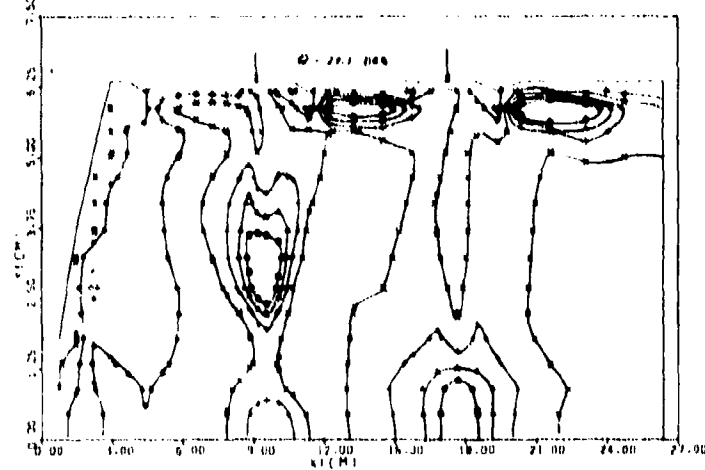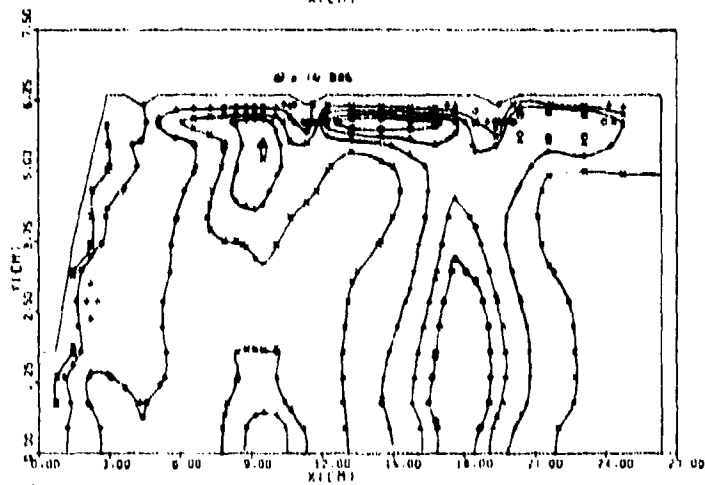
♦ 0.250 k_{MAX}

✗ 0.125 k_{MAX}

Figure 108.   Predicted Profiles of Turbulence Kinetic
Energy Combustor Liner Pressure Drop = 5%.
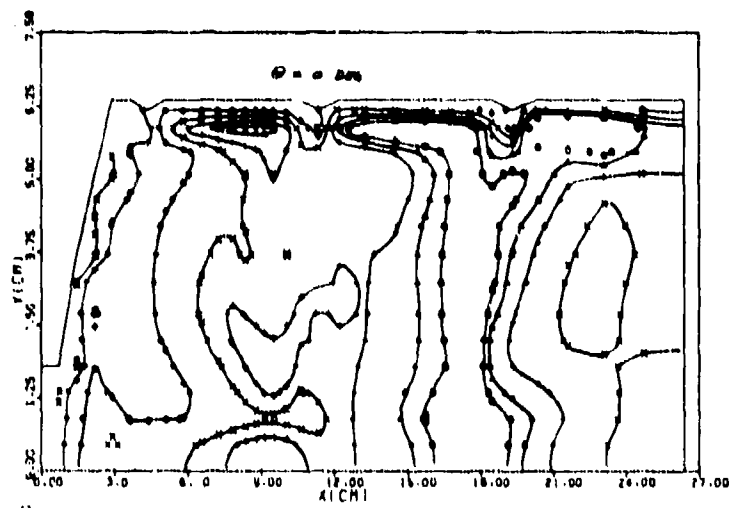
LEGEND
- ○ 0.875 k_{MAX}
- △ 0.750 k_{MAX}
- + 0.625 k_{MAX}
- × 0.500 k_{MAX}
- ◇ 0.375 k_{MAX}
- ⚐ 0.250 k_{MAX}
- ✕ 0.125 k_{MAX}
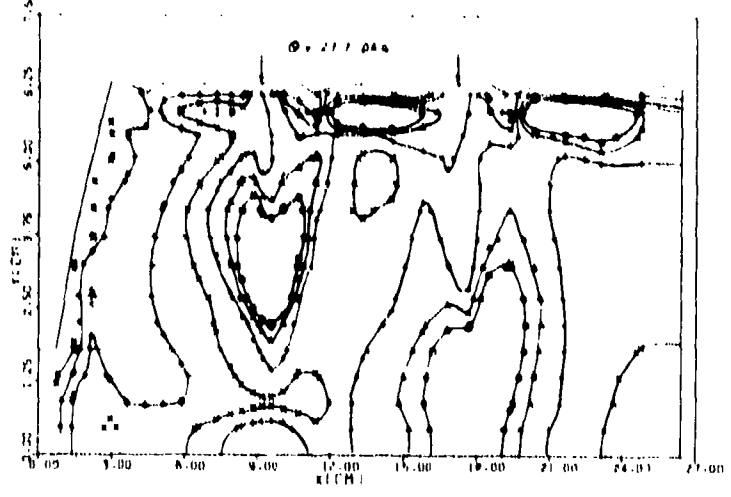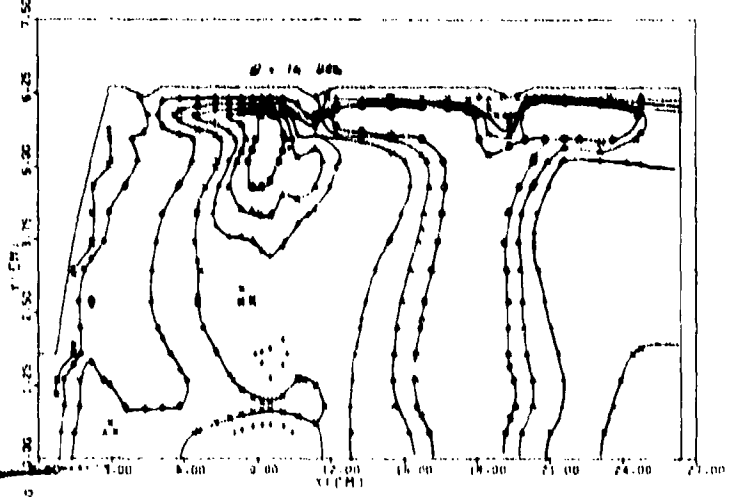
Figure 109.   Predicted Profiles of Turbulence
Kinetic Energy Combustor Liner Pressure
Drop = 7.4%.

$$R_{fu_{ch}} = 3.0 \times 10^{14} \rho^2 \, m_{fu} \, m_{ox}^{1/2} \, m_{H_2O}^{1/2} \, e^{\frac{28500}{T}}$$

Similarly, for CO oxidation, the following equation[26] was used:

$$R_{CO,ch} = 6.4 \times 10^8 \, \rho^2 \, m_{CO} \, m_{ox} \, e^{-\frac{12500}{T}} \tag{5}$$

The effect of turbulence on combustion was taken into account by using Equation 2 only with $C_{R1} = 1$. A similar expression was used to obtain $R_{CO,Turb}$. After a number of computer runs, the following set of equations was found to give reasonably good agreement with data for natural gas:

$$R_{fu,ch} = k_o \, \rho^{1.5} \, m_{fu}^{1/2} \, m_{ox} \, e^{-\frac{27000}{T}} \tag{6}$$

$$R_{fu,Turb} = 3 \, \rho \, m_{fu} \, \frac{\varepsilon}{k} \tag{7}$$

$$R_{fox,Turb} = 3 \, \rho \, \frac{m_{ox}}{i_1} \, \frac{\varepsilon}{k} \tag{8}$$

$$R_{CO,ch} = 6.0 \times 10^8 \, \rho^2 \, m_{CO} \, m_{ox} \, e^{-\frac{12500}{T}} \tag{9}$$

$$R_{CO,Turb} = 4 \, \rho \, m_{CO} \, \frac{\varepsilon}{k} \tag{10}$$

$$R_{CC_{ox},Turb} = 4 \, \rho \, \frac{m_{CO}}{i_2} \, \frac{\varepsilon}{k} \tag{11}$$

where i_1 and i_2 are stoichiometric oxygen-to-fuel and oxygen-to-CO ratios for the two-step scheme. The i_1 for natural gas and Jet-A fuels is 2.93 and 2.26, respectively. The corresponding values of k_o were 2.0×10^{16} and 3.3×10^{14}. The stoichiometric oxygen-to-CO ratio is 0.57.

Figure 110 presents a comparison between predicted and measured profiles of unburned fuel (HC) for the x-y plane lying in between the primary/dilution jets (refer to Figure 52 for combustor geometrical details). The x-y planes in between the primary jet have been arbitrarily denoted by θ = 0 degrees, thus making the θ location of the plane in line with the jet equal to 30 degrees. The results discussed in Figures 110 through 124 are for Set-2 of Table 15 with the natural gas burning at 2.0 atmospheres, with a combustor inlet temperature and pressure drop of 369 K and 3.28 percent, respectively. It may be recalled that the primary and dilution orifices are located at 9.09 and 17.21 cm from the nozzle face, respectively. The predicted recirculation zone extended up to approximately x = 9.75 cm. Consequently, the first two stations presented in Figure 92, i.e., x = 6.0 and 8.5 cm, are expected to contain the regions of reverse flow. The next three stations, x = 10, 13, and 15, lie in the intermediate zone between the primary and secondary orifices; whereas the last two stations are in the dilution zone.

Figure 111, like Figure 110, shows a comparison between measured and predicted HC for the x-y planes along θ = 15 degrees. The radial profiles for the first four axial stations are similar for both θ = 0- and 15-degree planes, indicating approximately a two-dimensional flow field with little variation along the circumferential direction. This, however, does not imply that a 2-D elliptic program could be used for analyzing practical combustor geometry (such as shown in Figure 52), because such an approximation would not give backflow created by strong primary jets. The profiles for the x-y plane (θ = 30 degrees) in line with the primary jet, as shown in Figure 112 are significantly different from those of the θ = 0- and 15-degree planes. The profiles for the last three stations; i.e., x = 15, 19, and 21 cm, for both θ = 0- and 15-degree planes are slightly different.
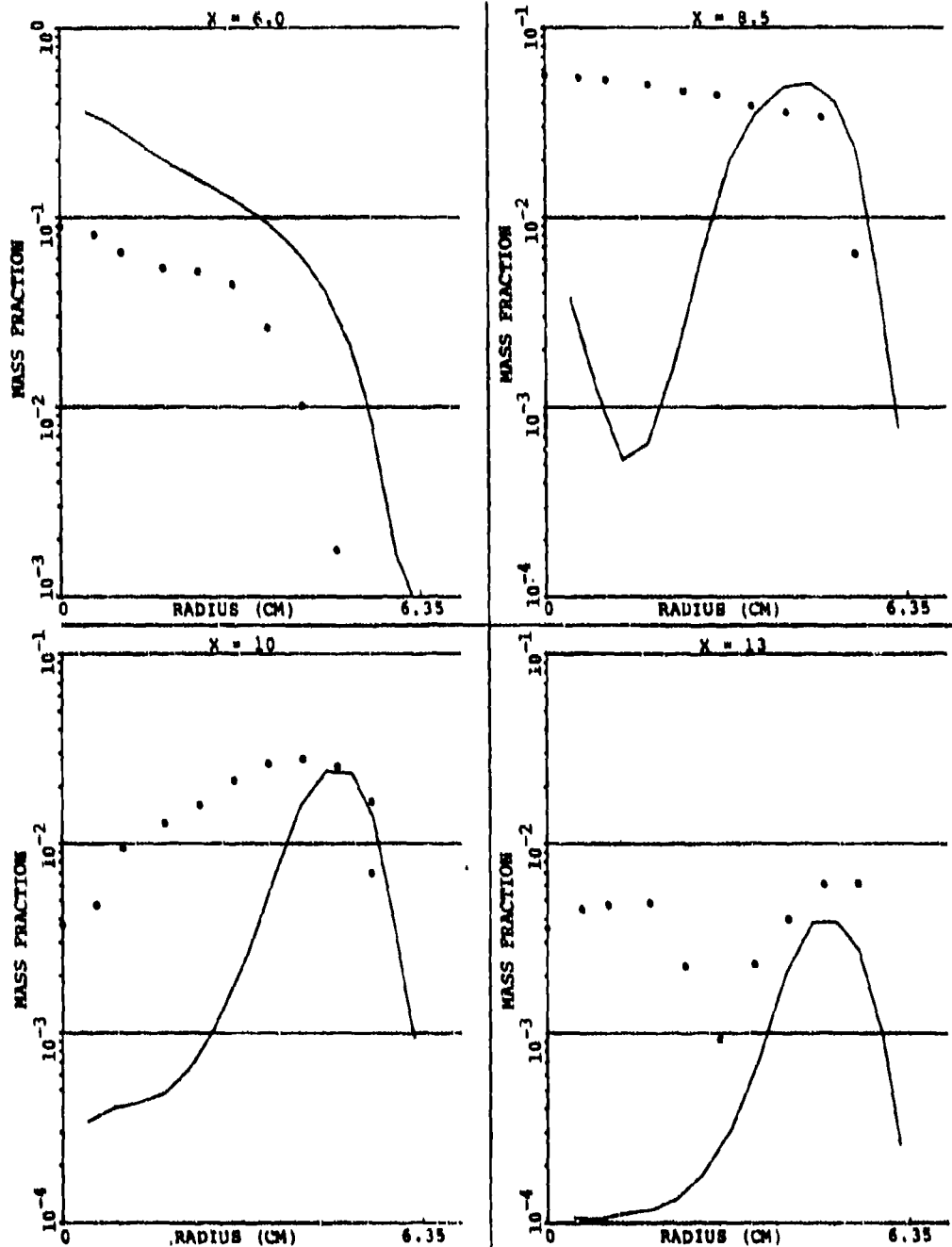
241

Figure 110. Comparison Between Predicted and Measured Unburned
Fuel at Different X-Y Planes (θ = 15°) In Between
Primary Jets (θ = 30°) for Set-2, Table 15.
(Sheet 1 of 2)
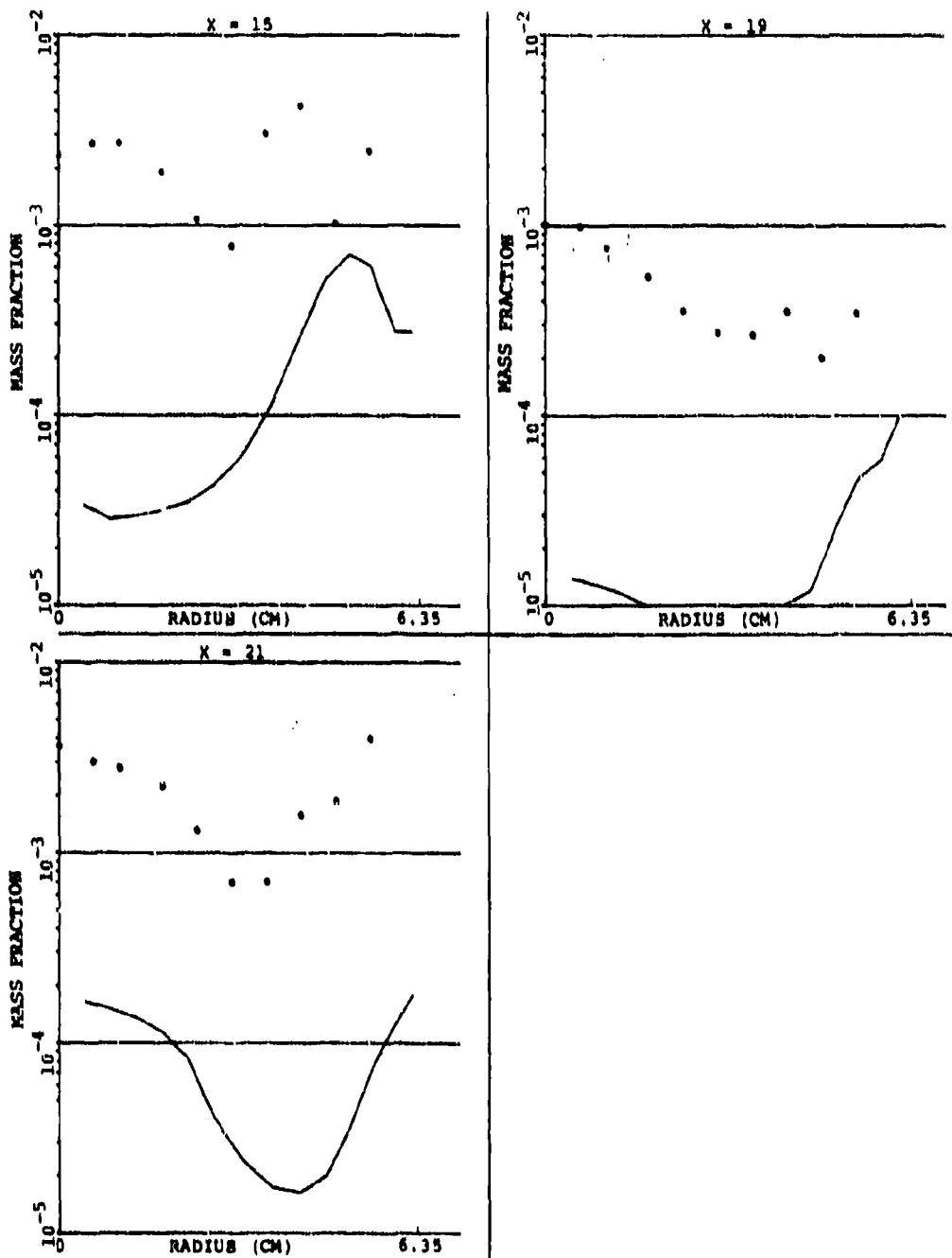
Figure 110.   Comparison Between Predicted and Measured Unburned
Fuel at Different X-Y Planes ($\theta = 0°$) In Between
Primary Jet ($\theta = 30°$) for Set-2, Table 15.
(Sheet 2 of 2)

243
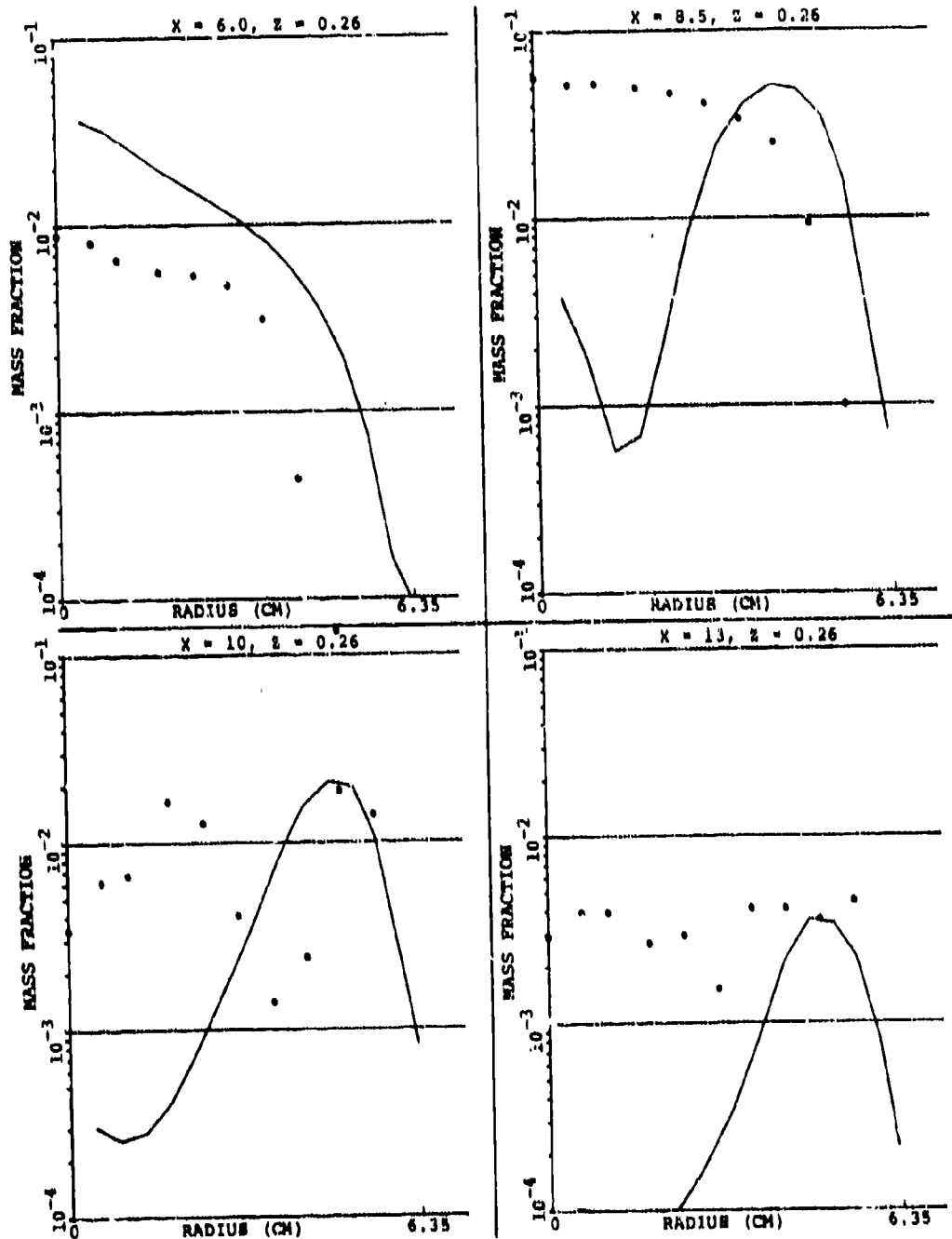
Figure 111. Comparison Between Predicted and Measured Unburned
Fuel At Different X-Y Planes ($\theta = 15°$) (As Compared
to the Primary Jet Located at $\theta = 30°$) for Set-2,
Table 15. (Sheet 1 of 2)
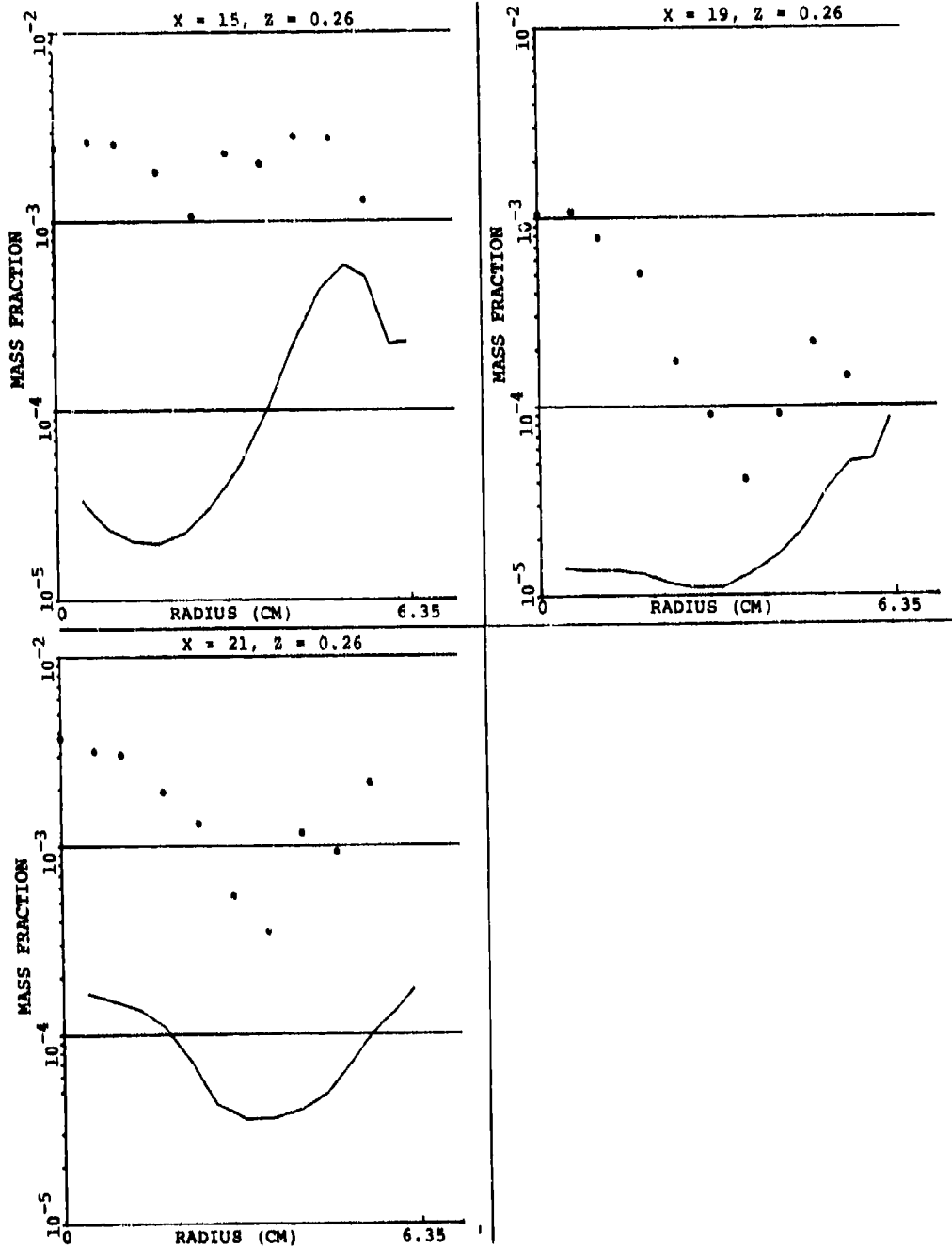
Figure 111. Comparison Between Predicted and Measured Unburned Fuel At Different X-Y Planes ($\theta = 15°$) (As Compared to the Primary Jet Located at $\theta = 30°$) for Set-2, Table 15. (Sheet 2 of 2)

Figure 112 gives a comparison between measured and predicted HC for the x-y plane in line with the primary and dilution jets. The measurement errors for this plane were expected to be quite large, compared to the θ = 0- and 15-degree planes because of: first, large transverse flow induced by radial jets; and second, blockage introduced by the probe in allowing the primary jet air to go upstream. The quality of correlation and shape of the profiles for the first two stations of the θ = 30-degree plane are comparable to those of the θ = 0-degree plane. However, t x = 10 cm, due to the presence of the primary jet, the peak is around Y = 2 cm for the in-line plane (θ = 30 degrees), compared to the θ = 0-degree plane where the peak is closer to the liner wall. Slightly downstream, at x = 13 cm, the profiles are similar for both planes, although the peak is about an order of magnitude smaller for the plane in line with the jet. A similar trend is observed at x = 15 cm.

Significant measurement errors are introduced by the physical presence of the emission probe in a recirculating flow field. In order to estimate the measurement errors, the 3-D model was run for Set-2 with the emission probe placed in line with the primary jet at x = 8.5 cm. Figure 113 compares predicted profiles of fuel/air ratio, unburned fuel, CO, and axial velocity component with and without the blockage introduced by the emission probe. Also shown in Figure 113 are measured values. The presence of the probe stops the primary jet air from going toward the dome, with the attendant absence of the reverse-flow region near the combustor center, as shown. Consequently, with probe blockage, significantly higher levels of total fuel are predicted near the combustor center, as compared to the results without blockage. The reverse is true near the liner wall. A difference of up to an order of magnitude in predicted fuel/air ratio exists between results with and without probe blockage, thereby making it difficult to verify the model within the primary zone.
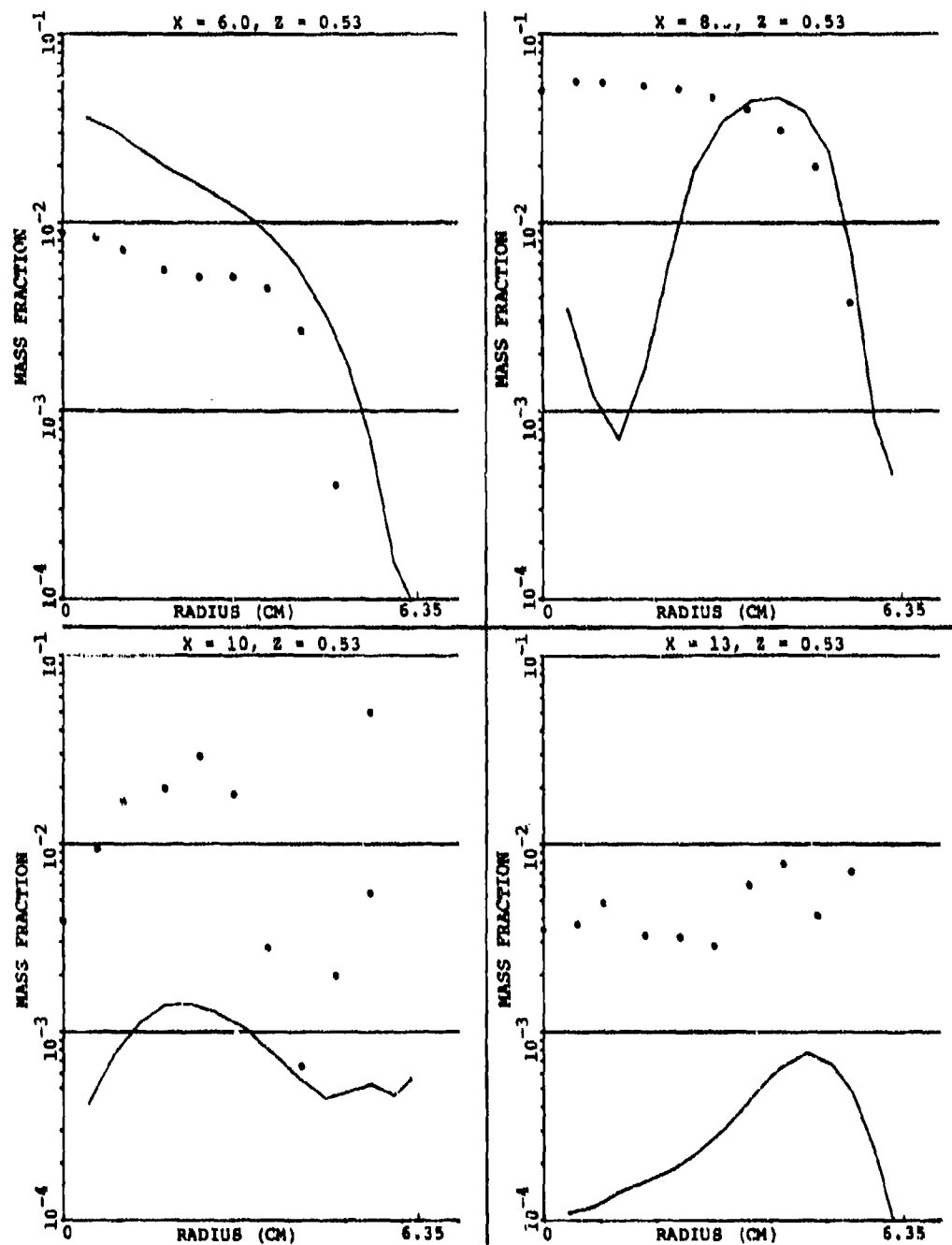
Figure 112.   Comparison Between Predicted and Measured Unburned
Fuel at Different X-Y Planes In Line With the Primary
Jet (θ = 30°) for Set-2, Table 15 (Sheet 1 of 2).
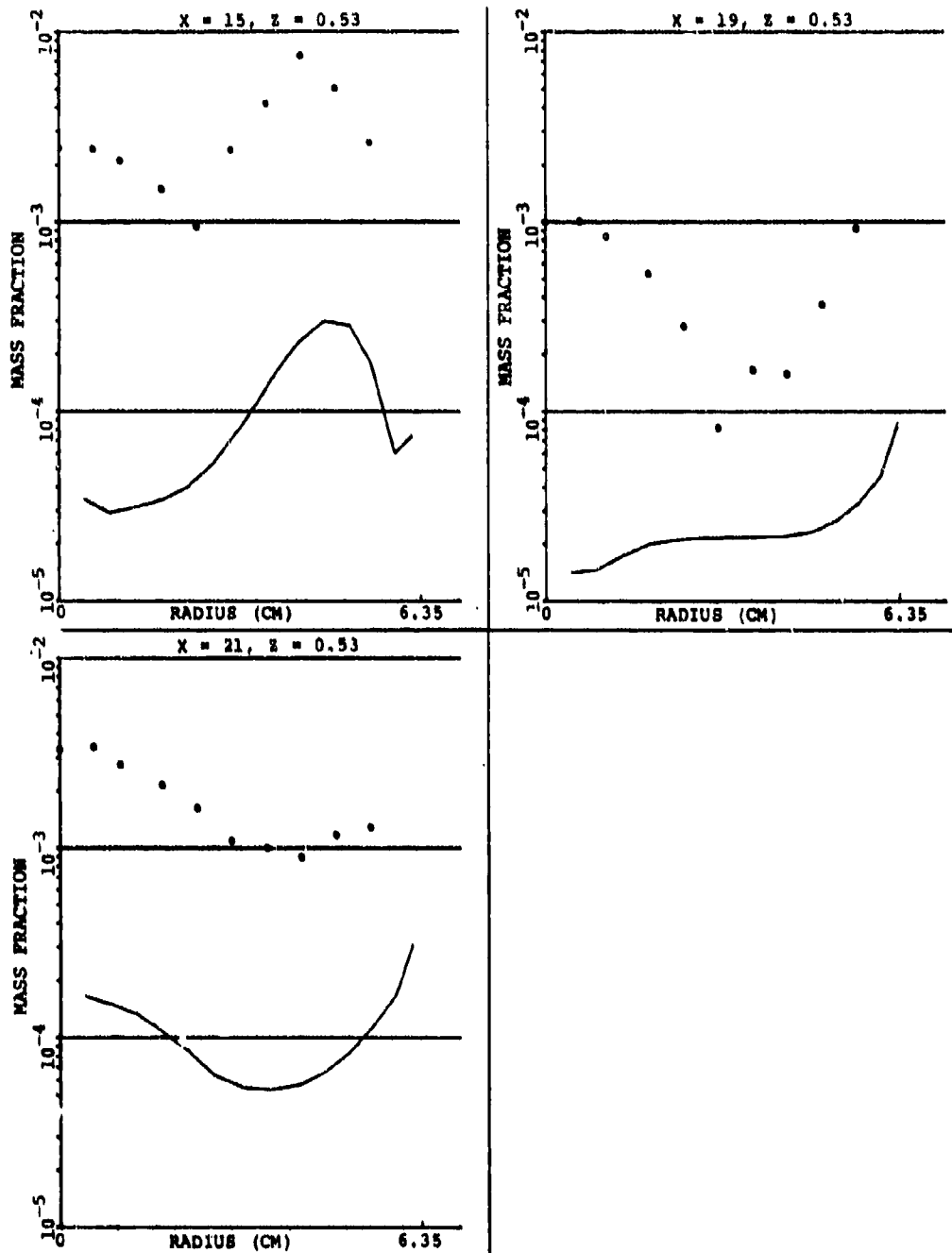
Figure 112. Comparison Between Predicted and Measured Unburned Fuel at Different X-Y Planes in Line With the Primary Jet ($\theta = 30°$) for Set-2, Table 15 (Sheet 2 of 2).
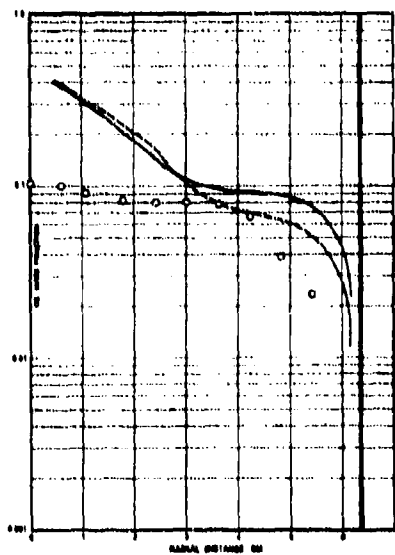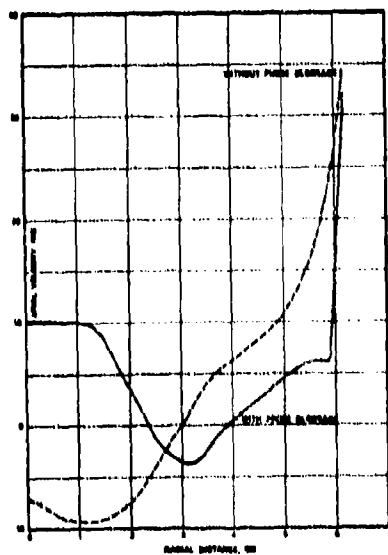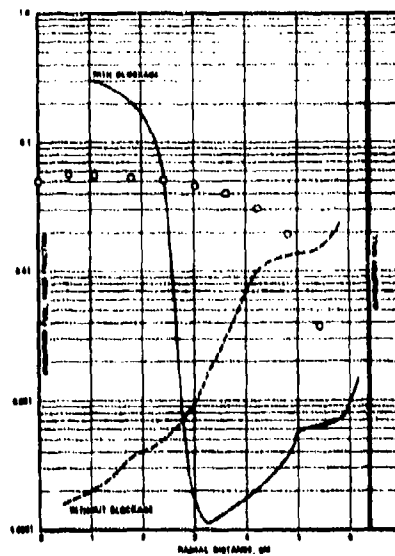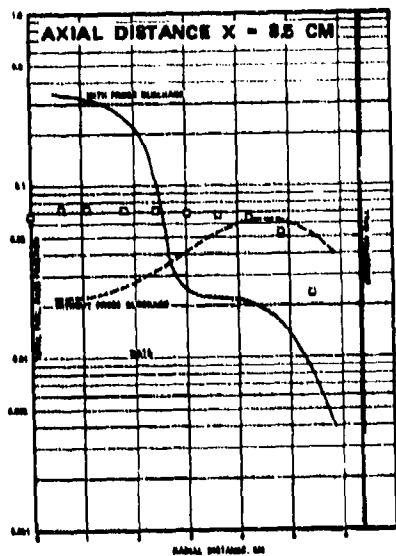
Figure 113.   Comparison Between Measurements and Predictions With
and Without Probe Blockage for the X-Y Plane in Line
With the Primary Jet for Set-2, Table 15.

The effect of probe blockage on predicted HC profiles is even more pronounced, as shown in Figure 113. The upstream flow induced by the primary jet, without the physical presence of the probe, reduces the HC concentration near the center by three orders of magnitude, compared to what one obtains with the blockage. However, a relatively small effect is felt on the CO profiles.

At x = 6 cm, the radial profiles of predicted and measured HC are qualitatively similar. The model underpredicts the fuel oxidation rate over the entire combustor radius. Further downstream at x = 8.5 cm, i.e., 0.6 cm upstream from the center of the primary orifices, the predictions for the center half of the can combustor do not agree qualitatively with the data, although the agreement for the region beyond Y = 3 cm is quite good. The model predicts two regions of minimum HC at approximately Y = 1.5 cm and close to the liner wall. Since the fuel nozzle (Figure 72) axially injects the gaseous fuel near the combustor centerline, a maximum level of HC is expected to be near the can center, such as shown for x = 6 cm, until the upstream flow from the primary jet displaces it toward the liner wall for the x-y plane in between the primary jet. Consequently, it appears that predictions for x = 9.5 cm appear to be more plausible than the measurements, as shown.

At x = 10 cm, i.e., approximately 1 cm downstream from the primary jet, the radial profiles of predicted and measured HC are again in qualitatively good agreement, although the model now overpredicts the fuel-oxidation rate for the region close to the center. The predicted HC is lower than the measured values by up to a factor of ten. At x = 13 cm, i.e., 4.21 cm upstream from the dilution jet, predictions agree reasonably well for the outer half-radius of the combustor. Whereas predictions show similarity of the radial profiles at x = 10 and 13 cm, with a continual oxidation of fuel over the combustor height, measurements show the freezing of the reaction near the combustor

250

center. Due to the impinging primary jets, the combustor center
is expected to have high turbulence with its attendant increase
in the fuel-oxidation rate; and one is at a loss to explain a
sudden loss in reactivity near the center, as inferred from the
data at x = 13 cm. It therefore appears that the data at both
the x = 13 and 15 cm locations must have considerable measure-
ment errors due to the physical presence of the probe. Neverthe-
less, it appears that the model is underpredicting HC in this
region, as well as for the dilution zone, by two-orders of
magnitude.

In the dilution zone at x = 19 and 21 cm, the predicted
profiles are in qualitative agreement with the data. Although
predicted values are lower than measurements by up to two orders
of magnitude, the absolute values are too small to cause signi-
ficant errors in the computed combustion efficiency (as shown
later in Figure 120).

Figure 114 presents a comparison between predicted and
measured profiles of CO for the planes in between the primary
and dilution jets for Set-2 of Table 15. The corresponding HC
profiles were previously presented in Figure 110. Relatively
flat profiles of CO were measured for the first four axial
stations in contrast to those of HC. The model overpredicts CO
in the region up to x = 13 cm; further downstream the model
underpredicts the data. At x = 6 cm, the location of the peak
is determined by the rate of fuel oxidation, and diminution of
CO by cooling air and CO oxidation rate. At x = 8.5 cm, the
profiles of CO and HC are quite similar. The quenching of CO
near the combustor center is due to the radial jet penetration
for the region downstream from x = 13 cm.

Like HC predictions, the radial profiles for the first two
stations along the θ = 0- and 15-degree planes are similar, as
shown in Figures 115 and 116, indicating again a 2-D flow field
for this region. Minor variations along the θ direction exist
at x = 10 and 13 cm. However, significant variation in the
profiles (up to a factor of 3) exists for the last three stations
of the θ = 0- and 15-degree planes, as shown. Figure 116 shows
the corresponding profiles of CO for the x-y plane in line with
the primary jet.

Figures 117, 118, and 119 present predicted and measured
fuel/air-ratio profiles for the x-y planes along θ = 0, 15, and
30 degrees, respectively. At x = 6 cm there was qualitatively
good agreement between predictions and data. However, the model
predicted an extremely rich fuel region near the center. This
discrepancy between the model and data can be partly explained
as follows. It was assumed that the fuel was exiting the nozzle
as an axial jet with velocity computed from the nozzle-pressure
drop; which in the case of Set-2, the initial fuel jet velocity
was estimated to be 57.9 m/s. Consequently, the fuel jet estab-
lished a positive axial velocity field near the center that
extended up to x = 7.5 cm. The length of this region could be
reduced by either decreasing the fuel jet initial velocity, or
by imparting some radial velocity component to the fuel jet.
Neither of these were attempted as it is well known that it is
possible to improve model correlation by changing boundary condi-
tions. Since boundary conditions such as these are not properly
known in practical combustors, the view taken was that one
should not generally expect good correlation near the nozzle
boundaries.

The poor comparison achieved from the x = 0.5 cm location
was due to measurement errors caused by the perturbing emission
probe, as previously discussed in Figure 113, especially for
the planes θ = 15 and 30 degrees. The error is expected to be
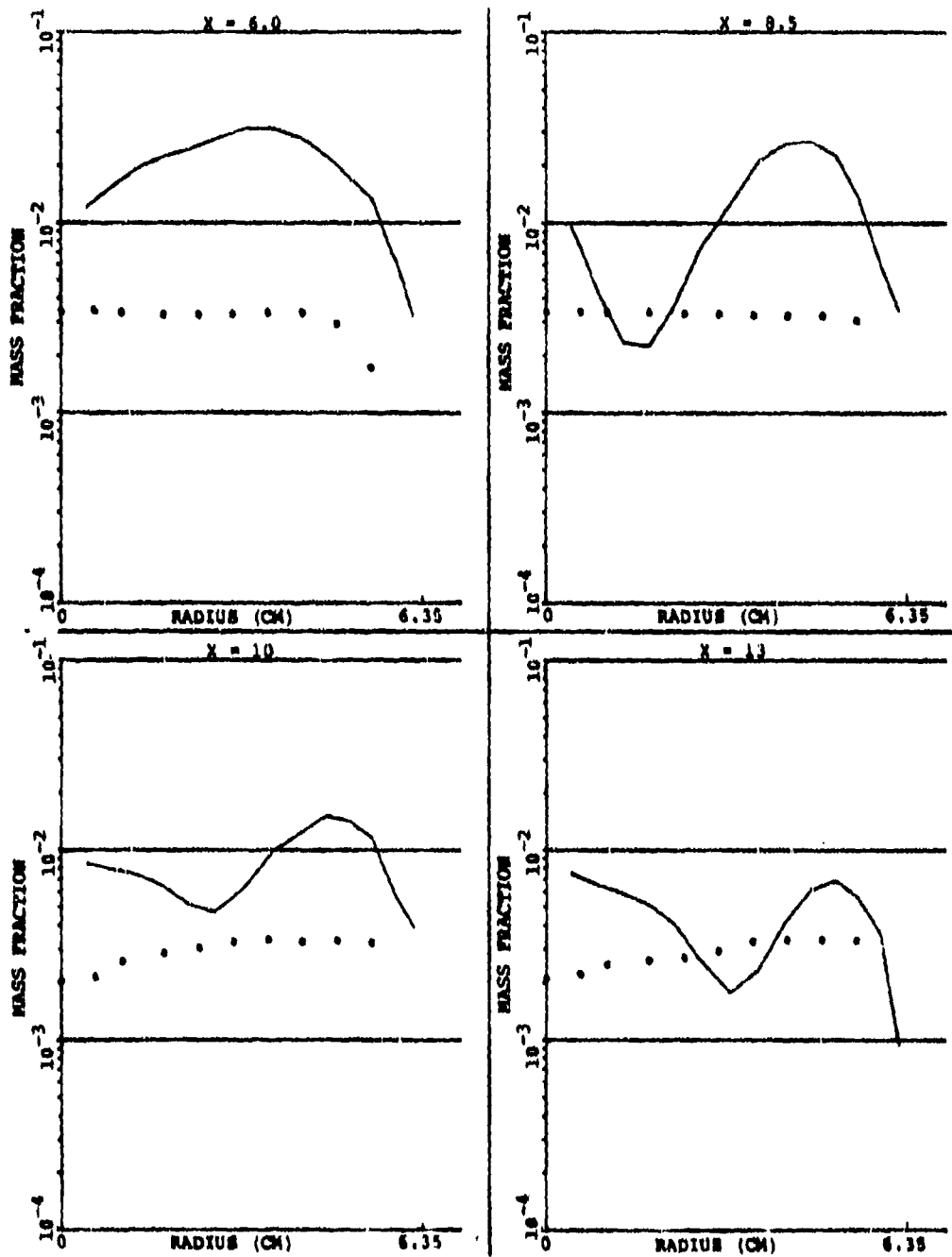
252

Figure 114. Comparison Between Predicted and Measured Profiles
of CO at Different X-Y Planes ($\theta = 0°$) In Between
the Primary Jet ($\theta = 30°$) for Set-2, Table 15
(Sheet 1 of 2).

253
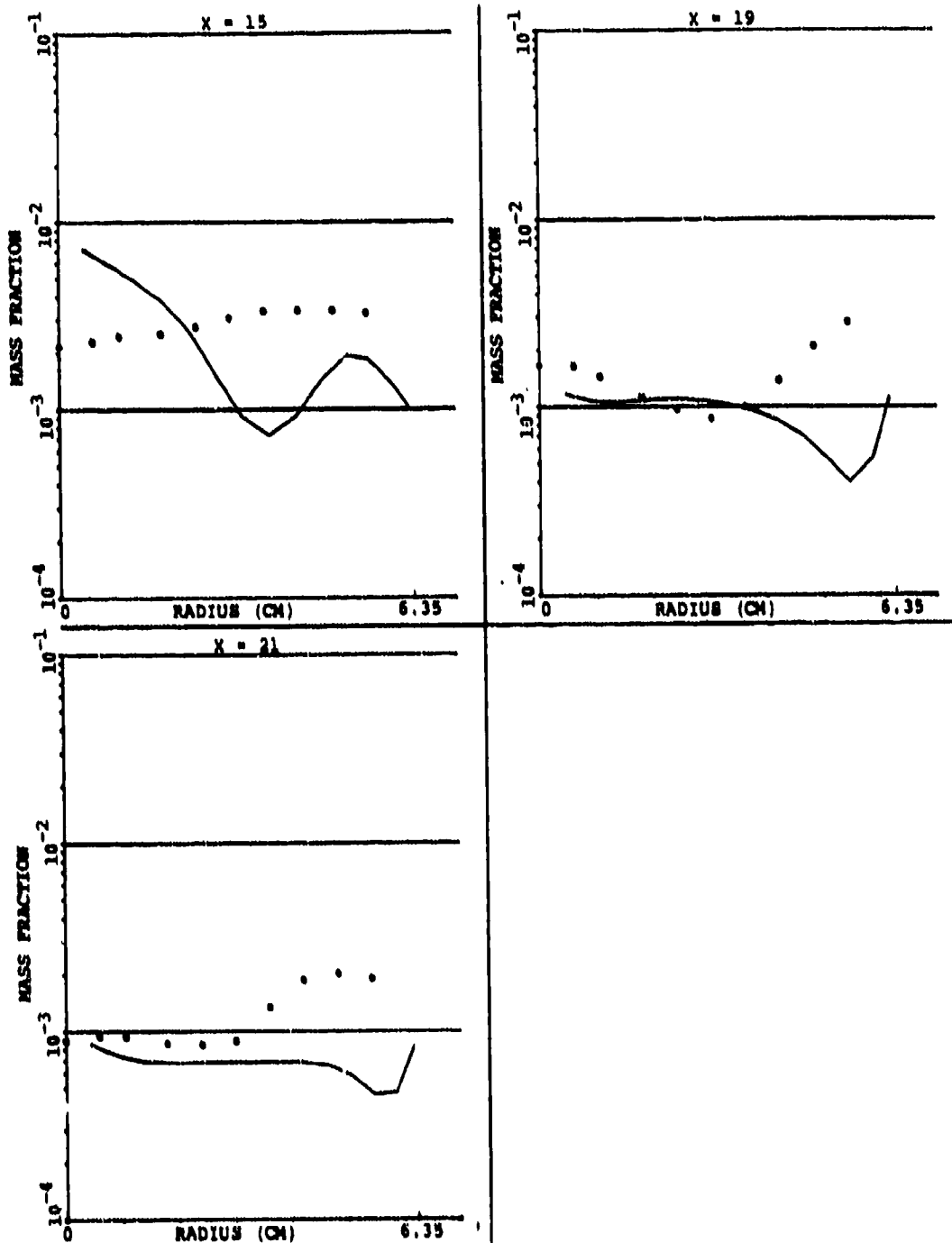
Figure 114. Comparison Between Predicted and Measured Profiles
of CO at Different X-Y Planes ($\theta = 0°$) In Between
the Primary Jet ($\theta = 30°$) for Set-2, Table 15
(Sheet 2 of 2)

Figure 115. Comparison Between Predicted and Measured CO at Different X-Y Planes (θ = 15°) for Set-2, Table 15 (Sheet 1 of 2).
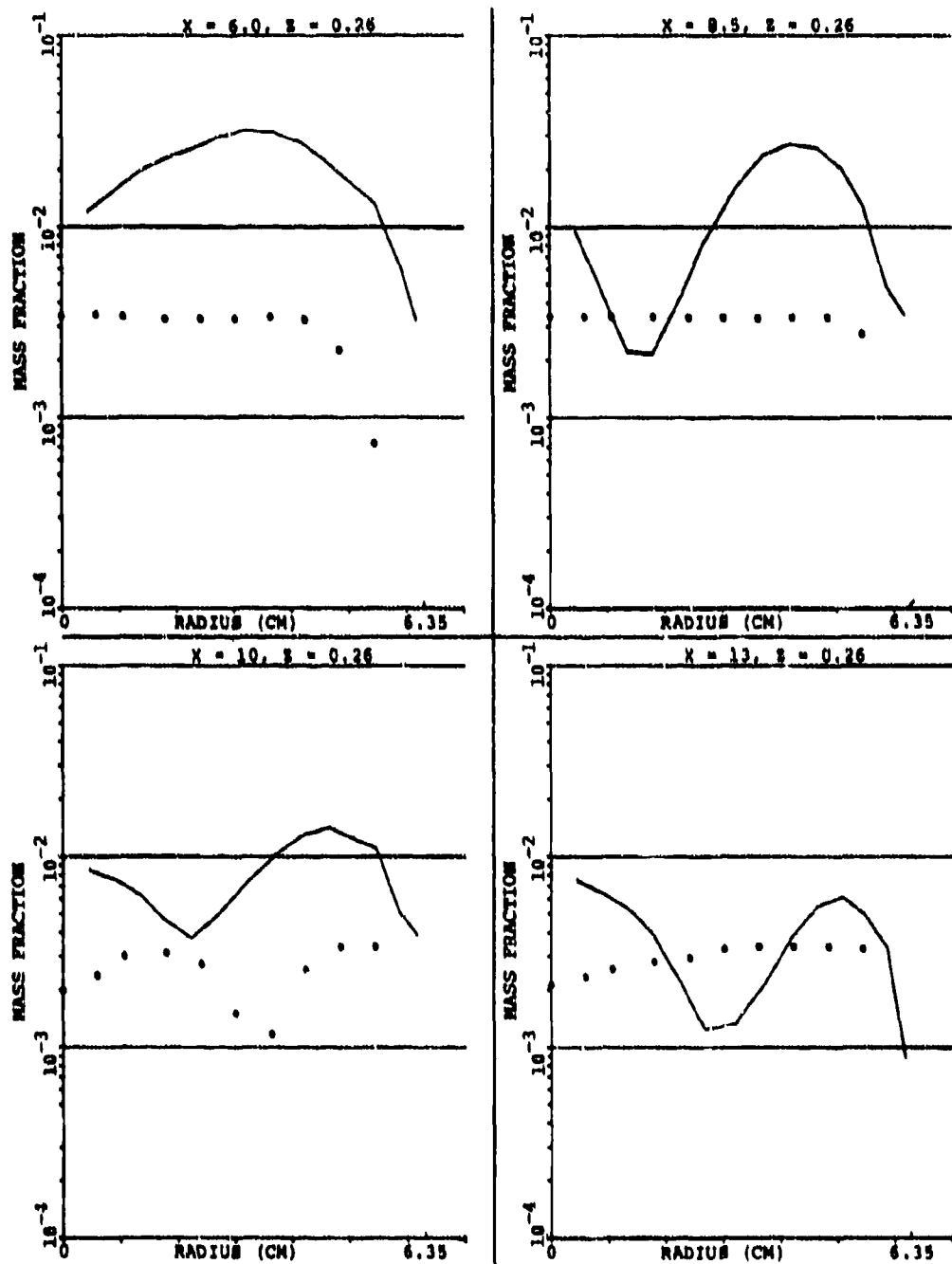
Figure 115.   Comparison Between Predicted and Measured CO at
Different X-Y Planes ($\theta = 15°$) for Set-2, Table 15
(Sheet 2 of 2).

256
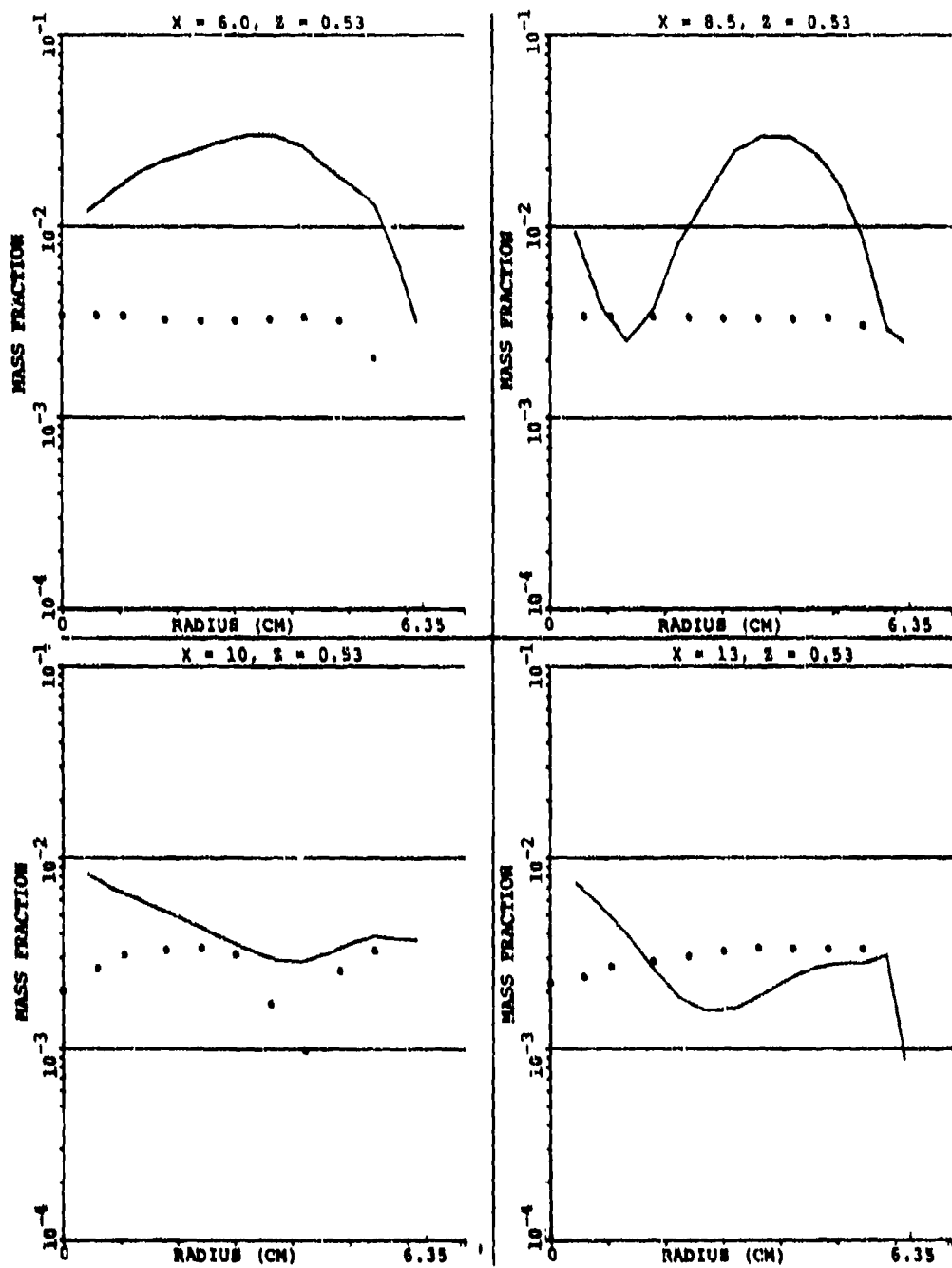
Figure 116. Comparison Between Predicted and Measured CO at
Different X-Y Planes ($\theta = 30°$) for Set-2, Table 15
(Sheet 1 of 2).

Figure 116. Comparison Between Predicted and Measured CO at
Different X-Y Planes (θ = 30°) In Line With the
Primary Jet (θ = 30°) for Set-5, Table 15
(Sheet 2 of 2).
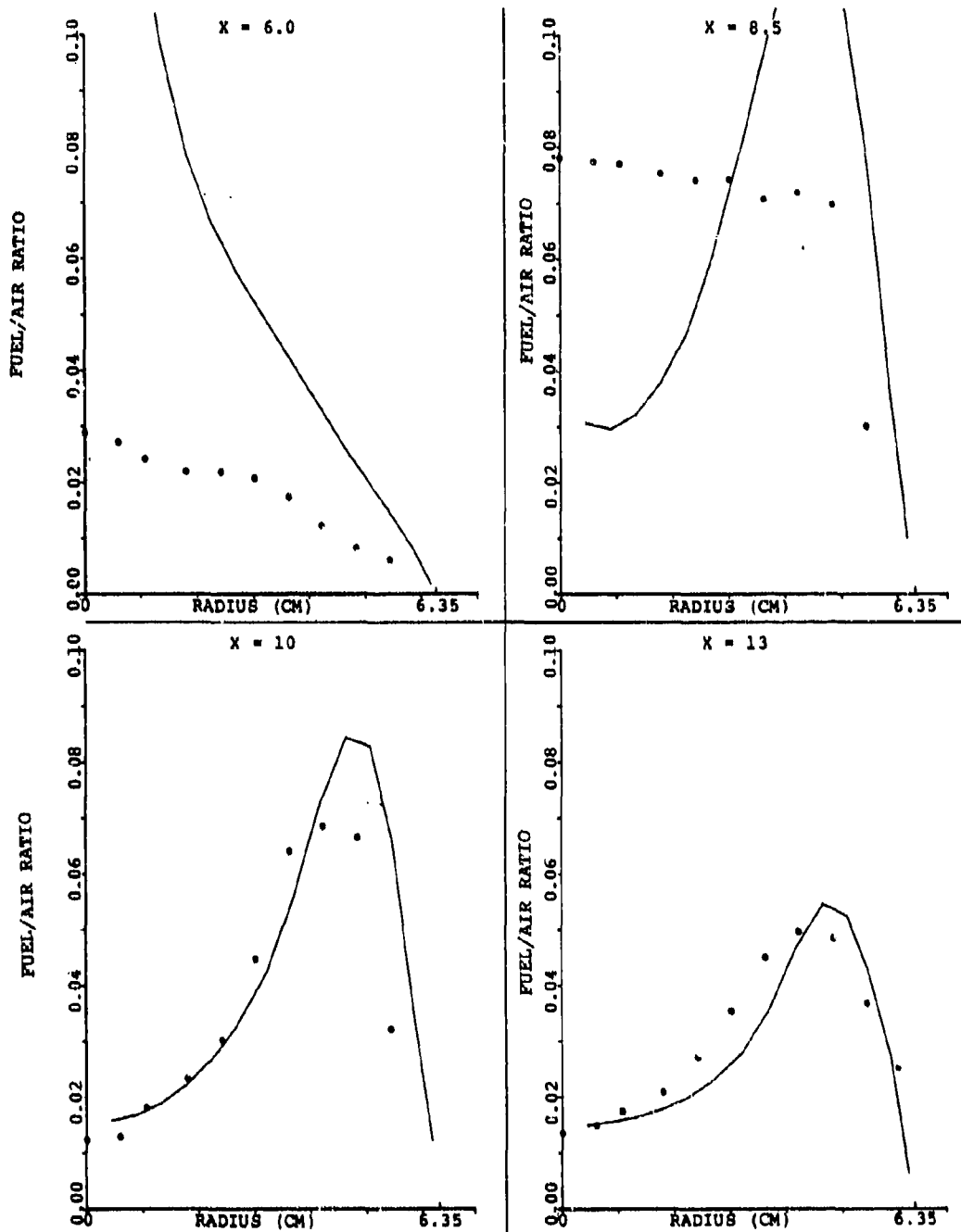
Figure 117.   Comparison Between Predicted and Measured Profiles
of Fuel/Air Ratio Along θ = 0° for Set-2, Table 15
(Sheet 1 of 2).

259
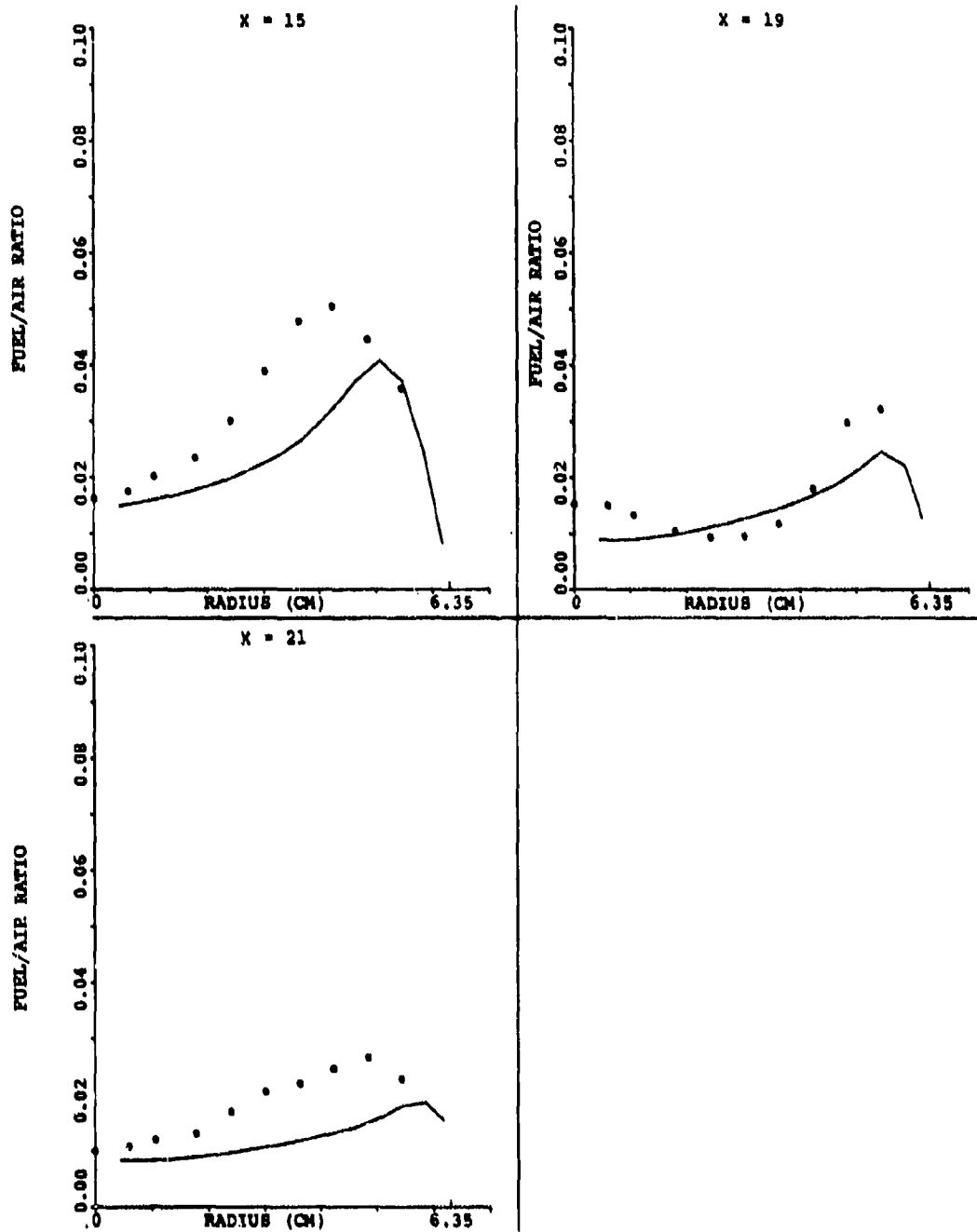
Figure 117. Comparison Between Predicted and Measured Profiles of Fuel/Air Ratio Along θ = 0° for Set-2, Table 15 (Sheet 2 of 2).

Figure 118. Comparison Between Predicted and Measured
Profiles of Fuel/Air Ratio Along θ = 15° for
Set-2, Table 15 (Sheet 1 of 2).

261
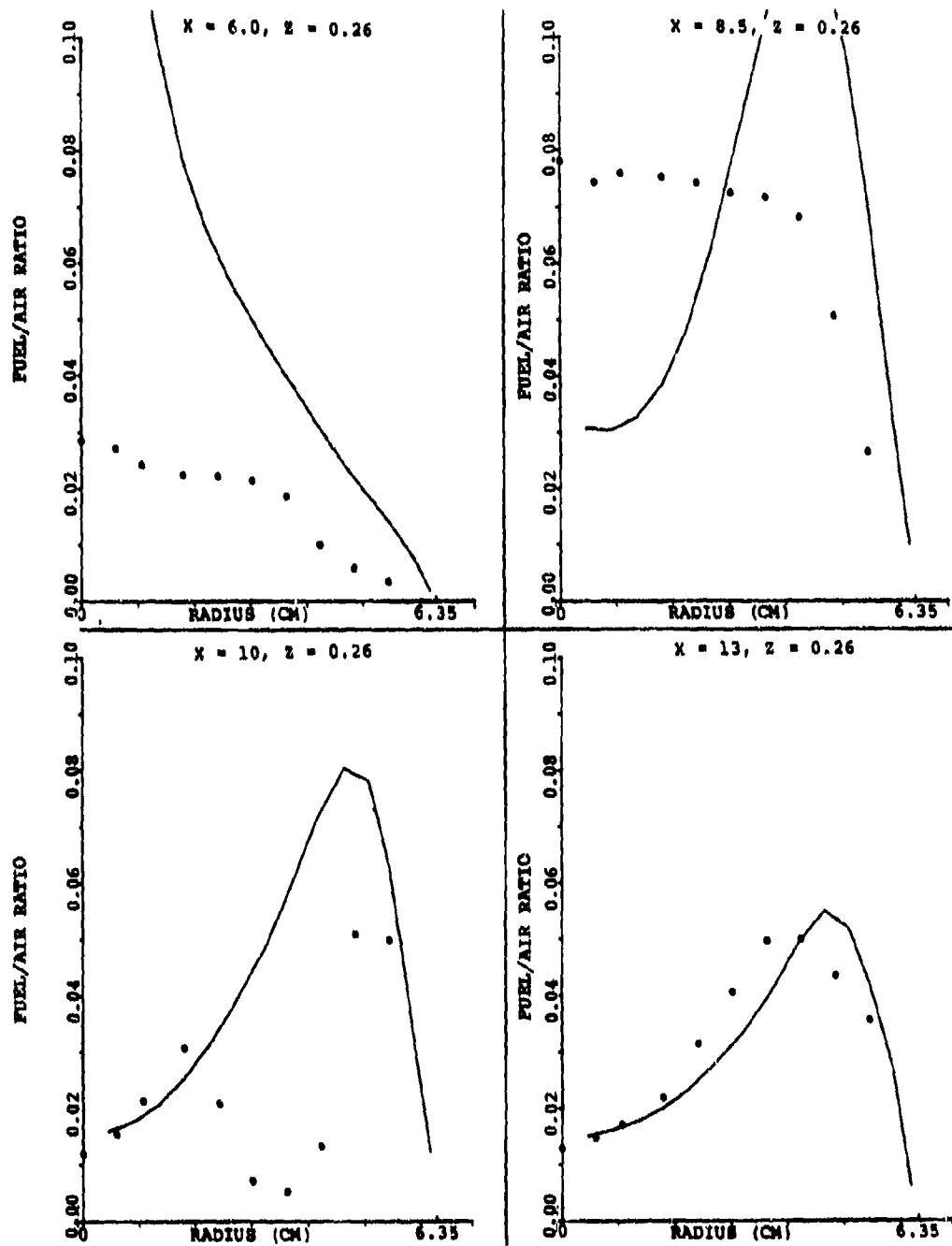
Figure 118. Comparison Between Predicted and Measured
Profiles of Fuel/Air Ratio Along $\theta = 15°$
for Set-2, Table 15 (Sheet 2 of 2).

Figure 119. Comparison Between Predicted and Measured
Profiles of Fuel/Air Ratio Along θ = 30°
for Set-2, Table 15 (Sheet 1 of 2).

263
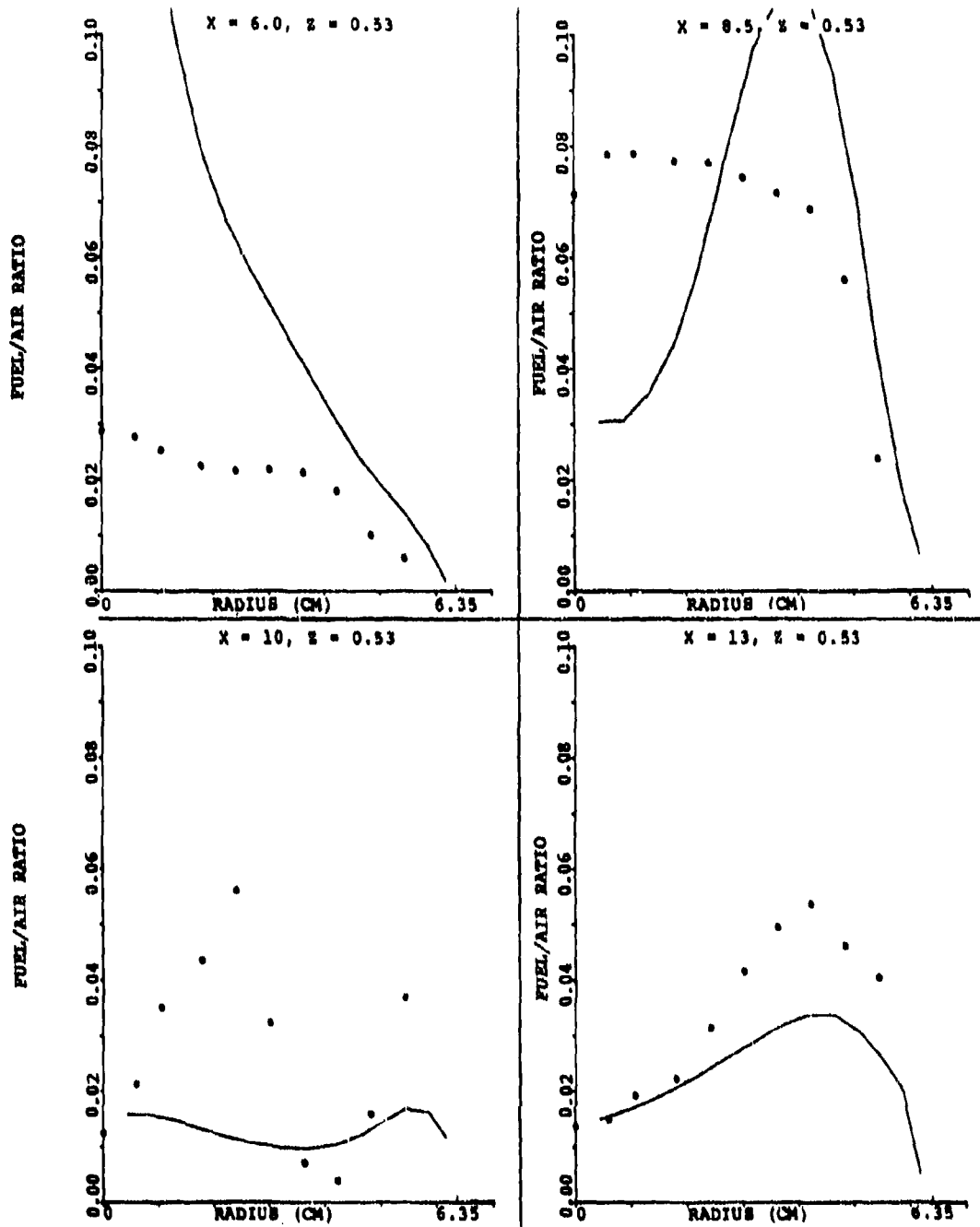
Figure 119. Comparison Between Predicted and Measured Profiles of Fuel/Air Ratio Along $\theta = 30°$ for Set-2, Table 15 (Sheet 2 of 2).

least for the x-y plane in between the primary and dilution jets, and other planes lying further away from the radial orifices. It can be seen that for the θ = 0-degree plane (Figure 117), good agreement between predictions and data was obtained for x = 10, 13, 15, 19, and 21 cm. On the other hand, reasonably good correlation was achieved for the θ = 15- and 30-degree planes at stations x = 13, 15, and 21 cm. For the remaining stations, it is believed that the quality of the data is not good enough to make any assertion. Nevertheless, it appears that the predicted results are plausible.

Combustion engineers are interested in knowing fuel/air ratio and combustion efficiency distributions at different stations within the combustor. The results presented in Figures 116 through 119 indicated good correlation for the fuel/air-ratio distribution. Figures 120, 121, and 122 present the corresponding results for combustion efficiency. Keeping in mind the measurement errors discussed for Figure 113, the model predictions are in good agreement with measurements. At x = 6 cm, a minimum combustion efficiency of 5 percent exists near the center (Figure 120), and efficiency reaches a maximum value of approximately 90 percent near the liner wall. The recirculation-zone combustion efficiency is around 90 percent at x = 8.5 cm, whereas the minimum efficiency is approximately 50 percent at Y = 4.5 cm. The overall combustion efficiency is approximately 85 percent at x = 10 cm (i.e., 0.91 cm downstream from the primary orifices), with the minimum value being 65 percent. A continual increase in combustion efficiency continues with increasing values of x, as shown by predictions at x = 8.5, 10, and 13 cm; the shape of the profiles remains relatively similar for this region. At x = 15 cm (i.e., 2.21 cm upstream from the dilution jet), the predicted combustion efficiency is approximately 95 percent. The minimum is near the center, which should be expected for a combustor using axial jet fuel nozzles. This type of radial profile is maintained for stations at

Figure 120.   Comparison Between Predicted and Measured Combustion
Efficiency Along θ = 0° for Set-2, Table 15
(Sheet 1 of 2).

266
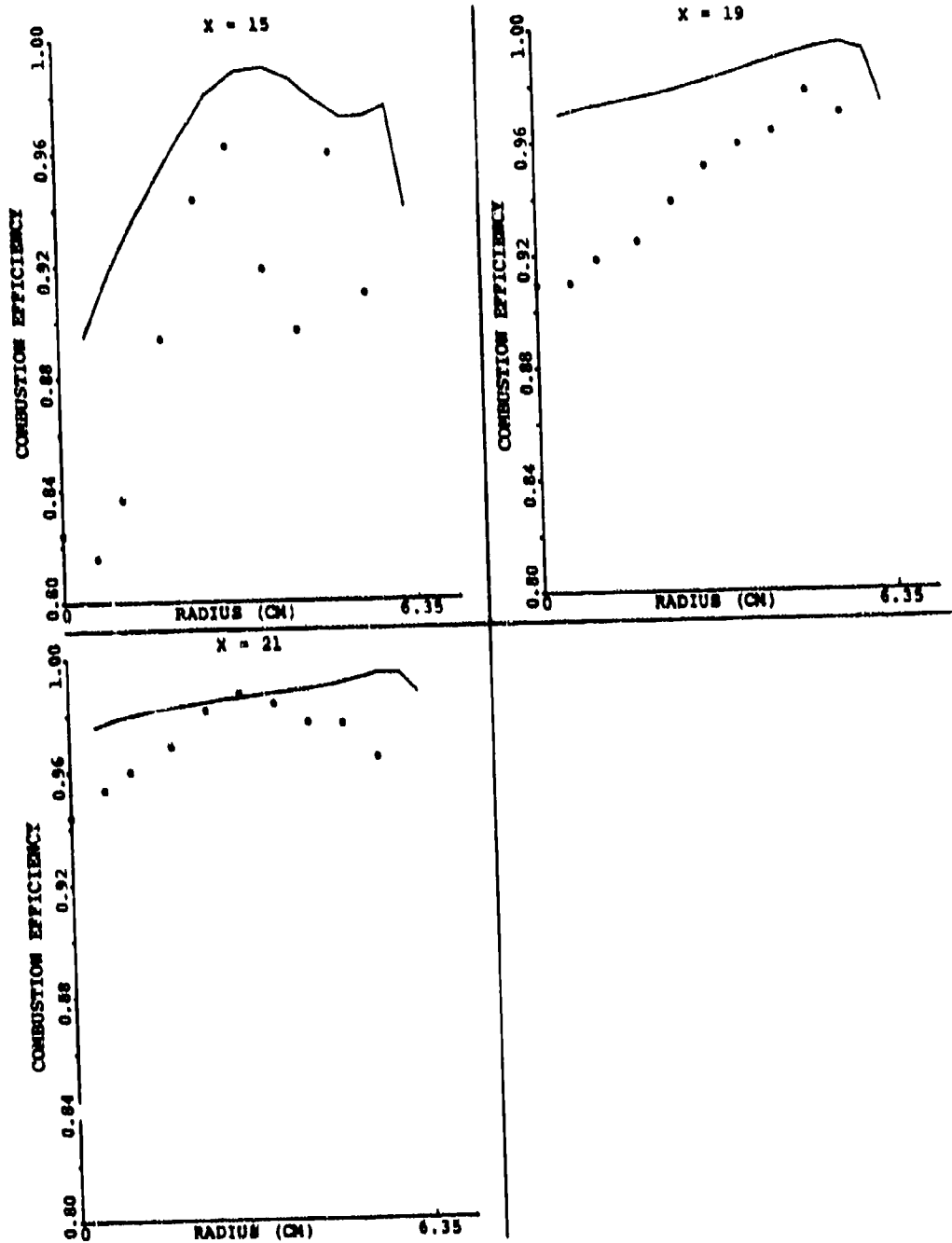
Figure 120.   Comparison Between Predicted and Measured
Combustion Efficiency Along θ = 0° for Set-2,
Table 15 (Sheet 2 of 2).
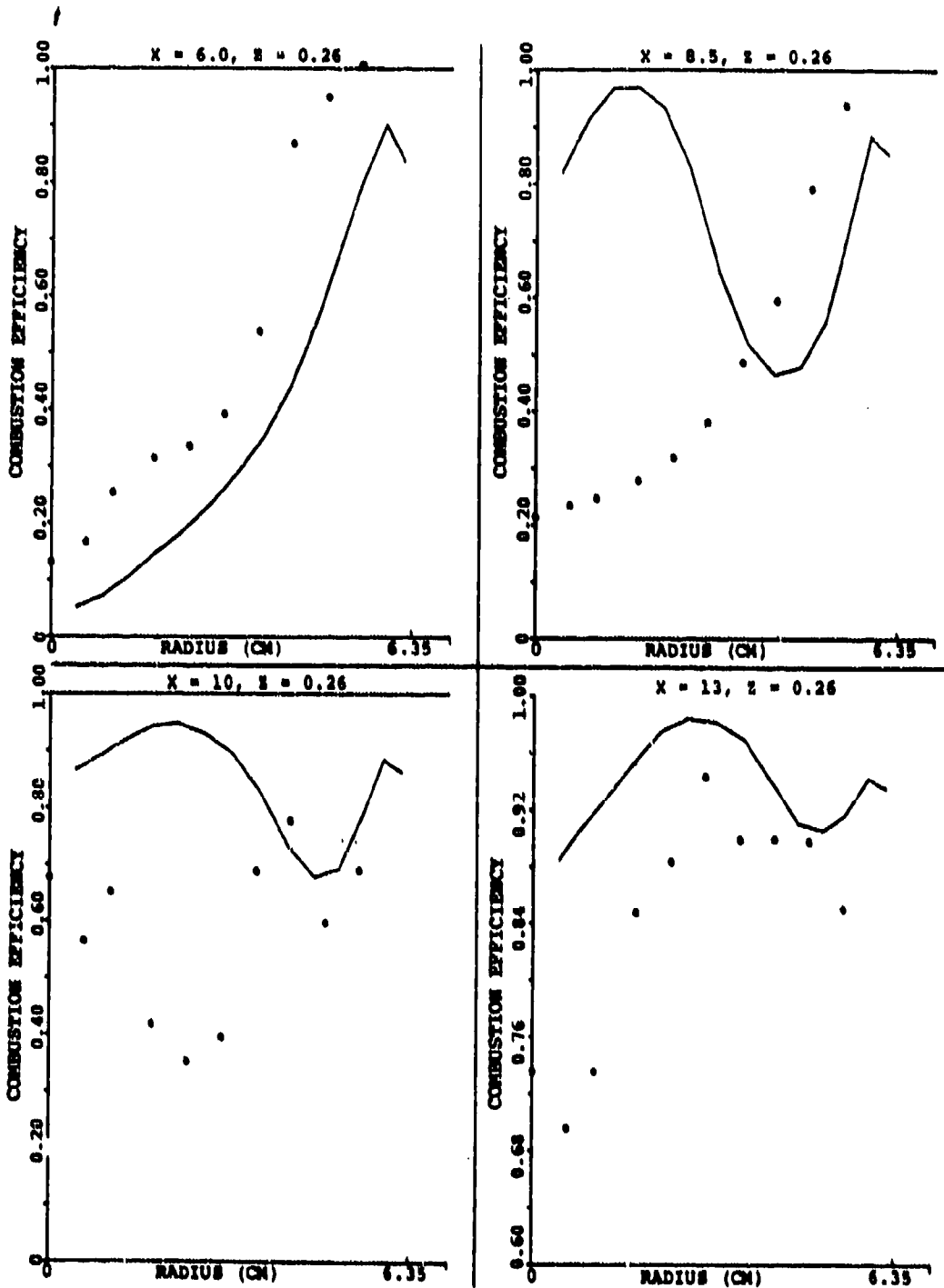
Figure 121. Comparison Between Predicted and Measured Combustion Efficiency Along θ = 15° for Set-2, Table 15 (Sheet 1 of 2).

Figure 121. Comparison Between Predicted and Measured
Combustion Efficiency Along θ = 15° for Set-2,
Table 15 (Sheet 2 of 2).

269
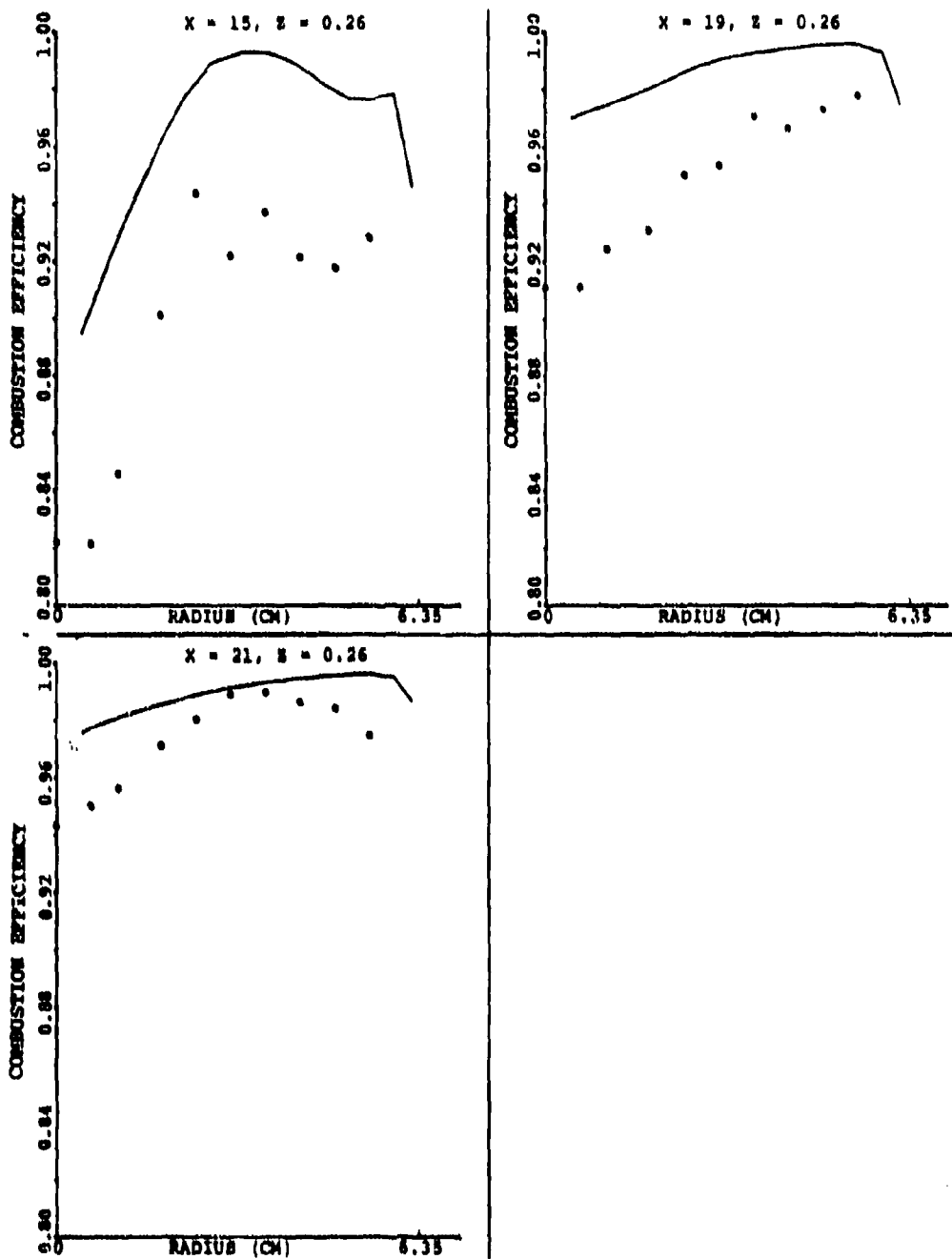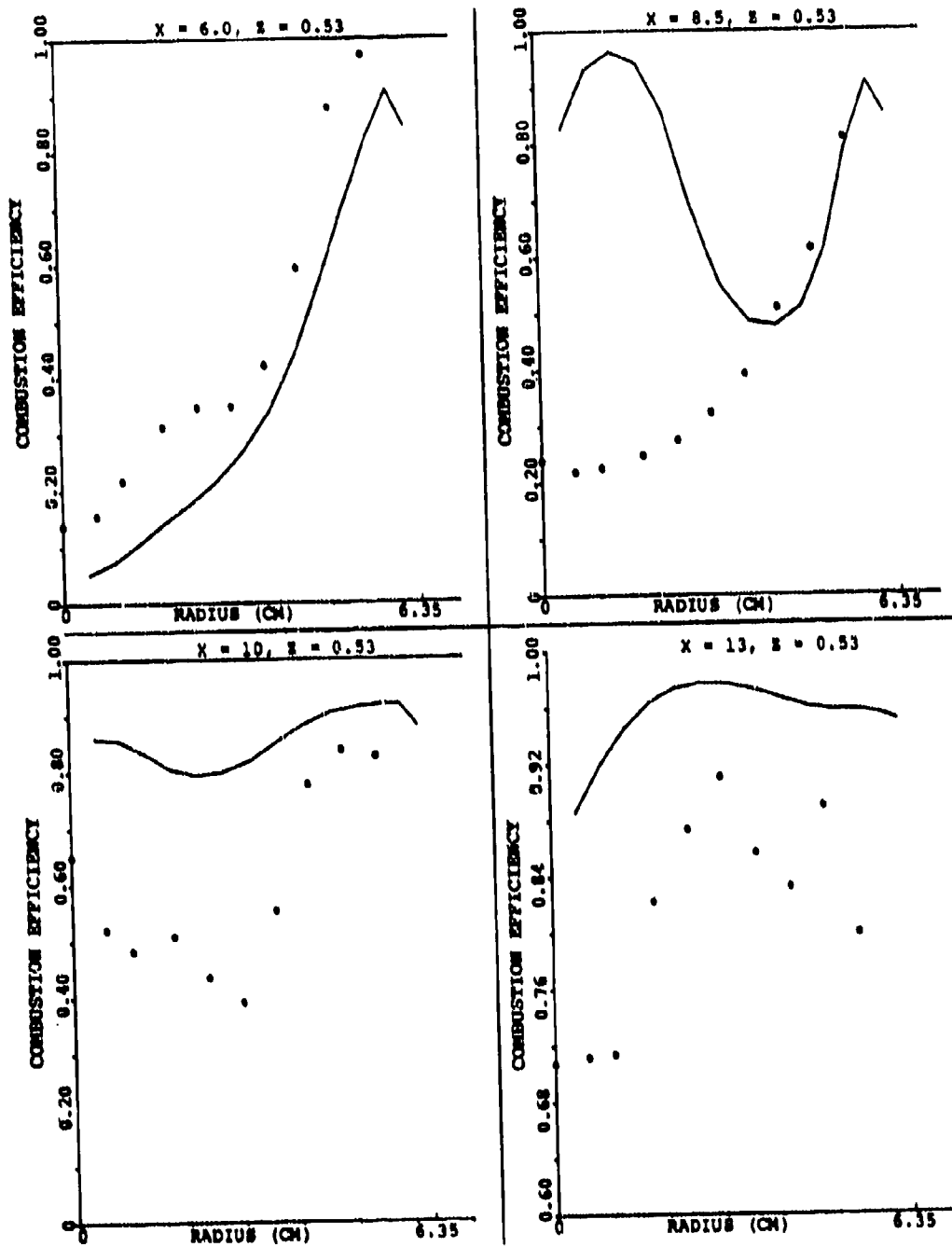
Figure 122.   Comparison Between Predicted and Measured Combustion
Efficiency Along θ = 30° for Set-2, Table 15
(Sheet 1 of 2).

Figure 122. Comparison Between Predicted and Measured Combustion
Efficiency Along θ = 30° for Set-2, Table 15
(Sheet 2 of 2).

x = 19 and 21 cm. The shape of the predicted combustion-
efficiency curve at x = 19 cm is similar to measurements. How-
ever, at x = 21 cm, the location of the measured peak efficiency
is quite different from that of the model. Nevertheless, the
predicted overall combustion efficiency of approximately 99 per-
cent compares favorably with the measured value of 97 percent.
Similar arguments apply to predictions and data for the θ = 15-
and 30-degree planes presented in Figures 121 and 122.

Before presenting comparisons for the remaining 12 sets of
emission mapping, it will be worthwhile to discuss Set-2 in
regard to regions where the fuel-oxidation rate is controlled
by chemical kinetics, and the rate of fuel and oxygen availabil-
ity. It may be recalled that the net fuel-combustion rate is
determined by the minimum of the three expressions, which cal-
culate reaction rates as controlled by kinetics, fuel concentra-
tion, and oxygen concentration. Figure 123 presents predicted
regions for Set-2 of Table 15 for the two x-y planes; i.e.,
θ = 0 and 30 degrees. For the plane in between the primary jet,
the gas temperatures in the regions near the dome, the liner wall,
and the middle half of the exit plane are low enough to make the
overall reaction rate controlled by chemical kinetics. The
region bounded by broken lines is fuel-rich and has high gas-
temperature levels so that the reaction rate is controlled by
oxygen. Regions like this are prone to producing carbon. The
rest of the combustion area is controlled by the availability
of fuel. The fuel-limited region contains a small kinetically-
controlled region created by the primary jet penetration.

Similarly, further downstream near the burner exit middle half,
the kinetically-controlled region is created by the dilution
jets. The regions predicted for the θ = 30-degree plane in
Figure 123 are similar to those of the θ = 0-degree plane inso-
far as the flow areas near the dome and liner walls are concerned.
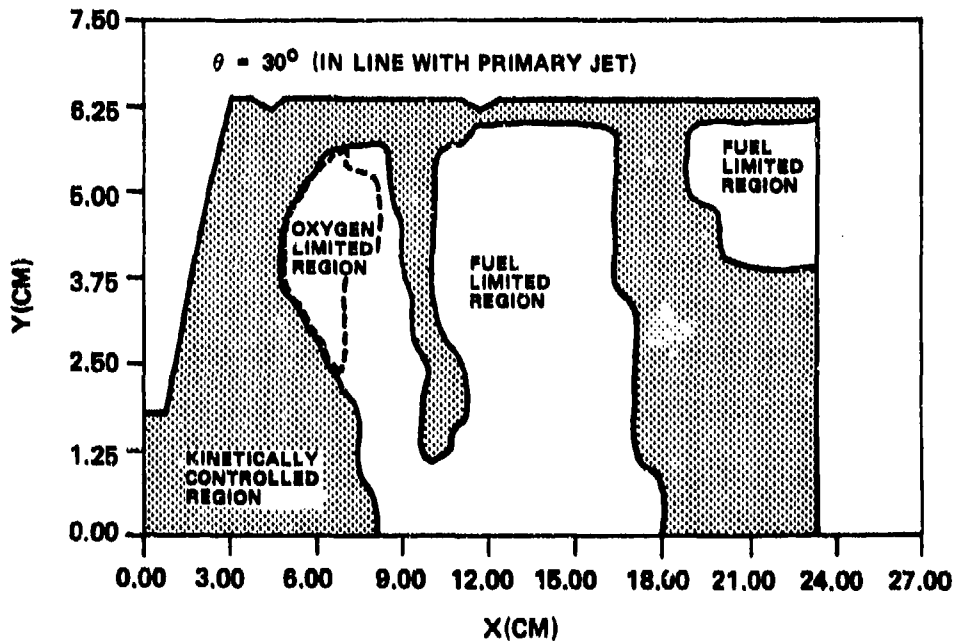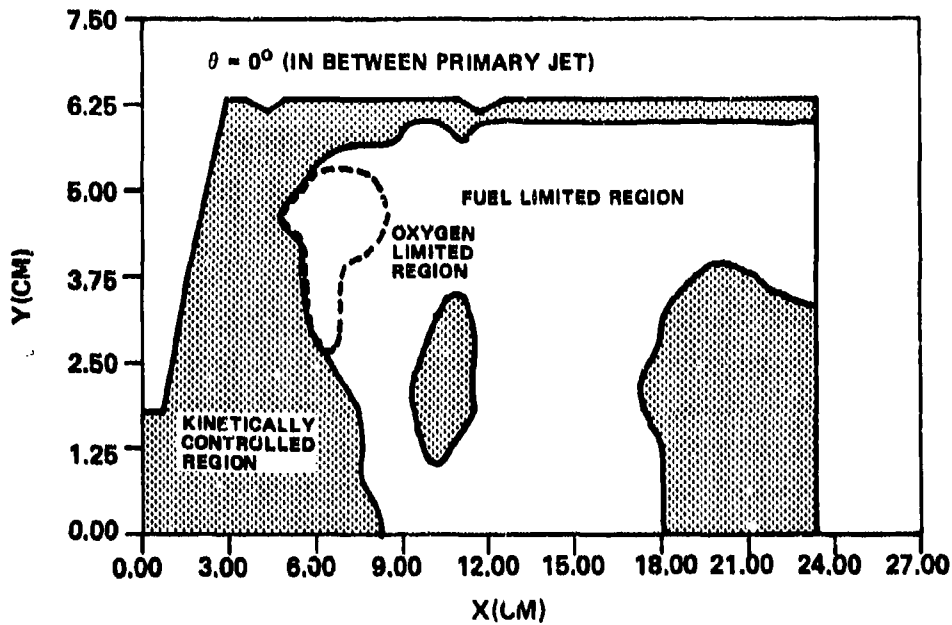
Figure 123. Predicted Regions Controlled by Availability of
Oxygen and Fuel and Chemical Kinetics for
Set-2 of Table 15.

273

The major difference is in the region covered by the primary and secondary jet trajectories, which have further increased the zones controlled by chemical kinetics.

Figure 124 shows the regions (similar to those of Figure 123) for Set-1 of Table 15. It may be recalled that the flow conditions for both Set-1 and Set-2 are identical, except the former has an overall combustor fuel/air ratio of 0.006, as compared to 0.0097 for Set-2. Due to a lower fuel/air ratio of Set-1, chemical kinetics control the reaction in most of the combustor region. This, along with the fuel-escaping ignition within the fuel-limited region, constitutes a majority of the inefficiency at idle. Plots like Figures 123 and 124 are very useful for improving fundamental understanding of the combustion processes occurring within a typical turbo-propulsion combustor.

A detailed discussion is given in the following paragraphs for a test set with Jet-A fuel. Set-8 of Table 16 was selected as it had combustor inlet-flow conditions and a fuel/air ratio similar to those of Set-2 with natural gas, discussed in Figures 110 through 124. It should be noted that no attempt is being made here to compare the combustor performance with liquid and gaseous fuels as the nozzles used in both cases were quite different. As pointed out earlier in Section IV.D, the main reason for selecting two different nozzles was to provide an opportunity to test the model predictions with data from different combustor flow fields, as influenced by both nozzle characteristics and the type of fuel.

Figure 125 presents results of fuel/air-ratio profiles for different x-y planes in between the primary jet for Set-0 of Table 16 and should be compared with the results of natural gas shown in Figure 117. The predictions are in good agreement

274
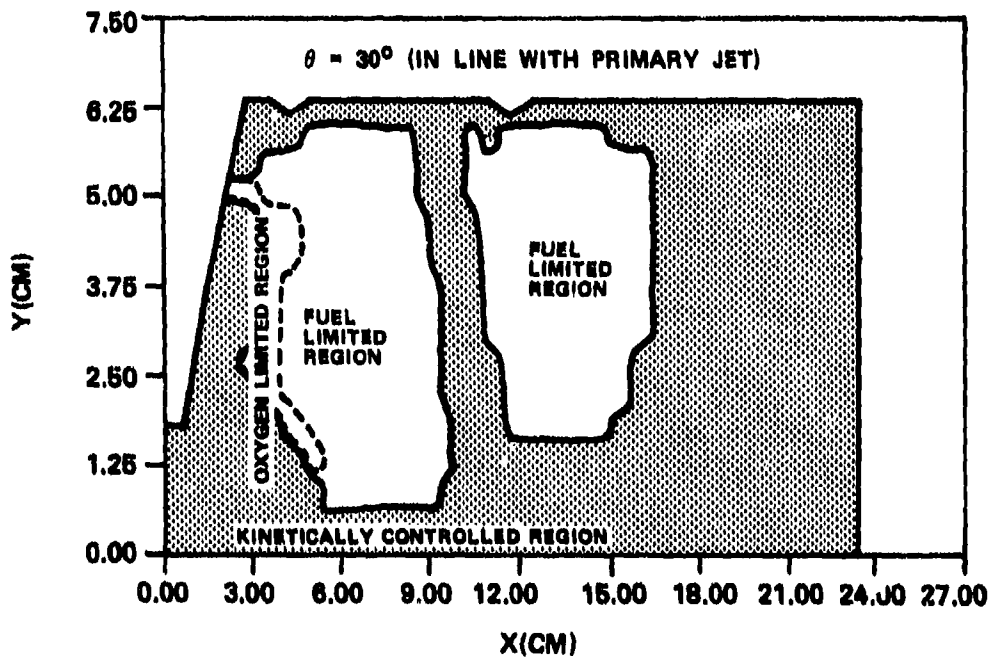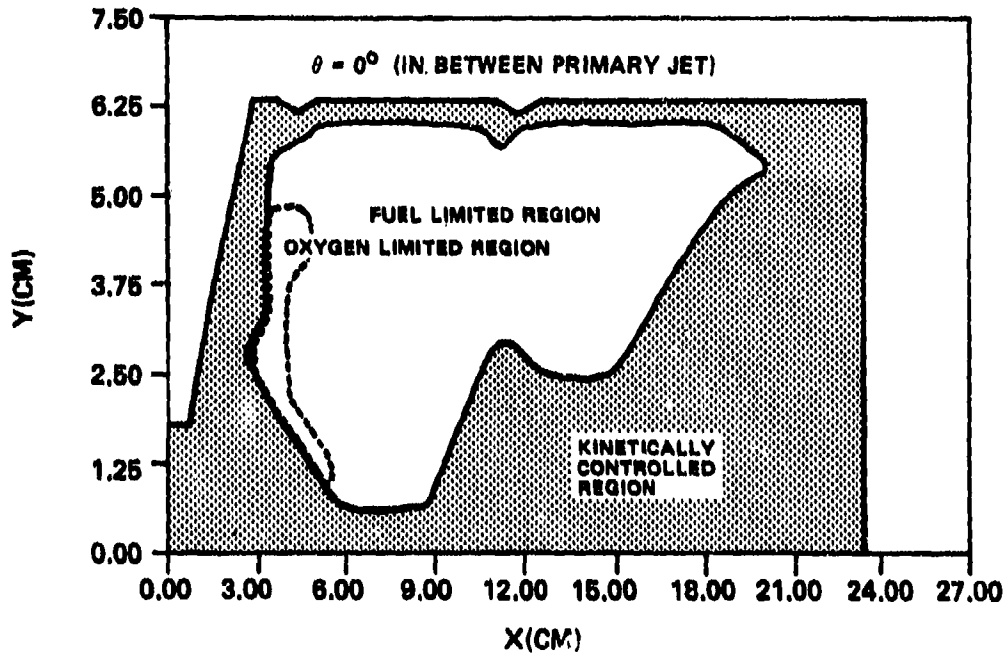
Figure 124. Predicted Regions Controlled by Availability of Oxygen and Fuel, and Chemical Kinetics for Set-1 of Table 15.
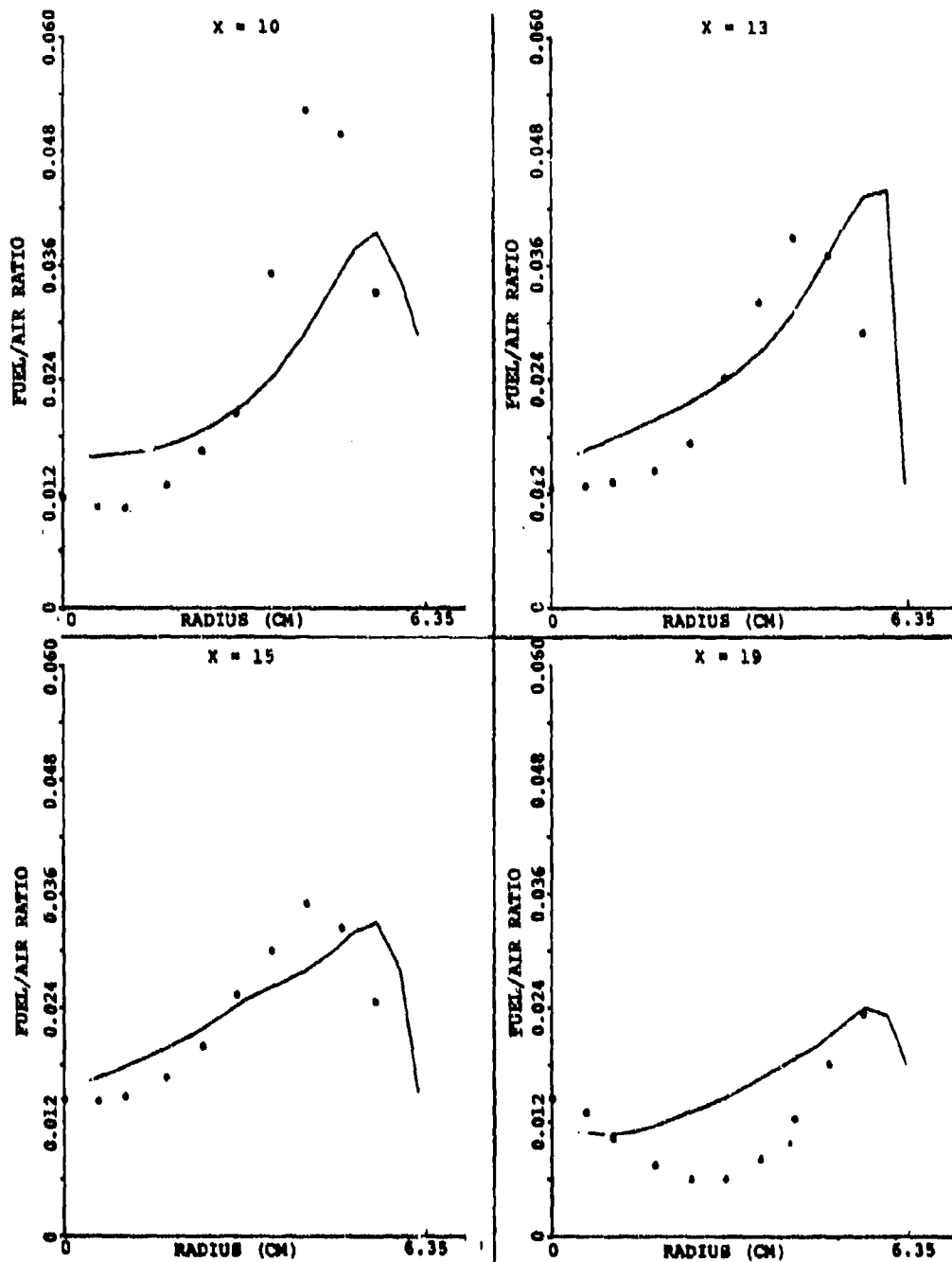
275

Figure 125. Comparison Between Predicted and Measured Profiles
of Fuel/Air Ratio for the X-Y Planes ($\theta = 0$) In
Between Primary Jet ($\theta = 30°$) for Set-8 of Table 16
(Sheet 1 of 2).

Figure 125. Comparison Between Predicted and Measured Pro-
files of Fuel/Air Ratio for the X-Y Planes
(θ = 0) In Between Primary Jet (θ = 30°) for
Set-8 of Table 16 (Sheet 2 of 2).

with measurements, especially at x = 10, 13, 15, and 21 cm. Compared to results with natural gas, the following observations can be made. At x = 10 cm using Jet-A fuel, the centerline fuel/air-ratio is equal to 0.016, whereas the peak value of 0.04 occurs at Y = 5.5 cm. On the other hand, with natural gas the corresponding values are 0.015, 0.084, and Y = 4.6 cm. By this station, approximately 75 percent of the spray has evaporated. The improved mixedness achieved with liquid fuel is due to a 90-degree cone, as opposed to an axial jet produced by the natural gas nozzle, and spray evaporation.

With liquid fuel the peak fuel/air ratio of 0.044 occurs at x = 13 cm, beyond which there is a continual decrease in the peak value (signifying a mixing process). With natural gas, the peak fuel/air ratio of 0.084 occurs at x = 10 cm. Of course, the maximum value of 1.0 is at the natural gas nozzle face. With both fuels, the centerline value remains relatively constant for axial stations located at x = 10, 13, and 15 cm. Due (in part) to the presence of dilution orifices at x = 17.2 cm, the centerline value is reduced at station x = 19.0 cm. Further reductions in the centerline value with increasing x is quite small, indicating that the dilution-jet penetration was more or less completed by x = 19 cm, with further mixing taking place through a shear layer-mixing process.

Figure 126 presents a comparison between predicted and measured profiles of fuel/air ratio for the plane lying 15 degrees from the center of the primary jet, for Set-8 conditions of Table 16. Due to large measurement errors at x = 10 and 19 cm (because of the presence of primary and dilution jets), good agreement is not expected at these stations. Relative to the v-y planes in between the jets, the profiles are similar, indicating a 2-D flow field in the case of liquid fuel, as was previously observed with gaseous fuel. The model correlated the data resonably well at x = 13, 15, and 21 cm.
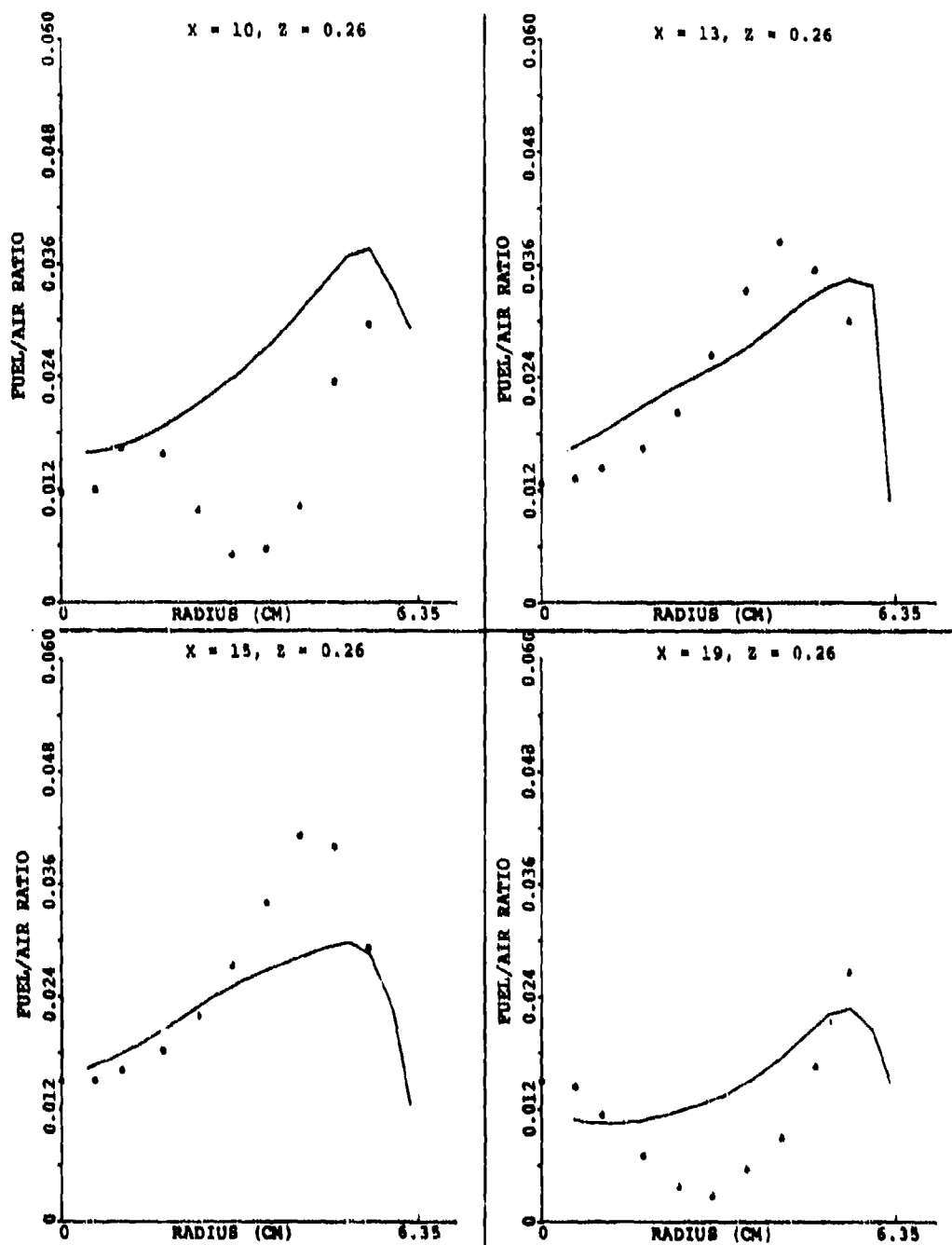
278

Figure 126. Comparison Between Predicted and Measured Profiles of Fuel/Air Ratio for the θ = 15° Plane for Set-8 of Table 16 (Sheet 1 of 2).
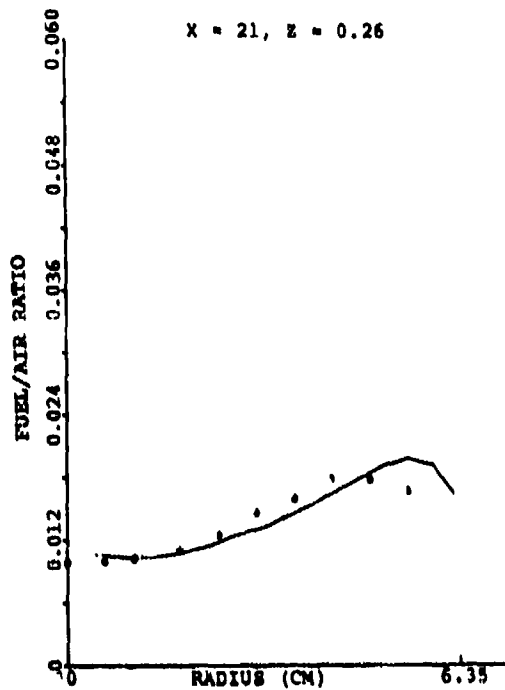
Figure 126.   Comparison Between Predicted and Measured Profiles
of Fuel/Air Ratio for the θ = 15° Plane for
Set-8 of Table 16 (Sheet 2 of 2).

Figure 127 presents fuel/air ratio profiles for the x-y planes in line with the primary jet. Compared to data for the plane in between the jet at stations adjacent to the primary and secondary orifices (i.e., x = 10 and 19 cm) as shown previously in Figure 125, the results are quite different. At x = 10 cm, the peak fuel/air ratio values at θ = 0 and 30 degrees are 0.021 and 0.029, respectively. The profile for the region up to γ = 4 cm is relatively flat for the in-line plane, caused by the primary jet. At x = 19 cm, the corresponding peaks are 0.024 and 0.012. It can therefore be concluded that at stations close to the radial injection points the circumferential variation is quite small for the region 0 < θ ≤ 15 degrees, whereas it is significant around θ = 30 degrees. However, the circumferential variation for other axial stations is quite small. This is an important conclusion as it justifies to some extent the use of the 2-D liner-cooling, emission, and transition-mixing models used in this program. However, as combustors with high heat-release rate are designed with discrete transverse jets, there might prevail a 3-D flow field encompassing most of the combustor. In such circumstances, the usefulness of 2-D auxiliary programs is expected to be limited.

A comparison between predicted and measured profiles of combustion efficiency for the x-y plane in between the primary jet is presented in Figure 128. The correlation is reasonably good for the first three x-stations. The results with liquid and gaseous fuel (Figure 120) are quite different because of the use of different fuel nozzles. It may be recalled that the gas nozzle injected the fuel axially, whereas the airblast nozzle used for liquid fuel injection had a 90-degree included spray angle. This resulted in a lean primary zone in the case of liquid fuel. In addition, more fuel was deposited near the liner wall. Consequently, at x = 10 cm the combustion efficiency near
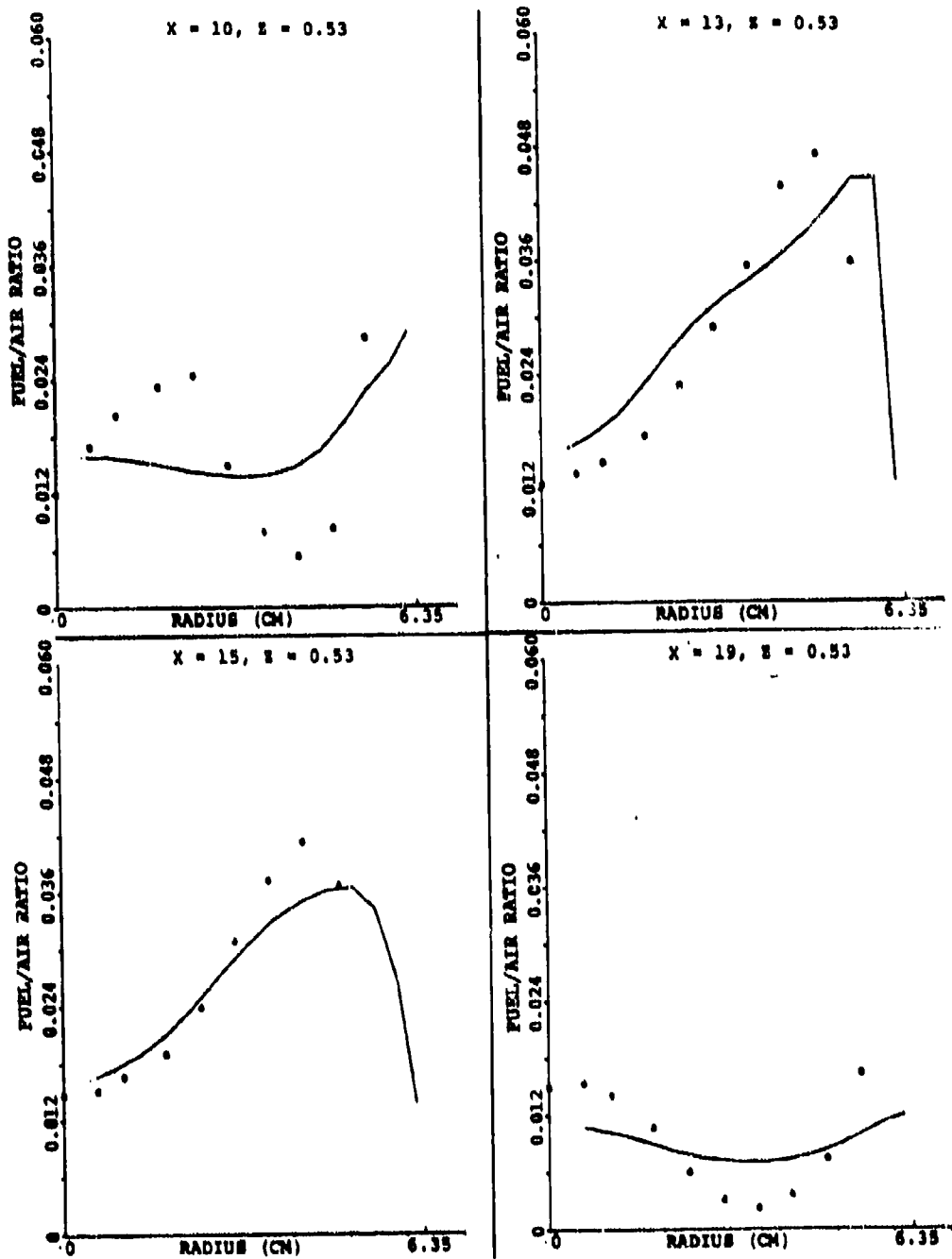
281

Figure 127.   Comparison Between Predicted and Measured Profiles
of Fuel/Air Ratio for the X-Y Planes In Line With
the Primary Jet for Set-8 of Table 15 (Sheet 1 of 2).

Figure 127. Comparison Between Predicted and Measured Profiles of Fuel/Air Ratio for the X-Y Planes In Line With the Primary Jet for Set-8 of Table 15 (Sheet 2 of 2).

283
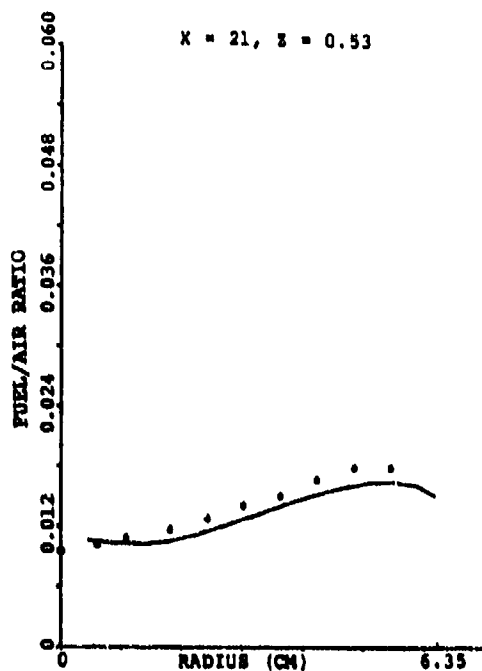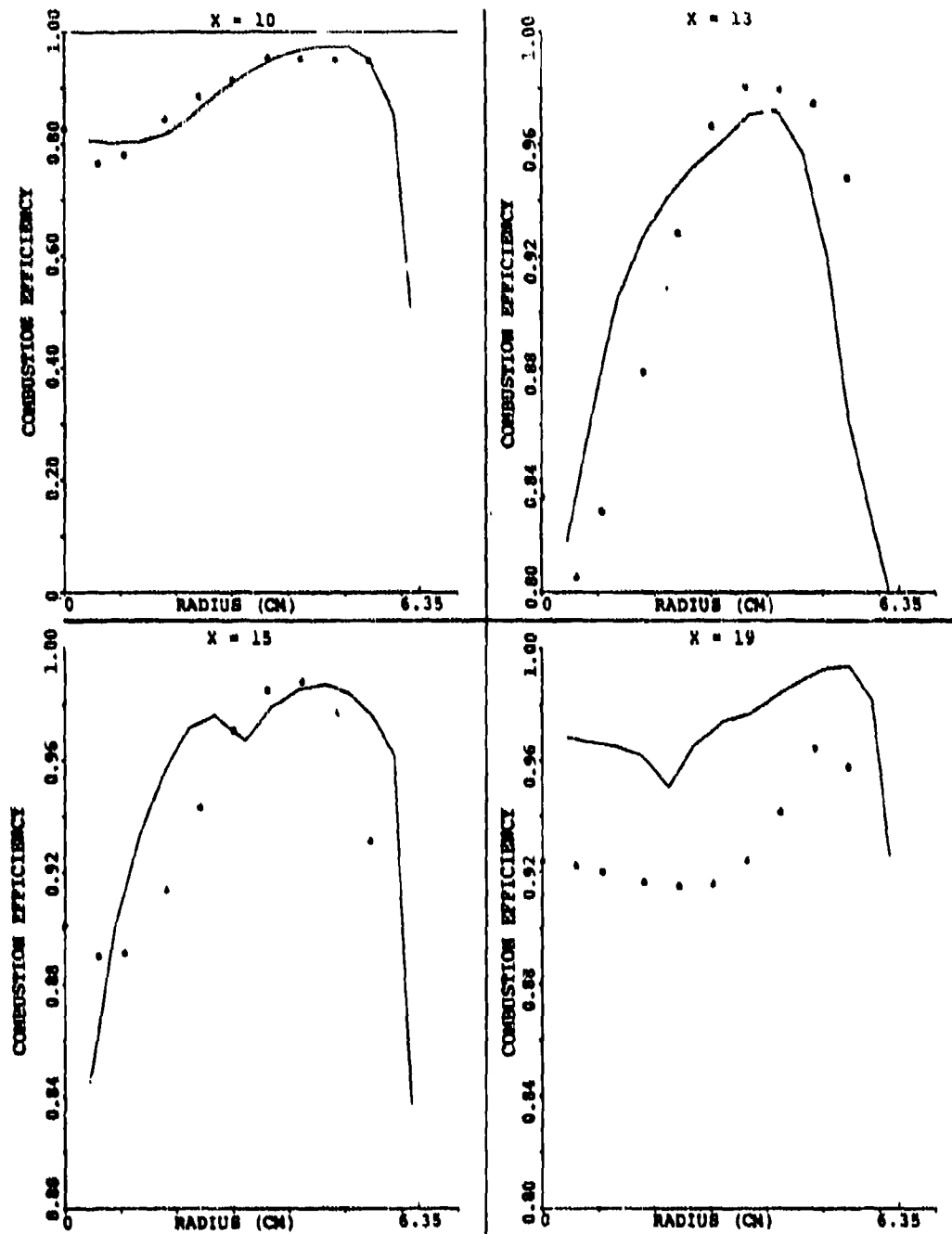
Figure 128.   Combustion Efficiency Profiles for the X-Y
Planes (θ = 0°) In Between the Primary Jet
for Set-8 of Table 16 (Sheet 1 of 2).
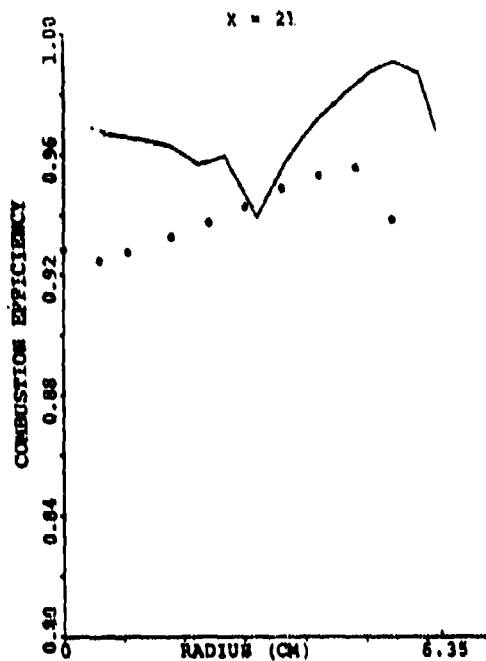
Figure 128. Combustion Efficiency Profiles for the X-Y
Planes (θ = 0°) In Between the Primary Jet
for Set-8 of Table 16 (Sheet 2 of 2).

the combustor center was lower with liquid fuel, and the peak was located near the wall. In addition, there was a significant drop in efficiency near the wall due to wall quenching. The shape of the curves were quite different at x = 13 cm, again due to different nozzle characteristics. The shapes of the curves begin to look similar at x = 16 cm, although the drop in efficiency near the center and near the wall is more pronounced with liquid fuel. A seemingly poor correlation for stations at x = 19 and 21 cm is perhaps due to measurement error at these stations because the average combustion efficiency appears to be lower than that at x = 15 cm.

Figures 129 and 130 present results for the planes at θ = 15 and 30 degrees, where the primary and dilution jets are located at θ = 30 degrees. Although it has been pointed out earlier that the measurement inaccuracies increase as θ approaches 30 degrees, the results are presented to illustrate inefficiencies at low-power points caused by the cooler primary and dilution jets. Notice a drop in efficiency at x = 10 and 19 cm for the plane in line with the primary/dilution jet. Consequently, combustion inefficiency near the wall is more for the θ = 30-degree plane. It also appears that the model correlation with combustion efficiency within the dilution zone is less satisfactory with liquid than with gaseous fuel. A plausible explanation is an increased level of wall quenching in the case of liquid fuel, that cannot be accurately predicted by the combustor performance model due to lack of required space resolution for the region adjacent to the liner wall. Nevertheless, the model gives adequate correlation with measurements to justify the usefulness for relative performance evaluations of combustor design changes.

286
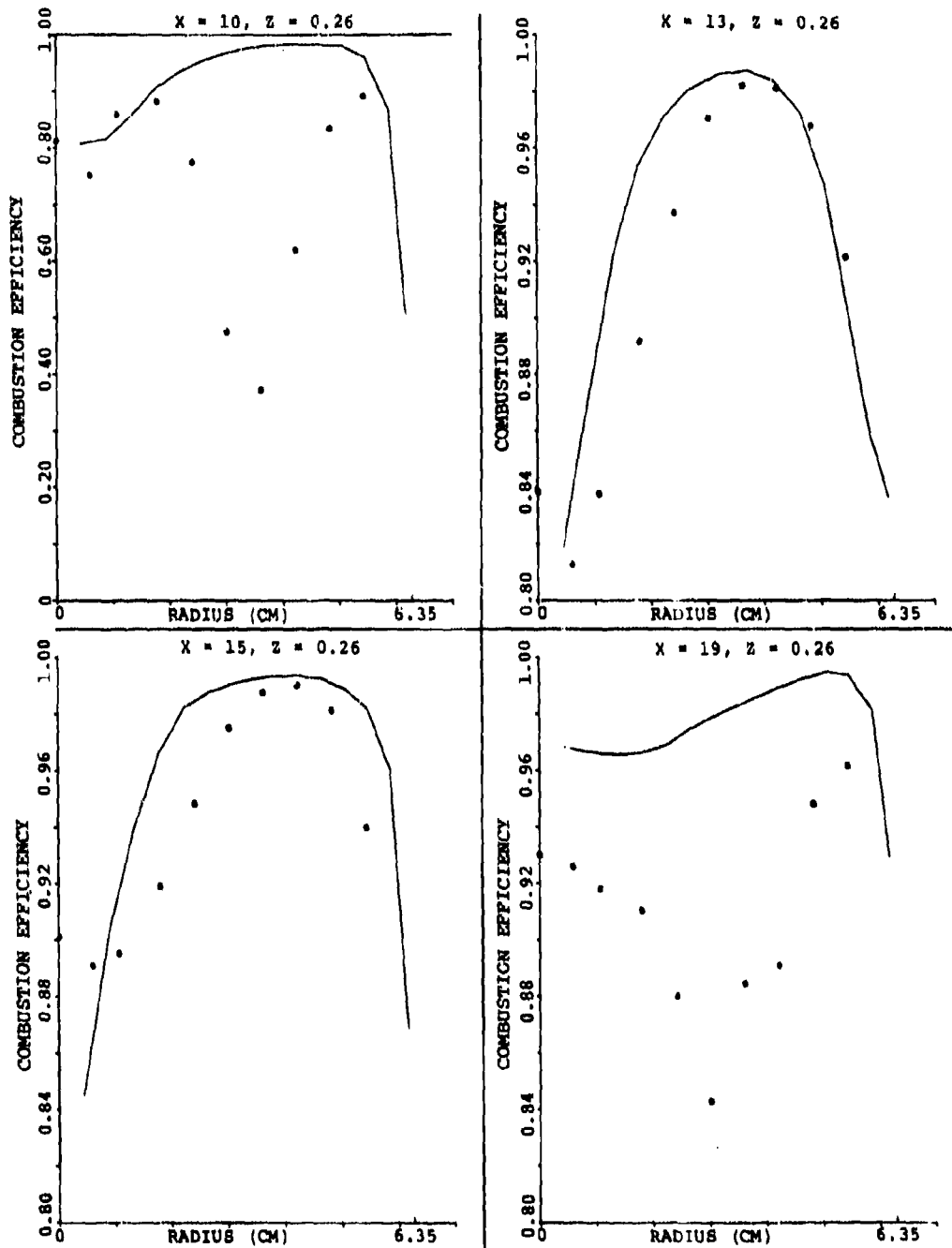
Figure 129.   Combustion Efficiency Profiles for the $\theta = 15°$ Planes
for Set-8 of Table 16 (Sheet 1 of 2).
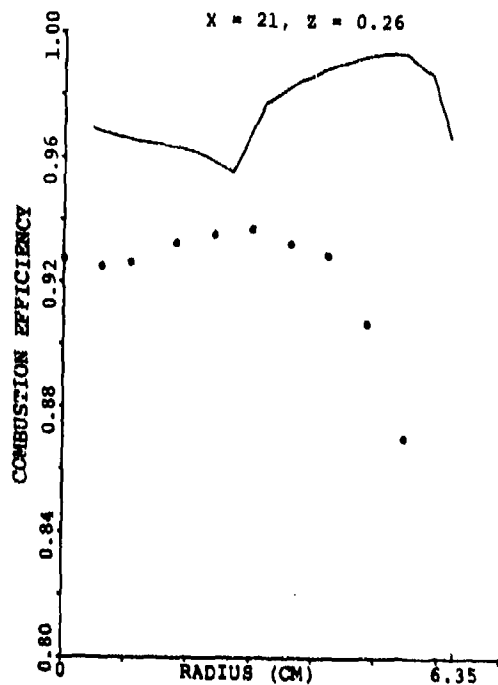
Figure 129.   Combustion Efficiency Profiles for the
$\theta = 15°$ Plane for Set-8 of Table 16
(Sheet 2 of 2).
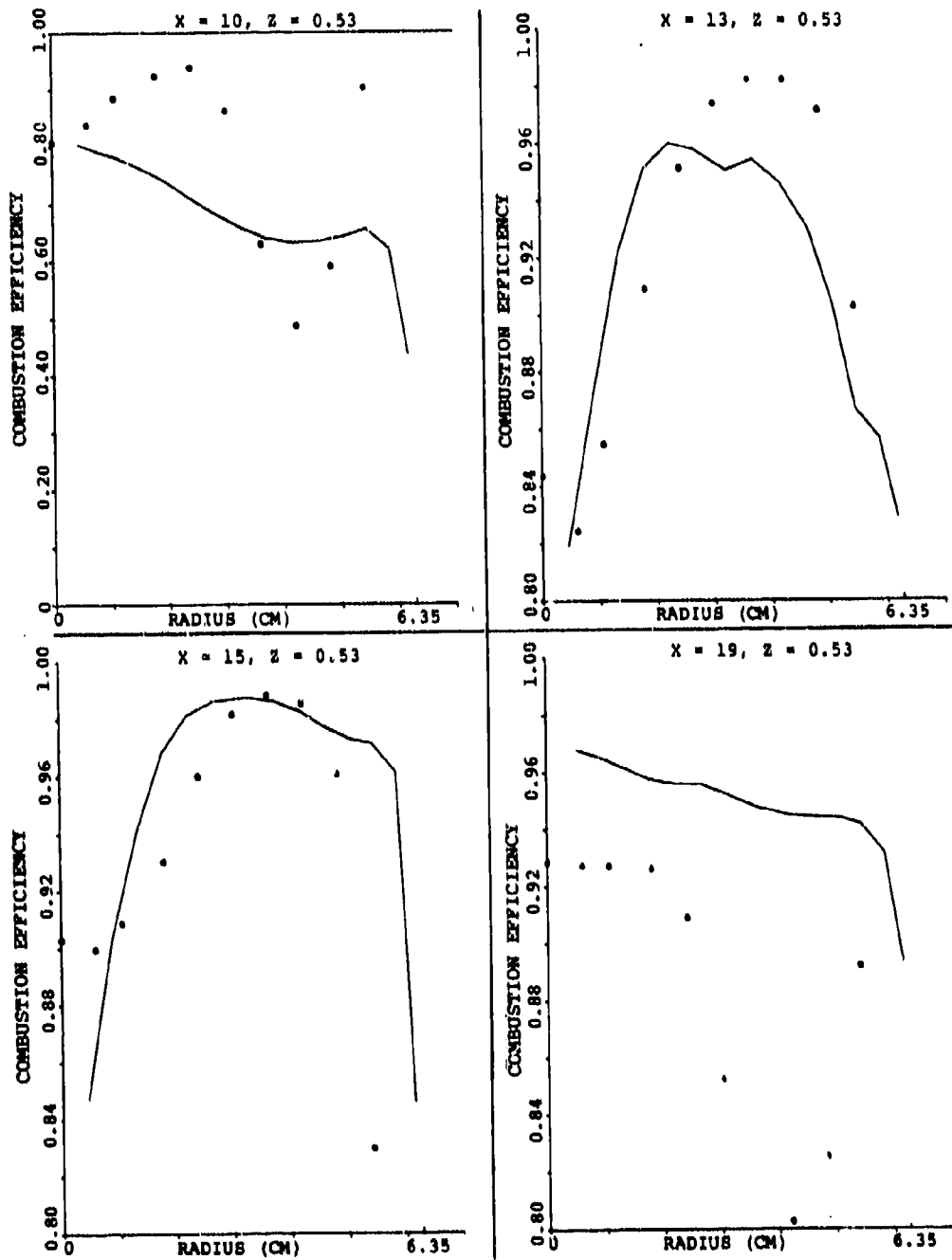
Figure 130. Combustion Efficiency Profiles for the X-Y
Planes In Line With the Primary Jet for
Set-8 of Table 16 (Sheet 1 of 2).

289
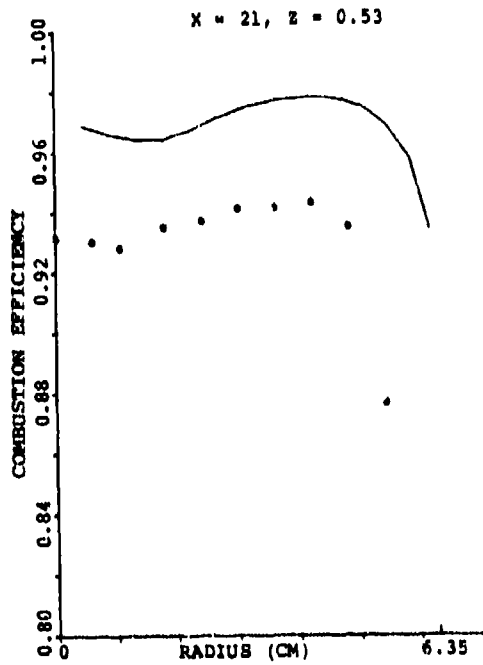
Figure 130. Combustion Efficiency Profiles for the
X-Y Planes In Line With the Primary Jet
for Set-8 of Table 16 (Sheet 2 of 2).

Figures 131 and 132 compare predicted and measured profiles of unburned fuel and CO for the x-y planes in betwween the primary jet for Set-8 (liquid fuel) and may be compared with the corresponding results of gaseous fuel presented previously in Figures 110 and 114. The correlation for the first three axial stations of the liquid fuel case is reasonabley good, and the profiles are quite different from those of the gaseous fuel (Figure 110). On the other hand, the correlation with the gaseous fuel data was not good. A possible explanation for this discrepancy might be due to poorly defined boundary conditions associated with the gas nozzle; in the case of liquid fuel, an increase in HC quenching near the center and liner wall. The CO correlation is also better with liquid fuel. For the region up to the intermediate zone, there also appears to be an increased level of CO near the center and near the wall. However, in the dilution zone, the CO quenching is more pronounced near the liner wall.

Figures 133 through 154 summarize results for the remaining 11 sets of emissions data. Only the profiles of fuel/air ratio and combustion efficiency are presented for the x-y planes in between the primary jet, as the measurement errors are expected to be minimal for these stations. Only the salient points will be presented while discussing these figures.

Figures 133 and 134 show the results for Set-1, and should be compared with Figures 117 and 120 for illustrating the effect of overall combustor fuel/air ratio on radial profiles of fuel/air ratio and combustion efficiency. Although the ratio of overall fuel/air ratios of Sets-2 and -1 was 1.6, the ratio of peak fuel/air ratios at x = 6 cm is 4.4. Also the shape of the fuel/air ratio profile is quite different at this station. The profiles are relatively similar at x = 10 cm, and at stations further downstream. The ratios of peak fuel/air value at x = 10, 13, 15, and 19 cm are 2.08, 1.95, 1.9, and 1.77, respectively,
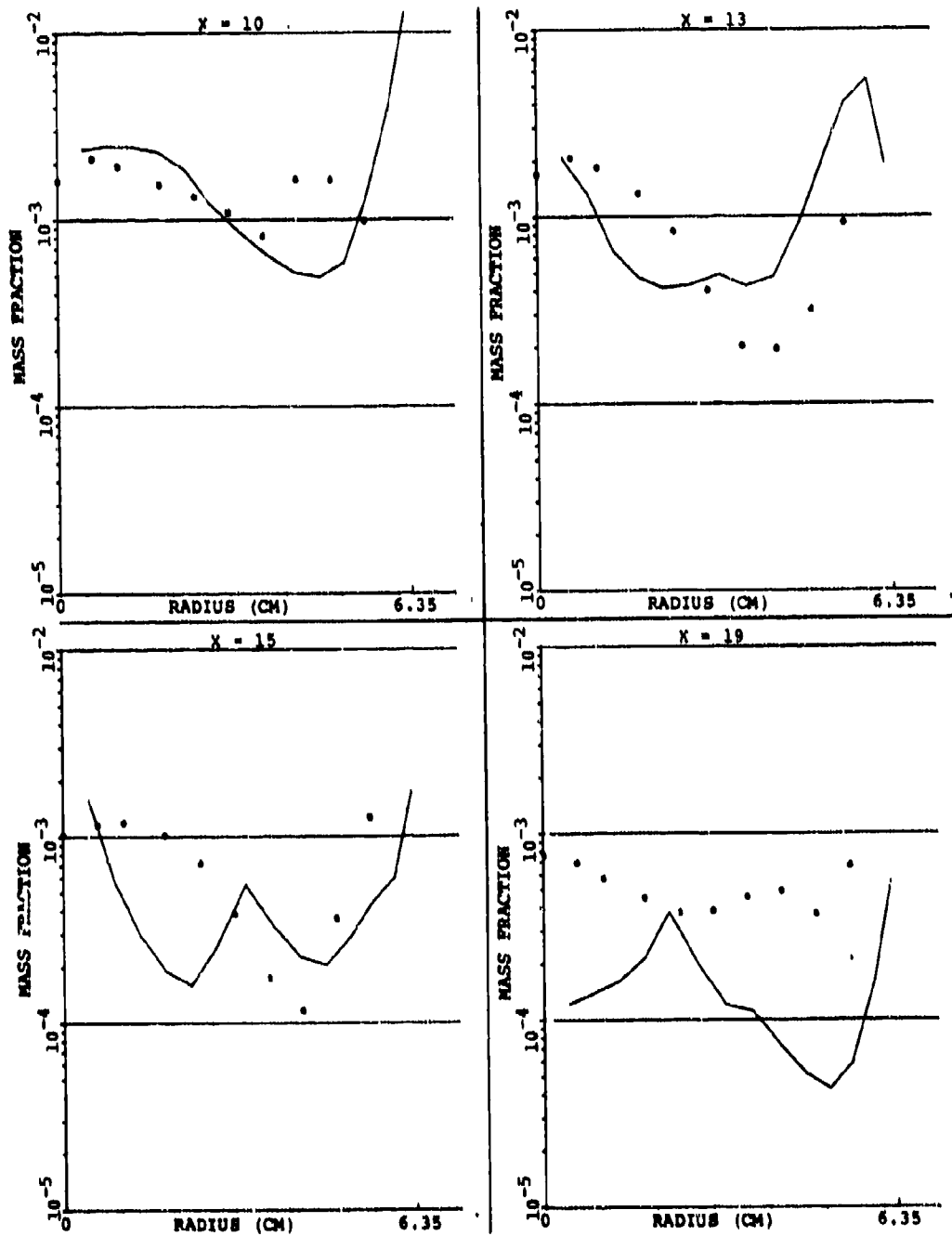
Figure 131. Comparison Between Measured and Predicted
Unburned Fuel for the X-Y Planes In Between
the Primary Jet for Set-8 of Table 16
(Sheet 1 of 2).

292

Figure 131. Comparison Between Measured and Predicted
Unburned Fuel for the X-Y Planes In Between
the Primary Jet for Set-8 of Table 16
(Sheet 2 of 2).

293
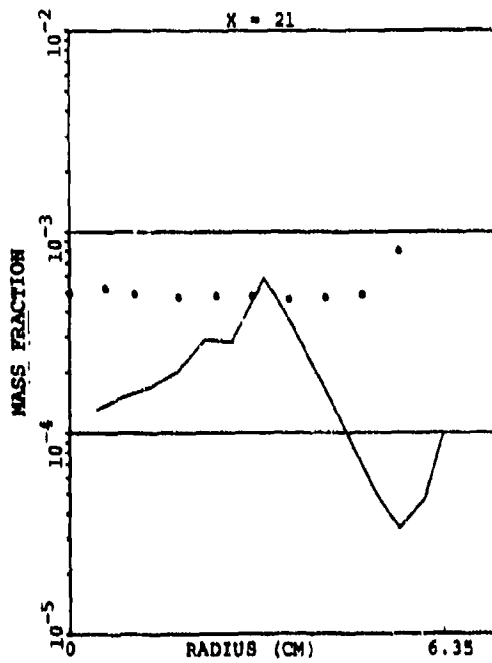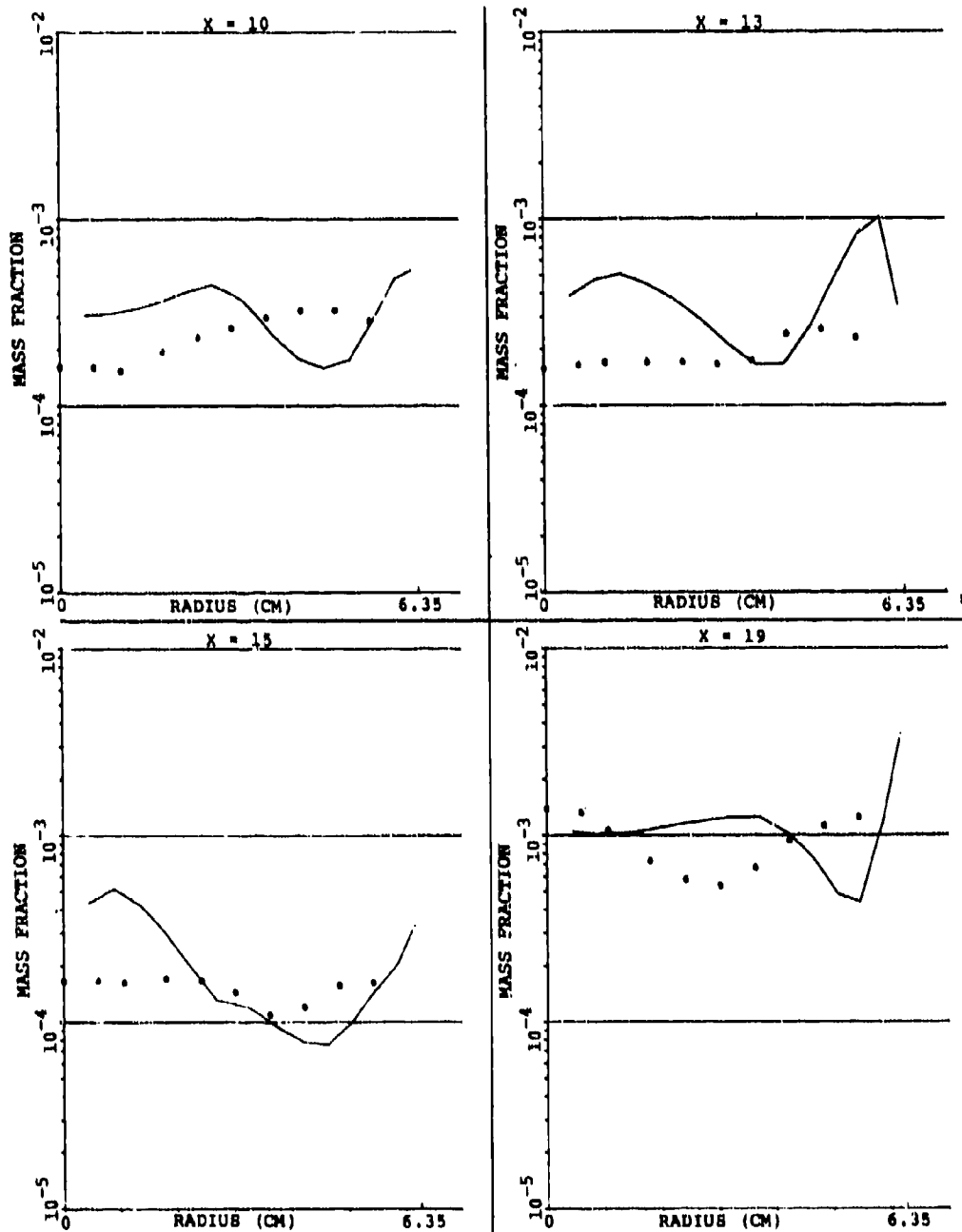
Figure 132.   Comparison Between Predicted and Measured CO
Profiles for the X-Y Planes In Between the
Primary Jet for Set-8 of Table 16
(Sheet 1 of 2).
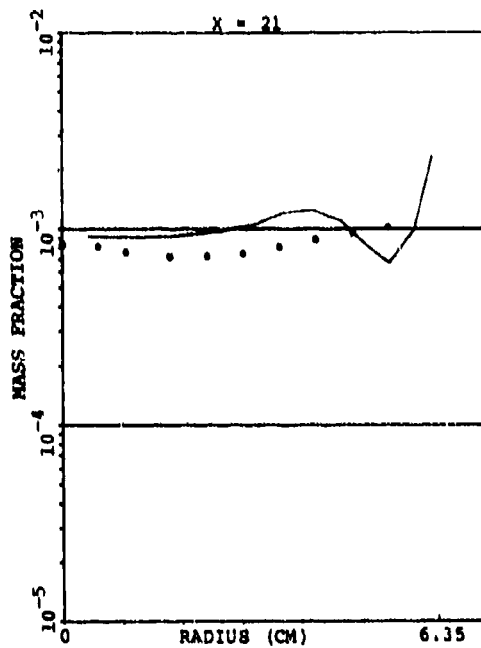
Figure 132. Comparison Between Predicted and Measured CO
Profiles for the X-Y Planes In Between the
Primary Jet for Set-8 of Table 16
(Sheet 2 of 2).
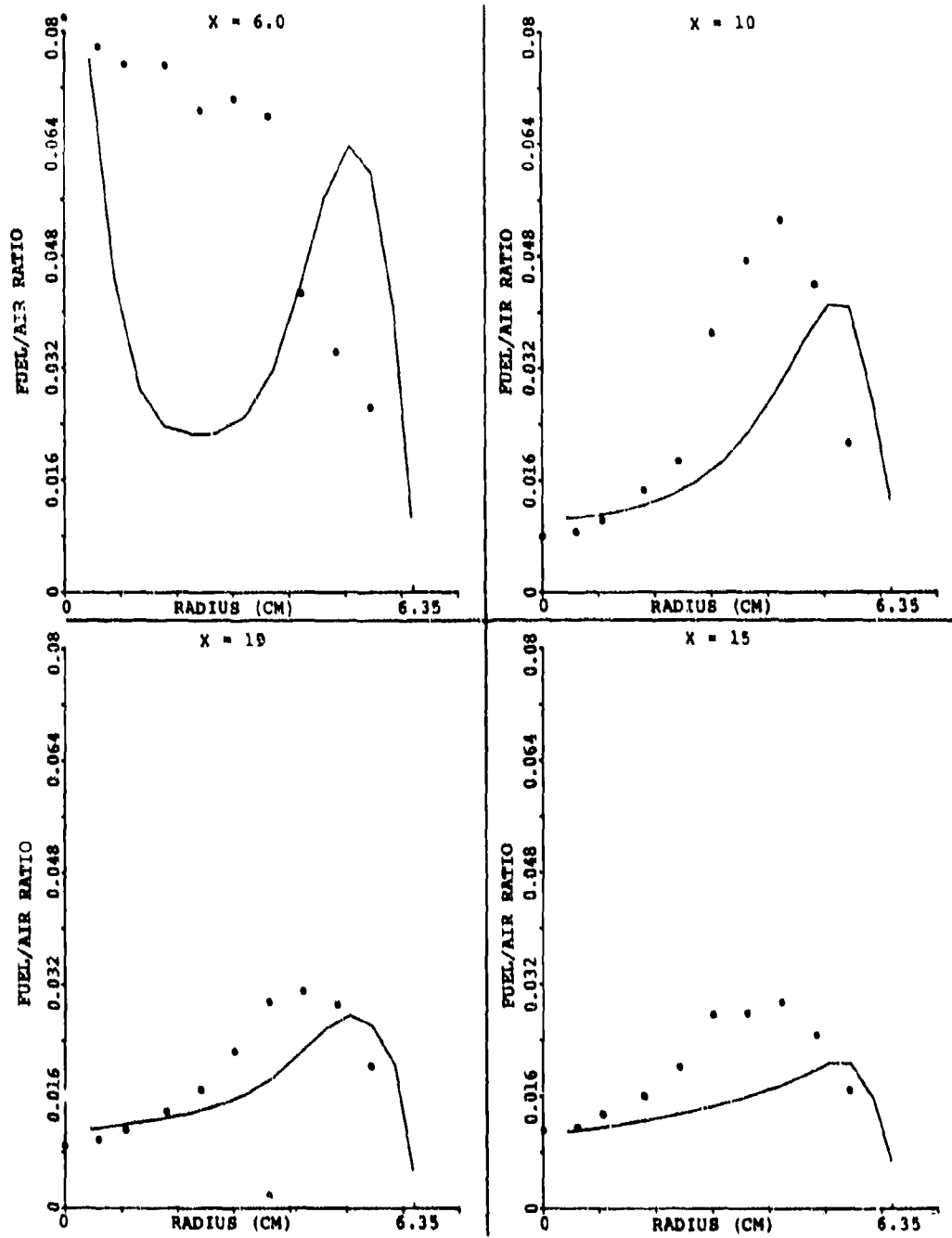
Figure 133. Comparison Between Predicted and Measured Profiles of Fuel/Air Ratio for the X-Y Planes In Between the Primary Jet for Set-8 of Table 15 (Sheet 1 of 2).

Figure 133. Comparison Between Predicted and Measured Profiles
of Fuel/Air Ratio for the X-Y Planes In Between
the Primary Jet for Set-8 of Table 15
(Sheet 2 of 2).

297
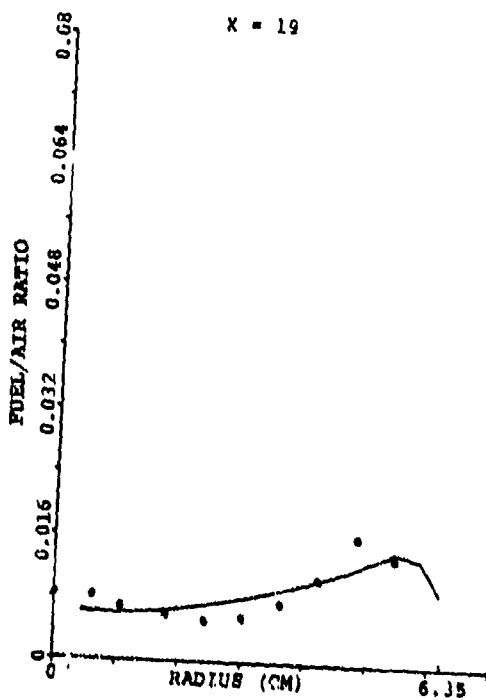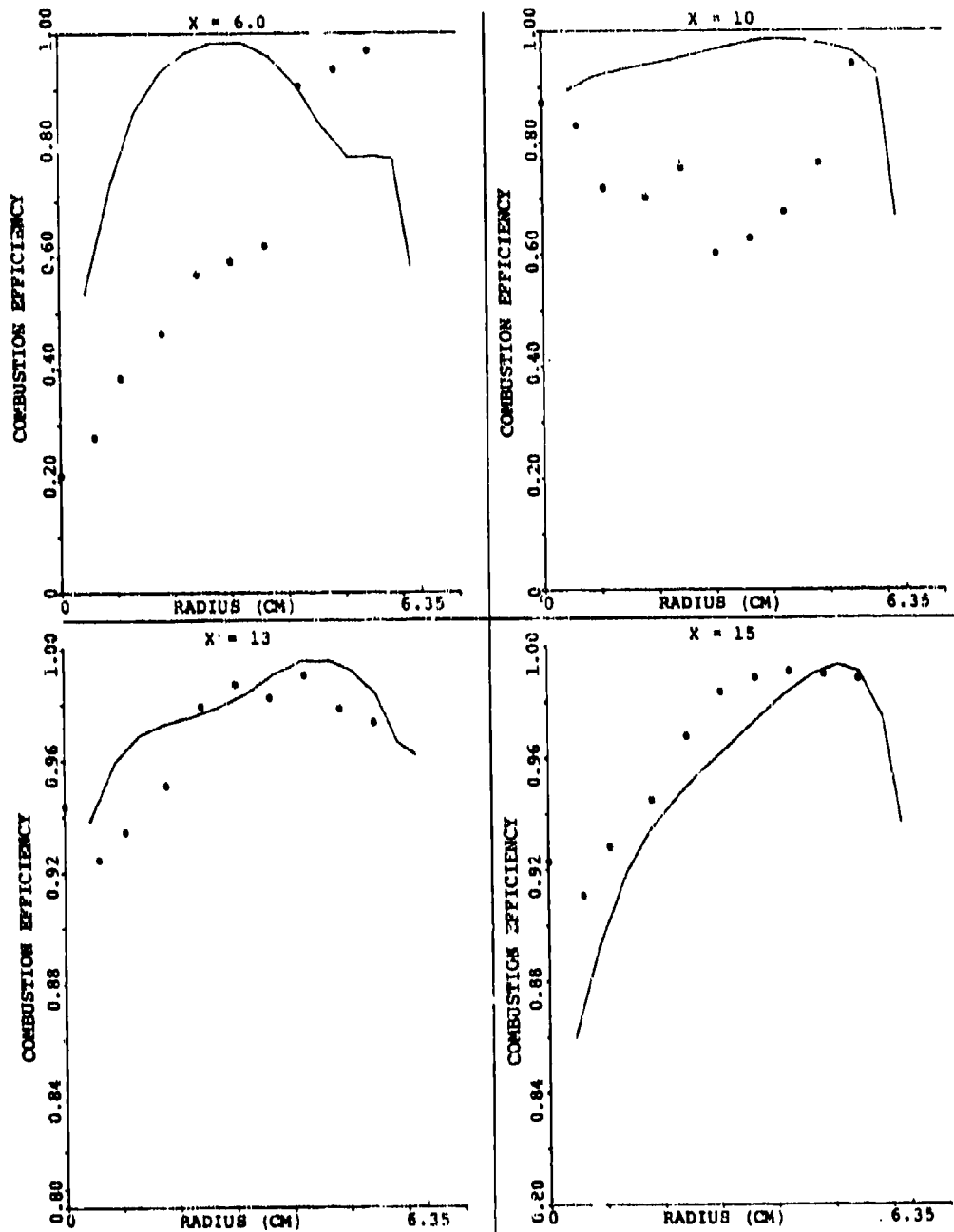
Figure 134. Comparison Between Predicted and Measured Combustion Efficiency for the X-Y Planes In Between the Primary Jet for Set-1 of Table 15 (Sheet 1 of 2).

Figure 124. Comparison Between Predicted and Measured Combustion Efficiency for the X-Y Plane In Between the Primary Jet for Set-1 of Table 15 (Sheet 2 of 2).
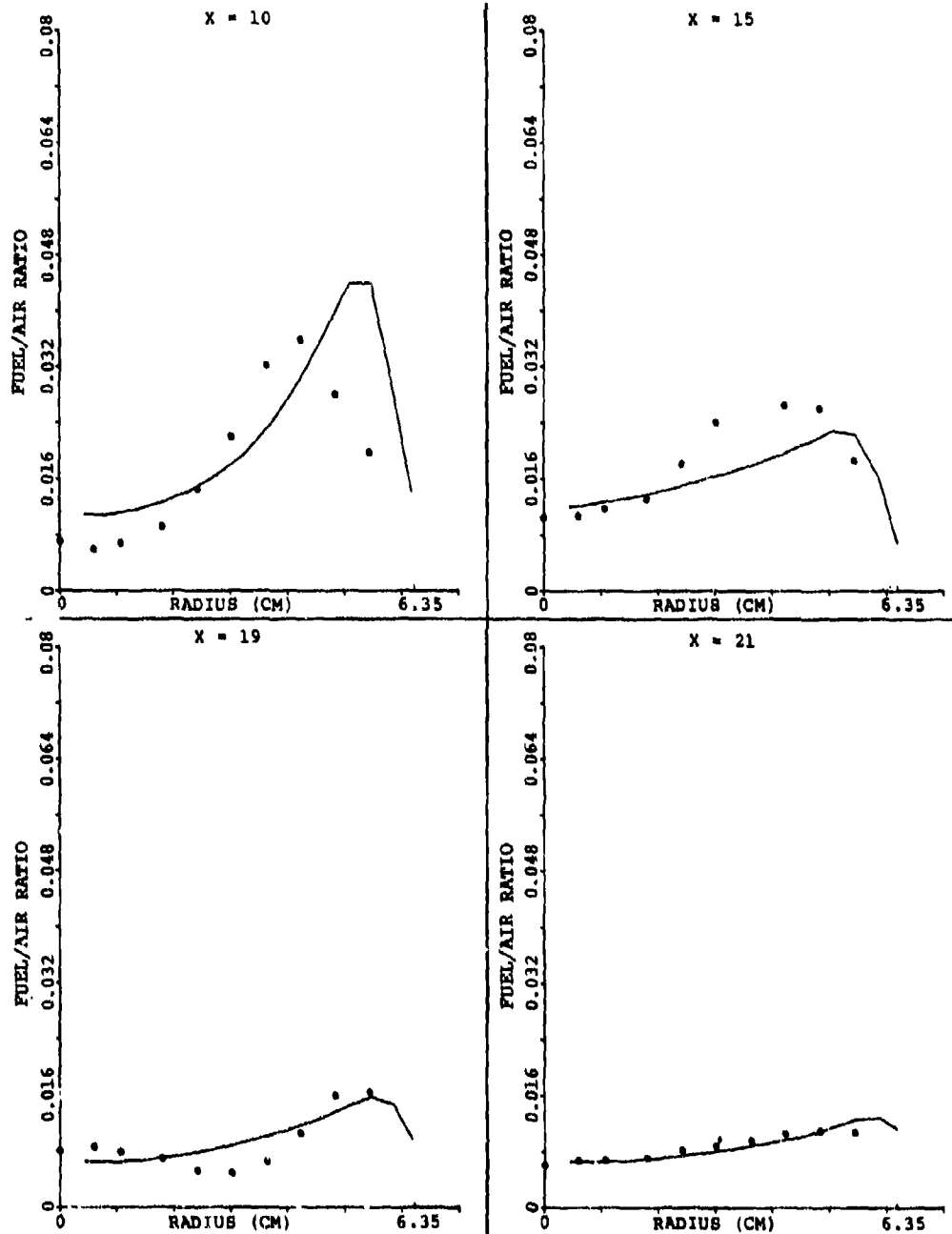
Figure 135. Comparison Between Predicted and Measured Profiles
of Fuel/Air Ratio for the X-Y Planes In Between
the Primary Jet for Set-3 of Table 15.

300
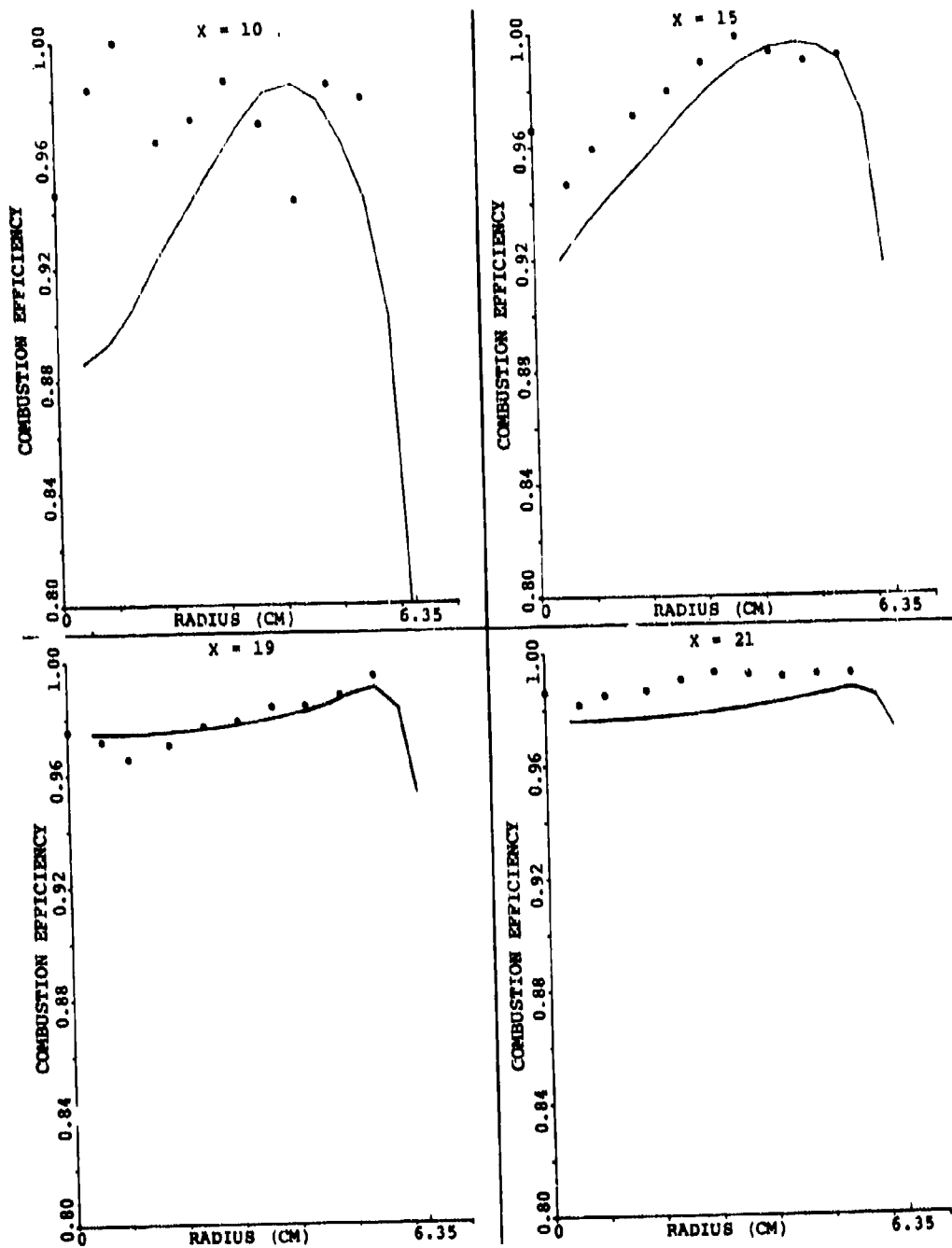
Figure 136. Comparison Between Predicted and Measured Combustion Efficiency for the X-Y Planes In Between the Primary Jet for Set-3 of Table 15.

301
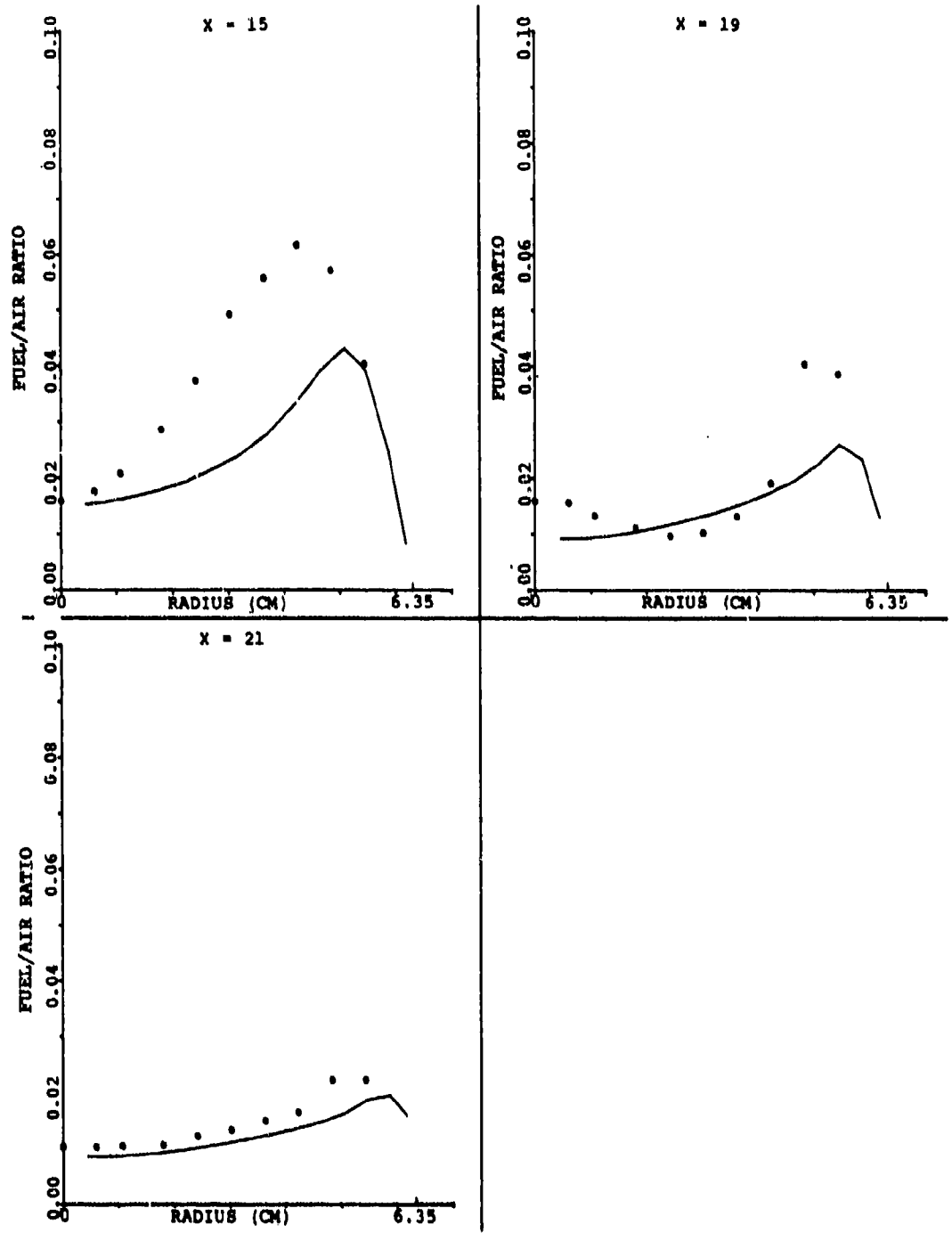
Figure 137. Comparison Between Predicted and Measured Profiles
of Fuel/Air Ratio for the X-Y Planes In Between
the Primary Jet for Set-4 of Table 15.

302
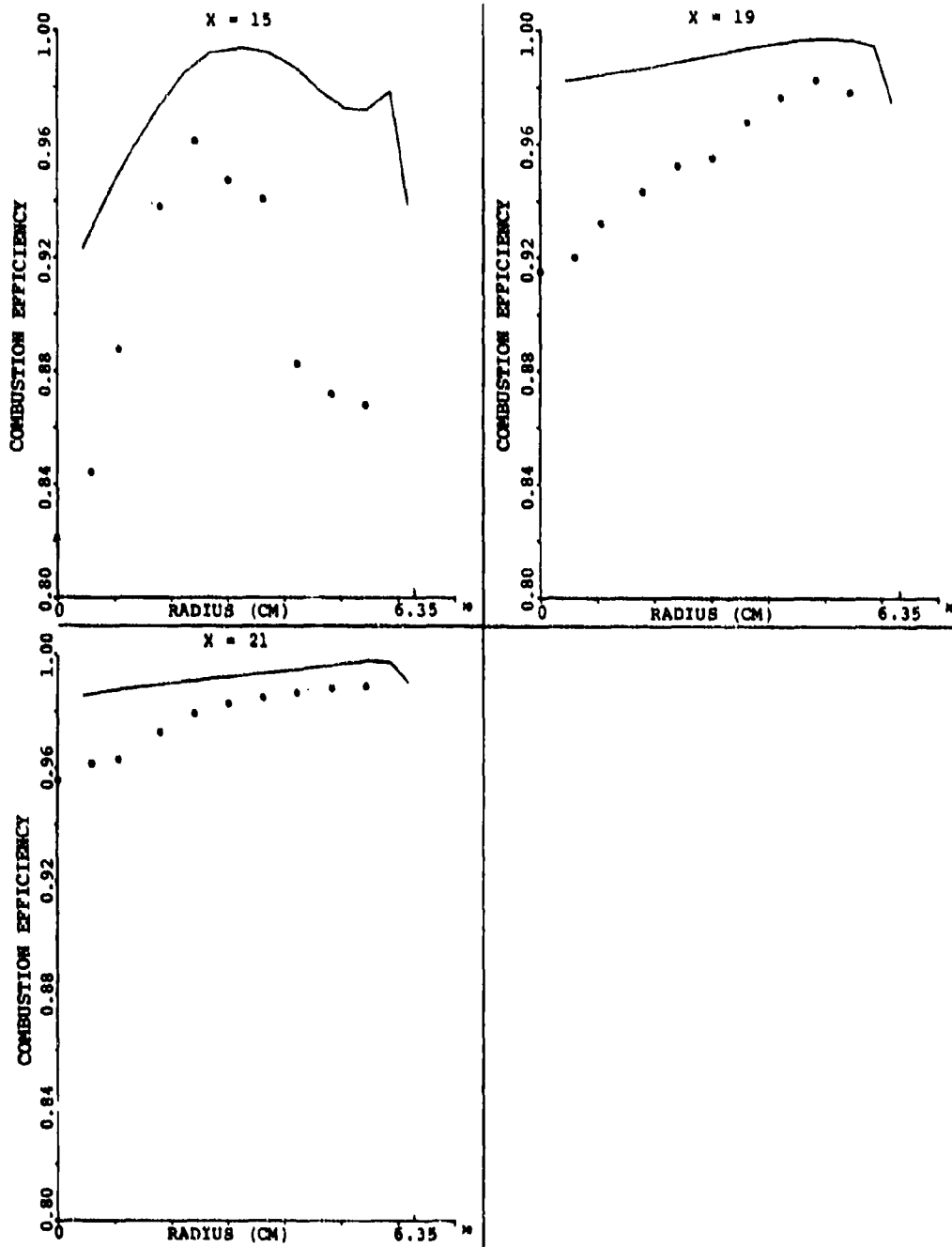
Figure 138. Comparison Between Predicted and Measured Combustion
Efficiency for the X-Y Planes In Between the Primary
Jet for Set-4 of Table 15.

303
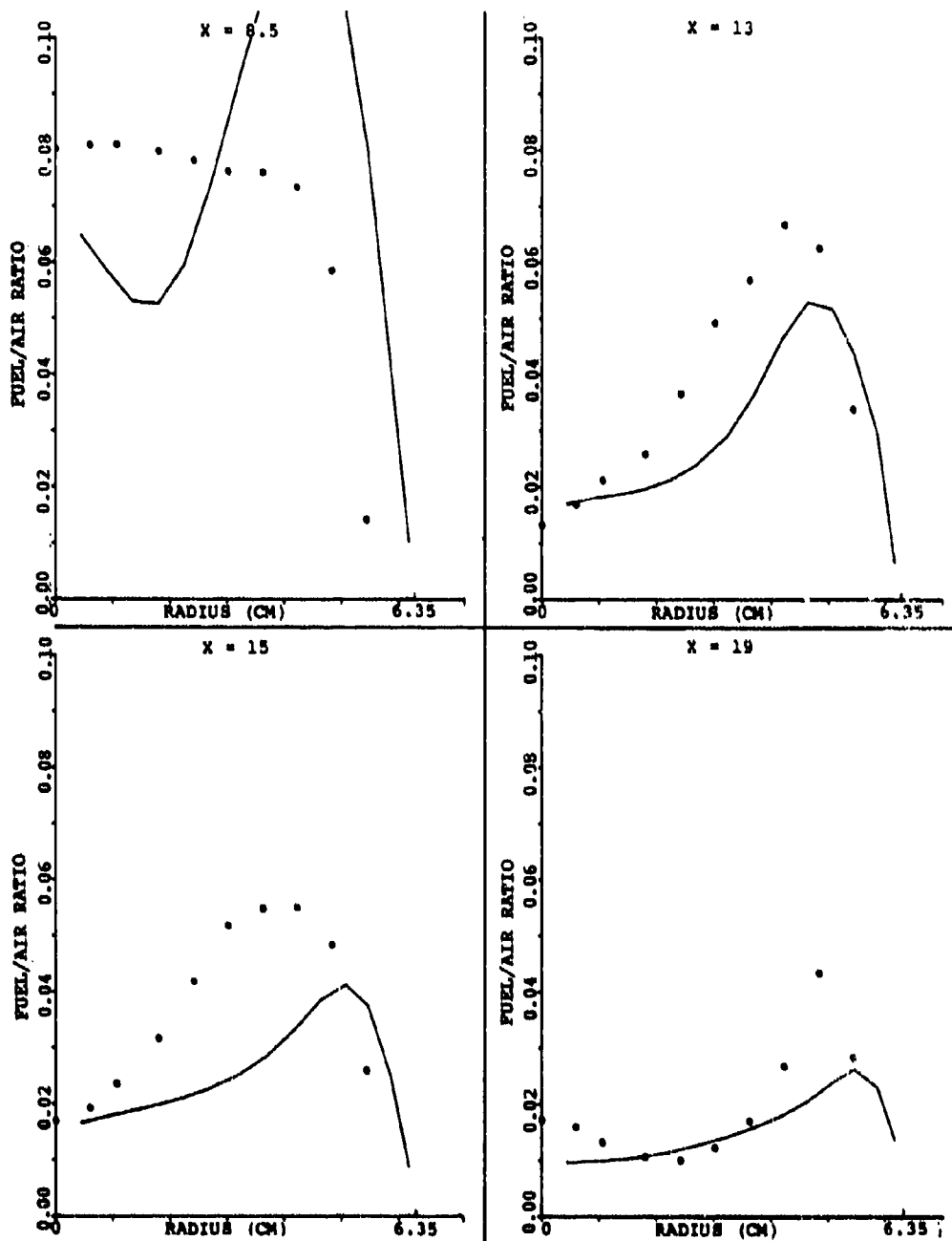
Figure 139. Comparison Between Predicted and Measured Profiles
of Fuel/Air Ratio for the X-Y Planes In Between
the Primary Jet for Set-6 of Table 15.

304
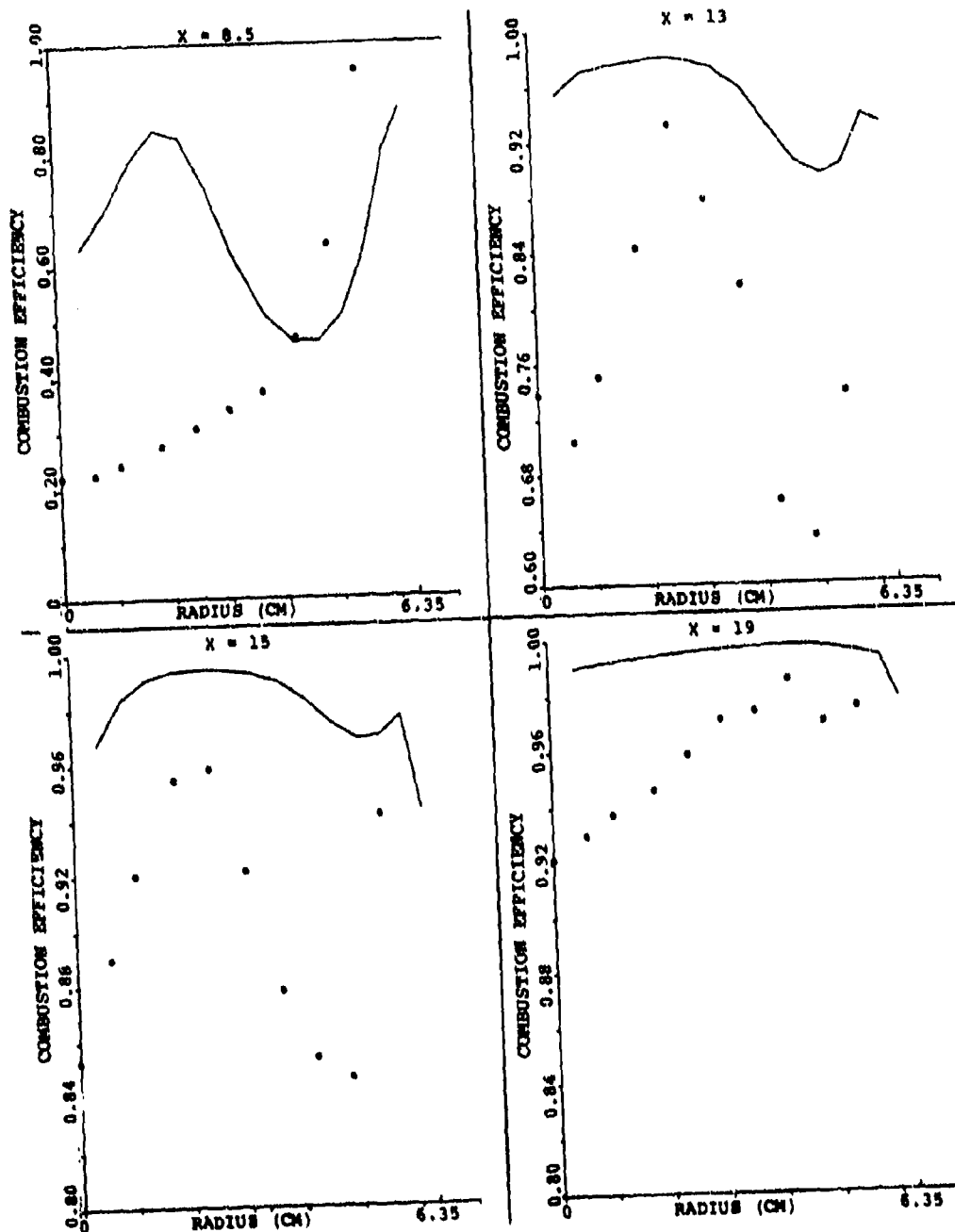
Figure 140. Comparison Between Predicted and Measured Combustion Efficiency for the X-Y Planes In Between the Primary Jet for Set-6 of Table 15.
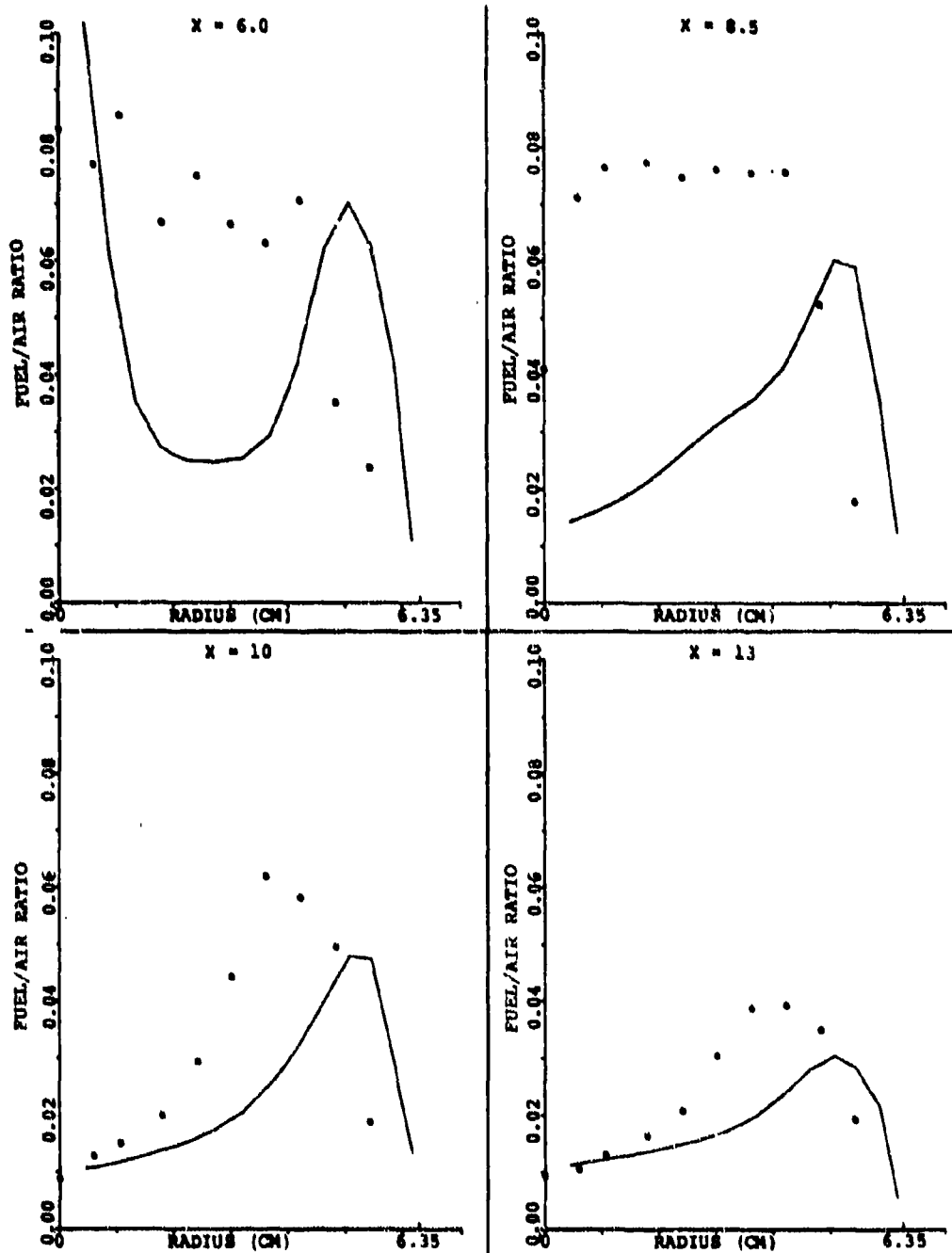
Figure 141. Comparison Between Predicted and Measured Profiles of Fuel/Air Ratio for the X-Y Planes In Between the Primary Jet for Set-5 of Table 15 (Sheet 1 of 2).

Figure 141. Comparison Between Predicted and Measured Profiles
of Fuel/Air Ratio for the X-Y Planes In Between
the Primary Jet for Set-5 of Table 15
(Sheet 2 of 2).

307
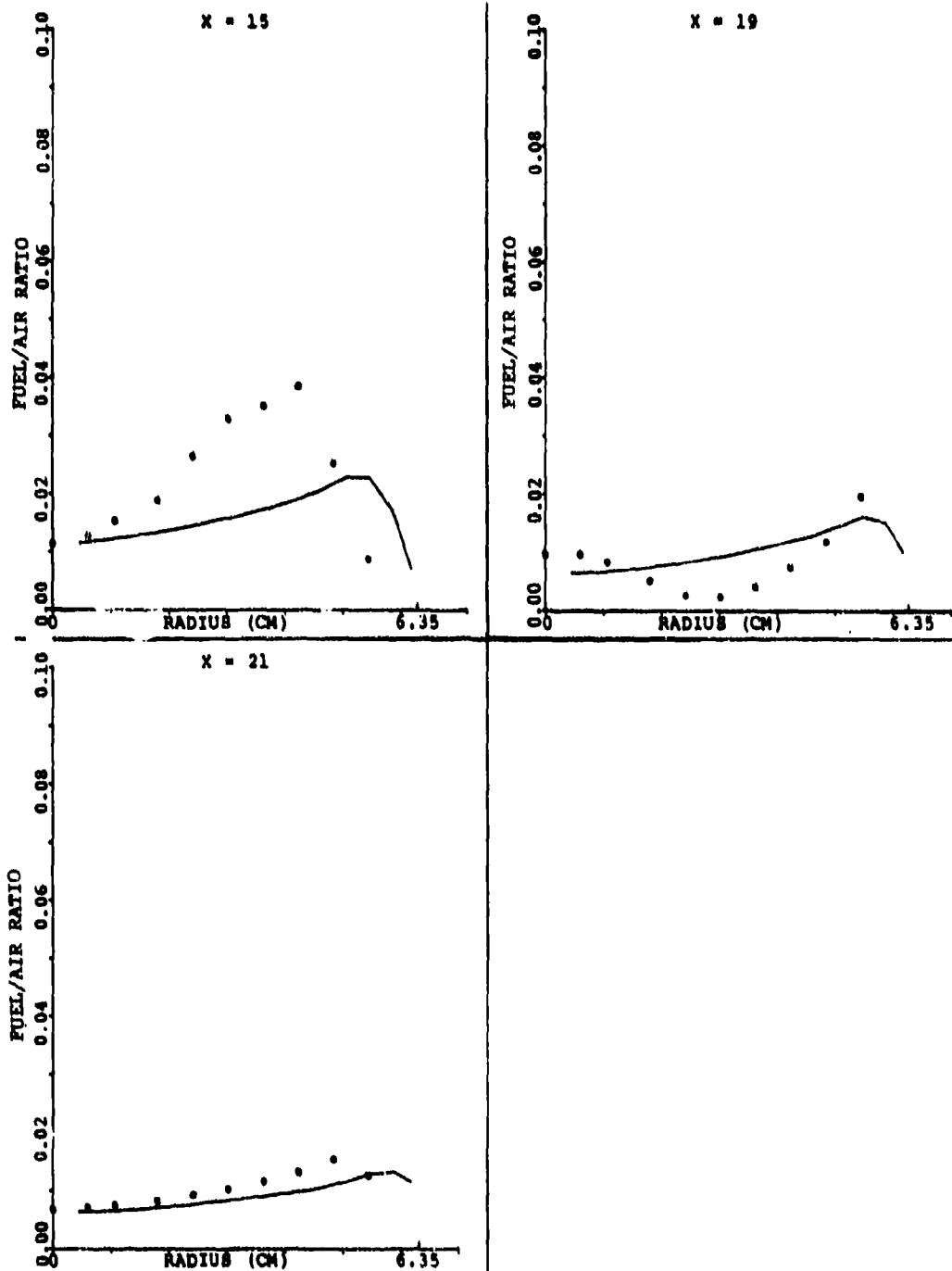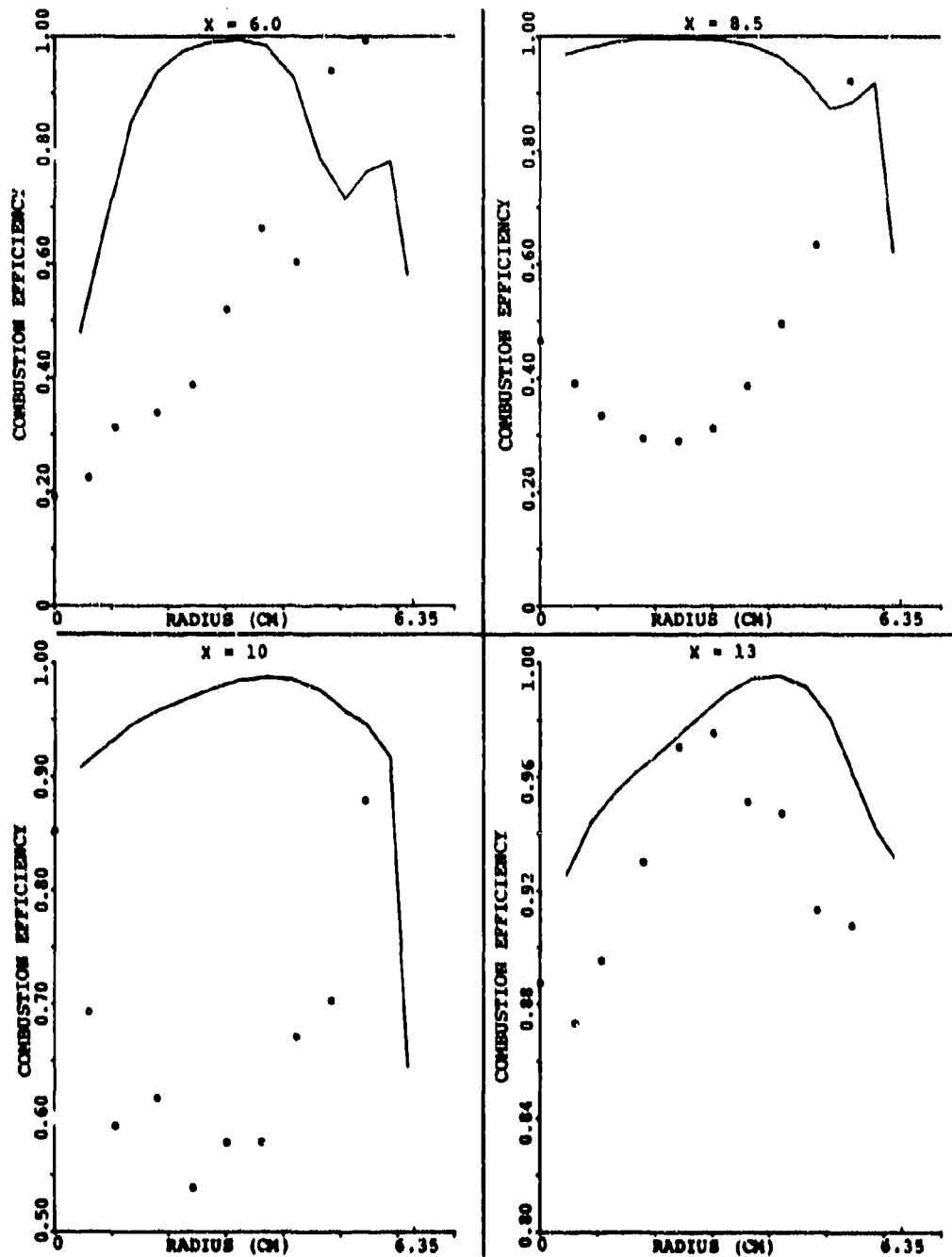
Figure 142. Comparison Between Predicted and Measured Combustion
Efficiency for the X-Y Planes In Between the Primary
Jet for Set-5 of Table 15 (Sheet 1 of 2).
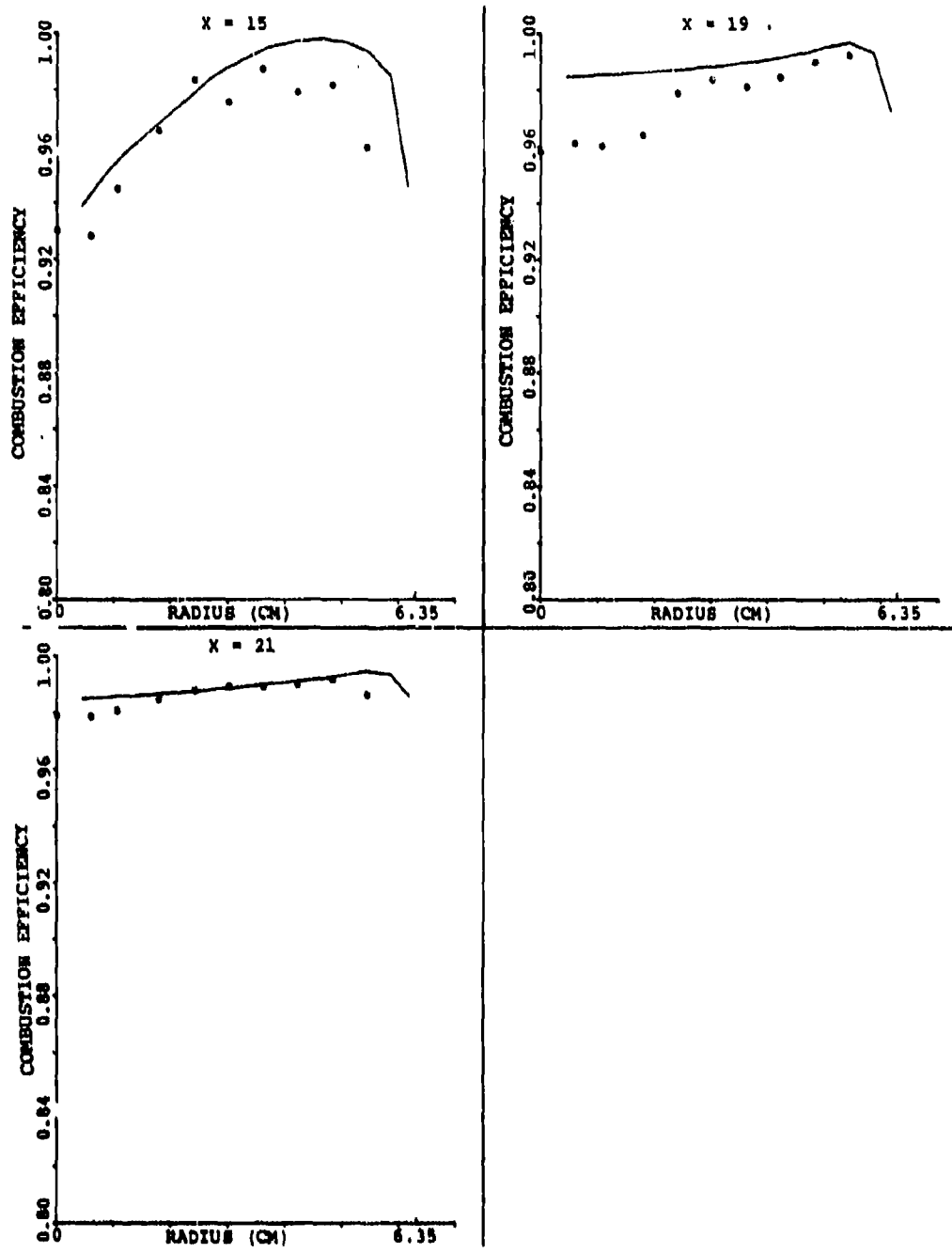
Figure 142. Comparison Between Predicted and Measured Combustion Efficiency for the X-Y Planes In Between the Primary Jet for Set-5 of Table 15 (Sheet 2 of 2).

Figure 143.   Comparison Between Predicted and Measured Profiles
              of Fuel/Air Ratio for the X-Y Planes In Between
              the Primary Jet for Set-7 of Table 15
              (Sheet 1 of 2).

310
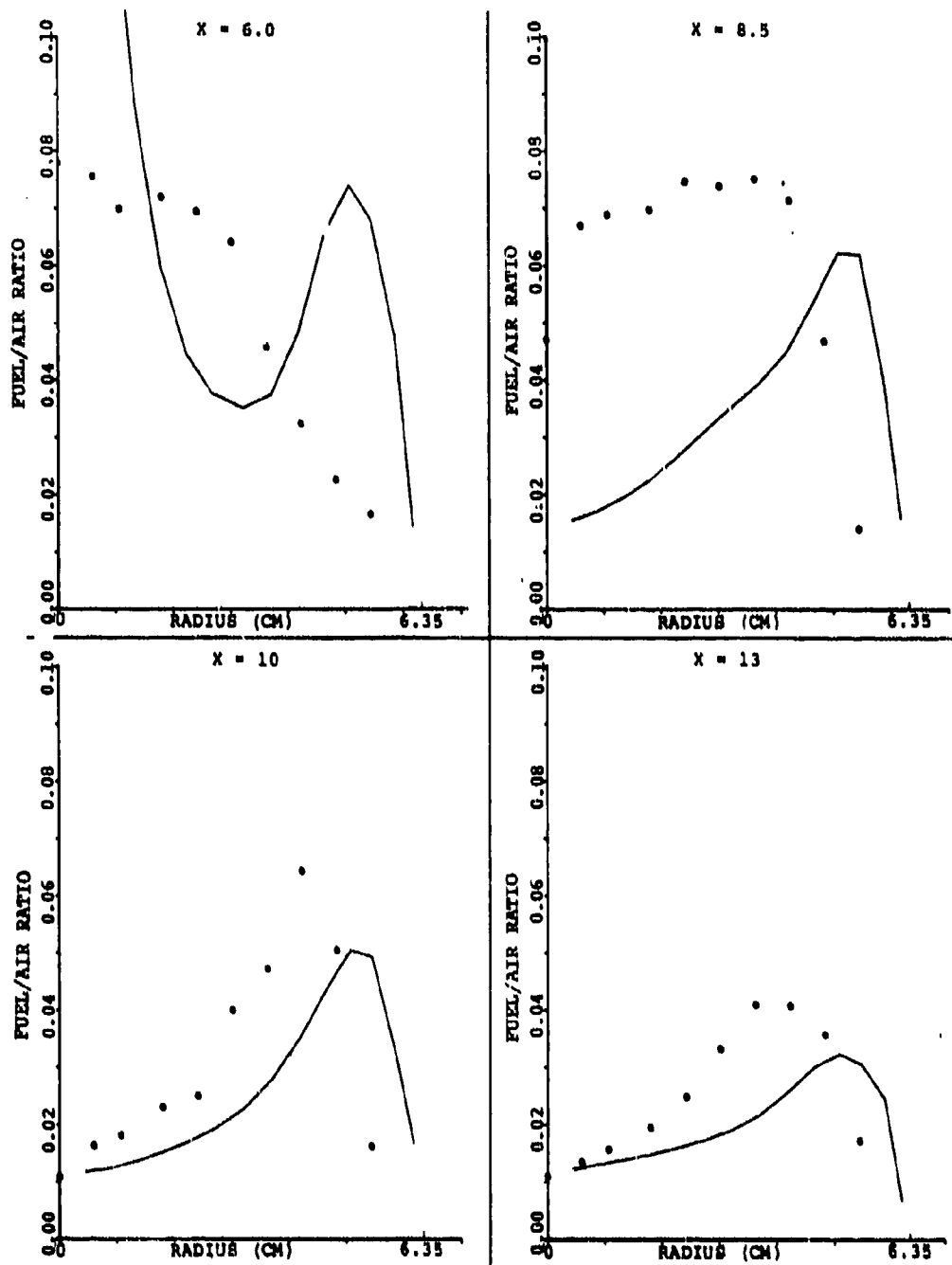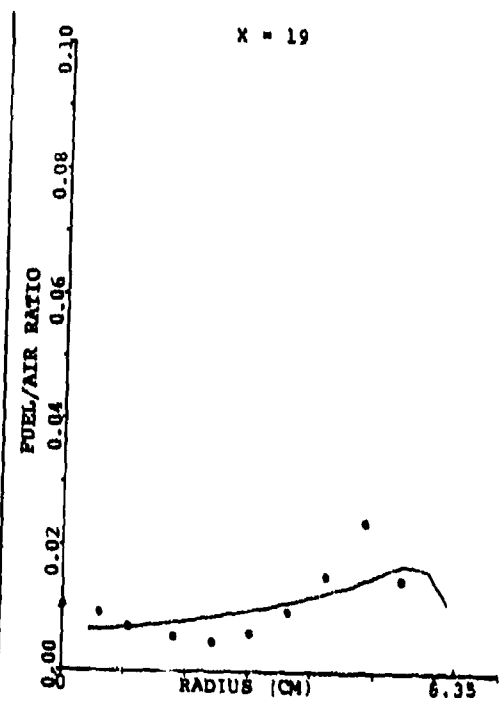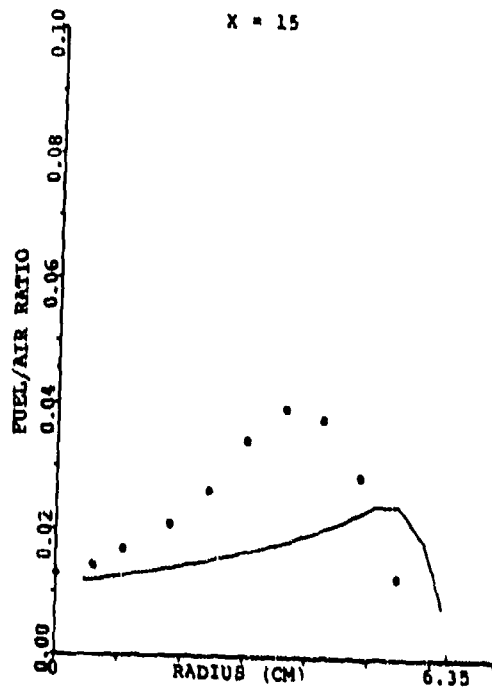
Figure 143. Comparison Between Predicted and Measured Profiles of Fuel/Air Ratio for the X-Y Planes In Between the Primary Jet for Set-7 of Table 15 (Sheet 2 of 2).
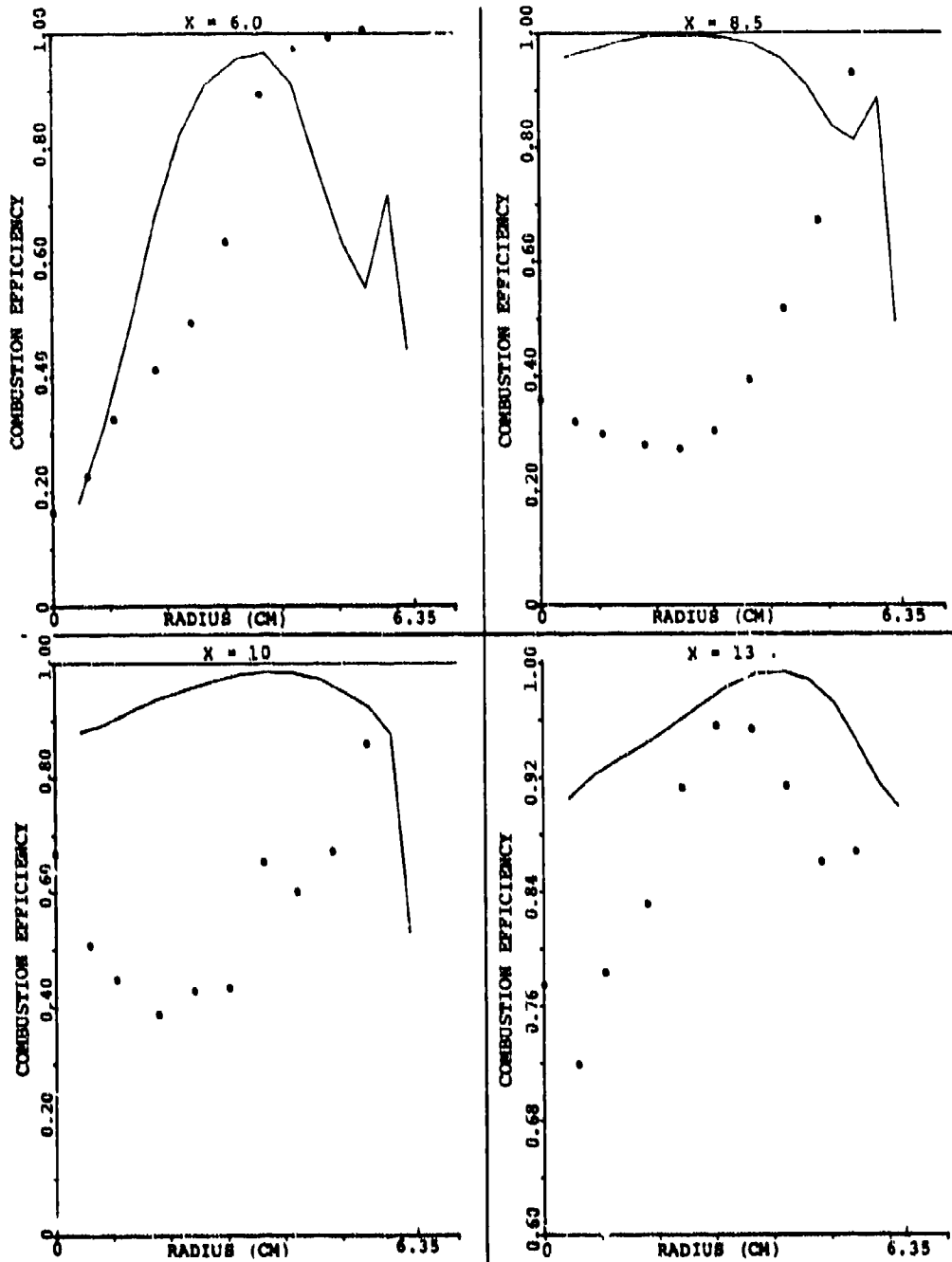
Figure 144. Comparison Between Predicted and Measured Combustion Efficiency for the X-Y Planes In Between the Primary Jet for Set-7 of Table 15 (Sheet 1 of 2).

Figure 1.44. Comparison Between Predicted and Measured Combustion
Efficiency for the X-Y Planes In Between the Primary
Jet for Set-7 of Table 15 (Sheet 2 of 2).

313
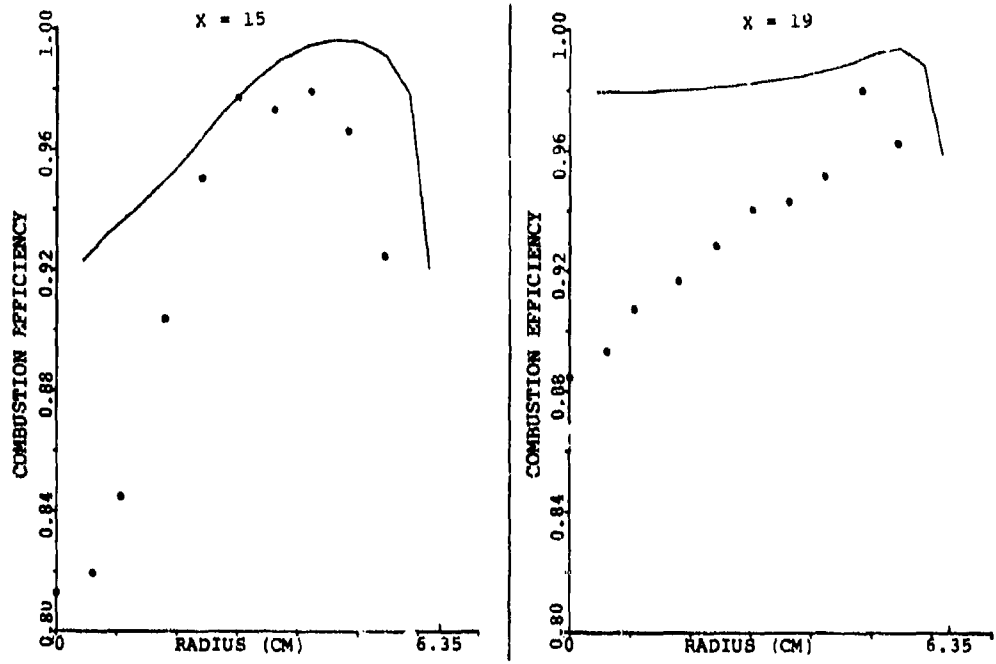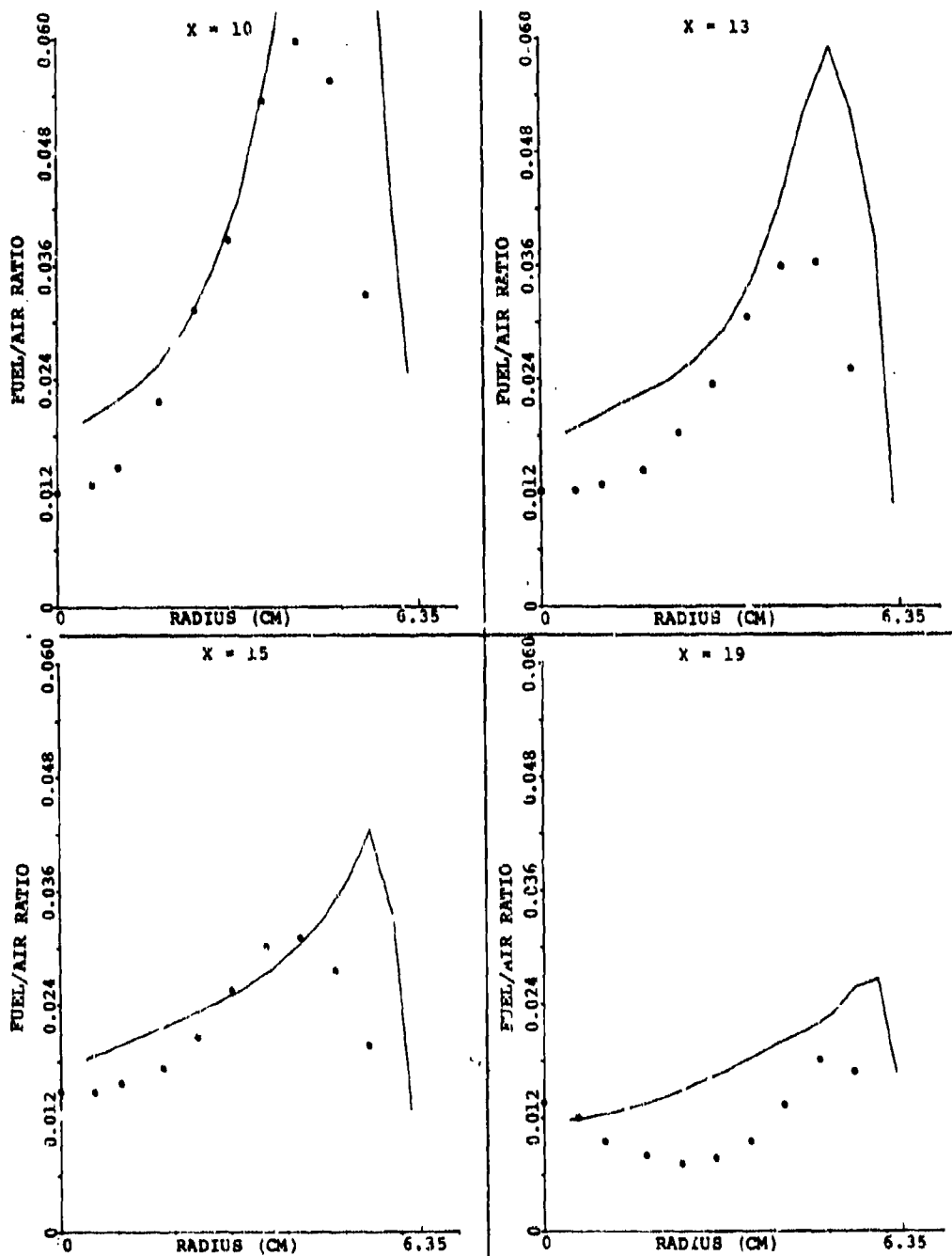
Figure 145. Comparison Between Predicted and Measured Profiles of Fuel/Air Ratio for the X-Y Planes In Between the Primary Jet for Set-9 of Table 16 (Sheet 1 of 2).
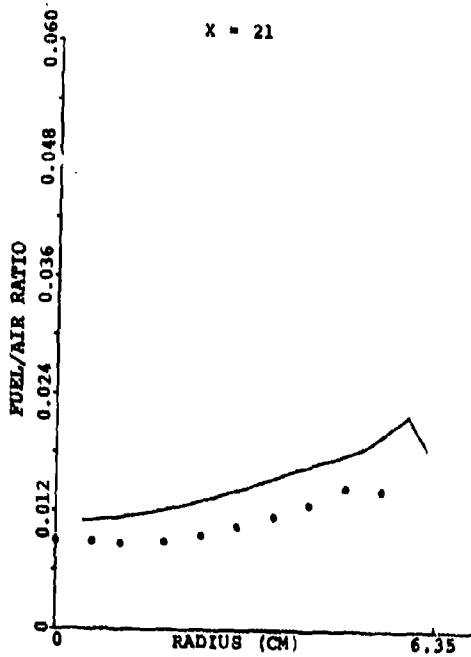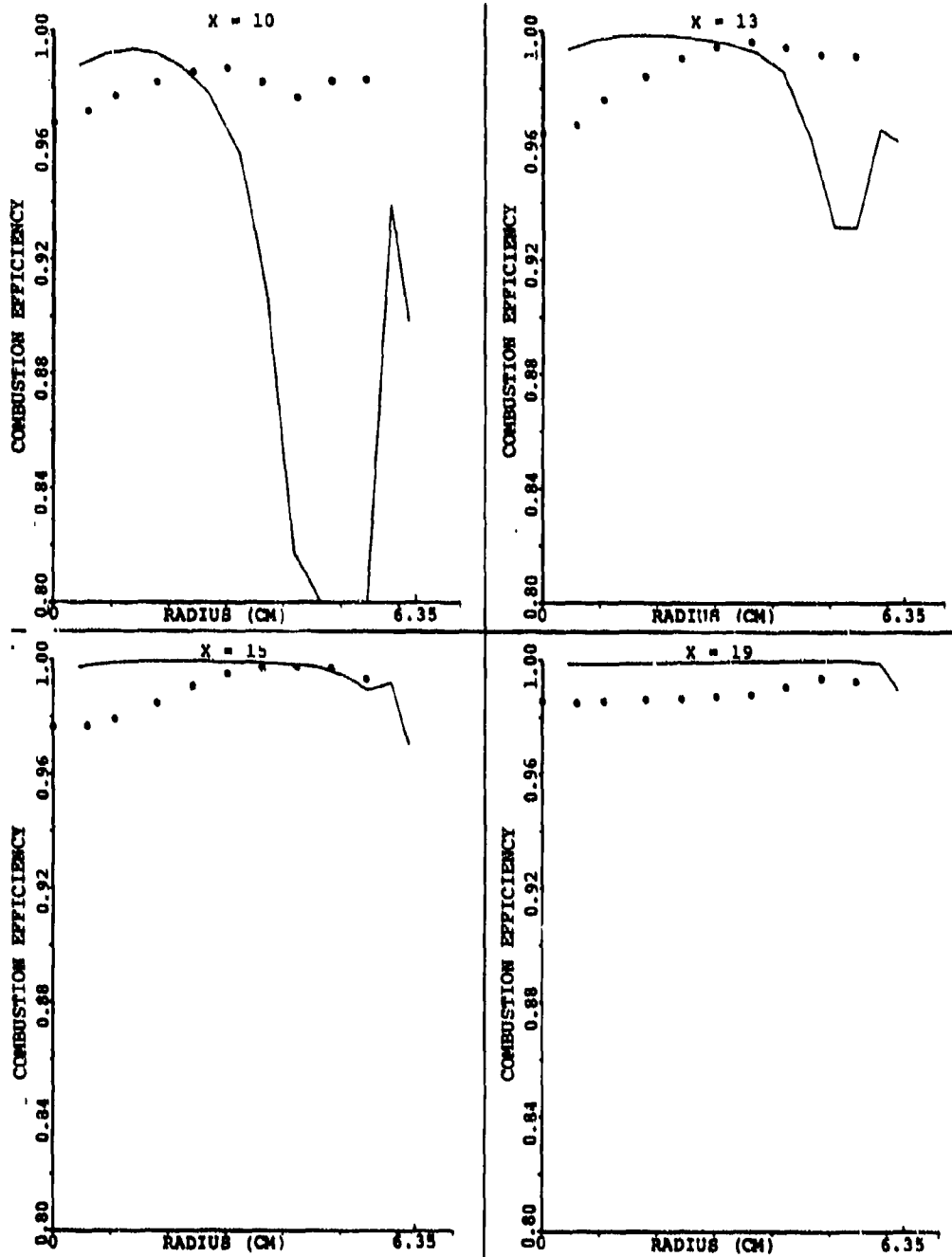
Figure 145.   Comparison Between Predicted and Measured Profiles
of Fuel/Air Ratio for the X-Y Planes In Between
the Primary Jet for Set-9 of Table 16
(Sheet 2 of 2).

Figure 146.   Comparison Between Predicted and Measured Combustion Efficiency for the X-Y Planes In Between the Primary Jet for Set-9 of Table 16 (Sheet 1 of 2).

316
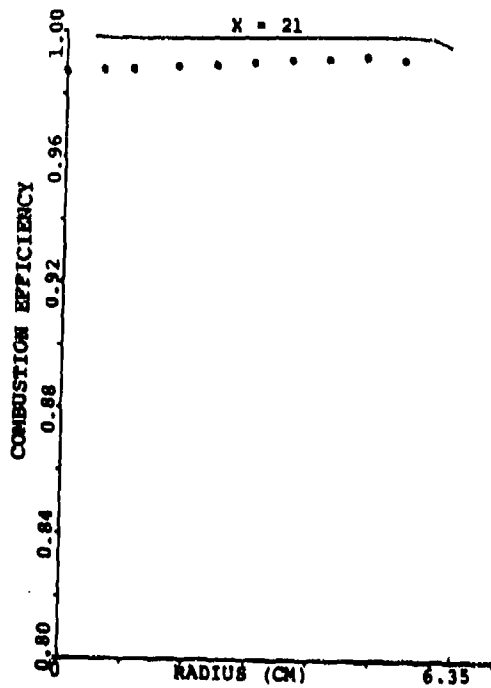
Figure 146. Comparison Between Predicted and Measured Combustion Efficiency for the X-Y Planes In Between the Primary Jet for Set-9 of Table 16 (Sheet 2 of 2).

Figure 147.   Comparison Between Predicted and Measured Profiles
of Fuel/Air Ratio for the X-Y Planes In Between
the Primary Jet for Set-10 of Table 16
(Sheet 1 of 2).

318
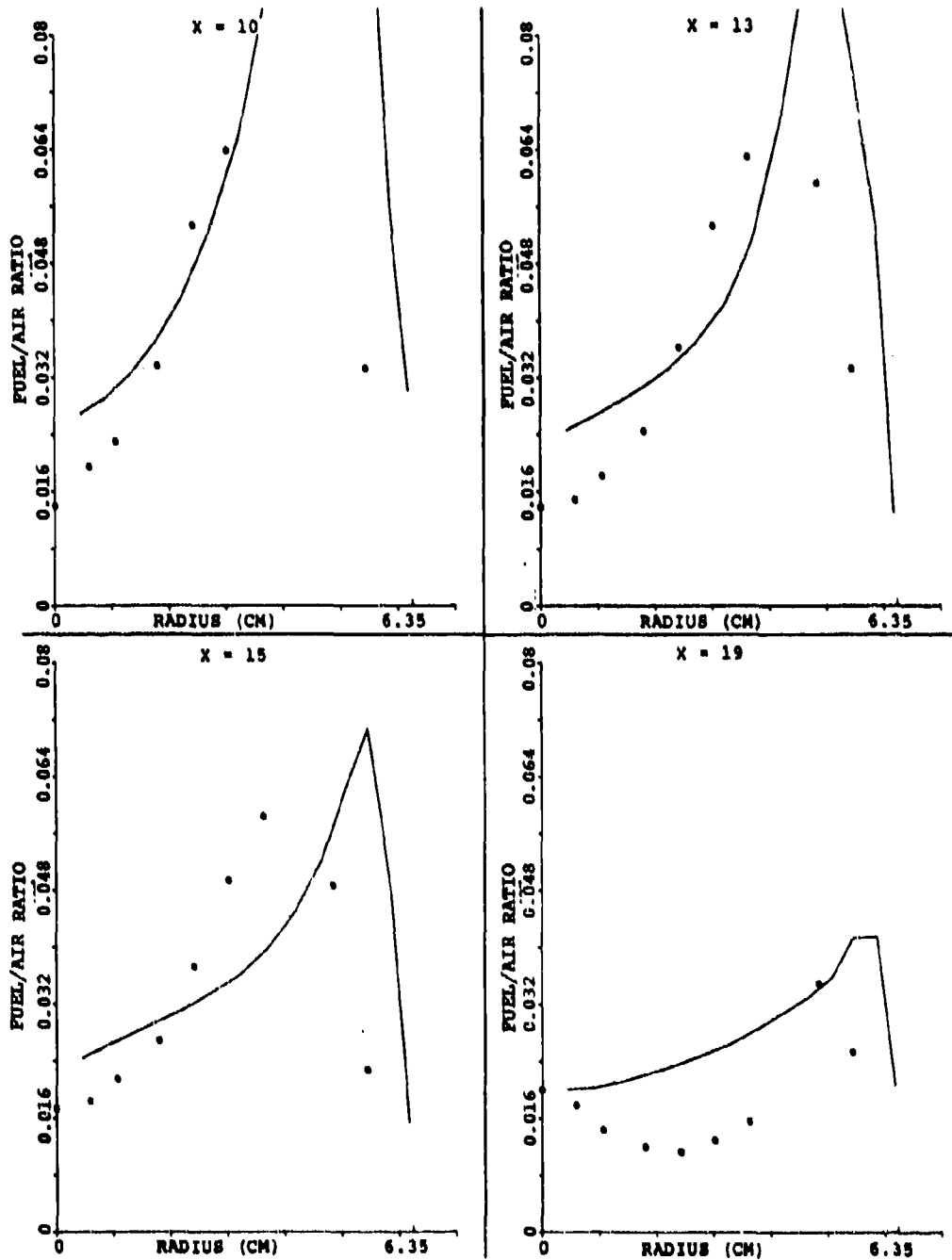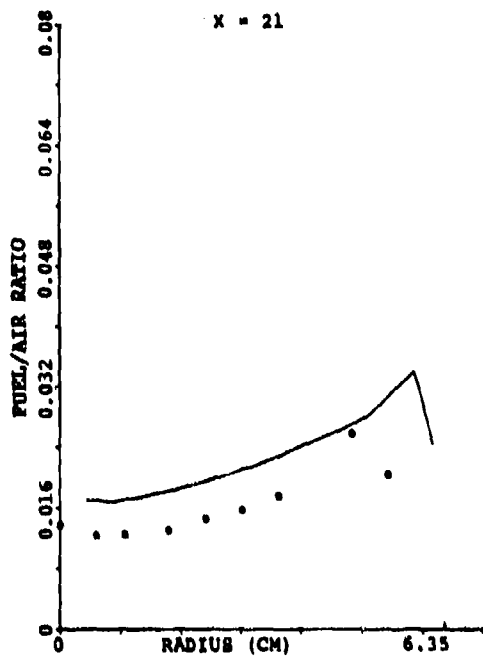
Figure 147. Comparison Between Predicted and Measured Profiles
of Fuel/Air Ratio for the X-Y Planes In Between
the Primary Jet for Set-10 of Table 16
(Sheet 2 of 2).
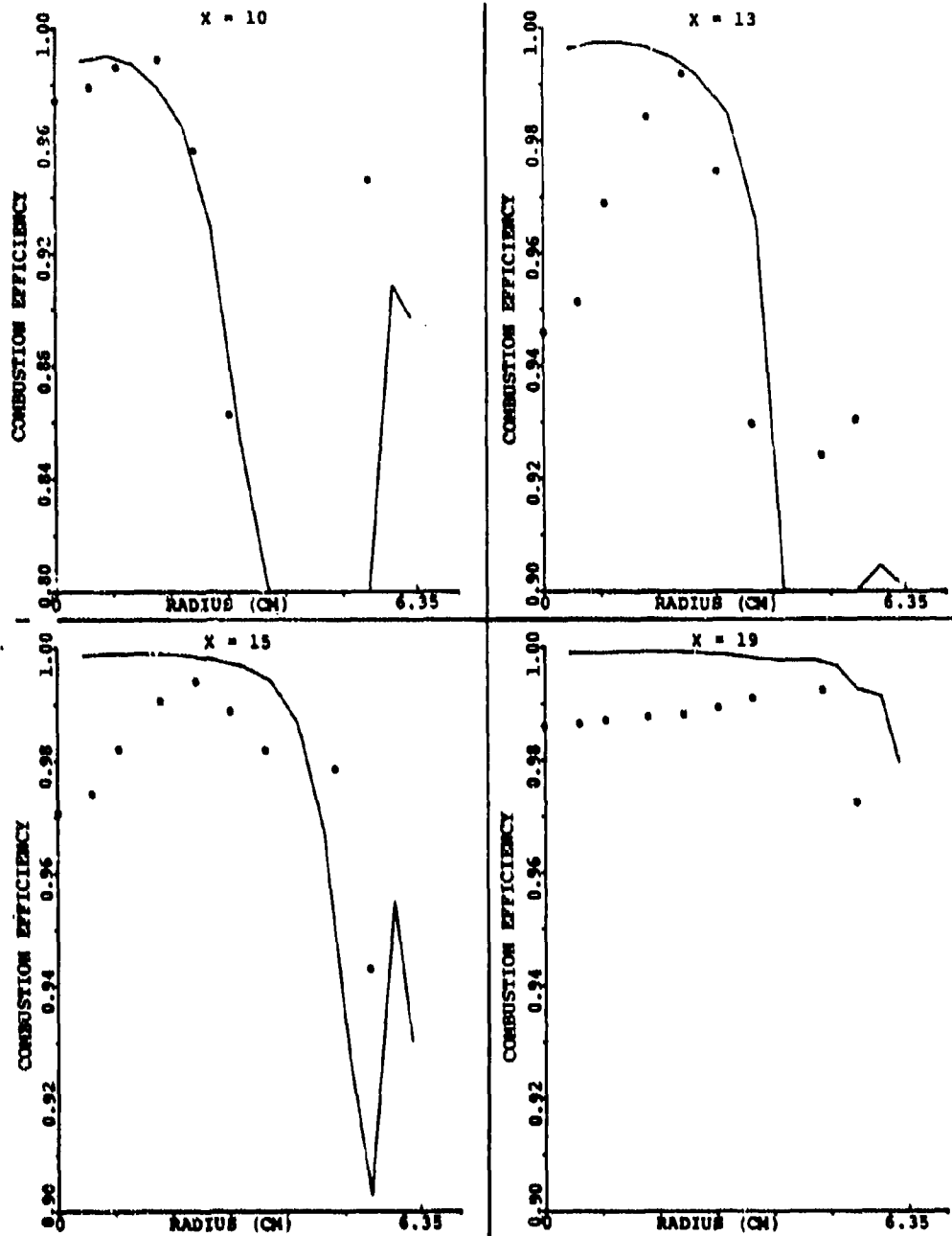
Figure 148. Comparison Between Predicted and Measured Combustion
Efficiency for the X-Y Planes In Between the Primary
Jet for Set-10 of Table 16 (Sheet 1 of 2).
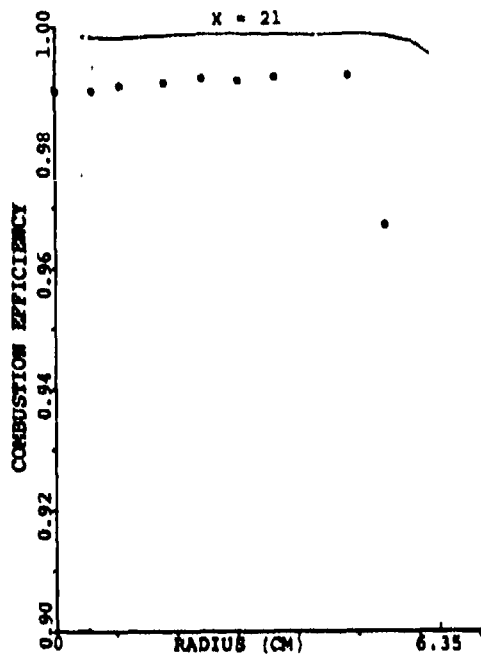
Figure 148. Comparison Between Predicted and Measured Combustion Efficiency for the X-Y Planes In Between the Primary Jet for Set-10 of Table 16 (Sheet 2 of 2).
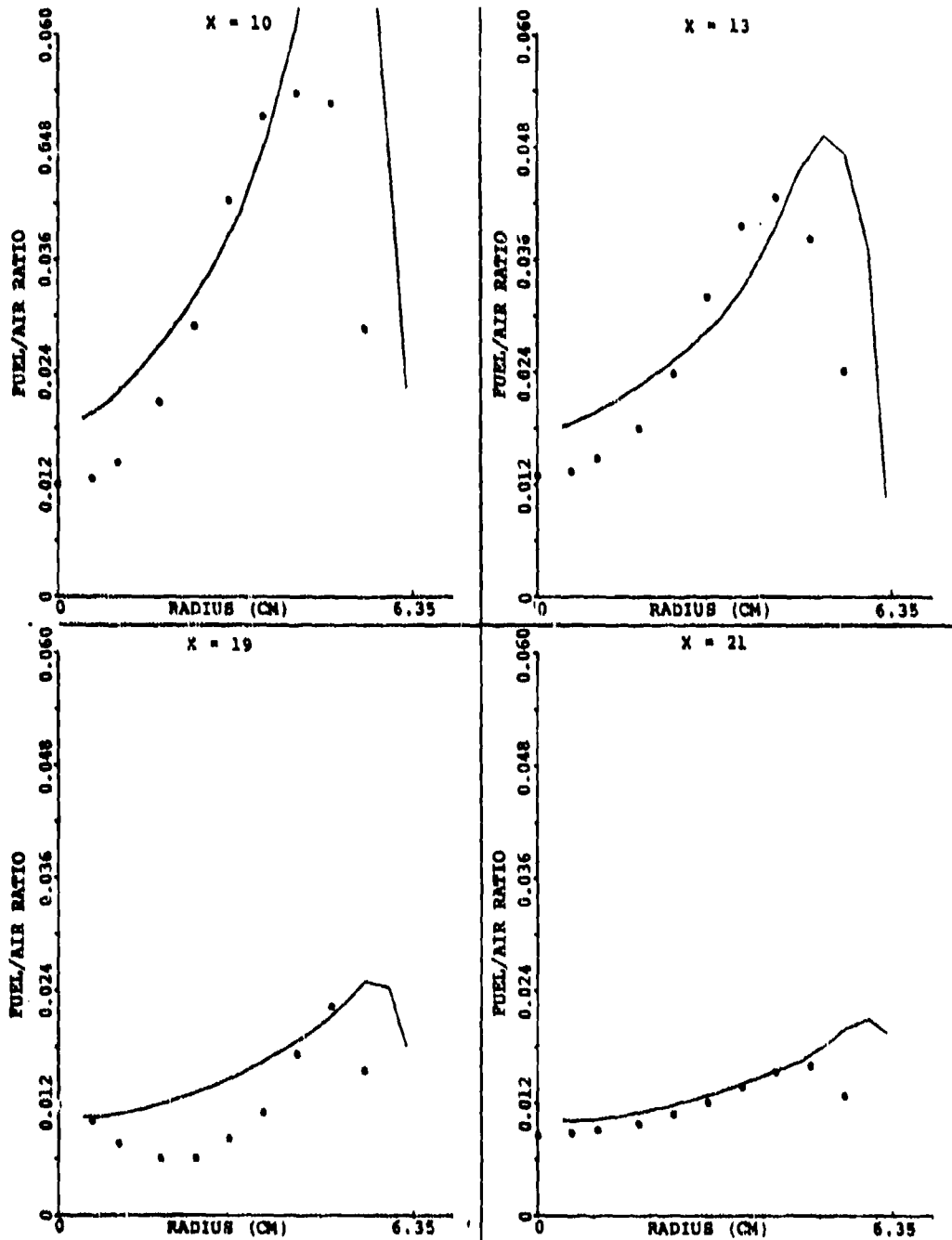
Figure 149. Comparison Between Predicted and Measured Profiles
of Fuel/Air Ratio for the X-Y Planes In Between
the Primary Jet for Set-11 of Table 16.

322
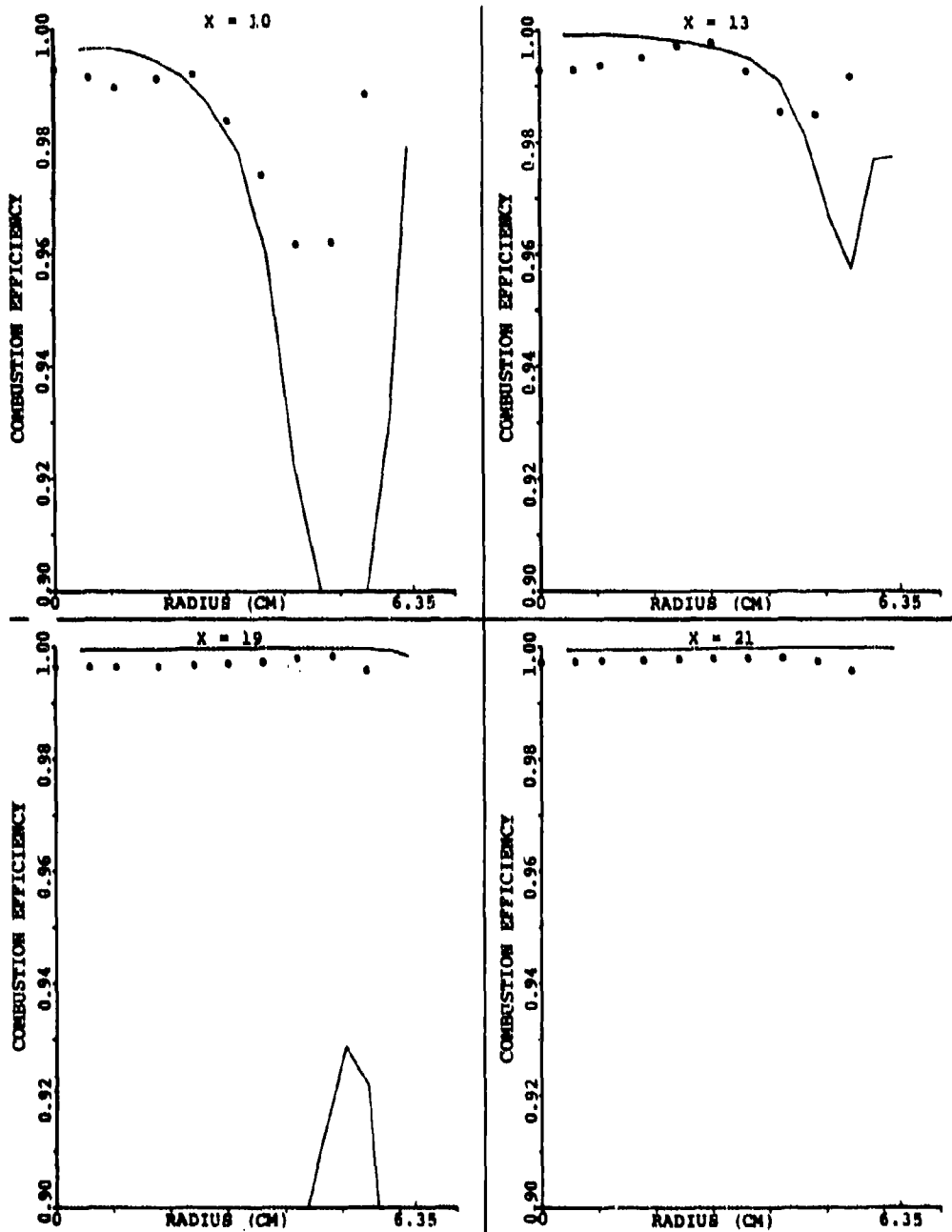
Figure 150.   Comparison Between Predicted and Measured Combustion
Efficiency for the X-Y Planes In Between the Primary
Jet for the Set-11 of Table 16.
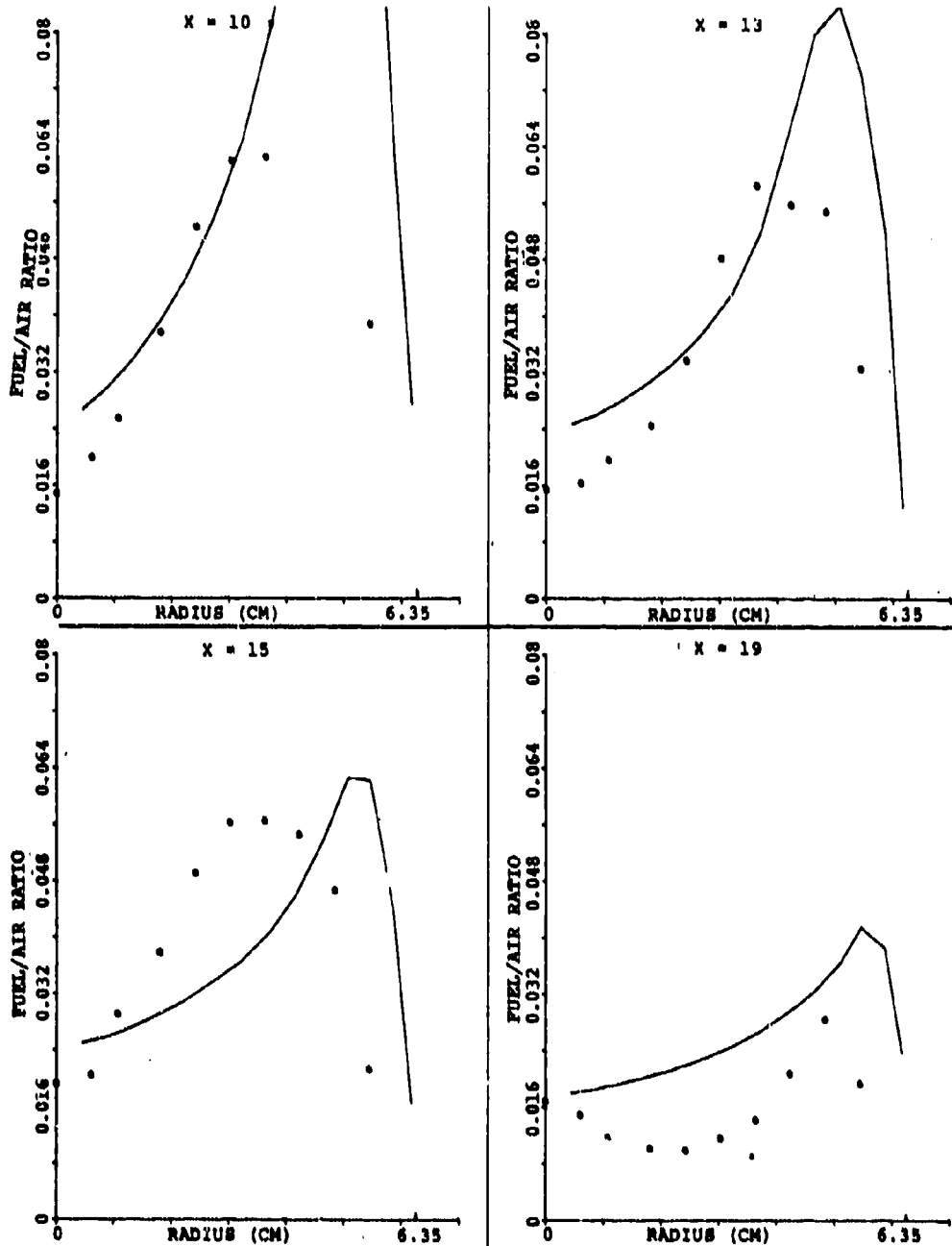
Figure 151. Comparison Between Predicted and Measured Profiles
of Fuel/Air Ratio for the X-Y Planes In Between
the Primary Jet for Set-12 of Table 16
(Sheet 1 of 2).
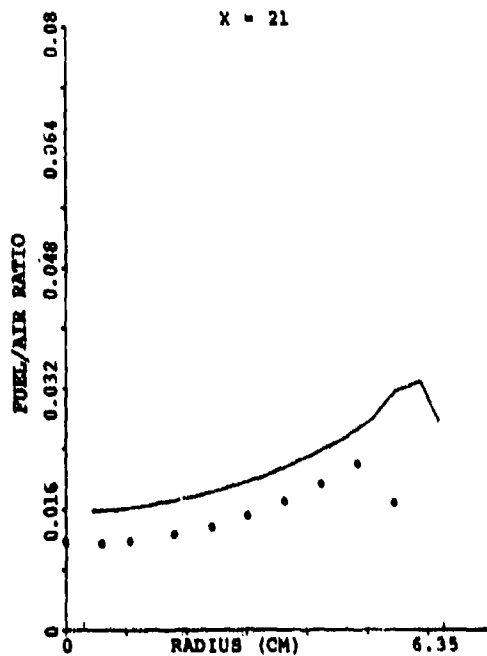
Figure 151. Comparison Between Predicted and Measured Profiles of Fuel/Air Ratio for the X-Y Planes In Between the Primary Jet for Set 12 of Table 16 (Sheet 2 of 2).
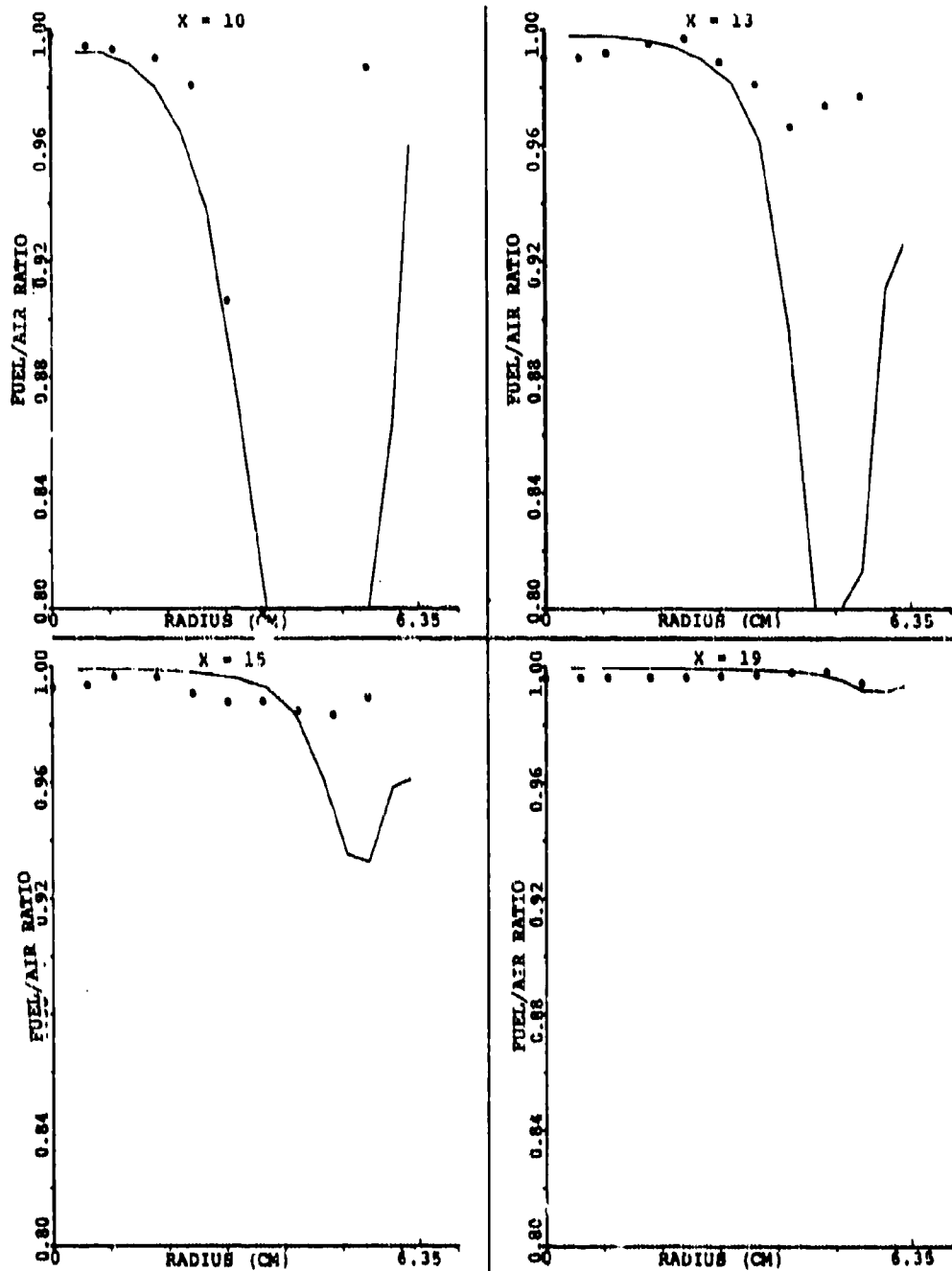
Figure 152.   Comparison Between Predicted and Measured Combustion
Efficiency for the X-Y Planes In Between the Primary
Jet for Set-12 of Table 16 (Sheet 1 of 2).

Figure 152.   Comparison Between Predicted and Measured Combustion
Efficiency for the X-Y Planes In Between the Primary
Jet for Set-12 of Table 16 (Sheet 2 of 2).

327
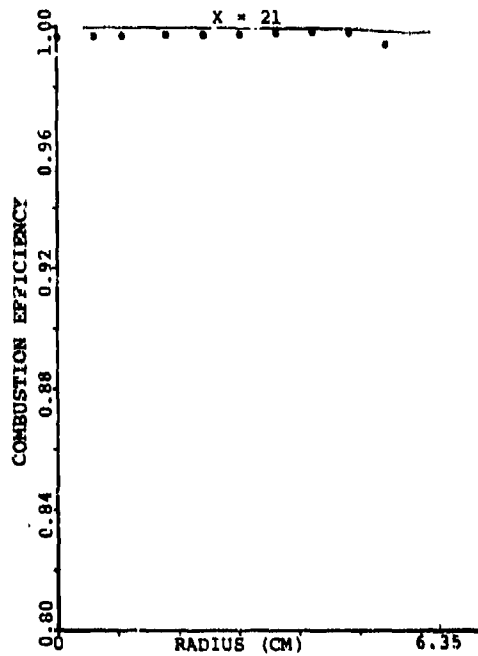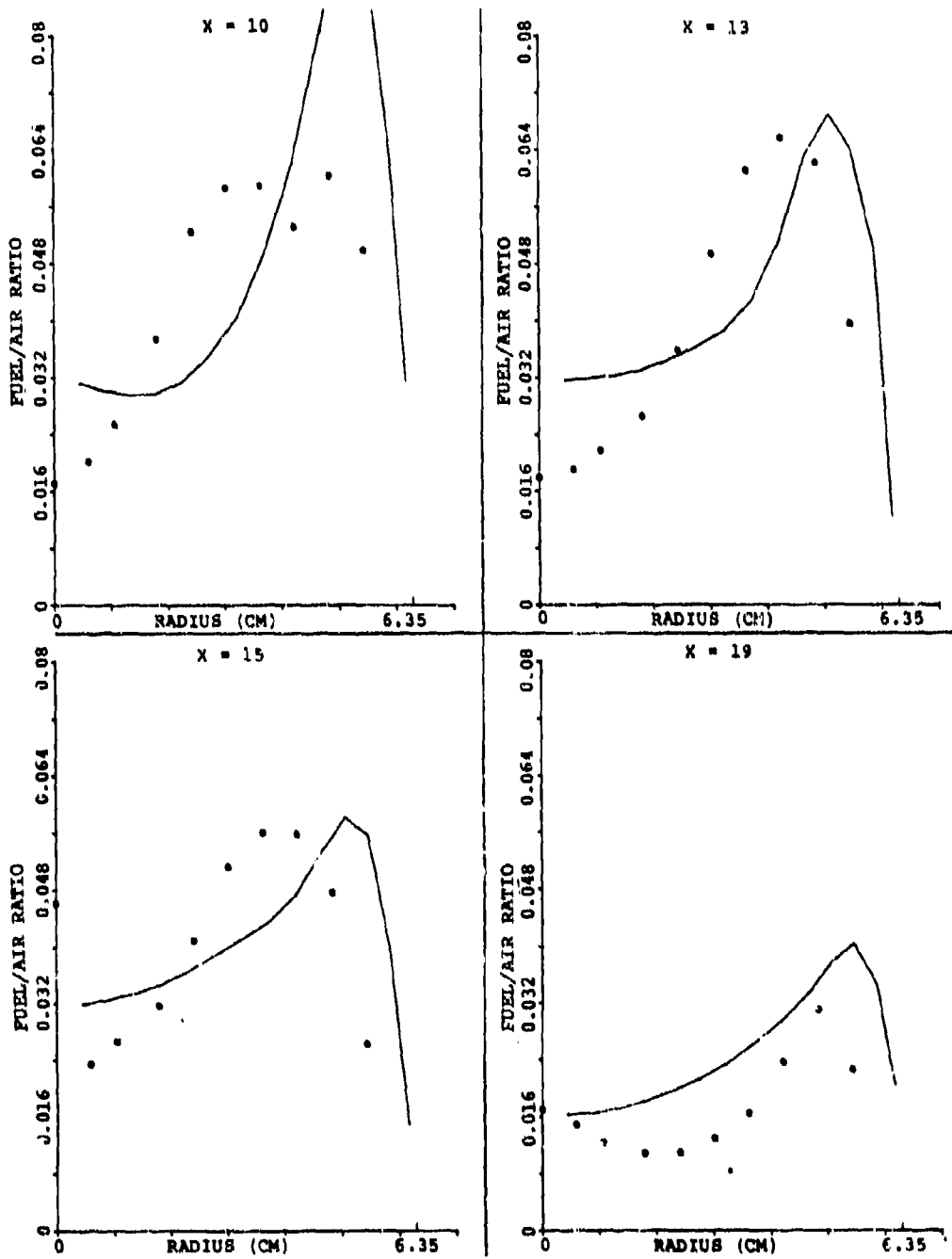
Figure 153. Comparison Between Predicted and Measured Profiles of Fuel/Air Ratio for the X-Y Planes In Between the Primary Jet for Set-13 of Table 16 (Sheet 1 of 2).
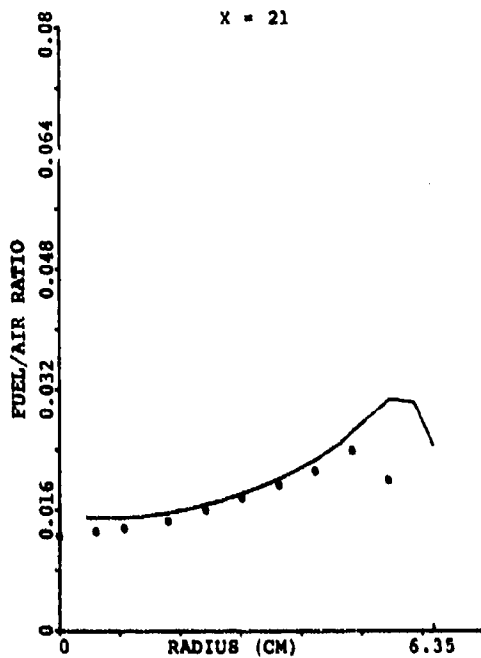
Figure 153. Comparison Between Predicted and Measured Profiles of Fuel/Air Ratio for the X-Y Planes In Between the Primary Jet for Set-13 of Table 16 (Sheet 2 of 2).

Figure 154.   Comparison Between Predicted and Measured Combustion
Efficiency for the X-Y Planes In Between the Primary
Jet for Set-13 of Table 16 (Sheet 1 of 2).

330
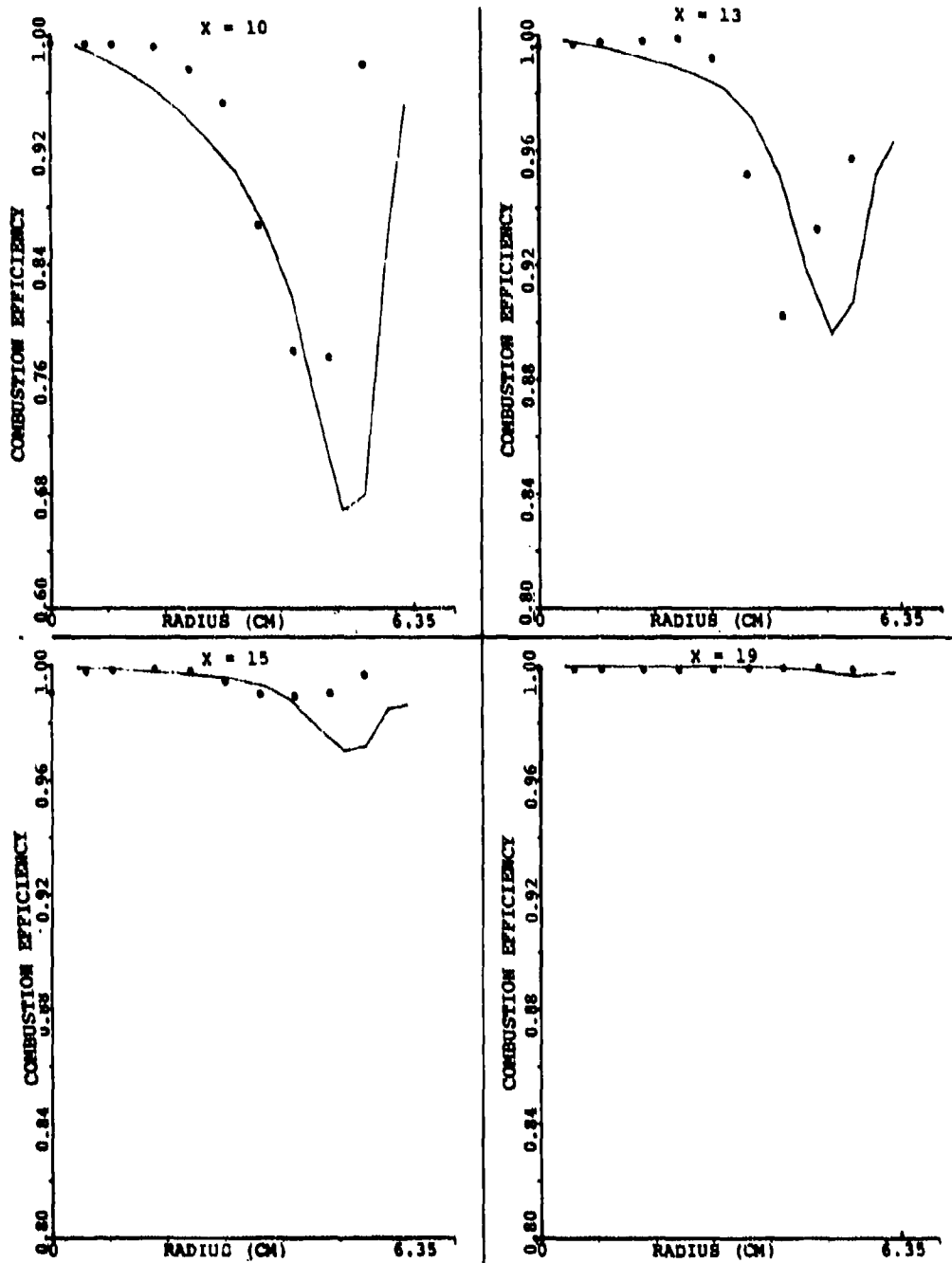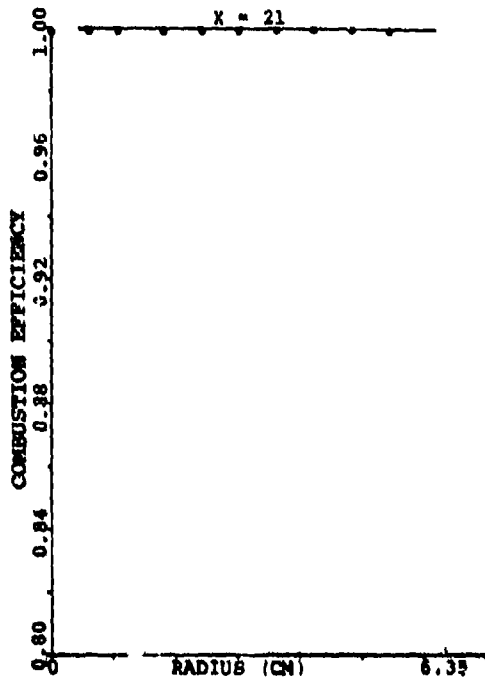
Figure 154. Comparison Between Predicted and Measured Combustion
Efficiency for the X-Y Planes In Between the Primary
Jet for Set-13 of Table 16 (Sheet 2 of 2).

versus the overall fuel/air ratio of 1.6. Decreasing the overall combustor fuel/air ratio increased combustion efficiency at x = 10 and 13 cm. However, further downstream overall combustion efficiency is lower for Set-1.

The effect of an increase in combustor-residence time, and a decrease in pressure drop on the profiles of fuel/air ratio and combustion efficiency can be estimated by comparing results of Set-1 and Set-3, as shown in Figures 133 through 136. Decreasing combustor pressure drop increased the peak value of the fuel/air ratio, and thus decreased the mixedness. Consequently, there was an increase in combustion efficiency; however, the profiles of fuel/air ratio remain similar.

The effect of an increase in pressure on the combustor performance for the same residence time, combustor inlet temperature, and overall fuel/air ratio can be obtained by comparing Sets-2, -4, and -6 (Figures 117, 120, 137-140). A similar comparison at the lower fuel/air ratio of 0.006 can be made by referring to Sets-1, -5, and -7 (Figures 133, 134, 141-144). A small decrease in the level of mixedness was noticed with increasing pressure. The profiles of fuel/air ratio remained unchanged with pressure. As expected there was an increase in overall combustion efficiency with pressure. However, the increase was mostly due to an improvement in combustion efficiency away from the liner wall. The level of wall quenching did not change with pressure. The conclusions in regard to fuel/air ratio profiles of Sets-1, -5, and -7 were similar to those made above for the high fuel/air ratio test cases. The improvement in combustion efficiency occurred over the entire cross-section of the combustor.

The test data with Jet-A fuel was taken at conditions simulating different cycle-pressure ratios at a constant combustor corrected-flow rate. Set-8 data was taken to compare performance

332

with liquid versus gaseous fuel, as given by Set-2. The effect of engine cycle-pressure ratio and fuel/air ratio can be illustrated by Sets-9 through -13, as presented in Figures 145 through 154.

The effect of pressure was negligible on the predicted fuel/air ratio profiles downstream from the dilution orifices. However, there was a significant increase in maximum values of fuel/air ratio in the primary and intermediate regions with an increase in pressure. The effect of pressure was more pronounced in this regard with liquid, as compared to gaseous fuel.

Increasing fuel/air ratio extended the flame further into the intermediate zone with a resulting decrease in combustion efficiency in the primary and intermediate zone. However, the reaction was mostly completed by $x = 21$ cm, where the effect of fuel/air ratio on combustion efficiency values and profiles was negligible. Increasing the pressure improved combustion efficiency in the primary and intermediate regions. But since reaction was mostly completed by $x = 21$ cm, the chamber pressure had no effect on the combustor efficiency.

E.   Radiation Model Validation

As previously reported in Section IV.E, radiation measurements through the primary and dilution orifices were made on the can combustor at various inlet flow conditions. The following set of conditions was selected to validate the six-flux radiation model employed in the 3-D Performance Model and simultaneously the two-flux model incorporated in the 2-D Program.

<div align="center">

RADIATION MODEL TEST CONDITIONS

P_3 = 1013 kPa

T_3 = 622 K

W_{a_3} = 1.07 Kg/Sec

f/a = 0.0132

</div>

The combustor was modeled using a grid network identical to that employed for the can reacting flow mapping comparisons. For the absorption and scattering coefficients, constant values of 0.1 and 0.01, respectively, were selected. Obviously, these quantities were not constant in a combustor since they vary with the chemical species present and their concentrations. However, data on the variation is scarce.

When the flow-field had converged to an acceptable level of mass-error, the net radiation flux, in the +y direction through the primary and dilution orifices, was calculated and is compared to the following measured values:

	Primary	Dilution
Measured Radiation Flux (J/M^2-Sec)	6.62×10^5	9.2×10^4
Calculated Radiation Flux (J/M^2-Sec)	5.21×10^5	1.44×10^5

Though the model is slightly underpredicting the flux, manipulation of the absorption and scattering coefficients, to obtain better agreement, was deemed pointless considering the quantity of unknowns involved in the experimental measurements, such as temperature and specie concentrations. Within the scope of the measurements, the above agreement is certainly acceptable.

Figure 155 shows a contour plot of the net radiation flux to the can combustor wall for the above case. Regions of low flux are clearly visible around the primary and dilution orifices and the cooling slots.

F.   Transition Mixing Model Validation

The transition mixing data, described in Section IV.B.4, was used to validate the Transition Mixing Model. Although the data was highly three-dimensional in nature it was concluded that a "first level" validation could be obtained.

First, the effect of step size on the predicted results was studied. It was found that with 98 equally spaced cross-stream nodes, there were only small differences between the results obtained with marching step sizes of 0.05 and 0.025 times the channel height. Therefore, all of the results reported here were obtained with maximum step size being less than 0.025 channel height.

The effect of initial turbulence kinetic energy level, normalized by the square of the time-mean velocity of individual streams, and length scale normalized by the channel height of cold and hot stream passages on the transition liner exit temperature profiles is shown in Figure 156. The computation was started with initially uniform mass averaged velocities for the 200-degree sector, which lies in between the main and start nozzle ports as explained in Section IV.H.
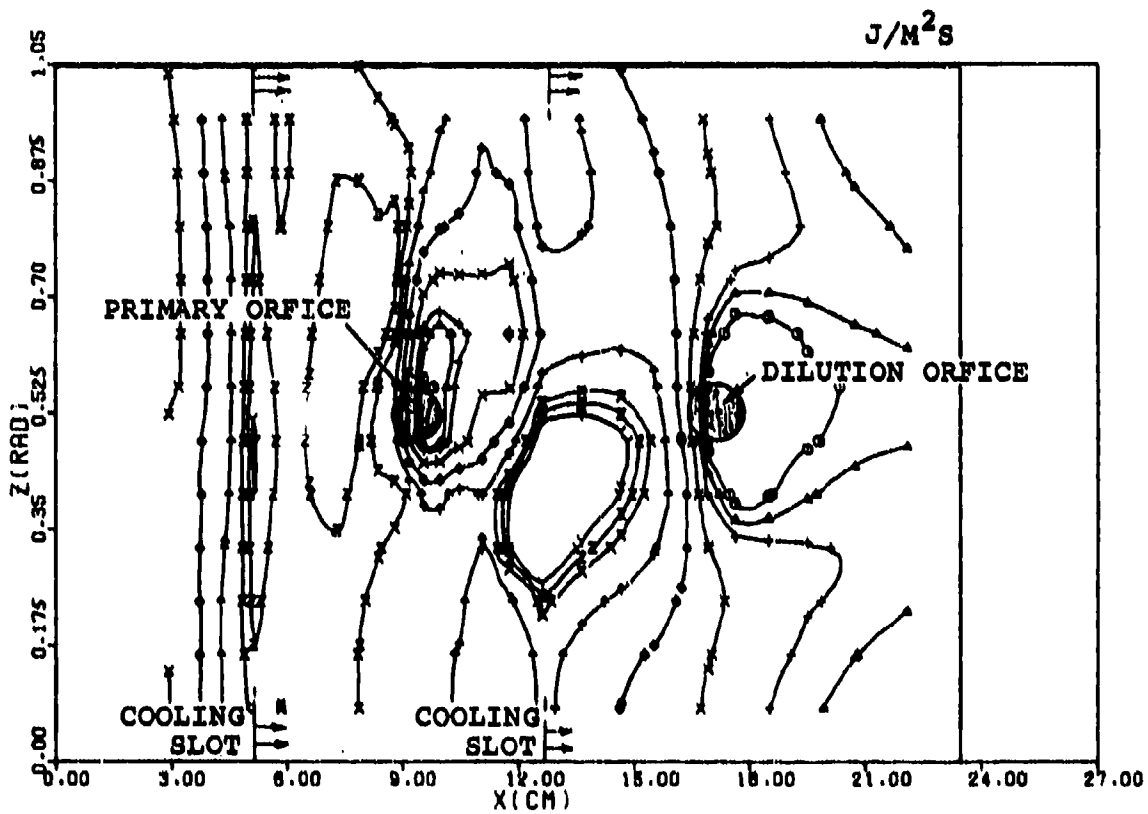
Figure 155. Contours of Net Radiation Flux to the
Liner Wall.

336
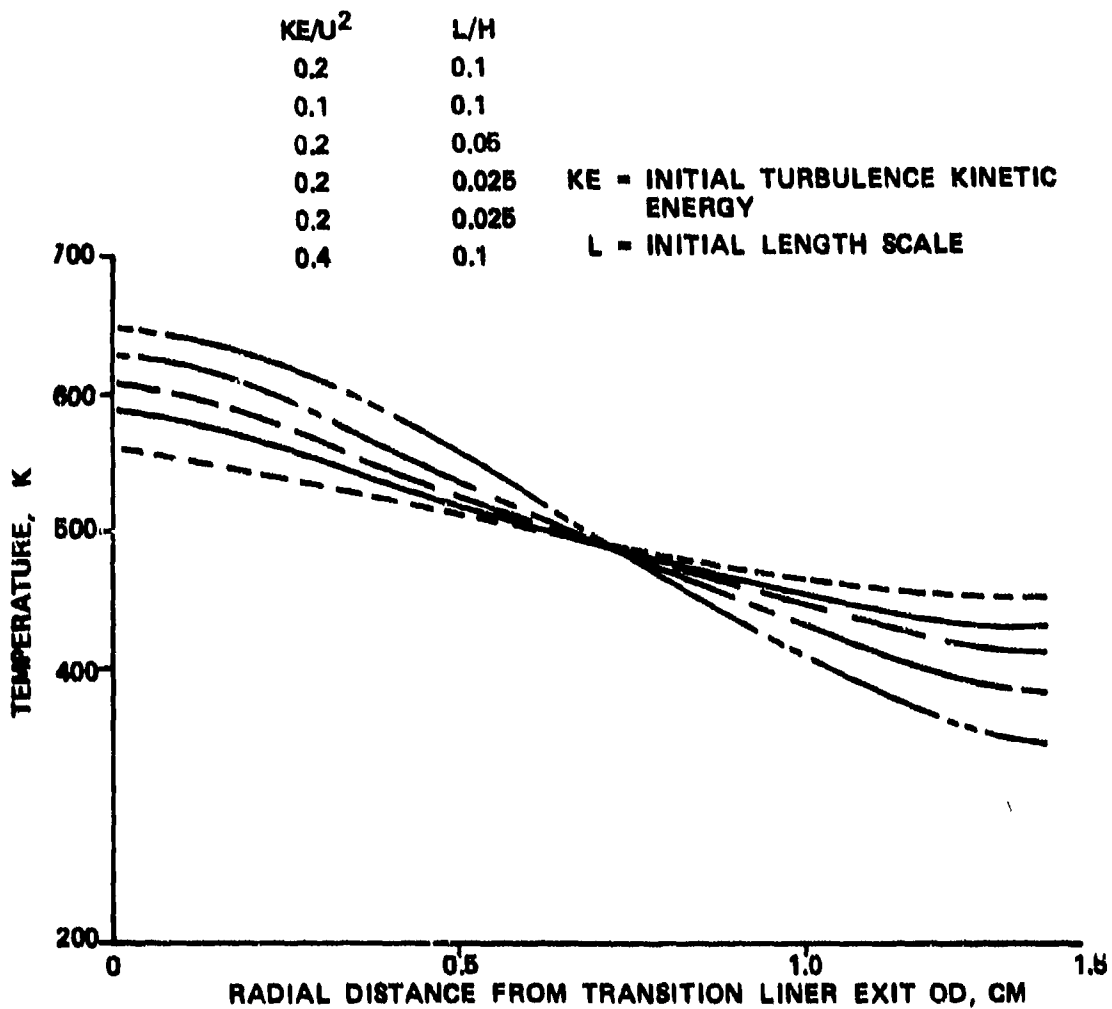
Figure 156. Effect of Initial Turbulence K.E. and
Length Scale on Exit Temperature
Profiles for Scan #1.

337

Predicted exit temperature profiles for scans 1 through 5 and 2-1 through 2-5 are shown in Figures 157 and 158, respectively. Each scan corresponds to a particular hot and cold flow rate as listed at the top of the figure with Figure 157 for cold flow from upper half and Figure 158 for cold flow from the lower half. Also given are the maximum, minimum, and average temperatures over the entire transition liner exit.

A comparison between measured and predicted TSF ($\Delta \left[T_{max} - T_{avg} \right] / T_{avg}$) is shown in Figure 159. The agreement is reasonably good in that the two-dimensional model is being used to correlate a three-dimensional flow with incomplete initial profile data, particularly with regard to the velocity and the turbulence intensity and scale profiles.

338
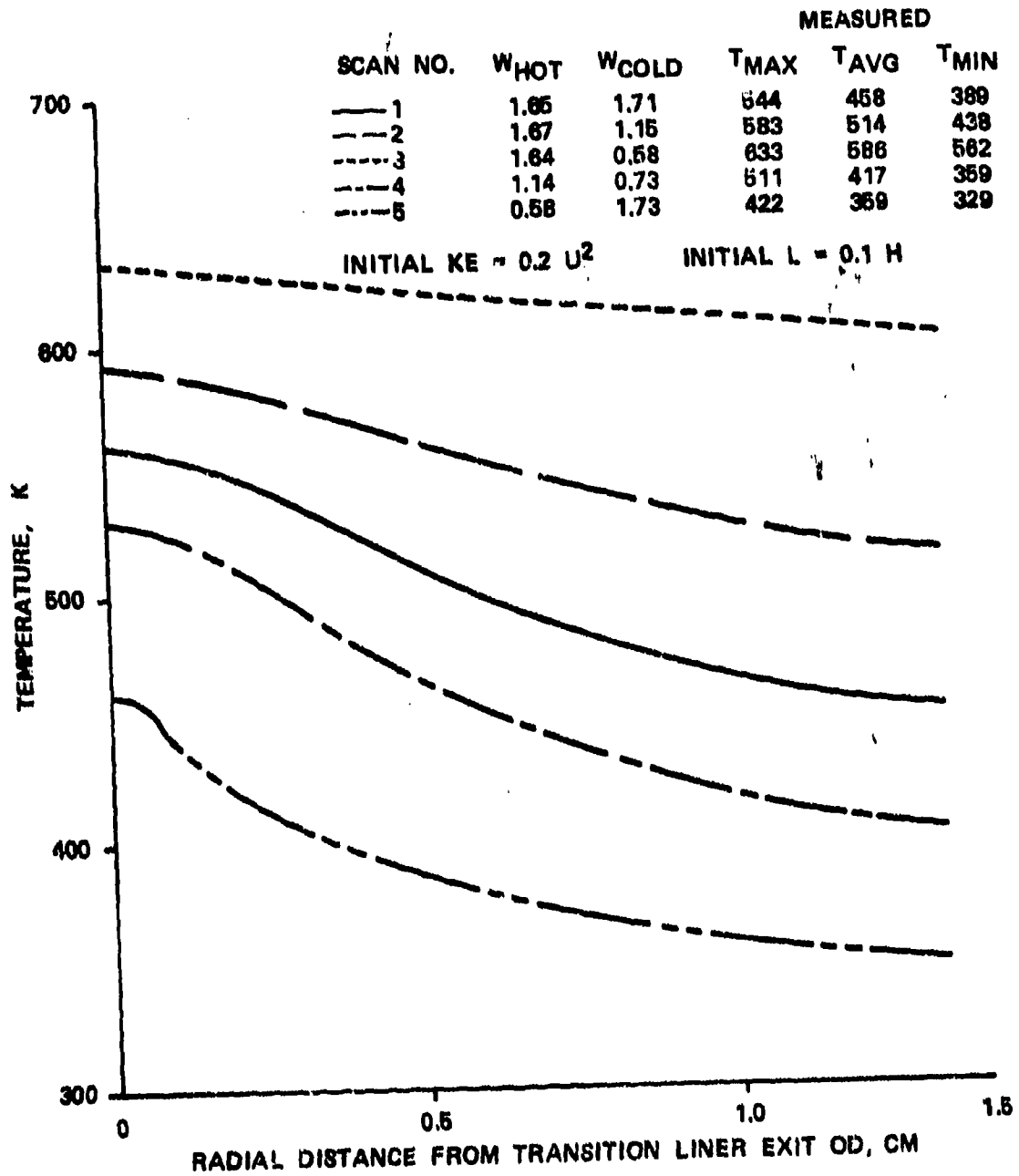
Figure 157. Predicted Exit Temperature Profiles
Cold Flow From Upper Half.

SCAN NO.	W_{HOT}	W_{COLD}	MEASURED		
			T_{MAX}	T_{AVG}	T_{MIN}
2-1	1.71	1.67	560	528	475
2-2	1.19	1.69	518	477	434
2-3	0.59	1.73	433	402	376
2-4	1.73	1.16	590	553	499
2-5	1.75	0.57	638	614	556

INITIAL KW = 0.2 U²   INITIAL L = 0.1 H
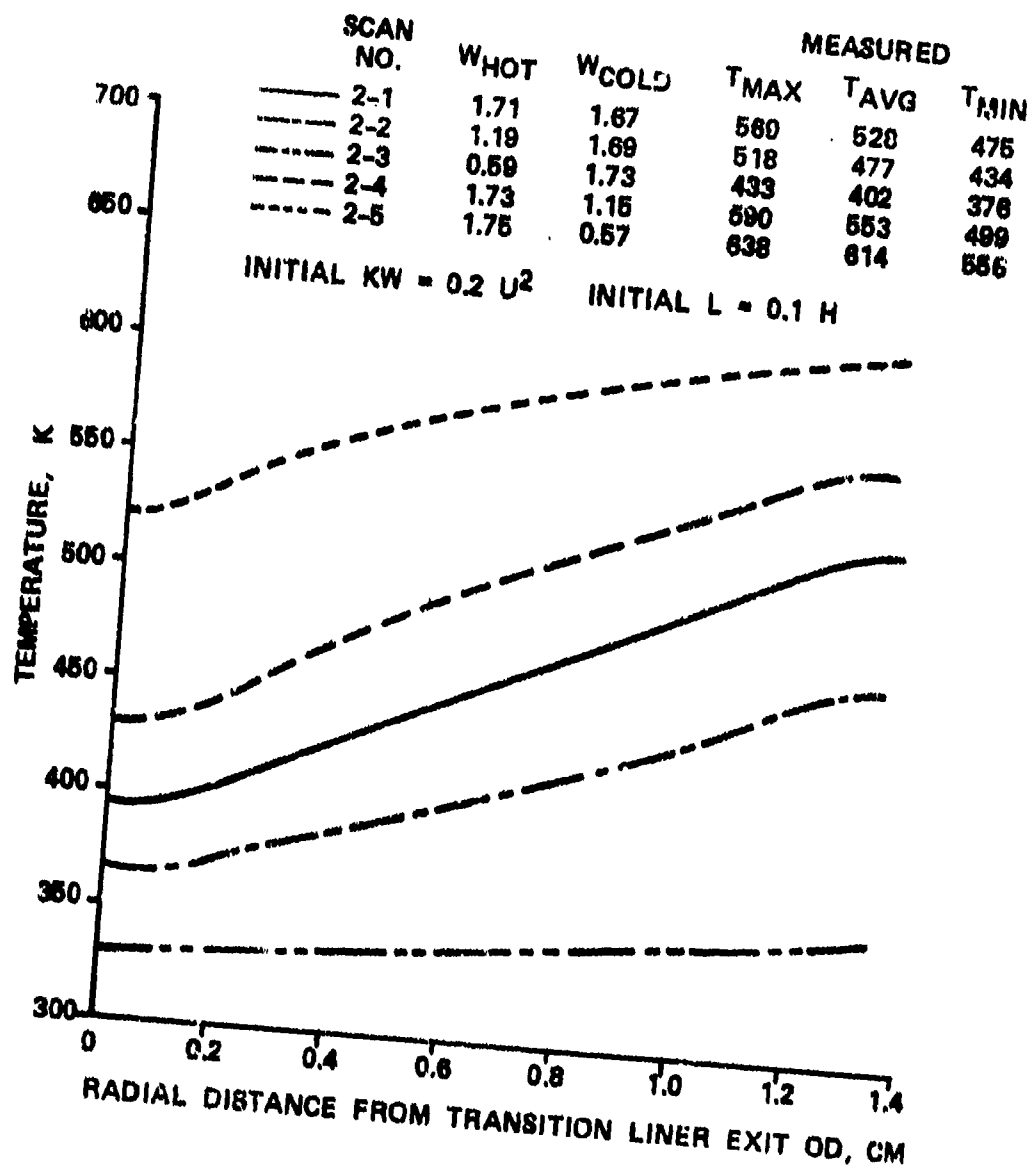
Figure 158.   Predicted Temperature Profiles for Cold Flow From Lower Half.
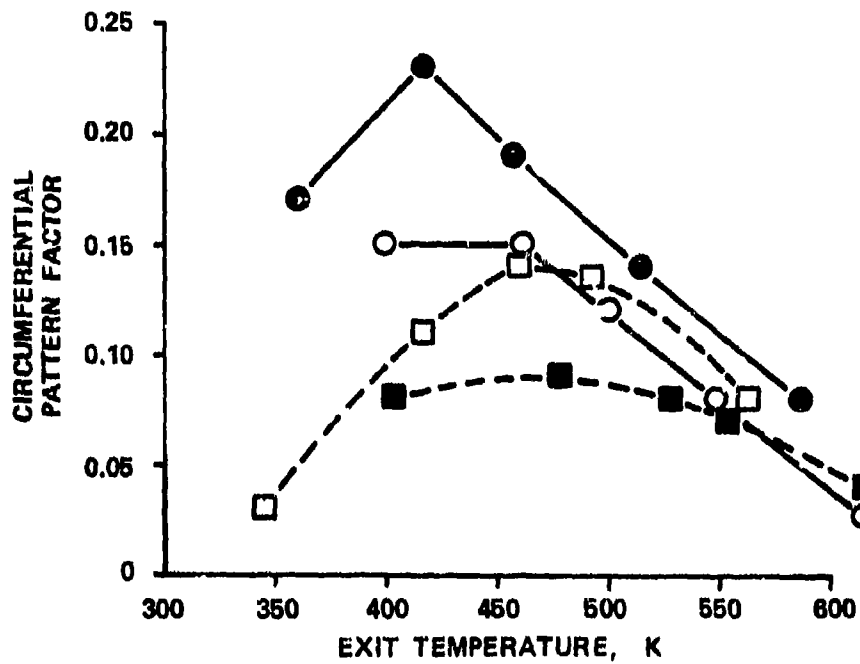
$$PF = (T_{MAX} - T_{AVG})/T_{AVG} \ (K/ K)$$

◡ PREDICTIONS, COLD FROM UPPER HALF

● MEASUREMENTS, COLD FROM UPPER HALF

□ PREDICTIONS, COLD FROM LOWER HALF

■ MEASUREMENTS, COLD FROM LOWER HALF

Figure 159.   Pattern Factor Comparison

341

VI. CONCLUSIONS

During Task I, the following six combustor performance models were formulated for application to small gas turbine combustor geometries:

- Annulus Flow Model - Calculates pressure losses and airflow distribution within the annulus external to the combustor liner

- 3-D Combustor Performance Model - Calculates axial, radial, and tangential velocity components; turbulence kinetic energy and disipacion rate; unburned hydrocarbons and composite fuel-mass fraction; stagnation enthalpy; radiation vectors along the x, y, and z directions, and fuel spray droplet size and distribution.

- Wall-Cooling Model - Calculates axial velocity, swirl velocity, turbulence, kinetic energy and dissipation, and stagnation enthalpy and liner wall temperatures.

- Transition Mixing Model - Calculates mixing rates in the combustor transition liner.

- 2-D Emissions Model - Calculates HC, CO, and NO_x emissions by using a detailed kinetic scheme.

- Fuel Insertion Model - Calculates the effect of fuel-spray cone angle, SMD, pressure drop, fuel physical properties on spray trajectory, and amount of fuel impingement on liner wall surfaces.

Element tests were conducted to provide input necessary for formulating each of the models and then to provide test cases for validating the models. The following conclusions are drawn regarding the model validation for each series of element tests run:

- Wall Cooling Tests - Correlation between 2-D program and measurements was made for profiles of velocity, temperature, and turbulence kinetic energy and dissipation rate downstream from a cooling geometry. The correlation was good for pressure drops encountered in reverse-flow combustors but only fair for liner pressure drops higher than 4 percent.

- Jet Mixing Tests - Correlation between the 3-D program and the measurements was made for jet trajectories of various configurations. The correlation was good but improvement is needed in regard to modeling the jet expansion rate.

- Can Combustor Cold-Flow Mapping Tests - Correlation between the 3-D program and measurements was made for internal flow profiles including axial velocity and turbulence without combustion. Good correlation was obtained, especially in the high velocity regions of the combustor, such as the liner walls, dome area, and in between the primary jets.

- Can Combustor Reacting Flow Mapping - Internal flow-profile correlations were made between the 3-D program and the measurements for reacting flows. Reasonably good correlation was obtained for unburned fuel calculations/measurements although

343

the agreement was more qualitative than quantative.
Measurement errors, due to emissions probe dis-
turbances, were the main reasons for the discrep-
ancies. However, despite the probe disturbances,
good correlation was obtained for fuel/air ratio
and combustion efficiency both for Jet-A and
natural gas fuels.

● Radiation Tests - Limited correlation between the
3-D and 2-D programs and radiation measurements was
made. Good correlation was obtained.

● Transition Mixing Tests - Correlations were made
with a 2-D model and test measurements in a
transition section which included 3-D flow
characteristics. Good correlation was obtained
especially in view of the limited initial profile
data that was available.

All of the combustor analysis models were sufficiently
developed and validated in Task I to permit advancement to the
next step of the program. This next step entailed the use of
the analytical models to assist in the design and successful
development of two combustor concepts. This work is reported
in Volume II of this report.

VII. REFERENCES

1. Patankar, S.V., "Numerical Prediction of Three-Dimensional Flows," Studies in Convection: Theory, Measurement and Applications, Volume 1 (B.E. Launder), Academic Press (1975).

2. Patankar, S.V., and D.B. Spalding, "Heat and Mass Transfer in Boundary Layers," Intertext Books (1970).

3. Carlson, N.G., "Development of High-Temperature Subsystem Technology to a Technology Readiness State: Phase I Topical Report, Preliminary Combustor Design," Technical Report FE-2292-11, November 1977, Work Performed Under Contract No. EX-76-C-01-2292.

4. Wood, M.P., and K.M. Johansen, "Advanced, Small, High-Temperature-Rise Combustor Program: Volume II Design and Test of Full-Scale Combustion System," AiResearch Manufacturing Co., USAAMRDL TR-74-3B, Eustis Directorate, U.S. Army Air Mobility R&D Laboratory, Fort Eustis, Va., AD776978, February 1974.

5. Odgers, J., "Combustion Modeling Within Gas Turbine Engines," AIAA Paper No. 77-52.

6. Hunter, S.C., K.M. Johansen, H.C. Mongia, and M.P. Wood, "Advanced, Small, High-Temperature-Rise Combustor Program, Volume I, Analytical Model Derivation and Combustor-Element Rig Tests (Phases I and II)," AiResearch Manufacturing Co., USAAMRDL TR74-3A, Eustis Directorate, U.S. Army Air Mobility R&D Laboratory, Fort Eustis, Va., AD 778766, February 1974.

7. Ballal, D.R., and A.H. Lefebvre, "A Proposed Method for Calculating Film Cooled Wall Temperatures in Gas Turbine Combustion Chambers," ASME Paper 72-WA/HT-24.

8. Mosier, S.A., and R. Roberts, "Low-Power Turbopropulsion Combustor Exhaust Emissions, Volume 3, Analysis," Technical Report AFAPL-TR-73-36, 1974.

9. Shapiro, A.H., "The Dynamics and Thermodynamics of Compressible Fluid Flow," The Ronald Press Company (1953).

10. Sturgess, G.J., "Gas Turbine Combustor Liner Durability-The Hot-Streak Problem," Project Squid (ONR) Workshop on Gas Turbine Combustor Design Problems, 1978.

11. Jones, W.P., and B.E. Launder, "The Calculation of Low-Reynolds Number Phenomena with a Two Equation Model of Turbulence," ASME Paper 72-HT-20.

12. Sanborn, J.W., R.S. Reynolds, and H.C. Mongia, "A Quasi-Three-Dimensional Calculation Procedure for Predicting the Performance and Gaseous Emissions of Gas Turbine Combustors," AIAA Paper NO. 76-682.

13. Edelman, R., J. Boccio, and G. Weilerstein, "The Role of Mixing and Kinetics in Combustion Generated NOx," Paper presented at Aiche Symposium on Control of NOx Emissions in Direct Combustion Power Sources, 1973.

14. Priem, R.J., and M.F. Heidmann, "Vaporization of Propellants in Rocket Engines," ARS Journal, Nov. 1959, pp. 836-842.

15. Burns, W.K. and J.L. Stollery, "The Influence of Foreign Gas Injection and Slot Geometry on Film Cooling Effectiveness," Int. J. Heat and Mass Transfer, Vol. 12, pp. 935-951, 1969.

16. Goldstein, R.J., "Film Cooling," Advances in Heat Transfer V. 7 (1971).

17. LeBrocq, P.V., B.E. Launder, and C.H. Priddin, "Discrete Hole Injection as a Means of Transpiration Cooling; An Experimental Study," Proceeding Instn. Mech. Engrs., 1973.

18. Holdeman, J.D., and R.E. Walker, "An Empirical Model for the Mixing of a Row of Dilution Jets with a Confined Crossflow," AIAA Paper 76-48.

19. Dobbins, R.A., Crocco, L., and Glassman, I., "Measurement of Mean Particle Sizes of Sprays from Diffractively Scattered Light," AIAA J. 1, 1882-1886 (1963).

20. Rizkalla, A.A., and A.H. Lefebvre, "The Influence of Air and Liquid Properties on Airblast Atomization," ASME Journal of Fluids Engineering, Sept. 1975.

21. Mugele, R.A. and Evans, H.D., "Droplet Size Distribution in Sprays," Ind. Eng. Chem. 43, 1317-1324 (1951).

22. Roberts, J.H. and Webb, M.J., "Measurements of Droplet Size for Wide Range Particle Distributions," AIAA J. 2, 583-585 (1964).

23. Hiroyasu, H., and T. Kadota, "Fuel Droplet Size Distribution in Diesel Combustion Chamber," SAE Paper 740715, 1974.

24. Williams, G.C., H.C. Hottel, and A.C. Morgan, "The Combustion to Methane in a Jet-Mixed Reactor," Twelfth Symposium (International) on Combustion, The Combustion Institutes (1969).

APPENDIX A

TABULATION OF INTERNAL EMISSIONS DATA OF
SET-1 THROUGH SET 13 OF
TABLE 15 AND TABLE 16

DATA SET-01   CIRCUMFERENTIAL POSITION = 0.0 DEG.
                          (IN BETWEEN JETS)

AX.POS.(CM)	6.05	10.43	12.90	15.37	18.82	24.22
RAD. POS. (CM)		UNBURNED HYDROCARBONS (PPM)				
5.44	665.4	1064.6	915.5	61.2	125.1	111.8
4.84	2395.3	14638.0	1093.9	75.9	270.1	123.8
4.23	4923.7	24485.9	109.1	43.9	439.1	139.7
3.63	36462.0	25283.9	1038.0	139.7	227.6	114.8
3.02	40587.3	21424.8	455.1	280.8	190.6	190.1
2.42	42051.1	6387.5	676.0	564.2	187.6	124.1
1.80	57069.4	6121.4	1636.8	894.9	258.9	194.4
1.07	65871.2	4125.3	1855.0	1015.8	306.6	149.0
.60	79977.7	1863.0	1924.2	1183.0	459.1	170.3
.00	91421.2	1197.7	1211.0	942.2	419.7	162.3
RAD. POS. (CM)		CO (PPM)				
5.44	1739.9	2665.3	2329.3	747.3	449.9	304.4
4.84	2923.0	3263.6	2530.7	953.2	713.1	372.3
4.23	3318.1	3340.2	2435.1	1120.3	669.7	379.7
3.63	3329.6	3291.4	1645.0	1029.6	501.6	385.6
3.02	3297.7	3044.0	1315.8	1256.3	399.5	395.6
2.42	3261.7	2498.9	1295.7	1374.1	391.5	372.3
1.80	3244.3	2215.7	1485.6	1489.3	469.6	374.7
1.07	3274.9	1557.1	1412.9	1541.9	591.1	360.7
.60	3332.9	1405.8	1285.8	1367.2	497.7	359.4
.00	3343.1	1272.6	1190.0	1259.5	474.4	347.6
RAD. POS. (CM)		NOX (PPM)				
5.44	52.7	38.4	43.5	36.6	23.4	14.1
4.84	60.0	52.5	47.0	52.4	29.3	17.4
4.23	61.8	55.5	42.0	53.9	14.5	20.1
3.63	62.5	42.2	33.2	56.5	11.3	19.9
3.02	58.0	28.0	24.2	28.4	9.6	19.8
2.42	54.9	20.3	18.6	20.6	8.5	18.4
1.80	47.8	16.4	16.6	17.4	9.5	17.3
1.07	36.3	14.2	15.8	14.4	11.4	14.3
.60	29.6	15.1	16.9	13.3	12.8	19.8
.00	25.1	17.0	19.3	13.4	13.2	12.5
RAD. POS. (CM)		CO2 (PERCENT)				
5.44	4.37	3.37	3.25	2.92	2.40	1.28
4.84	5.35	5.48	4.68	4.24	2.79	1.66
4.23	6.38	5.80	5.13	5.01	1.93	1.97
3.63	6.70	4.82	4.85	4.75	1.91	1.99
3.02	6.59	3.64	3.76	4.67	.99	1.94
2.42	6.20	2.35	2.80	3.37	.89	1.89
1.80	5.46	1.68	2.13	2.61	.99	1.59
1.07	4.49	1.24	1.65	2.14	1.16	1.53
.60	3.30	1.21	1.41	1.80	1.37	1.40
.00	2.96	1.18	1.39	1.76	1.39	1.31

DATA SET-01   CIRCUMFERENTIAL POSITION = 7.6 DEG.

AX.POS.(CM)   6.05   10.43   12.90   15.37   18.82   26.22

RAD. POS. (CM)	UNBURNED HYDROCARBONS (PPM)					
5.44	I	10778.9	798.4	I	97.1	81.7
4.84	I	20094.0	53.2	I	254.7	87.1
4.23	I	34332.9	705.3	I	295.5	119.9
3.63	I	11710.4	146.4	I	176.4	195.7
3.02	I	13706.5	159.7	I	85.9	127.8
2.42	I	9847.4	771.8	I	145.0	179.1
1.80	I	7185.9	1330.7	I	770.1	127.9
1.07	I	9991.3	1596.9	I	432.5	147.7
.60	I	2794.5	2395.3	I	424.5	177.0
.00	I	2262.2	1557.0	I	443.1	167.7

RAD. POS. (CM)	CO (PPM)					
5.44	I	2812.4	2192.3	I	491.6	274.6
4.84	I	3345.1	2497.9	I	607.4	354.3
4.23	I	3343.1	2093.8	I	629.3	382.6
3.63	I	2942.7	1678.9	I	264.5	304.4
3.02	I	2252.2	1240.8	I	249.9	376.7
2.42	I	2384.8	1292.4	I	317.3	979.7
1.80	I	2366.5	1500.5	I	479.5	375.8
1.07	I	2293.3	1434.4	I	658.7	965.0
.60	I	1744.0	1275.9	I	752.5	359.7
.00	I	1367.2	1144.0	I	723.0	344.7

RAD. POS. (CM)	NOX (PPM)					
5.44	I	33.3	48.1	I	27.1	19.7
4.84	I	45.3	46.9	I	24.1	17.7
4.23	I	37.4	45.3	I	16.4	20.5
3.63	I	18.4	34.3	I	10.7	21.7
3.02	I	11.2	23.9	I	6.7	21.2
2.42	I	11.1	17.5	I	7.3	20.6
1.80	I	11.2	14.2	I	8.7	18.4
1.07	I	11.4	13.2	I	9.7	16.6
.60	I	10.9	13.5	I	11.9	15.5
.00	I	12.0	12.6	I	13.2	14.7

RAD. POS. (CM)	CO2 (PERCENT)					
5.44	I	3.39	3.21	I	2.52	1.19
4.84	I	5.72	4.72	I	2.55	1.62
4.23	I	4.92	5.10	I	1.93	1.97
3.63	I	2.54	4.98	I	1.08	1.98
3.02	I	1.42	3.89	I	.69	1.98
2.42	I	1.37	2.97	I	.71	1.92
1.80	I	1.27	2.28	I	.94	1.75
1.07	I	1.36	1.76	I	1.25	1.55
.60	I	1.14	1.41	I	1.44	1.43
.00	I	1.15	1.35	I	1.42	1.32

DATA SET-01   CIRCUMFERENTIAL POSITION = 15.1 DEG.

AX.POS.(CM)	6.05	10.43	12.90	15.37	1°.°2	26.22

RAD. POS. (CM)   UNBURNED HYDROCARBONS (PPM)

RAD. POS. (CM)	6.05	10.43	12.90	15.37	1°.°2	26.22
5.44	0.0	6387.5	692.0	45.2	79.8	87.8
4.84	1863.0	14505.0	79.8	10.6	137.1	104.5
4.23	9049.0	3326.8	731.9	58.6	99.9	101.1
3.63	24884.7	1596.9	385.9	101.1	37.3	110.8
3.02	35796.7	2927.6	133.1	207.6	34.6	122.4
2.42	47241.0	10246.6	372.6	415.2	141.7	134.4
1.80	58019.9	7585.2	1224.3	1250.9	934.0	143.7
1.07	66935.8	5056.8	2169.1	1370.7	454.4	140.0
.60	83170.7	3859.1	2115.9	1280.2	585.5	140.0
.00	89691.9	2395.3	1956.2	992.7	455.1	170.9

RAD. POS. (CM)			CO (PPM)			
5.44	804.6	3236.0	1887.1	570.5	469.6	249.1
4.84	2348.2	3291.1	2357.3	935.6	539.8	357.7
4.23	3291.4	1974.0	2252.2	1189.7	327.4	390.0
3.63	3314.2	851.6	1982.7	1246.6	196.4	389.5
3.02	3238.1	973.8	1459.8	1200.4	144.7	389.5
2.42	3218.2	2265.9	1360.2	1230.6	255.3	394.4
1.80	3218.2	2890.9	1549.5	1332.8	451.0	376.7
1.07	3279.8	2820.8	1405.8	1377.6	719.1	367.0
.60	3342.5	2044.6	1279.2	1240.2	774.4	353.4
.00	3338.8	1423.6	1138.0	1132.1	723.0	337.4

RAD. POS. (CM)			NOX (PPM)			
5.44	39.9	36.2	42.8	30.4	75.4	13.4
4.84	54.1	29.8	48.2	41.7	26.5	17.5
4.23	60.8	12.9	45.5	47.9	12.1	20.4
3.63	57.6	9.5	36.8	46.3	9.1	27.0
3.02	36.7	10.2	28.0	31.6	6.0	21.9
2.42	51.9	13.8	19.4	28.1	7.1	20.7
1.80	43.5	18.5	15.2	20.9	10.3	19.3
1.07	33.5	21.2	14.1	18.2	12.7	14.6
.60	27.6	18.4	15.5	17.8	14.0	15.5
.00	24.4	21.1	15.6	21.3	14.7	14.7

RAD. POS. (CM)			CO2 (PERCENT)			
5.44	2.72	4.80	3.25	2.33	2.49	1.19
4.84	4.10	3.97	4.51	3.93	3.10	1.61
4.23	6.13	1.40	5.28	4.88	1.79	1.89
3.63	6.58	.53	5.34	5.07	.69	2.08
3.02	6.13	.45	4.39	4.45	.43	2.05
2.42	5.90	1.03	3.34	3.34	.51	1.89
1.80	5.20	1.98	2.39	2.55	.97	1.80
1.07	4.00	2.27	1.74	2.15	1.35	1.57
.60	2.98	1.33	1.42	1.85	1.50	1.43
.00	2.41	1.15	1.39	1.79	1.45	1.34

DATA SET-01   CIRCUMFERENTIAL POSITION = 22.5 DEG.

AX.POS.(CM)	6.05	10.43	12.90	15.37	18.92	26.22

RAD. POS. (CM)		UNBURNED HYDROCARBONS (PPM)				
5.44	I	3326.8	918.2	I	50.6	71.0
4.84	I	14904.2	1131.1	I	83.8	111.8
4.23	I	25683.1	425.8	I	68.9	94.9
3.63	I	39522.7	1809.8	I	33.3	102.5
3.02	I	50833.9	332.7	I	57.2	122.4
2.42	I	71194.1	519.0	I	130.4	142.4
1.80	I	21424.8	1636.8	I	255.5	154.4
1.07	I	46575.6	1969.9	I	503.5	144.4
.60	I	22489.4	1650.1	I	465.1	194.4
.00	I	7452.1	1569.6	I	488.4	147.7

RAD. POS. (CM)		CD (PPM)				
5.44	I	2765.6	1934.7	I	479.5	201.4
4.84	I	3337.3	2634.2	I	462.4	375.3
4.23	I	3341.9	2739.6	I	391.5	394.1
3.63	I	3319.5	2369.4	I	341.8	409.3
3.02	I	3165.5	1764.7	I	185.4	404.8
2.42	I	3119.0	1456.2	I	250.6	399.8
1.80	I	2927.0	1515.4	I	509.5	384.1
1.07	I	2584.9	1430.8	I	770.2	367.9
.60	I	2062.5	1279.2	I	822.2	354.9
.00	I	1809.1	1097.0	I	757.1	341.8

RAD. POS. (CM)		NOX (PPM)				
5.44	I	48.5	45.6	I	22.2	17.5
4.84	I	65.6	52.7	I	23.4	16.0
4.23	I	50.5	50.6	I	17.2	19.0
3.63	I	31.2	41.8	I	14.1	20.8
3.02	I	27.1	31.5	I	8.8	20.8
2.42	I	22.8	21.8	I	7.6	20.2
1.80	I	17.8	17.6	I	10.4	18.4
1.07	I	14.7	16.9	I	13.2	15.9
.60	I	12.7	17.0	I	14.0	14.7
.00	I	14.0	14.7	I	13.7	13.6

RAD. POS. (CM)		CO_2 (PERCENT)				
5.44	I	4.08	3.58	I	2.14	1.20
4.84	I	6.49	4.81	I	2.89	1.69
4.23	I	6.58	5.89	I	1.82	2.09
3.63	I	5.74	5.61	I	1.34	2.07
3.02	I	4.73	4.68	I	.61	2.10
2.42	I	4.23	3.55	I	.97	2.09
1.80	I	3.30	2.48	I	1.01	1.49
1.07	I	2.57	1.77	I	1.42	1.40
.60	I	1.76	1.46	I	1.36	1.45
.00	I	1.22	1.37	I	1.47	1.34

351

DATA SET-01   CIRCUMFERENTIAL POSITION = 30.1 DEG.
                                  (IN LINE WITH JETS)

AX.POS.(CM)   6.05   10.43   12.90   15.37   18.92   26.22

RAD. POS. (CM)	UNBURNED HYDROCARBONS (PPM)					
5.44	5855.2	2928.4	971.4	116.8	97.1	47.5
4.84	26219.4	1197.7	2102.6	93.2	71.9	67.1
4.23	50967.0	7	2321.1	111.8	62.5	134.4
3.65	63608.9	665.4	292.8	167.7	47.9	111.8
3.02	70262.6	19694.8	838.4	268.8	38.9	127.8
2.42	73585.5	2927.6	745.2	606.8	96.8	122.6
1.80	85892.2	35491.5	1250.9	1104.5	372.0	143.7
1.07	92352.7	75319.4	2129.2	1344.0	505.7	144.4
.60	89824.3	45244.9	2421.9	1274.8	525.6	143.7
.00	85166.8	16231.0	1942.8	1192.4	510.0	127.4

RAD. POS. (CM)	CO (PPM)					
5.44	2757.0	2444.2	2589.4	612.1	580.7	305.9
4.84	3344.8	1305.7	2988.8	1370.6	451.6	362.1
4.23	3256.1	957.7	3065.1	1591.8	391.9	345.6
3.65	3203.9	570.5	2878.8	1619.2	243.6	425.8
3.02	3225.0	2075.8	1965.2	1496.2	150.0	435.4
2.42	3277.4	3047.5	1627.1	1412.9	240.8	417.8
1.80	3332.9	2969.8	1588.0	1420.1	582.5	345.6
1.07	3346.6	2557.9	1541.9	1423.6	826.7	367.9
.60	3346.5	1965.2	1282.5	1262.8	847.1	357.7
.00	3346.0	1282.5	1041.2	1114.4	730.2	334.0

RAD. POS. (CM)	NOX (PPM)					
5.44	44.2	16.3	51.4	42.0	13.2	17.4
4.84	53.2	11.8	57.3	48.8	18.1	16.7
4.23	48.9	13.8	53.4	49.5	13.1	18.0
3.65	35.2	19.8	41.2	38.8	10.1	20.3
3.02	28.2	31.6	32.1	30.8	6.8	21.0
2.42	26.1	28.7	22.1	23.7	7.9	19.8
1.80	22.8	21.6	17.8	20.2	11.5	19.0
1.07	21.8	18.1	17.0	18.4	14.2	17.0
.60	21.5	17.2	17.5	18.4	14.5	17.0
.00	22.3	19.1	19.7	19.3	14.1	15.5

RAD. POS. (CM)	CO2 (PERCENT)					
5.44	3.60	3.95	4.31	1.64	2.39	1.24
4.84	5.80	1.64	5.69	3.89	2.21	1.56
4.23	5.90	.38	6.51	5.06	1.12	1.95
3.65	4.81	.49	5.97	4.88	.95	2.06
3.02	3.94	1.80	4.88	4.72	.42	2.08
2.42	3.57	3.95	3.77	3.59	.59	2.01
1.80	2.88	3.79	2.50	2.83	1.12	1.87
1.07	2.59	2.70	1.88	2.26	1.53	1.54
.60	2.70	1.76	1.40	1.92	1.55	1.45
.00	3.01	1.21	1.37	1.77	1.49	2.33

DATA SET-02　　　CIRCUMFERENTIAL POSITION = 0.0 DEG.
　　　　　　　　　　(IN BETWEEN JETS)

AX.POS.(CM)	6.05	8.51	10.43	12.90	15.37	18.82	21.29	24.22
RAD. POS. (CM)			UNBURNED HYDROCARBONS (PPM)					
5.44	133.1	10246.6	11045.1	9714.3	3872.4	845.4	687.1	238.2
4.84	2794.5	52297.7	39788.9	9581.3	1410.2	910.4	299.4	145.0
4.23	19835.7	55092.3	43115.7	6254.4	6667.0	959.3	250.7	89.3
3.63	40567.3	59882.9	41119.6	3593.0	4737.4	625.0	111.6	74.5
3.02	67001.1	68733.4	34066.7	1463.8	1774.3	430.1	111.8	110.5
2.42	79577.7	71726.4	28417.0	3593.0	1716.4	672.2	210.3	175.7
1.80	82372.2	77182.4	20493.3	7716.4	3024.1	848.2	390.3	206.8
1.07	99804.8	87505.3	15170.3	7585.2	4351.5	1274.3	447.1	324.7
.60	123225.7	84767.6	7585.2	7185.9	4238.3	1570.3	485.7	335.3
.00	136000.7	86763.7	5988.3	9722.1	3764.0	1623.5	588.2	419.2
RAD. POS. (CM)			CO (PPM)					
5.44	1752.2	3072.1	3282.0	3343.1	3841.4	2825.3	1926.0	699.3
4.84	2962.1	3211.2	3286.9	3343.5	3346.3	2120.7	2040.2	705.2
4.23	3336.5	3221.6	3250.3	3345.5	3244.1	1408.8	1805.7	660.7
3.63	3305.5	3234.9	3337.6	3293.2	3814.1	1021.5	1360.2	642.7
3.02	3238.1	3261.7	3292.0	2950.5	3041.6	884.4	901.1	644.5
2.42	3211.2	3209.7	3072.1	2722.4	2741.3	996.7	880.9	682.0
1.80	3192.6	3328.4	2903.0	2665.3	2853.4	1193.0	877.3	711.1
1.07	3274.9	3345.2	2625.3	2530.7	2495.3	1481.8	960.9	768.1
.60	3345.9	3345.9	2179.4	2270.4	2330.5	1673.9	948.6	787.2
.00	3270.0	3343.6	2075.8	2143.2	2202.1	1696.3	910.9	766.0
RAD. POS. (CM)			NOX (PPM)					
5.44	0.0	.9	.2	.2	0.0	T	T	21.0
4.84	0.0	.1	.3	.2	T	T	T	29.7
4.23	0.0	.1	.4	.3	T	T	T	29.6
3.63	0.0	0.0	.2	.3	T	T	T	29.2
3.02	0.0	0.0	.2	.3	T	T	T	26.3
2.42	0.0	.1	.3	.3	0.0	T	T	24.0
1.80	0.0	0.0	.3	.3	T	T	T	20.6
1.07	0.0	T	.4	.4	T	T	T	17.3
.60	0.0	0.0	.3	.3	0.0	T	T	13.5
.00	0.0	0.0	.3	.2	0.0	T	T	13.1
RAD. POS. (CM)			CO2 (PERCENT)					
5.44	4.14	3.77	4.00	4.90	4.43	5.22	3.76	2.30
4.84	5.13	5.20	6.11	6.75	7.05	4.02	4.43	3.11
4.23	6.17	5.19	6.06	7.31	7.39	2.39	4.11	3.53
3.63	6.45	4.49	5.61	6.89	7.21	1.04	3.74	3.74
3.02	5.39	4.06	3.44	5.63	5.22	1.57	3.54	3.49
2.42	4.65	3.64	2.08	4.05	4.77	1.51	2.92	3.20
1.80	4.42	3.20	1.50	2.56	3.53	1.46	2.29	2.70
1.07	3.70	2.84	1.23	1.99	2.84	2.09	2.02	2.41
.60	2.64	2.69	1.24	1.63	2.40	2.33	1.91	2.11
.00	2.08	2.52	1.34	1.56	2.24	2.35	1.64	1.45

DATA SET-02   CIRCUMFERENTIAL POSITION = 15.1 DEG.

AX.POS.(CM)	6.05	8.51	10.43	12.90	15.37	18.82	21.29	26.22
RAD. POS. (CM)		UNBURNED HYDROCARBONS (PPM)						
5.44	I	1596.9	21957.1	7052.9	2049.3	275.?	340.7	312.7
4.84	1064.6	14638.0	29409.2	5589.1	4311.6	244.0	147.7	198.3
4.23	6919.8	38090.4	3859.1	6367.5	4391.4	144.4	185.0	114.4
3.63	48438.6	52164.7	2262.2	6387.5	3180.4	64.5	55.9	79.8
3.02	72791.0	63742.0	6520.6	2395.3	3606.3	144.4	86.5	91.8
2.42	82372.2	71726.4	20227.1	4657.6	1690.0	275.5	210.3	134.4
1.80	89699.1	77049.3	26481.5	4258.3	2914.3	811.7	309.7	211.6
1.07	99937.9	81174.6	10645.8	6254.4	4125.3	1290.0	488.4	288.8
.60	123092.6	81041.5	9847.4	6254.4	4231.7	1716.4	511.0	267.5
.00	134004.6	87029.8	5456.0	4657.6	3925.7	1676.7	508.8	401.9
RAD. POS. (CM)		CO (PPM)						
5.44	743.2	2778.5	3344.8	3282.0	2719.7	2730.8	1541.9	703.2
4.84	2293.3	3343.6	3346.5	3345.7	3293.2	1710.4	1635.0	743.2
4.23	3272.0	3305.5	2575.9	3345.9	3340.9	785.1	1956.8	709.1
3.63	33??.1	3267.1	1199.0	3342.6	3272.0	453.1	1048.9	659.3
3.02	32??.8	3279.8	1541.9	3250.2	3141.2	320.7	860.9	650.1
2.42	3211.2	3305.5	2769.9	2946.6	2735.4	629.8	877.7	637.2
1.80	3200.2	3327.2	3134.9	2841.7	2571.4	1156.0	847.1	699.3
1.07	3279.8	3344.4	3044.0	2616.3	2508.0	1690.3	882.0	735.1
.60	3345.1	3342.6	2426.0	2375.6	2361.9	1756.4	960.9	741.2
.00	3280.1	3338.1	2031.3	2161.3	2224.5	1685.0	915.8	751.4
RAD. POS. (CM)		NOX (PPM)						
5.44	0.0	I	.1	.3	I	I	I	18.6
4.84	0.0	I	0.0	.3	I	I	I	24.4
4.23	0.0	I	.2	.4	I	I	I	27.9
3.63	0.0	I	.1	.4	I	I	I	31.1
3.02	0.0	I	.1	.4	0.0	I	I	31.0
2.42	0.0	I	0.0	.3	I	I	I	27.0
1.80	0.0	0.0	.2	.3	I	I	I	23.8
1.07	0.0	I	.1	.3	I	I	I	18.8
.60	0.0	I	.1	.4	I	I	I	16.0
.00	I	I	.1	.4	0.0	I	I	14.4
RAD. POS. (CM)		CO2 (PERCENT)						
5.44	2.44	4.18	5.59	5.02	4.18	5.51	3.64	2.06
4.84	3.76	6.53	4.91	6.44	6.62	3.65	4.81	3.01
4.23	5.79	6.44	1.70	7.96	7.11	1.97	5.02	3.79
3.63	6.30	5.48	.59	7.31	7.00	.78	4.46	3.90
3.02	5.18	4.30	.43	6.33	6.03	.57	3.79	3.95
2.42	4.55	3.66	1.14	4.62	4.76	1.91	2.70	3.76
1.80	4.30	3.21	2.05	3.09	3.72	1.79	2.21	3.17
1.07	3.67	2.84	2.28	2.07	2.92	2.29	1.90	2.57
.60	2.61	2.63	1.41	1.67	2.44	2.85	1.74	2.19
.00	2.11	2.50	1.33	1.56	2.30	2.48	1.54	1.98

DATA SET-02   CIRCUMFERENTIAL POSITION = 30.1 DEG.
(IN LINE WITH JETS)

AX.POS.(CM)	6.05	8.51	10.43	12.90	15.37	18.82	21.29	26.22
RAD. POS. (CM)	**UNBURNED HYDROCARBONS (PPM)**							
5.44	399.2	5988.3	8649.8	11178.1	4145.2	1443.9	204.9	271.5
4.84	6387.5	30873.0	3193.8	6520.6	7017.8	585.5	187.6	158.4
4.23	41119.6	47906.3	1064.6	12242.7	11597.1	252.8	143.7	103.8
3.63	68931.9	62012.1	4524.5	9448.2	6540.5	264.1	161.0	102.5
3.02	79444.6	71460.3	29143.0	4524.5	3752.7	133.1	175.7	101.1
2.42	79178.5	79178.5	45777.1	5055.8	1490.4	452.4	260.8	126.4
1.80	86098.3	82372.2	31272.2	5189.9	2369.7	851.7	346.0	220.9
1.07	108553.8	86098.3	26747.7	7716.2	3366.7	1344.0	443.1	300.7
.60	126685.6	86763.7	15037.3	5968.3	3872.4	1623.5	552.3	328.7
.00	133738.5	77591.6	6254.4	5589.1	3912.3	1596.9	532.3	435.1
RAD. POS. (CM)	**CO (PPM)**							
5.44	2098.2	3085.8	3283.9	3337.3	2744.1	2375.4	1434.4	729.0
4.84	3236.0	3334.0	2607.4	3321.9	3330.0	1982.7	1126.2	715.0
4.23	3312.6	3258.9	1010.7	3323.3	3346.5	1230.4	955.8	761.8
3.63	3214.7	3274.9	1760.5	3344.4	3341.5	661.2	815.6	723.0
3.02	3176.8	3279.8	3131.8	3247.9	3215.9	342.1	787.2	653.8
2.42	3164.4	3303.6	3335.8	3061.6	2841.7	612.1	778.7	680.1
1.80	3211.2	3330.8	3296.7	2907.1	2538.4	1295.7	813.3	683.9
1.07	3315.8	3345.7	3125.4	2726.7	2538.0	1744.0	806.3	743.2
.60	3338.8	3345.7	2669.7	2421.4	2366.5	1802.2	933.1	755.6
.00	3322.0	3338.8	2044.6	2256.7	2211.2	1601.0	913.3	749.4
RAD. POS. (CM)	**NOX (PPM)**							
5.44	0.0	0.0	I	.3	I	I	I	19.0
4.84	0.0	I	.1	.1	I	I	I	26.0
4.23	0.0	0.0	0.0	.3	I	I	I	28.9
3.63	0.0	I	I	.3	I	I	I	30.7
3.02	I	0.0	0.0	.4	I	I	I	29.8
2.42	0.0	I	0.0	.2	I	I	I	27.3
1.80	0.0	0.0	0.0	.2	I	I	I	24.1
1.07	0.0	0.0	0.0	.1	I	I	I	19.7
.60	0.0	0.0	0.0	.2	I	I	I	17.4
.00	I	0.0	.1	.4	I	I	I	16.0
RAD. POS. (CM)	**CO2 (PERCENT)**							
5.44	3.90	3.19	5.05	5.32	3.47	4.49	4.06	2.23
4.84	5.87	5.54	2.22	6.75	6.75	3.27	3.53	3.27
4.23	6.75	5.52	.49	7.27	7.49	2.01	2.84	3.97
3.63	5.54	4.37	.61	6.93	7.24	.07	2.46	4.11
3.02	4.66	3.71	2.00	6.25	5.76	.49	2.32	3.96
2.42	4.62	3.23	3.88	4.56	5.28	1.02	2.10	3.83
1.80	4.30	2.90	3.57	3.04	4.09	2.01	1.92	3.12
1.07	3.25	2.67	2.74	2.26	3.13	2.44	1.73	2.59
.60	2.46	2.57	1.79	1.74	2.55	2.65	1.70	2.21
.00	2.23	2.59	1.33	1.59	2.28	2.47	1.64	1.98

DATA SET-03   CIRCUMFERENTIAL POSITION = 0.0 DEG.
                          (IN BETWEEN JETS)

AX.POS.(CM)	10.43	15.37	18.82	21.29	24.22
RAD. POS. (CM)		UNBURNED HYDROCARBONS (PPM)			
5.44	0.0	0.0	51.9	61.2	53.2
4.84	0.0	169.0	178.3	63.9	41.3
4.23	2129.2	35.9	145.0	75.9	33.3
3.63	505.7	87.8	90.5	50.6	47.9
3.02	I	207.6	105.1	39.9	75.9
2.42	212.9	363.3	115.8	65.2	54.6
1.80	252.8	367.3	219.6	85.2	57.2
1.07	I	507.0	310.1	93.2	62.5
.60	I	673.3	254.2	123.8	61.2
.00	332.7	348.7	194.3	74.5	75.9
RAD. POS. (CM)		CO (PPM)			
5.44	1870.0	729.0	269.0	217.6	157.5
4.84	1982.7	763.9	398.9	230.4	176.0
4.23	2837.6	791.5	369.4	215.7	202.1
3.63	2778.5	460.8	242.2	204.5	201.2
3.02	2004.8	552.0	192.2	178.7	202.6
2.42	1233.8	659.3	235.2	184.6	194.2
1.80	806.7	709.1	325.9	198.9	193.3
1.07	476.3	747.3	379.7	207.7	194.2
.60	511.1	699.3	401.8	215.2	169.6
.00	828.9	653.8	366.5	181.4	163.3
RAD. POS. (CM)		NOX (PPM)			
5.44	50.9	43.5	28.2	23.1	16.8
4.84	75.1	57.2	27.6	23.7	20.0
4.23	69.8	52.1	19.6	21.4	22.9
3.63	65.2	49.6	15.0	19.7	22.2
3.02	46.6	41.1	11.6	18.3	22.5
2.42	33.1	31.2	12.9	17.0	22.5
1.80	22.9	24.0	14.1	15.7	20.3
1.07	20.5	20.6	16.5	14.4	19.3
.60	19.1	19.2	17.2	13.1	17.6
.00	21.6	19.6	17.3	12.4	16.5
RAD. POS. (CM)		CO2 (PERCENT)			
5.44	3.30	3.22	2.90	1.90	1.48
4.84	4.68	4.46	2.77	1.94	1.72
4.23	5.63	4.56	1.84	1.86	1.97
3.63	5.23	16.59	1.15	1.69	2.01
3.02	3.70	4.14	.87	1.58	2.02
2.42	2.43	3.11	.91	1.46	1.86
1.80	1.56	2.24	1.20	1.25	1.72
1.07	1.21	1.97	1.36	1.19	1.57
.60	1.03	1.78	1.49	1.18	1.48
.00	1.17	1.78	1.40	1.07	1.40

DATA SET-03   CIRCUMFERENTIAL POSITION = 1°.1 DEG.

AX.POS.(CM)	10.43	15.37	19.82	21.29	26.22
RAD. POS. (CM)		UNBURNED	HYDROCARBONS	(PPM)	
5.44	1317.4	16.0	37.3	16.0	14.0
4.84	8450.1	21.3	37.3	17.3	74.6
4.23	479.1	33.3	21.3	37.3	39.9
3.63	186.3	87.8	6.7	50.6	34.6
3.02	958.1	159.7	16.0	50.6	74.6
2.42	425.8	328.7	51.9	70.5	47.8
1.80	1982.8	439.1	235.5	93.2	87.2
1.07	452.4	560.2	328.7	97.1	47.9
.60	1184.4	540.3	286.1	102.5	41.2
.00	1197.7	457.8	235.5	101.1	63.2

RAD. POS. (CM)			CO	(PPM)	
5.44	2517.1	504.7	197.7	187.8	111.8
4.84	2722.4	923.1	218.5	165.1	144.5
4.23	1040.6	1026.9	130.0	176.0	141.0
3.63	409.3	1010.7	69.6	205.4	198.4
3.02	608.6	585.9	65.9	204.0	195.2
2.42	1420.1	639.1	203.3	198.9	204.0
1.80	1445.3	761.8	375.3	211.5	155.9
1.07	628.2	768.1	473.2	232.8	154.7
.60	782.9	687.7	451.6	226.1	170.1
.00	787.2	630.0	415.3	219.0	177.9

RAD. POS. (CM)			NOX	(PPM)	
5.44	49.3	38.7	31.0	21.2	15.6
4.84	43.2	55.1	26.9	22.8	20.4
4.23	18.4	51.7	11.8	28.0	24.8
3.63	11.4	55.4	8.5	22.4	25.3
3.02	14.1	41.7	7.7	25.7	26.6
2.42	22.0	31.1	10.9	20.6	24.6
1.80	23.1	25.5	15.8	15.9	27.3
1.07	20.6	21.7	18.5	14.9	19.9
.60	16.5	20.2	17.6	13.5	14.9
.00	18.0	21.3	16.7	12.9	14.2

RAD. POS. (CM)			CO2	(PERCENT)	
5.44	3.64	2.72	2.28	1.99	1.14
4.84	3.83	3.46	2.08	1.54	1.54
4.23	1.47	4.36	.96	1.85	1.99
3.63	.63	4.31	.65	2.44	2.19
3.02	.70	3.09	.46	2.21	2.17
2.42	1.72	2.41	.78	1.82	2.06
1.80	2.19	2.11	1.33	1.53	1.85
1.07	1.35	1.68	1.69	1.34	1.65
.60	1.09	1.57	1.64	1.19	1.51
.00	1.15	1.56	1.58	1.17	1.40

DATA SET-03   CIRCUMFERENTIAL POSITION = 30.1 DEG.
(IN LINE WITH JETS)

AX.POS.(CM)	10.43	15.37	18.82	21.29	26.22
RAD. POS. (CM)		UNBURNED HYDROCARBONS (PPM)			
5.44	692.0	6.7	12.0	47.9	24.0
4.84	173.0	8.0	14.6	17.3	20.3
4.23	I	89.2	10.6	33.3	46.6
3.63	252.8	134.4	6.7	27.9	54.6
3.02	1384.0	227.6	42.6	34.6	46.5
2.42	2142.5	352.6	141.1	69.2	42.5
1.80	1969.5	492.4	264.8	73.2	60.2
1.07	2115.9	409.9	208.9	91.8	79.2
.60	1503.7	608.1	280.8	115.8	65.2
.00	811.7	417.8	236.9	79.8	74.5

RAD. POS. (CM)		CO (PPM)			
5.44	1493.0	363.6	152.7	162.0	123.1
4.84	519.2	547.0	87.1	213.8	187.5
4.23	105.1	559.4	62.2	170.5	193.9
3.63	356.3	497.3	15.9	224.2	223.7
3.02	1445.3	553.7	70.8	216.6	222.8
2.42	2713.7	659.6	228.3	220.9	216.2
1.80	2297.9	753.5	492.0	232.3	202.5
1.07	1230.6	759.7	457.7	241.0	202.6
.60	918.2	729.0	447.7	225.6	191.0
.00	745.3	680.1	405.9	198.9	185.1

RAD. POS. (CM)		NOX (PPM)			
5.44	39.7	31.5	18.9	24.9	17.5
4.84	16.8	45.0	19.0	25.4	23.9
4.23	9.1	46.1	10.7	35.0	24.5
3.63	15.3	47.2	5.6	21.9	27.4
3.02	31.2	41.0	7.3	28.1	29.7
2.42	45.7	32.5	11.0	23.0	27.3
1.80	32.6	26.6	19.8	19.0	25.9
1.07	24.7	22.5	19.9	15.3	21.3
.60	16.0	21.0	17.4	13.3	18.9
.00	14.2	21.1	16.4	13.1	18.1

RAD. POS. (CM)		CO2 (PERCENT)			
5.44	2.59	2.06	1.56	1.89	1.28
4.84	1.22	3.79	.82	2.92	1.67
4.23	.19	3.53	.47	2.02	1.92
3.63	.57	3.40	.26	2.91	2.11
3.02	2.36	3.12	.55	2.56	2.29
2.42	4.30	2.58	1.19	2.05	2.15
1.80	3.41	2.06	1.85	1.45	1.92
1.07	2.31	1.75	1.71	1.40	1.67
.60	1.58	1.59	1.67	1.22	1.49
.00	1.15	1.60	1.54	1.14	1.39

DATA SET-04   CIRCUMFERENTIAL POSITION = 0.0 DEG.
(IN BETWEEN JETS)

AX.POS.(CM)	15.37	18.82	21.29	26.22

RAD. POS. (CM)	UNBURNED HYDROCARBONS (PPM)			
5.44	7052.9	359.3	117.1	200.9
4.84	9714.3	306.1	141.1	129.1
4.23	9514.7	372.6	121.1	75.9
3.69	3779.3	385.9	155.7	87.8
3.02	2834.5	465.8	174.3	111.8
2.42	1423.9	465.8	215.6	153.0
1.80	2036.0	692.0	270.1	196.9
1.07	2954.2	1024.7	403.2	283.4
.60	3632.9	1503.7	396.6	324.7
.00	3359.1	1650.1	489.7	356.6

RAD. POS. (CM)	CO (PPM)			
5.44	3162.6	2765.6	822.2	563.7
4.84	3346.6	2275.0	815.6	540.4
4.23	3346.0	994.7	680.1	503.1
3.63	3316.8	856.2	610.3	484.2
3.02	3119.0	785.1	565.4	506.3
2.42	2357.3	798.0	567.1	527.3
1.80	2102.7	915.8	594.6	572.2
1.07	2143.2	1195.9	642.7	594.6
.60	2031.3	1402.3	709.1	610.3
.00	1874.3	1434.4	731.0	599.8

RAD. POS. (CM)	NOX (PPM)			
5.44	58.9	58.0	36.9	27.8
4.84	75.3	51.2	34.8	36.7
4.23	85.5	28.6	27.3	40.2
3.63	77.6	20.0	24.5	39.3
3.02	60.9	17.1	22.4	36.3
2.42	41.4	16.2	20.0	32.4
1.80	29.9	17.1	17.6	27.8
1.07	23.0	19.3	16.3	24.2
.60	20.3	21.0	16.0	21.4
.00	19.4	21.4	15.7	20.1

RAD. POS. (CM)	CO2 (PERCENT)			
5.44	5.61	6.30	3.84	2.55
4.84	8.10	6.63	3.94	3.63
4.23	8.90	3.24	2.85	3.95
3.63	8.95	2.22	2.59	3.85
3.02	7.62	1.70	2.31	3.53
2.42	6.02	1.60	2.11	3.30
1.80	4.55	1.81	1.89	2.90
1.07	3.14	2.14	1.77	2.48
.60	2.81	2.48	1.74	2.23
.00	2.80	2.50	1.74	2.04

DATA SET-04   CIRCUMFERENTIAL POSITION = 15.1 DEG.

AX.POS.(CM)   15.37   18.82   21.29   26.22

RAD. POS. (CM)		UNBURNED HYDROCARBONS (PPM)		
5.44	I	998.0	323.4	319.4
4.84	I	199.6	202.3	159.7
4.23	I	212.9	81.2	97.1
3.63	I	146.4	79.8	70.5
3.02	I	106.5	90.5	90.5
2.42	I	346.0	218.2	126.4
1.80	I	705.3	291.4	189.0
1.07	I	1224.3	376.6	200.9
.60	I	1423.9	488.4	299.4
.00	I	1783.2	512.3	343.3

RAD. POS. (CM)		CO (PPM)		
5.44	I	2996.3	1427.2	605.0
4.84	I	1642.9	1553.3	610.3
4.23	I	596.3	948.2	548.7
3.63	I	318.7	678.2	492.0
3.02	I	287.4	599.8	492.0
2.42	I	527.3	599.8	530.6
1.80	I	879.6	640.9	575.6
1.07	I	1305.7	661.2	591.1
.60	I	1463.5	731.0	601.5
.00	I	1474.5	721.0	605.0

RAD. POS. (CM)		NOX (PPM)		
5.44	I	56.8	45.1	25.7
4.84	I	33.4	56.4	36.3
4.23	I	11.7	48.6	40.5
3.63	I	7.4	42.0	40.9
3.02	I	8.4	32.5	38.5
2.42	I	12.2	24.7	33.3
1.80	I	16.3	19.3	26.9
1.07	I	19.7	17.2	23.0
.60	I	21.0	16.6	19.5
.00	I	21.1	16.6	18.7

RAD. POS. (CM)		CO2 (PERCENT)		
5.44	I	7.13	4.59	2.43
4.84	I	4.26	6.01	3.47
4.23	I	1.18	5.21	4.19
3.63	I	.54	4.98	4.10
3.02	I	.59	3.30	3.97
2.42	I	1.06	2.58	3.40
1.80	I	1.66	2.14	2.95
1.07	I	2.31	1.87	2.49
.60	I	2.57	1.60	2.18
.00	I	2.57	1.73	2.00

```
DATA SET-04            CIRCUMFERENTIAL POSITION = 30.1 DEG.
                            (IN LINE WITH JETS)

AX.POS.(CM)    15.37    18.82    21.29    26.22

  RAD. POS.
    (CM)              UNBURNED HYDROCARBONS (PPM)
   5.44
   4.84       I        625.4    338.0    254.2
   4.23       I        279.5    250.5    150.4
   3.63       I        319.4    138.4    102.5
   3.02       I        239.5     69.2     69.2
   2.42       I        119.8    102.5     99.8
   1.80       I        266.1    175.7    170.3
   1.07       I        958.1    294.1    195.6
    .60       I       1477.1    411.2    234.2
    .00       I       1663.4    447.1    326.0
             I       1769.9    500.4    338.0

  RAD. POS.
    (CM)                     CO (PPM)
   5.44
   4.84       I       2026.9   1650.9    621.0
   4.23       I       1398.7   1412.9    635.4
   3.63       I        966.0   1132.1    562.1
   3.02       I        366.5    886.7    528.9
   2.42       I        239.4    640.9    525.7
   1.80       I        482.6    608.6    532.0
   1.07       I       1016.1    624.6    584.2
    .60       I       1452.6    689.6    606.8
    .00       I       1538.1    727.0    619.2
             I       1500.5    727.0    610.3

  RAD. POS.
    (CM)                    NOX (PPM)
   5.44
   4.84       I         34.3     41.7     26.7
   4.23       I         25.6     48.2     34.8
   3.63       I         19.6     45.7     37.6
   3.02       I          7.6     41.5     37.9
   2.42       I          4.8     36.4     35.9
   1.80       I         10.2     28.9     30.6
   1.07       I         19.0     22.4     24.4
    .60       I         24.5     19.3     17.8
    .00       I         24.4     18.1     16.2
             I         24.1     18.3     15.2

  RAD. POS.
    (CM)                   CO2 (PERCENT)
   5.44
   4.84       I          4.48     4.64     2.78
   4.23       I          3.24     4.99     3.86
   3.63       I          1.83     4.62     4.13
   3.02       I           .88     3.98     4.16
   2.42       I           .42     3.53     4.08
   1.80       I           .97     2.74     3.90
   1.07       I          1.94     2.24     2.96
    .60       I          2.61     1.92     2.49
    .00       I          2.68     1.82     2.18
             I          2.51     1.78     2.01
```

DATA SET-05   CIRCUMFERENTIAL POSITION = 0.0 DEG.
(IN BETWEEN JETS)

AX.POS.(CM)	6.05	9.51	10.43	12.90	15.37	18.82	21.29	26.22
RAD. POS. (CM)	UNBURNED HYDROCARBONS (PPM)							
5.44	0.0	1730.0	2927.6	2022.7	359.3	89.9	147.7	119.4
4.84	2395.3	27413.1	20892.5	3579.7	319.4	86.5	101.1	89.2
4.23	39389.6	53761.5	27146.9	2049.9	337.7	99.5	110.5	105.1
3.63	30074.5	65605.0	37127.4	1836.4	144.4	67.9	107.8	93.2
3.02	45377.9	74254.8	27013.8	402.4	652.1	33.3	91.8	99.8
2.42	69072.7	75492.4	19961.0	625.4	385.9	55.9	101.1	99.8
1.80	63209.7	77192.4	11045.1	1397.9	731.9	219.2	177.4	123.8
1.07	82239.2	71692.5	8915.9	1793.2	1024.7	395.2	159.0	123.8
.60	84634.5	61745.9	5589.1	1809.6	1197.7	435.1	157.0	147.7
.00	94619.0	32336.8	1730.0	1437.2	1011.4	479.7	147.7	162.3
RAD. POS. (CM)	CO (PPM)							
5.44	804.6	1448.9	1861.4	2207.6	636.8	463.0	314.2	230.9
4.84	2602.9	3309.6	3330.0	3150.5	1177.4	310.2	297.8	276.2
4.23	3301.7	3259.1	3293.5	3261.4	2625.3	261.0	292.3	289.5
3.63	3297.7	3234.9	3339.9	3009.3	1572.5	169.0	244.1	274.7
3.02	3225.0	3256.1	3221.0	1956.5	1723.6	90.9	241.5	271.7
2.42	3291.7	3282.2	2929.2	1010.7	892.0	103.9	228.5	294.7
1.80	3253.2	3289.1	2638.7	1227.4	853.9	242.2	225.7	250.3
1.07	3247.3	3259.1	2238.5	1129.1	928.1	412.3	234.7	240.1
.60	3345.7	3329.6	1961.4	953.2	857.9	493.6	240.8	236.2
.00	3340.2	3039.2	1018.8	755.6	759.6	489.7	237.6	227.6
RAD. POS. (CM)	NOX (PPM)							
5.44	61.0	43.5	37.2	38.0	19.7	37.0	25.1	17.9
4.84	77.5	69.3	60.8	61.0	55.3	74.4	29.6	29.2
4.23	83.5	61.2	60.0	75.2	79.9	15.1	25.9	29.7
3.63	70.8	40.8	47.3	73.1	76.1	8.8	23.1	26.2
3.02	54.9	30.9	31.6	58.7	61.4	6.5	20.4	25.1
2.42	43.5	28.2	20.4	37.8	44.3	7.0	18.1	23.0
1.80	33.6	29.3	16.5	26.3	30.5	11.2	16.0	20.7
1.07	34.5	28.6	14.5	20.9	23.0	15.5	14.7	18.5
.60	29.8	28.7	14.5	18.3	19.8	17.0	13.9	17.1
.00	21.6	27.8	13.9	17.9	18.6	17.2	13.9	17.1
RAD. POS. (CM)	CO2 (PERCENT)							
5.44	4.10	2.81	2.81	2.95	1.49	3.49	2.21	1.45
4.84	5.54	5.36	5.68	5.31	4.27	2.09	2.71	2.04
4.23	6.76	5.87	6.30	6.16	6.30	1.31	2.33	2.33
3.63	6.70	4.54	5.73	6.13	5.87	.71	2.05	2.37
3.02	5.48	3.65	4.16	5.04	5.64	.49	1.91	2.91
2.42	4.52	3.32	2.58	3.51	4.50	.47	1.64	2.14
1.80	3.53	3.48	2.01	2.64	2.18	.80	1.44	1.94
1.07	4.09	3.95	1.49	2.02	2.52	1.49	1.31	1.72
.60	2.60	4.33	1.47	1.40	2.06	1.65	1.24	1.55
.00	2.37	3.08	1.28	1.46	1.84	1.61	1.19	1.44

DATA SET-05　　　CIRCUMFERENTIAL POSITION = 15.1 DEG.

AX.POS.(CM)	6.05	8.51	10.43	12.90	15.37	19.82	21.29	26.22
RAD. POS. (CM)		UNBURNED HYDROCARBONS (PPM)						
5.44	266.1	0.0	3726.0	2515.1	186.3	91.8	175.7	98.5
4.84	1863.0	10912.0	18630.2	2235.6	119.8	66.5	90.8	99.8
4.23	13440.4	36062.8	5456.0	3752.7	625.4	97.9	95.8	85.2
3.63	56689.1	55092.3	395.2	2155.8	399.2	55.0	86.5	87.8
3.02	57886.6	57221.4	2528.4	372.6	252.9	49.7	75.0	93.2
2.42	69472.0	66931.9	5189.9	439.1	306.1	66.9	97.1	119.8
1.80	69475.9	61346.7	13041.2	1290.8	652.1	150.7	142.4	95.8
1.07	77980.8	64806.6	11843.5	1570.3	951.5	275.5	154.4	95.8
.60	88094.4	49837.8	6653.7	1916.3	1144.4	429.5	185.0	153.0
.00	88360.5	36861.2	2528.4	1144.4	1104.5	443.1	179.6	161.0
RAD. POS. (CM)		CO (PPM)						
5.44	375.3	709.1	2179.4	1719.4	433.9	379.7	375.9	221.8
4.84	1227.4	3291.4	3333.0	3014.9	1135.1	397.7	341.6	281.8
4.23	3202.5	3295.6	1939.0	3191.5	1823.2	240.9	313.2	291.1
3.63	3315.8	3225.0	808.9	3075.5	1555.3	162.7	285.4	283.4
3.02	3228.4	3234.9	844.8	2161.3	1108.6	101.2	264.6	270.2
2.42	3225.0	3258.9	1939.0	1057.2	770.2	115.5	244.4	262.1
1.80	3269.8	3284.6	2602.9	1111.5	977.6	207.4	244.4	253.2
1.07	3330.8	3309.1	2977.5	1189.7	925.5	362.1	240.8	240.1
.60	3346.5	3343.0	2252.2	986.8	860.9	470.1	240.3	233.8
.00	3339.5	3168.5	1221.0	733.1	731.0	477.9	241.0	225.2
RAD. POS. (CM)		NOX (PPM)						
5.44	31.7	36.1	35.5	39.4	25.3	32.4	22.2	16.1
4.84	55.6	83.6	40.8	58.3	50.5	44.5	28.9	22.1
4.23	81.6	76.6	17.4	72.4	75.1	17.5	31.4	25.5
3.63	64.6	53.4	9.1	76.2	78.6	9.5	29.0	26.2
3.02	49.3	50.2	8.0	65.9	64.1	7.1	25.2	25.2
2.42	36.8	36.7	10.6	42.7	44.7	7.3	23.8	23.4
1.80	28.3	37.0	16.2	26.4	31.0	10.1	17.8	20.8
1.07	25.3	35.6	23.2	22.1	24.6	13.9	15.0	18.6
.60	23.5	35.5	17.9	18.4	21.4	14.0	14.4	17.2
.00	23.0	30.7	16.5	18.3	20.6	14.7	15.2	18.8
RAD. POS. (CM)		CO2 (PERCENT)						
5.44	2.12	2.27	3.17	3.24	1.95	2.89	1.89	1.38
4.84	3.63	6.07	5.32	5.01	4.55	4.15	2.52	2.01
4.23	5.84	6.68	1.85	6.36	6.01	1.59	2.92	2.32
3.63	6.23	5.23	.66	6.42	6.15	.73	2.44	2.42
3.02	4.76	5.46	.44	5.61	5.17	.53	2.27	2.30
2.42	4.32	4.06	.76	4.26	4.12	.47	1.83	2.19
1.80	3.63	4.30	1.62	3.05	3.25	.79	1.55	1.96
1.07	2.88	4.85	3.29	2.14	2.45	1.24	1.35	1.72
.60	2.47	4.97	1.92	1.67	2.05	1.58	1.74	1.58
.00	2.42	3.90	1.29	1.43	1.40	1.40	1.10	1.42

DATA SET-05   CIRCUMFERENTIAL POSITION = 30.1 DFG.
                      (IN LINE WITH JETS)

AX.POS.(CM)	6.05	8.51	10.43	12.90	15.37	18.92	21.79	26.22
RAD. POS. (CM)			UNBURNED HYDROCARBONS (PPM)					
5.44	0.0	399.2	798.4	2661.5	519.0	Y	269.8	91.8
4.84	2395.3	1996.1	133.1	5216.5	104.5	Y	194.4	109.1
4.23	32869.1	42317.2	I	7731.5	119.8	Y	96.5	89.2
3.63	58552.2	64673.5	0.0	4724.1	457.4	Y	75.0	122.4
3.02	71061.0	72697.9	2395.3	1623.5	173.0	Y	103.5	98.5
2.42	80509.2	73589.4	13972.7	638.8	413.5	Y	139.1	109.1
1.80	86497.5	72258.7	37925.8	1104.5	771.9	Y	175.1	110.5
1.07	88360.5	64141.2	14771.1	1906.1	865.0	Y	166.3	118.4
.60	91022.0	50833.9	4524.6	1916.3	998.0	Y	190.5	133.1
.00	89170.7	19428.7	1730.0	1038.0	984.7	Y	174.9	129.1
RAD. POS. (CM)			CO (PPM)					
5.44	467.0	889.1	2102.7	2403.1	608.6	Y	459.6	295.7
4.84	2462.5	2075.8	731.0	9291.4	1074.1	Y	347.2	282.3
4.23	3343.0	3336.8	226.9	3383.0	2791.3	Y	290.8	287.0
3.63	3231.7	3256.1	126.0	3278.1	2302.4	Y	271.2	282.3
3.02	3244.3	3258.9	831.2	2704.9	1474.5	Y	259.7	269.2
2.42	3309.1	3289.1	2761.3	1315.6	915.8	Y	252.3	260.2
1.80	3346.8	3310.9	3247.9	1243.4	849.3	Y	249.8	240.5
1.07	3340.2	3334.0	3075.5	1214.7	920.7	Y	255.2	237.2
.60	3345.1	3331.0	1852.9	960.9	444.8	Y	251.8	229.0
.00	3346.0	2850.0	908.4	703.2	743.2	Y	247.4	222.8
RAD. POS. (CM)			NOX (PPM)					
5.44	45.4	26.9	41.5	50.3	20.1	Y	24.6	16.8
4.84	77.2	36.9	16.9	70.0	52.6	Y	29.9	21.6
4.23	77.9	52.9	6.2	78.1	81.4	Y	29.1	24.2
3.63	48.3	36.5	5.0	75.0	77.9	Y	24.5	29.3
3.02	30.1	28.2	8.9	63.8	65.4	Y	24.3	25.8
2.42	25.3	27.7	20.7	45.0	47.5	Y	20.5	23.7
1.80	23.5	27.0	32.1	30.2	32.4	Y	17.4	21.4
1.07	22.1	27.7	29.0	21.5	24.2	Y	14.6	19.1
.60	23.5	28.2	18.1	18.3	20.8	Y	13.6	17.4
.00	24.7	25.4	15.1	15.7	19.6	I	13.1	16.4
RAD. POS. (CM)			CO2 (PERCENT)					
5.44	2.70	1.71	3.97	4.21	1.42	Y	2.76	1.47
4.84	5.01	2.97	1.70	6.50	4.35	Y	2.68	1.92
4.23	7.05	6.22	.30	7.16	6.90	Y	2.61	2.16
3.63	5.15	4.52	.09	6.64	6.90	Y	2.41	2.27
3.02	4.00	3.71	.43	5.97	4.97	Y	2.19	2.37
2.42	2.83	3.58	2.23	4.49	4.50	Y	1.95	2.17
1.80	2.71	3.92	4.25	3.28	3.18	Y	1.60	1.93
1.07	2.18	4.17	3.89	2.31	2.60	Y	1.37	1.71
.60	2.41	4.34	2.04	1.71	2.10	Y	1.27	1.56
.00	2.79	3.16	1.32	1.47	1.99	I	1.18	1.42

DATA SET-06   CIRCUMFERENTIAL POSITION = 0.0 DEG.
                         (IN BETWEEN JETS)

AX.POS.(CM)   8.51   12.90   15.37   18.92   24.22

RAD. POS. (CM)	UNBURNED HYDROCARBONS (PPM)				
5.44	798.4	12508.9	1469.8	212.9	399.3
4.84	30207.6	32469.8	9990.5	918.2	194.4
4.23	55092.3	31937.5	10778.9	239.5	109.8
3.63	67601.1	14371.9	8782.8	425.8	69.8
3.02	71194.1	7851.3	4923.7	319.4	66.5
2.42	76917.0	2927.6	1596.9	439.1	124.1
1.80	81706.9	5496.0	1469.8	665.4	190.3
1.07	86630.6	7452.1	2262.2	984.7	248.8
.60	88493.6	7185.9	2661.5	1357.3	293.4
.00	88227.5	4923.7	3926.8	1676.7	308.7

RAD. POS. (CM)	CO (PPM)				
5.44	928.1	3282.0	2718.0	2625.3	912.7
4.84	3344.8	3309.1	3344.8	3095.9	507.9
4.23	3196.4	3289.1	3327.2	1108.6	427.9
3.63	3184.8	3323.3	3327.2	815.6	394.4
3.02	3203.9	3267.9	3346.6	717.0	394.4
2.42	3234.9	2638.7	3025.9	649.1	427.9
1.80	3277.4	2457.9	2252.2	791.4	456.2
1.07	3317.4	2416.8	2026.9	986.8	498.4
.60	3339.2	2098.2	2004.8	1266.1	516.0
.00	3345.2	1735.8	1831.7	1377.6	524.9

RAD. POS. (CM)	NOX (PPM)				
5.44	39.5	46.7	42.3	49.4	26.7
4.84	65.0	63.4	72.8	80.4	39.9
4.23	51.8	74.7	88.4	49.0	47.0
3.63	41.0	77.3	94.5	29.9	51.0
3.02	36.0	68.4	82.4	22.0	48.7
2.42	31.4	46.7	59.0	19.0	42.2
1.80	27.5	31.8	42.8	19.6	36.7
1.07	24.8	24.8	30.1	22.5	31.2
.60	23.2	21.9	24.6	25.6	26.5
.00	22.8	21.9	22.6	26.8	24.3

RAD. POS. (CM)	CO2 (PERCENT)				
5.44	2.36	4.12	4.12	4.67	2.35
4.84	6.00	6.35	6.70	6.98	3.61
4.23	5.42	7.03	7.64	4.56	3.90
3.63	4.40	7.52	7.64	2.91	4.11
3.02	4.03	7.08	7.80	2.10	3.90
2.42	3.70	5.70	6.65	1.69	3.95
1.80	3.34	3.67	5.10	1.77	3.11
1.07	2.96	2.66	3.70	2.17	2.82
.60	2.74	1.99	2.92	2.58	2.42
.00	2.67	1.64	2.46	2.74	2.19

365

DATA SET-06   CIRCUMFERENTIAL POSITION = 15.1 DEG.

AX.POS.(CM)	8.51	12.90	15.37	18.82	26.22
RAD. POS. (CM)	UNBURNED HYDROCARBONS (PPM)				
5.44	0.0	7851.3	798.4	758.5	448.5
4.84	8782.8	8117.5	5589.1	565.5	270.1
4.23	38857.3	24086.2	7052.9	266.1	190.4
3.63	92430.8	16900.3	3593.0	53.2	77.2
3.02	66536.6	9847.4	5056.8	119.8	91.9
2.42	74254.8	2661.5	1197.7	186.3	119.9
1.80	78779.3	5189.9	1197.7	372.6	223.6
1.07	84102.2	8516.7	2395.3	984.7	267.5
.60	88360.5	6919.8	3499.9	1357.3	320.7
.00	91155.1	5722.1	3593.0	1530.3	323.4
RAD. POS. (CM)	CO (PPM)				
5.44	522.4	3141.2	1549.5	2211.2	545.4
4.84	3282.0	3336.5	3250.2	2704.9	570.5
4.23	3277.4	3321.9	3341.9	657.5	504.7
3.63	3192.6	3339.2	3344.4	363.6	474.8
3.02	3207.6	3335.7	3346.5	215.7	444.9
2.42	3241.2	2911.1	3058.1	320.8	450.1
1.80	3277.4	2557.9	2211.2	610.3	479.5
1.07	3318.9	2467.1	2066.9	1026.9	509.5
.60	3341.9	2134.2	1995.9	1336.2	540.4
.00	3346.0	1711.2	1931.7	1405.8	535.5
RAD. POS. (CM)	NOX (PPM)				
5.44	42.3	46.1	36.2	50.9	23.1
4.84	95.0	60.5	73.4	63.2	36.5
4.23	89.7	70.2	91.3	16.1	45.0
3.63	67.9	77.8	93.7	9.0	48.5
3.02	37.7	73.9	82.8	7.3	47.2
2.42	30.1	51.0	62.1	10.1	42.3
1.80	27.2	33.8	41.1	16.4	37.0
1.07	25.2	25.3	30.7	22.9	31.3
.60	24.2	21.8	29.6	26.3	26.5
.00	22.9	21.8	24.5	27.0	24.1
RAD. POS. (CM)	CO2 (PERCENT)				
5.44	2.39	4.02	3.27	4.78	2.06
4.84	6.70	5.91	6.96	5.55	3.74
4.23	7.11	7.06	7.71	1.49	3.76
3.63	5.87	7.49	7.85	.60	4.06
3.02	4.54	7.13	7.58	.42	3.90
2.42	3.67	6.13	6.79	.76	3.58
1.80	3.28	4.30	4.78	1.41	3.19
1.07	2.92	2.91	3.76	2.33	2.72
.60	2.64	2.02	2.91	2.78	2.41
.00	2.33	1.60	2.44	2.68	2.15

DATA SET=06   CIRCUMFERENTIAL POSITION = 90.1 DEG.
                        (IN LINE WITH JETS)

AX.POS.(CM)	8.51	12.90	15.37	18.82	26.22

RAD. POS. (CM) — UNBURNED HYDROCARBONS (PPM)

RAD. POS. (CM)	8.51	12.90	15.37	18.82	26.22
5.44	133.1	7585.2	1730.0	1069.5	205.4
4.84	3060.7	24086.2	7185.9	692.0	171.7
4.23	10379.7	36462.0	3450.9	465.8	85.8
3.63	47107.9	24086.2	7185.9	252.8	89.2
3.02	79855.6	8649.8	9714.3	93.2	85.2
2.42	82239.2	3593.0	2528.4	173.0	114.8
1.80	87429.0	5322.9	1197.7	452.4	190.4
1.07	93151.2	5189.9	2129.2	1077.9	246.2
.60	94881.1	6919.8	2927.6	1400.4	204.1
.00	90866.9	9056.8	2927.6	1966.9	357.4

RAD. POS. (CM) — CO (PPM)

RAD. POS. (CM)	8.51	12.90	15.37	18.82	26.22
5.44	1269.3	3322.0	1381.1	2675.5	457.0
4.84	2566.9	3324.6	3308.1	1707.2	562.1
4.23	3337.3	3272.4	3299.7	823.9	511.1
3.63	3318.9	3312.6	3301.7	468.6	460.6
3.02	3247.9	3339.9	3339.7	208.6	499.9
2.42	3253.2	3102.6	3171.4	284.5	452.4
1.80	3289.1	2833.4	2426.0	711.1	492.0
1.07	3324.6	2966.9	2003.8	1211.6	528.9
.60	3338.4	2184.0	1965.2	1374.1	535.8
.00	3338.4	1719.4	1810.6	1381.1	535.5

RAD. POS. (CM) — NOX (PPM)

RAD. POS. (CM)	8.51	12.90	15.37	18.82	26.22
5.44	37.6	61.2	27.5	46.4	27.8
4.84	65.1	69.9	74.1	31.3	41.8
4.23	75.4	72.5	92.3	20.2	49.0
3.63	61.0	72.9	95.4	11.6	51.1
3.02	38.3	68.0	86.2	7.0	40.2
2.42	30.2	51.9	66.2	10.1	44.4
1.80	26.0	34.8	45.4	16.7	38.8
1.07	24.2	25.8	32.5	27.7	30.6
.60	23.5	21.0	26.7	25.2	26.0
.00	23.8	20.9	24.8	25.4	23.6

RAD. POS. (CM) — CO2 (PERCENT)

RAD. POS. (CM)	8.51	12.90	15.37	18.82	26.22
5.44	2.48	5.15	2.29	4.81	2.46
4.84	5.05	6.87	6.64	3.58	3.47
4.23	7.21	7.26	7.61	1.79	4.04
3.63	6.47	7.26	7.73	.98	4.16
3.02	4.11	7.34	7.41	.38	3.96
2.42	3.25	6.32	7.08	.63	3.67
1.80	2.93	4.66	5.11	1.73	3.16
1.07	2.68	3.11	3.60	2.41	2.73
.60	2.56	2.09	2.96	3.02	2.35
.00	2.69	1.64	2.48	2.96	3.11

367

DATA SET-C7   CIRCUMFERENTIAL POSITION = 0.0 DEG.
(IN BETWEEN JETS)

AX.POS.(CM)	6.05	8.51	10.43	12.90	15.37	18.82	26.22
RAD. POS. (CM)		UNBURNED HYDROCARBONS (PPM)					
5.44	I	1197.7	3060.7	2914.3	1157.7	595.4	309.0
4.84	0.0	21957.1	23553.9	6547.2	785.1	425.9	391.2
4.23	665.4	48571.7	34329.0	4271.6	372.6	839.4	451.1
3.63	6121.4	64407.4	23420.9	1840.7	811.7	425.4	307.9
3.02	33002.1	72924.1	33401.3	1384.0	519.0	412.9	362.0
2.42	49769.3	77182.4	21291.7	2661.5	1437.2	309.2	387.2
1.80	6C016.0	71859.5	21159.6	4418.0	2561.7	859.8	306.6
1.07	67201.9	69064.9	14904.2	4657.6	3589.7	825.1	468.4
.60	83037.6	65338.9	11843.5	5369.5	3526.4	1264.2	497.0
.00	92485.8	44313.3	5189.9	3446.6	3940.1	1970.9	436.5
RAD. POS. (CM)		CO (PPM)					
5.44	321.6	1074.1	1627.1	2018.0	1177.4	870.2	527.3
4.84	640.9	3112.5	3250.2	3068.6	2147.9	959.3	642.7
4.23	2019.6	3346.9	3340.2	3109.2	2451.4	981.4	646.8
3.63	3265.7	3336.8	3289.6	3138.1	2390.2	725.0	649.6
3.02	3142.5	3349.2	2966.0	2575.9	2009.2	512.7	622.8
2.42	3320.4	3344.0	2696.4	2161.3	1764.7	437.9	610.3
1.80	3323.3	3330.0	2465.3	2270.4	1904.3	522.4	979.0
1.07	3346.0	3308.1	2398.5	2116.2	1881.4	701.3	862.1
.60	3318.1	3245.6	2247.6	1760.5	1703.1	929.1	557.1
.00	3207.9	2958.3	1572.9	1405.8	1467.2	1015.1	522.4
RAD. POS. (CM)		NOX (PPM)					
5.44	37.0	26.1	26.2	24.9	20.7	23.4	13.4
4.84	49.4	51.6	50.3	48.4	47.7	34.5	18.2
4.23	68.9	53.8	51.4	60.4	64.9	20.9	23.9
3.63	60.2	38.4	35.4	57.7	66.4	13.3	21.6
3.02	67.2	26.9	20.1	44.9	52.8	9.8	21.1
2.42	52.8	23.5	13.8	29.0	35.5	8.2	19.5
1.80	45.7	21.7	11.9	21.0	24.9	8.4	17.5
1.07	32.9	22.1	11.5	16.4	19.6	10.6	15.6
.60	23.7	21.7	11.4	14.0	17.1	12.8	14.5
.00	18.2	20.4	11.4	14.6	16.2	14.0	13.4
RAD. POS. (CM)		CO2 (PERCENT)					
5.44	2.96	2.27	2.38	2.54	2.08	2.51	1.42
4.84	3.93	5.14	5.51	5.10	4.75	4.06	1.97
4.23	5.34	5.84	6.17	6.17	5.23	2.55	2.27
3.63	6.75	4.61	5.01	6.48	5.47	1.50	2.20
3.02	6.51	3.47	2.79	5.35	5.69	1.02	2.24
2.42	5.42	3.12	1.71	3.85	4.30	.77	2.11
1.80	4.65	3.00	1.41	2.74	3.25	.88	1.91
1.07	3.54	3.19	1.29	2.06	2.44	1.13	1.70
.60	2.59	3.33	1.33	1.62	1.99	1.49	1.59
.00	1.87	2.69	1.20	1.43	1.79	1.59	1.49

DATA SET-07   CIRCUMFERENTIAL POSITION = 15.1 DEG.

AX.POS.(CM)   6.05   8.51   1C.43   12.90   15.37   1⁸.⁸²   2⁶.²²

RAD. POS. (CM)	UNBURNED HYDROCARBONS (PPM)						
5.44	I	1330.7	4391.4	2515.1	8⁹1.⁶	745.²	⁴⁰⁰.⁰
4.84	I	13041.2	4524.5	2980.8	⁶12.1	²12.⁰	45².⁴
4.23	0.0	42716.5	1463.8	5²⁸³.0	51⁹.0	346.⁰	43².5
3.63	14638.0	5935C.6	5³².3	2368.7	⁹11.7	23⁹.⁵	416.5
3.02	45644.1	70661.8	3060.7	1024.7	⁸7⁸.⁹	193.1	³44.0
2.42	5C967.0	69996.5	8915.9	1730.0	1²24.3	224.²	3⁹1.⁹
1.80	57620.7	71859.5	19694.⁸	⁻779.3	²²²2.3	⁵05.7	2⁵⁶.⁶
1.07	⁶613⁷.³	70262.6	25550.0	3859.1	3140.⁵	951.7	47².1
.60	82239.2	54959.2	11710.4	405⁸.7	3¹⁰³.⁹	1450.5	4⁸³.1
.00	93550.4	42450.3	599⁸.3	3153.8	²741.3	1⁵03.7	4⁶⁶.4

RAD. POS. (CM)	CO (PPM)						
5.44	190.⁹	1079.⁸	22⁸⁸.7	1384.6	⁹2⁹.1	⁹45.5	⁵4².1
4.84	362.1	3228.6	2669.7	2782.8	11⁶².1	770.²	⁶5².⁸
4.23	1⁊44.0	3346.2	116⁸.2	3134.9	20⁹³.⁹	⁵27.3	⁶⁹⁰.⁶
3.63	2950.⁵	3340.6	430.3	312⁵.4	217⁰.4	347.6	⁶7⁸.²
3.02	3344.⁸	3343.0	631.⁸	2731.1	²⁰04.⁹	22⁸.3	⁶44.4
2.42	3325.⁹	3346.6	1760.⁵	2120.7	16⁵⁸.⁸	260.⁵	⁶²².⁸
1.80	3325.⁹	3344.0	26⁸7.4	2261.3	1⁸²³.2	447.0	⁶⁸⁶.⁹
1.07	3346.⁵	3340.2	2938.⁸	2107.2	179⁸.0	74³.2	⁻570.⁵
.60	3303.4	3303.4	249⁸.⁹	1760.5	16⁵⁸.⁹	976.4	540.⁴
.00	3185.⁹	3079.0	1654.⁸	1391.⁻	1470.⁸	10³³.4	⁵²⁶.7

RAD. POS. (CM)	NOX (PPM)						
5.44	15.5	29.2	2⁶.7	23.5	1⁵.1	24.⁹	1².⁸
4.84	2⁸.2	67.9	26.3	44.2	3⁸.5	3⁸.4	17.1
4.23	4⁸.2	59.8	9.1	5⁸.3	⁶².⁸	13.3	2⁰.0
3.63	75.2	43.⁸	5.0	62.5	6⁶.4	7.⁵	²1.⁰
3.02	70.1	34.7	4.7	52.7	53.0	5.⁸	²1.⁰
2.42	4⁸.2	31.9	7.⁶	35.5	³⁵.7	5.⁹	1⁰.1
1.80	39.2	31.1	12.2	24.6	2⁵.0	⁸.3	1⁴.⁹
1.07	30.1	30.7	16.⁰	1⁸.0	1⁹.6	11.6	1⁸.2
.60	23.0	30.3	12.6	15.2	17.1	13.⁹	¹³.9
.00	18.7	25.9	11.3	14.5	1⁴.3	14.7	1².³

RAD. POS. (CM)	CO2 (PERCENT)						
5.44	1.09	2.1⁸	³.19	2.31	1.41	2.7⁶	1.3⁸
4.84	2.13	6.26	3.3⁸	4.62	3.7⁵	4.0³	1.⁹1
4.23	3.75	⁶.30	.99	6.23	⁵.⁹³	1.4⁵	².²⁹
3.63	6.13	4.96	.35	6.67	6.2²	.7²	².³1
3.02	⁶.61	3.87	.24	6.04	5.7⁹	.4⁶	2.²⁹
2.42	⁵.04	3.5⁶	.62	4.43	4.4⁵	.43	².1³
1.80	4.51	3.66	1.40	3.04	³.2⁹	.7⁵	1.⁹1
1.07	3.54	3.88	2.27	2.12	2.4²	1.19	1.4⁹
.60	2.34	4.21	1.53	1.⁶4	2.04	1.⁵⁶	1.⁵⁹
.00	1.76	3.20	1.21	1.41	1.⁸³	1.⁶1	1.⁶1

369

DATA SET-07   CIRCUMFERENTIAL POSITION = 90.1 DEG.
                           (IN LINE WITH JETS)

AX.POS.(CM)	6.05	8.51	10.43	12.90	15.37	18.92	26.22
RAD. POS. (CM)		UNBURNED HYDROCARBONS (PPM)					
5.44	I	1330.7	3326.8	1400.4	479.1	465.8	424.5
4.84	133.1	7458.1	798.4	4351.5	505.7	385.9	431.2
4.23	6520.6	44446.4	0.0	5562.5	771.8	306.1	440.5
3.63	35929.7	62677.4	399.2	5602.4	346.0	245.1	375.3
3.02	51765.4	70129.5	7718.2	2326.9	1064.6	173.0	400.6
2.42	56023.8	72258.7	26215.4	1869.6	1171.0	196.3	347.3
1.80	64939.7	71327.2	30606.8	3459.6	2739.0	479.1	412.5
1.07	73855.6	62810.5	25293.9	6201.2	2947.9	1091.2	423.2
.60	84900.6	55092.3	8117.5	5243.1	3459.9	1423.0	377.0
.00	93683.5	35929.7	3992.2	3353.4	3034.1	1517.0	383.3
RAD. POS. (CM)		CO (PPM)					
5.44	366.5	1183.9	2462.5	1926.0	966.0	1123.2	548.7
4.84	984.2	2439.7	1074.1	3177.3	1240.2	793.4	639.1
4.23	2930.9	3327.9	291.6	3329.0	2349.2	637.2	695.4
3.63	3342.0	3346.0	317.3	3265.8	2189.5	497.3	683.0
3.02	3315.8	3346.5	1627.1	3090.3	2147.8	263.3	663.1
2.42	3305.5	3342.6	2934.9	2303.9	1682.9	228.3	622.8
1.80	3312.8	3324.5	3171.4	2234.0	1764.7	454.7	502.8
1.07	3345.7	3291.4	2996.3	2179.4	1708.0	708.0	562.1
.60	3311.1	3180.1	2279.6	1748.1	1446.9	1024.2	847.0
.00	3228.6	2795.5	1445.3	1374.1	1459.8	1045.1	524.1
RAD. POS. (CM)		NOX (PPM)					
5.44	22.3	16.9	32.9	25.9	11.3	28.8	13.8
4.84	47.9	29.8	8.9	56.8	29.9	21.0	17.6
4.23	76.8	44.1	4.0	68.2	63.7	13.0	19.7
3.63	62.8	34.5	4.2	63.6	63.1	9.5	21.2
3.02	59.9	27.2	9.0	54.4	54.0	5.9	21.3
2.42	45.8	24.8	17.1	35.6	36.2	4.3	19.0
1.80	38.6	24.4	20.8	26.6	24.1	9.2	17.2
1.07	29.7	25.0	18.0	19.0	19.0	12.6	19.2
.60	21.3	25.0	13.9	15.9	16.6	14.6	13.8
.00	18.4	23.1	11.6	15.0	15.3	14.9	13.1
RAD. POS. (CM)		CO2 (PERCENT)					
5.44	1.52	1.33	4.10	2.63	1.00	3.33	1.44
4.84	3.94	2.49	1.00	5.97	3.01	2.23	1.92
4.23	6.53	5.02	.18	7.27	5.93	1.49	2.21
3.63	6.92	4.25	.12	7.08	5.39	.09	2.29
3.02	5.81	3.39	.71	6.13	5.40	.45	2.31
2.42	4.87	3.13	2.08	4.86	4.46	.26	2.12
1.80	4.55	3.21	3.09	3.26	3.34	.75	1.91
1.07	3.17	3.32	2.71	2.20	2.47	1.29	1.69
.60	2.35	3.29	1.76	1.65	2.05	1.57	1.54
.00	1.89	2.48	1.27	1.42	1.80	1.61	1.41

DATA SET-06   CIRCUMFERENTIAL POSITION = 0.0 DEG.
                    (IN BETWEEN JETS)

AX.POS.(CM)	10.43	12.90	15.37	18.82	21.29	26.27
RAD. POS. (CM)		UNBURNED HYDROCARBONS (PPM)				
5.44	202.5	192.0	262.5	139.5	166.5	187.5
4.84	337.5	66.0	75.0	76.5	100.5	147.5
4.23	339.0	40.5	24.0	102.0	97.5	171.0
3.63	168.0	42.0	36.0	94.5	96.0	150.0
3.02	225.0	84.0	79.5	79.5	99.0	124.5
2.42	273.0	172.5	148.5	78.0	99.0	117.5
1.80	318.0	276.0	210.0	93.0	97.5	105.5
1.07	400.5	370.5	246.0	118.5	102.0	91.5
.60	439.5	429.0	238.5	144.0	108.0	47.0
.00	336.0	349.5	211.5	197.5	102.0	81.0
RAD. POS. (CM)		CO (PPM)				
5.44	2923.0	2371.1	1678.9	1285.8	1054.4	881.1
4.84	3335.7	2629.7	1619.2	1156.0	986.8	1111.5
4.23	3338.8	2494.4	1243.4	968.6	809.4	1192.8
3.63	3047.5	1785.5	1129.1	687.7	831.2	1192.7
3.02	2674.1	1715.3	1449.3	552.0	772.3	1144.0
2.42	2393.9	1756.4	1711.2	594.6	747.3	1004.1
1.80	2009.2	1760.5	1768.8	753.5	743.2	986.8
1.07	1591.8	1756.4	1678.9	1091.2	792.9	994.4
.60	1662.6	1703.1	1727.6	1363.7	839.4	847.1
.00	1662.6	1627.1	1699.1	1430.8	852.9	831.2
RAD. POS. (CM)		NOX (PPM)				
5.44	72.0	50.2	36.3	27.2	20.9	17.3
4.84	116.5	82.7	65.7	23.3	23.1	22.5
4.23	108.2	83.7	74.9	15.4	20.5	23.5
3.63	65.0	62.5	63.0	13.7	20.4	27.3
3.02	27.7	32.5	38.0	10.9	16.5	22.0
2.42	18.0	19.0	23.7	10.4	14.5	20.4
1.80	12.7	14.2	19.1	11.4	13.7	18.5
1.07	10.7	13.8	17.8	13.1	13.7	17.4
.60	9.8	12.5	16.9	13.4	13.1	14.4
.00	10.5	12.7	17.3	13.4	12.7	13.2
RAD. POS. (CM)		CO2 (PERCENT)				
5.44	6.16	5.39	4.55	4.46	3.24	2.31
4.84	9.15	7.06	6.26	3.48	3.11	2.84
4.23	9.62	7.46	6.86	2.33	2.82	3.09
3.63	6.56	6.22	5.87	1.51	2.47	3.02
3.02	3.66	4.62	4.90	1.12	2.19	3.11
2.42	2.85	3.20	3.72	1.11	1.98	2.97
1.80	2.12	2.50	3.01	1.37	1.90	2.75
1.07	1.61	2.15	2.58	1.90	1.75	2.44
.60	1.60	2.02	2.50	2.40	1.75	2.25
.00	1.85	2.06	2.57	2.66	1.90	2.11

DATA SET-08   CIRCUMFERENTIAL POSITION = 15.1 DEG.

AX.POS.(CM)	10.43	12.90	15.37	18.82	21.29	26.22

RAD. POS. (CM)   UNBURNED HYDROCARBONS (PPM)

RAD. POS. (CM)	10.43	12.90	15.37	18.82	21.29	26.22
5.44	499.5	354.0	253.5	138.0	384.0	282.0
4.84	658.5	108.0	57.0	130.5	276.0	240.4
4.23	736.5	37.5	16.5	168.0	201.0	252.0
3.63	712.5	37.5	30.0	111.0	169.0	207.0
3.02	522.0	72.0	66.0	75.0	141.0	166.5
2.42	361.5	162.0	144.0	75.0	123.0	133.5
1.80	265.5	267.0	208.5	96.0	112.5	102.5
1.07	366.0	384.0	252.0	133.5	115.5	97.5
.60	320.5	424.5	247.5	147.0	112.5	93.0
.00	366.0	340.5	220.5	144.0	106.5	91.5

RAD. POS. (CM)   CO (PPM)

RAD. POS. (CM)	10.43	12.90	15.37	18.82	21.29	26.22
5.44	3085.8	2939.8	2134.2	1456.2	1205.3	1040.0
4.84	2748.4	2548.8	1934.7	958.3	1292.4	1253.5
4.23	1343.0	2261.3	1384.6	709.1	1230.6	1395.2
3.63	524.1	1760.5	1153.0	485.7	1102.9	1367.2
3.02	751.4	1823.2	1522.9	276.0	1008.0	1343.0
2.42	1952.1	2053.5	1823.2	390.0	910.9	1240.9
1.80	2435.1	2031.3	1943.4	725.0	853.9	1094.1
1.07	2229.4	1965.2	1952.1	1227.4	847.1	984.9
.60	1861.4	1760.5	1840.2	1489.3	879.6	886.7
.00	1752.2	1670.8	1756.4	1485.6	858.8	933.4

RAD. POS. (CM)   NOX (PPM)

RAD. POS. (CM)	10.43	12.90	15.37	18.82	21.29	26.22
5.44	49.5	42.7	38.1	33.4	16.6	17.1
4.84	34.5	68.2	79.4	19.9	21.0	22.7
4.23	11.0	77.2	86.8	11.8	21.0	21.4
3.63	8.5	62.2	66.7	11.0	22.4	24.0
3.02	8.2	37.5	41.6	8.5	19.1	23.9
2.42	11.0	22.2	23.6	9.3	15.7	22.5
1.80	15.2	16.2	17.8	11.3	14.3	23.5
1.07	14.2	15.0	16.1	14.2	14.1	18.7
.60	10.0	14.0	15.4	14.5	13.2	14.9
.00	10.0	14.0	15.3	14.8	13.0	14.9

RAD. POS. (CM)   CO2 (PERCENT)

RAD. POS. (CM)	10.43	12.90	15.37	18.82	21.29	26.22
5.44	5.14	5.43	5.40	5.10	2.89	2.32
4.84	3.83	6.73	7.70	3.16	3.21	2.90
4.23	1.24	7.41	8.03	1.61	3.30	3.38
3.63	.41	6.47	6.65	1.00	2.97	3.39
3.02	.47	5.07	5.28	.46	2.75	3.41
2.42	1.46	3.75	4.12	.66	2.35	3.30
1.80	2.72	2.88	3.30	1.28	2.06	2.98
1.07	2.77	2.36	2.84	2.08	1.91	2.44
.60	1.75	2.11	2.64	2.64	1.85	2.36
.00	1.85	2.09	2.67	2.77	1.83	2.13

DATA SET-08   CIRCUMFERENTIAL POSITION = 30.1 DEG.
                     (IN LINE WITH JETS)

AX.POS.(CM)	10.43	12.90	15.37	18.82	21.29	24.22
RAD. POS. (CM)			UNBURNED HYDROCARBONS (PPM)			
5.44	415.5	549.0	690.0	301.5	382.5	372.0
4.84	643.5	118.5	171.0	238.5	175.5	321.0
4.23	532.5	39.0	50.0	132.0	139.0	223.5
3.63	534.0	34.5	18.0	84.0	190.5	177.0
3.02	294.0	57.0	42.0	82.5	171.5	155.7
2.42	165.0	124.5	106.5	85.5	120.0	120.0
1.80	226.5	225.0	178.5	112.5	111.0	117.0
1.07	349.5	345.0	217.5	139.5	115.5	105.0
.60	442.5	402.0	223.5	151.5	102.0	103.5
.00	381.0	321.0	208.5	147.0	94.5	91.5
RAD. POS. (CM)			CO (PPM)			
5.44	2942.7	3092.4	2206.7	1269.3	1409.8	981.5
4.84	1192.8	3128.6	2485.3	621.0	1289.1	1147.0
4.23	808.9	2602.9	1947.7	379.7	1165.1	1237.0
3.63	1448.9	1052.1	1459.8	240.8	1094.4	1221.0
3.02	2575.9	2018.0	1926.7	295.9	1000.0	1343.9
2.42	2895.0	2147.8	1835.9	594.6	953.2	1285.8
1.80	2769.9	2129.7	1934.7	1048.9	943.1	1165.1
1.07	2665.3	1970.4	1969.6	1485.6	975.6	1009.0
.60	2430.5	1831.7	1865.7	1623.1	906.0	894.7
.00	1827.5	1654.8	1756.4	1504.2	840.2	435.7
RAD. POS. (CM)			NOX (PPM)			
5.44	42.7	47.5	19.6	15.0	18.1	16.9
4.84	12.0	92.2	62.5	11.0	22.5	22.9
4.23	9.5	57.7	82.5	8.8	21.9	25.6
3.63	13.8	63.2	73.7	9.6	22.8	31.2
3.02	18.5	42.0	46.8	9.6	17.3	27.7
2.42	26.5	26.5	24.5	11.3	15.4	24.5
1.80	22.0	17.5	16.1	13.6	14.1	21.1
1.07	15.7	14.7	14.2	15.3	13.5	19.1
.60	11.7	13.5	13.1	15.6	12.7	15.3
.00	10.9	13.5	12.6	15.6	12.1	14.9
RAD. POS. (CM)			CO2 (PERCENT)			
5.44	5.00	6.28	3.75	2.92	9.12	2.15
4.84	.95	5.85	6.92	1.23	9.34	2.47
4.23	.50	9.36	7.99	.59	9.15	9.49
3.63	.95	6.84	7.27	.36	2.95	9.67
3.02	2.49	5.55	6.01	.54	9.65	3.95
2.42	4.49	4.29	4.55	1.10	9.41	9.59
1.80	4.19	3.13	3.50	1.98	9.20	9.19
1.07	3.50	2.47	2.98	2.54	9.01	2.75
.60	2.76	2.20	2.69	2.88	1.99	2.94
.00	1.87	2.06	2.62	2.76	1.79	2.14

DATA SET-09   CIRCUMFERENTIAL POSITION = 0.0 DEG.
(IN BETWEEN JETS)

AX.POS.(CM)	10.43	12.90	15.37	18.82	21.29	26.??
RAD. POS. (CM)	UNBURNED HYDROCARBONS (PPM)					
5.44	18.0	10.8	10.6	10.3	8.4	11.1
4.84	33.0	4.2	2.8	4.9	5.4	13.7
4.23	114.0	1.6	1.6	7.3	6.0	13.7
3.63	97.5	1.5	2.2	8.5	8.1	11.4
3.02	0.0	3.1	4.5	7.3	7.2	8.3
2.42	3.0	7.0	9.0	7.5	7.6	8.7
1.80	6.0	15.1	17.4	7.8	6.6	8.5
1.07	16.5	27.1	24.7	8.5	7.3	8.0
.60	28.5	40.8	27.3	11.1	7.0	9.4
.00	36.0	45.4	27.9	11.7	7.8	9.4
RAD. POS. (CM)	CO (PPM)					
5.44	1991.5	709.1	344.7	311.6	287.4	252.1
4.84	3327.9	1205.3	298.7	390.0	294.9	327.4
4.23	3344.4	833.4	266.1	395.9	251.7	375.3
3.63	3162.6	476.3	294.5	315.9	264.7	308.0
3.02	2143.2	493.6	439.4	270.4	252.1	373.7
2.42	1861.4	605.0	610.3	263.3	246.4	362.1
1.80	1541.9	653.8	755.6	317.3	254.9	340.3
1.07	1091.2	759.7	867.9	415.3	290.3	327.4
.60	963.5	882.0	906.0	545.4	305.9	317.3
.00	906.0	920.7	910.9	558.0	324.5	325.0
RAD. POS. (CM)	NOX (PPM)					
5.44	113.0	98.2	72.0	59.4	48.4	31.8
4.84	190.9	147.7	108.0	62.9	45.9	43.1
4.23	197.0	146.2	116.2	41.7	42.1	47.4
3.63	168.2	117.0	110.2	30.2	37.9	46.5
3.02	122.0	84.0	88.7	24.8	33.1	43.1
2.42	90.5	60.0	67.0	22.9	29.4	41.5
1.80	63.5	46.0	51.2	24.7	27.7	38.7
1.07	44.0	39.0	43.8	29.2	26.3	34.7
.60	37.2	33.8	40.0	35.3	25.9	37.4
.00	36.0	33.5	40.0	39.2	25.5	30.7
RAD. POS. (CM)	CO2 (PERCENT)					
5.44	6.38	4.97	3.95	3.40	2.87	2.07
4.84	10.52	7.11	5.52	3.65	2.99	2.47
4.23	11.20	7.08	6.20	2.68	2.58	2.93
3.63	10.14	6.07	6.03	1.91	2.96	3.74
3.02	7.51	4.68	5.10	1.58	2.17	3.08
2.42	6.09	3.65	4.10	1.43	1.93	2.88
1.80	4.23	2.84	3.42	1.61	1.80	2.71
1.07	2.88	2.52	3.08	1.89	1.75	2.60
.60	2.50	2.38	2.89	2.39	1.80	2.78
.00	2.33	2.35	2.90	2.71	1.80	2.19

DATA SET-09   CIRCUMFERENTIAL POSITION = 15.1 DEG.

AX.POS.(CM)	10.43	12.90	15.37	18.82	21.29	25.22

UNPURNED HYDROCARBONS (PPM)

RAD. POS. (CM)	10.43	12.90	15.37	18.82	21.29	25.22
5.44	35.0	24.7	19.8	13.2	25.1	25.9
4.84	52.5	5.1	3.4	6.1	18.6	24.4
4.23	24.0	1.5	2.2	13.8	13.0	29.5
3.63	45.0	1.5	1.5	6.7	10.9	15.2
3.02	33.0	2.1	3.6	6.1	9.6	15.7
2.42	19.5	6.7	9.0	7.0	8.9	11.2
1.80	12.0	14.8	18.4	8.5	9.4	9.4
1.07	9.0	30.4	26.4	10.3	7.9	7.9
.60	25.5	44.5	30.6	12.1	7.9	8.9
.00	37.5	44.8	27.7	12.7	9.2	9.0

CO (PPM)

RAD. POS. (CM)	10.43	12.90	15.37	18.82	21.29	25.22
5.44	2541.7	682.0	473.2	367.9	351.9	347.4
4.84	3319.5	697.4	430.3	318.7	387.0	445.5
4.23	2053.5	655.6	366.5	196.4	345.6	492.0
3.63	1441.7	473.2	336.0	101.2	376.7	503.1
3.02	1500.5	504.7	470.1	94.8	344.7	445.5
2.42	1930.0	664.9	640.9	166.3	310.2	413.9
1.80	1921.6	776.6	831.2	314.4	301.4	367.0
1.07	1615.3	874.9	930.6	498.4	311.6	336.0
.60	1005.6	953.2	963.5	626.4	325.9	327.4
.00	923.1	950.7	955.8	648.2	334.6	319.7

NOX (PPM)

RAD. POS. (CM)	10.43	12.90	15.37	18.82	21.29	25.22
5.44	120.5	84.2	65.5	73.3	45.7	30.7
4.84	151.0	118.5	107.5	57.1	54.6	41.3
4.23	61.7	129.7	124.7	22.5	55.4	45.9
3.63	29.2	116.2	122.0	12.9	50.9	49.8
3.02	29.0	87.0	99.0	11.7	41.6	47.9
2.42	39.0	61.5	73.2	15.8	39.3	46.9
1.80	49.2	47.7	54.7	22.5	29.8	41.4
1.07	55.2	38.5	49.2	31.6	28.0	35.1
.60	34.7	33.3	41.2	38.4	26.9	32.2
.00	31.3	34.0	41.5	30.9	26.4	29.4

CO2 (PERCENT)

RAD. POS. (CM)	10.43	12.90	15.37	18.82	21.29	25.22
5.44	7.68	4.37	3.74	4.16	2.77	2.18
4.84	10.40	6.10	5.87	3.44	3.28	2.86
4.23	4.57	6.87	6.73	1.41	3.30	3.71
3.63	1.91	6.48	6.79	.64	3.12	3.45
3.02	2.01	5.01	5.91	.49	2.75	3.47
2.42	2.90	3.92	4.94	.84	2.93	3.74
1.80	3.55	3.13	3.76	1.43	2.04	2.94
1.07	3.90	2.67	3.22	2.16	1.92	2.55
.60	2.32	2.43	3.00	2.64	1.85	2.42
.00	2.10	2.40	2.96	2.89	1.40	2.19

DATA SET-09   CIRCUMFERENTIAL POSITION = 30.1 DEG.
(IN LINE WITH JETS)

AX.POS.(CM)	10.43	12.90	15.37	18.82	21.29	26.77

RAD. POS. (CM)   UNBURNED HYDROCARBONS (PPM)

RAD. POS. (CM)	10.43	12.90	15.37	18.82	21.29	26.77
5.44	69.0	53.4	79.8	49.0	48.0	49.0
4.84	78.0	13.2	16.6	31.3	21.7	43.8
4.23	28.5	9.0	3.1	22.9	13.6	37.4
3.63	33.0	1.2	1.3	9.4	10.6	20.4
3.02	39.0	1.5	3.7	5.8	11.8	14
2.42	6.0	4.8	8.7	7.2	10.6	13.4
1.80	15.0	14.7	16.6	9.3	10.5	9.4
1.07	12.0	32.4	25.0	10.9	8.5	7.3
.60	39.0	47.1	28.8	12.4	9.3	8.4
.00	37.5	44.4	29.6	12.9	9.4	8.5

RAD. POS. (CM)   CO (PPM)

RAD. POS. (CM)	10.43	12.90	15.37	18.82	21.29	26.77
5.44	1764.7	1957.1	703.2	495.2	565.4	437.0
4.84	798.0	2407.7	898.7	340.3	538.8	547.7
4.23	166.3	2040.2	680.1	204.6	450.1	547.1
3.63	186.7	833.4	476.3	89.7	407.8	511.1
3.02	1305.7	608.6	493.6	63.4	372.3	501.6
2.42	2161.3	737.1	651.9	166.3	344.7	450.1
1.80	2430.5	867.9	842.5	400.3	340.3	399.9
1.07	1887.1	955.8	945.6	603.3	343.2	359.2
.60	1530.5	986.8	968.6	607.7	344.7	340.5
.00	997.4	955.9	923.1	670.6	344.7	334.0

RAD. POS. (CM)   NOX (PPM)

RAD. POS. (CM)	10.43	12.90	15.37	18.82	21.29	26.77
5.44	63.0	90.2	40.7	39.4	48.0	29.7
4.84	22.0	158.7	109.0	22.3	60.0	41.5
4.23	8.5	159.0	137.2	14.0	54.5	50.4
3.63	9.5	129.2	134.0	10.5	53.4	57.8
3.02	26.7	97.7	107.2	9.9	44.4	55.4
2.42	86.0	69.7	78.2	16.7	38.6	53.2
1.80	115.0	49.7	56.5	28.3	92.7	44.2
1.07	75.2	38.5	47.2	38.8	30.1	36.5
.60	44.0	33.0	42.7	41.1	29.0	32.2
.00	36.7	33.2	42.2	39.8	27.5	29.0

RAD. POS. (CM)   CO2 (PERCENT)

RAD. POS. (CM)	10.43	12.90	15.37	18.82	21.29	26.77
5.44	4.61	5.48	2.84	2.93	3.25	2.25
4.84	1.48	8.89	6.11	1.55	3.64	3.17
4.23	.21	9.25	7.52	.98	3.37	3.44
3.63	.16	7.82	7.42	.42	3.12	4.24
3.02	1.78	6.07	6.48	.29	2.84	4.03
2.42	6.00	4.46	4.85	.92	2.49	3.77
1.80	8.45	3.41	3.92	1.92	2.19	3.25
1.07	5.51	2.78	3.37	2.76	2.06	2.90
.60	3.31	2.48	3.02	2.97	1.90	2.60
.00	2.42	2.38	2.94	2.98	1.83	2.71

376

DATA SET-10   CIRCUMFERENTIAL POSITION = 0.0 DEG.
                          (IN BETWEEN JETS)

AX.POS.(CM)	10.43	12.90	15.37	18.82	21.29	26.27
RAD. POS. (CM)		UNBURNED	HYDROCARBONS	(PPM)		
5.44	225.0	330.0	193.0	80.1	85.9	37.5
4.84	I	723.0	63.6	3.9	6.9	19.9
4.23	I	I	I	I	I	I
3.63	I	708.0	57.3	3.7	3.3	3.0
3.02	1560.0	127.5	2.4	4.3	3.4	2.5
2.42	300.0	I	2.1	5.2	3.3	1.9
1.80	I	10.5	7.2	5.5	9.3	2.2
1.07	I	40.5	20.5	6.4	3.3	2.9
.60	I	76.5	21.9	8.2	4.0	3.4
.00	0.0	85.5	36.7	10.0	4.5	3.9
RAD. POS. (CM)			CO (PPM)			
5.44	2833.4	2825.0	1670.8	1279.2	1081.7	522.4
4.84	I	3332.9	3029.5	1043.3	727.0	555.4
4.23	I	I	I	I	I	Y
3.63	I	3325.9	3162.6	525.7	548.7	449.5
3.02	3267.1	2966.0	2256.7	503.1	517.6	416.0
2.42	3306.5	1299.1	889.1	474.8	462.4	417.3
1.80	2575.9	1448.9	933.1	519.2	449.5	428.9
1.07	2339.0	1588.0	1224.2	664.9	456.2	445.5
.60	2075.8	1522.9	1374.1	863.2	482.4	468.5
.00	1564.8	1445.3	1409.4	992.1	542.1	485.7
RAD. POS. (CM)			NOX (PPM)			
5.44	75.2	68.0	54.5	71.0	59.8	41.5
4.84	I	143.8	151.0	117.5	82.5	63.2
4.23	I	I	I	I	I	Y
3.63	I	153.5	192.7	47.7	55.5	76.7
3.02	126.7	126.7	162.0	36.7	48.5	71.7
2.42	102.7	90.0	117.2	32.2	44.0	67.5
1.80	80.5	56.5	79.0	33.2	38.7	60.7
1.07	57.2	39.0	56.7	29.5	36.7	54.7
.60	47.7	30.5	47.0	46.3	36.0	47.0
.00	37.7	28.2	43.0	50.7	37.0	44.0
RAD. POS. (CM)			CO2 (PERCENT)			
5.44	6.16	6.04	4.25	4.90	3.94	2.93
4.84	I	10.54	9.23	6.87	5.15	3.98
4.23	I	I	I	I	I	I
3.63	I	11.25	11.03	3.11	3.54	4.49
3.02	10.61	10.05	9.51	2.58	3.14	4.45
2.42	9.85	7.11	7.34	2.26	2.94	4.23
1.80	6.51	4.80	5.32	2.39	2.64	3.84
1.07	4.46	3.51	4.21	2.86	2.91	3.63
.60	3.76	2.81	3.55	3.53	2.49	3.22
.00	2.70	2.61	3.34	3.95	2.75	3.09

DATA SET-10   CIRCUMFERENTIAL POSITION = 15.1 DEG.

AX.POS.(CM)	10.43	12.90	15.37	18.82	21.29	26.22

RAD. POS. (CM)	UNBURNED HYDROCARBONS (PPM)					
5.44	480.0	I	144.0	64.2	121.2	45.4
4.84	I	I	11.7	4.8	23.8	21.4
4.23	I	I	I	I	21.9	I
3.63	480.0	I	54.1	8.4	.5	4.3
3.02	525.0	I	5.2	6.0	.4	7.4
2.42	300.0	0.0	2.5	6.0	1.5	1.6
1.80	285.0	12.0	8.4	6.6	3.0	1.9
1.07	0.0	46.5	23.1	7.5	3.4	2.7
.60	30.0	79.5	35.4	7.9	4.0	3.6
.00	105.0	91.5	40.5	9.9	4.3	4.2

RAD. POS. (CM)	CO (PPM)					
5.44	3254.8	I	1635.0	1395.2	1149.1	960.4
4.84	I	Y	2302.4	1094.1	973.9	627.8
4.23	I	I	I	I	1010.7	Y
3.63	2841.7	I	2833.4	445.5	513.8	471.7
3.02	2907.1	I	2198.5	304.4	540.4	439.4
2.42	3022.3	1256.3	953.2	334.6	503.1	416.8
1.80	3036.8	1441.7	1035.1	468.6	481.0	434.8
1.07	2886.9	1627.1	1305.7	695.4	482.6	451.6
.60	2799.8	1568.6	1434.4	903.6	509.5	467.0
.00	2147.8	1481.9	1467.2	1010.7	539.5	481.0

RAD. POS. (CM)	NOX (PPM)					
5.44	54.0	I	61.7	79.7	50.2	41.7
4.84	I	I	141.7	137.0	95.0	64.2
4.23	I	I	I	I	94.2	Y
3.63	30.7	I	192.0	29.7	89.5	91.7
3.02	18.7	I	162.5	20.7	72.2	76.5
2.42	23.7	91.3	112.0	22.0	56.5	74.2
1.80	31.7	60.2	75.0	29.0	44.7	69.2
1.07	55.5	43.2	55.2	39.0	39.5	54.5
.60	36.3	34.0	46.5	49.0	34.7	50.0
.00	26.7	32.0	44.0	52.7	34.7	45.7

RAD. POS. (CM)	CO2 (PERCENT)					
5.44	7.41	I	4.56	5.46	4.05	2.79
4.84	I	I	8.83	7.87	5.97	4.11
4.23	I	I	I	I	6.16	Y
3.63	2.97	I	11.20	2.04	5.51	4.89
3.02	2.97	I	9.66	1.27	4.52	4.97
2.42	3.64	6.71	7.27	1.48	3.59	4.51
1.80	3.56	4.77	5.40	2.12	3.07	4.09
1.07	5.96	3.52	4.25	3.01	2.70	3.59
.60	4.42	2.90	3.61	3.72	2.41	3.91
.00	2.63	2.63	3.44	4.05	2.64	3.09

DATA SET-10   CIRCUMFERENTIAL POSITION = 30.1 DEG.
(IN LINE WITH JETS)

AX.POS.(CM)	10.43	12.90	15.37	18.82	21.29	26.22

RAD. POS. (CM) — UNBURNED HYDROCARBONS (PPM)

RAD. POS. (CM)	10.43	12.90	15.37	18.82	21.29	26.22
5.44	109.0	I	97.8	30.0	40.2	39.2
4.84	285.0	I	41.7	29.2	7.0	91.4
4.23	I	I	I	I	I	I
3.63	150.0	I	20.4	12.9	1.2	4.9
3.02	585.0	I	3.0	6.6	1.2	9.1
2.42	225.0	I	2.4	7.9	1.9	1.5
1.80	735.0	6.0	10.6	7.8	1.9	1.9
1.07	1110.0	45.0	15.8	7.5	3.5	2.2
.60	940.0	79.5	39.7	8.7	4.5	3.3
.00	945.0	99.0	97.5	9.6	6.0	4.2

RAD. POS. (CM) — CO (PPM)

RAD. POS. (CM)	10.43	12.90	15.37	18.82	21.29	26.22
5.44	2598.4	I	1744.0	1189.7	1102.9	691.9
4.84	2040.2	I	3144.9	1062.8	904.6	693.9
4.23	I	I	I	I	I	I
3.63	144.7	I	3144.3	457.7	649.7	509.1
3.02	1773.0	I	2490.7	178.5	614.7	424.3
2.42	3210.6	1395.2	1033.3	222.7	562.1	393.0
1.80	3291.3	1391.7	1037.6	498.4	524.9	412.9
1.07	3253.2	1607.4	1255.7	815.6	510.2	439.9
.60	2782.8	1538.1	1429.6	973.8	530.5	455.2
.00	1835.9	1463.5	1430.8	1010.7	555.4	474.3

RAD. POS. (CM) — NOX (PPM)

RAD. POS. (CM)	10.43	12.90	15.37	18.82	21.29	26.22
5.44	69.7	I	82.2	75.2	190.8	90.0
4.84	27.0	I	154.3	54.5	231.7	75.9
4.23	I	I	I	I	I	I
3.63	10.2	I	197.0	21.0	199.5	96.9
3.02	15.2	I	141.0	9.8	172.7	90.0
2.42	57.2	106.5	113.7	14.7	192.2	94.5
1.80	115.2	66.0	73.0	30.7	171.0	71.2
1.07	110.5	42.7	53.2	47.2	100.7	61.2
.60	61.5	34.0	44.5	52.5	90.7	51.7
.00	34.5	32.5	43.7	54.0	90.2	47.2

RAD. POS. (CM) — CO2 (PERCENT)

RAD. POS. (CM)	10.43	12.90	15.37	18.82	21.29	26.22
5.44	6.13	I	4.70	5.40	5.76	3.39
4.84	2.46	I	10.66	3.85	4.00	4.89
4.23	I	I	I	I	I	I
3.63	I	I	11.57	1.39	4.52	5.51
3.02	.76	I	15.00	.47	4.59	5.52
2.42	7.29	7.91	7.39	.95	3.84	4.99
1.80	10.94	5.20	5.50	2.21	3.72	4.34
1.07	10.52	3.52	4.29	3.53	3.79	3.99
.60	5.98	2.78	3.67	4.03	2.49	3.24
.00	2.85	2.58	3.42	4.08	2.54	3.07

DATA SET-11   CIRCUMFERENTIAL POSITION = 0.0 DEG.
(IN BETWEEN JETS)

AX.POS.(CM)	10.43	12.90	16.82	21.29	26.22
RAD. POS. (CM)		UNBURNED HYDROCARBONS (PPM)			
5.44	6.0	5.4	2.7	2.4	1.3
4.84	235.5	9.4	.6	1.2	1.2
4.23	244.5	10.0	.4	.6	.9
3.63	106.5	2.8	.6	.6	.7
3.02	20.7	.1	.6	.6	.4
2.42	.9	.1	.6	.6	.3
1.80	I	.8	.6	.7	.3
1.07	0.0	.4	.4	.4	.4
.60	0.0	.4	.6	.4	.3
.00	0.0	.4	.4	.6	.3

RAD. POS. (CM)		CO (PPM)			
5.44	1259.5	737.1	215.2	183.7	121.8
4.84	3316.8	2220.3	139.8	149.9	146.8
4.23	3346.1	2389.4	129.2	112.8	158.0
3.63	3254.8	1138.0	115.2	98.4	169.5
3.02	2426.0	288.8	90.3	93.3	149.5
2.42	945.6	273.2	73.2	84.7	140.2
1.80	793.7	363.6	79.2	84.7	129.6
1.07	639.1	394.4	111.8	82.6	171.5
.60	463.9	398.9	145.5	86.4	117.9
.00	375.3	380.5	176.9	86.5	113.5
				92.8	112.2

RAD. POS. (CM)		NOX (PPM)			
5.44	14.4	56.8	31.6	67.0	47.3
4.84	21.8	86.0	96.8	77.9	62.9
4.23	22.4	88.1	74.8	72.6	72.1
3.63	19.8	78.7	50.2	65.8	74.8
3.02	16.0	61.8	37.2	58.4	72.9
2.42	11.5	42.9	29.6	51.8	71.6
1.80	8.4	32.4	30.7	47.1	67.0
1.07	6.3	25.8	39.4	43.6	63.6
.60	6.0	24.3	48.5	42.5	55.9
.00	5.4	25.6	54.5	42.6	53.9

RAD. POS. (CM)		CO_2 (PERCENT)			
5.44	5.62	4.80	3.13	2.59	1.09
4.84	9.79	7.37	4.50	3.24	2.62
4.23	9.96	8.21	3.47	3.12	3.16
3.63	9.66	7.77	2.24	2.79	3.19
3.02	8.14	6.39	1.67	2.45	3.14
2.42	5.72	4.78	1.25	2.20	3.16
1.80	4.13	3.63	1.24	2.00	2.92
1.07	2.87	2.98	1.56	1.87	2.77
.60	2.54	2.70	2.09	1.80	2.47
.00	2.41	2.60	2.40	1.74	2.27

```
DATA SET-11        CIRCUMFERENTIAL POSITION = 15.1 DEG.

AX.POS.(CM)    10.43    12.90    18.82    21.29    26.22
```

RAD. POS. (CM)	UNBURNED HYDROCARBONS (PPM)				
5.44	21.0	10.8	2.4	2.8	.9
4.84	228.0	1.5	.8	1.9	1.9
4.23	10.5	1.2	1.2	1.2	.9
3.63	10.5	.6	1.0	.7	.7
3.02	6.0	.1	.7	.6	.7
2.42	4.5	.1	.6	.4	.4
1.80	1.5	0.0	.6	.6	.4
1.07	0.0	.3	.6	.4	.4
.60	1.5	.4	.4	.6	.4
.00	0.0	.3	.4	.4	.3

RAD. POS. (CM)	CO (PPM)				
5.44	2152.3	594.6	212.4	197.0	116.5
4.84	3346.6	1141.0	125.7	192.9	151.7
4.23	1561.0	971.2	104.0	158.0	164.2
3.63	874.9	749.4	69.4	133.6	159.7
3.02	795.8	224.1	39.4	111.8	140.9
2.42	1114.4	245.0	41.5	98.0	140.2
1.80	1230.6	351.9	78.8	96.3	125.7
1.07	817.8	392.9	130.1	95.8	115.7
.60	689.6	401.8	175.1	98.0	107.4
.00	401.8	400.3	198.4	99.7	106.6

RAD. POS. (CM)	NOX (PPM)				
5.44	11.5	46.3	32.8	60.5	49.9
4.84	15.6	69.0	38.5	76.7	66.7
4.23	8.0	80.5	20.0	81.5	75.7
3.63	3.5	77.3	9.4	77.1	78.6
3.02	3.3	61.7	6.1	66.9	77.1
2.42	4.6	46.0	7.5	58.5	75.4
1.80	6.6	34.6	12.3	90.7	60.3
1.07	8.1	27.9	17.7	46.5	62.9
.60	6.0	26.5	22.2	43.0	57.2
.00	6.8	31.6	24.8	40.6	53.7

RAD. POS. (CM)	CO2 (PERCENT)				
5.44	5.84	4.21	3.33	2.51	2.02
4.84	10.34	6.38	4.72	3.26	2.83
4.23	4.62	7.51	2.29	3.48	3.29
3.63	1.64	7.64	1.03	3.36	3.39
3.02	1.90	6.53	.55	2.88	2.39
2.42	2.15	5.07	.57	2.52	3.41
1.80	3.13	3.76	1.24	2.17	3.21
1.07	3.67	3.10	1.84	1.97	2.79
.60	2.61	2.76	2.37	1.84	2.31
.00	2.22	2.60	2.61	1.79	2.30

DATA SET-11

CIRCUMFERENTIAL POSITION = 30.1 DEG.
(IN LINE WITH JETS)

AX.POS.(CM)	10.43	12.90	18.82	21.29	26.22
RAD. POS. (CM)	**UNBURNED HYDROCARBONS (PPM)**				
5.44	9.0	4.6	1.3	1.6	
4.84	19.5	2.5	1.2	1.0	1.0
4.23	7.5	.9	1.0	.7	.9
3.63	3.0	.4	.7	.6	.9
3.02	6.0	0.0	.7	.6	.7
2.42	6.0	0.0	.7	.6	.7
1.80	16.5	.1	.6	.6	.4
1.07	0.0	.3	.6	.6	.4
.60	0.0	.4	.4	.6	.4
.00	0.0	.6	.7	.6	.4
RAD. POS. (CM)	**CO (PPM)**				
5.44	1237.0	903.6	170.5	157.0	117.9
4.84	759.7	2238.5	110.9	163.8	134.0
4.23	159.5	2026.9	70.3	134.8	137.1
3.63	132.6	703.2	39.8	134.8	134.0
3.02	948.2	285.8	28.0	123.5	134.0
2.42	1707.2	274.6	49.8	110.9	132.5
1.80	2704.9	372.3	104.9	107.4	128.5
1.07	1013.4	392.9	171.4	107.9	117.9
.60	557.0	406.3	202.6	108.3	110.9
.00	409.3	400.3	202.6	109.2	104.4
				108.7	103.6
RAD. POS. (CM)	**NOX (PPM)**				
5.44	9.9	58.7	26.8	74.6	
4.84	3.9	88.0	15.1	84.8	51.2
4.23	1.6	94.8	8.2	79.6	63.9
3.63	2.0	82.2	4.9	71.8	71.8
3.02	5.0	65.5	5.8	77.0	77.5
2.42	12.5	48.0	10.8	68.9	80.3
1.80	15.2	34.9	17.4	63.3	78.9
1.07	10.5	27.0	23.1	56.9	71.5
.60	6.9	23.5	26.1	51.4	67.0
.00	6.9	22.5	26.6	46.9	60.2
				43.5	54.0
RAD. POS. (CM)	**CO2 (PERCENT)**				
5.44	5.32	5.40	3.26	3.04	2.59
4.84	2.06	8.72	1.66	2.46	2.69
4.23	.33	9.29	.88	3.34	3.10
3.63	.15	8.17	.61	3.19	3.30
3.02	1.70	7.11	.37	2.86	3.25
2.42	6.38	5.48	.94	2.58	3.45
1.80	8.27	4.65	1.72	2.41	3.28
1.07	5.34	3.40	2.55	2.17	2.49
.60	3.30	2.92	2.86	1.99	2.59
.00	2.50	2.75	2.62	1.84	2.24

DATA SET-12 CIRCUMFERENTIAL POSITION = 0.0 DEG.
(IN BETWEEN JETS)

AX.POS.(CM)	10.43	12.90	15.37	18.82	21.30	26.22

RAD. POS. (CM)	UNBURNED HYDROCARBONS (PPM)					
5.44	I	49.5	10.8	4.8	5.9	2.4
4.84	I	124.5	24.4	.4	.0	.3
4.23	I	210.0	17.8	.5	.0	1.3
3.63	2310.0	58.5	4.6	.7	.5	.7
3.02	975.0	1.5	4.0	.9	.5	.4
2.42	45.0	I	2.5	1.0	.4	.3
1.80	I	I	.6	.8	.7	.2
1.07	I	0.0	.6	.8	.9	.2
.60	I	0.0	1.0	.7	.9	.3
.00	I	0.0	1.3	.7	.8	.3

RAD. POS. (CM)	CO (PPM)					
5.44	2752.7	2134.2	729.0	360.8	311.4	171.0
4.84	I	3344.4	2687.4	204.0	181.4	173.7
4.23	I	3324.6	3054.1	155.3	154.5	149.2
3.63	3142.6	3333.0	2576.5	159.7	153.0	129.6
3.02	3282.2	2202.1	2722.4	140.2	151.7	121.3
2.42	3223.6	506.3	1789.6	127.4	147.7	117.4
1.80	1874.3	545.4	507.9	132.3	132.7	123.1
1.07	1353.3	666.8	367.9	162.4	134.0	131.4
.60	1117.3	678.2	527.3	218.5	135.9	133.1
.00	766.0	648.2	557.0	258.7	151.3	134.4

RAD. POS. (CM)	NOX (PPM)					
5.44	13.5	14.8	11.4	39.8	33.7	27.8
4.84	I	23.9	25.4	59.5	45.2	28.7
4.23	I	25.1	30.6	39.4	39.9	43.7
3.63	17.3	23.6	31.9	26.3	34.5	43.5
3.02	16.1	21.2	31.7	21.3	30.5	42.5
2.42	14.0	14.7	26.3	17.9	27.7	40.1
1.80	11.5	10.5	19.0	18.4	25.2	38.7
1.07	7.8	8.0	12.9	20.7	23.0	33.7
.60	6.4	6.8	9.0	25.8	22.2	32.5
.00	5.8	6.4	8.6	29.6	22.1	28.1

RAD. POS. (CM)	CO2 (PERCENT)					
5.44	7.51	6.26	4.24	3.88	3.41	2.91
4.84	I	10.29	8.93	5.70	4.45	3.74
4.23	I	10.38	10.38	4.19	3.52	4.11
3.63	9.64	11.03	10.80	2.88	3.44	4.12
3.02	10.80	9.29	10.75	2.37	3.08	4.05
2.42	9.96	6.71	9.49	2.02	2.79	3.87
1.80	7.34	4.88	7.49	2.07	2.59	3.49
1.07	5.04	3.90	5.81	2.37	2.41	3.31
.60	3.96	3.26	4.09	3.01	2.35	3.36
.00	2.97	3.07	3.84	3.39	2.23	2.85

DATA SET-12   CIRCUMFERENTIAL POSITION = 15.1 DEG.

AX.PCS.(CM)	10.43	12.90	15.37	18.82	21.24	26.22
RAD. POS. (CM)		UNBURNED HYDROCARBONS (PPM)				
5.44	465.0	46.5	14.2	8.0	11.5	2.6
4.84	2580.0	114.0	8.4	.5	7.2	1.4
4.23	165.0	147.0	13.9	.9	.7	.7
3.63	15.0	67.5	5.6	1.3	.4	.4
3.02	0.0	0.0	1.6	1.1	.3	.4
2.42	I	I	.7	1.0	.4	.3
1.80	I	I	.4	.9	.5	.3
1.07	I	I	.6	.7	.6	.4
.60	I	0.0	.9	.6	.6	.4
.00	I	0.0	1.0	.6	.6	.5

RAD. POS. (CM)		CO (PPM)				
5.44	3325.6	2120.7	913.3	399.8	377.1	181.0
4.84	3142.6	3247.9	1646.9	210.5	279.8	181.4
4.23	3213.2	3326.8	2544.3	192.4	188.7	155.7
3.63	2111.7	3207.9	2769.9	143.3	167.4	130.1
3.02	2202.1	1917.3	1919.0	82.2	158.4	114.1
2.42	2307.0	440.9	433.3	63.9	152.6	116.5
1.80	2134.2	520.8	307.3	110.0	145.1	119.4
1.07	1764.7	651.9	135.8	169.6	141.5	131.0
.60	1474.5	674.4	152.0	234.7	140.6	132.7
.00	896.3	639.1	171.0	268.7	145.5	142.8

RAD. POS. (CM)		NOX (PPM)				
5.44	14.8	13.8	10.5	45.1	32.1	31.0
4.84	10.6	22.1	22.9	71.4	45.7	42.2
4.23	9.7	24.8	30.2	36.4	50.2	47.7
3.63	4.3	24.5	31.6	15.8	47.2	48.7
3.02	4.7	20.1	27.2	9.6	40.4	47.7
2.42	6.2	14.9	20.0	9.9	33.9	44.5
1.80	8.5	10.5	14.0	13.9	28.2	40.7
1.07	11.1	8.1	10.4	20.8	24.4	35.2
.60	6.5	6.9	9.0	27.0	23.0	31.0
.00	5.0	6.5	8.6	30.9	22.4	28.7

RAD. POS. (CM)		CO2 (PERCENT)				
5.44	9.17	6.59	4.49	4.40	3.44	2.99
4.84	9.94	10.22	9.03	6.76	4.73	4.10
4.23	8.07	11.45	10.94	3.48	4.77	4.44
3.63	3.02	11.37	11.32	1.73	4.55	4.52
3.02	2.93	9.68	10.29	1.02	3.94	4.51
2.42	4.16	6.98	7.92	1.10	3.31	4.19
1.80	5.38	5.19	5.07	1.58	2.89	3.57
1.07	7.54	4.05	4.78	2.45	2.59	3.39
.60	4.11	3.39	4.12	3.28	2.49	3.15
.00	2.74	3.07	3.84	3.59	2.41	2.90

DATA SET-12   CIRCUMFERENTIAL POSITION = 30.1 DEG.
                          (IN LINE WITH JETS)

AX.POS.(CM)	10.43	12.90	15.37	18.82	21.29	24.22

RAD. POS. (CM)   UNBURNED HYDROCARBONS (PPM)

RAD. POS. (CM)						
5.44	0.0	22.5	5.9	1.7	2.5	1.3
4.84	15.0	141.0	42.9	1.9	.7	.8
4.23	0.0	126.0	5.5	2.0	.3	.5
3.63	I	51.0	3.4	1.6	.3	.5
3.02	0.0	4.5	.5	1.3	.3	.4
2.42	100.0	I	.4	1.1	.3	.3
1.80	585.0	I	.5	.8	.3	.4
1.07	525.0	I	.6	.6	.4	.4
.60	I	0.0	1.0	.6	.5	.4
.00	I	0.0	1.1	.6	.5	.4

RAD. POS. (CM)   CO (PPM)

RAD. POS. (CM)						
5.44	2018.0	2607.4	224.2	317.5	264.1	171.0
4.84	1367.2	3326.8	542.5	328.9	206.9	175.5
4.23	284.5	3343.1	553.0	223.7	199.9	149.5
3.63	177.2	3147.4	473.7	128.8	194.3	131.8
3.02	1735.8	1752.2	333.8	59.8	194.6	119.5
2.42	3263.6	416.8	124.4	63.6	172.8	115.1
1.80	3305.5	503.1	104.4	126.1	151.1	119.5
1.07	3344.0	621.0	142.4	204.0	150.8	123.5
.60	1272.6	663.1	167.8	251.3	149.5	135.5
.00	751.4	630.0	173.2	266.6	147.7	139.5

RAD. POS. (CM)   NOX (PPM)

RAD. POS. (CM)						
5.44	10.3	15.8	10.5	47.3	45.1	34.4
4.84	4.4	21.9	26.0	30.0	49.0	47.2
4.23	1.2	25.9	30.8	16.8	48.9	52.3
3.63	1.3	25.8	31.7	12.4	42.8	52.9
3.02	5.6	21.2	103.2	6.0	38.9	53.7
2.42	14.2	15.3	74.0	8.6	34.1	49.1
1.80	15.9	10.3	51.7	17.0	29.2	44.9
1.07	13.3	8.2	39.7	26.4	25.7	39.5
.60	7.7	6.9	34.1	30.6	23.0	32.3
.00	6.5	6.7	32.7	31.0	22.1	29.5

RAD. POS. (CM)   CO2 (PERCENT)

RAD. POS. (CM)						
5.44	6.51	8.10	4.49	4.86	4.51	3.50
4.84	3.08	11.42	10.43	3.08	4.49	4.37
4.23	.42	12.11	11.50	2.07	4.49	4.43
3.63	.12	11.55	11.37	1.20	4.25	4.97
3.02	2.00	10.00	9.85	.63	3.59	4.73
2.42	9.41	7.27	7.70	.80	3.50	4.53
1.80	10.87	5.10	5.89	1.66	3.04	4.13
1.07	10.22	4.04	4.70	3.01	2.71	3.53
.60	4.71	3.40	4.04	3.63	2.55	3.38
.00	3.18	3.09	3.78	3.67	2.41	2.94

385

DATA SET-13   CIRCUMFERENTIAL POSITION = 0.0 DEG.
                           (IN BETWEEN JETS)

AX.POS.(CM)	10.43	12.90	15.37	16.82	21.79	26.22

RAD. POS.   UNBURNED HYDROCARBONS (PPM)

RAD. POS. (CM)	10.43	12.90	15.37	16.82	21.79	26.22
5.44	39.0	225.0	.4	.3	.3	.?
4.84	2520.0	660.0	2.5	.1	.1	.?
4.23	2172.0	1095.0	1.2	.1	.1	.1
3.63	1380.0	420.0	.9	.1	.1	.1
3.02	381.0	0.0	.3	.1	.1	.1
2.42	91.5	I	.1	.2	.1	.1
1.80	0.0	I	.1	.2	.1	.1
1.07	0.0	I	.1	.2	.1	.1
.60	0.0	I	0.0	.1	.2	.1
.00	1.5	0.0	2.4	.1	.?	.1

CO (PPM)

RAD. POS. (CM)	10.43	12.90	15.37	16.82	21.79	26.22
5.44	3318.1	2366.5	334.6	119.6	93.7	43.3
4.84	3079.2	3289.6	1835.9	90.7	59.4	44.8
4.23	3023.6	3343.5	2403.1	73.2	56.0	40.?
3.63	3147.1	3270.0	2234.0	64.8	56.5	35.3
3.02	3338.4	1599.6	1153.0	56.4	53.9	33.7
2.42	3144.3	233.8	288.8	48.1	51.0	34.1
1.80	1230.6	236.6	143.3	45.2	60.2	35.3
1.07	668.7	287.4	164.9	50.2	47.7	37.9
.60	495.2	297.3	188.1	58.5	49.1	41.1
.00	367.9	285.9	1773.0	67.8	49.3	43.5

NOX (PPM)

RAD. POS. (CM)	10.43	12.90	15.37	16.82	21.79	26.22
5.44	1.0	60.0	201.0	197.7	176.0	124.0
4.84	2.0	83.7	406.0	247.7	213.0	175.0
4.23	5.0	97.2	508.0	204.7	191.0	202.0
3.63	254.0	92.7	519.0	130.0	173.0	203.0
3.02	233.0	75.2	421.0	102.0	151.0	204.0
2.42	209.0	53.0	302.0	94.0	141.0	194.0
1.80	172.0	38.0	217.0	84.2	127.0	179.0
1.07	122.0	29.7	172.0	93.8	114.0	153.0
.60	112.0	25.7	146.0	110.2	107.0	142.3
.00	114.0	25.7	398.0	123.2	103.0	133.7

CO2 (PERCENT)

RAD. POS. (CM)	10.43	12.90	15.37	16.82	21.79	26.22
5.44	9.45	7.41	5.27	4.57	4.04	3.94
4.84	9.05	11.13	9.23	6.23	4.83	4.03
4.23	8.05	11.35	10.68	4.80	4.31	4.45
3.63	9.87	11.15	10.75	3.36	3.04	4.62
3.02	10.75	9.56	9.96	2.66	3.59	4.52
2.42	9.90	7.13	8.10	2.24	3.27	4.31
1.80	7.34	5.32	6.35	2.24	2.94	4.00
1.07	5.05	4.37	5.35	2.53	2.79	3.50
.60	4.04	3.83	4.73	3.04	2.53	3.40
.00	3.44	3.61	8.95	3.46	2.56	3.07

DATA SET-13   CIRCUMFERENTIAL POSITION = 15.1 DFG.

AX.POS.(CM)   10.43   12.90   15.37   18.92   21.29   26.22

RAD. POS. (CM)	UNBURNED HYDROCARBONS (PPM)					
5.44	1272.0	21.0	.4	.2	.4	.2
4.84	849.0	54.0	1.8	.1	.1	.1
4.23	3.0	48.0	2.1	.2	.1	.1
3.63	1.5	15.0	.4	.2	.1	.1
3.02	0.0	0.0	.3	.3	.1	.1
2.42	3.0	I	.1	.3	.1	.1
1.80	19.5	I	.1	.2	.1	.1
1.07	33.0	I	.1	.2	.1	.1
.60	I	0.0	0.0	.1	.1	.1
.00	I	0.0	0.0	.1	.2	.2

RAD. POS. (CM)	CO (PPM)					
5.44	3258.0	2152.3	313.0	130.3	111.3	49.3
4.84	3297.7	3233.6	1467.2	107.0	72.4	45.2
4.23	1470.8	3315.4	2426.0	92.8	62.7	41.1
3.63	1099.9	3188.7	2503.5	55.2	44.8	37.0
3.02	1336.2	1588.0	1569.6	34.5	53.9	35.1
2.42	1427.2	325.9	522.4	33.3	53.9	36.1
1.80	1430.8	228.3	177.2	45.2	50.5	34.1
1.07	1538.1	276.0	159.5	57.7	49.3	39.9
.60	582.5	284.5	188.1	69.9	48.9	44.4
.00	363.6	288.8	200.5	74.1	48.1	44.4

RAD. POS. (CM)	NOX (PPM)					
5.44	222.0	235.0	194.0	252.7	172.0	134.0
4.84	180.0	335.0	379.0	286.5	221.0	186.0
4.23	97.0	399.0	503.0	124.5	241.0	219.0
3.63	61.0	395.0	535.0	60.0	224.0	224.0
3.02	87.0	335.0	445.0	42.5	196.0	212.0
2.42	135.0	235.0	326.0	48.8	157.0	204.0
1.80	170.0	171.0	231.0	76.5	139.0	199.0
1.07	157.0	129.0	177.0	104.7	120.0	162.0
.60	101.0	115.0	152.0	121.5	109.0	141.0
.00	93.0	112.0	143.0	129.7	103.0	132.0

RAD. POS. (CM)	CO2 (PERCENT)					
5.44	10.49	7.32	5.23	5.66	4.13	3.24
4.84	10.31	10.68	9.33	6.36	5.17	4.32
4.23	4.57	11.57	11.06	3.12	5.39	4.49
3.63	2.41	11.67	11.65	1.58	5.19	5.02
3.02	4.11	10.00	10.56	1.07	4.45	4.55
2.42	6.38	7.59	8.62	1.30	3.23	4.32
1.80	7.47	5.84	6.76	2.06	3.23	3.76
1.07	7.31	4.57	5.57	2.98	2.97	3.76
.60	4.26	3.94	4.85	3.55	2.75	3.43
.00	3.23	3.65	4.43	3.77	2.65	3.22

DATA SET-13

CIRCUMFERENTIAL POSITION = 90.1 DEG.
(IN LINE WITH JETS)

AX.POS.(CM)	10.43	12.90	15.37	18.42	21.20	26.22

RAD. POS. (CM) — UNBURNED HYDROCARBONS (PPM)

RAD. POS. (CM)	10.43	12.90	15.37	18.42	21.20	26.22
5.44	21.0	132.0				
4.84	0.0	226.5	.1	.1		
4.23	0.0	72.0	7.6	.1	.1	.5
3.63	1.5	12.0	1.6	.3	.1	.5
3.02	1.5	0.0	.9	.3	.1	.5
2.42	81.0		.3	.3	.1	.5
1.80	388.5	I	.1	.3	.1	.5
1.07	96.0	I	.1	.3	.1	.5
.60	I	I	0.0	.3	.1	.5
.00	I	I	.1	.2	.1	.5
			0.0	.1	.1	.5

RAD. POS. (CM) — CO (PPM)

RAD. POS. (CM)	10.43	12.90	15.37	18.42	21.20	26.22
5.44	1823.2	3298.4				
4.84	568.8	3297.7	434.8	134.0		
4.23	160.8	3259.1	2954.4	108.7	92.0	47.3
3.63	245.0	3306.5	2907.1	89.4	65.7	46.9
3.02	1082.6	2553.4	2954.1	49.3	72.4	37.6
2.42	3278.1	463.9	1874.3	29.2	65.2	31.2
1.80	3343.5	226.9	548.7	28.0	62.7	30.0
1.07	3131.8	261.9	174.4	36.5	58.9	29.2
.60	462.4	281.7	163.5	53.9	55.6	31.5
.00	350.5	280.9	186.7	69.9	51.9	34.3
			199.1	74.1	50.6	39.3
					48.0	39.9

RAD. POS. (CM) — NOX (PPM)

RAD. POS. (CM)	10.43	12.90	15.37	18.42	21.20	26.22
5.44	164.0	269.0				
4.84	86.0	357.0	175.0	190.5	221.0	137.0
4.23	28.0	413.0	405.0	110.5	244.0	188.0
3.63	28.0	401.0	515.0	73.5	235.0	210.0
3.02	85.0	341.0	527.0	42.5	213.0	227.0
2.42	206.0	252.0	443.0	30.7	105.0	233.0
1.80	241.0	177.0	318.0	28.0	147.0	229.0
1.07	202.0	133.0	225.0	50.2	141.0	195.0
.60	130.0	114.0	174.0	92.0	176.0	170.0
.00	113.0	119.0	149.0	124.5	117.0	147.0
			142.0	134.5	105.0	137.0

RAD. POS. (CM) — CO2 (PERCENT)

RAD. POS. (CM)	10.43	12.90	15.37	18.42	21.20	26.22
5.44	7.14	9.64				
4.84	3.52	11.45	5.43	5.27	5.40	2.71
4.23	.62	11.72	11.06	3.12	4.43	4.40
3.63	.36	11.83	11.75	2.31	5.15	5.14
3.02	3.19	10.66	11.80	1.26	4.47	5.31
2.42	10.03	8.36	10.52	.72	4.65	5.27
1.80	11.03	6.09	8.54	.70	4.90	5.17
1.07	9.11	4.63	6.76	1.34	3.47	4.46
.60	4.83	3.93	5.62	2.99	3.11	3.94
.00	3.68	3.99	4.83	3.45	2.85	3.45
			4.36	4.03	2.61	3.73

1556-79